UNIVERSITÀ DEGLI STUDI DI MILANO

PhD COURSE IN INDUSTRIAL CHEMISTRY, 38th cycle

Department of Chemistry

PhD thesis

Preparation of nano- and molecular compounds for antitumoral applications triggered by light

Schifano Veronica

R13888

ORCID n. 0009-0008-7359-968X

SUPERVISOR Prof. Daniela Maggioni

CO-SUPERVISOR Prof. Silvia Cauteruccio

PhD COORDINATOR Prof. Laura Prati

A.A. 2024-2025

Table of contents

Aim of the thesis

During my PhD, I worked on several projects focusing on the preparation of compounds for antitumoral applications, involving different types of species: nanocomposites, organometallic complexes, and organic compounds. The antitumoral action of most of these systems was based on the photodynamic therapy (PDT), often with the aim of combining it with a secondary antitumoral strategy to enhance its efficiency. A smaller part of the thesis was instead devoted to the preparation of a luminescent metformin-derivative to investigate the antitumoral activity of this antidiabetic drug.

Thus, after a first general introduction on PDT, in which the mechanisms, the photosensitizers, the limitations and the strategies to improve this therapy are presented, the thesis is divided in two main parts. The first one is dedicated to nanocomposites and nanoparticles-metal complexes hybrids, starting with two introductions on nanoparticles employed in many of the projects – the gold nanostars (GNS), in Chapter 2, and halloysite nanotubes (HNT), in Chapter 4. In Chapter 3 we functionalized GNS surface with a polyamidoamine-Ru(II) complex to increase the PDT efficiency of the complex, i.e. to produce ROS upon irradiation, due to the metal enhanced $^1O_2$ generation promoted by GNS. Another possible advantage of such functionalized nanostructures that was not studied yet is the possibility to combine PDT with plasmon photothermal therapy (PTT) promoted by the same GNS. Differently, in Chapter 5 we employed GNS to decorate the external surface of HNT, aiming to obtain a nanocomposite carrier for small molecules loaded into HNT tubular structure, whose release would be triggered by the local hyperthermia produced by GNS. The action of the released drug is combined with the PTT. In this thesis we chose the antitumoral drug mitoxantrone, but as a future perspective, it can be replaced with an organic photosensitizing agent to introduce the additional PDT treatment. In Chapter 6, HNT were functionalized in their inner lumen to serve as carriers for hydrophobic photosensitizers. Perfluorinated porphyrins, in their non-coordinated- and Zn-coordinated form, were loaded into HNT and the ends of the loaded nanotubes were capped to slow down their release.

On the other hand, the focus of the second part of the thesis was moved to luminecent organometallic and organic compounds. This second part is composed of two chapters, the first (Chapter 7) concerning the preparation of a bioconjugate between a tris-cyclometalled Ir(III) complex and a peptide nucleic acid (PNA). The aim of this work was to obtain a multifunctional compound with anticancer activity based on a possible synergic effect between PDT, promoted by the Ir complex, and an antisense/antigene strategy induced by specific PNA sequences that can target an RNA or DNA chains and interfere with their transcription. However, in this thesis we only evaluated the bioconjugate

features in PDT, while the investigation on the potential synergistic effect remains the object of future work. Lastly, Chapter 8 was dedicated to the preparation of a luminescent molecule containing a terminal biguanide group to study how this moiety interacts with tumoral cells and can be related to the activity of the anti-diabetic drug metformin in inhibiting the proliferation of various types of tumors. Unfortunately, more investigation is still needed as for timing issues we could only investigate one synthetic strategy.

Moreover, for three of these projects a biological investigation at cellular level was carried out confirming their efficacy for antitumoral therapies. In particular, the biological investigation on GNS-polyamidoamine-Ru(II) compounds was performed during my exchange period at the University of Groningen under the supervision of prof. Anna Salvati.

GENERAL INTRODUCTION

Photodynamic Therapy (PDT)

Mechanisms of PDT

Photodynamic Therapy (PDT) is a non-invasive medical treatment developed since 1970s, initially clinically approved against a small number of tumors and lately has expanded to different areas. It is based on the uptake of a photosensitizer (PS) that, when excited by a suitable light, reacts with oxygen and generates reactive oxygen species (ROS) in target tissues (i.e. nucleic acids, lipids and proteins), leading to cell death by severe alteration in cell signaling cascades or in gene expression regulation.[1,2]

There are two possible mechanisms of PDT, schematized by the Jablonski diagram in Scheme 1. The ^{1}PS* excited to the excited single state (S_1) can undergo intersystem crossing (ISC) and populate the triplet excited state (T_1), which possesses a relatively long life due to the prohibited spin inversion. From the T_1 state, the ^{3}PS* can either relax back to ground state by phosphorescence or transfer energy to another molecule, such as oxygen. The longer the life of the ^{3}PS* in this state, the higher the chances of transferring energy to O_2.

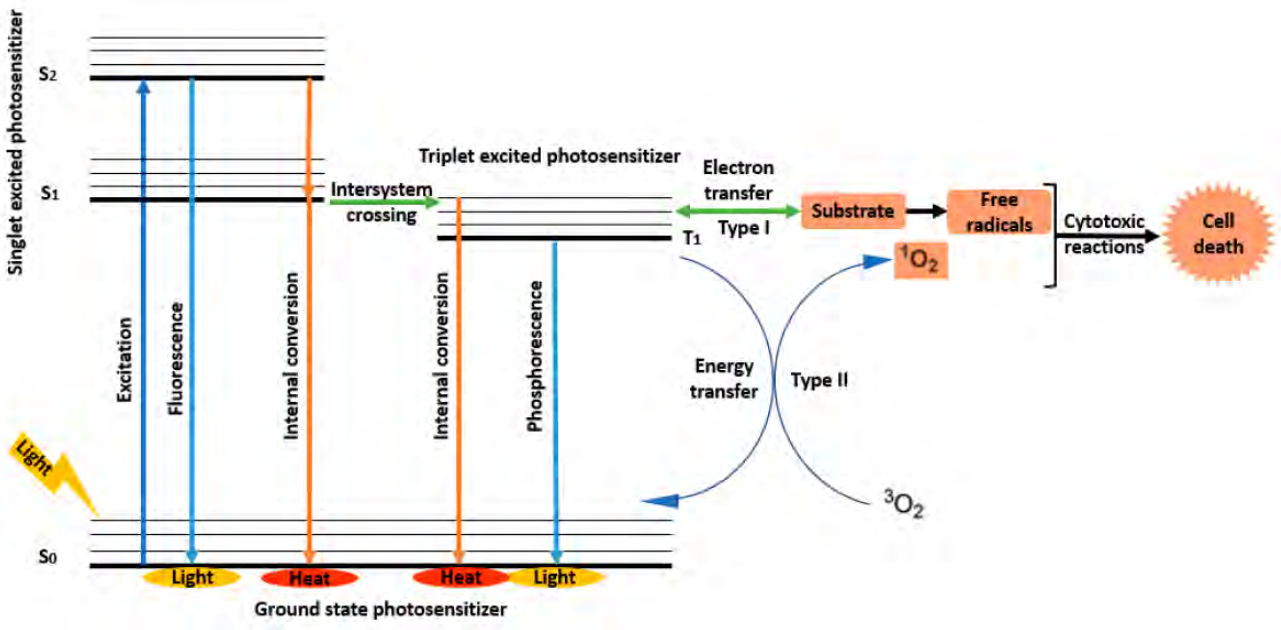

Scheme 1. *Schematization of the mechanism of the two types of PDT. From Ref. 3*

In Type I PDT, the energy transfer occurs via electron/hydrogen transfer through direct contact reactions: ^{3}PS* takes an electron from a nearby reducing molecule, such as NADPH, guanidine, tryptophan or tyrosine, forming a pair of radical species ($PS^{-\bullet}$ and biomolecule$^{+\bullet}$). The PS radical anion subsequently transfers the extra electron to O_2, generating the superoxide anion radical ($O_2^{-\bullet}$) and restoring the ground-state PS. This mechanism ultimately leads to specific damage to biomolecules and triggers radical chain reactions.

On the other hand, in Type II PDT the energy is transferred directly from the $^3PS^*$ to molecular oxygen, whose ground state is a triplet one ($^3O_2$), which is converted to the reactive singlet oxygen ($^1O_2$). Molecular oxygen possesses two S_1 excited states ($^1\Delta_g$ and $^1\Sigma_g$): $^1\Sigma_g$ is very short-lived, as electrons easily populate the lower energy $^1\Delta_g$ state. Its lifetime, however, is determined by both physical quenching, in which the energy of $^1O_2$ is transferred to another molecule without O_2 consumption or formation of new products, and chemical quenching, which involves chemical reactions that generate products. Due to its extreme electrophilic character, it rapidly reacts with unsaturated C-C bonds, anions and neutral electrophiles such as sulfides and amines, producing first peroxide, which in turn generates radicals initiating a variety of chemical reactions, damaging membranes, proteins and DNA. In water, the lifespan of $^1O_2$ is ca. 4 μs due to physical quenching, but in cells it is shorter due to the addition of chemical quenching contribution and the maximum length that the molecule can travel is ca 150 nm in neat water and 10-55 nm in cells, a lot shorter compared to the typical eukaryotic cell diameter (ca. 10-30 μm)[4]. Thus, the localization of the PS is fundamental to determine which cellular structures will be damaged by PDT.[1,2,5,6]

The two mechanisms are competitive, although it is believed that most PS generate both radicals and $^1O_2$. In addition, Type II PDT is considered the most efficient, due to the higher reactivity of $^1O_2$ compared to $O_2^{-\bullet}$ and the biological systems being enzymatically protected against superoxide but not against $^1O_2$. In most cases the cellular damage caused by single oxygen leads to apoptotic cellular mechanisms, which are preferred on necrotic ones, usually associated with an inflammatory response.[7] While Type II PDT mechanism is prevalent in oxygenated tissues, Type I can also occur in hypoxic tissues.[8] In both cases the formation of the triplet excited state is a key step for the performance of the PS.

Photosensitizers

The intrinsic properties of photosensitizers determine the therapeutic efficiency of PDT. An ideal photosensitizer should possess a chemically pure and uniform composition, effectively accumulate in the target tissue and generate ROS when irradiated, while being innocuous in the dark. It should also be stable in solution, serum or plasma and easily eliminated by the organism.[3,9] Optimally, it should absorb light in the near IR, in a part of the spectrum called phototherapeutic window, indicatively placed in the 600-900 nm range that allows the deepest tissue penetration (Figure 1). Conversely, at lower wavelengths the light absorption by biomolecules such as hemoglobin and melanin becomes relevant, while at higher wavelength light is prevailingly absorbed by water.

Another important characteristic of PS is their autofluorescence, allowing their use as theranostic agents combining treatment with imaging to detect pre-cancer lesion, early malignances and tumor margins, as well as monitoring the progress of the PDT treatment.[1]

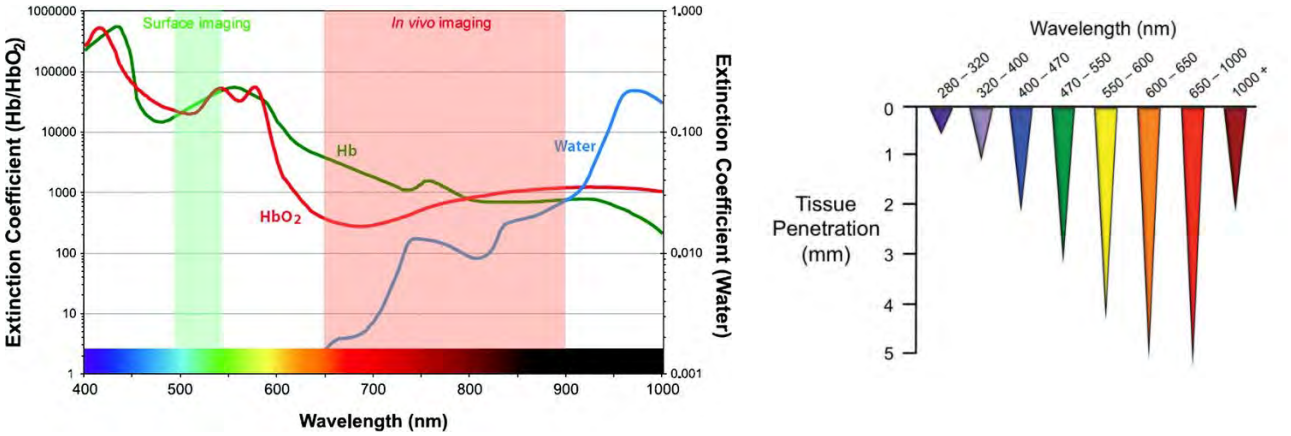

Figure 1. *Left panel: The spectral region between 650 and 900 nm, referred to as phototherapeutic window. From Ref. 10 Right panel: Schematization of the dependence of light penetration through tissues on the wavelength. From Ref. 11*

The first photosensitizer, introduced in the 1970s, was the so-called "hematoporphyrin derivative", a water-soluble mixture of various kind of porphyrins with their derivatives, monomers, dimers, oligomers and esters. The first generation of photosensitizers consist of various forms of this derivative and it has been used for over 30 years to treat several types of cancer, such as non-small lung, bladder, esophageal and brain. Nonetheless, these PS showed low chemical purity, limited tissue penetration and could be excited only with wavelengths below 640 nm. Additionally, they possessed long half-life that rendered the skin hypersensitive to light for weeks. Thus, since late 1980s a second generation of photosensitizers was developed, consisting of pure synthetic compounds with aromatic macrocycles. These PS allowed a better tumor specificity and penetration (due to excitation in the biotherapeutic window) and faster elimination from the body, but their low water solubility affected their yield of ROS production due to aggregation and limited the possibility of intravenous administration. Consequently, third generation PS are being developed with higher affinity to target cells, to facilitate delivery and cell uptake and improve pharmacodynamics and biodistribution in vivo.[3,12]

A wide variety of PS have been developed, including tetrapyrrole structures such as porphyrins, chlorins, bacteriochlorins and phthalocyanines with appropriate functionalization. In addition, synthetic dyes classes including phenothiazinium (like methylene blue), rose bengal, squaraine, phenanelones and BODIPY (boron-dipyrromethene) and natural products such as hypericin, riboflavin and curcumin have been investigated.[9]

One major drawback of organic photosensitizers is their tendency to photobleach, reducing their efficiency and reusability. Conversely, transition metal complexes have acquired growing interest as PS

for their high photostability to both one- and two- photon illumination, together with other interesting characteristics required to the optimal PS: although they absorb visible light, their two-photon cross-section in the NIR are often high. Additionally, they have accessible and easily populated excited triplet states due to the spin-orbit coupling promoted by the presence of heavy atoms and, consequently, they often possess high yields of singlet oxygen generation and due to their long emission lifetimes can be employed as theranostic compounds. Their properties can be tuned by combining several ligands and metals. The most studied complexes for this aim are ruthenium, rhodium, rhenium and cyclometalated iridium complexes.[9,13]

Cellular mechanisms induced by PDT

PDT is involved in three main mechanisms of tissues damages: the first consists in the direct kill of cells through the action of ROS generated by the irradiated PS, that causes damages to specific target as membranes and organelles. In addition, the tumor destruction can involve the damage of tumor vasculature, compromising the supply of oxygen and nutrients, and the activation of immune system.[1]

Depending on various conditions as the type of PS used, the tumor microenvironment and the sensitivity of the target cells, PDT can induce cell death through several mechanisms, including apoptosis, necrosis and autophagy (the first two are schematized in Figure 2).

Apoptosis is a regulated form of programmed cell death that involves hydrolytic enzymes, including proteases and nucleases, that generate morphological changes in cells as a consequence of various disturbances in the cell microenvironment (i.e. DNA damage, accumulation of ROS, endoplasmic reticulum stress and growth factor withdrawal). After initiation, signaling pathways from either the cell surface or the site of the cell damage converge to mitochondria and lead to the activation of caspases (a family of proteases) and finally to program the cell death. In the first case, the extrinsic pathway, transmembrane receptor activates first FADD (FAS-associated death domain protein, an adaptor protein also associated with cell proliferation, cell cycle regulation and development), pro-caspase 8 and finally caspases 8 and 3. On the other end, the intrinsic apoptosis is initiated independently of cell-surface receptors and involves the cleavage of a protein called Bid, that is transported to mitochondria and activates proteins (Bax and Bak) that leads to mitochondrial permeability and the release of cytochrome c, that triggers pro-caspase 9 and the activation of caspases 3 and 7.[14,15]

Conversely, autophagy is a cellular recycling process in which cells engulf organelles and cytosol in vacuoles (autophagosomes). Depending on the intensity of cytotoxicity during treatment, it can lead to cell survival, recycling damaged mitochondria or endoplasmic reticulum before apoptosis is triggered, or death, observed especially in cells resistant to apoptosis.[14]

PDT at its highest dose may also lead to necrosis, which results from severe cell damage causing the rupture of the cell membrane and the leakage of cellular content into the surrounding tissues, triggering an inflammatory response. Unlike apoptosis, necrosis is energy-independent and is induced by radiation, heat, chemicals or hypoxia.[14]

Results of various studies suggest that the mechanism of cell death strongly influences the clinical outcome of the therapy. PDT might provoke apoptosis, necrosis or a combination of the two, although in many cases PDT was found to induce apoptotic mechanisms with higher efficiency, especially when a low light fluence is employed, a very important feature because of the lower doses required to induce apoptosis and because of the reduction of side effects and the improvement of tumor control. Additionally, it implies that PDT can bypass those mechanisms that lead to apoptosis resistance in response to chemotherapeutic drug and ionizing radiations.[15,16]

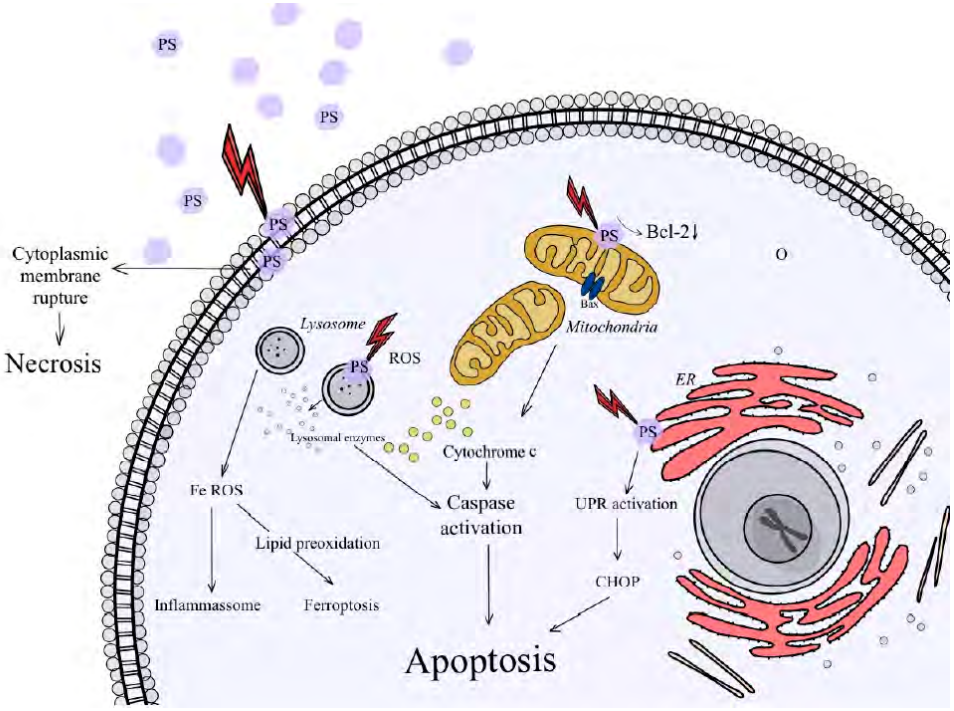

Figure 2. *Schematization of mechanisms that lead to apoptosis or necrosis. From Ref. 14*

Thus, PS localization in the cell is fundamental in determining the mechanisms of cellular response. Lysosomes were initially considered the main intracellular PDT target, believing that the photo-induced disruption of lysosomal membranes would lead to cell digestion by the released hydrolytic enzymes. However, PS targeting lysosomes either delay or block apoptosis and lead to cell death by necrosis, while targeting other organelles such as mitochondria has been revealed more efficient, being directly involved in the apoptotic response and in mechanisms fundamental for the survival of the cell. Another important target are biomembranes, as a PS anchored to them would encounter a high concentration of oxygen, improving PDT efficiency, and the produced $^1O_2$ has higher chances to react with sensitive membrane components as saturated fatty acids, resulting in the loss of membrane barrier function, the

inactivation of protein complexes on the membrane and the inhibition of cell signaling. Conversely, if the PS remains at the membrane boundary or in the water environment, the $^1O_2$ generated might be inactivated before meeting sensitive cellular components. Finally, cytoskeletal elements, such as non-polymerized tubulin, are another strategic target.

The PS uptake and intracellular localization depend on its chemical characteristics like charge, lipophilicity, shape and size. Cationic PS can bind to anionic regions of proteins, possibly resulting in more efficient transport and accumulation in tumor tissues compared to negatively charged molecules. Other than the total net charge, the charges distribution in the molecule also influences the PS uptake.[2]

Limitations and strategies to improve PDT

The main drawback associated with PDT is the limited penetration of light, generating the idea that it might only treat superficial lesions. However, the possibility of delivering light using optical fibers that can be placed within the tumor site using interstitial, endoscopic, intraoperative or laparoscopic systems is a way to overcome this major drawback.[1] The development of PS absorbing and emitting in the NIR with either one- or two-photon excitation is also fundamental to further improve light penetration, as already discussed in the previous subsections.

Additionally, PDT strongly depends on tissue oxygenation state. First, it should be noted that almost all solid tumors show hypoxia in their tumor microenvironment, due to the dysfunctional tumor vasculature not able to supply sufficient oxygen to balance the demand of cancer. Hypoxia is exploited by tumoral cells to defend against the attack of immune cells or therapeutic interventions.[17] Moreover, oxygen level can be reduced too fast during the treatment with a high light fluence, reducing the treatment efficiency. Among various strategies to provide self-oxygen supply (such as the use of red blood cells to deliver the PS, perfluorocarbons NP to deliver O_2 and the suppression of hypoxia related proteins), the decomposition of H_2O_2 into O_2 water through a catalase-like activity results highly interesting. H_2O_2 is indeed implicated in malignant tumor cells with enhanced concentrations over normal cells, being responsible for the progression and proliferation of tumors.[18] A work by Lin and coworkers[19] employed PAMAM dendrimers encapsulating gold nanoclusters, which exhibit a catalase-like activity in a pH range of 4.8-7.4 resulting in a great improvement of the PDT efficacy on H460 cells (lung cancer) when combined with commercial PS.

Other drawbacks already mentioned in one of the previous sections are the limited water solubility of many PS and the lack of good tumor targeting efficiency. Integrating the PS into nanoparticles (NP), by either encapsulation or immobilization on the nanoparticle surface, is a highly promising solution to increase their therapeutic efficiency. The concentration delivery and uptake of PS in target cells can be

increased due to the high surface-to-volume ratio of NP, their small size that allow them to easily pass through the immune system barrier and the possibility to be functionalized with ligands recognized only by specific receptors.[20] A wide range of nanostructures are employed, including metallic, organic, inorganic (mesoporous silica NP, carbon nanotubes) and polymeric (especially water soluble and biodegradable polymer as polyacrylamide and dendrimers, as well as natural polymers) materials. In particular metal-based nanoparticles, especially gold, silver, CuS, TiO_2 and MnO_2, are promising due to their long cycle time, slow degradation, targeted and controlled release due to the enhanced permeability retention (EPR) effect.[3,21] In addition, the specificity toward tumoral cells and the pharmacological properties of PS can be improved through their linkage to DNA- or peptide-based vehicles.[22]

Lastly, PDT might also be combined with other therapies to improve the overall antitumoral efficacy. For instance, PDT has been employed to stimulate immunological response in combination with immunotherapy against metastatic breast cancer, showing a higher efficiency compared to the two therapies alone.[23]

References

(1) Dos Santos, A. F.; De Almeida, D. R. Q.; Terra, L. F.; Baptista, M. S.; Labriola, L. Photodynamic Therapy in Cancer Treatment - an Update Review. *J. Cancer Metastasis Treat.* **2019**, *5* (25). https://doi.org/10.20517/2394-4722.2018.83.

(2) Benov, L. Photodynamic Therapy: Current Status and Future Directions. *Medical Principles and Practice* **2015**, *24* (1), 14–28. https://doi.org/10.1159/000362416.

(3) Niculescu, A. G.; Grumezescu, A. M. Photodynamic Therapy—an up-to-Date Review. *Applied Sciences* **2021**, *11* (8). https://doi.org/10.3390/app11083626.

(4) Maharjan, P. S.; Bhattarai, H. K. Singlet Oxygen, Photodynamic Therapy, and Mechanisms of Cancer Cell Death. *J. Oncol.* **2022**, *2022*, 1–20. https://doi.org/10.1155/2022/7211485.

(5) Mroz, P.; Bhaumik, J.; Dogutan, D. K.; Aly, Z.; Kamal, Z.; Khalid, L.; Kee, H. L.; Bocian, D. F.; Holten, D.; Lindsey, J. S.; Hamblin, M. R. Imidazole Metalloporphyrins as Photosensitizers for Photodynamic Therapy: Role of Molecular Charge, Central Metal and Hydroxyl Radical Production. *Cancer Lett.* **2009**, *282* (1), 63–76. https://doi.org/10.1016/j.canlet.2009.02.054.

(6) DeRosa, M. Photosensitized Singlet Oxygen and Its Applications. *Coord. Chem. Rev.* **2002**, *233–234*, 351–371. https://doi.org/10.1016/S0010-8545(02)00034-6.

(7) Wang, S.; Gao, R.; Zhou, F.; Selke, M. Nanomaterials and Singlet Oxygen Photosensitizers: Potential Applications in Photodynamic Therapy. *J. Mater. Chem.* **2004**, 487–493. https://doi.org/10.1039/b311429e.

(8) Lv, Z.; Wei, H.; Li, Q.; Su, X.; Liu, S.; Zhang, K. Y.; Lv, W.; Zhao, Q.; Li, X.; Huang, W. Achieving Efficient Photodynamic Therapy under Both Normoxia and Hypoxia Using Cyclometalated Ru(II) Photosensitizer through Type I Photochemical Process. *Chem. Sci.* **2018**, *9* (2), 502–512. https://doi.org/10.1039/C7SC03765A.

(9) Abrahamse, H.; Hamblin, M. R. New Photosensitizers for Photodynamic Therapy. *Biochemical Journal* **2016**, *473* (4), 347–364. https://doi.org/10.1042/BJ20150942.

(10) Vickerman, B. M.; Zywot, E. M.; Tarrant, T. K.; Lawrence, D. S. Taking Phototherapeutics from Concept to Clinical Launch. *Nat. Rev. Chem.* **2021**, *5* (11), 816–834. https://doi.org/10.1038/s41570-021-00326-w.

(11) Ruggiero, E.; Alonso-de Castro, S.; Habtemariam, A.; Salassa, L. Upconverting Nanoparticles for the near Infrared Photoactivation of Transition Metal Complexes: New Opportunities and Challenges in Medicinal Inorganic Photochemistry. *Dalton Transactions* **2016**, *45* (33), 13012–13020. https://doi.org/10.1039/C6DT01428C.

(12) Park, W.; Cho, S.; Han, J.; Shin, H.; Na, K.; Lee, B.; Kim, D.-H. Advanced Smart-Photosensitizers for More Effective Cancer Treatment. *Biomater. Sci.* **2018**, *6* (1), 79–90. https://doi.org/10.1039/C7BM00872D.

(13) McKenzie, L. K.; Bryant, H. E.; Weinstein, J. A. Transition Metal Complexes as Photosensitisers in One- and Two-Photon Photodynamic Therapy. *Coord. Chem. Rev.* **2019**, *379*, 2–29. https://doi.org/10.1016/j.ccr.2018.03.020.

(14) Przygoda, M.; Bartusik-Aebisher, D.; Dynarowicz, K.; Cieślar, G.; Kawczyk-Krupka, A.; Aebisher, D. Cellular Mechanisms of Singlet Oxygen in Photodynamic Therapy. *Int. J. Mol. Sci.* **2023**, *24* (23). https://doi.org/10.3390/ijms242316890.

(15) Oleinick, N. L.; Morris, R. L.; Belichenko, I. The Role of Apoptosis in Response to Photodynamic Therapy: What, Where, Why, and How. *Photochemical and Photobiological Sciences*. January 1, 2002, pp 1–21. https://doi.org/10.1039/b108586g.

(16) Mroz, P.; Yaroslavsky, A.; Kharkwal, G. B.; Hamblin, M. R. Cell Death Pathways in Photodynamic Therapy of Cancer. *Cancers (Basel).* **2011**, *3* (2), 2516–2539. https://doi.org/10.3390/cancers3022516.

(17) Liao, C.; Liu, X.; Zhang, C.; Zhang, Q. Tumor Hypoxia: From Basic Knowledge to Therapeutic Implications. *Semin. Cancer Biol.* **2023**, *88*, 172–186. https://doi.org/10.1016/j.semcancer.2022.12.011.

(18) Dang, J.; He, H.; Chen, D.; Yin, L. Manipulating Tumor Hypoxia toward Enhanced Photodynamic Therapy (PDT). *Biomater. Sci.* **2017**, *5* (8), 1500–1511. https://doi.org/10.1039/C7BM00392G.

(19) Liu, C. P.; Wu, T. H.; Liu, C. Y.; Chen, K. C.; Chen, Y. X.; Chen, G. S.; Lin, S. Y. Self-Supplying O2 through the Catalase-Like Activity of Gold Nanoclusters for Photodynamic Therapy against Hypoxic Cancer Cells. *Small* **2017**, *13* (26). https://doi.org/10.1002/smll.201700278.

(20) Montaseri, H.; Kruger, C. A.; Abrahamse, H. Inorganic Nanoparticles Applied for Active Targeted Photodynamic Therapy of Breast Cancer. *Pharmaceutics* **2021**, *13* (3), 296. https://doi.org/10.3390/pharmaceutics13030296.

(21) Sun, J.; Kormakov, S.; Liu, Y.; Huang, Y.; Wu, D.; Yang, Z. Recent Progress in Metal-Based Nanoparticles Mediated Photodynamic Therapy. *Molecules* **2018**, *23* (7), 1704. https://doi.org/10.3390/molecules23071704.

(22) Klara Stefflova; Juan Chen; Gang Zheng. Killer Beacons for Combined Cancer Imaging and Therapy. *Curr. Med. Chem.* **2007**, *14* (20), 2110–2125. https://doi.org/10.2174/092986707781389655.

(23) Li, X.; Ferrel, G. L.; Guerra, M. C.; Hode, T.; Lunn, J. A.; Adalsteinsson, O.; Nordquist, R. E.; Liu, H.; Chen, W. R. Preliminary Safety and Efficacy Results of Laser Immunotherapy for the Treatment of Metastatic Breast Cancer Patients. *Photochemical & Photobiological Sciences* **2011**, *10* (5), 817–821. https://doi.org/10.1039/c0pp00306a.

PART ONE:

NANOCOMPOSITES AND NANOPARTICLES-METAL COMPLEXES HYBRIDS

Gold Nanostars (GNS)

Gold nanoparticles

In the last few decades, noble metal nanoparticles have acquired increasing interest in a wide range of applications including optics, catalysis, electronic, chemical and bio-sensing and in biomedical and environmental applications due to their peculiar electronic and physicochemical features. In nanomaterials, differently from their corresponding continuous bulk conformation, the electronic energy levels are quantized. This effect is known as the quantum confinement effect and, together with the high surface-to-volume ratio, causes some properties of nanoparticles such as chemical reactivity, melting point, electrical conductivity, fluorescence, and magnetic permeability to differ from those of the corresponding bulk materials and to be a function of their size.[1-3] In particular, among noble metal nanoparticles, gold ones (AuNP) have gained considerable attention because of their the good biocompatibility and chemical inertness as well as the possibility of an easy functionalization with thiols, amines, and disulfides.[4]

Synthesis of gold nanoparticles

The wide variety of NP syntheses can be classified into two basic classes. In top-down approaches bulk materials are separated into nanodimensional particles, adopting different physicochemical methods. On the contrary, bottom-up methods consist of the self-assembly of single species (atoms, molecules, or clusters) by using chemical or biological methods. The bottom-up syntheses are usually cheaper and provide great control over the development of the final product with a more homogeneous size, shape, and chemical composition. Conversely, one major drawback of top-down syntheses is the imperfect surface structure of the resulting nanoparticles.[2]

The colloidal approach is the most promising among the bottom-up procedures to prepare noble metal nanoparticles, because it allows their synthesis without the necessity of specialized equipment, and the reaction system might be easily scaled up. In general, the colloidal process can be divided into two steps: the reduction of metallic ions of salts precursors are first reduced to form small metal nuclei, which then grow into large nanoparticles. It is widely accepted that the morphology of the final product is mainly determined by the seed structure and dimensions, the surfactant, and the reaction kinetics. Thus, by selecting different reducing agents, solvent systems, capping agents, and other synthetic conditions, colloidal synthesis can produce plasmonic nanoparticles with various shapes and sizes, other than the classic spherical shape.[5]

Both spherical and anisotropic Au NP can be either prepared by one-in-situ or seed-growth syntheses. Anisotropic shape is obtained through the preferential interaction of shape-directing agents to specific facets of the growing nanoparticles, slowing down their growth kinetics and facilitating an anisotropic growth. Compared to the in-situ procedures, the seed-growth method enlarges the particles step by step and is widely used in the most recent size- and shape controlled AuNP syntheses. In the first step, small AuNP seeds are prepared. These seeds are then added to a "growth" solution containing $HAuCl_4$, the stabilizing and reducing agents. The reducing agents used in the growth step are always mild ones, that reduce Au(III) to Au^0 only in the presence of Au seeds as catalysts, while in their absence Au(III) is reduced to Au(I), preventing any new nucleation and forcing the assembling of the newly reduced Au^0 only on the seeds.[6]

The Localized Surface Plasmon Resonance (LSPR)

The optical properties of noble-metal nanoparticles are one of their most interesting aspects. Applications in surface-enhanced spectroscopies, nanoscale waveguides, optoelectronics and catalysis derive from the Localized Surface Plasmon Resonance (LSPR) phenomenon.[5]

LSPR refers to the collective oscillations of the free conduction-band electrons, also named plasmons, in the presence of the oscillating electromagnetic field. For nanoparticle sizes much smaller than the wavelength of the incident light, the plasmon polarization result confined and concentrated into the nanoparticle. When the electron cloud is displaced from the nuclei, a restoring force arises from the Coulomb attraction between electrons and nuclei and generates the oscillation of the electron cloud (Figure 1). The frequency of this oscillation is determined by the electron density, mass, and shape and size of the charge distribution. The resonance condition is reached when the frequency of the collective oscillation is approximately the same as the incident light, causing large absorption and scattering cross-sections at the resonance frequency, together with a strong electric field enhancement near the surface of the structure. Other than NP size, shape, and geometry, the extinction spectra of metal nanoparticles originated by the LSPR phenomenon is determined by several factors, such as the dielectric properties of the surrounding medium and the interparticle coupling interactions.[5,7-9]

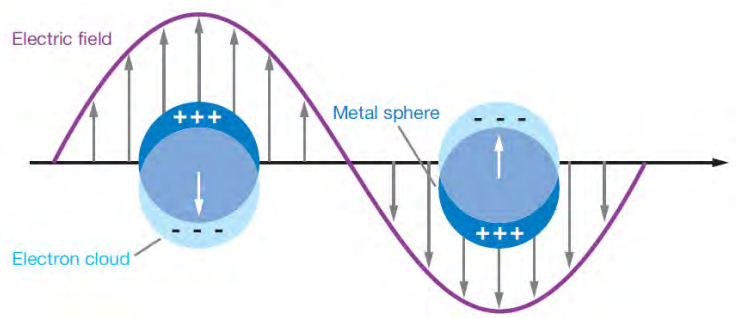

Figure 1. *LSPR phenomenon for a spherical nanoparticle. From Ref. 10*

In particular, the LSPR band of AuNP derives from the sum between scattered and absorbed photons, strongly dependent on particle size: the increase in dimensions is associated with a red shift and a broadening of its LSPR band.[9] Spherical gold nanoparticles in the 10-nm size range have a strong absorption maximum around 520 nm in water due to their LSPR. However, size tunability of the LSPR band of nanospheres is limited: for instance, an increase of the nanoparticle size to ca. 40 nm generates only a red shift of ca. 10 nm (to ca. 530 nm). In many biological applications, it is desirable to work in the NIR spectral region, as already discussed in the previous chapter, due to the higher penetration of light through tissues, blood and water in the 650-900 nm window (i.e. the phototherapeutic window). Changing the particle shape into an anisotropic morphology is the easiest and the most common strategy to tune the position and the number of its LSPR bands.[11]

Indeed, changes in the shape of the nanoparticles are associated with a variation of their surface geometry, and in a shift of the local electric field density on the particle surface upon irradiation, which finally causes a change in the oscillation frequency. For instance, the LSPR absorption of gold nanorods splits into two bands corresponding to the oscillation of the free electrons along and perpendicularly to their long axis, named respectively longitudinal and transverse modes, schematized in Figure 2. An absorption at around 520 nm is related to the transverse LSPR, analogous to the LSPR band of spherical NP, while an additional LSPR band at longer wavelengths derives from the longitudinal oscillation. This latter strongly depends on the aspect ratio of the nanorods (i.e. the width-to-height ratio), as red shifting of this band is associated with the elongation of the nanorod.[12]

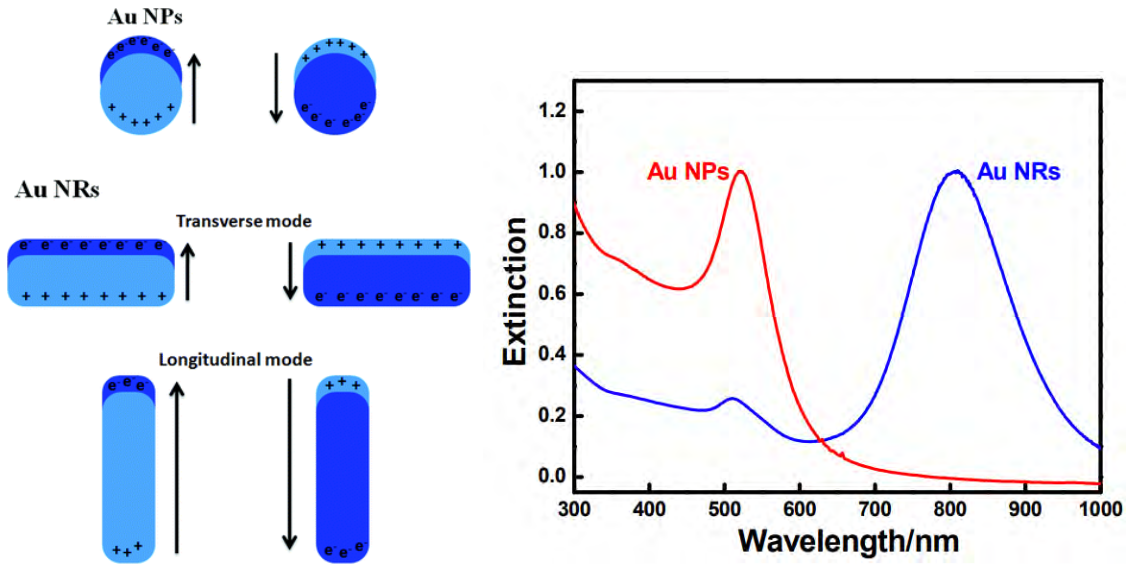

Figure 2. *Left panel: LSPR oscillation for a spherical gold nanoparticle and the two LSPR oscillations (transverse and longitudinal modes) in a gold nanorod. Right panel: Extinction spectra of a gold nanosphere (red trace) and of a gold nanorod (blue trace). From Ref. 12*

The second method to tune LSPR bands is by introducing a metal nanoshell on the plasmonic nanoparticle: the decrease of its thickness is associated to a red shift of the extinction band due to increased coupling between the inner and outer shell surface plasmons.[11]

The photoexcitation of nanoparticles resulting from LSPR is a global non-equilibrium, where the plasmons dephase and decay at ultrafast speed. To restore the equilibrium, the absorbed energy can thus be released through either the radiative emissions of photons or the nonradiative generation of electron–hole pairs.[7] The non-radiative relaxation is associated with the photothermal effect and will be discussed afterwards. The photoluminescence (PL) efficiency of LSPR is typically very low (below 10^{-3}-10^{-5}) due to the fast non-radiative processes typical of metals. However, anisotropic morphologies can promote the 'lightning rod' effect, consisting in the enhanced radiative recombination efficiency of sp band electrons with d band holes, thanks to the local electric field associated with LSPR.[9] The PL of metal nanoparticles do not follow Kasha's rule, as their behavior is strongly dependent on the excitation wavelengths, possibly attributed to the fact that the extinction spectrum of a metal nanoparticle is composed of many nonconjugated and localized surface plasmon resonances of different crystalline facets, and the LSPR of each metal nanoparticle behaves independently.[13]

Gold nanostars

Among the possible different anisotropic morphologies, gold nanostars (GNS) are of particular interest, due to the possibility to tune LSPR bands by branch and core dimensions, the strong near-field enhancements at the tips of the branches and the three different curvatures affecting adsorbed ligands.

GNS can be schematized in a central core from which a certain number of branches develop, whose length and number depend on the synthetic conditions. Depending on the morphology, GNS display at least two LSPR bands, one associated to the core (at ca. 530 nm) and one to the branches, even though the first one has low intensity. Hence, by changing the aspect ratio of the branches from spheroidal shapes to star-like shapes with more elongated branches, the main LSPR band shifts toward the NIR, as schematized in Figure 3. Furthermore, by tuning the core size it is possible to control the ratio between absorbance and scattering of the plasmons. Absorption is the fraction of electromagnetic radiation that after interacting with the plasmon is released through nonradiative decay, while scattering is the fraction of energy that after interacting with the plasmon is re-emitted. Both increase with particle size, although scattering more significantly. Hence, GNS grown from seeds or nanoparticles smaller than 60 nm display stronger absorption and are preferred for catalytic and photothermal applications, while those grown from larger seed possess stronger scatter coefficients and are more suitable for labelling or sensing applications.[14,15]

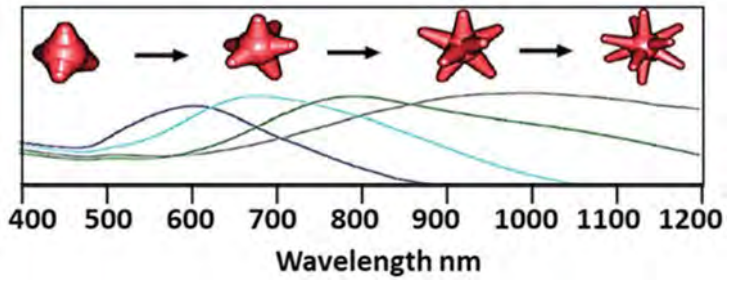

Figure 3. *Dependence of the position and the broadness of the main LSPR band of GNS on the aspect ratio of the branches. Adapted from Ref. 16*

A consequence of the LSPR phenomenon is the concentration of the energy of the electromagnetic radiation to subwavelength dimensions, generating strong electromagnetic field in proximity of the NP surface. Due to their characteristic shape with long sharp branches, GNS produce one of the highest enhancements of the electromagnetic field (Figure 4), ca. 10-fold higher compared to nanospheres and nanorods. Moreover, this effect is further enhanced by the proximity of two or more GNS (below 3 nm), in the so-called hotspots (panel e of Figure 4). Due to this effect, different types of optical phenomena in materials and molecules located in close proximity to GNS surface are enhanced, such as fluorescence emission, Raman scattering, absorption of radiation and the subsequent production of reactive oxygen species.[15]

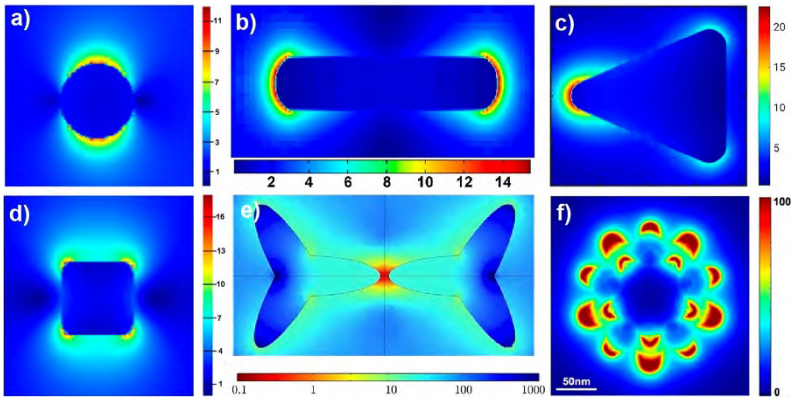

Figure 4. *Simulated electric field distribution of plasmonic nanoparticles with different shapes: nanospheres (a), nanorods (b), nanotriangles (c), nanocubes (d), nanotripods (e) and nanostars (f) when interacting with light. From Ref. 17*

Thus, a precise control over their size and shape becomes necessary to tune the GNS properties depending on their applications. GNS morphology is controlled during their synthesis by adjusting different synthetic factors. It is known that Ag^+ ions have a role in directing the formation of the branches, although its mechanism of action is still uncertain. It has been proposed that due to the gold precursor ($HAuCl_4$) AgCl might form and precipitate, adsorbing on the surface of the growing GNS and directing the formation of the star-like morphology.[4] A wide variety of synthetic strategies have been developed. For instance, Liz-Marzán and coworkers[18] prepared GNS with extremely high yield in a seed-mediated method using dimethylformamide (DMF) as solvent and reducing agent and polyvinylpyrrolidone (PVP) as the shape directing agent. Alternatively, by exploiting the synergistic effect between cetyltrimethylammonium bromide (CTAB) and $AgNO_3$, GNS with high aspect ratio can be prepared, yielding to strong extinction coefficients in the second NIR window (1200-1500 nm).[19]

However, to prepare GNS for biomedical applications it is useful to carry out the synthesis in water employing non-toxic reagents. For this reason, surfactant free syntheses[20,21] or in-situ syntheses employing biocompatible surfactants have been proposed, for instance, buffers such as HEPES, EPPS, and MOPS that function both as reducing and shape directing agents and controlling the aspect ratio of the branches by the buffer/$HAuCl_4$ ratio. However, the absence of a seed-growth procedure resulted in the production of highly heterogeneous GNS.[14,22]

Another interesting synthesis proposed by Pallavicini and coworkers[23] employs the surfactant Triton X-100 as directing and stabilizing agent producing regular, flat, 5-branched GNS that show three LSPR bands: other than the short one at ca. 520 nm and the intermediate tunable one in the phototherapeutic window, another band at ca. 1300 nm is present, assigned to oscillation along collinear branches. Moreover, the easy replacement of the surfactant, that adheres weakly with the gold surface, offers easy surface functionalization and makes such particles interesting for a range of bio-medical applications.

Gold nanostars in the biomedical field

As already described in the previous section, due to the promising optical properties, the possibility to tune size and shape, their facile surface modification and their biocompatibility and chemical inertness make GNS and more in general gold nanoparticles highly attractive for various sensing, imaging and therapeutic applications.[24]

The main GNS applications in biosensing are based on metal enhanced fluorescence (MEF) or surface enhanced Raman spectroscopy (SERS). Both depend on the enhancement of the electromagnetic field in close proximity of the nanoparticle surface, already described above. MEF, that will be described more in detail in the next chapter, consists in the increase of the excitation rate of a fluorophore placed within the near-field of the nanoparticle resulting in enhanced fluorescence. Similarly, it also strongly affects the polarizability of adsorbed molecules, leading to an enhancement of their characteristic Raman scattering by many orders of magnitude. The great interest toward SERS is associated with a great sensitivity, which can reach detection limits down to attomolar concentrations, combined with the molecular specificity provided by the characteristic vibrational fingerprint of each molecule. Biosensors based on these two effects exploit biomolecules immobilized to a transducer and selective to very specific disease biomarkers or disease-specific micro-RNAs. The biological response derived from this interaction results in a measurable signal from the transducer, whose intensity is dependent on the biomarker concentration.[24,25]

Other biomedical applications of GNS are photothermal and photodynamic therapies (PTT and PDT respectively). Subsequently to LSPR, gold nanostructures can convert electromagnetic radiation energy into heat, which in turn can eliminate tumors through PTT, discussed more in detail in the next section, or can be combined with suitable photosensitizers to trigger the production of ROS for PDT applications (see next chapter). GNS have also been exploited for the development of efficiently targeted delivery of anticancer drugs and genetic agents, mostly based on the large number of hotspots on plasmonic nanostars to enhance light-triggered heating effects, resulting in faster drug release compared to those of other plasmonic nanostructures.[17]

Furthermore, all these applications can be combined to achieve a variety of multimodal imaging, theranostic and combination therapies.

Photothermal Therapy (PTT)

Photothermal therapy (PTT) is a highly applied antitumoral therapy with minimal invasiveness, derived from the photothermal effect, i.e. the non-radiative relaxation of plasmons, that collide with low-energy

electrons through inelastic Coulombic collisions, converting the energy of plasmons into heat. These low-energy electrons then couple with the metallic lattice through electron-phonon scattering processes, leading to the lattice thermalization of the nanostructure and, finally, the release of thermal energy to the surrounding environment through phonon-phonon collisions, generating a local hyperthermia in the surroundings of the nanostructure.[7,26]

Upon irradiation by light at a specific wavelength, the excited PTT agent relaxes to the ground state through collision with the surrounding molecules, heating the tumor microenvironment (Figure 5).[27] When the temperature reaches 42 °C, irreversible tissue damage occurs and, above 60 °C, cell death is instantaneous, due to the denaturation of proteins and the destruction of the plasma membrane.[28] In particular, temperatures in the range of 41–47 °C induces apoptosis, while an increase above 50 °C is associated with necrosis.[29]

GNS with small core size and multiple long thin branches are particularly efficient photothermal transducers due to their high absorption cross sections tunable in the near-infrared region with relatively low scattering effect. Indeed, GNS resulted ca. 3-fold more efficient in inducing local hyperthermia compared to gold nanorods and ca. 100-fold more efficient than magnetite nanoparticles.[29] Moreover, due to the enhanced permeability retention (EPR) effect, nanoparticles can accumulate preferentially in tumoral site, allowing to target selectively tumoral tissues without affecting healthy ones, overcoming one limitation of PTT linked to the non-specific laser absorption by both tumor and healthy tissues, that might cause potential thermal damage to the healthy surrounding tissues.[28]

However, PTT might induce thermotolerance in cancer cells mediated by heat-shock proteins. This drawback can be overcome by combining PTT with another therapeutic modality, such as PDT, chemotherapy, radiotherapy, and immunotherapy, leading to additive or even synergistic therapeutic effect.[27,29]

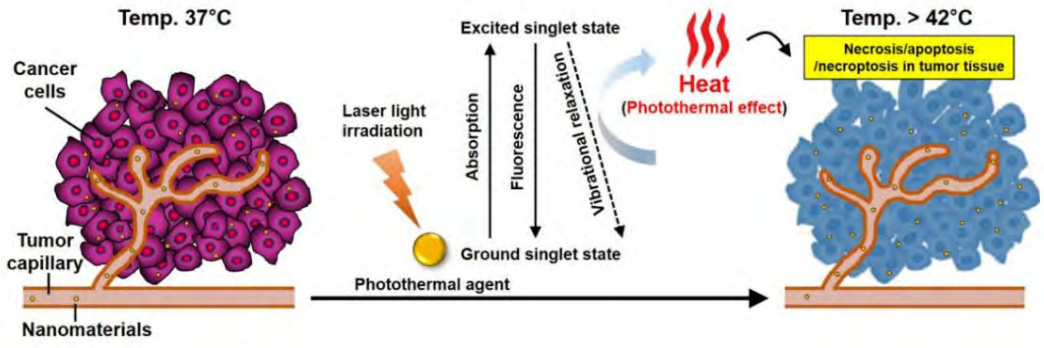

Figure 5. *Schematic representation of the mechanism of PTT mediated by plasmonic nanoparticles. From Ref. 27*

Biocompatibility of gold nanoparticles

Although gold nanoparticles are usually considered biocompatible, there are some parameters that might be associated with some kind of cytotoxicity, such as shape, size, surface chemistry and coatings, purity, production method, solvent, type of functionalization, aggregation level, concentration and exposure time to the cells, as well as the type of cell line. Among these parameters, nanoparticle morphology is one of the most important.

The cytotoxicity of bare gold nanoparticles with various shapes (nanospheres, nanorods, nanoprisms, nanostars and nanoflowers, in the size range between 10 and 400 nm) was evaluated toward HeLa and HEK293T cell lines, showing overall a good biocompatibility and some cytotoxicity dependent on dose and exposure. Moreover, dimensions ranging between 100-200 nm were associated to a more efficient internalization by endocytosis and to a minor aggregation between the nanoparticles, yielding to a lower cytotoxicity.[30]

Another important parameter to determine NP cytotoxicity is their surface chemistry. When suspended in biological fluids, proteins adsorb on the NP surface affecting properties such as optical features, circulation times and interactions with cells. The thickness and density of protein corona adsorbed on the NP surface are strongly dependent on the particle size and shape, as well as on the surface charge. The different curvatures of GNS branches promote distinct protein orientations, resulting in larger protein coronas. Since some applications (for instance, targeting) might be affected by large protein corona formation, surface-modification strategies have been developed to minimize the formation of protein corona on the GNS.[15,31]

The interaction cells with nanoparticles and the internalization mechanisms are described in more detail in the next chapter.

References

(1) Kvítek, O.; Siegel, J.; Hnatowicz, V.; Švorčík, V. Noble Metal Nanostructures Influence of Structure and Environment on Their Optical Properties. *J. Nanomater.* **2013**, *2013*. https://doi.org/10.1155/2013/743684.

(2) Ielo, I.; Rando, G.; Giacobello, F.; Sfameni, S.; Castellano, A.; Galletta, M.; Drommi, D.; Rosace, G.; Plutino, M. R. Synthesis, Chemical–Physical Characterization, and Biomedical Applications of Functional Gold Nanoparticles: A Review. *Molecules* **2021**, *26* (19), 5823. https://doi.org/10.3390/molecules26195823.

(3) Sau, T. K.; Rogach, A. L. Nonspherical Noble Metal Nanoparticles: Colloid-Chemical Synthesis and Morphology Control. *Advanced Materials* **2010**, *22* (16), 1781–1804. https://doi.org/10.1002/adma.200901271.

(4) Mousavi, S. M.; Zarei, M.; Hashemi, S. A.; Ramakrishna, S.; Chiang, W. H.; Lai, C. W.; Gholami, A. Gold Nanostars-Diagnosis, Bioimaging and Biomedical Applications. *Drug Metab. Rev.* **2020**, *52* (2), 299–318. https://doi.org/10.1080/03602532.2020.1734021.

(5) Yang, P.; Zheng, J.; Xu, Y.; Zhang, Q.; Jiang, L. Colloidal Synthesis and Applications of Plasmonic Metal Nanoparticles. *Advanced Materials* **2016**, *28* (47), 10508–10517. https://doi.org/10.1002/adma.201601739.

(6) Li, N.; Zhao, P.; Astruc, D. Anisotropic Gold Nanoparticles: Synthesis, Properties, Applications, and Toxicity. *Angewandte Chemie - International Edition* **2014**, *53* (7), 1756–1789. https://doi.org/10.1002/anie.201300441.

(7) Cui, X.; Ruan, Q.; Zhuo, X.; Xia, X.; Hu, J.; Fu, R.; Li, Y.; Wang, J.; Xu, H. Photothermal Nanomaterials: A Powerful Light-to-Heat Converter. *Chem. Rev.* **2023**, *123* (11), 6891–6952. https://doi.org/10.1021/acs.chemrev.3c00159.

(8) Kelly, K. L.; Coronado, E.; Zhao, L. L.; Schatz, G. C. The Optical Properties of Metal Nanoparticles: The Influence of Size, Shape, and Dielectric Environment. *J. Phys. Chem. B* **2003**, *107* (3), 668–677. https://doi.org/10.1021/jp026731y.

(9) Amendola, V.; Pilot, R.; Frasconi, M. Surface Plasmon Resonance in Gold Nanoparticles : A Review. *Journal of Physics: Condensed Matter* **2017**, *29* (20). https://doi.org/https://doi.org/10.1088/1361-648X/aa60f3.

(10) Willets, K. A.; Van Duyne, R. P. Localized Surface Plasmon Resonance Spectroscopy and Sensing. *Annu. Rev. Phys. Chem.* **2007**, *58*, 267–297. https://doi.org/10.1146/annurev.physchem.58.032806.104607.

(11) Jain, P. K.; Huang, X.; El-Sayed, I. H.; El-Sayed, M. A. Noble Metals on the Nanoscale: Optical and Photothermal Properties and Some Applications in Imaging, Sensing, Biology, and Medicine. *Acc. Chem. Res.* **2008**, *41* (12), 1578–1586. https://doi.org/10.1021/ar7002804.

(12) Jayabal, S.; Pandikumar, A.; Lim, N. A Gold Nanorod-Based Localized Surface Plasmon Resonance Platform for the Detection of Environmentally Toxic Metal Ions. *Analyst* **2015**, *140*, 2540–2555. https://doi.org/10.1039/c4an02330g.

(13) Vankayala, R.; Sagadevan, A.; Vijayaraghavan, P.; Kuo, C. L.; Hwang, K. C. Metal Nanoparticles Sensitize the Formation of Singlet Oxygen. *Angewandte Chemie - International Edition* **2011**, *50* (45), 10640–10644. https://doi.org/10.1002/anie.201105236.

(14) M. Pallares, R.; Stilson, T.; Choo, P.; Hu, J.; Odom, T. W. Using Good's Buffers To Control the Anisotropic Structure and Optical Properties of Spiky Gold Nanoparticles for Refractive Index Sensing. *ACS Appl. Nano Mater.* **2019**, *2* (8), 5266–5271. https://doi.org/10.1021/acsanm.9b01117.

(15) Xi, Z.; Zhang, R.; Kiessling, F.; Lammers, T.; Pallares, R. M. Role of Surface Curvature in Gold Nanostar Properties and Applications. *ACS Biomater. Sci. Eng.* **2024**, *10* (1), 38–50. https://doi.org/10.1021/acsbiomaterials.3c00249.

(16) Gao, M.; Zhu, L.; Peh, C. K.; Ho, G. W. Solar Absorber Material and System Designs for Photothermal Water Vaporization towards Clean Water and Energy Production. *Energy Environ. Sci.* **2019**, *12* (3), 841–864. https://doi.org/10.1039/C8EE01146J.

(17) Ngo, N. M.; Tran, H.-V.; Lee, T. R. Plasmonic Nanostars: Systematic Review of Their Synthesis and Applications. *ACS Appl. Nano Mater.* **2022**, *5* (10), 14051–14091. https://doi.org/10.1021/acsanm.2c02533.

(18) Senthil Kumar, P.; Pastoriza-Santos, I.; Rodríguez-González, B.; Javier García de Abajo, F.; Liz-Marzán, L. M. High-Yield Synthesis and Optical Response of Gold Nanostars. *Nanotechnology* **2008**, *19* (1), 015606. https://doi.org/10.1088/0957-4484/19/01/015606.

(19) Trigari, S.; Rindi, A.; Margheri, G.; Sottini, S.; Dellepiane, G.; Giorgetti, E. Synthesis and Modelling of Gold Nanostars with Tunable Morphology and Extinction Spectrum. *J. Mater. Chem.* **2011**, *21* (18), 6531. https://doi.org/10.1039/c0jm04519e.

(20) Yuan, H.; Khoury, C. G.; Hwang, H.; Wilson, C. M.; Grant, G. A.; Vo-Dinh, T. Gold Nanostars: Surfactant-Free Synthesis, 3D Modelling, and Two-Photon Photoluminescence Imaging. *Nanotechnology* **2012**, *23* (7), 075102. https://doi.org/10.1088/0957-4484/23/7/075102.

(21) Vega, M. M.; Bonifacio, A.; Lughi, V.; Marsi, S.; Carrato, S.; Sergo, V. Long-Term Stability of Surfactant-Free Gold Nanostars. *Journal of Nanoparticle Research* **2014**, *16* (11). https://doi.org/10.1007/s11051-014-2729-z.

(22) Xi, W.; Haes, A. J. Elucidation of HEPES Affinity to and Structure on Gold Nanostars. *J. Am. Chem. Soc.* **2019**, *141* (9), 4034–4042. https://doi.org/10.1021/jacs.8b13211.

(23) Dacarro, G.; Pallavicini, P.; Bertani, S. M.; Chirico, G.; D'Alfonso, L.; Falqui, A.; Marchesi, N.; Pascale, A.; Sironi, L.; Taglietti, A.; Zuddas, E. Synthesis of Reduced-Size Gold Nanostars and Internalization in SH-SY5Y Cells. *J. Colloid Interface Sci.* **2017**, *505*, 1055–1064. https://doi.org/10.1016/J.JCIS.2017.06.102.

(24) Joyce, C.; Fothergill, S. M.; Xie, F. Recent Advances in Gold-Based Metal Enhanced Fluorescence Platforms for Diagnosis and Imaging in the near-Infrared. *Mater. Today Adv.* **2020**, *7*, 100073. https://doi.org/10.1016/j.mtadv.2020.100073.

(25) Lenzi, E.; Jimenez De Aberasturi, D.; Liz-Marzán, L. M. Surface-Enhanced Raman Scattering Tags for Three-Dimensional Bioimaging and Biomarker Detection. *ACS Sens.* **2019**, *4* (5), 1126–1137. https://doi.org/10.1021/acssensors.9b00321.

(26) Elahi, N.; Kamali, M.; Baghersad, M. H. Recent Biomedical Applications of Gold Nanoparticles: A Review. *Talanta* **2018**, *184*, 537–556. https://doi.org/10.1016/j.talanta.2018.02.088.

(27) Han, H. S.; Choi, K. Y. Advances in Nanomaterial-Mediated Photothermal Cancer Therapies: Toward Clinical Applications. *Biomedicines* **2021**, *9* (3), 305. https://doi.org/10.3390/biomedicines9030305.

(28) Zhao, J.; Long, X.; Zhou, M. Clearable Nanoparticles for Cancer Photothermal Therapy; 2021; pp 121–134. https://doi.org/10.1007/978-3-030-58174-9_6.

(29) Pallavicini, P.; Cabrini, E.; Borzenkov, M.; Sironi, L.; Chirico, G. Applications of Gold Nanostars: Nanosensing, Thermal Therapy, Delivery Systems. In *SpringerBriefs in Materials*; Springer, 2015; pp 43–59. https://doi.org/10.1007/978-3-319-20768-1_3.

(30) Woźniak, A.; Malankowska, A.; Nowaczyk, G.; Grześkowiak, B. F.; Tuśnio, K.; Słomski, R.; Zaleska-Medynska, A.; Jurga, S. Size and Shape-Dependent Cytotoxicity Profile of Gold Nanoparticles for Biomedical Applications. *J. Mater. Sci. Mater. Med.* **2017**, *28* (6), 92. https://doi.org/10.1007/s10856-017-5902-y.

(31) Liu, J.; Peng, Q. Protein-Gold Nanoparticle Interactions and Their Possible Impact on Biomedical Applications. *Acta Biomater.* **2017**, *55*, 13–27. https://doi.org/10.1016/j.actbio.2017.03.055.

Decoration of gold nanostars with a polyamidoamine-Ru(II) complex to increase $^1O_2$ generation in Photodynamic Therapy.

Introduction

Nanoparticles uptake by cells

Cell internalization of molecules and nanoparticles across the cell membrane is highly dependent on their size and chemical properties. First, the molecule or nanoparticle charge can strongly affect uptake efficiency and the cell membrane being a lipid bilayer with an external negative charge on both surfaces, usually positively charged molecules interact more strongly with it and are more easily internalized in respect to neutral and negatively charged molecules due to the electric potential gradient.[1] The second component of the membrane are the proteins, directly involved in cellular signaling and in the exchange of molecules between the inside and the outside of the cell. Interactions with the cell membrane proteins and other biomolecules on the cell surface further modulate uptake

Depending on the molecule size, three classes of transport mechanisms inside the cell can be identified: i) simple diffusion, which consists of the passive transport of small lipophilic molecules across the membrane driven by a concentration or electric potential gradient; ii) facilitated diffusion, a passive process that involves membrane proteins; and iii) active transport, in which large molecules transported against gradient are internalized requiring energy from the cell.[1]

The active internalization of large molecules, such as macromolecules and nanoparticles, occurs through endocytosis, in which the substance is enveloped by the membrane itself and released inside the cytoplasm in a vesicle formed by the membrane lipids.[2] Depending on the nature of the cells, different kinds of endocytosis are possible, listed and schematized in Figure 1. Phagocytosis mostly involves specialized cells (called phagocytes) and it first consists in the recognition and tagging of the foreign particle in the bloodstream by proteins called opsonins, followed by their attachment on the membrane of phagocytes through specific receptor-ligand interactions and internalization in these cells. Here the vesicle containing the particle matures and fuses with endosomes and lysosomes, forming a phagolysosome, which acidifies and acquires enzymes to degrade the particle material.[3]

Other main endocytic mechanisms are clathrin-mediated endocytosis, caveolae-mediated endocytosis and macropinocytosis. The clathrin-mediated endocytosis occurs in all mammalian cells and for most of them is the main physiological mechanism of internalization for macromolecules. It can be receptor-dependent or independent, in a membrane region rich in clathrin proteins, that polymerize and assembly to form vesicles with an average size of 100-120 nm. The vesicle delivers its content to early endosomes, at first slightly (pH ca. 6) and then further acidified until pH ca. 5 when mature into

late endosomes. Once mature, their fusion with prelysosomal vesicles containing acid hydrolases generate an environment for the degradation of the internalized particles.[3]

The caveolae-mediated endocytosis is instead a highly regulated and much slower pathway in which the particle interacting with the cell membrane moves into caveolae invaginations on the surface, that engulf it forming vesicles that does not contain any enzyme for its degradation. Folic acid, albumin and cholesterol are known to be internalized with this process, that is believed to escape lysosomal degradation, hence it is considered useful when the nanocarrier is highly sensitive to enzymes to escape lysosomal degradation (although whether this pathway is active in every cells and capable to escape lysosomal accumulation remains debated).[3]

Finally, micropinocytosis is a non-selective process that consists of the formation of membrane protrusions that collapse and fuse with the membrane, internalizing the particles through the formation of vesicles larger than 1 μm and called macropinosomes, that, analogously to the other endocytic mechanisms, acidify or fuse with lysosomes to degrade the particle.[3]

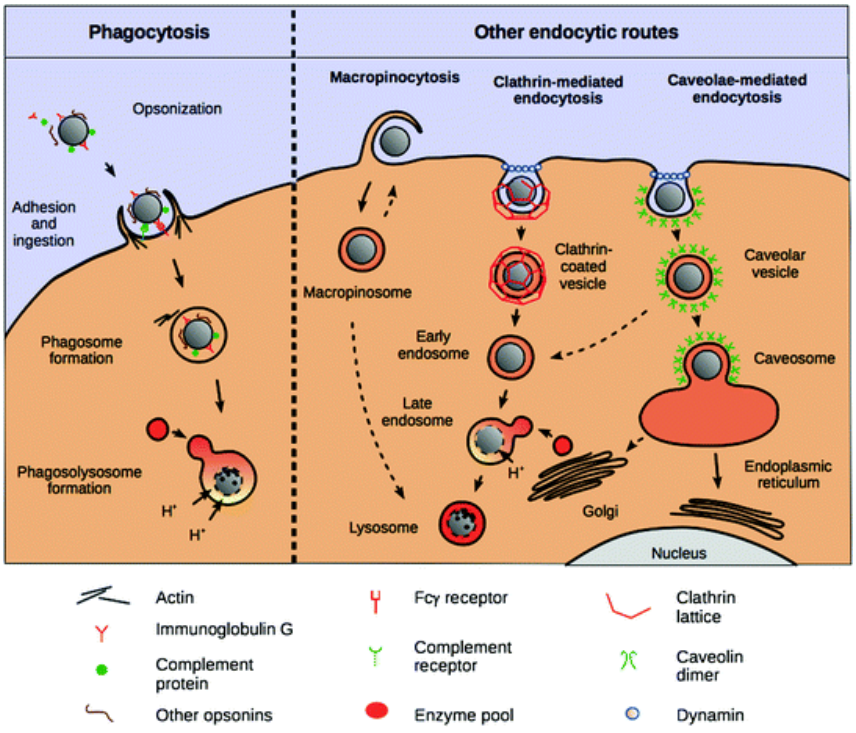

Figure 1. *Schematization of the endocytic pathways followed by nanoparticles to be internalized by cells. From Ref. 3*

Even though biomolecules and nanoparticles are taken up by cells following the same endocytic processes, the internalization of larger nanoparticles through endocytosis seems easier compared to biological macromolecules such as proteins and nucleic acids. Nanoparticles smaller than 200 nm, indeed, enter the cells very easily and those with a size less than 35 nm sometimes even the nucleus.[4] Nanoparticles possess a highly energy surface that interacts with cells with great affinity thought

multiple weak interactions. For the same reason, when suspended in biological medium, proteins and other biomolecules adsorb on their surface forming a so-called protein corona of a certain thickness, that increases the hydrodynamic diameter of the nanoparticles and influences their ζ-potential depending on the properties of the adsorbed proteins.

The formation of the protein corona on nanoparticles, as well as its density and thickness, highly depends on features of both the nanoparticles, the proteins and the medium in which they are suspended, i.e. the protein and nanoparticle type and size, the conformational flexibility of the protein and the nanoparticle's shape, electric charge, and hydrophilicity.[5] Also the nanoparticles functionalization plays an important role in the formation of the protein corona, as it changes their surface properties, and it is often exploited to tune the pharmacokinetic of nanoparticles in drug delivery systems. The proteins adsorbed on the nanoparticle surface indeed influences their cellular uptake, targeting, biodistribution, pharmacokinetics and nanotoxicity. For instance, the adsorption of serum albumin might prolong the circulation time in the blood,[6] while a protein corona containing the antibodies IgG and fibrinogen might trigger the clearance of the nanoparticles[7] and the adsorption of a large amount of apolipoproteins might help the nanoparticle to pass through the blood-brain barrier.[8] However, the nanoparticle-protein system is highly dynamic, as the corona composition changes over time and in different environments through continuous adsorption and desorption of the proteins, making difficult to predict the biological fate of the nanoparticle.[5]

Another key factor influencing the uptake of nanoparticles by cells is their cycle phase. The cell cycle comprehends the events that the cell undergoes to divide and replicate and it can be divided into four phases: G1, S, G2 and M. During the first one, G1, the cell increases its size, in the S phase replicates its DNA and in the G2 synthesizes the proteins necessary for cell division, until its effective division in phase M, that generates two daughter cells in the G1 phase and so on.[9] A schematization of these four phases is shown in the upper part of Figure 2.

In the lower panel of Figure 2, the cell cycle is taken into account during their nanoparticle uptake. It has been found that the rate of nanoparticles uptake by cells is independent by their phase in the cell cycle, but that their accumulation in the cell after treating times shorter than a cell phase greatly depends on it, being higher for cells in the G2 and M phases and lower for cells in the G1 phase. Cells in the G2 and M phases have indeed taken up nanoparticles for a longer time and are not yet divided, those in G1 phase have just divided and not yet internalized any particle, while those in the S phase are in an intermediate situation. Once cells enter the M phase, the internalized nanoparticles are divided into the daughter cells, diluting the overall nanoparticle concentration. On the other hand, for longer treatment times, the average nanoparticle uptake deviates from linearity as the cell culture commonly used at laboratory scale contains cells that are in a different phase one to each other and simultaneously

undergo growth and cell division. Additionally, the dilution of nanoparticles into daughter cells is expected to be higher for tumoral cells with respect to healthy cells, as they divide faster.[9]

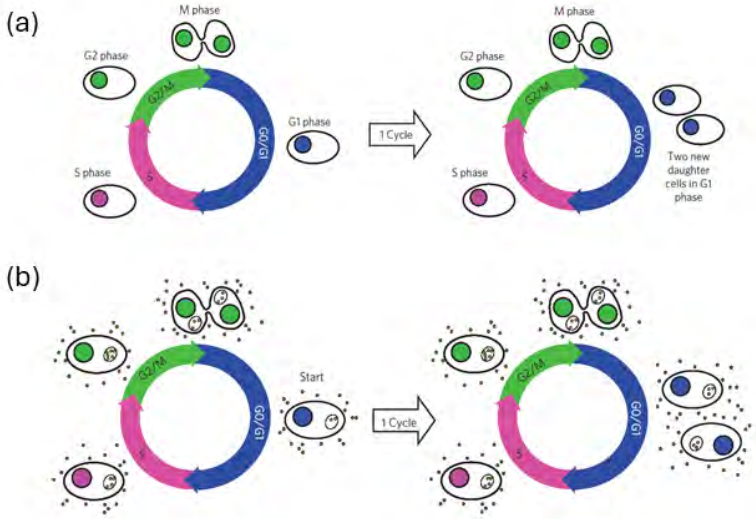

Figure 2. *(a) The normal cell cycle that leads to cell division is schematized, marking the four stages involved in the cycle. (b) Nanoparticle uptake by a cycling cell. From Ref. 9*

PAA-transition metal complexes for biomedical applications

Poly-amidoamines (PAAs) are a class of polymers, most of them water-soluble and biocompatible, obtained by a Michael-type polyaddition of primary or secondary amines with bisacrylamides. Their synthesis is highly versatile, as they can be easily designed to possess linear, grafted or hyperbranched architecture and to bear various chemical functions. Thus, PAAs can be exploited for various biomedical applications, as antibacterial, antiviral, antimalarial or antitumoral agents.[10]

Over the years, various PAA-transition metal complexes have been prepared by our research group, most of them through the insertion of a phenanthroline pendant derived from 4-aminobutyl-1,10-phenantroline (BAP), whose structure is shown in Scheme 1, into the PAA structure.

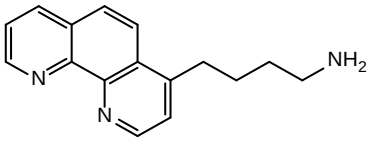

Scheme 1. *Structure of the 4-aminobutyl-1,10-phenantroline (BAP), previously used by our research group to prepare various PAA-transition metal complexes.*

The first, Re-ISA23SH (see the upper structure of Scheme 2A), was prepared as a radiopharmaceutical agent for applications in diagnostics involving the $^{186/188}$Re γ/β emitters.[11] It showed an excellent biocompatibility both in vitro (no toxic effect was recorded on HeLa cells for doses up to 100 ng/mL), and in vivo, tested on mice models in doses up to 20 mg/kg without any toxic sign.[11] The same Re-containing polymer was also used to coat superparamagnetic iron oxide nanoparticles to obtain a

bifunctional imaging probe with an active cancer targeting, to be used in MRI or SPECT that could also be exploited in radiotherapy.[12]

Starting from the same main monomer of the ISA23SH copolymer, PhenISA was then prepared by introducing the phenanthroline pendant, and this polymer was used to form Re, Ru and Ir complexes with a general structure schematized in the lower part of Scheme 2A (respectively named Re-PhenISA and Ru-PhenISA) and in Scheme 2B (Ir-PhenISA). The complexation of Ru and Re by PhenISA produced stable, water soluble and highly luminescent complexes to be used for imaging application, being them easily internalized by HEK-293 cells (a human embryonic kidney cell line) through an endocytic pathway and escaping across the vesicular membrane with the pH reduction inside the endosomes to spread homogeneously in the cytosol without any cytotoxic effect for doses up to 50 μM.[13] Polyamidoamines dendrimers (PAMAMs), i.e. highly branched polymer with a chemical structure similar to that of linear PAAs and a globular shape,[10] are indeed known to disrupt and escape endosomes by the proton sponge effect when their pH drops from 7 to 5.5.[1] This effect consists of the increase in the ionic concentration in the endosome due to an influx of Cl^- anions with pH reduction, causing its osmotic swelling together with the expansions of the polymeric network because of the internal charge repulsion.[14]

Ir-PhenISA complex was tested as a PS for $^1O_2$ production in PDT, yielding to a water-soluble cell staining agent easily internalized by HeLa cells and excited with two-photon absorption (TPA), and with improved photophysical properties compared to the analogue $[Ir(ppy)_2(phen)]^+$ complex, even though it showed a bit lower efficiency in $^1O_2$ production and cellular death via apoptosis after irradiation. However, the necrotic death of cells resulted reduced as well, suggesting that the Ir coordination to PhenISA allowed to avoid significant cell damaging that the complex alone possessed.[15] Given the good results obtained using Ir-PhenISA for PDT, Ru-PhenISA was tested as well, both its internalization and photocytotoxicity resulted lower compared to the analogous $[Ru(phen)_2(BAP)]^{2+}$ complex.[16]

On the other hand, the Ru complex of a PAA polymer with a different structure, named Ru-PhenAN and schematized in Scheme 2C, resulted in a highly promising PS for PDT: it showed an increased cell death via apoptosis after the irradiation when compared to $[Ru(phen)_2(BAP)]^{2+}$, with a light EC_{50} value (i.e. the dose required to reduce cell viability to 50%) of 0.7 μM (vs 9 μM for the free complex).[16] Additionally, Ru-PhenAN was found to escape the endolysosomal internalization pathway upon irradiation and accumulate at the nuclear level, which would possibly cause its higher photocytotoxicity.[17] However, the main drawback of PhenAN was the difficult multi-step synthesis required to obtain the BAP molecule, starting from the expensive 4-methyl-1,10-phenantroline, and thus in this work we developed a new synthetic route to obtain a PAA analogous to PhenAN, that we named PhenVS and in which the phenanthroline moiety derives from a more easily obtained molecule, phen-cysteamine, as will be extensively discussed in the next section “Results and Discussion”.

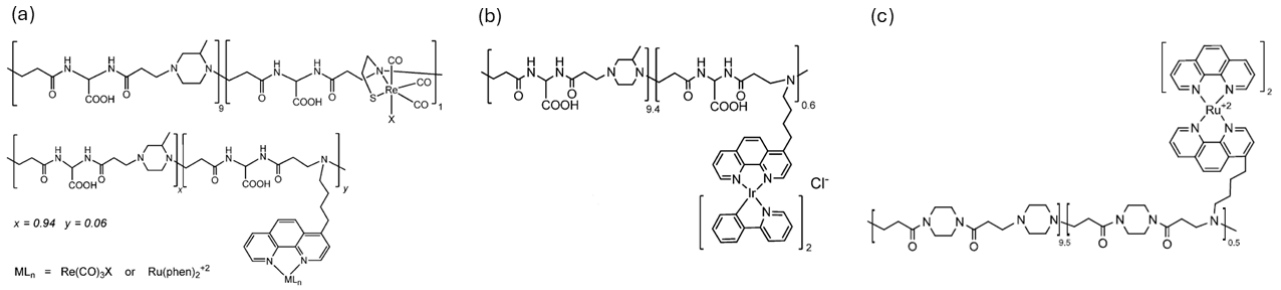

Scheme 2. *Structures of the PAA-transition metal complexes prepared by our research group: (a) $Re(CO)_3$-ISA23SH and ML_n-PhenISA (with ML_n = $Re(CO)_3X$ and $Ru(phen)_2^{2+}$. From Ref. 13 (b) $Ir(ppy)_2$-PhenISA. From Ref. 15 (c) $Ru(phen)_2$-PhenAN. From Ref. 16*

Metal Enhanced $^1O_2$ generation (ME$^1O_2$)

As already discussed in the Introduction chapter on gold nanostars, Localized Surface Plasmon Resonance (LSPR) is a key optical property of metal nanoparticles, consisting of the coherent oscillation of the free electrons of the NP with the incident light. This oscillation produces a strong localized electromagnetic field in the nanoparticle surroundings, that increases the absorption and emission cross section of the molecules in close proximity, yielding to a phenomenon called Metal Enhanced Fluorescence (MEF). In particular, the fluorescence enhancement is recorded when the fluorophore is 5-90 nm from their surface, even though there are some inconsistencies in the literature regarding the optimal distance. However, when the fluorophore is in direct contact with or too close (less than 5 nm) to the nanoparticle, the quenching of its emission prevails, due to the dipole energy around the nanoparticle that reduces the ratio between radiative/non-radiative decays and the fluorescence quantum yield.[18-21] MEF occurs due to coupling to the plasmonic structure, which produces the re-radiation phenomenon, i.e. the transfer of the near field to the far field at the fluorescence frequency.[22] The re-radiation rate depends on the absorption and scattering cross sections of the nanoparticle at the emission wavelength, as the band overlap determine whether the dominant effect is the Forster Resonance Energy Transfer (FRET), for fluorophore-NP distances of ca. 10 nm, or the Purcell Effect, when the separation is larger (10-50 nm).[19,22] Another important parameter is the shape and size of the nanoparticle, being the local electromagnetic field produced by the LSPR stronger around sharp corners and edges.[21]

Analogously, the Metal Enhanced Phosphorescence (MEP) and Metal Enhanced $^1O_2$ generation (ME$^1O_2$) might occur as the enhanced absorption produced by the closeness to the metal nanostructure can facilitate both an enhanced S_1 fluorescence and the intersystem crossing, with the consequent population of the T_1 state with a higher yield. The highly populated triplet state can both enhance the phosphorescence emission and increase the yield in $^1O_2$ generation, provided that the luminophore

sensitizes its production.[23] In Figure 3 the Jablonski diagram describing the possible mechanisms of MEF, MEP and ME$^1O_2$ is schematized.

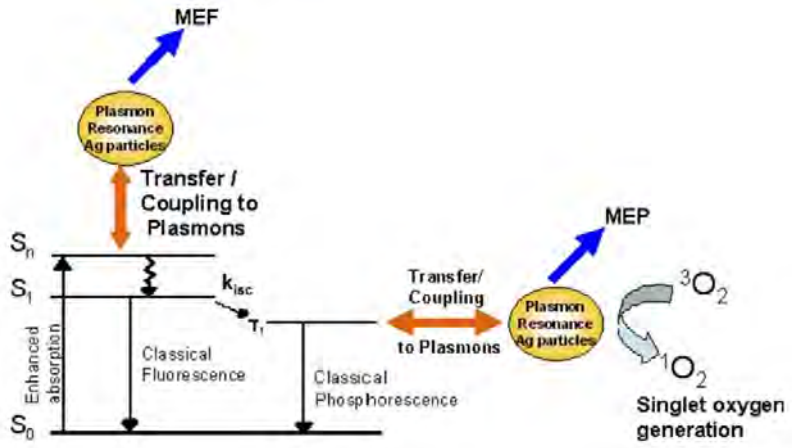

Figure 3. *Schematization Jablonski diagram for Metal Enhanced Fluorescence (MEF), Metal Enhanced Phosphorescence (MEP) and Metal Enhanced $^1O_2$ generation (ME$^1O_2$). From Ref. 23*

Gold and silver nanoparticles are widely reported for applications based on MEF, MEP and ME$^1O_2$ among the metal NPs, mainly due to their high quality factor (Q), i.e. the strength of the generated surface plasmon, directly linked to the enhancement of the electromagnetic field and of the MEF and MEP factors.[19] However, due to the higher chemical stability and easiness of Au functionalization, AuNP are considered ideal delivery systems for carrying photosensitizers for $^1O_2$ production. Their use is not limited to the spherical shape, as anisotropic shapes like nanorods, nanostars and nanoclusters are used in the literature for this purpose.[23,24]

Thus, $^1O_2$ yield can be adjusted by the same parameters that influence MEF and MEP: the distance between the photosensitizer and the nanoparticle, the shape and size of the nanoparticle and the emission wavelength of the photosensitizing molecule.[23] Regarding ME$^1O_2$ some authors have also observed an inverse relationship between the singlet oxygen enhancement factor and the singlet oxygen quantum yield of the free molecule, in agreement with what observed for MEF, even though tracing a general trend is not possible.[22,25]

Moreover, some works[26] claim that noble metal nanoparticles (of Ag, Pt and Au) are able to generate $^1O_2$ per se, without the presence of any organic nanoparticles, through an energy transfer directly from the nanoparticle to the oxygen molecule.

Given this background, this work aimed at the functionalization of GNS with a PAA-Ru complex to explore and exploit the enhancement in $^1O_2$ production by the gold nano-objects to improve its features as a photosensitizer for PDT, choosing Ru-PhenAN based on the great results obtained in our previous work, as described in the previous section. However, we slightly modified the polymer structure, attempting a different procedure to easily obtain a phenanthroline with a similar functionalization

(phen-cysteamine) given the costly and multi-step procedure required to synthetize the functionalized phenanthroline (BAP) in the PhenAN polymer.

Results and discussion

Preparation of the Ru-PhenVS polymer

Synthesis of 5-(2-aminoethanesulfanyl)-1,10-phenanthroline (phen-cysteamine)

The first synthetic step in the preparation of the Ru-PhenVS complex polymer consisted of the preparation of a phenanthroline substituted with a pendant bearing a terminal amino group, as schematized in Scheme 3. The amino functional group is indeed necessary for the incorporation of the free phenanthroline into the polyamidoamine chain as for the preparation of the previous polymer PhenAN, where, as described in the Introduction, the substituted phenanthroline was achieved by an expensive starting precursor. For this reason, we moved to an easier and cheaper pathway to obtain 5-(2-aminoethanesulfanyl)-1,10-phenanthroline (phen-cysteamine), an analogously amino-substituted phenanthroline depicted in Scheme 3.

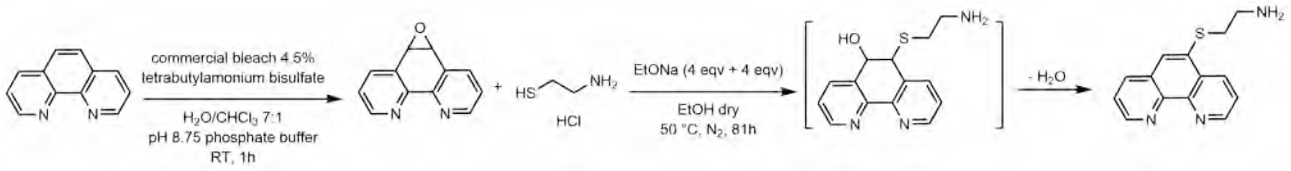

Scheme 3. *Synthetic route followed to prepare the phen-cysteamine, as a first step of the preparation of the phenAN polymer.*

The starting point was the oxidation of the central ring of 1,10-phenanthroline to obtain an epoxide that could be easily opened in the following step. This first step, taken from the literature,[27] involves the use of commercial bleach in an aqueous/$CHCl_3$ biphasic environment, in which the phase transferring agent tetrabutylammonium bisulfate allows the reaction to proceed. The control of the pH plays a crucial role in the epoxidation and directs the outcome toward the desired product rather than one of the possible byproducts: accordingly to the literature,[28] the epoxide is the only product when the pH of the solution is fixed around 9. At lower but still basic pH, it is obtained in a mixture with the 5,6-dichloro- and 5,6-dihydro-1,10-phenantroline, while when the pH is below 7 the only products obtained are the dichloro derivative together with two of its oxidation products (5,5-dichloro-6-oxo-1,10-phenanthroline and 5,6-dioxo-1,10-phenanthroline). The different products and byproducts of this reaction depending on the pH are schematized in Scheme 4.

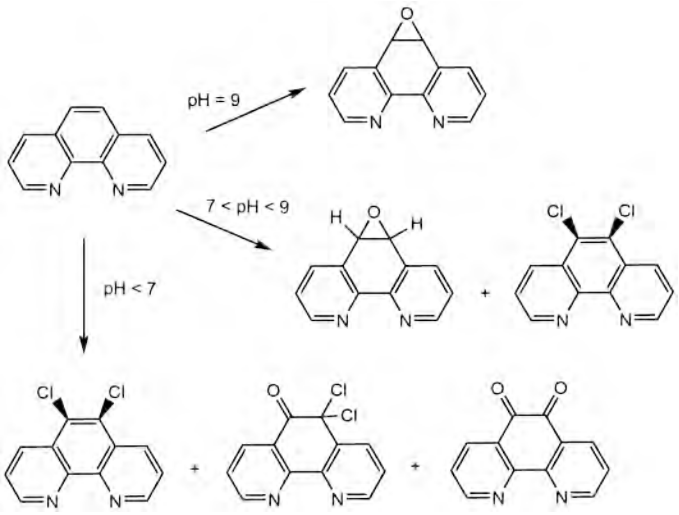

Scheme 4. *The different products of the epoxidation reaction at different pH ranges.*

The ^{1}H NMR spectrum (Figure 4) recorded after the washes and the trituration with Et_2O shows the epoxide as the only product obtained. A second set of signals is assigned to the unreacted phenanthroline, which accounts for only 1% in moles of the main product. Thus, the product was used for the following steps without any further purification.

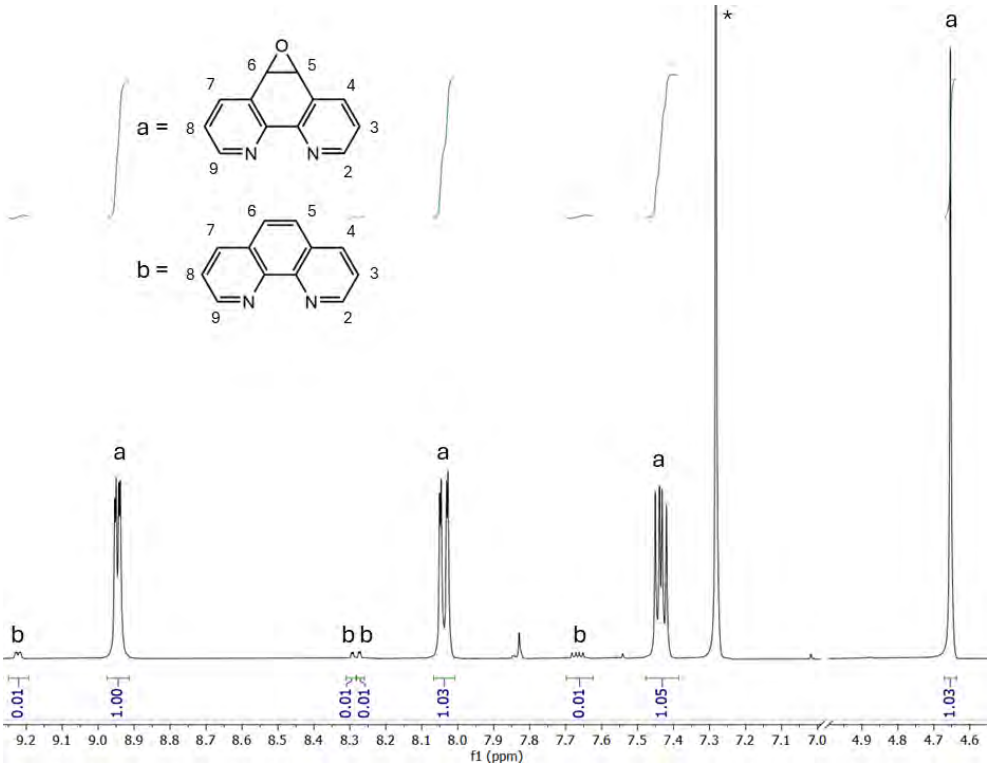

Figure 4. *^{1}H NMR (9.4 T, 300 K, $CDCl_3$) of the purified product of the epoxidation reaction. In the spectrum, the only visible product is 5,6-epoxy-1,10-phenantroline (signals marked with a), as expected when the reaction is carried out at pH ca. 9. The second set of signals (marked with b) is attributed to the unreacted phenanthroline, while * marks the signal of the solvent.*

The epoxy-derivative was then exploited to further functionalize the central ring of the phenanthroline with a linear molecule exposing a terminal amino group, as it promptly reacts with a wide range of

nucleophiles, such as thiols, leading to the opening of the ring and the restoration of the aromaticity of the central ring through dehydration. The reaction was carried out in anhydrous EtOH under N_2 atmosphere, using an excess of EtONa (4 eqv).

After a total of 81 h of reaction time and the addition of another 4 equivalents of EtONa, the mixture was filtered to remove the excess of EtONa, dried and precipitated from $CHCl_3$/hexane. The ^1H NMR spectrum of the obtained powder (Figure 5) showed the full conversion of the starting epoxy-derivative and a full re-aromatization of the central ring of the phenanthroline. For this reason, we decided not to purify the product further and to use it as it was to prepare the PhenVS polymer.

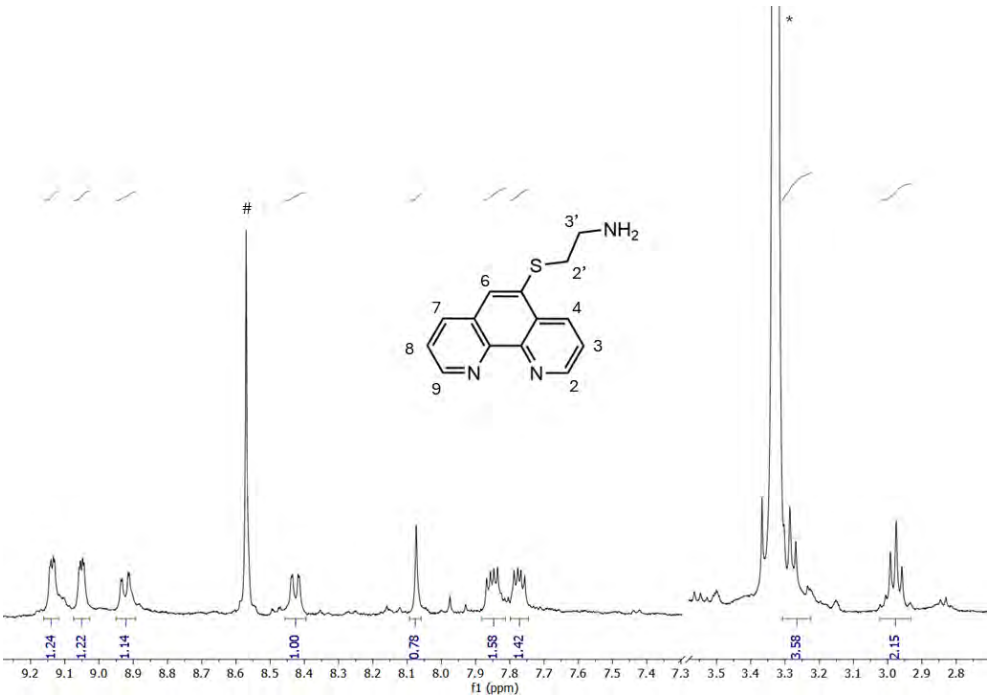

Figure 5. *^1H NMR (9.4T, 300 K, MeOD) of the crude phen-cysteamine. From the spectrum the molecule appears fully reacted and re-aromatized. The solvent, marked with *, is partially overlapped with one of the aliphatic signals of the product, while the # marks an impurity present in the dry EtOH used.*

Synthesis of the PhenVS polymer

The PhenVS polymer was prepared following a Michael addition procedure, which is the usual way to synthesize the polyamidoamines and already employed by our group for the preparation of a very similar polymer named PhenAN (already discussed in the Introduction part and whose structure is shown in Scheme 6 in the next section).[16] The main involved polymerization reagent is the 1,4-bisacryloylpiperazine, which reacts with piperazine and phen-cysteamine to obtain a linear copolymer. As the secondary diamine reacts faster, the functionalized phenanthroline was first treated with a large excess of bisacrylamide for one day, and the piperazine was added later to the reaction mixture to obtain a good distribution of the phenanthroline moiety in the polymeric chain, as suggested by the literature.[29] A schematization of the synthetic route is represented in the following Scheme 5.

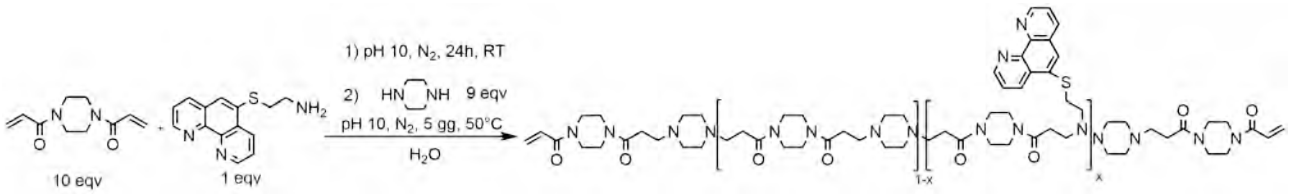

Scheme 5. *Synthesis followed to prepare the PhenVS polymer. The x values for the two batches prepared are reported in the last column of Table 1.*

Two batches of PhenVS were prepared using slightly different reaction times. The obtained polymers differed in their length and the % of the phenanthroline moiety. The concentration of the reagents at the beginning of the reaction was the same, but during the preparation of batch A, despite the sealed Schlenk used for the reaction, the bubbling of the N_2 to assure the inertness of the environment was strong enough to evaporate the small amount of water, replaced more than once with fresh H_2O which could not completely solubilize the reagents. Thus, their actual concentration resulted uncertain and varied during the reaction time. On the other hand, during the preparation of batch B, the mixture solidified and 0.5 mL of water were added to dissolve the reagents again, decreasing their concentration.

This is probably the main reason for the differences in the obtained polymer, as reagent concentration plays a strategic role in this synthesis, as well as temperature modulation. A higher monomer concentration is indeed correlated to a higher molecular weight of polyamidoamine, while a higher temperature increases the reaction rate but tends to limit the molecular weight to a lower maximum value.[29]

In both cases, the reaction was stopped with the addition of an HCl solution to decrease the pH to 3 diluting the reaction mixture to 5 mL.

Table 1. *The first two columns list the phen-cysteamine concentration and reaction time of the phenVS synthesis, while the last two columns report the molecular weights (Mw) of the obtained polymers and the molar % of the minor repeating unit containing the phenanthroline moiety.*

Batch	Starting [phen-cysteamine] (M)[i]	Reaction time (days)	Mw (kDa)	Mn (kDa)	% mol phenanthroline[ii]
A	0.149	2 (step 1) + 7 (step 2)	15.21	4.44	3
B	0.154	1 (step 1) + 6 (step 2)	4.99	1.98	2

After the reaction, batch A was recovered by ultrafiltration by centrifugation using a 3 kDa cutoff filter, while batch B was diluted to 50 mL and filtered using a 1 kDa cutoff membrane.

[i] Concentration of the phen-cysteamine reagent at the beginning of the reaction. The concentration of the other two reagents is easily calculated by multiplying this number by 10 (for 1,4-bisacryloyl piperazine) or 9 (piperazine).
[ii] This value represents the x in Scheme 5

The ^{1}H NMR spectra (Figure 6) of the two freeze-dried polymers show that in both cases the phenanthroline was successfully included into the polymeric chain. The molar % content of phenanthroline, whose value for each batch is presented in Table 1, is calculated from the ratio between one of the aromatic signals and the aliphatic signals between 3.0-3.75 ppm. Notably, even though the different substitution procedure to obtain the phenanthroline bearing a pendant with a terminal -NH_2 simplified the reaction in terms of both costs and number of synthetic steps, it resulted in a slightly shorter pendant (S and two CH_2 instead of four CH_2). This unfortunately reduced the efficiency of the phenanthroline incorporation in the PhenVS polymer, resulting in 2-3 % in moles instead of the 4.5-5 % obtained for PhenAN.[16]

Moreover, the spectrum depicted in Figure 6B shows two small signals between 5.0-5.5 ppm assigned to the terminal C=C double bonds in the polymeric chain. These bonds must be saturated before using this polymer with cells, as they are cytotoxic to a certain extent. Interestingly, these signals are not visible in batch A (Figure 6A), indicating that the ratio of these protons is significantly lower, and thus the polymeric chain is longer. Because of the absence of these signals and the smaller amount of polymer produced, we decided not to saturate the terminal bonds before testing batch A on cells.

A portion of the freeze-dried polymer was used for its characterization with Size Exclusion Chromatography (SEC). The Mw and Mn values for the two batches are reported in Table 1 and reflect the discussion above regarding the reagent concentration during synthesis.

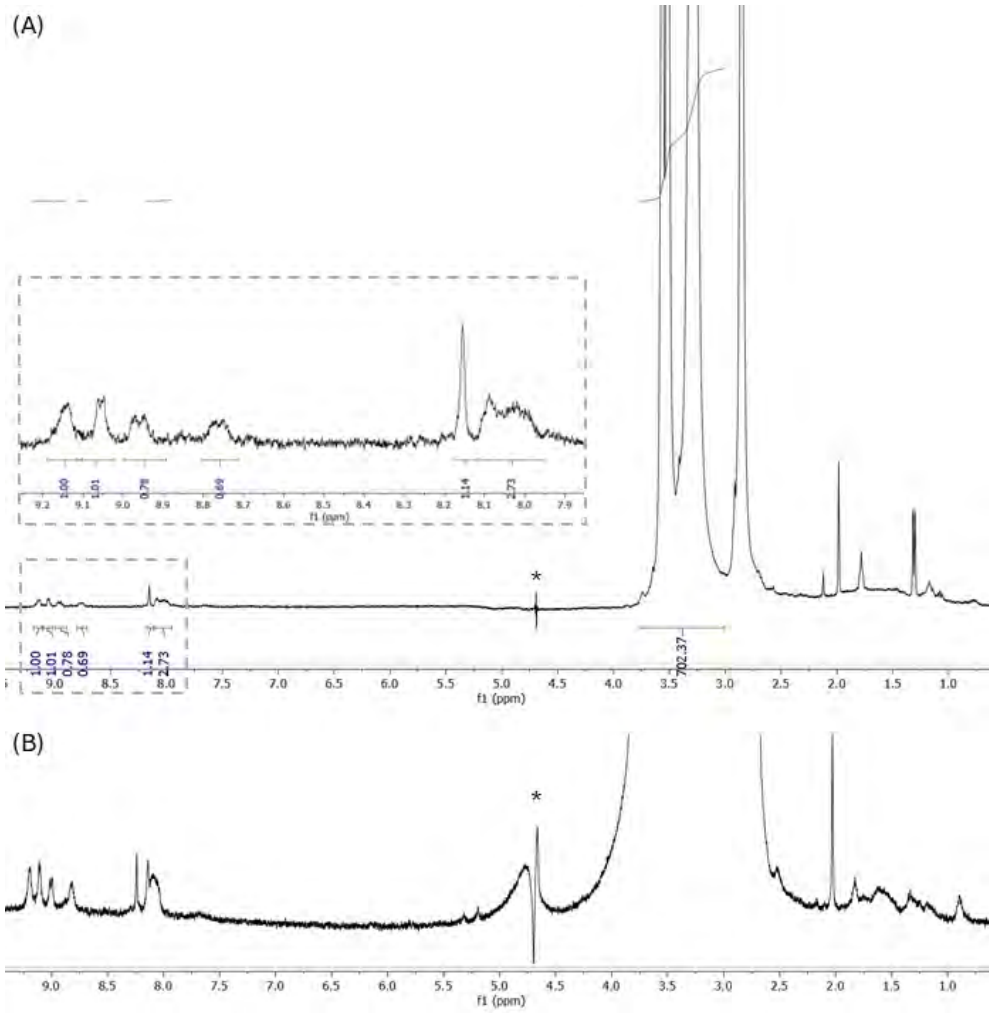

Figure 6. *^{1}H NMR (9.4T, 300 K, D_2O) of the freeze-dried PhenVS. The * marks the suppressed signal of the solvent (A) Batch A. The insert shows a magnification of the aromatic signals attributed to the phenanthroline moiety, whose attribution is analogous to the spectrum shown in Figure 5. From the ratio between the aromatic signals and the most intense aliphatic signal between 3.0-3.75 ppm it is possible to calculate the molar % of phenanthroline. (B) Magnification of the spectrum of batch B. The two signals assigned to the protons of the terminal double bonds of the polymeric chain are visible between 5.0 and 5.5 ppm.*

Synthesis of the Ru (II) complexes: Ru-PhenVS and [Ru(phen)$_2$(phen-cysteamine)]$^{2+}$

PhenVS copolymer was then reacted with a Ru(II) precursor to give rise to its complexation by the free phenanthroline pendent present in the polymer chain. The reaction was carried out heating through microwave irradiation after the addition of an equimolar amount of Ru(phen)$_2^{2+}$ precursor (with either Cl^- or OTf^- as counterions) with respect to minority part of the repeating units containing the phenantholine (2-3% of the whole polymer), following the protocol schematized in Scheme 6A, similar to the one our group previously used to prepare Ru-phenAN.[16]

The heating process was divided into 15-minute slots, to control the pH and possibly correct it by adding HCl to maintain it between 6 and 7 and so maximizing the ability of the phenanthroline to complex the metal moiety avoiding the formation of the neutral dihydroxide derivative [Ru(phen)$_2$(OH)$_2$], which is

promptly formed at higher pH. Moreover, the luminescence was checked under a UV lamp to monitor the progress of the reaction, as the Ru precursor is not luminescent as well as the byproduct $[Ru(phen)_2(OH)_2]$, hence its presence would be due only to the formation of Ru-PhenVS.

The last synthetic step, carried out only on the shorter Ru-PhenVS (derived from batch B of PhenVS), was the saturation of the terminal double bonds of the polymeric chain with morpholine. The choice of this molecule was based on the literature, in which it is ascribed as a targeting group for lysosomes, a strategic target for PDT agents since they are fundamental in cell survival and apoptosis, which occurs when the lysosomal membrane is disrupted, causing the leakage of protons and hydrolases in the cytosol.[30-33]

The reaction was performed in water at pH 3 and room temperature, as shown in Scheme 6B. After three days under stirring, the solubilized polymer was filtered through ultrafiltration to remove the morpholine excess. Then it was lyophilized, obtaining batch B of Ru-PhenVS used for the biological investigation and to functionalize part of the GNS using the layer-by-layer strategy, as described in the following sections.

The NMR spectrum of the polymer, reported in Figure 7, confirmed the success of the step, from the disappearance of the signals between 5.0 and 5.5 ppm, assigned to the terminal double bonds, and the appearance of two new signals, partially overlapped with the aliphatic backbone of the polymer, whose chemical shifts are compatible with those reported in the literature for the free molecule.

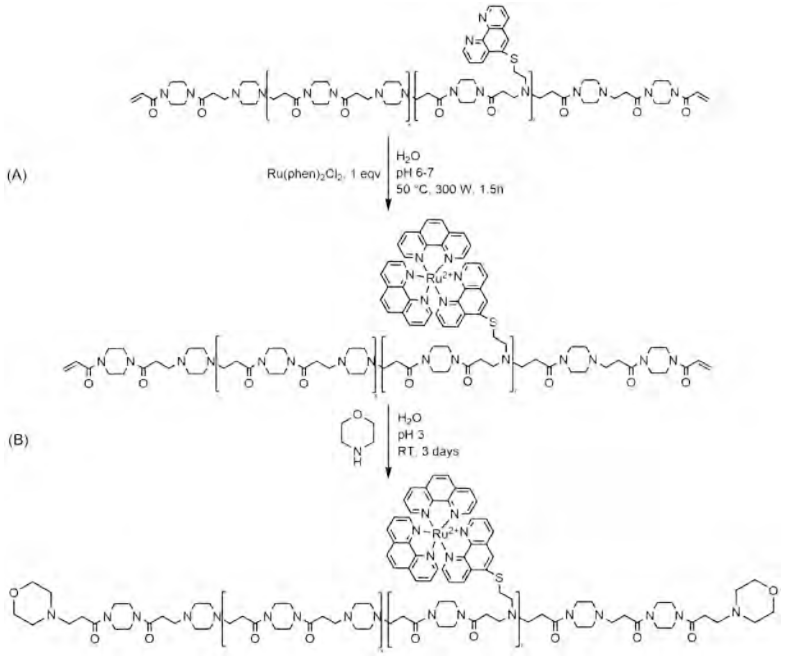

Scheme 6. *Synthetic route for the preparation of the Ru-PhenVS complex and the saturation of the terminal double bonds of the polymer with morpholine.*

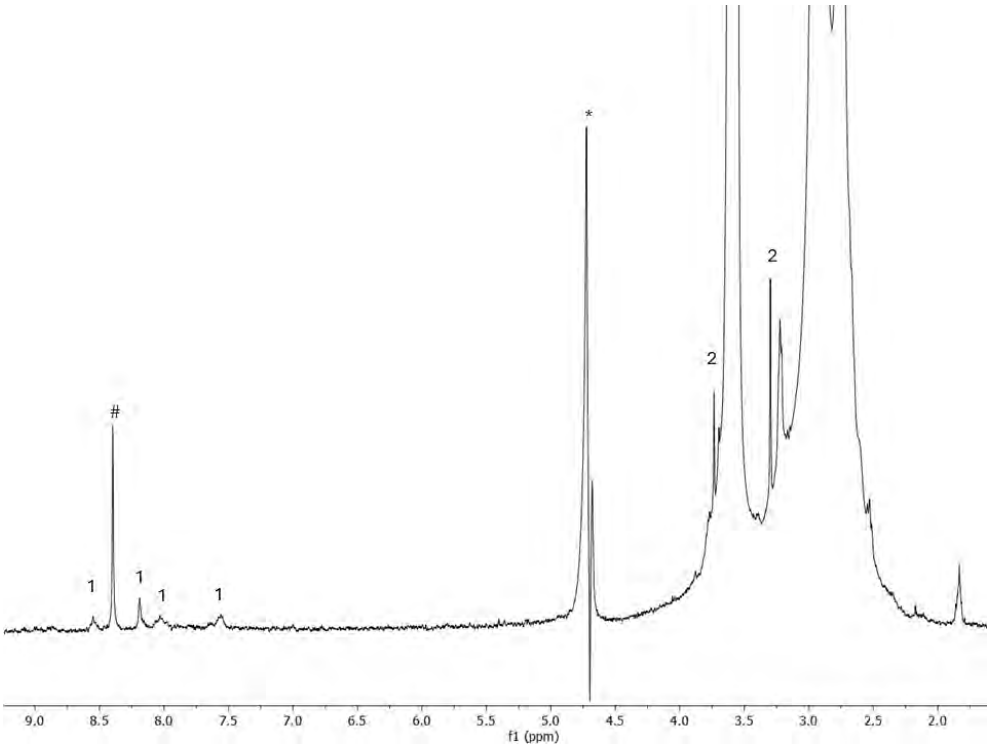

Figure 7. *^{1}H NMR (9.4T, 300 K, D_2O) of the freeze-dried Ru-PhenVS-morpholine. The * marks the suppressed signal of the solvent and # an impurity present in the dry EtOH used during the synthesis of phen-cysteamine. The signal set marked with 1 is assigned to the ancillary phenanthroline ligands of the Ru (II) complex and those marked with 2 to the terminal morpholine groups.*

The analogous Ru(II) complex, bearing the free phen-cysteamine instead of PhenVS as the third ligand, was prepared to check how the photophysical properties are influenced by the presence of the sulfur atom in the α-position of the central phenanthroline ring, in comparison to the already prepared and characterized $[Ru(phen)_2(BAP)](OTf)$.[1] The complex was prepared according to the procedure shown in Scheme 7, by reacting in D_2O the $Ru(phen)_2Cl_2$ precursor with one equivalent of phen-cysteamine.

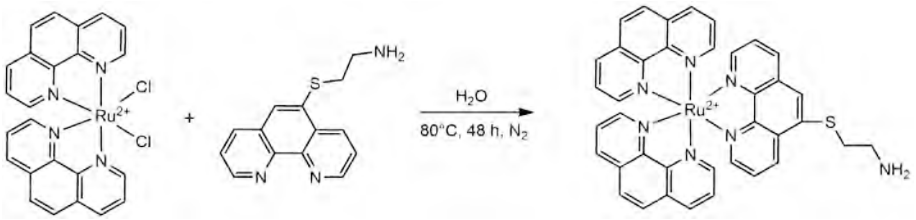

Scheme 7. *Synthesis of the analogue Ru (II) complex using the sole phen-cysteamine as the third ligand.*

The reaction was monitored by checking the increasing luminescence of the product under irradiation at 365 nm and by ^{1}H NMR spectroscopy (Figure 8), monitoring the simultaneous disappearance of the signals attributed to phen-cysteamine and the appearance of new peaks, indicating the complexation of the third cyclometalled ligand. Finally, the complex was purified by precipitation and the final $[Ru(phen)_2(phen\text{-}cysteamine)](PF_6)_2$ was characterized by NMR (Figure 9).

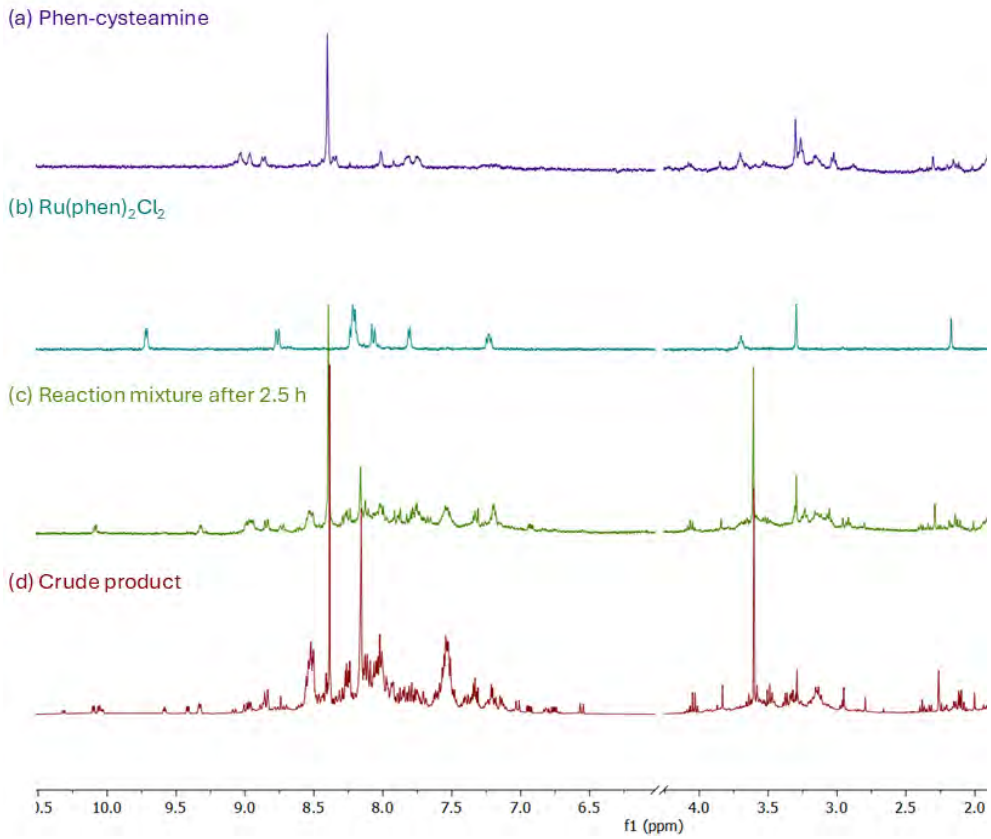

Figure 8. *^{1}H NMR (9.4T, 300 K, D_2O) of phen-cysteamine (a), the $Ru(phen)_2Cl_2$ precursors (b), the reaction mixture after 2.5 h of reaction (c) and the crude product (d).*

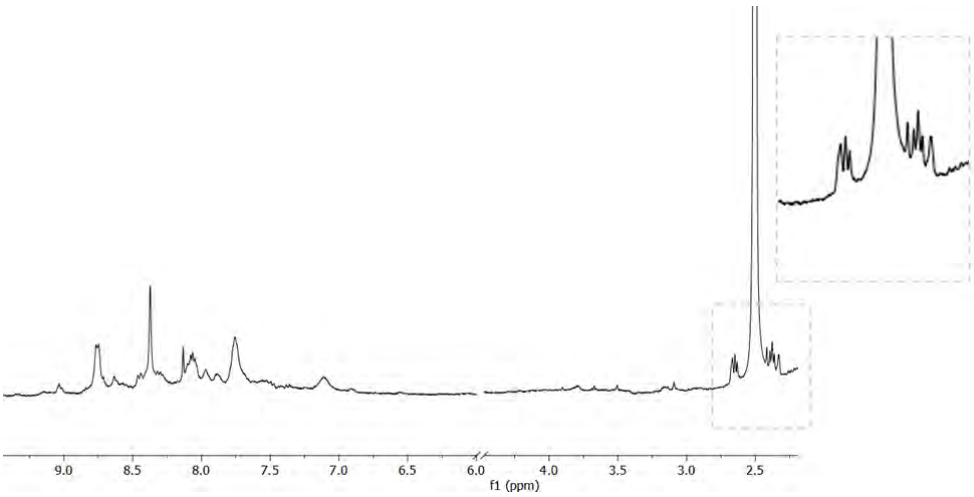

Figure 9. *^{1}H NMR (9.4T, 300 K, DMSO-d_6) of $[Ru(phen)_2(phen\text{-}cysteamine)](PF_6)_2$.*

The absorption, excitation and emission spectra of the two Ru complexes are shown in Figure 10, while in Table 2 their photophysical properties are listed and compared to those of the analogous Ru complex containing 4-(4'-aminobutyl)-1,10-phenanthroline (BAP) as the third ligand and of Ru-PhenAN. The different phenanthroline substituent containing a sulfur atom slightly influences the emission wavelength of the complex, resulting in just a 3 nm red shift. In a study on Cu(I) complexes containing substituted phenanthrolines as one of the ligands,[34] the authors observed in apolar solvent a ca. 15 nm

red shift in the emission wavelength moving from a methyl-substituted phenanthroline (-Me) to a -SMe substituted one (substitutions in positions 2 and 9 of the phenanthroline). They also studied the influence of this substitution in other positions (3,8 and 4,7), which resulted in a larger red shift both in apolar and polar solvents. Anyhow, the presence of substituents in positions 5 and 6 influences the electronic properties of phenanthroline, but less strongly compared to positions 3,8 and 4,7.[35] Moreover, the emission wavelength of the Ru complex appears slightly blue-shifted when the complex is incorporated into the polymer structure, with a parallel increase in both the lifetime (τ) and the photoluminescence quantum yield (PLQY). This behavior, explained by the more rigid surrounding of the complex when inside the polymer, is similar to what observed moving from $[Ru(phen)_2(BAP)](OTf)_2$ to Ru-PhenAN with a more important increase of τ and PLQY due to the shorter pendant that the $[Ru(phen)_2(phen\text{-}cysteamine)](PF_6)_2$ complex possess and that keeps the complex more blocked inside the polymer aggregates in solution.

Moreover, the MLCT absorption and excitation bands of the two Ru complexes containing a phen-cysteamine (or the derived polymer) as one of the ligands peaks at the same wavelength, in the 350-500 nm range. Both spectra show under 300 nm the absorption and excitation bands attributed to the phenanthrolines that, in the Ru-PhenVS absorption spectrum, are overlapped with the LC transitions of the amide groups of the polymer backbone. In this last spectrum, the MLCT absorption band is slightly visible due to the scattering caused by the polymer aggregated in the solution.

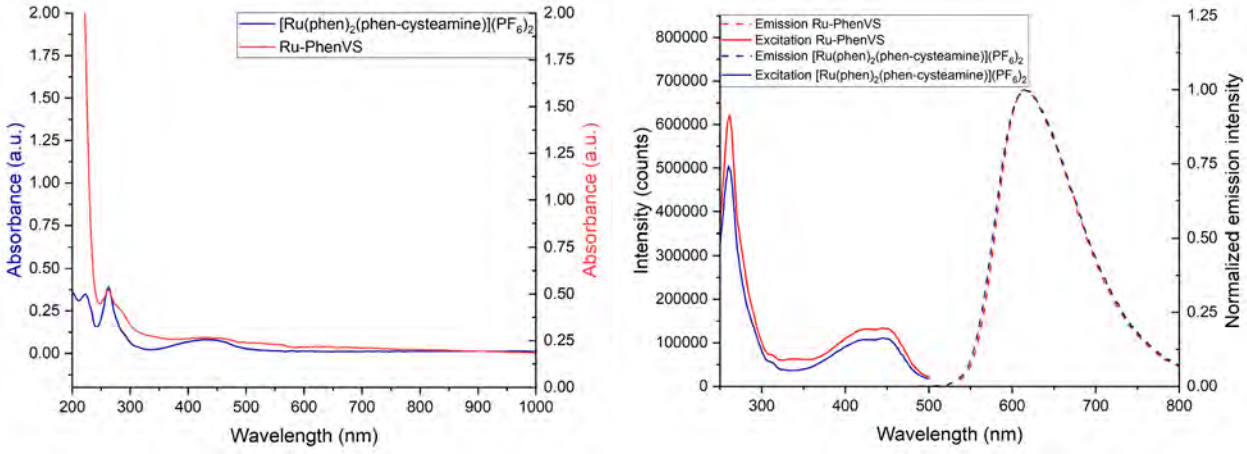

Figure 10. *Left panel: UV-vis absorption spectra of $[Ru(phen)_2(phen\text{-}cysteamine)](PF_6)_2$ (in blue) and Ru-PhenVS (in red) in water. Right panel: UV-vis excitation (full lines) and emission (dashed lines) spectra of $[Ru(phen)_2(phen\text{-}cysteamine)](PF_6)_2$ (in blue) and Ru-PhenVS (in red), measured in water at RT.*

Table 2. *Photophysical properties (measured in aerated water at RT) of the Ru complexes containing phen-cysteamine or BAP as the third ligand and of the respective Ru-PhenVS or Ru-PhenAN copolymers.*

Complex	λ_{exc} (nm)	λ_{em} (nm)	τ (ns)	Φ (%)
$[Ru(phen)_2(phen\text{-}cysteamine)](PF_6)_2$	427-446	615	598	1.9
Ru-PhenVS	425-445	613	754	4.2
$[Ru(phen)_2(BAP)](OTf)_2$ [iii]	425-446[iv]	612	492	2.5
Ru-PhenAN [iii]	419-448[iv]	608	533	3.6

Functionalization of gold nanostars with Ru-PhenAN/Ru-PhenVS

Ligand exchange between Triton X-100 and Ru-PhenAN

For the functionalization of gold nanostars (GNS) with the Ru-PhenVS polymer, various approaches were followed. The first attempt consisted of a ligand exchange between the Triton X-100 surfactant (TX-100), which stabilizes the GNS in the synthesis that we followed,[36] and the Ru-PhenVS, exploiting the weak interactions between the gold surface and the amino groups of the piperazine moieties and carbonyl groups of the amide ones present in the polymer structure. Three different Au:polymer mass ratios were tested, equal to 1:0.35, 1:1.5 and 1:3.45.

In this first approach, a batch of Ru-PhenAN previously prepared by our research group was used, whose structure is slightly different from the one described in the paragraph above (see introduction). The polymer differs in the aliphatic chain that links the phenanthroline moiety to the backbone, which is slightly longer in this case since it consists of four -CH_2-. The structure of the polymer is depicted in the following Scheme 8.

[iii] Data taken from Ref. 16

[iv] The values listed show the absorption wavelengths rather than the excitation ones showed for the other two complexes

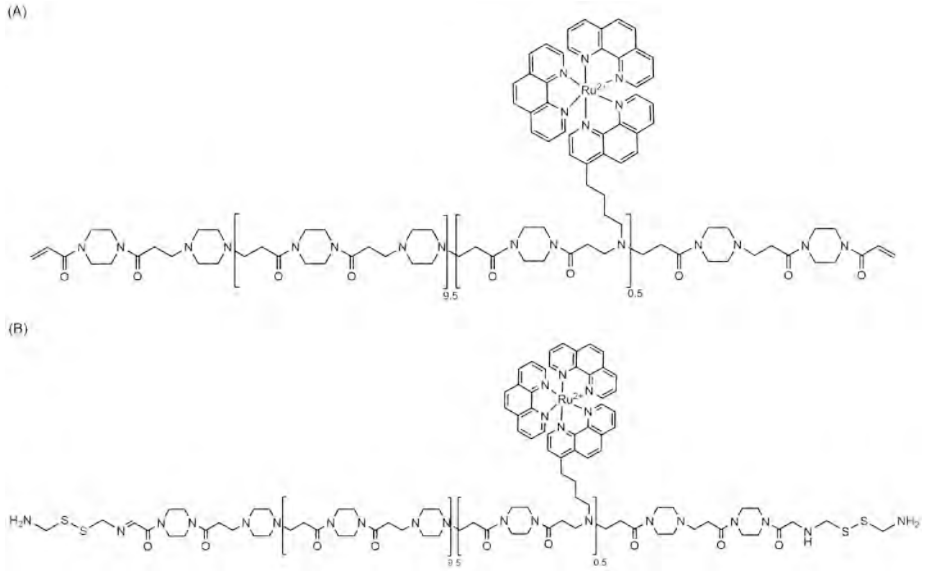

Scheme 8. *Structures of the Ru-PhenAN polymer used in the attempt at GNS functionalization via ligand exchange. (A) with unsaturated terminal double bonds and (B) after the saturation of the terminal double bonds with cystamine*

The freshly prepared GNS@TX-100 were functionalized with the polymer (Scheme 8A) through an overnight interaction at RT, followed by separation through centrifugation of the GNS forming a easily re-suspendable pellet and of TritonX-100 and the possible excess of Ru-phenAN, which remained in the supernatant. Then additional centrifugation cycles were performed to wash the sample properly, replacing the old supernatant with fresh milliQ water until the complete disappearance of the TX-100 foam and its relative UV-vis absorption bands. The re-suspendability of the GNS after multiple centrifugation cycles was used as a first macroscopic indicator of the success in their stabilization with Ru-PhenAN polymer.

The obtained GNS@Ru-phenAN samples were then characterized through DLS and ζ-potential measurements and UV-vis spectroscopy.

DLS measurements

The DLS measurements (Figure 11) gave a first insight into the stabilization of the GNS by different amounts of polymer. Of the two populations distinguishable for the GNS@TX-100 sample, the smallest one (slightly bigger than 10 nm) is assigned to the excess of Triton X-100 residual of the synthesis and fundamental to stabilize the unfunctionalized GNS, while the biggest one (ca. 100-150 nm depending on the synthesis) is assigned to the actual GNS.

The hydrodynamic size of GNS measured shifts from 142 (± 62) nm to 220 (± 47) nm for the 1:0.35 ratio and to 156 (± 45) nm for the 1:3.45 ratio.[v] It is thus noticeable that larger amount of Ru-phenAN added

[v] The size values are here reported as the maximum of the peak assigned to the population, using the half of the full width at half maximum (HWHM) of the peak as the standard deviation for the size value.

corresponds to a less shifted peak compared to the pristine GNS, which could depend on a lower aggregation state of the GNS, as also suggested by the absence of the small peak between 1000 and 10000 nm. This is particularly true for the 1:3.45 ratio sample, in which the size remained about the same after the functionalization. The 1:1.5 ratio sample was not taken into account in this comparison since it was prepared and from another batch of GNS@TX-100, with a different dimension. We thus proceeded to study the differences in ζ-potential between GNS@TX-100 and GNS@Ru-PhenAN only for the highest ratio, since we considered it to be the best one in stabilizing the GNS.

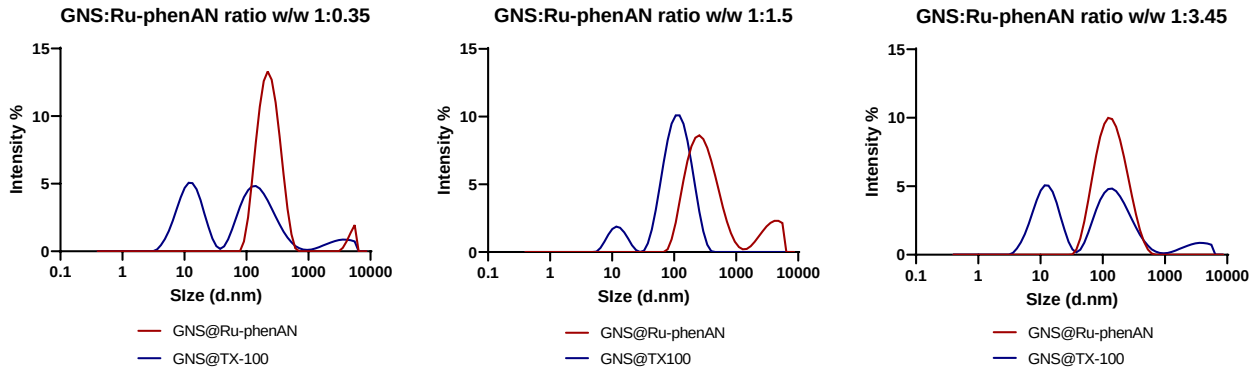

Figure 11. *DLS of GNS before (blue line) and after (red line) their functionalization with Ru-phenAN polymer by ligand exchange, using three different mass ratios of Au:polymer (from left to right: 1:0.35, 1:1.5 and 1:3.45).*

ζ-potential measurements

In Figure 12, ζ-potential measurements at various pH are reported for the two samples. For GNS@TX-100, ζ-potential values are around neutrality becoming slightly negative at the higher pH, in agreement with the non-ionic character of the surfactant and its poor ability to interact with the Au surface that, hence, leave room to the increasingly higher amount of OH^- to cover the Au surface to some extent.

When GNS are instead functionalized with the cationic Ru-PhenAN, the ζ-potential of the suspension is strongly positive at low pH and drops to a slightly negative value at high pH, in agreement with the pK_a values of the polymer (pK_{a1} = 3.35; pK_{a2} = 7.40).[16] The great difference between the two samples, especially at acidic pH, further supports the success in the stabilization of GNS by Ru-PhenAN and helps in the characterization of GNS functionalized with this kind of polymer.

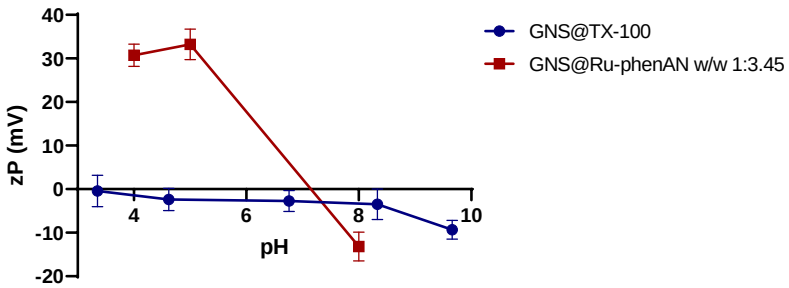

Figure 12. *Zeta potential vs pH titration for the GNS@TX-100 (in blue) and GNS@Ru-phenAN w/w 1:3.45 (in red).*

UV-vis spectroscopy

Moving to the absorption UV-vis spectra of the two samples (Figure 13, left graph), the absorption bands assigned to the Ru-PhenAN polymer and to the GNS are both visible. In the sample with a 3.45 mass excess of polymer, these first bands are more intense, confirming the higher amount of polymer on the GNS surface. Even though the GNS came from the same batch, a difference in the absorption maximum is observed for this sample compared to the other two. We tentatively attributed this evidence to the GNS being more sterically and electrostatically separated from one another, which results in a blue-shift maximum compared to the other two less stabilized samples. The presence of the Ru-PhenAN is recognizable mainly from the peaks between 200 nm and 300 nm. In particular, the one at 200 nm is attributed to the amide groups in the PhenAN backbone[13] and is partially overlapped with the absorption bands assigned to the π-π* transitions of the phenanthroline (visible between 200-270 nm[37]). On the contrary, the ^{3}MLCT absorption bands of the Ru(II) complex, which plateaus between 400-450 nm are just a shoulder above the scattering given by the GNS suspension and because of the low concentration of the complex estimated on the nanoparticle surface.

Moreover, the absorption spectra of the supernatants collected after the first centrifuge (Figure 13, right graph), showed an excess of Ru-PhenAN mainly for the sample with the higher polymer:Au ratio, with much less intense Ru-PhenAN bands for the other ratio, suggesting a saturation in the amount of polymer that can functionalize the GNS. Anyway, in both cases the absorption of GNS is only slightly visible, indicating this method as suitable to recover almost all the functionalized GNS, with a minimal loss.

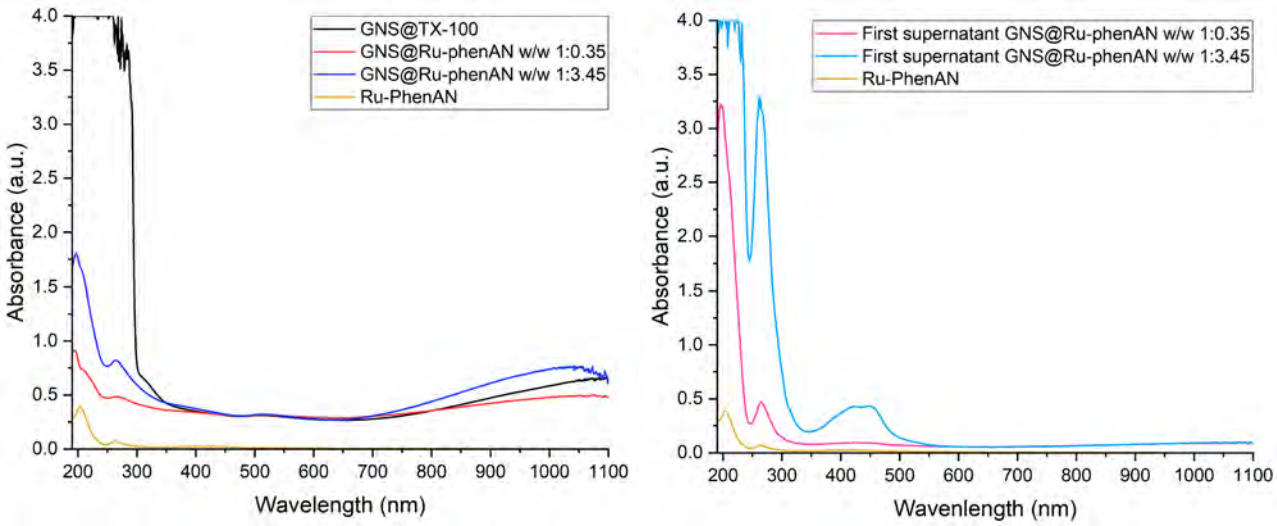

Figure 13. *Left: UV-vis absorption spectra of GNS before (black line) and after the functionalization with Ru-PhenAN via ligand exchange (red line Au:polymer w/w 1:0.35 and blue line 1:3.45). Right: UV-spectra of the first supernatant after the functionalization.*

Another attempt at the functionalization of GNS with the polymer via ligand exchange was followed using the same Ru-PhenAN with a prior saturation of the terminal double bonds with cystamine (as

depicted in Scheme 8B). This saturation aimed to functionalize the polymeric chain with a disulfur bridge, reduced in the presence of the GNS to expose thiols and possibly bind more strongly to the GNS than the unfunctionalized PhenAN thanks to the strong Au-S interaction.

In this case, the only GNS:polymer mass ratio tested was 1:2.89, which is a value close to the highest amount of polymer used in the previous attempts, due to the reasons discussed above on the stabilization of the GNS. The procedure followed and the characterization methods used are analogous too and are represented in the following Figure 14.

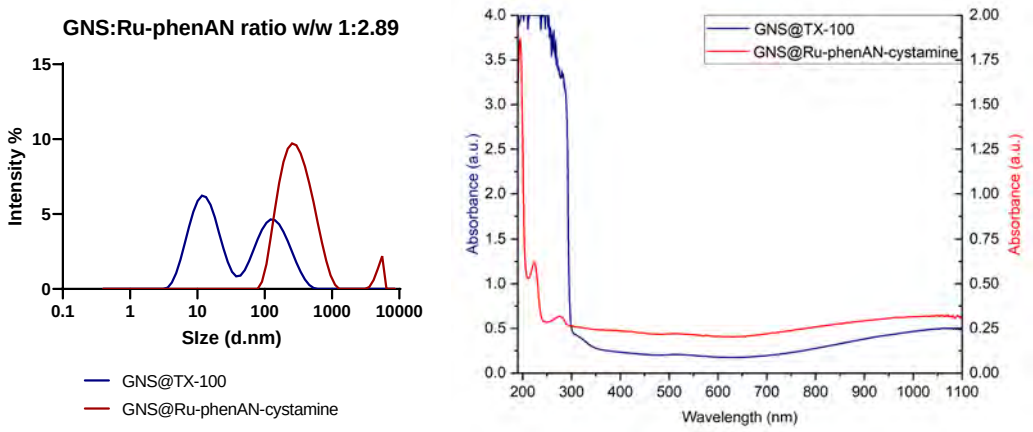

Figure 14. *Left: DLS measurement of GNS@TX-100 (blue line) and of GNS@Ru-phenAN-cystamine (red line). Right: UV-vis spectra of the GNS@TX-100 (in blue) and of GNS@Ru-phenAN-cystamine (in red) after the washing steps via centrifugation.*

The DLS measurements show the two already discussed populations for GNS@TX-100 sample and only one for the functionalized GNS@Ru-PhenAN-cystamine. The shift in the GNS size from (148 ± 41) nm to (255 ± 91) nm was not attributed to a weaker stabilization by the functionalized polymer, but to the possibility of cross-linking through the formation of new disulfuric bonds between the Ru-phenAN-cystamine chains.

Similarly to the previous samples, the UV-vis spectrum shows mainly the absorption band of the GNS, while the PhenAN polymer is recognizable only from the bands in the UV region.

As shown in Figure 15, neither the GNS:Ru-phenAN 1:0.35 nor 1:3.45 showed any emission when excited using the same excitation wavelength used to record the emission spectrum of Ru-PhenAN alone. On the other hand, the polymer exhibited a quite sharp emission band, peaking at ca. 610 nm, and a plateau between 415-450 nm in the excitation spectrum.

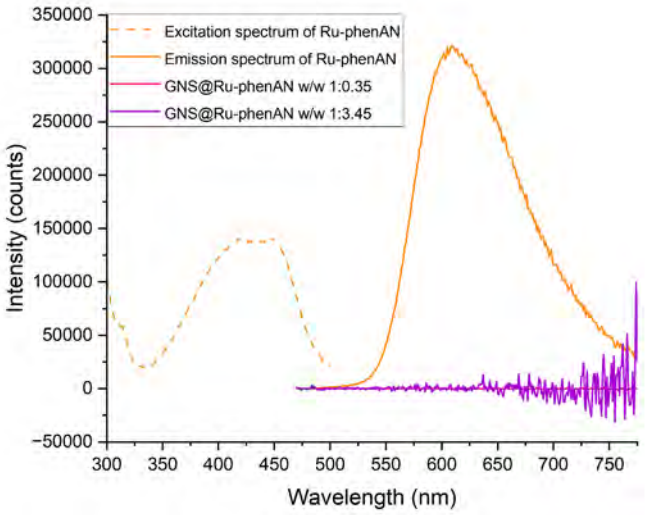

Figure 15. *In orange: excitation (dashed line, emission λ at 608 nm) and emission (full line, excitation λ at 470 nm) spectra of the Ru-phenAN polymer alone. In pink and purple: emission spectra of the GNS@Ru-phenAN samples prepared with an Au:polymer ratio of 1:0.35 and 1:3.45, respectively (excitation λ at 470 nm).*

The absence of the Ru(II) complex luminescence in the GNS@Ru-phenAN samples can be easily explained by the proximity between the gold surface and the fluorophore when this synthetic strategy is used. It is indeed known from the literature[21,38,39] that the presence of metal nanostructures near fluorophore molecules modifies their emissive properties due to the plasmon coupling between the two components in a phenomenon called metal-enhanced fluorescence (MEF). MEF occurs when the spacing is 5-90 nm. Nonetheless, when the fluorophore is directly linked to the metal surface or too close to it (< 5 nm), the quenching effect by the nanostructure becomes prevalent over the enhancement.

Given the results obtained and the findings in the literature, we decided to move to another approach to functionalize the GNS with the Ru-phenAN polymer to obtain a larger spacing and recover Ru-phenAN luminescence.

Functionalization of GNS with four polymeric layers with a layer-by-layer approach (GNS@Ru with 4 layers)

To achieve a larger spacing between the Ru-PhenAN polymer and the gold surface, we adopted a different approach, involving the stacking of negative and positive layers through electrostatic interactions, with the Ru-PhenAN as the outermost layer. For this purpose, we chose the polyamidoamine $ISA23SH_{20\%}$ (or simply ISA23SH, as it will be indicated from now on) as the negatively charged polymer. ISA23SH (whose structure is schematized in Scheme 9) is a copolymer with a different backbone compared to PhenAN, having a zwitterionic slightly negative character at physiological pH because of the presence of carboxylic groups. This feature gives the polymer a “stealth-like” behavior, which is not captured by the reticulo-endothelial system and has longer circulation times in the

bloodstream.[11] Moreover, it bears a thiol pendant in the minor unit (20% of the whole polymer in molar terms) that interacts strongly with Au, allowing a better GNS stabilization.

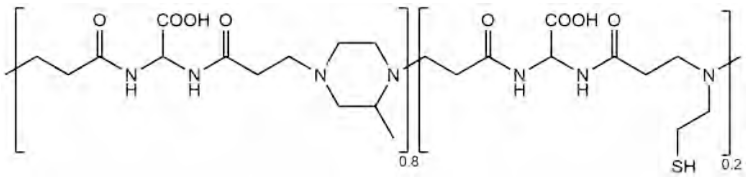

Scheme 9. *Schematic depiction of ISA23SH, used as the negative layer to functionalize the GNS with the layer-by-layer approaches.*

The first step of the layer-by-layer approach, which is schematized in Scheme 10, consisted of a first ligand exchange between Triton X-100 and ISA23SH, similar to the one used with Ru-PhenAN. The freshly prepared GNS interacted overnight at RT with a mass excess of ISA23SH (given our results previously obtained with Ru-PhenAN, we chose a polymer:Au w/w ratio of 2:1), after setting the pH of the mixture at ca. 9 to help the interaction by partly deprotonating the thiol groups. The mixture was then centrifuged to remove both the excess of TX-100 and the unbound polymer, and immediately after resuspended in the same volume of milliQ water. Then, three serial interactions with the polymer of the opposite charge were carried out: first with PhenAN (bearing the free phenanthroline), followed by ISA23SH and finally with Ru-PhenAN. For the preparation of the GNS@(ISA23SH@phenAN)$_2$-Ru, the PhenAN and Ru-phenAN polymers used are the unsatured ones (see Scheme 8A). Given the ζ-potential vs pH titration curves of the two copolymers (Figure 16) and of GNS@polymer layers (Figure 17, left picture), the pH of the mixture was set to ca. 6 for the addition of the PhenAN or Ru-phenAN layers and to ca. 7 for the second layer of ISA23SH, to maximize at the same time the negative and positive charge of both components of the mixture for each step. After each functionalization step, the suspension was centrifuged, and the pellet was diluted again for the next step.

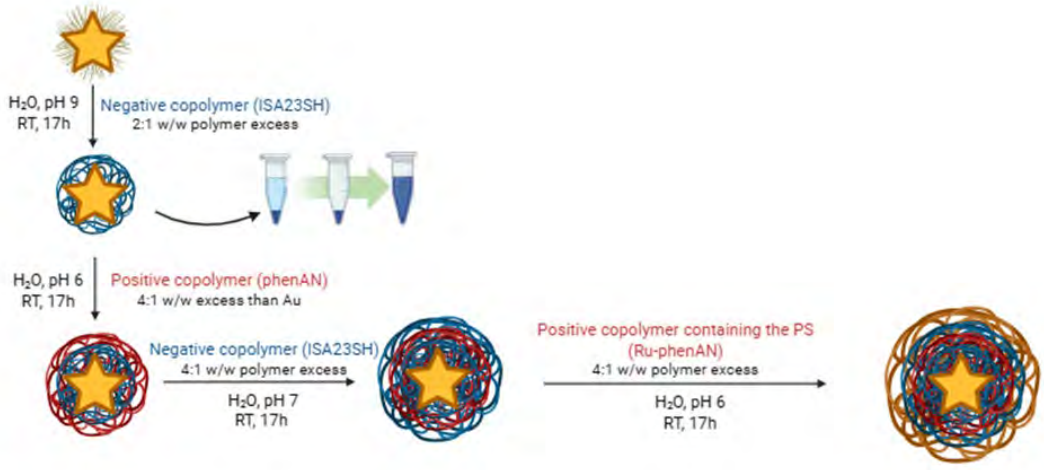

Scheme 10. *Schematic representation of the protocol used for the functionalization of GNS with 4 polymeric layers with the layer-by-layer approach. Picture made using Biorender software.*

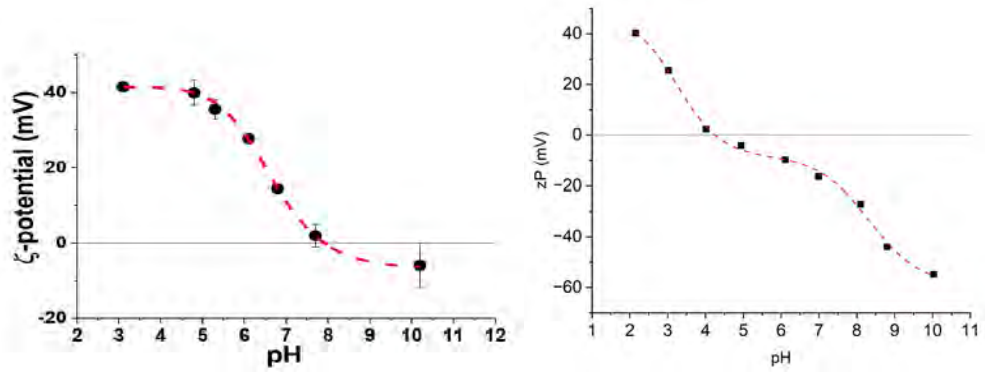

Figure 16. *ζ-potential vs pH titration for PhenAN (left picture, from Ref 16) and ISA23SH (right picture, data taken from Ref 12).*

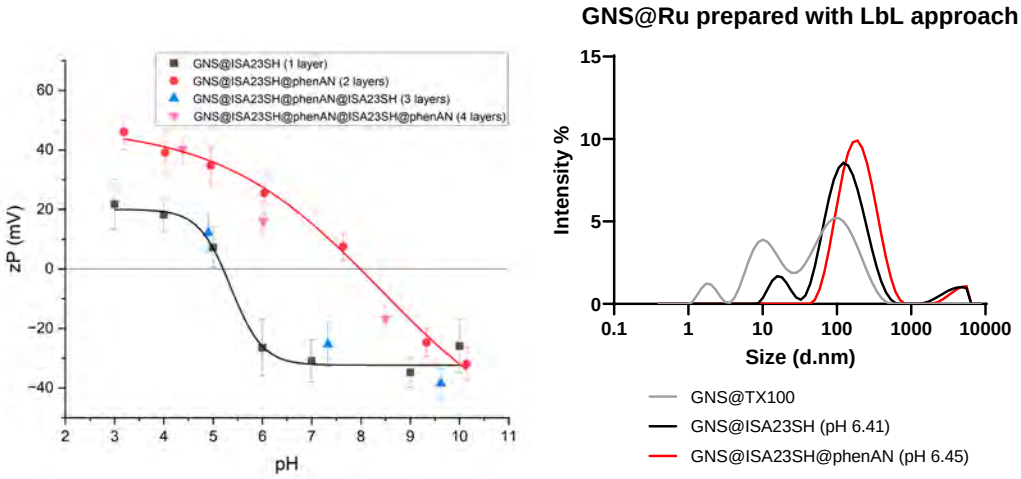

Figure 17. *Left: ζ-potential vs pH titration of the GNS functionalized with 1-4 layers of polymers. The black points are the values measured for GNS@ISA23SH (1 layer), while the red ones for GNS@ISA23SH@PhenAN (2 layers) with the respective fittings. The blue and purple ones are measured respectively when the external layer is the ISA23SH (3 layers) and PhenAN (4 layers). Right: DLS measurements of unfunctionalized GNS (gray line) and GNS functionalized with 1 layer (ISA23SH, black line) and 2 layers (ISA23SH and PhenAN, red line).*

DLS measurements were carried out to characterize the GNS functionalized with the first two layers, as shown in the right panel of Figure 17. The GNS@TX-100 presents three populations: other than the main one, centered at 115 (± 37) nm and assigned to the GNS, a second peak at 13 (± 3) nm, and a third at 2 ± (0.2) nm, are visible, assigned to aggregates and single molecules of TX-100, respectively (Figure 18). The main GNS peak shifts to 151(± 43) nm after the functionalization of the first ISA23SH layer and to 212 (± 57) nm after the addition of the PhenAN layer. At the same time, the GNS@ISA23SH@phenAN sample does not show the peak assigned to TX-100, still visible in the GNS@ISA23SH sample.

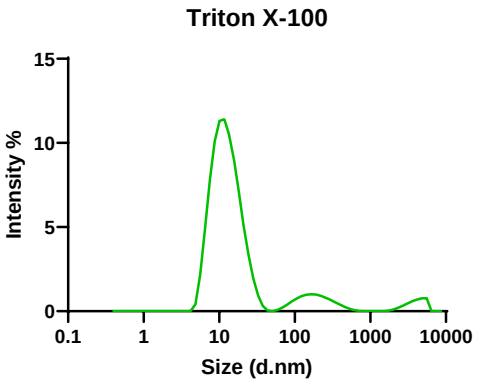

Figure 18. *DLS measurement of Triton X-100 in the same concentration employed in the synthesis of GNS.*

In Figure 19 the UV-vis absorption spectra for the three samples are shown. By focusing on the main GNS absorption band that peaks at ca. 850 nm, a slight shift of the peak (of about 10 nm) is visible after their functionalization with ISA23SH. Nonetheless, when the second copolymer PhenAN is added, the peak remains superimposable, suggesting that the close surrounding of the GNS did not change, as it would be expected if another ligand exchange occurred instead of the polymers stacking.

Moreover, the ζ-potential values measured at three different pH for the GNS functionalized with 3 and 4 layers (Figure 17, left panel) follow the curves fitted for the samples with the same external copolymer, confirming the success of the last two covering steps.

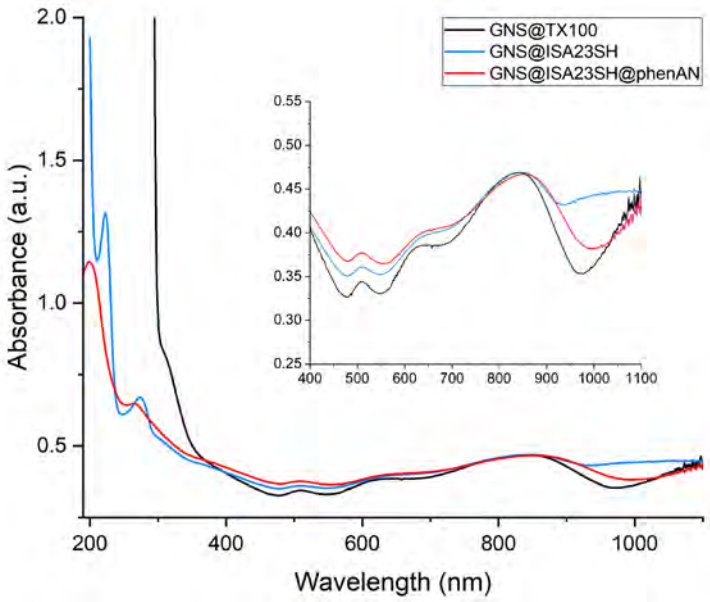

Figure 19. *UV-vis spectra of GNS@TX-100 (black line) and after the functionalization of GNS with one layer of ISA23SH (blue line) and two layers (ISA23SH and phenAN, red line). The insert shows a magnification of the spectra between 400-1100 nm to highlight the main GNS absorption band.*

TEM images of the GNS functionalized with the three polymeric layers before the addition of Ru-PhenAN were then recorded to further confirm the success of the layer-by-layer functionalization. The following Figure 20 shows a close-up of such GNS, around some of which a polymeric layer is visible and

highlighted by the purple arrows. Even though not all the GNS seem to be surrounded by this layer, this is due to the little contrast of the organic polymer compared to Au, which makes it hardly and not homogeneously visible. Trying to overcome this contrast problem, we used for this analysis a Holey carbon-supported Cu grid, which helps to visualize materials with low contrast since it possesses larger meshes in the polymer coating that minimizes the interference of this film. The thickness of this polymeric layer was measured to be ca. 3 nm, employing ImageJ software.

Moreover, an EDS elemental analysis (Figure 21, left two panels) of an area containing the GNS suggested the presence of ISA23SH around the GNS from the presence of N, O, and S highlighted in the picture with the red boxes. The same elements are also visible in another area analyzed without GNS (Figure 21, right two panels); however, some other analyzed regions did not show the elements present in either of the polymers. This observation supported our hypothesis that the polymer stacking collapses when the sample is placed on the grid, since the affinity of the polymers for the carbon film is likely higher than the electrostatic interactions between them. As a result, it is possible that only the first ISA23SH layer remains around the GNS due to the strong Au-S interactions.

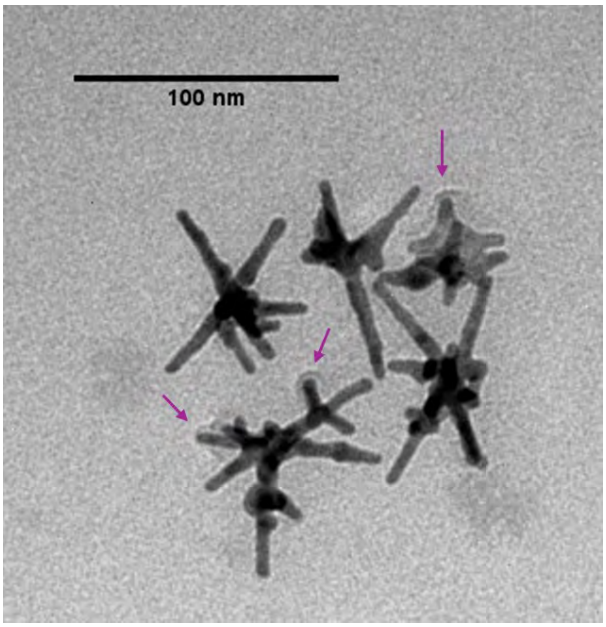

Figure 20. *TEM picture of the functionalized GNS. The shadows around some of the GNS, highlighted with the purple arrows, are attributed to the first ISA23SH layer, whose thickness was measured using ImageJ software (ca. 3 nm). Scale bar: 100 nm.*

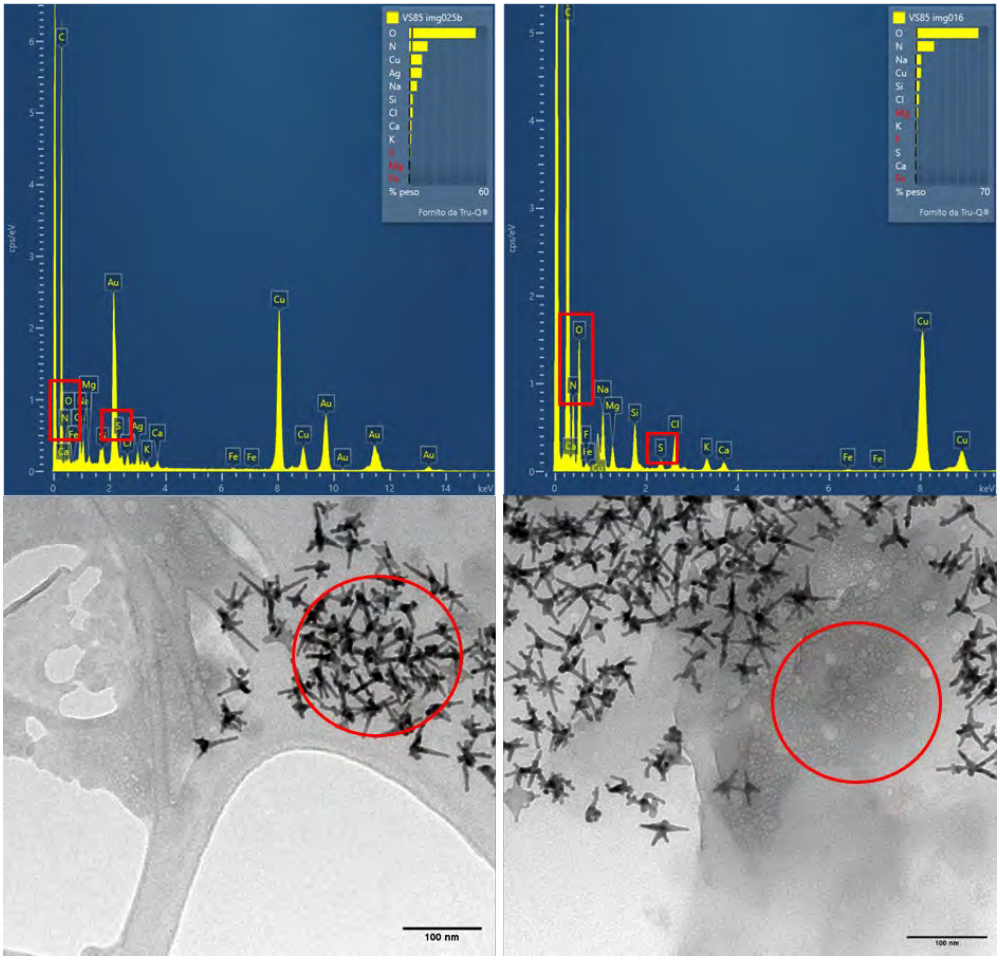

Figure 21. *EDS (upper figures) of two areas of the sample and the corresponding TEM pictures (bottom figures). The red circles mark the areas in which the two EDS analyses were made, while the red squares highlight the elements present in the ISA23SH and phenAN polymers. Scale bar: 100 nm.*

The GNS@(ISA23SH@phenAN)$_2$-Ru (or GNS@Ru, as the nanoparticles prepared using the layer-by-layer approach will be called from now on) nanoparticles were finally characterized by UV-vis absorption and emission spectroscopy. In the absorption spectrum (shown in the left panel of Figure 22), the plasmonic band of GNS, peaking around 900 nm and highlighted with green in the figure, is clearly visible, while the absorption band of the Ru(II) complex appears as a shoulder over the scattering of the GNS, as highlighted in yellow in the picture. Between 200-300 nm the absorption bands of the polymers and of phenanthroline are also evident.

Moreover, the sample shows the same emission and excitation of Ru-PhenAN (Figure 22, right panel), suggesting that Ru-PhenAN and the gold surface are distanced enough by the three layers in the middle to prevent any influence of GNS on its emission wavelength, peaking at 609 nm for Ru-PhenAN alone and at 607 nm for GNS@Ru). Thus, by using the layer-by-layer approach, we managed to overcome the quenching of Ru-PhenAN, allowing us to characterize the biological behaviour of the GNS@Ru system and test the efficacy of GNS to boost the Ru-PhenAN photocytotoxicity, as described in the following section.

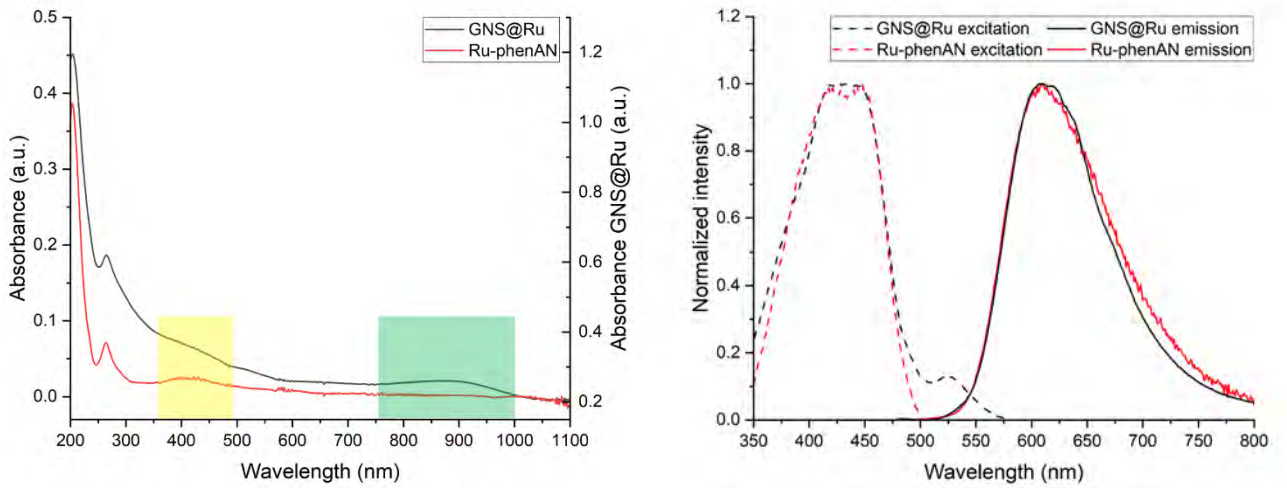

Figure 22. *Left graph: UV-vis absorption spectra of the GNS@Ru (black line) and of the Ru-phenAN copolymer (red line). The yellow and green squares highlight the absorption peak of the Ru(II) complex and of the GNS, respectively. Right graph: Normalized excitation (dashed lines) and emission (full lines) spectra of Ru-phenAN (red lines) and GNS@Ru (black lines).*

Unfortunately, the GNS@Ru nanoparticles prepared with this method presented some stability problems over longer times when the same samples were measured 3 months after preparation. The multi-angle DLS (MADLS) measurements of the sample recorded in milliQ water, PBS and cMEM (Minimum Essential Medium + 10% Fetal Bovine Serum or FBS) show the presence of two populations in all three dispersants (see Figure 23 and Table 3), whose size is measured between ca. 250-350 nm (peak 1 in the table) and 530-750 nm (peak 2). The smaller population is much bigger than the corresponding population of Ru-phenAN, whose dimension remains quite constant at ca. 130-140 nm, even though their size in water is compatible with the one measured using DLS during the preparation of these samples (ca. 211 nm for GNS functionalized with two polymeric layers). The bigger population is also visible for the Ru-phenAN alone, even if the size of these aggregates is still smaller compared to GNS@Ru.

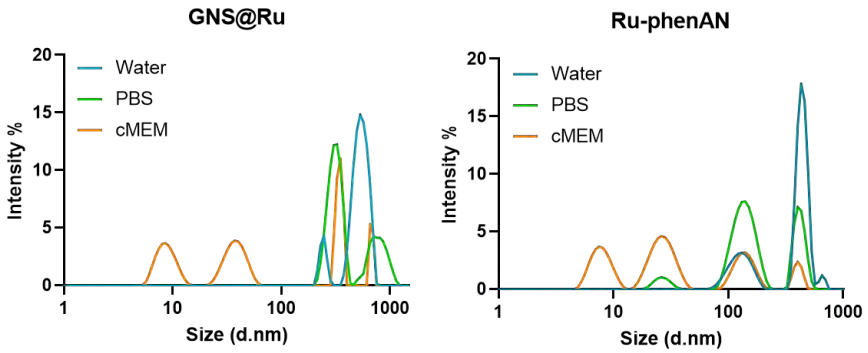

Figure 23. *MADLS measurements of GNS@Ru (left graph) and Ru-PhenAN (right graph) in water (blue lines), DPBS (green lines) and cMEM (orange lines). The two smaller populations visible in cMEM (centered at ca. 8 and 30 nm) are due to the free proteins present in cMEM.*

By just looking at these DLS measurements, it is difficult to say something about the stability of this compound. Nonetheless, when coupled with the ζ-potential measured in the same three dispersants (listed in the last column of Table 3), these values are different from our expectations: in water at a pH of 5.4, this kind of nanoparticles (i.e. GNS functionalized with 4 polymeric layers, being Ru-phenAN the external one) presented a positive ζ-potential of 30-40 mV in the measurement taken during their preparation, as shown in Figure 17, instead of the -5.4 mV recorded after several months. For the other two dispersants, the values are compatible with both the GNS functionalized with an external positive or negative polymer, since the ζ-potential expected for all four samples is similar at basic pH.

Table 3. *Size of the populations shown in the MADLS measurements of GNS@Ru (with four layers) and Ru-phenAN in water, DPBS and cMEM (Figure 23). The two smaller populations visible in cMEM (centered at ca. 8 and 30 nm) are due to the free proteins present in cMEM and thus are not reported in the table. In the last column, the ζ-potential values of GNS@Ru (four layers) in each dispersant and of Ru-phenAN in water are listed.*

Compound	Dispersant	Peak 1 (nm)	Peak 2 (nm)	ζ-potential (mV)
GNS@Ru	Water	242 ± 9	542 ± 40	-5 at pH 5.4
	DPBS	312 ± 22	671 ± 35	-8 at pH 7.3
	cMEM	342 ± 11	676 ± 12	-12 at pH 7.9
Ru-PhenAN	Water	129 ± 14	439 ± 22	16 at pH 6.5
	DPBS	139 ± 15	418 ± 23	-
	cMEM	139 ± 13	404 ± 17	-

Functionalization of GNS with two polymeric layers with the layer-by-layer approach

Given the stability problem of GNS@Ru with four polymeric layers, we simplified the synthesis, aiming to obtain more stable nanoparticles and to check whether the ISA23SH layer alone provided enough spacing between Ru-PhenAN and the gold surface. The preparation of these GNS@Ru nanoparticles (GNS@ISA23SH@Ru-phenAN, schematized in Scheme 11) followed a protocol similar to that used previously, with adjustments to the pH of the interaction and the volumes involved, as described in the experimental part.

Another difference was the use of the Ru-PhenVS polymer instead of the PhenAN and Ru-PhenAN used in the previous strategies.

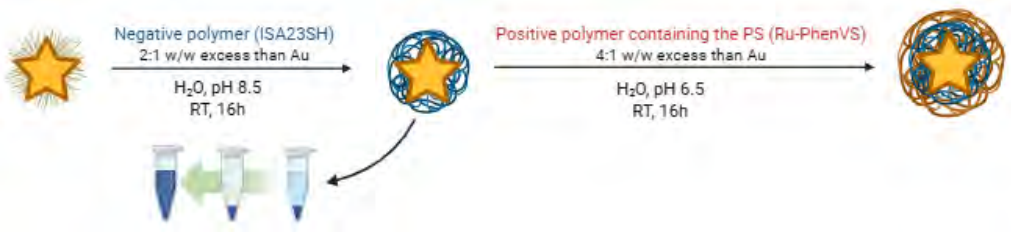

Scheme 11. *Representation of the synthetic procedure followed to obtain GNS@Ru with only two polymeric layers. Figure prepared using BioRender.*

The size and the stability over time of these new GNS@Ru particles were measured with MADLS in the three dispersants already used in the previous measurements (milliQ water, DPBS and cMEM). As reported in Table 4, which shows the sizes measured immediately after diluting the concentrated GNS@Ru stock in each dispersant, two populations are still detectable. However, their dimensions are markedly smaller than those of the GNS@Ru prepared with 4 polymeric layers and are instead comparable to the size of the polymer Ru-PhenAN alone. The first one (peak 1), centered between 90-160 nm depending on the dispersant, can be assigned to the single particles in the dispersion, while the second population (peak 2), lying between 325-390 nm, is attributed to few aggregates. Notably, the size of GNS@Ru is smaller than that of GNS functionalized with one layer of ISA23SH and one of PhenAN measured with DLS (shown in the previous section in Figure 17). This is due to the higher resolution of MADLS compared to DLS, since MADLS measurements detect the light scattered at three different angles, providing narrower peaks for each population. On the other hand, in DLS measurements only the backscattered light is detected, generating larger peaks whose nominal size is the average of all the unresolved populations. Indeed, by extrapolating from the MADLS of GNS@Ru with 2 layers (GNS@ISA23SH@Ru-PhenVS) only the measurement at 173 degrees, it possesses the same size of the GNS@ISA23SH@PhenAN (right panel of Figure 24). In the left panel of Figure 24 the MADLS measurement of GNS@Ru with 2 layers is split in the measurements recorded at each angle (173, 90 and 13 degrees).

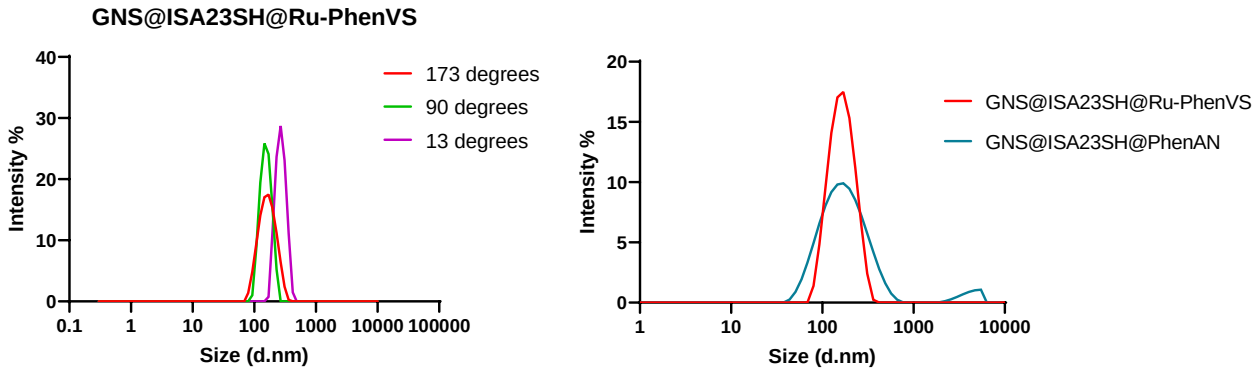

Figure 24. *Left panel: MADLS measurement of GNS@ISA23SH@Ru-PhenVS split in the three angles singularly (173 degrees: red trace, 90 degrees: green trace and 13 degrees: purple trace). Right panel: MADLS measurement recorded at 173 degrees of GNS@ISA23SH@Ru-PhenVS (red trace) and DLS measurement of GNS@ISA23SH@PhenAN (blue trace).*

Moreover, Figure 25 shows that these GNS@Ru nanoparticles are quite stable over time, especially in water, where an increase in the relative intensity of peak 2 over the un-aggregated particles is visible only after 24 hours from their dilution. In PBS, bigger aggregates are detected from the first measurement, with the appearance of a second aggregated population after 6 hours, but the overall distribution of all the samples in both dispersants remained quite stable throughout the measurements.

Another hint that confirmed the success and stability of the so-prepared GNS@Ru was the ζ-potential, measured in all three dispersants as for the size measurements and showed in Table 4 as well: the strongly positive value in water at pH 4.7, the almost neutral at pH 7.0 and the slightly negative one at pH 8.1 all agree with the curves produced for the functionalized GNS in which the positive polymer is the external layer, as shown in the left panel of Figure 17.

Table 4. *Size and ζ-potential of GNS@Ru (with 2 layers) and Ru-PhenVS in water and DPBS, recorded right after the suspension of the concentrated stock in dispersant. In the last column, the ζ-potential values of GNS@Ru (two layers) in each dispersant and of Ru-PhenVS in water are listed.*

Compound	Dispersant	Peak 1 (nm)	Peak 2 (nm)	ζ-potential (mV)
GNS@Ru	Water	165 ± 12	326 ± 13	41.1 at pH 4.7
	DPBS	96 ± 1	374 ± 9	-1.2 at pH 7.0
	cMEM	96 ± 10	386 ± 21	-12.1 at pH 8.1
Ru-phenAN	Water	151 ± 10	270 ± 8	15.7 at pH 6.5
	DPBS	147 ± 2	434 ± 13	-
	cMEM	127 ± 13	418 ± 18	-

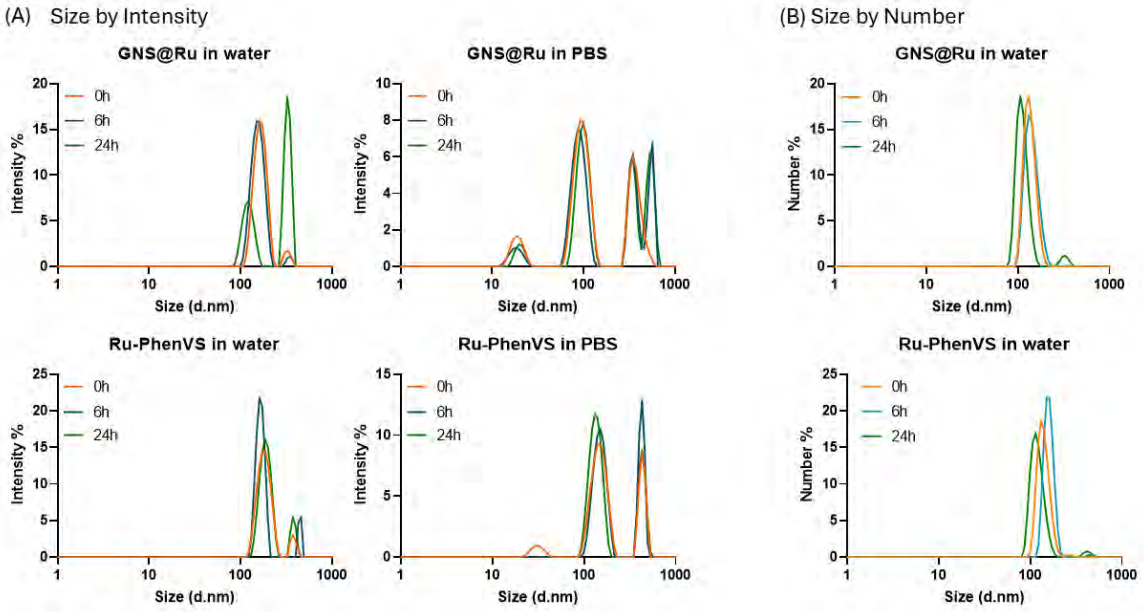

Figure 25. *MADLS measurements of GNS@Ru with 2 layers (upper two graphs) and of Ru-PhenVS (bottom two graphs) recorded over time (0h: orange lines, 6h: blue lines, 24h: green lines). Size data shown by Intensity (A) and by Number (B).*

The absorption and emission spectra of these GNS@Ru were finally recorded to check if the only layer of ISA23SH was still enough to avoid the complete quenching of Ru-PhenAN emission by GNS. As shown in the right panel of Figure 26, the two emission spectra are completely superimposable. The UV-vis absorption spectra (left graph of Figure 26) present some differences, mainly related to the LSPR bands of GNS, due to the different batches used. The spectrum of GNS@Ru with two layers (black line) shows a main peak at ca. 850 nm and a shoulder at ca. 630 nm, typically assigned respectively to asymmetrical five-branched GNS and smaller and symmetrical four-trapezoidal-branched GNS,[40] while only the main

band (peaking at ca. 900 nm) is present in the other sample spectrum. The Ru-PhenAN absorption bands (the shoulder at ca. 400-450 nm for the Ru complex and the two peaks between 200-300 nm for the phenanthroline and the polymer chain) are still visible for both samples.

Additionally, analogously to what already said for the GNS@Ru with four polymeric layers, the LC absorption bands of the amide groups in the polymer backbone and the phenanthroline (below 350 nm) are visible for both Ru-PhenVS and GNS@Ru, while the one assigned to the ^{3}MLCT transition of the Ru complex is barely visible over the scattering of GNS (left panel of Figure 27). On the other hand, there is a slight blue shift in the emission wavelength of GNS@Ru compared to Ru-PhenVS alone, peaking at 605 nm and 613 nm, respectively, consistent with the lower distance between Ru-PhenVS and the gold surface in this sample and suggesting a higher influence of gold on the emissive features of this sample. Additionally, another emission band is visible in the GNS@Ru sample, peaking at ca. 467 nm and assigned to the emission of GNS.[36] The emission spectra described in this last paragraph are shown in the right panel of Figure 27.

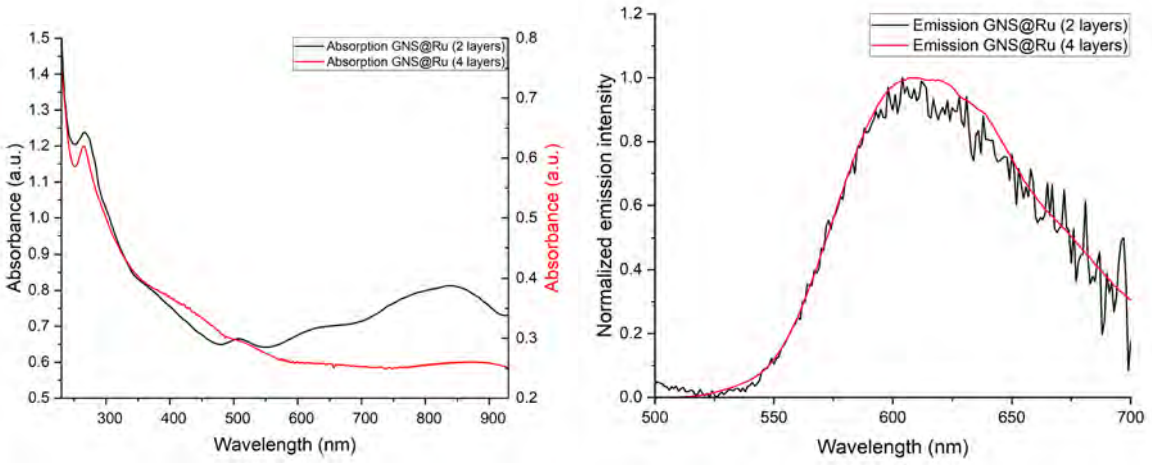

Figure 26. *UV-vis absorption (left panel) and normalized emission (right panel) spectra of GNS@Ru with two polymeric layers (in black) and with four polymeric layers (in red).*

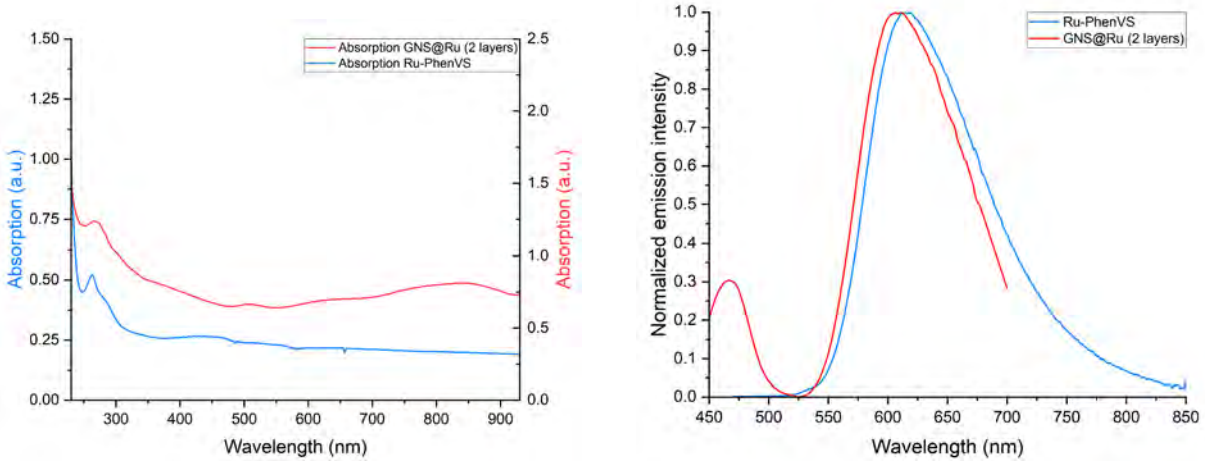

Figure 27. *Uv-vis absorption (left panel) and emission (right panel) spectra of Ru-PhenVS (blue traces) and of GNS@Ru with 2 polymeric layers (red traces).*

Biological investigation on GNS@Ru

Uptake of Ru-PhenVS and GNS@Ru

Before starting the biological investigation of GNS@Ru, the uptake of Ru-PhenVS by HeLa cells was compared to that of Ru-PhenAN to determine if the change in the minority part of the polymeric structure provided any difference. HeLa cells were treated with suspensions of both Ru-PhenVS (prepared from batch A of PhenVS) and Ru-PhenVS whose terminal double bonds were saturated with morpholine (prepared form batch B of PhenVS and marked as Ru-PhenVS-morpholine) in cMEM, at the same Ru concentrations as the published data for Ru-PhenAN.[16] After incubation for 24 hours (see experimental for details), the cells were properly washed to remove any polymer excess and harvested in order to quantify the fluorescence of the internalized compound. As shown in Figure 28, the median fluorescence intensity (MFI) values measured in the Violet610 channel (ranging from 600 to 620 nm) after excitation at 405 nm are ca. the double for Ru-PhenAN compared to the two batches of Ru-PhenVS at the same Ru concentration. This is possibly due to the different dimensions and monodispersity of the two polymers (M_w=48 kDa for Ru-PhenAN, 15.2 kDa for Ru-PhenVS and 4.99 kDa for Ru-PhenVS-morpholine), which could influence their interaction with the cells and their uptake. Additionally, the higher total positive charge of Ru-PhenAN compared to Ru-PhenVS, (the bis-acryloyl monomer provides a 0.5 positive charge per repeating unit at physiological pH)[16,41] also contributes to the higher uptake observed for this polymer. The two batches of Ru-PhenVS, on the other hand, showed a similar uptake suggesting that the internalization of the two polymers could also be affected by the different substituent of the phenanthroline contained in the polymeric backbone. Thus, both the shorter aliphatic chain on the phenanthroline and the presence of the sulfur atom seem to reduce uptake efficiency by the cells. This difference is even higher considering that Ru-PhenVS possesses a slightly increased photoluminescence quantum yield (PLQY) compared to that of Ru-PhenVS (respectively 3.6% for Ru-PhenAN and 4.2% for Ru-PhenVS, as listed in Table 2) and thus a higher emission intensity when the concentration of the two polymers is the same.

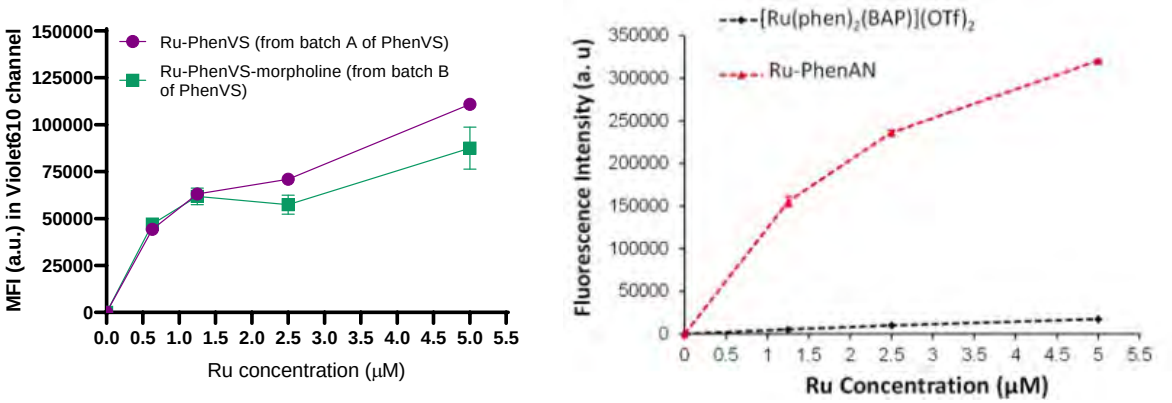

Figure 28. *Left panel: Uptake of Ru-PhenVS from batch A of PhenVS (in purple) and of Ru-PhenVS-morpholine from batch B of PhenVS (in green) by HeLa cells after 24h of treatment. Right panel: Uptake of Ru-PhenAN by HeLa cells (red line) after 24h of treatment. Picture adapted from Ref. 16. In both panels, the uptake is measured by quantification of the Ru complex luminescence in the HeLa cells. The results are the average and standard*

deviation of the median fluorescence intensity obtained by flow cytometry from 3 replicate samples in 1 representative experiment.

Then, the uptake of GNS@Ru by HeLa cells was studied after either 5 or 24 h of treatment. Figure 29 shows that after an incubation of 5 h the uptake of GNS@Ru, covered by 4 polymeric layers, and Ru-PhenVS is comparable. After 24 h incubation, instead, no increment in MFI is visible for GNS@Ru, while the fluorescence measured for the corresponding Ru concentration of Ru-PhenVS is much higher. This result suggests that the GNS and the free Ru are internalized by cells with different kinetics. Additionally the lower uptake of GNS@Ru may be due to instability in the biological medium over time, and potential disruption of the layer-by-layer stacking over the 24h incubation due to the high ionic strength of the medium.[42] Further studies to test the layer stability over time in cell culture medium may help to address this point.

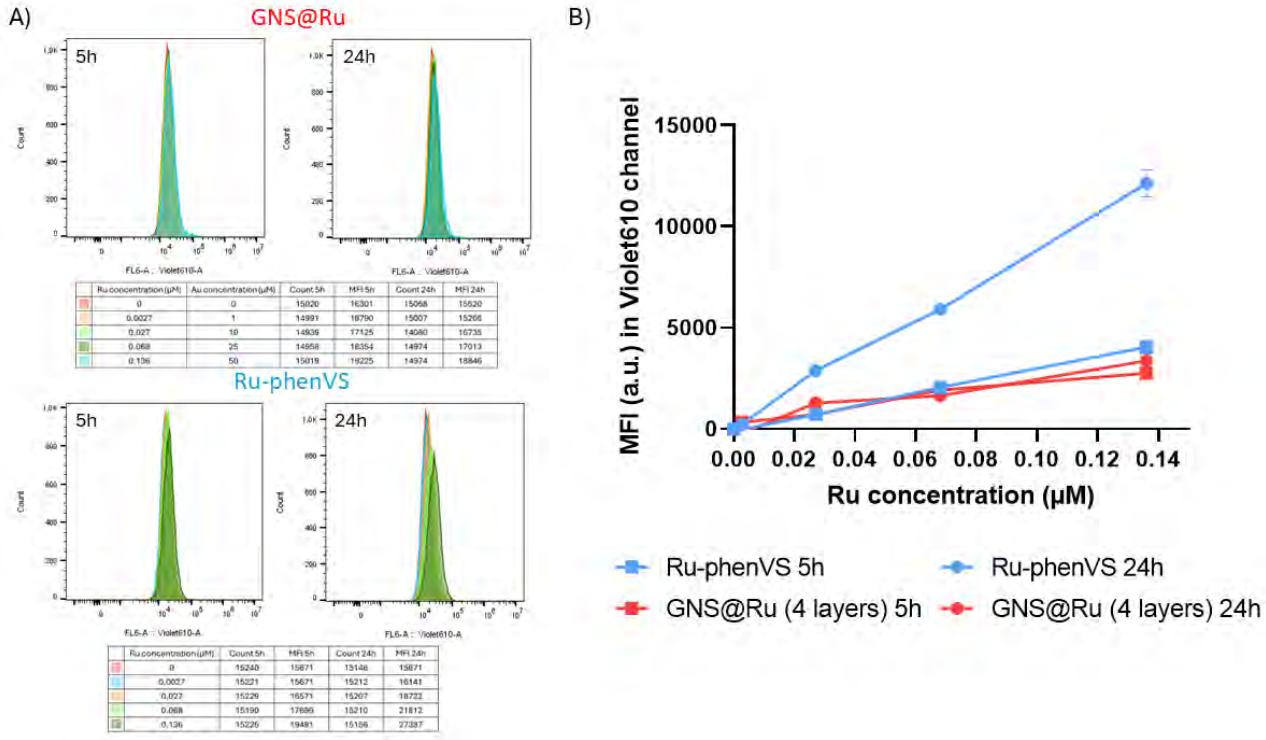

Figure 29. *Dose-response of Ru-phenVS (in blue) or GNS@Ru with 4 polymeric layers (in red) showing the luminescence of the Ru complex in HeLa cells. (A) Median fluorescence intensity (MFI) distributions of HeLa cells incubated with the two compounds for 5h (histograms in the left column) or 24h (histograms on the right column). (B) Cell fluorescence intensity as a function of Ru concentration. The results are the average and standard deviation of the median fluorescence intensity obtained by flow cytometry from 3 replicate samples in 1 representative experiment.*

Based on the results of this experiment, we investigated the stability of GNS@Ru in various dispersants. Then, we prepared the GNS@Ru sample with only 2 polymeric layers to overcome the stability issue, as discussed in the previous sections.

For the GNS@Ru with 2 polymeric layers uptake by HeLa cells, was comparable (even slightly higher) to Ru-PhenVS both at 5 and 24 h (Figure 30). When increasing the treatment time to 24 h, uptake for

GNS@Ru and Ru-PhenVS was similar. The difference between the results for 5 and 24 h of treatment may be explained as a difference in the uptake kinetics, being GNS@Ru internalized faster by cells and thus showing brighter luminescence for shorter treatment times.

To exclude the possible influence of GNS on GNS@Ru emission in the uptake experiment, suspensions in DPBS (Dubecco's PBS) of GNS@Ru (with both 4 and 2 polymeric layers) and Ru-PhenVS were excited at 405 nm, and their luminescence was recorded at 610 nm. The three samples were prepared so that they possessed the same Ru concentration, which was measured with UV-vis spectroscopy for Ru-PhenVS, using the molar extinction coefficient at 448-450 nm,[vi] while it was calculated from the data obtained with ICP analysis for the GNS@Ru samples. The emission recorded for Ru-PhenAN and GNS@Ru with 2 layers was similar, while for GNS@Ru with 4 layers it was much lower. For this reason, GNS@Ru with 4 layers were not further involved in the biological investigation and were replaced by the analogous sample with only two polymeric layers.

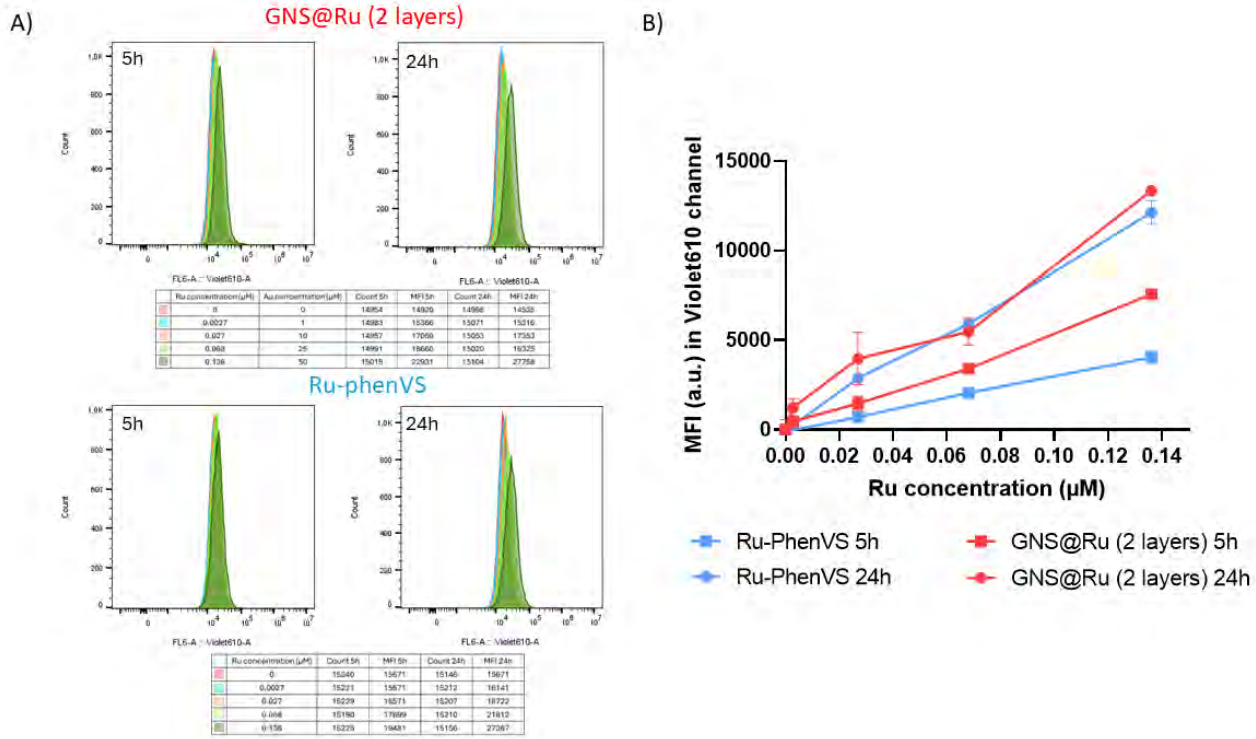

Figure 30. *Dose-response of Ru-phenVS (in blue) or GNS@Ru with 2 polymeric layers (in red) showing the luminescence of the Ru complex inside the cells. (A) Median fluorescence intensity (MFI) after treating HeLa cells with the two compounds for 5h (histograms in the left column) or 24h (histograms on the right column. (B) Cell fluorescence intensity as a function of Ru concentration. The results are the average and standard deviation of the median fluorescence intensity obtained by flow cytometry from 3 replicate samples in 1 representative experiment.*

Lastly, cells were incubated with GNS without Ru-PhenVS to verify whether it causes any cytotoxicity to HeLa cells. Since these nanostars as prepared were incompatible with cells because of the high amount

[vi] ε (448 - 458 nm) = 19100 M^{-1} cm^{-1}, data published for Ru-PhenAN and an analogous polyamidoamine, Ru-PhenISA, bearing the same Ru complex as Ru-PhenAN, in Ref. 13,16

of Triton X-100 provided by the synthesis, known to induce cell lysis, for testing potential toxicity of the GNS alone they were functionalized with either just one layer of ISA23SH or a first layer of ISA23SH and a second one of PhenAN, to obtain nanocompounds similar to GNS@Ru, but without the Ru complex.

HeLa cells were treated for 24 h with increasing concentrations of GNS@ISA23SH or GNS@ISA23SH@PhenAN (suspended in cMEM), and eventual changes in forward-side scattering of cells by flow cytometry were monitored. The Side scattering (SSC), i.e. the scattered light measured at 90° when the laser hits a cell during a flow cytometry measurement, measures the complexity of the cells and in the case of metal and highly scattering particles, it can indeed be used to evaluate uptake of nanoparticles, that provoke changes in the cell light scattering.[43] Analogously, forward scattering (FSC), the scattered light measured at a small angle, is generally linked to cells dimensions. Thus, it is possible to have some indications of potential cytotoxicity of nanoparticles from the changes in the scattered light, since cytotoxic agents can drastically influence their morphology and forward-side scattering properties, until reaching the extreme situation of dead cells, which can be detected as smaller debris at a decreased FSC and an increased SSC.[44] However, one has to take into account that in the case of cells incubated with metal nanoparticles such as gold, changes in cell scattering could also be due to simple scattering of the internalized gold nanoparticles, as opposed to toxicity (hence other tests are required to fully confirm whether toxicity is present).

Figure 31A shows the SSC vs FSC plots of the untreated HeLa cells and of the same cells treated with the four concentrations of the two compounds. While a dose-dependent cytotoxicity of the GNS@ISA23SH is clearly visible from the rise of a new subset of cells between the one in the left corner (assigned to the cell debris) and the big right one (assigned to healthy cells), the GNS@ISA23SH@PhenAN did not cause the same effect and the two mentioned populations remained clearly distinguished. This difference is easily visible in Figure 31B, that shows an overlay of the untreated cells and the cells treated with the highest concentration of the two compounds. Moreover, a shift toward higher SSC values is noticeable, suggesting uptake of both functionalized nanoparticles by HeLa cells. Further tests are required to fully discriminate whether the observed change in SSC vs FSC plots and the formation of a separate subset of cells at lower FSC is due to an effect of the nanoparticle on cell viability.

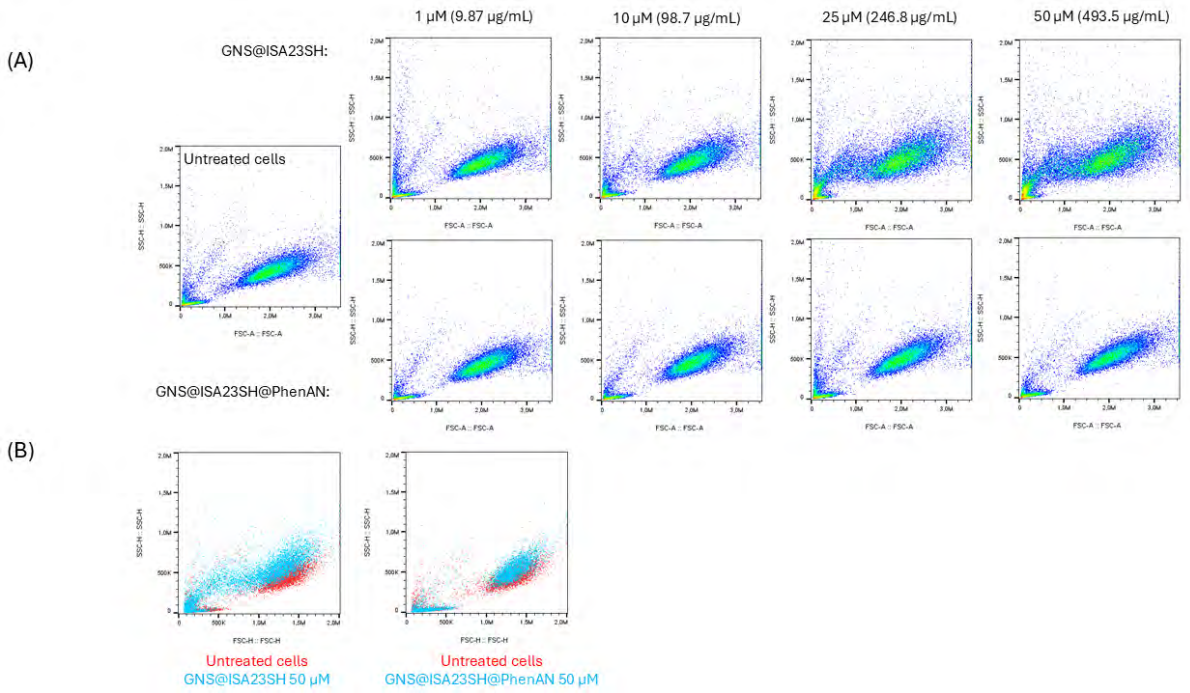

Figure 31. *(A) Side scattering (SSC) vs Forward scattering (FSC) plots of untreated HeLa cells or cells treated for 24h with increasing Au concentrations (from left to right: 1 µM, 10 µM, 25 µM and 50 µM, respectively corresponding to 9.87 µg/mL, 98.7 µg/mL, 246.8 µg/mL and 493.5 µg/mL) of GNS@ISA23SH (upper row) or GNS@ISA23SH@PhenAN (bottom row). (B) Comparison of SSC vs FSC distributions of untreated HeLa cells (in red) and cells treated for 24h (in blue) with 50 µM GNS@ISA23SH (left plot) or GNS@ISA23SH@PhenAN (right plot).*

Photostability of Ru-PhenVS

Before testing the photocytotoxicity of Ru-PhenVS and GNS@Ru, the photostability of Ru-PhenVS under irradiation was tested employing the same commercial lamp (with an emission intensity of 1.3 mW/cm^2) used in the following experiments involving light in the visible range (its emission spectrum is shown in Figure 32). The measurements were carried out both in cuvette and on cells.

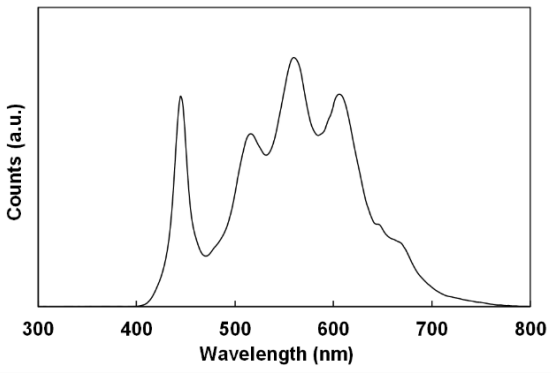

Figure 32. *The emission spectrum of the commercial lamp used to irradiate the compounds during photostability, photocytotoxicity and ROS production experiments.*

For the in-cuvette experiment, a Ru-PhenVS solution was prepared in PBS (with a Ru concentration of 1.25 µM). The two cuvettes were irradiated for 15 minutes, at ca. 2 cm distance from the light source,

and stored in the dark at room temperature for a total time of 24h. UV-vis spectra recorded after 1h, 3h, 5h and 24h from the irradiation were comparable (Figure 33, left panel), proving the high photostability of the PS in both dispersants with these irradiation conditions.

To carry out the same photostability experiment on cells, HeLa cells were treated with a suspension of the compound (Ru concentration of 1.25 μM) in cMEM for 24 h, after which they were washed with DPBS to remove the possible non-internalized compound and the medium was replaced with a fresh one without compounds. This protocol was performed in parallel on two plates of cells, and one was irradiated for 15 minutes with the same lamp used for the in-cuvette experiment, while the other plate was kept in the dark outside of the incubator for the same amount of time. Then, the cells were incubated for additional 2, 4, 6 and 24 h in the incubator, and harvested after each time point to measure the emission of Ru-PhenVS using flow cytometry. This protocol was the same as followed for all the experiments involving light, as described in the following sections.

The measured emissions at each timepoint for the irradiated plate, shown as red squares in Figure 33, remained stable over time, confirming the good photostability of Ru-PhenVS also in the cell environment. The non-irradiated plate, used as a negative control, showed on contrary a good stability in the emission for the first 4 h, followed by a decrease in the last two time points. The decrease in emission can be explained by cell division and the subsequent "dilution" of the compound in the forming daughter cells (as discussed earlier in the Introduction section).[9] The fact that for the irradiated plate a similar decrease in fluorescence is not seen after 24 h suggests that for these cells, cell division may not occur, possibly because of the toxicity induced by the irradiation. Further studies to count cell numbers and check proliferation should be performed to elucidate this. By comparing the emissions of the two plates, it is evident that the values recorded for the non-irradiated one are very different and, especially for the first points, higher than those in the other plate. This difference is simply explained by the partial quenching effect of O_2 on the emission of Ru(II) polypyridyl complexes due to the formation of $^1O_2$ and thus its non-radiative decay to the ground state.[45] $[Ru(phen)_3]^{2+}$, archetypical of the photosensitizer $[Ru(phen)_2(phen\text{-}cysteamine)]^{2+}$ incorporated in the chain of PhenVS, and the similar $[Ru(ppy)_3]^{2+}$ are indeed vastly used in the literature as probes for the detection of O_2 in vitro and in vivo.[45,46]

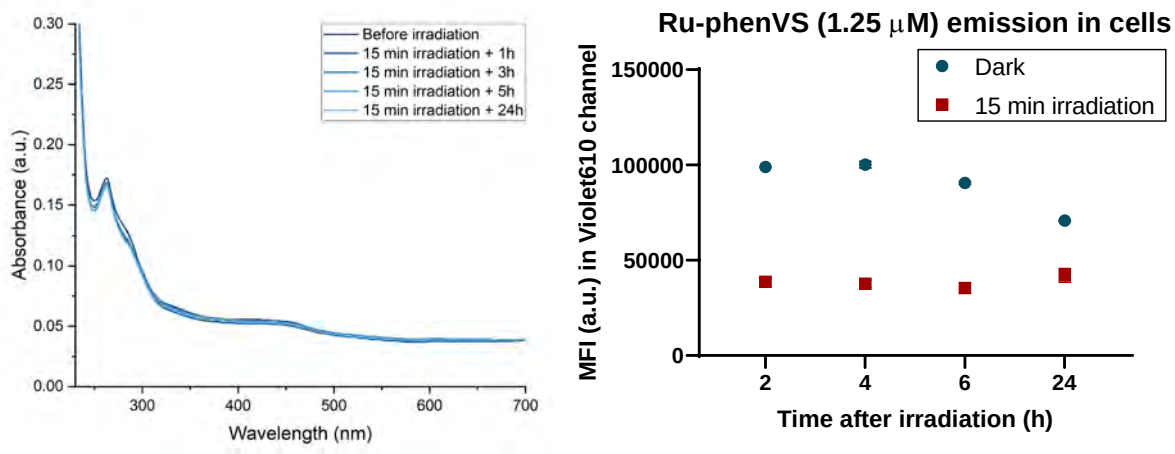

Figure 33. *Left panel: UV-vis spectra of Ru-PhenVS suspended in PBS (Ru concentration: 1.25 μM), recorded before and after (1, 3, 5 and 24 h) 15 minutes of irradiation with a commercial lamp emitting in the visible spectral range. Right panel: Plot MFI (median fluorescence intensity) recorded in the Violet610 channel using flow cytometry vs incubation time after the irradiation, measured on Ru-PhenVS (1.25 μM) internalized by HeLa cells, and irradiated for 15 minutes with a commercial lamp emitting in the visible spectral range.*

Photocytotoxicity of Ru-PhenVS and GNS@Ru

Being the photostability of Ru-PhenVS ascertained, the photocytotoxicity of this compound and of its derivative GNS@Ru nanoparticles was investigated. The protocol used for the illumination, already mentioned in the previous section, and to determine the cellular viability after the treatment with the two photosensitizers, is schematized in Scheme 12. HeLa cells, seeded in two 96-well plates, were treated with Ru-PhenVS and/or GNS@Ru for 24 h, after which the cells were washed with PBS and the medium replaced with a new one to remove the compound that was not taken up by cells. At this point one plate was irradiated outside of the incubator for either 5 or 15 min, while the second plate was covered and kept in the dark, outside of the incubator for the same amount of time, i.e. in the very same conditions as the irradiated plate. Then, the two plates were additionally incubated for either 4 or 24 h and, lastly, the cells viability was assessed by an MTT assay to compare the photo-cytotoxic effect of GNS@Ru to that of Ru-PhenVS.

First, we optimized this protocol using various concentrations of the Ru-PhenVS, in order to find the best combination between the irradiation time and incubation after it in order to detect effects on viability. The Ru-PhenVS doses used in this optimization process were chosen to obtain a photocytotoxic effect similar to that of Ru-PhenAN of previously published data,[16] produced with a longer irradiation and with a different lamp. In Figure 34 the four different combinations of illumination and exposure times tested are reported. The one chosen for the following experiments was 15 minutes of irradiation followed by 4 h of incubation, since the longer irradiation produced a more evident cytotoxic effect already at 4 h compared to the 5 min. On the contrary, when using the 15 min irradiation, 4 h of incubation were

preferred to 24 h to avoid too strong toxicity and be able to discriminate the effect of different doses of photosensitizer.

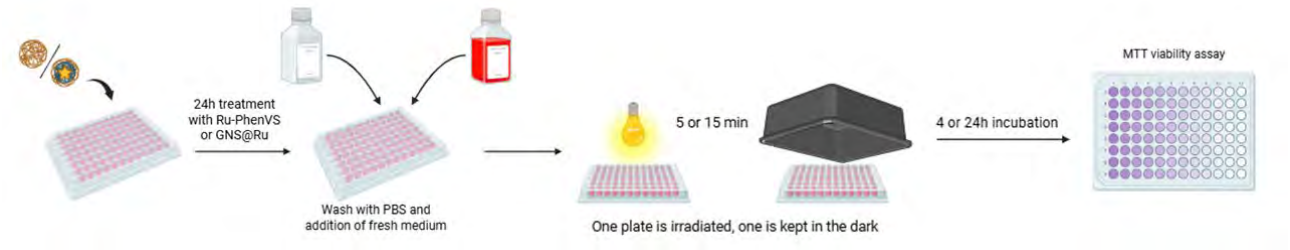

Scheme 12. *Schematic representation of the general protocol followed in the photocytotoxicity experiments. Picture made using Biorender software.*

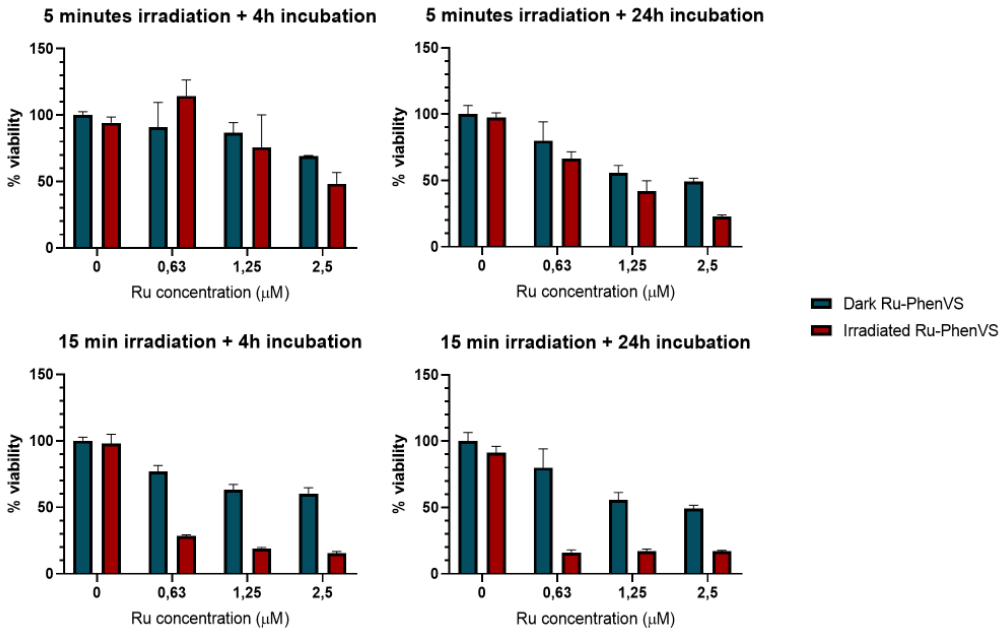

Figure 34. *Viability of HeLa cells after the treatment with various concentrations of Ru-PhenVS in the dark (blue bars) or after the irradiation with a commercial lamp emitting in the visible spectral range (red bars), resulting in the optimization of the irradiation and incubation times involved in the protocol: 5 min irradiation + 4h incubation (upper left), 5 min irradiation + 24h incubation (upper right), 15 min irradiation + 4h incubation (bottom left) and 15 min irradiation + 24h incubation (bottom right). The graph represents the mean relative absorbance (Abs ± SD for 3 independent samples).*

The photo-cytotoxicity of Ru-PhenVS was then compared with that of Ru-PhenAN using the same irradiation conditions, to obtain a more precise comparison of the two compounds and check whether the differences in the polymer structure and length influenced their efficiency in $^1O_2$ generation when irradiated, other than their uptake in HeLa cells. The results are reported in Figure 35, showing that Ru-PhenAN gives a higher photocytoxicity than Ru-PhenVS when low concentrations are used (as visible for the lowest concentration tested, 0.63 μM). When increasing its concentration, the efficiency of the two compounds becomes more similar. This might be a consequence of the more efficient uptake of Ru-PhenAN, causing a better $^1O_2$ generation efficiency from lower concentrations than those necessary with Ru-PhenVS.

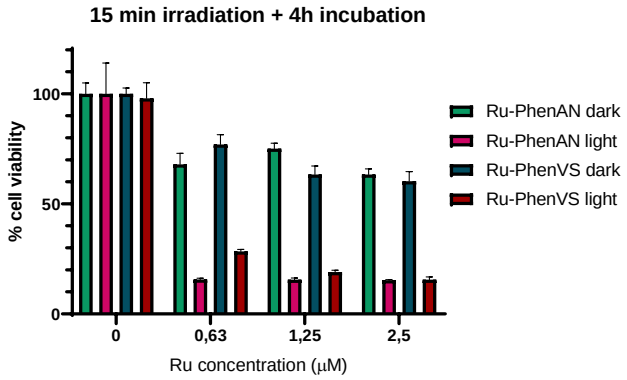

Figure 35. *Viability of HeLa cells after the treatment with increasing concentrations (Ru concentrations of 0.63, 1.25 and 2.5 μM) of Ru-PhenVS and Ru-PhenAN in the dark (blue bars for Ru-PhenVS and green bars for Ru-PhenAN) or after 15 minutes of irradiation with a commercial lamp emitting in the visible spectral range (red bars for Ru-PhenVS and magenta bars for Ru-PhenAN), followed by 4h of incubation. The graph represents the mean relative absorbance (Abs ± SD for 3 independent samples).*

After fixing the irradiation and incubation times, the GNS@Ru were introduced to study their photo-cytotoxicity and check whether the proximity to the GNS provided the enhancement of $^1O_2$ generated by the photosensitizer. In the left plot of Figure 36 the comparison between the photo-cytotoxicity of GNS@Ru and of Ru-PhenVS, after 15 minutes of irradiation and 4 h of incubation is reported. Because of the high cytotoxicity observed for the GNS@Ru upon illuminations, the concentrations tested were lower than those used for the optimization process with Ru-PhenVS, ranging from 0.04 μM to 1.25 μM. The GNS@Ru sample started to show an evident photo-cytotoxicity starting from a Ru concentration of 0.8 μM, while for the Ru-PhenVS alone no cytotoxicity was visible until a Ru concentration of 0.63 μM. These results showed indeed an increased cytotoxic effect of the photosensitizer when in the proximity of the GNS, which resulted toxic starting from a dose about an order of magnitude lower. This enhancement effect is more evident in the plot shown in the right panel of Figure 36, in which the cell viability after irradiation, measured for each concentration tested, was normalized to the viability of cells incubated with the corresponding concentration of compounds in the dark plate. This allowed to exclude from this analysis any other toxic effect independent from the irradiation, and thus $^1O_2$ generation. From this plot the 10-fold increase in photocytotoxicity of Ru-PhenVS in the presence of GNS is clear, since the same reduction of viability is obtained with a concentration ca. 10 times lower when the GNS are introduced, confirming the success in employing GNS to boost the photocytotoxicity of Ru-PhenVS.

However, the viability of the cells treated with GNS@Ru and irradiated (i.e. the pink bars and dots in Figure 36) seem to not further decrease after a certain nanocompound concentration. We assumed this to be due to an interference with the assay when the dose of GNS is too high, being it a colorimetric assay that measures the absorbance at 550 nm and possessing the GNS one of the LSPR bands around

that wavelength. For this reason, it might be worth to try a non-colorimetric assay in the future, like the Alamar blue assay, already employed with cells treated with Ru-PhenAN.[16]

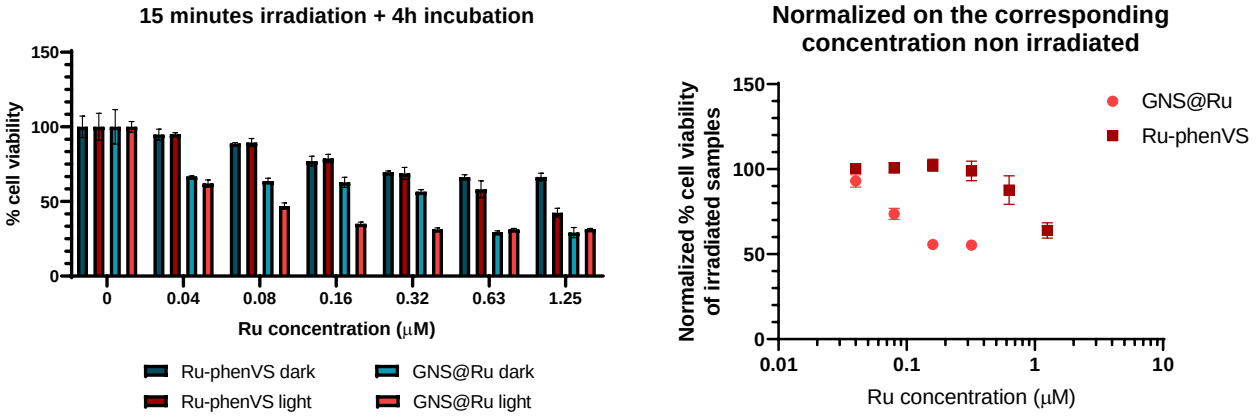

Figure 36. *Left panel: viability of HeLa cells after the treatment with increasing concentrations (Ru concentrations of 0.04, 0.08, 0.16, 0.32, 0.63 and 1.25 μM) of Ru-PhenVS and GNS@Ru in the dark (blue bars for Ru-PhenVS and light blue bars for GNS@Ru) or after 15 minutes of irradiation with a commercial lamp emitting in the visible spectral range (red bars for Ru-PhenVS and pink bars for GNS@Ru) followed by 4 h of incubation. Right panel: viability of HeLa cells in the same experiment, treated with increasing concentrations (Ru concentrations of 0.04, 0.08, 0.16, 0.32, 0.63 and 1.25 μM) of Ru-PhenVS (red squares) and GNS@Ru (pink dots) and irradiated 15 min with a commercial lamp emitting in the visible spectral range, followed by 4h of incubation. These data were normalized on the viability of the corresponding Ru concentration of the plate kept in the dark. The results shown in both panels represent the mean relative absorbance (Abs ± SD for 3 independent samples).*

Anyhow, in all the cell viability plots shown so far, as well as in the published biological study of Ru-PhenAN,[16] a certain dose-dependent cytotoxicity of the photosensitizer is visible also for the non-irradiated plate, possibly given by the slightly positive charge of the polymer, that favors its uptake but, at the same time, causes some cytotoxicity. In addition to this, some cytotoxicity in the dark plate is measured also for GNS@Ru (left plot of Figure 36): similarly to what observed with Ru-PhenVS and Ru-PhenAN, this effect is dose dependent, but it is visible for all the concentration tested and too strong to depend only on the positive charge of the polymer. For this reason, we attributed this effect to the GNS, which in the literature are proven to be biocompatible in concentrations ranging between 1 and 300 μg/mL (when HeLa cells are treated for 24, 48 and 72 h)[47] but are likely to induce some toxicity for the higher concentrations tested. Additionally, GNS synthesized with the same procedure that we followed and possessing similar dimensions to those adopted in our study, showed no or little cytotoxicity toward SH-SY5Y cells for 24 h treatment times at concentrations between 1-50 μg/mL when their surface was functionalized with a neutral PEG polymeric layer.[36] On the other hand, the cytotoxicity of the same GNS functionalized with a positively charged PEG, increased drastically starting from a concentration of ca. 25 μg/mL.[36] Our results obtained in the uptake experiment for GNS@ISA23SH@PhenAN (Figure 31) agree with those reported in the literature, as the SSC vs FSC plot of HeLa cells treated for 24 h did not suggest any toxicity from this nanocompound in the concentration tested (10-500 μg/mL).

The Au amount in the samples used in the photocytotoxicity experiments was determined with ICP-MS and reported in Table 5. The gold concentrations shown in the table are indeed higher than both those tested in the literature and those involved in the uptake experiment with GNS@ISA23SH@PhenAN (9.9-494 μg/mL, Figure 31) and thus the too high gold concentration might be the possible reason for the cytotoxicity in the dark of GNS@Ru.

To confirm our hypothesis, the same viability experiment was carried out using GNS@ISA23SH@PhenAN, employing the same concentrations shown in the table below (corresponding to that used in the experiment with GNS@Ru). HeLa cells were treated with the compounds for 24 h, then one plate of cells was irradiated for 15 min and the other was kept in the dark the same time, after which both plates were incubated for additional 4 h. The results are shown in Figure 37, confirming that the cytotoxic effect in the dark is caused by the high GNS concentrations involved. Interestingly, no differences were measured between the viability of the irradiated plate and of the non-irradiated one, except for a slight decrease in cell viability after the irradiation for the two highest concentrations tested. This proved that the increase in photocytotoxicity of GNS@Ru is due to an enhancement of the Ru-PhenVS action rather than an additional toxic effect from the GNS, further confirming the success in using GNS to boost Ru-PhenVS photocytotoxicity. Further studies to increase the Ru load would allow to achieve similar effects while reducing the amount of GNS added to cells, hence avoiding additional toxicity due to too high GNS concentrations.

Table 5. *In the left column of the table are reported the Ru concentration of the GNS@Ru samples employed in the MTT viability experiments, while in the right column the corresponding Au concentrations in the same samples.*

Ru concentration in GNS@Ru samples (μM)	Corresponding Au concentration (mg/mL)
0.04	0.7
0.08	1.4
0.16	2.8
0.32	5.6
0.63	11.2
1.25	22.3

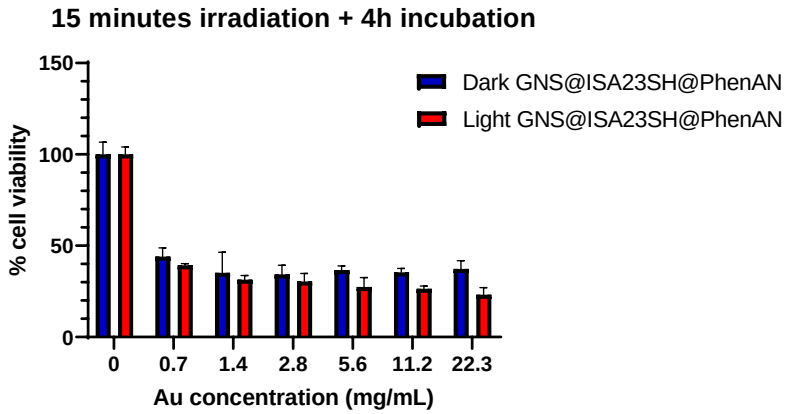

Figure 37. *Viability of HeLa cells after the treatment with GNS@ISA23SH@PhenAN, employing the same Au concentrations used in the experiments with GNS@Ru (0.7, 1.4, 2.8, 5.6, 11.2 and 22.3 mg/mL) in the dark (blue bars) or after 15 min of irradiation with a commercial lamp emitting in the visible spectral range (red bars), followed by 4 h of incubation. The graph represents the mean relative absorbance (Abs ± SD for 3 independent samples).*

ROS generation by Ru-PhenVS and GNS@Ru with irradiation

After confirming the higher photo-cytotoxicity of GNS@Ru compared to that of Ru-PhenVS we tested whether this effect was due to ROS production, to finally confirm the boosting of the PDT action of Ru-PhenVS by GNS.

An optimization of the protocol to measure the intracellular ROS generation was carried out investigating four parameters: the cell seeding density, the ROS probe concentration and volume, and the number of centrifugation cycles used to wash the cells after the treatment with the ROS probe. In a first experiment, untreated HeLa cells seeded at two different densities (15000 cells/well and 20000 cells/well) were harvested 48 h after the seeding (replacing cMEM after 24 h) and a PBS solution of the ROS probe (CM-H_2DCFDA) was added. CM-H_2DCFDA is a commercially available chloromethyl derivative of the 2',7'-dichlorodihydrofluorescein diacetate that passively enters live cells, and it is oxidized by intracellular ROS, yielding to a fluorescent product. The high retention of the molecule in live cells, both in the reduced and oxidized form, makes this probe suitable for long-term studies.[48] To one quarter of the samples, 100 µL of the ROS probe with a concentration of 2.5 µM were added, to a second quarter 50 µL with the same concentration, to a third 100 µL with a concentration of 1.25 µM and to the last quarter 50 µL of the same 1.25 µM concentration. The emission of the oxidized ROS probe was measured with flow cytometry (detected in the FITC channel, ranging from 485 to 564 nm). As shown in Figure 38A, the best results in terms of cell count and of the emission intensity were measured using 100 µL of the ROS probe, with a concentration of 2.5 µM for the 20000 cells/well density and 1.25 µM for the 15000 cells/well one.

These two conditions were adopted in the second experiment, in which cells were treated with increasing concentrations (between 2.5-10 µg/mL) of commercially available polystyrene nanoparticles

functionalized with amino groups (PS/R-NH_2), that are known to possess a certain cytotoxicity due to their positive charge.[49] To half of the cells, that were seeded with a density of 20000 cells/well, 100 µL of the ROS probe was added with a concentration of 2.5 µM, while to the other half, seeded 15000 cells/well, with a concentration of 1.25 µM. After the treatment with the ROS probe, the cells were washed with one or two centrifugation cycles with PBS. For both cell densities, the addition of the second wash drastically reduced the number of the measured cells, while the emission values changed only slightly (Figure 38B). Overall, the best condition was the cell density of 20000 cells/well, treated with 100 µL of 2.5 µM ROS probe and washed once. These conditions were used for all the following ROS generation experiments.

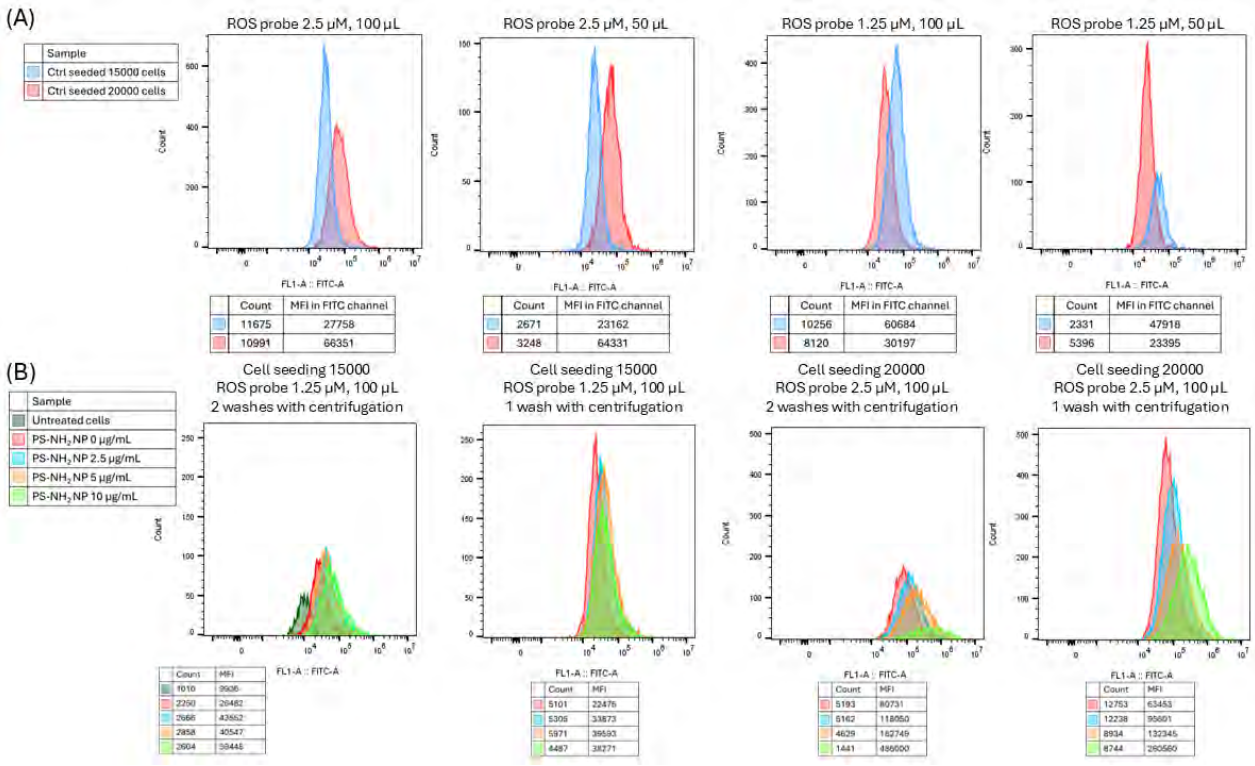

Figure 38. *Median fluorescence intensity (MFI) measured during the optimization of the protocol for the intracellular ROS production measurement. (A) Fluorescence distributions of HeLa cells (seeded 15000 cells/well, in blue, or 20000 cells/well, in red) after their treatment with various volumes and concentrations of the ROS probe (first graph: 100 µL 2.5 µM, second graph: 50 µL 2.5 µM, third graph: 100 µL 1.25 µM and fourth graph: 50 µL 2.5 µM). (B) Fluorescence distributions of HeLa cells treated with PS/R-NH_2 nanoparticles at increasing dose (2.5-10 µg/mL). Cells were seeded 15000 cells/well and treated with 100 µL of ROS probe 1.25 µM (first and second graph) or seeded 20000 cells/well and treated with 100 µL of ROS probe 2.5 µM (third and fourth graph), after either one (second and fourth graphs) or two (first and third graphs) washes with centrifugation. In the first graph, the "untreated" sample refers to HeLa cells without the addition of neither the nanoparticles nor the ROS probe and is used as negative control.*

In Scheme 13 the whole procedure followed for the measurement of intracellular ROS generated after the irradiation is schematized. Working again with two plates in parallel, HeLa cells were treated with Ru-PhenVS and GNS@Ru for 24h, washed once with DPBS and the old medium was replaced. One plate was then irradiated for 15 minutes with the commercial lamp emitting in the visible range (already

described in the previous sections), while the other was kept in the dark outside of the incubator for the same time. After another incubation time, depending on the experiment, the intracellular ROS levels were quantified using the protocol discussed above and in the experimental section.

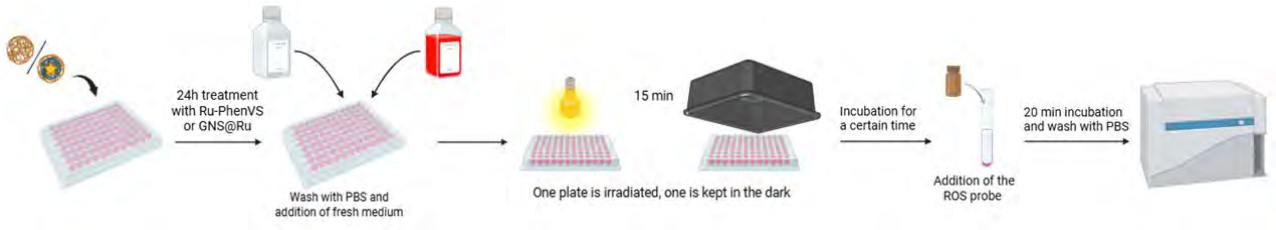

Scheme 13. *Schematic representation of the general protocol followed in the experiments to measure intracellular ROS generation after irradiation. Figure made using Biorender software.*

First, we compared the kinetics of ROS generation by GNS@Ru and Ru-PhenVS, by treating the cells with a fixed concentration of the two, 0.08 μM for GNS@Ru and 1.25 μM for Ru-PhenVS (in terms of Ru concentration). These concentrations were chosen based on the results of the cell viability experiments after irradiation, since they showed the same photo-cytotoxicity. After the irradiation, the cells were incubated for increasing times ranging from 30 min to 4 h prior to ROS quantification. In Figure 39A the distribution of ROS fluorescence in the cells is shown: neither compound produced any ROS if not irradiated, while after the irradiation a second peak at higher intensity values appeared. The two peaks were separated and the obtained subsets superimposed in an SSC vs FSC plot, to determine if the two populations showed differences in morphology (Figure 39B). Since the two subsets were completely superimposable, they were considered as one population and the median of their emission intensities was plot against the incubation time after the irradiation, producing the graph in Figure 39C. The ROS generated by GNS@Ru increased until 1h from the irradiation, until reaching a plateau with 4-fold increase compared to the non-irradiated samples, while the Ru-PhenVS showed a faster kinetics in ROS production, reaching a maximum (ca. 8-fold increase compared to the dark samples), followed by a decrease until reaching a ROS production similar to GNS@Ru. Notably, the decrease in ROS production registered for the 4 h incubation might be due to the too high toxicity of the compounds at those concentrations and to a high rate of dead cells, being this incubation time the same adopted in the cell viability experiments. It is also important to stress that, even though this kinetics experiment shows a similar ROS production for the two compounds, slightly higher for Ru-PhenVS, its concentration is more than 10 times higher than GNS@Ru (in relation to Ru amounts), again confirming that GNS@Ru enables a much higher ROS production in comparison to the polymer alone at the same Ru concentration.

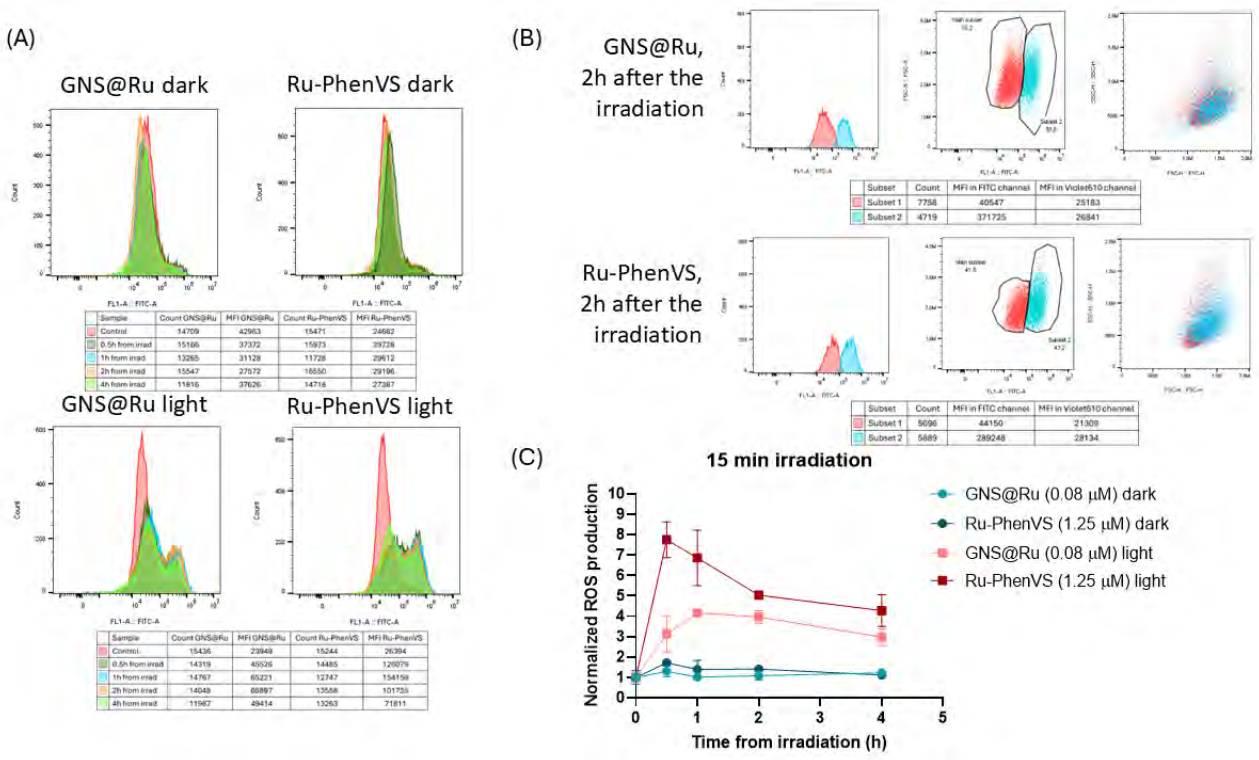

Figure 39. *ROS generation kinetics by Ru-PhenVS (1.25 µM) and GNS@Ru (0.08 µM). (A) Total MFI measured. (B) Separation of of the two MFI peaks and of the respective two subsets (FSC vs MFI in the FITC channel plot) and superposition of the two subsets in a SSC vs FSC plot. C: Intracellular ROS production (normalized on the emission intensities recorded on the untreated cells) vs incubation time after irradiation plot of HeLa cells treated with Ru-PhenVS (1.25 µM) or GNS@Ru (0.08 µM), irradiated for 15 minutes (red and pink plots respectively) or kept in the dark the same time (blue and light blue plots respectively) and incubated for increasing times (30 min-4h). The results are the average and standard deviation of the median fluorescence intensity obtained by flow cytometry from 3 replicate samples in 1 representative experiment*

Given the results of the kinetics, we carried out two dose-response experiments measuring the ROS production after 1 and 2 h from the irradiation and employing the same doses of the two PS (ranging from 0.01 to 0.04 µM Ru) for a better comparison of their PDT effect.

The results of the experiments are shown in Figure 40. While Ru-PhenVS in the concentrations used did not generate any ROS neither in the dark nor after the irradiation, a visible ROS production is measured after the irradiation when the cells were treated with GNS@Ru, reaching, for the highest concentration tested, respectively a 3-fold and 10-fold increase for 1 h (left plot) and 2 h (right plot) of incubation. The results of these two experiments showed a slower ROS production kinetics when the GNS are present, that might be due to differences in the uptake of the two compounds or in a different mechanism of ROS generation involved. The results also confirmed that the higher cytotoxicity after irradiation measured during the cell viability assays is really due to a boost in ROS production, corroborating that the proximity of Ru-PhenAN to GNS might favor the generation of a higher amount of $^1O_2$, resulting in a better photosensitizing activity in PDT.

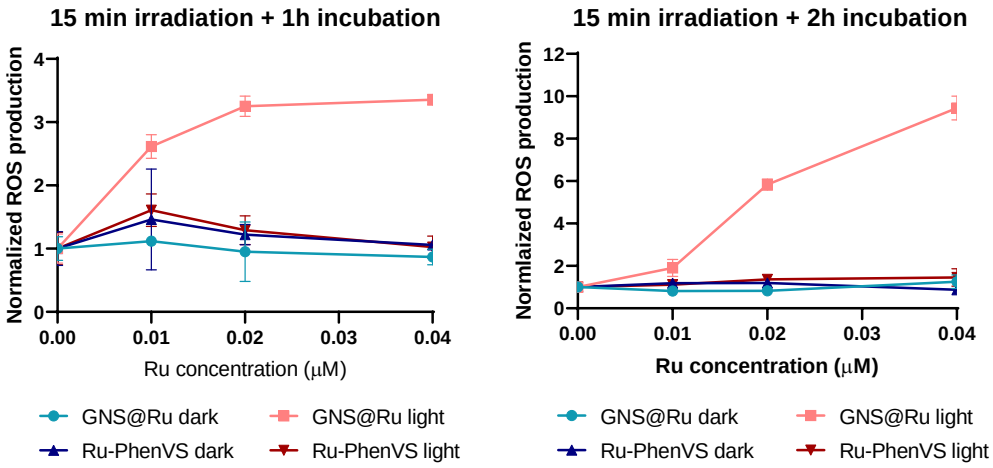

Figure 40. *Intracellular ROS generation (normalized on the emission measured for the untreated cells) vs Ru concentration plot of HeLa cells treated with Ru-PhenVS and GNS@Ru in the concentration range of 0-01-0.04 μM, irradiated for 15 minutes (red and pink plots respectively) or kept in the dark for the same time (blue and light blue plots respectively) and incubated for 1h (left graph) or 2h (right graph) after the irradiation. The results are the average and standard deviation of the median fluorescence intensity obtained by flow cytometry from 3 replicate samples in 1 representative experiment.*

Internalization studies of GNS@Ru and Ru-PhenVS using confocal microscopy and two-photon microscopy

Finally, confocal microscopy and two-photon microscopy pictures of HeLa cells treated with the two compounds were recorded to visualize differences in uptake and location inside the cells of GNS@Ru as well as Ru-PhenVS.

HeLa cells were treated with 0.08 μM suspensions of the two compounds and incubated for 14 h, after which they were fixed with formalin, their nuclei stained with Hoechst dye and observed under confocal microscopy (Figure 41). The Hoechst stain was detected in the blue channel (430-536 nm), while the emission of the Ru complex, for both Ru-PhenVS and GNS@Ru, in the red channel (604-696 nm). The GNS were visualized through the reflected light, collected at the same wavelength as the incident light (430-450 nm).

As visible in Figure 41A, showing the pictures recorded with a lower magnification (63x), both Ru-PhenVS and GNS@Ru were efficiently internalized by all the cells present in the frame, where they seem to be localized in vesicles in the cytosol in the perinuclear regions, as expected for particles internalized via endocytosis along the endo-lysosomal compartment. In Figure 41B, the same samples are recorded with a higher magnification, that shows more clearly that the GNS and Ru-PhenVS are co-localized, confirming the stability of the GNS functionalization and of the overall GNS@Ru samples.

Moreover, two-photon (TP) microscopy pictures were taken, as shown in Figure 42, by treating HeLa cells with a higher concentration of the two compounds (0.63 μM for GNS@Ru and 1.25 μM for Ru-

PhenVS). Unfortunately, in this case we could not record the reflectance of GNS, due to the microscope set-up. Anyhow, the visible emission of the compounds, excited with an 810 nm laser, confirms the possibility of a two-photon excitation. This opens up the possibility of testing in the future whether the proximity of GNS to Ru-PhenVS boosts its $^1O_2$ generation also when excited with a two-photon excitation. Using two photons illumination would allow the use of these GNS@Ru compounds for TP-PDT exploiting light in the NIR range, hence allowing a deeper penetration through tissues.

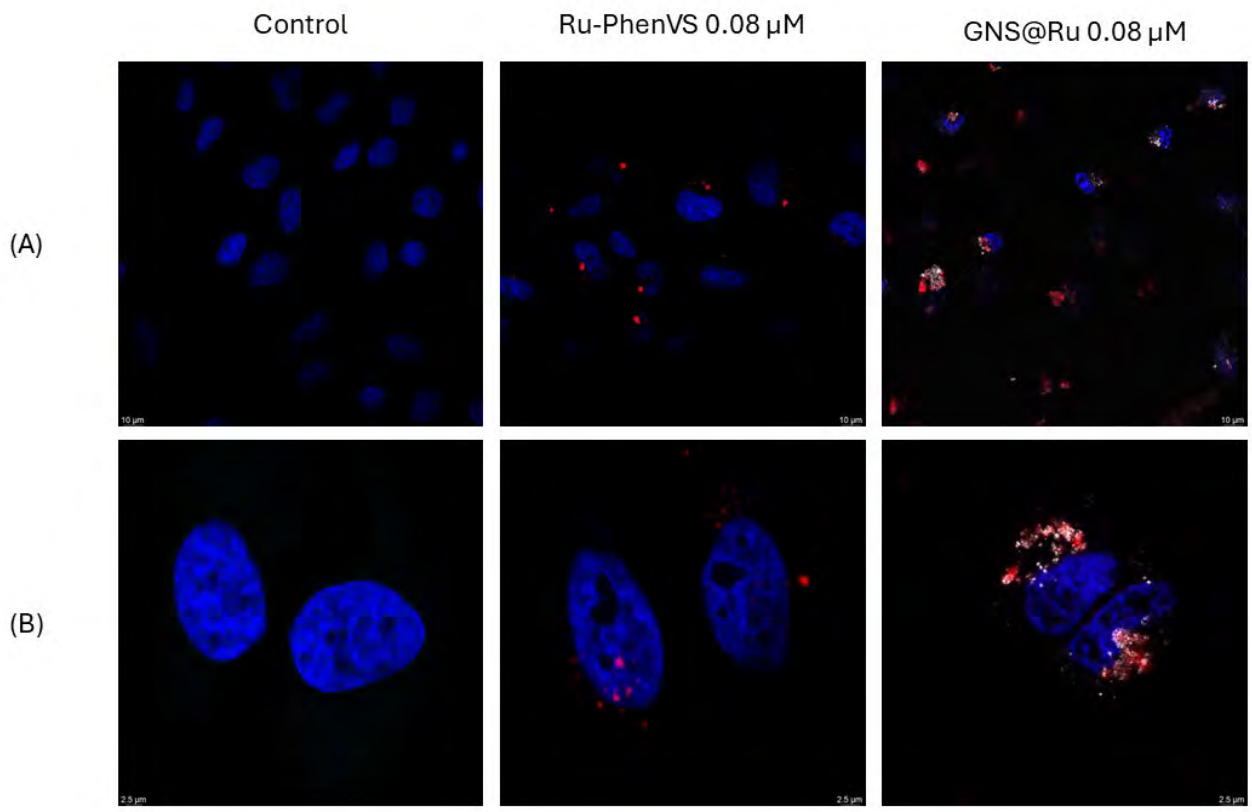

Figure 41. *Confocal microscopy pictures of untreated HeLa cells (first column), treated with Ru-PhenVS 0.08 µM (second column) or GNS@Ru 0.08 µM (third column) for 24h and fixed with formalin. Nuclei are stained with Hoechst dye. Pictures were recorded exciting the Hoechst dye at 405 nm and recording the emission at 430-536 nm (blue channel), and Ru-PhenVS and GNS@Ru at 440 nm, recording their emission at 604-696 nm (red channel). GNS were visualized in reflectance mode (grey channel), by collecting the light at the same wavelength as the incident laser (430-450 nm).*

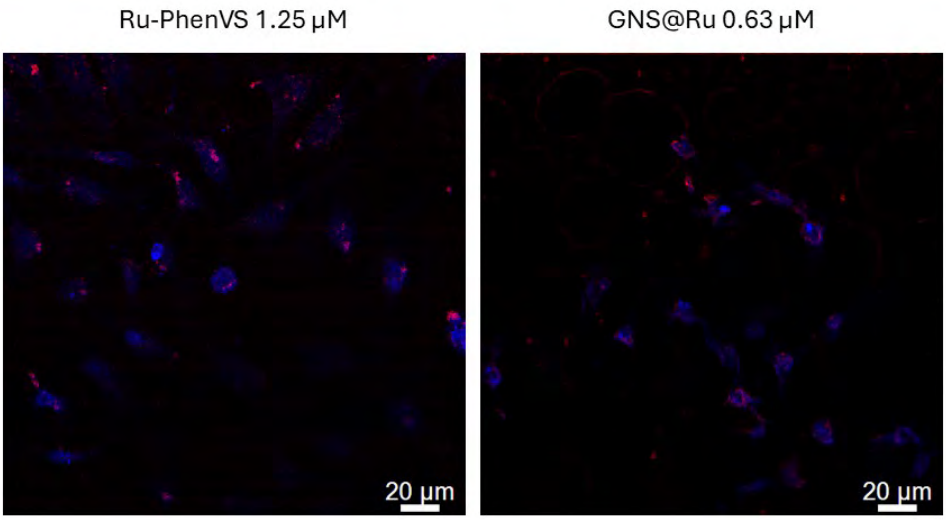

Figure 42. *Two-photon microscopy pictures of HeLa cells treated with Ru-PhenVS 1.25 µM (left picture) and GNS@Ru 0.63 µM (right panel) for 24h and fixed with formalin. Nuclei are stained with DAPI dye. Pictures were recorded exciting both compounds, as well as the DAPI stain, at 810 nm, measuring the emission at 430-536 nm (blue channel) and 570-652 nm (red channel).*

Conclusions

This work aimed at the functionalization of GNS with a polyamidoamine-Ru(II) complex to boost its $^1O_2$ generation and obtain a more efficient photosensitizer for Photodynamic Therapy. The photosensitizing properties and the cell trafficking of the same polymer containing a similar Ru(II) complex in its minor repetition unit, namely Ru-PhenAN, were previously studied by our groups,[16,17] showing a high efficiency of $^1O_2$ photosensitization upon irradiation with a lamp emitting in the visible range and an accumulation of the photosensitizer in the nucleus due to a photo-activated lysosomal escape.

Given the high interest in Ru-PhenAN for PDT but the costly and multi-step procedure required to synthetize the functionalized phenanthroline in the polymer, in this work we carried out a different procedure to obtain a phenanthroline bearing a pendant that expose a terminal amino group (phen-cysteamine). The shorter pendant of Phen-cysteamine compared to that of BAP (used in the preparation of PhenAN) that possibly resulted in greater steric hindrance at the primary amine to be incorporated in the backbone of the new polyamidoamine (PhenVS), originating shorter polymeric chains (Mw: 15.21 and 4.99 kDa for PhenVS vs 48 kDa for PhenAN) with a lower phenanthroline molar content (2 and 3 % in moles for PhenVS vs 4.5-5 % for PhenAN).

On the free phenanthroline pendents present in the polymer chain, a Ru(II)-based moiety was complexed to afford the copolymer complex Ru-PhenVS. Its photophysical properties were compared to those of an analogous molecular Ru complex prepared using the free phen-cysteamine as the third ligand. When the Ru complex is incorporated into the polymeric structure, its emission wavelength

appears slightly blue shifted (613 nm vs 615 nm) and its lifetime and PLQY are increased (respectively 754 ns and 4.2% vs 598 ns and 1.9%), accordingly to the more rigid surroundings.

Subsequently, Ru-PhenVS was used to decorate the surface of GNS. After attempting various strategies, the approach that successfully overcame the quenching of Ru-PhenVS emission by GNS and provided the best result in terms of stability consisted of the layer-by layer stacking of two polymeric layers on the nanoparticle surface (GNS@Ru). The first layer was a negatively charged polyamidoamine (ISA23SH) with a "stealth-like" behavior, followed by an outer positively charged Ru-PhenVS layer. The layer stacking was monitored by DLS measurements of the size and ζ-potential, yielding nanohybrid particles whose size is comparable to those of free Ru-PhenVS (in water 165 ± 12 nm for GNS@Ru vs 151 ± 10 nm). These nanohybrid exhibited an overall strongly positive charge at acidic pH, neutral at physiological pH and became slightly negative when suspended in cell culture medium (cMEM).

GNS@Ru and Ru-PhenVS were taken up efficiently by HeLa cells both after short and long incubation times and lead to comparable Ru accumulation inside cells. Confocal microscopy pictures recorded on HeLa cells treated with a low concentration of the two compound (Ru concentration 0.08 μM) showed both compounds localized in vescicles in a perinuclear zone and the two components of GNS@Ru (i.e. the GNS and the Ru complex) resulted co-localized, confirming the stability of the GNS decoration by Ru-PhenVS even after their uptake.

The cytotoxicity of GNS@Ru and Ru-PhenVS was measured and compared both on cells treated and incubated in the dark and with the addition of an irradiation step using a low power commercial lamp (1.3 mW/cm^2) emitting in the visible range. After the irradiation, the dose of GNS@Ru required to see an evident cytotoxicity started from a Ru concentration of 0.08 μM, about an order of magnitude lower compared to the Ru dose needed for Ru-PhenVS alone (0.63 μM). These results confirmed the boosting of the photocytotoxicity of Ru-PhenVS when in close proximity of the GNS. Indeed, an analogous test carried out on cells treated with GNS decorated with a layer of ISA23SH and one of PhenVS (thus prepared in the same way as GNS@Ru but using the PhenVS polymer without the Ru complex) did not show any difference in cytotoxicity between the irradiated and non-irradiated samples and confirmed that the system possess a photocytotoxic effect only when the Ru complex is present and it is not due neither to the GNS alone nor the polymer before complexing the Ru.

Finally, the intracellular ROS produced by the two compounds after the irradiation was tested to confirm that the enhanced photocytotoxicity was due to an increased ROS production. The experiment confirmed an increased ROS production when cells were treated GNS@Ru and irradiated, reaching an 8-fold increase in ROS production at a Ru concentration that did not generate any neither in the dark nor without the closeness to GNS.

On the other hand, a certain dose-dependent cytotoxicity in the dark of GNS@Ru was also observed and attributed to the very high gold concentration for the GNS@Ru doses employed in the experiment (0.7-22.3 mg/mL). According to the literature and to an additional experiment we carried out treating the cells with GNS@ISA23SH@PhenVS, GNS should not exhibit any evident cytotoxicity up to a gold concentration of 300-500 μg/mL. For this reason, future work will focus on improving the phenanthroline loading into the polymeric chain, as well as further modifying the phenanthroline substitution strategy, in order to increase the amount of Ru complex in the polymer and decrease the Au:Ru ratio per particle in the GNS@Ru samples. This optimization aims to exploit the effective boosting of ROS generation while avoiding additional gold cytotoxic effect observed at high GNS concentration.

Also, the mechanism of ROS generation by GNS@Ru should be further studied employing various assays. In addition, $^1O_2$ generation by two-photon excitation should also be explored to exploit the GNS absorption in the NIR region, enabling deeper light penetration into tissues when GNS@Ru are applied to 3D cellular models, solid tumors, and tissue samples.

In conclusion, even though further optimization work and more studies on these GNS@Ru nanohybrid compounds are needed, the GNS decoration strategy employed in this work and the preliminary biological tests resulted extremely promising in exploiting the LSPR effect of GNS to boost the of $^1O_2$ generation of a polyamidoamine-based photosensitizer, for its future antitumoral application in PDT.

Experimental

Materials and instruments

Ultrapure water (Milli-Q, Millipore, resistivity = 18 MΩcm^{-2}) was used for the preparation of the aqueous solutions. THF was distilled from sodium/benzophenone just before its use. Commercial reagents were used without further purification. The Ru precursors $Ru(phen)_2Cl_2$ and $Ru(phen)_2(OTf)_2$ were prepared following the same literature procedure employed for the synthesis of $Ru(bpy)_2Cl_2$ and $Ru(bpy)_2(OTf)_2$.[50] The positive charged polystyrene nanoparticles (PS/R-NH_2) used in the optimization of the ROS generation experiments protocol were bought from Bangs laboratories (PA02N, INV# L150902B, LOT# 11638). ^{1}H NMR experiments were performed on a Bruker DRX400 spectrometer with a Bruker 5 mm BBI Z-gradient probe head with a maximum gradient strength of 53.5 G/cm (π/2 pulse: 1 H 8.5 μs, 13C 13 μs) operating at 400.13 MHz. UV–vis absorption spectra were acquired on an Agilent (model 8543) single beam spectrophotometer equipped with a diode array detector using a quartz cuvette with a 1 cm path length at room temperature. A ThermoMAX microplate reader was employed to measure the absorbance and the luminescence in the biological assays, using either multiwell plates (96- or 48-well plates, depending on the experiment) or a support for quartz cuvettes. Emission spectra of Ru-PhenAN, GNS@Ru-PhenAN, $[Ru(phen)_2(phen\text{-}cysteamine)]^{2+}$ and of Ru-PhenVS were acquired using an Edinburgh FLS980 spectrofluorimeter equipped with a 450 W xenon arc lamp, while those of GNS@Ru with 4 polymeric layers on a Shimadzu RF-6000. All the spectra were corrected for source intensity (lamp and grating) and emission spectral response (detector and grating) by standard correction curves.

Time-resolved measurements were performed using the time-correlated single photon counting (TCSPC) option on the FLS980. A monochromatic LED emitting at 445 nm was used as the pulsed excitation source, it was mounted directly on the sample chamber, and the emission was collected by a multichannel plate MCP-PMT Hamamatsu H10720−01 single photon-counting detector, correlating the detected photons to the excitation pulse by a time-to-amplitude converter (TAC). The data analysis was performed using the commercially available F980 software (Edinburgh Instruments). The goodness of the data fitting was assessed by minimizing the reduced chi-squared function (χ^2). Photoluminescence quantum yields (Φ) were collected for an optically diluted solution with a Hamamatsu C11347−11 Quantaurus-QY absolute PL quantum yield spectrometer, equipped with a xenon light source (150 W), a monochromator, and a Spectralon integrating sphere, and employing the commercially available U6039−05 PLQY measurement software (Hamamatsu Photonics Ltd., Shizuoka, Japan). The samples were excited in the 400-500 nm range. TEM measurements were carried out on a FEI TECNAI G2 F20, equipped with a Multiscan 794 GATAN detector. EDS microanalyses were performed employing an Azec Energy instrument equipped with an Xplore OXFORD detector. The size distribution by dynamic light scattering and zeta potential of the samples were determined using a Malvern ZetaSizer Nano ZS (Malvern Instruments Ltd.) at 25 °C, using as dispersants milliQ water, DPBS, and complete cell culture medium (cMEM) consisting of MEM (Gibco, Thermo Fisher Scientific) supplemented with 10% v/v Fetal Bovine Serum (FBS, Serana). Every sample was measured 3 times and the size results are the average of at least 10 runs for each replicate measurement. The uptake, photostability and intracellular ROS generation experiments that involve flow cytometry were carried out using a Cytoflex S flow cytometer (Beckman Coulter). Data was analyzed using FlowJo software (FlowJo, LLC), gating the forward and side scattering plots to select live and single cells. For each condition, 15000 cells were acquired for three replicate samples and the mean and standard deviation of the median cell fluorescence intensity of each sample calculated. Confocal microscopy pictures of the cells treated with the two compounds were recorded using a Leica Stellaris CRS microscope. Ru-PhenVS and GNS@Ru were excited at 440 nm and Hoechst stain at 405 nm, while the fluorescence was detected respectively between 604-696 nm and 430-536 nm. The light reflected by GNS was collected at the same wavelength as the incident laser (430-450 nm).

Synthesis of 5-(2-aminoethanesulfanyl)-1,10-phenanthroline(phen-cysteamine)

The functionalized phenanthroline exposing a terminal amino group was prepared from the commercial 1,10-phenanthroline with a two-step synthesis, consisting first in the formation of an epoxide on the central ring of phenanthroline (1,10-phenanthroline-5,6-epoxide) and then in its opening with the thiol group of a cysteamine molecule, restoring the aromaticity of the phenanthroline central ring.

For the first step, we followed and slightly modified a literature procedure,[27] Consisting of a two-phase $CHCl_3/H_2O$ reaction in which commercial bleach is used as a reagent. 1,10-phenanthroline·H_2O (1 g, 5.055 mmol) and tetrabutylammonium hydrogensulfate (858 mg, 2.527 mmol) were dissolved in 10 mL of $CHCl_3$. Na_2HPO_4 (6.03 g, 34.6 mmol) was dissolved in 20 mL of milliQ water, and 50 mL of commercial bleach was added to obtain a final hypochlorite concentration of 3.2%. The pH of the solution was adjusted to 8.75, and the chloroform solution was added. After mixing the two phases, the organic one turned to a bright yellow color that slowly faded during the reaction. The pH was monitored and kept around 8.75. After 1 h, the TLC plate (AcOEt:hexane:MeOH 8:2:0.1) confirmed the formation of the sole product (R_f = 0.14), which was extracted with $CHCl_3$ (3 x 10 mL) and washed first with $Na_2S_2O_5$ 10% (2 x 12.5 mL) and then with H_2O (3 x 10 mL). During the washing steps, the organic phase turned from

transparent to orange and then to orange-yellowish. It was finally dried over anhydrous $MgSO_4$, filtered, dried under vacuum with the mechanical pump, and triturated with Et_2O, obtaining a brown-whitish solid with almost a quantitative yield (1.1051 g). ^{1}H NMR (9.4 T, 300 K, $CDCl_3$) δ 8.95 ppm (2H, dd, CH(2,9), J= 4.7, 1.7 Hz), 8.95 ppm (2H, dd, CH(2,9), J= 4.7, 1.7 Hz), 8.04 ppm (2H, dd, CH (4,7), J= 7.7, 1.8 Hz), 7.44 ppm (2H, dd, CH(3,8), J= 7.7, 4.7 Hz), 4.66 ppm (2H, s, CH(5,6)).

Half of this solid (500 mg, 2.548 mmol) was then dissolved under inert N_2 atmosphere in 3.5 mL of dry EtOH with 1 equivalent of cysteamine·HCl (289.5 mg, 2.548 mmol). A suspension of EtONa (693.9 mg, 4 eq) in 35 mL of dry EtOH was then added, following a procedure from the literature.[51] The reaction was carried out at 50 °C for 45 h under inert N_2 atmosphere. The mixture was then filtered, dried under vacuum with the mechanical pump and triturated with Et_2O, obtaining 326.6 mg of a brownish solid. A ^{1}H NMR experiment showed the presence of the non-aromatized subproduct. For this reason, the solid was mixed again with an EtONa suspension in dry EtOH (325.2 mg, 4 eq) to further react for another 36 h. The mixture was filtered and dried, obtaining an oily brown solid that was dissolved in 3 mL of $CHCl_3$ and precipitated with hexane (15 mL). The solid was dried again and triturated with hexane, obtaining 259.7 mg of powder (yield 40%). ^{1}H NMR of phen-cysteamine: (9.4 T, 300 K, MeOD-d_4) δ 9.14 (dd, 1H, CH(2), J= 4.4, 1.6 Hz), 9.05 (dd, 1H, CH(9), J= 4.4, 1.8 Hz), 8.92 (dd,1H, CH(4), J= 8.4, 1.7 Hz), 8.43 (dd, 1H, CH(7), J= 8.1, 1.8 Hz), 8.07 (s, 1H, CH(6)), 7.85 (dd, 1H, CH(3), J= 4.4, 4.1 Hz), 7.77 (dd, 1H, CH(8), J= 4.4, 3.8 Hz), 3.30 (m, 2H, CH_2(3')), 2.98 (t, 2H, CH_2(2'), J= 6.8 Hz).

Synthesis of the complex $[Ru(phen)_2(phen\text{-}cysteamine)](PF_6)_2$

Phen-cysteamine (3.8 mg, 0.0149 mmol) and $[Ru(phen)_2Cl_2]$ (7.4 mg, 0.0139 mmol) were suspended in 2.5 mL of D_2O to follow the reaction through NMR spectroscopy. The pH was adjusted to ca. 6 and the mixture was heated to 50°C using a microwave reactor. After 2.5h of heating (divided into 30 min cycles to monitor the reaction progress under a 366 nm UV lamp), the mixture appeared dark brown, given by the Ru precursor partially dissolved and still partially solid. Since the NMR spectra showed the absence of the phen-cysteamine signals, one additional equivalent (3.6 mg, 0.0141 mmol) was added, two more heating cycles of 30 min using the microwave were carried out and the reaction was finally heated at 60 °C for 2 days, yielding to a solution with an intense orange color and a bright orange luminescence under UV lamp. The solution was filtered to remove the remaining dark solid, washed with 0.5 mL of milliQ water, and the product was precipitated adding a saturated NH_4PF_6 solution (0.74 g for 1 mL of solution) and filtered, obtaining 11.5 mg of orange powder (yield 91.4%). The product was analyzed by NMR experiments.

Synthesis of the cationic copolymer PhenVS

Batch B: Phen-cysteamine (39.5 mg, 0.154 mmol) and 1,4-bis(acryloyl)piperazine (300.1 mg, 1.545 mmol, 10 eq) were dissolved in 900 µL of H_2O under inert N_2 atmosphere and the pH was adjusted to ca. 10. The mixture was left under magnetic stirring at room temperature for 24 h, after which the piperazione·$6H_2O$ (270.9 mg, 1.395 mmol, 9 eq) was added. The reaction was carried out under N_2 for 6 days at 60°C during the days and at room temperature during the nights. After the nights the solidification of the mixture occurred, and it was melted again by sonicating and heating at 60 °C. When a caramel-like viscous mixture was obtained, the reaction was stopped by adding 5 mL of H_2O to dilute and by lowering the pH to ca. 3 with HCl 2 M. The suspension was first filtered with a syringe cellulose filter (cutoff 20 µm), then further diluted to 50 mL and finally filtered using an Amicon membrane with a

nominal cutoff of 1000 Da. The retained solution was lyophilized, obtaining 191.5 mg of a pink fluffy solid, with a M_w of 4.99 kDa. The polymer was further characterized by NMR, from whose integrals the molar percentage of the phenanthroline units was calculated, between 2-3% depending on the different batches of polymer.

Synthesis of the complex Ru-PhenVS

173.3 mg of phenAN (0.555 mmol) was dissolved in 8 mL of H_2O and $[Ru(phen)_2Cl_2]$ or $[Ru(phen)_2OTf_2]$ was added (6.2 mg, 0.0116, 1 eqv compared to the phenanthroline units in the polymer). The mixture was vigorously magnetically stirred, and the reaction was carried out at 50 °C for 90 minutes in a microwave reactor. The black suspension turned orange and clear, showing an orange luminescence under a 365 nm UV lamp. The solution was diluted to 50 mL and filtered first from the solid unreacted Ru precursor with a syringe cellulose filter, and then with an Amicon membrane with a nominal cutoff of 1000 Da. The retained solution was finally lyophilized, obtaining 93.4 mg of an orange fluffy solid.

Saturation of the terminal double bonds of Ru-PhenVS

The terminal double bonds of the polymer were saturated before its use with the cells, through a treatment with an excess of morpholine. The freeze-dried Ru-PhenVS was dissolved in 3 mL of milliQ water (pH of the solution 3) and 15 µL of morpholine were added, carrying out the reaction for 3 days at RT. The obtained product was purified with ultrafiltration using first a centrifugal filter with a cut-off of 3000 Da (3 cycles of 3000 g for 40 minutes each). To reduce the product loss, the filtered aliquots were unified and filtered again using another filter with a lower cut-off of 1000 Da. All the collected products were freeze-dried and analyzed with ^1H NMR.

Synthesis of gold nanostars with Triton X-100 (GNS@TX-100)

The lab glassware was treated with aqua regia for 15 min prior to the GNS synthesis and all the synthetic steps involving GNS, followed by 3 washing cycles with milliQ-H_2O and sonication for 3 min.

Gold nanostars (GNS@TX-100) were prepared following a literature procedure[36] with slight variations. First the gold seeds were prepared by adding to a 0.2 M Triton X-100 solution (5 mL), 5 mL of a 0.5 mM of $HAuCl_4$ and 600 µL of a 0.01 M $NaBH_4$ ones. The resulting solution was gently hand-shaked and its color turned to orange-brune. The reagents were kept at 0 °C in an ice bath for 1.5 h before the seed preparation. Then GNS were growth from the seeds, by adding to a 0.2 Triton X-100 solution (15 mL) 750 µL of $AgNO_3$ 4 mM, 15 mL of $HAuCl_4$ 1 mM, 510 µL of ascorbic acid 0.0788 M and 36 µL of the seed solution in this order, at RT and under stirring. After 1h the GNS@TX-100 were obtained, as confirmed by the blueish-grayish color of the solution, depending on the dimensions of the obtained nano-objects. Both the seeds and the $HAuCl_4$ solutions were kept at 0 °C for 2h before the GNS growth step. The prepared GNS were characterized with UV-vis spectroscopy as well as size DLS and ζ-potential measurements before their use.

To determine the yield of the synthesis, an aliquot of the fresh prepared GNS@TX-100 was centrifugated at 20817 rcf for 15 minutes and washed various time with H_2O. The residual pellet was dried overnight at 50 °C and weighed. The calculated yield (79.9%) is in accordance with the literature data reported for

this kind of synthesis (75%)[52]. From our experimental yield we calculated a GNS concentration of 0.079 mg/mL.

Functionalization of GNS with phenAN-Ru via ligand exchange (GNS@Ru-phenAN)

To a 10 mL aliquot of GNS@TX-100, a certain amount of the Ru-phenAN solution was added, aiming to exchange the Triton X-100 molecules on the gold surface with the polyamidoamine polymer. The interaction was carried out overnight at RT, testing different polymer:Au ratios and two different purification procedures.

Regarding its purification, both dialysis and centrifugation were tested. The functionalized GNS@phenAN-Ru was either dialyzed for 5 days using a cut-off of 12-14 kDa or centrifuged 5 times at 6500 g for 15 min, until the complete disappearance of the UV-vis bands assigned to the TX-100 (at 300 nm). Even though with the first method the TX-100 was selectively removed, it resulted longer and less effective than the centrifugation, which was chosen for the purification of such nanoparticles for all the next attempts and preparation.

With this approach, three different polymer:Au ratios were tested to find the best one in stabilizing the GNS, calculated from the experimental yield of the GNS synthesis: 0.35:1, 1.5:1 and 3.45.

Functionalization of GNS with Ru-phenAN-cystamine via ligand exchange (GNS@Ru-phenAN-cystamine)

The functionalization of GNS with Ru-phenAN-cystamine was carried out similarly to the optimized procedure followed for GNS@Ru-phenAN. To 10 mL of GNS@TX-100, 2.6 mL of Ru-phenAN-cystamine (0.87 mg/mL in water) were added, to obtain a polymer:Au ratio of 2.89. The mixture was left under magnetic stirring to interact overnight at RT, after which the GNS@Ru-phenAN-cysteamine were purified from the excess of Triton X-100 and unreacted polymer through centrifugation (6500 g for 15 min) and washed with fresh water until the disappearance of the UV-vis bands assigned to TX-100.

Functionalization of GNS with four polymeric layers with a layer-by-layer approach (GNS@(ISA23SH@PhenAN)$_2$-Ru)

For the functionalization of the GNS with a first polymeric layer, a ligand exchange with the Triton X-100 was carried out similarly to the procedure described above. To a 10 mL aliquot of GNS@TX-100, a certain volume of ISA23SH (concentration of the stock solution 1.5-2 mg/mL) was added to obtain a polymer:Au mass ratio of 2:1. The pH of the mixture was adjusted to 9 and the interaction was carried out overnight at RT. The so-obtained GNS@ISA23SH were purified through centrifugation (7000 rcf for 1h) and resuspended in 10 mL of fresh water for the stacking of other polymeric layers (either the positive PhenAN or the negative ISA23SH) exploiting the electrostatic interactions between them.

From the second to the fourth layer, the polymer:Au mass ratio was increased to 4:1 (starting again from polymer stocks of 1.5-2 mg/mL). The pH was adjusted to 6.5 for the addition of the positive polymer layers (the second and the fourth) and to 7 for the third layer. The product of each step was purified via centrifugation as described above. For the preparation of the fourth and most external layer, the PhenAN bearing the Ru complex (Ru-PhenAN) was used instead of the same polymer with the free phenantroline used for the second layer.

The product of each step was characterized by UV-vis spectroscopy and DLS and ζ-potential measurements, to confirm the success of the layer-by-layer approach.

Functionalization of GNS with two polymeric layers with a layer-by-layer approach (GNS@ISA23SH@PhenVS-Ru and GNS@ISA23SH@PhenVS)

The functionalization of the GNS with only two polymeric layers was carried out similarly to the one described above. To 4 mL of GNS@TX-100 a solution of ISA23SH was added (400 µL of a 1.94 mg/mL stock) to obtain a 2:1 polymer:Au mass ratio. The pH was adjusted to ca. 8.5 and the interaction was carried out overnight at RT. The GNS@ISA23SH were divided into 1 mL aliquots and centrifuged at 7000 rcf for 15 min. The supernatants were then centrifuged again, and all the pellets unified and resuspended in 4 mL of fresh milliQ water.

For the second layer (Ru-PhenVS) different amounts of polymer were added to the GNS suspension to maintain the polymer:Au mass ratio around 4 and the concentration of Ru in the different batches the same. The pH was adjusted to ca. 6.5 and the interaction was carried out overnight at RT. For the samples in which the external layer is PhenVS, the amount of polymer added was the same as the corresponding polymer bearing the Ru complex.

The final compound was purified via centrifugation as for the first layer, the functionalized GNS were washed once with milliQ water and resuspended in 50 µL of sterile water for their use with cells, to obtain a Ru concentration in the sample of 26.4 µM.

Cell culture of HeLa cells

The HeLa cell line was cultured at 37 °C with 5% CO_2 in complete MEM (Minimum Essential Medium) supplement, enriched with FBS (Fetal Bovine Serum) (50 mL added to 500 mL of MEM), without the addition of any antibiotic. The cells with ca. 80% confluence were split every 2/3 days, in order to keep a cell concentration of 10^6 cells in a 75 cm^2 polystyrene flask.

Flow cytometry cell uptake experiment

In a 24-well plate, HeLa cells were seeded with a density of either 50000 cells/well or 30000 cells/well, depending on the experiment, in 500 µL of complete MEM (cMEM). After 24h the medium was removed from the wells and replaced with 250 µL of fresh one (for the negative control samples) or with 250 µL of a solution of Ru-PhenVS, GNS@Ru (2 or 4 layers) or GNS@ISA23SH@PhenAN in cMEM. Cells were then incubated for either 5h or 24h at 37 °C in a 5% CO_2 atmosphere.

After the incubation time, the cells were washed once with 500 µL of fresh cMEM, twice with DPBS (500 µL x2) and harvested through a 5 min incubation with trypsin (TEP, 250 µL) at 37 °C. 500 uL of cMEM were added and the cells were transferred into FACS tubes. The cells were then centrifuged (300 rcf for 5 min), the supernatant discarded by inversion of the tubes, and the pellet suspended in 100 µL of DPBS for flow cytometry analysis (excitation laser: 405 nm, fluorescence channel: 610/20 BP).

Photocytotoxicity assay (MTT viability assay)

In two 96-well plates, HeLa cells were seeded with a density of either 5000 cells/well or 7000 cells/well in 200 µL of cMEM. After 24h the medium was replaced with 100 µL of fresh one (for the negative control samples) or with 100 µL of a solution of Ru-PhenVS, GNS@Ru (2 or 4 layers) or GNS@ISA23SH@PhenVS in cMEM. Cells were then incubated for 24h at 37 °C in a 5% CO_2 atmosphere.

After the incubation time, the wells were emptied with a pipet, washed once with 200 µL of DPBS and filled with 50 µL of fresh cMEM. One of the two plates was then irradiated for either 5 or 15 min with a commercial lamp emitting in the visible, while the other was kept in the dark outside of the incubator for the same time. 150 µL of fresh cMEM were then added to each well and an additional incubation of the plates was carried out.

After an incubation of either 4h or 24h, 20 µL of 3-(4,5-di methyl thiazol-2-yl)-2,5-diphenyltetrazolium bromide (MTT) (5 mg/mL in DPBS) were added to each well and the plates were incubated for 90 min at 37 °C with 5% CO_2. The wells were then emptied with a pipette and the dark powder at the bottom of the wells was solubilized with 200 µL of DMSO (and gently mixed at 400 rpm for 15 min in the plate shaker). If needed the solution was additional mixed with the pipet.

The absorbance at 550 nm was read for each well. Three replicas were prepared for each condition and the average absorbance values and standard deviation were calculated. The cell viability % was then calculated and normalized by the value obtained for untreated cells not incubated with the compounds for each plate.

Intracellular ROS generation assay

In the protocol optimization, HeLa cells were seeded with a density of 15000 or 20000 cells/well in 250 µL of cMEM in a 48-well plate. After 24h the medium was replaced with either 125 µL of fresh one or with suspensions of PS/R-NH_2 nanoparticles (2.5-10 µg/mL) in 125 µL of cMEM. The cells were incubated for 24h, after which they were washed twice 250 µL of DBPS and harvested with 125 µL of TEP (5 min at 37 °C with 5% CO_2). 250 uL of cMEM were added and the cells were transferred into FACS tubes and centrifuged (300 rcf for 5 min). The supernatant was discarded and the pellets were suspended in either 50 µL or 100 µL of CM-H_2DCFDA (ROS probe), with a concentration of either 1.25 µM or 2.5 µM in DPBS. After 20 min of incubation at 37 °C with 5% CO_2, 500 µL of DPBS were added to wash, the cells were centrifuged (once or twice) at 400 g for 5 min, the pellets resuspended in 50 µL of DPBS and analyzed with flow cytometry (excitation laser: 488 nm, fluorescence channel: 525/40 BP).

For the experiments with Ru-PhenVS and GNS@Ru, in two 48-well plates, HeLa cells were seeded with a density of 20000 cells/well in 250 µL of cMEM. After 24h the medium was replaced with 125 µL of fresh one (for the negative control) or with 125 µL of a suspension of Ru-PhenVS or GNS@Ru (2 layers). The cells were incubated for 24h, after which they were washed once with DPBS (250 µL) and 100 µL of fresh cMEM were added. One of the two plates was then irradiated for either 5 or 15 min with a commercial lamp emitting in the visible, while the other was kept in the dark outside of the incubator for the same time. 150 µL of fresh cMEM were then added to each well and an additional incubation of the plates was carried out.

After another incubation (whose time varied depending on the experiment), cells were washed twice with 250 µL of DBPS and harvested with 125 µL of TEP (5 min at 37 °C with 5% CO_2). 250 uL of cMEM

were added and the cells were transferred into FACS tubes and centrifuged (300 rcf for 5 min). The supernatant was the discarded and the pellets were suspended in 100 µL of CM-H_2DCFDA (2.5 µM in DPBS). After 20 min of incubation at 37 °C with 5% CO_2, 500 µL of DPBS were added to wash, the cells were centrifuged at 400 g for 5 min, the pellets resuspended in 50 µL of DPBS and analyzed with flow cytometry (excitation laser: 488 nm, fluorescence channel: 525/40 BP).

Preparation of samples for Confocal Microscopy

In a 24-well plate, sterile round glass coverslips with a 12 mm diameter were put in each well before the seeding of HeLa cells (50000 cells/well in 500 µL of cMEM). After 24 of incubation at 37 °C in a 5% CO_2 atmosphere, the medium was replaced with 250 µL of a solution of Ru-PhenVS or GNS@Ru (2 layers) or with fresh one (for the control samples) and the cells additionally incubated for 24h.

After the exposure time, the cells were washed with cMEM and DPBS as for the uptake experiment and fixed with 500 µL of 4% formalin (15 min of incubation at RT, keeping the plate in the dark with aluminum foil). Cells were incubated for 5 min with 500 µL of a Hoechst stain solution (3 µg/mL) to stain the nuclei, rewashed with DPBS, and mounted on microscope coverslip slides using a drop of MOWIOL mounting medium.

References

(1) Mosquera, J.; García, I.; Liz-Marzán, L. M. Cellular Uptake of Nanoparticles versus Small Molecules: A Matter of Size. *Acc. Chem. Res.* **2018**, *51* (9), 2305–2313. https://doi.org/10.1021/acs.accounts.8b00292.

(2) Doherty, G. J.; McMahon, H. T. Mechanisms of Endocytosis. *Annu. Rev. Biochem.* **2009**, *78* (1), 857–902. https://doi.org/10.1146/annurev.biochem.78.081307.110540.

(3) Hillaireau, H. Investigating Interactions Between Nanoparticles and Cells: Internalization and Intracellular Trafficking. In *Polymer Nanoparticles for Nanomedicines*; Springer International Publishing, 2016; pp 291–323. https://doi.org/10.1007/978-3-319-41421-8_10.

(4) Salvati, A.; Åberg, C.; dos Santos, T.; Varela, J.; Pinto, P.; Lynch, I.; Dawson, K. A. Experimental and Theoretical Comparison of Intracellular Import of Polymeric Nanoparticles and Small Molecules: Toward Models of Uptake Kinetics. *Nanomedicine* **2011**, *7* (6), 818–826. https://doi.org/10.1016/j.nano.2011.03.005.

(5) Liu, J.; Peng, Q. Protein-Gold Nanoparticle Interactions and Their Possible Impact on Biomedical Applications. *Acta Biomater.* **2017**, *55*, 13–27. https://doi.org/10.1016/j.actbio.2017.03.055.

(6) Sasidharan, A.; Riviere, J. E.; Monteiro-Riviere, N. A. Gold and Silver Nanoparticle Interactions with Human Proteins: Impact and Implications in Biocorona Formation. *J. Mater. Chem. B* **2015**, *3* (10), 2075–2082. https://doi.org/10.1039/C4TB01926A.

(7) Peng, Q.; Mu, H. The Potential of Protein–Nanomaterial Interaction for Advanced Drug Delivery. *Journal of Controlled Release* **2016**, *225*, 121–132. https://doi.org/10.1016/j.jconrel.2016.01.041.

(8) Monopoli, M. P.; Walczyk, D.; Campbell, A.; Elia, G.; Lynch, I.; Baldelli Bombelli, F.; Dawson, K. A. Physical−Chemical Aspects of Protein Corona: Relevance to in Vitro and in Vivo Biological Impacts of Nanoparticles. *J. Am. Chem. Soc.* **2011**, *133* (8), 2525–2534. https://doi.org/10.1021/ja107583h.

(9) Kim, J. A.; Aberg, C.; Salvati, A.; Dawson, K. A. Role of Cell Cycle on the Cellular Uptake and Dilution of Nanoparticles in a Cell Population. *Nat. Nanotechnol.* **2012**, *7* (1), 62–68. https://doi.org/10.1038/nnano.2011.191.

(10) Ranucci, E.; Manfredi, A. Polyamidoamines: Versatile Bioactive Polymers with Potential for Biotechnological Applications. *Chemistry Africa* **2019**, *2* (2), 167–193. https://doi.org/10.1007/s42250-019-00046-1.

(11) Donghi, D.; Maggioni, D.; D'Alfonso, G.; Amigoni, F.; Ranucci, E.; Ferruti, P.; Manfredi, A.; Fenili, F.; Bisazza, A.; Cavalli, R. Tricarbonyl-Rhenium Complexes of a Thiol-Functionalized Amphoteric Poly(Amidoamine). *Biomacromolecules* **2009**, *10* (12), 3273–3282. https://doi.org/10.1021/bm9008638.

(12) Maggioni, D.; Arosio, P.; Orsini, F.; Ferretti, A. M.; Orlando, T.; Manfredi, A.; Ranucci, E.; Ferruti, P.; D'Alfonso, G.; Lascialfari, A. Superparamagnetic Iron Oxide Nanoparticles Stabilized by a Poly(Amidoamine)-Rhenium Complex as Potential Theranostic Probe. *Dalton Trans.* **2014**, *43* (3), 1172–1183. https://doi.org/10.1039/C3DT52377B.

(13) Maggioni, D.; Fenili, F.; D'Alfonso, L.; Donghi, D.; Panigati, M.; Zanoni, I.; Marzi, R.; Manfredi, A.; Ferruti, P.; D'Alfonso, G.; Ranucci, E. Luminescent Rhenium and Ruthenium Complexes of an Amphoteric Poly(Amidoamine) Functionalized with 1,10-Phenanthroline. *Inorg. Chem.* **2012**, *51* (23), 12776–12788. https://doi.org/10.1021/ic301616b.

(14) Behr, J.-P. The Proton Sponge: A Trick to Enter Cells the Viruses Did Not Exploit. *Chimia (Aarau).* **1997**, *51* (1–2), 34. https://doi.org/10.2533/chimia.1997.34.

(15) Maggioni, D.; Galli, M.; D'Alfonso, L.; Inverso, D.; Dozzi, M. V.; Sironi, L.; Iannacone, M.; Collini, M.; Ferruti, P.; Ranucci, E.; D'Alfonso, G. A Luminescent Poly(Amidoamine)-Iridium Complex as a New Singlet-Oxygen Sensitizer for Photodynamic Therapy. *Inorg. Chem.* **2015**, *54* (2), 544–553. https://doi.org/10.1021/ic502378z.

(16) Mascheroni, L.; Dozzi, M. V.; Ranucci, E.; Ferruti, P.; Francia, V.; Salvati, A.; Maggioni, D. Tuning Polyamidoamine Design to Increase Uptake and Efficacy of Ruthenium Complexes for Photodynamic Therapy. *Inorg. Chem.* **2019**, *58* (21), 14586–14599. https://doi.org/10.1021/acs.inorgchem.9b02245.

(17) Mascheroni, L.; Francia, V.; Rossotti, B.; Ranucci, E.; Ferruti, P.; Maggioni, D.; Salvati, A. Light-Triggered Trafficking to the Cell Nucleus of a Cationic Polyamidoamine Functionalized with Ruthenium Complexes. *ACS Appl. Mater. Interfaces* **2020**, *12* (31), 34576–34587. https://doi.org/10.1021/acsami.0c08033.

(18) Kang, K. A.; Wang, J.; Jasinski, J. B.; Achilefu, S. Fluorescence Manipulation by Gold Nanoparticles: From Complete Quenching to Extensive Enhancement. *J. Nanobiotechnology* **2011**, *9*. https://doi.org/10.1186/1477-3155-9-16.

(19) Badshah, M. A.; Koh, N. Y.; Zia, A. W.; Abbas, N.; Zahra, Z.; Saleem, M. W. Recent Developments in Plasmonic Nanostructures for Metal Enhanced Fluorescence-Based Biosensing. *Nanomaterials* **2020**, *10* (9), 1749. https://doi.org/10.3390/nano10091749.

(20) Fernández-Lodeiro, J.; Nuñez, C.; Lodeiro, A. F.; Oliveira, E.; Rodríguez-González, B.; Dos Santos, A. A.; Capelo, J. L.; Lodeiro, C. New-Coated Fluorescent Silver Nanoparticles with a Fluorescein Thiol Esther Derivative: Fluorescent Enhancement upon Interaction with Heavy Metal Ions. *Journal of Nanoparticle Research* **2014**, *16* (3). https://doi.org/10.1007/s11051-014-2315-4.

(21) Jeong, Y.; Kook, Y.-M.; Lee, K.; Koh, W.-G. Metal Enhanced Fluorescence (MEF) for Biosensors: General Approaches and a Review of Recent Developments. *Biosens. Bioelectron.* **2018**, *111*, 102–116. https://doi.org/10.1016/j.bios.2018.04.007.

(22) Li, J.-F.; Li, C.-Y.; Aroca, R. F. Plasmon-Enhanced Fluorescence Spectroscopy. *Chem. Soc. Rev.* **2017**, *46* (13), 3962–3979. https://doi.org/10.1039/C7CS00169J.

(23) Zhang, Y.; Aslan, K.; Previte, M. J. R.; Geddes, C. D. Metal-Enhanced Singlet Oxygen Generation: A Consequence of Plasmon Enhanced Triplet Yields. *J. Fluoresc.* **2007**, *17* (4), 345–349. https://doi.org/10.1007/s10895-007-0196-y.

(24) García Calavia, P.; Bruce, G.; Pérez-García, L.; Russell, D. A. Photosensitiser-Gold Nanoparticle Conjugates for Photodynamic Therapy of Cancer. *Photochemical & Photobiological Sciences* **2018**, *17* (11), 1534–1552. https://doi.org/10.1039/c8pp00271a.

(25) Zhang, Y.; Aslan, K.; Previte, M. J. R.; Geddes, C. D. Plasmonic Engineering of Singlet Oxygen Generation. *Proceedings of the National Academy of Sciences* **2008**, *105* (6), 1798–1802. https://doi.org/10.1073/pnas.0709501105.

(26) Vankayala, R.; Sagadevan, A.; Vijayaraghavan, P.; Kuo, C. L.; Hwang, K. C. Metal Nanoparticles Sensitize the Formation of Singlet Oxygen. *Angewandte Chemie - International Edition* **2011**, *50* (45), 10640–10644. https://doi.org/10.1002/anie.201105236.

(27) Howell, B. A.; Dumitrascu, A. Thermal Stability of Bidendate Nitrogen Ligands Tethered to Multiwall Carbon Nanotubes. *J. Therm. Anal. Calorim.* **2010**, *102* (2), 505–512. https://doi.org/10.1007/s10973-010-0774-0.

(28) Z. Antkowiak, W.; Antkowiak, R. On the Chlorine Addition to the C(5)-C(6) Bridge and the N-Oxidation of 1,10-Phenanthroline. *Heterocycles* **1998**, *47* (2), 893. https://doi.org/10.3987/COM-97-S(N)99.

(29) Ferruti, P. Poly(Amidoamine)s: Past, Present, and Perspectives. *J. Polym. Sci. A Polym. Chem.* **2013**, *51* (11), 2319–2353. https://doi.org/10.1002/pola.26632.

(30) Liu, X.; Zhang, X.; Han, Y.; Li, X.; Li, J. Application and Suggestions of Morpholine Ring as a Lysosome Targeting Group. *Chemistry (Easton).* **2025**, *7* (3), 82. https://doi.org/10.3390/chemistry7030082.

(31) Yu, H.; Xiao, Y.; Jin, L. A Lysosome-Targetable and Two-Photon Fluorescent Probe for Monitoring Endogenous and Exogenous Nitric Oxide in Living Cells. *J. Am. Chem. Soc.* **2012**, *134* (42), 17486–17489. https://doi.org/10.1021/ja308967u.

(32) Wu, L.; Li, X.; Ling, Y.; Huang, C.; Jia, N. Morpholine Derivative-Functionalized Carbon Dots-Based Fluorescent Probe for Highly Selective Lysosomal Imaging in Living Cells. *ACS Appl. Mater. Interfaces* **2017**, *9* (34), 28222–28232. https://doi.org/10.1021/acsami.7b08148.

(33) Bader, C. A.; Simpson, P. V.; Dallerba, E.; Stagni, S.; Johnson, I. R. D.; Hickey, S. M.; Sorvina, A.; Hackett, M.; Sobolev, A. N.; Brooks, D. A.; Massi, M.; Plush, S. E. Synthesis and Cellular Uptake of Neutral Rhenium(I) Morpholine Complexes. *Dalton Transactions* **2024**, *53* (7), 3407–3413. https://doi.org/10.1039/D3DT03067A.

(34) Nohara, I.; Wegeberg, C.; Devereux, M.; Prescimone, A.; Housecroft, C. E.; Constable, E. C. The Surprising Effects of Sulfur: Achieving Long Excited-State Lifetimes in Heteroleptic Copper(I) Emitters. *J. Mater. Chem. C Mater.* **2022**, *10* (8), 3089–3102. https://doi.org/10.1039/D1TC05591G.

(35) Queffélec, C.; Pati, P. B.; Pellegrin, Y. Fifty Shades of Phenanthroline: Synthesis Strategies to Functionalize 1,10-Phenanthroline in All Positions. *Chem. Rev.* **2024**, *124* (11), 6700–6902. https://doi.org/10.1021/acs.chemrev.3c00543.

(36) Dacarro, G.; Pallavicini, P.; Bertani, S. M.; Chirico, G.; D'Alfonso, L.; Falqui, A.; Marchesi, N.; Pascale, A.; Sironi, L.; Taglietti, A.; Zuddas, E. Synthesis of Reduced-Size Gold Nanostars and Internalization in SH-SY5Y Cells. *J. Colloid Interface Sci.* **2017**, *505*, 1055–1064. https://doi.org/10.1016/J.JCIS.2017.06.102.

(37) Crosby, G. A.; Perkins, W. G.; Klassen, D. M. Luminescence from Transition-Metal Complexes: Tris(2,2'-Bipyridine)- and Tris(1,10-Phenanthroline)Ruthenium(II). *J. Chem. Phys.* **1965**, *43* (5), 1498–1503. https://doi.org/10.1063/1.1696960.

(38) Fernández-Lodeiro, J.; Nuñez, C.; Lodeiro, A. F.; Oliveira, E.; Rodríguez-González, B.; Dos Santos, A. A.; Capelo, J. L.; Lodeiro, C. New-Coated Fluorescent Silver Nanoparticles with a Fluorescein Thiol Esther Derivative: Fluorescent Enhancement upon Interaction with Heavy Metal Ions. *Journal of Nanoparticle Research* **2014**, *16* (3), 2315. https://doi.org/10.1007/s11051-014-2315-4.

(39) Kang, K. A.; Wang, J.; Jasinski, J. B.; Achilefu, S. Fluorescence Manipulation by Gold Nanoparticles: From Complete Quenching to Extensive Enhancement. *J. Nanobiotechnology* **2011**, *9* (1), 16. https://doi.org/10.1186/1477-3155-9-16.

(40) Bassi, B.; Dacarro, G.; Galinetto, P.; Giulotto, E.; Marchesi, N.; Pallavicini, P.; Pascale, A.; Perversi, S.; Taglietti, A. Tailored Coating of Gold Nanostars: Rational Approach to Prototype of Theranostic Device Based on SERS and Photothermal Effects at Ultralow Irradiance. *Nanotechnology* **2018**, *29* (23), 235301. https://doi.org/10.1088/1361-6528/aab74f.

(41) Ranucci, E.; Spagnoli, G.; Ferruti, P.; Sgouras, D.; Duncan, R. Poly(Amidoamine)s with Potential as Drug Carriers: Degradation and Cellular Toxicity. *J. Biomater. Sci. Polym. Ed.* **1991**, *2* (4), 303–315. https://doi.org/10.1163/156856291X00197.

(42) Orts-Gil, G.; Natte, K.; Drescher, D.; Bresch, H.; Mantion, A.; Kneipp, J.; Österle, W. Characterisation of Silica Nanoparticles Prior to in Vitro Studies: From Primary Particles to Agglomerates. *Journal of Nanoparticle Research* **2011**, *13* (4), 1593–1604. https://doi.org/10.1007/s11051-010-9910-9.

(43) Suzuki, H.; Toyooka, T.; Ibuki, Y. Simple and Easy Method to Evaluate Uptake Potential of Nanoparticles in Mammalian Cells Using a Flow Cytometric Light Scatter Analysis. *Environ. Sci. Technol.* **2007**, *41* (8), 3018–3024. https://doi.org/10.1021/es0625632.

(44) Preobrazhensky, S.; Malugin, A.; Wentz, M. Flow Cytometric Assay for Evaluation of the Effects of Cell Density on Cytotoxicity and Induction of Apoptosis. *Cytometry* **2001**, *43* (3), 199–203. https://doi.org/10.1002/1097-0320(20010301)43:3<199::AID-CYTO1050>3.0.CO;2-H.

(45) Ruggi, A.; van Leeuwen, F. W. B.; Velders, A. H. Interaction of Dioxygen with the Electronic Excited State of Ir(III) and Ru(II) Complexes: Principles and Biomedical Applications. *Coord. Chem. Rev.* **2011**, *255* (21–22), 2542–2554. https://doi.org/10.1016/j.ccr.2011.05.012.

(46) Huntosova, V.; Horvath, D.; Seliga, R.; Wagnieres, G. Influence of Oxidative Stress on Time-Resolved Oxygen Detection by [Ru(Phen)3]2+ In Vivo and In Vitro. *Molecules* **2021**, *26* (2), 485. https://doi.org/10.3390/molecules26020485.

(47) Woźniak, A.; Malankowska, A.; Nowaczyk, G.; Grześkowiak, B. F.; Tuśnio, K.; Słomski, R.; Zaleska-Medynska, A.; Jurga, S. Size and Shape-Dependent Cytotoxicity Profile of Gold Nanoparticles for Biomedical Applications. *J. Mater. Sci. Mater. Med.* **2017**, *28* (6), 92. https://doi.org/10.1007/s10856-017-5902-y.

(48) Oparka, M.; Walczak, J.; Malinska, D.; van Oppen, L. M. P. E.; Szczepanowska, J.; Koopman, W. J. H.; Wieckowski, M. R. Quantifying ROS Levels Using CM-H 2 DCFDA and HyPer. *Methods* **2016**, *109*, 3–11. https://doi.org/10.1016/j.ymeth.2016.06.008.

(49) Wang, F.; Bexiga, M. G.; Anguissola, S.; Boya, P.; Simpson, J. C.; Salvati, A.; Dawson, K. A. Time Resolved Study of Cell Death Mechanisms Induced by Amine-Modified Polystyrene Nanoparticles. *Nanoscale* **2013**, *5* (22), 10868. https://doi.org/10.1039/c3nr03249c.

(50) Sullivan, B. P.; Salmon, D. J.; Meyer, T. J. Mixed Phosphine 2,2'-Bipyridine Complexes of Ruthenium. *Inorg. Chem.* **1978**, *17* (12), 3334–3341. https://doi.org/10.1021/ic50190a006.

(51) Dotsenko, I. A.; Curtis, M.; Samoshina, N. M.; Samoshin, V. V. Convenient Synthesis of 5-Aryl(Alkyl)Sulfanyl-1,10-Phenanthrolines from 5,6-Epoxy-5,6-Dihydro-1,10-Phenanthroline, and Their Activity towards Fungal β-d-Glycosidases. *Tetrahedron* **2011**, *67* (39), 7470–7478. https://doi.org/10.1016/j.tet.2011.07.058.

(52) Pallavicini, P.; Donà, A.; Casu, A.; Chirico, G.; Collini, M.; Dacarro, G.; Falqui, A.; Milanese, C.; Sironi, L.; Taglietti, A. Triton X-100 for Three-Plasmon Gold Nanostars with Two Photothermally Active NIR (near IR) and SWIR (Short-Wavelength IR) Channels. *Chemical Communications* **2013**, *49* (56), 6265–6267. https://doi.org/10.1039/c3cc42999g.

Halloysite nanotubes (HNT)

Chemical composition and physical properties of HNT

Halloysite is a 1:1 phyllosilicate clay mineral with $Al_2Si_2O_5(OH)_4 \cdot nH_2O$ chemical formula, whose each layer is composed by an octahedral (Si-O) and tetrahedral (Al-O) sheet, separated by an interlayer of water that reduces the electrostatic interaction between adjacent layers and facilitates their curvature due to mismatches in dimension between octahedral and tetrahedral sheets. This results in their consequent rolling to form their characteristic hollow tubular morphology that exposes the -Si-O sheet on the outer surface and the Al-O one in the inner lumen, as schematized in Figure 1.[1,2] Other morphologies of halloysite are possible, such as platy, spheroidal and short tubular, although the elongated tubular one is the most common.[1] The length of the interlayer varies from 10 Å (n=2 in the chemical formula) to 7 Å (n= 0 in the chemical formula) due to fast and irreversible dehydration in a temperature range between 50-100 °C. Being the H_2O interlayer held weakly, it is difficult to handle halloysite-10Å without modifying their hydration status.[3]

Halloysite nanotubes (HNT) share the same chemical structure as kaolinite beside the water interlayer, whose absence results in a platy morphology. The main constituents are aluminum (20.90 %), silicon (21.76 %) and hydrogen (1.56 %). Both HNT and kaolinite are naturally occurring clays with similar conditions of formation, as the two polytypes often occur together.[2,4] They form under various geological conditions of hydrothermal alteration and weathering, extracted mainly from deposits in the United States, New Zealand, Australia, China and Brazil, although there are deposits of this mineral also in Turkey, Poland, Mexico, Malaysia, Kazakhstan and Russia.[1,5-7] Depending on the extraction site, HNT may possess different properties as a result of the local conditions of formation, including the presence of various impurities such as associated clay minerals, iron oxides or poorly organized minerals, that might be localized within the HNT.[1,8]

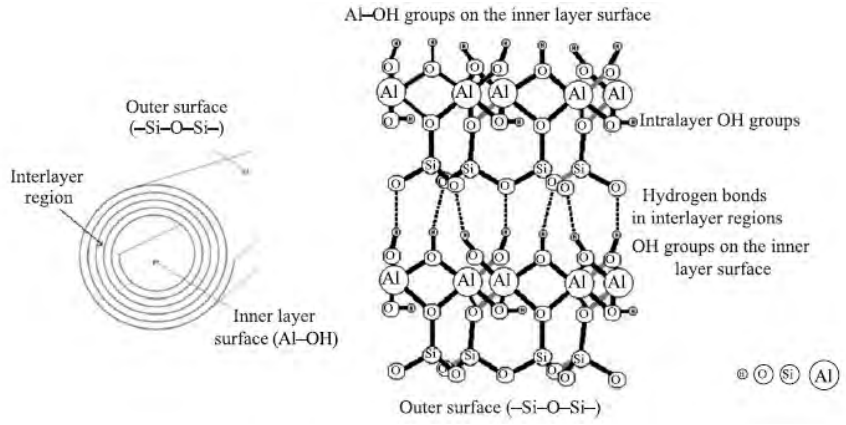

Figure 1. *Schematic representation of the tubular structure of HNT (left panel) and of the composition of their inner and external surfaces (right panel). From Ref. 7*

Usually, HNT are formed by the rolling of 15 or more layers and have average internal and external diameters of ca. 10-50 nm and 50-200 nm, respectively, and an average length between 1-2 μm. They possess a developed surface area, of 20-50 $m^2 g^{-1}$, but it can reach 150-200 $m^2 g^{-1}$.[7]

However, the most interesting feature of HNT is the different composition, charge and chemical activity between the external surface and the inner lumen, due to their rolling and the exposure of two different sheets. In a pH range indicatively between 2 and 8, the outer silica surface possesses a negative charge, while the inner alumina one is positively charged (a more precise estimation of the dependence of these charges on pH is carried out in the next chapter). Consequently, also their adsorption properties differ, since cations and positively charged species are adsorbed on the outer surface, while anions and negatively charged compounds on the inner one. In addition, many inorganic salts can be adsorbed in the interlayer space of nanotubes.[7] Additionally, the huge inner lumen area can host active substances and ca be further enlarged by the selective etching of aluminum oxide.[9]

Consequently, these structural and chemical properties, together with the easy availability, the environmental friendliness, non-toxic nature and high thermal and chemical stability, offer a great potential for developing cost-effective and efficient nanomaterials to store and release active agents in a wide range of applications, spacing from fillers in polymers, carriers for the loading and controlled release of guest molecules, adsorbents for pollution remediation, to nanoreactors/nanotemplates for the synthesis of functional materials.[8,10]

HNT in the biomedical field

In general, clay minerals are commonly used in the USA as excipients in commercialized pharmaceutical products and included in the FDA Inactive Ingredient Database.[11]

HNT shows numerous applications in the biomedical field for wound healing and tissue engineering, due to their biocompatibility and hemostatic properties associated with a high strength and modulus, and bioimaging and biosensing, through proper functionalization.[12] For instance, HNT modified with the cell adhesion molecule P-selectin is employed to capture the leukemic cells circulating in the blood vessels by altering their flow behavior and slowing down their velocity.[13] Nonetheless, the main application of HNT remains the drug delivery, in which HNT are employed as carriers for proper molecules as they present enhanced loading features compared to clays with the same chemical composition due to their hollow tubular morphology and the possibility to load the drug in the inner lumen other than on the external surface. Literature reports various examples highlighting the possibility of loading of different drugs including anticancer drugs, antibiotics, analgesics, antihypertension, anti-inflammatory drugs, and therapeutic nucleic acids.[3] The anticancer drug doxorubicin was introduced in

both kaolin and HNT to reduce its toxicity and increase its release efficiency, showing an 80 % (w/w) incorporation in HNT in respect to 54 % in kaolin.[14,15] The loaded HNT can be incorporated into creams, providing a controlled release of active agents in the cosmetic field, in gel matrixes to form a modern wound dressing releasing antibacterial agents, in tablets, by modifying the HNT outer layer with pH-responsive polymer stimulating release in either acid stomach or basic intestinal pH or form antibacterial sprays by loading antiseptic drug due to their high colloidal stability provided by the high zeta potential.[12,16]

Loading and releasing strategies

The incorporation of molecules into HNT can be performed by either their encapsulation into the inner lumen or their linkage to the external surface properly functionalized.

There are three main loading strategies of molecules into pristine HNT: adsorption, intercalation and tubular entrapment. In the first strategy the drug and HNT are mixed by stirring for ca. 24 h, reaching the thermodynamic equilibrium between the loaded and free drug molecules. The drug-loaded HNT is then recovered by centrifugation and dried at ca. 50 °C. The second involves the intercalation of small organic and inorganic substances in the interlayer spaces of HNT, causing their expansion. Finally, the third one consists of the removal of air and water molecules contained inside the inner lumen of HNT and their replacement with guest molecules by alternating low pressure and room pressure cycles. In the most common procedure, the clay dry powder is suspended into the saturated solution of the guest molecule under sonication or stirring, followed by vacuum pumping in/out operations, in which the dispersion is transferred from atmospheric pressure to a vacuum jar and, finally, centrifugation and drying (Scheme 1). An alternative procedure involves mixing an equal amount of drug and HNT and, at the end of the vacuum cycles, dehydration of the loaded HNT directly under vacuum.[3,17,18] Typically, a successful drug loading reaches 5-10 % w/w of the tube weight, although the loading capacity of HNT is affected by several factors, such as the morphology of HNT, the pH of the solution, and the solvent.[10,19]

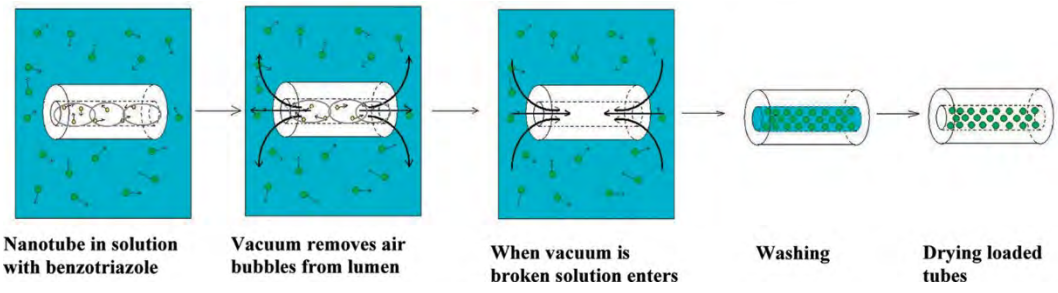

Scheme 1. *Loading procedure of HNT by tubular entrapment. From Ref. 18*

However, pristine HNT shows weak affinity (ion exchange, hydrogen bonding, and van der Waals forces) for guest molecules. This affinity is thus improved by surface modification of HNT, normally site-specific and sometimes selective. The Al–OH groups on the inner lumen surface of HNT have a high chemical activity toward many organic compounds such as organosilanes and alkyl phosphonic acids, to increase the affinity of the guest molecules toward the inner lumen but sacrificing part of the porosity of HNT. Analogously, on the external siloxane surface covalent bonding of molecules like organosilanes can be established at the surface defects, to work as linkers for the further decoration with nanoparticles or biologically active molecules with targeting moieties to improve the accumulation of HNT into target cells. Moreover, the external surface can be coated with cationic substances, such as polymers, biopolymers and surfactants, helping to improve the dispersibility and biocompatibility of halloysite.[10,11,16,20]

The release of guest molecules from HNT depends on the physical and chemical property of the guest and on the interactions with HNT. The complete release of inorganic salts from HNT is reached within 1-2 h, due to the high solubility in water, great mobility and weak interactions with HNT, while the release kinetics of organic compounds depends on the dimension of the molecule and the number of functional groups. In general, the drug release from HNT is characterized by a first burst dispersion of molecules adsorbed on the external surface followed by a slow drug release from nanotube lumen. Encapsulation of drugs within HNT might the drug release time by more than 20 times.[10,12] To further retard the release of guest molecules and prevent their leakage during the circulation before reaching the target, various kind of cappers are added at the ends of loaded HNT (usually polymers such as dextrin or stimuli responsive ones) whose conformation varies with and external stimuli as redox reactions, temperature increase, pH changes, enzymatic reactions and light, allowing the release of the drug.[11,21]

The possibility of a dual functionalization of the external surface and the inner lumen opens the way to various antitumoral applications in which the efficacy of an antitumoral drug loaded into the inner lumen might be increased by the action of a different functionalization of the external surface. This strategy may enhance a synergism between different drugs, increasing therapeutic target selectivity and reducing the drug resistance through distinct mechanisms of action.[11] For instance, in a work by Paemka and coworkers[22] the anticancer potential of curcumin-loaded HNT functionalized on the external surface with TiO_2 nanoparticles coated with an Ag shell was evaluated on HeLa cells, showing an increased antitumoral efficacy compared to curcumin alone, due to the low bioavailability of the anticancer drug and the synergistic effect with the ROS produced by the Ag-TiO_2 NP. In another work by Liu et al.[23] the external surface of HNT was decorated with folate, while their inner lumen was loaded with the antitumoral drug doxorubicin, resulting in the selective target of MCF-7 tumoral cells, whose express positive folate receptors, and in the inhibition of their proliferation, that was not recorded, on

contrast, in cells that did not express those receptors (L02 cells). Additionally, MCF-7 cells showed an increased ROS production due to the release of the drug into the targeted cells.

Biocompatibility and HNT uptake by cells

Tumoral tissues possess large gaps compared to healthy tissues and organs, a phenomenon known as the enhanced permeability and retention (EPR) effect, that allows large molecules and nanoparticles with a diameter under 100 nm to penetrate and accumulate in tumoral sites.[21,24] Other than size and surface characteristics, the nanoparticle shape plays a role in circulation time, biodistribution, cellular uptake and targeting in cancer drug delivery. In particular, there is evidence that elongated shapes provide a higher circulation time into the blood vessel, associated with a strong hydrodynamic shear that easily disrupts adhesion to phagocyte cell surfaces, minimizing their uptake and subsequent elimination in healthy organs. Differently, it has been proposed that their penetration and accumulation in tumoral sites might be easier due to the EPR effect compared to spherical nanoparticles with the same volume, that must deform to pass through the small tubular pores (left panel of Figure 2).[24]

Usually, the penetration of particles that are smaller, more elongated or more positively charged through the cell membrane occurs by either passive diffusion, active non-receptor mediated phagocytosis or receptor-mediated endocytosis, as discussed in the previous chapter. Regarding HNT, their uptake by HeLa and MCF-7 cells was demonstrated to be a two-step process consisting of a first concentration on the cell perimeter, followed by the accumulation in the cell through clathrin-dependent and independent endocytosis. The HNT internalization in A549 cells (human lung cancer) consisted in an endocytotic pathway, both caveolae- and clathrin-mediated, followed by an intracellular transport by microtubules and actin filaments in the cytosol to the Golgi apparatus and lysosomes, resulting in a final aggregation in the perinuclear region of the cells, as schematized in the right panel of Figure 2.[25-27] Analogously, the internalization of HNT by HT-29 cells (human colon cancer) consisted in a first accumulation in the cell membrane due to endocytosis, traffic through the cytoplasm toward the lysosomes, escape from the lysosomes and finally exocytosis as the HNT accumulate in the cell.[28]

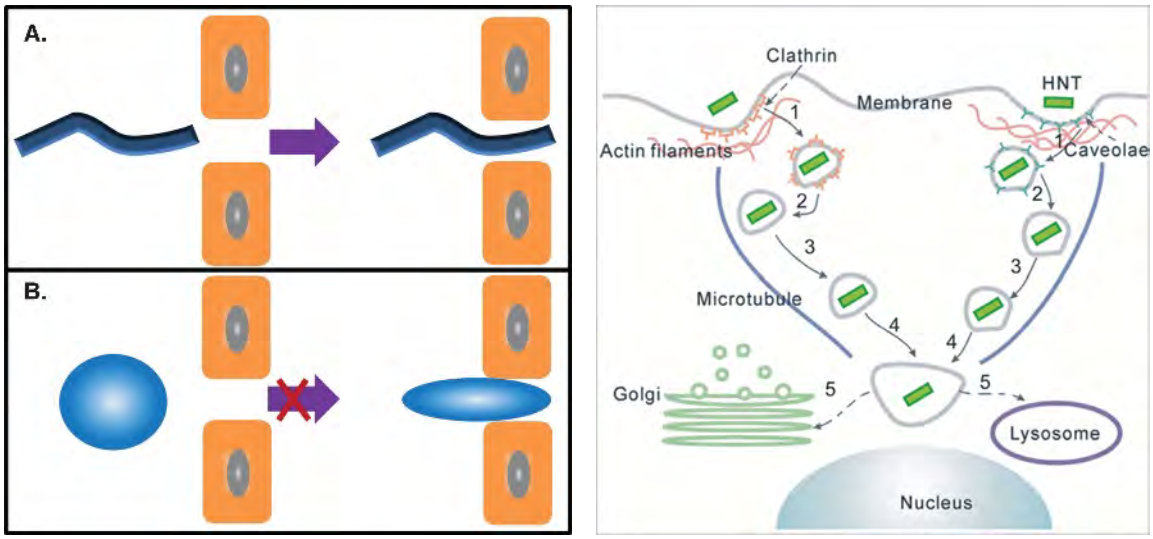

Figure 2. *Left panel: Schematization of the passage through a vascular pore to the tumoral site by a work-like nanocarrier and by a spherical nanocarrier with the same hydrodynamic volume. From Ref. 24 Right panel: proposed internalization pathway of HNT by human lung cancer cells (A549). From Ref. 25*

Cytotoxicity studies of pristine HNTs towards various tumoral and human cells revealed intracellular accumulation and a concentration dependent effect in the 75-1000 μg mL^{-1} concentration range, depending on the cell line and the exposure time. Nonetheless, HNT surface coating with PEG and proteins, as well as their incorporation into polymer matrixes were shown to improve their biocompatibility.[26] For instance, HNT functionalized with PEG resulted less cytotoxic toward HeLa and HepG2 cells compared to pristine HNT, with thresholds of 500 μg mL^{-1} and 100 μg mL^{-1}, respectively.[29]

Currently, HNT as nanomaterials are not yet approved for any sort of intake, although several preclinical studies have demonstrated the successful tumor growth inhibition without significant toxic effects, administered in various mouse models either intratumorally or intravenously.[30] Some studies have also shown that HNT are eliminated through gastrointestinal metabolism, concluding that HNTs are relatively biocompatible nanomaterials which can be used in many fields by governing their toxicity.[12]

References

(1) Joussein, E.; Petit, S.; Churchman, J.; Theng, B.; Righi, D.; Delvaux, B. Halloysite Clay Minerals — a Review. *Clay Miner.* **2005**, *40* (4), 383–426. https://doi.org/10.1180/0009855054040180.

(2) Ramadass, K.; Singh, G.; Lakhi, K. S.; Benzigar, M. R.; Yang, J. H.; Kim, S.; Almajid, A. M.; Belperio, T.; Vinu, A. Halloysite Nanotubes: Novel and Eco-Friendly Adsorbents for High-Pressure CO2 Capture. *Microporous and Mesoporous Materials* **2019**, *277*, 229–236. https://doi.org/10.1016/j.micromeso.2018.10.035.

(3) Fizir, M.; Dramou, P.; Dahiru, N. S.; Ruya, W.; Huang, T.; He, H. Halloysite Nanotubes in Analytical Sciences and in Drug Delivery: A Review. *Microchimica Acta* **2018**, *185* (8). https://doi.org/10.1007/s00604-018-2908-1.

(4) El Amrani El Hassani, I.; Sadik, C. Geology and Mineralogy of Clays for Nanocomposites: State of Knowledge and Methodology; 2016; pp 85–113. https://doi.org/10.1007/978-981-10-1953-1_4.

(5) Dube, S.; Rawtani, D.; Khatri, N.; Parikh, G. A Deep Delve into the Chemistry and Biocompatibility of Halloysite Nanotubes: A New Perspective on an Idiosyncratic Nanocarrier for Delivering Drugs and Biologics. *Advances in Colloid and Interface Science*. Elsevier B.V. November 1, 2022. https://doi.org/10.1016/j.cis.2022.102776.

(6) Wilson, I.; Keeling, J. Global Occurrence, Geology and Characteristics of Tubular Halloysite Deposits. *Clay Miner.* **2016**, *51* (3), 309–324. https://doi.org/10.1180/claymin.2016.051.3.12.

(7) Atyaksheva, L. F.; Kasyanov, I. A. Halloysite, Natural Aluminosilicate Nanotubes: Structural Features and Adsorption Properties (A Review). *Petroleum Chemistry*. Pleiades journals August 1, 2021, pp 932–950. https://doi.org/10.1134/S0965544121080119.

(8) Pasbakhsh, P.; Churchman, G. J.; Keeling, J. L. Characterisation of Properties of Various Halloysites Relevant to Their Use as Nanotubes and Microfibre Fillers. *Appl. Clay Sci.* **2013**, *74*, 47–57. https://doi.org/10.1016/j.clay.2012.06.014.

(9) Abdullayev, E.; Joshi, A.; Wei, W.; Zhao, Y.; Lvov, Y. Enlargement of Halloysite Clay Nanotube Lumen by Selective Etching of Aluminum Oxide. *ACS Nano* **2012**, *6* (8), 7216–7226. https://doi.org/10.1021/nn302328x.

(10) Yuan, P.; Tan, D.; Annabi-Bergaya, F. Properties and Applications of Halloysite Nanotubes: Recent Research Advances and Future Prospects. *Appl. Clay Sci.* **2015**, *112–113*, 75–93. https://doi.org/10.1016/j.clay.2015.05.001.

(11) Lazzara, G.; Riela, S.; Fakhrullin, R. F. Clay-Based Drug-Delivery Systems: What Does the Future Hold? *Therapeutic Delivery*. Newlands Press Ltd July 1, 2017, pp 633–646. https://doi.org/10.4155/tde-2017-0041.

(12) Kushwaha, S. K. S.; Kushwaha, N.; Pandey, P.; Fatma, B. Halloysite Nanotubes for Nanomedicine: Prospects, Challenges and Applications. *Bionanoscience* **2021**, *11* (1), 200–208. https://doi.org/10.1007/s12668-020-00801-6.

(13) Hughes, A. D.; King, M. R. Use of Naturally Occurring Halloysite Nanotubes for Enhanced Capture of Flowing Cells. *Langmuir* **2010**, *26* (14), 12155–12164. https://doi.org/10.1021/la101179y.

(14) Zhang, Y.; Long, M.; Huang, P.; Yang, H.; Chang, S.; Hu, Y.; Tang, A.; Mao, L. Emerging Integrated Nanoclay-Facilitated Drug Delivery System for Papillary Thyroid Cancer Therapy. *Sci. Rep.* **2016**, *6* (1), 33335. https://doi.org/10.1038/srep33335.

(15) Li, L.; Fan, H.; Wang, L.; Jin, Z. Does Halloysite Behave like an Inert Carrier for Doxorubicin? *RSC Adv.* **2016**, *6* (59), 54193–54201. https://doi.org/10.1039/C6RA09198A.

(16) Abdullayev, E.; Lvov, Y. Halloysite for Controllable Loading and Release. In *Developments in Clay Science*; Elsevier B.V., 2016; Vol. 7, pp 554–605. https://doi.org/10.1016/B978-0-08-100293-3.00022-4.

(17) Lisuzzo, L.; Cavallaro, G.; Pasbakhsh, P.; Milioto, S.; Lazzara, G. Why Does Vacuum Drive to the Loading of Halloysite Nanotubes? The Key Role of Water Confinement. *J. Colloid Interface Sci.* **2019**, *547*, 361–369. https://doi.org/10.1016/j.jcis.2019.04.012.

(18) Abdullayev, E.; Price, R.; Shchukin, D.; Lvov, Y. Halloysite Tubes as Nanocontainers for Anticorrosion Coating with Benzotriazole. *ACS Appl. Mater. Interfaces* **2009**, *1* (7), 1437–1443. https://doi.org/10.1021/am9002028.

(19) Lvov, Y.; Wang, W.; Zhang, L.; Fakhrullin, R. Halloysite Clay Nanotubes for Loading and Sustained Release of Functional Compounds. *Advanced Materials* **2016**, *28* (6), 1227–1250. https://doi.org/10.1002/adma.201502341.

(20) Biddeci, G.; Spinelli, G.; Colomba, P.; Di Blasi, F. Nanomaterials: A Review about Halloysite Nanotubes, Properties, and Application in the Biological Field. *International Journal of Molecular Sciences*. MDPI October 1, 2022. https://doi.org/10.3390/ijms231911518.

(21) Hu, Y.; Chen, J.; Li, X.; Sun, Y.; Huang, S.; Li, Y.; Liu, H.; Xu, J.; Zhong, S. Multifunctional Halloysite Nanotubes for Targeted Delivery and Controlled Release of Doxorubicin In-Vitro and in-Vivo Studies. *Nanotechnology* **2017**, *28* (37). https://doi.org/10.1088/1361-6528/aa8393.

(22) Nyankson, E.; Awuzah, D.; Tiburu, E. K.; Efavi, J. K.; Agyei-Tuffour, B.; Paemka, L. Curcumin Loaded Ag-TiO2-Halloysite Nanotubes Platform for Combined Chemo-Photodynamic Therapy Treatment of Cancer Cells. *RSC Adv.* **2022**, *12* (51), 33108–33123. https://doi.org/10.1039/d2ra05777h.

(23) Wu, Y.-P.; Yang, J.; Gao, H.-Y.; Shen, Y.; Jiang, L.; Zhou, C.; Li, Y.-F.; He, R.-R.; Liu, M. Folate-Conjugated Halloysite Nanotubes, an Efficient Drug Carrier, Deliver Doxorubicin for Targeted Therapy of Breast Cancer. *ACS Appl. Nano Mater.* **2018**, *1* (2), 595–608. https://doi.org/10.1021/acsanm.7b00087.

(24) Truong, N. P.; Whittaker, M. R.; Mak, C. W.; Davis, T. P. The Importance of Nanoparticle Shape in Cancer Drug Delivery. *Expert Opin. Drug Deliv.* **2015**, *12* (1), 129–142. https://doi.org/10.1517/17425247.2014.950564.

(25) Liu, H.; Wang, Z. G.; Liu, S. L.; Yao, X.; Chen, Y.; Shen, S.; Wu, Y.; Tian, W. Intracellular Pathway of Halloysite Nanotubes: Potential Application for Antitumor Drug Delivery. *J. Mater. Sci.* **2019**, *54* (1), 693–704. https://doi.org/10.1007/s10853-018-2775-5.

(26) Prinz Setter, O.; Segal, E. Halloysite Nanotubes-the Nano-Bio Interface. *Nanoscale* **2020** *12* (46), 23444–23460. https://doi.org/10.1039/d0nr06820a.

(27) Biddeci, G.; Spinelli, G.; Massaro, M.; Riela, S.; Bonaccorsi, P.; Barattucci, A.; Di Blasi, F. Study of Uptake Mechanisms of Halloysite Nanotubes in Different Cell Lines. *Int. J. Nanomedicine* **2021**, *Volume 16*, 4755–4768. https://doi.org/10.2147/IJN.S303816.

(28) Liao, J.; Peng, S.; Long, M.; Zhang, Y.; Yang, H.; Zhang, Y.; Huang, J. Nano-Bio Interactions of Clay Nanotubes with Colon Cancer Cells. *Colloids Surf. A Physicochem. Eng. Asp.* **2020**, *586*, 124242. https://doi.org/10.1016/j.colsurfa.2019.124242.

(29) Paola, M. Di; Quarta, A.; Pisani, P.; Conversano, F.; Sbenaglia, E. A.; Leporatti, S.; Gigli, G.; Casciaro, S. Surface Coating Highly Improves Cytocompatibility of Halloysite Nanotubes: A Metabolic and Ultrastructural Study. *IEEE Trans. Nanotechnol.* **2016**, *15* (5), 770–774. https://doi.org/10.1109/TNANO.2016.2546955.

(30) Pereira, I.; Saleh, M.; Nunes, C.; Reis, S.; Veiga, F.; Paiva-Santos, A. C. Preclinical Developments of Natural-Occurring Halloysite Clay Nanotubes in Cancer Therapeutics. *Adv. Colloid Interface Sci.* **2021**, *291*, 102406. https://doi.org/10.1016/j.cis.2021.102406.

Decoration of halloysite nanotubes with gold nanostars to obtain a dual therapeutic carrier exploiting Photothermal Therapy

Introduction

Mitoxantrone (MTX)

Mitoxantrone (MTX, structure shown in the left panel of Scheme 1) is an antitumoral drug first approved by FDA in 1987 for the treatment of acute myeloid leukemia and commercialized under the name of Novantrone, even though nowadays it is also used to treat breast cancer, prostate cancer and multiple sclerosis. It has been developed as a derivative of the antitumoral doxorubicin (DOX), whose structure is shown in the right panel of Scheme 1, to overcome the cardiotoxicity issues of this last one. The antitumoral action of MTX is mainly based on its intercalation into DNA duplexes and its weak electrostatic interactions with the anionic phosphate residues of DNA. The intercalation activates the topoisomerase II, an enzyme responsible for breaking DNA strands to relieve the topological stress generated by the intercalation. This enzyme normally possesses a physiological role, being involved in the regulation of DNA topology, by introducing and resealing transient breaks in the two strands. However, the introduction of MTX increases the concentration of the topoisomerase II, that turns into a cellular toxin, triggering frameshifts mutations, permanent double-strand breaks, illegitimate recombination and cellular apoptosis. The -OH groups are critical for the drug-stimulated DNA scission and the subsequent cell death. Moreover, mitoxantrone induces single strands breaks not dependent on proteins. The molecule is indeed sensitive to oxidation by enzymes like peroxidase and myeloperoxidase, generating conjugates that could bind covalently with DNA strands. The proposed mechanism is a first nucleophilic attack of formaldehyde, generating a highly reactive Schiff base that the secondary amino groups of mitoxantrone target for a subsequent nucleophilic attack. Thus, formaldehyde is required for the covalent DNA-mitoxantrone adduct, which is produced by the hydrogen peroxide mediated oxidation of cellular substrates. The MTX intercalation might be the first stage in the formation of these adducts, able to block the progression of RNA polymerase through a DNA template, blocking DNA replication and RNA transcription.[1] These various antitumoral mechanisms of mitoxantrone are schematized in Figure 1.

The molecules penetrate cells by passive diffusion through a “flip-flop” mechanism, consisting of a first interaction between the positively charged drug and the negative phospholipids of the cellular membrane, followed by a slow flip-flop through the lipid core and its dissociation from the membrane on the opposite side. Inside the cell, mitoxantrone distributes in the nucleus, the endoplasmic reticulum and vesicular compartments like the lysosomes. Mitoxantrone also interacts with hydrophobic components of the cell cytoskeleton: cytokeratin, lamin intermediate filaments and inhibits the assembly of tubulin into microtubules, that play an essential role in cell division. For this

reason, tumoral cells in late S phase (i.e. right before cell division) are particularly sensitive to MTX-induced cytotoxicity.[1]

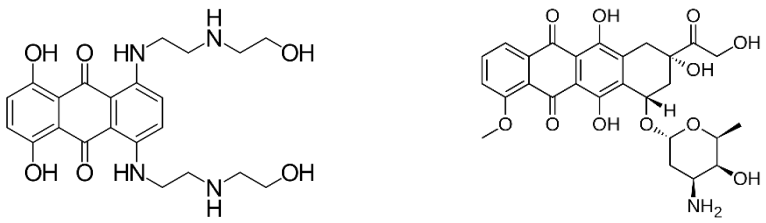

Scheme 1. *The structures of mitoxantrone (MTX), on the left, and doxorubicin (DOX), on the right.*

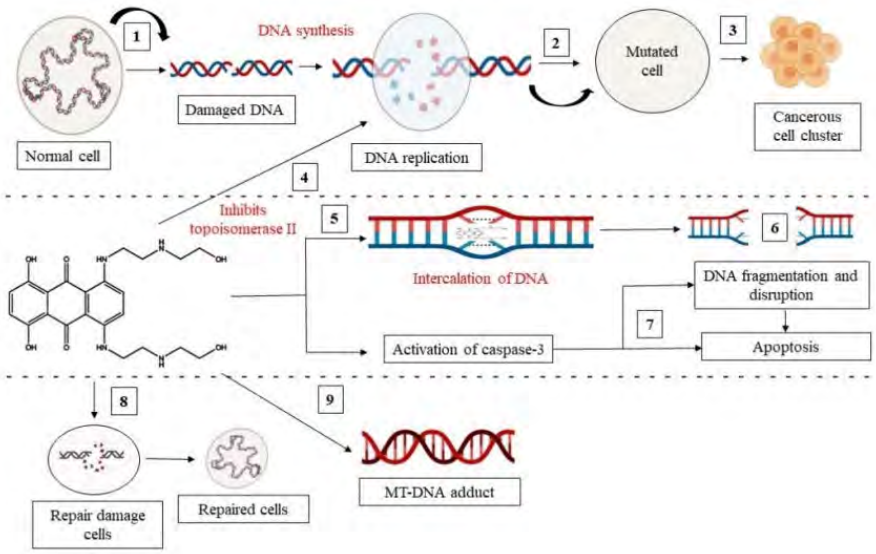

Figure 1. *Mechanisms of the antitumoral action of mitoxantrone. From Ref. 2*

Despite all these important features, mitoxantrone still shows severe cardiotoxicity issues, even though significantly reduced in comparison to DOX, in addition to hematological (i.e. a decrease of white blood cells and amenorrhea)[3] and gastrointestinal nature. MTX was also found to accumulate in the liver, thyroid and heart, commonly with a lower concentration in tumoral tissues compared to the neighboring normal ones.[1] Additionally, the drug is a substrate of efflux transporter breast cancer resistance protein, resulting in cancer resistance against MTX.[4]

The incorporation of the drug into nanocarriers might reduce the efflux and prolong the retention in drug-resistant tumoral cells, as well as reduce the side effects of the drug in normal tissues, increasing the overall antitumoral efficiency of the drug. As already discussed in the Introduction section on HNT, compared to spherical nanoparticles with the same hydrodynamic diameter, elongated nanoparticle shapes might be more effective for the delivery of drugs, as these shapes might be linked to longer circulation times, reduced clearance, more efficient tumor targeting and enhanced accumulation in tumors.[5] In the literature there are some examples of MTX incorporation into functionalized carbon nanotubes carriers:[3,6-9] for instance, MTX adsorbed on oxidized multiwalled carbon nanotubes

(MWCNT-OX) showed a higher effectiveness in cytotoxicity toward MDA231 (triple-negative human breast cancer cells) and NIH3T3 (mouse embryonic fibroblast cell line) compared to the free drug in a similar dose, even though the delivery system could not distinguish cancer from non-cancer cells.[9] Nonetheless, no example of HNT-based drug delivery systems for mitoxantrone was found, but HNT conjugated with PEG and folate were employed as drug delivery systems to load DOX.[10]

Results and discussion

In this work, three different strategies were attempted to obtain the Halloysite nanotubes-gold nanostars nanocomposites (HNT@GNS), involving two different functionalization of the external surface of HNT (with either 3-aminopropylethoxysilan or PVP 10kDa polymer) and the interaction with two types of GNS.

The first procedure to synthetize the GNS aimed to obtain a gold surface free from any surfactant that could hinder their interaction with HNT. Obviously, the absence of any stabilizing agent drastically reduced the stability of the GNS, and thus we moved to a different synthetic approach obtaining GNS stabilized by a surfactant that weakly interacts with the gold surface but strong enough to ensure temporary stability of the GNS, allowing an easy and fast ligand exchange.

Additionally, we worked with three different kinds of HNT, both commercial (HNT ALD, purchased by Sigma-Aldrich) and non-commercial (HNT USA, extracted from Northstar Mine in USA, and HNT AUS, extracted from Camel Lake in Australia). This choice depended on the different properties that HNT possess based on the geographical area of extraction, as already described in the introduction chapter about HNT. The HNT ALD sample contains a lot of kaolinite clay and unrolled sheets difficult to separate from the rolled HNT, whose presence reduces the effective HNT content and compete with the "capture" of the GNS. For this reason, we tested also non-commercial batches from USA and Australia. In particular, HNT USA should present a larger inner lumen (diameter: 100-180 nm, with an average of 140 nm)[11] compared to the commercial ones, i.e. HNT ALD (30-70 nm),[vii] allowing the loading of bigger molecules, and a more monodispersed length (0.9-1.5 μm vs 1-3 μm[i] of HNT ALD). Because of the absence of published values, the inner lumen, the external diameter and the length of HNT USA were measured using Image-J software from the TEM images recorded, obtaining respectively 20 (± 7) nm, 83 (± 30) nm and 464 (± 286) nm. On the other hand, HNT AUS possess a length of 0.5-4 μm and a diameter of 50-80 nm, smaller compared to that of HNT USA.[12] However, the high uniformity in their shape and size and the improved dispersibility (possibly due to the natural increased amount of -OH groups on

[vii] Data taken from the Sigma-Aldrich website

their external surface as suggested by some ζ-potential characterization, see further) makes these HNT the most suitable as carriers among all three HNT types.[13]

First synthetic strategy: decoration of HNT-NH_2 with f-GNS

Synthesis of surfactant-free GNS (f-GNS)

The first synthetic route we followed to prepare the HNT-GNS nanocomposite, consisted in the interaction of HNT functionalized with 3-aminopropylethoxysilane (APTES) and GNS prepared without any surfacing agent (f-GNS). Indeed, there are several papers indicating the use of APTES as cross-link agent to make silica surface suitable for the interaction with metal gold nanoparticles.[14,15] To obtain this kind of GNS, we developed a two-steps seed-growth synthesis inspired by some literature procedures,[16,17] which started from the preparation of small size spherical AuNP to be used as seeds in the second synthetic step. Such AuNP were prepared following a literature procedure by Puntes and coworkers,[18] consisting in a variation of the inverse Turkevich method that involves a sub-stoichiometric amount of tannic acid together with the commonly used sodium citrate for the reduction of $HAuCl_4$. The synthesis yields citrate-stabilized AuNP whose hydrodynamic diameter was measured 8 (± 1) nm, as shown in Figure 2, and thus promising as seeds for the GNS growth due to their small size and high monodispersity. Since these AuNP were used as seed for the growth of f-GNS within a period of some months, various UV-vis spectra were recorded over time (Figure 3). The LSPR absorption band was centered at 507 nm immediately after the synthesis and slightly red shifted to 511 nm after 6 days (coherently to what observed at the DLS), and blue shifting again to the original wavelength in the spectrum recorded after 2 months from the synthesis and thus confirming the high stability of these nanoparticles.

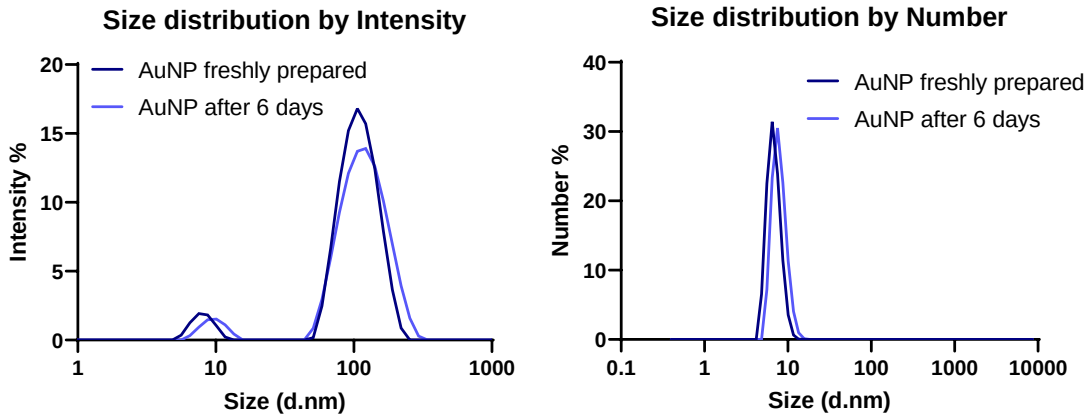

Figure 2. *Size measurements of AuNP freshly prepared (dark lines) and after 6 days from the synthesis (light lines), data shown by Intensity (left plot) and by Numbers (right plot), which confirms that the population at ca. 100 nm is negligible.*

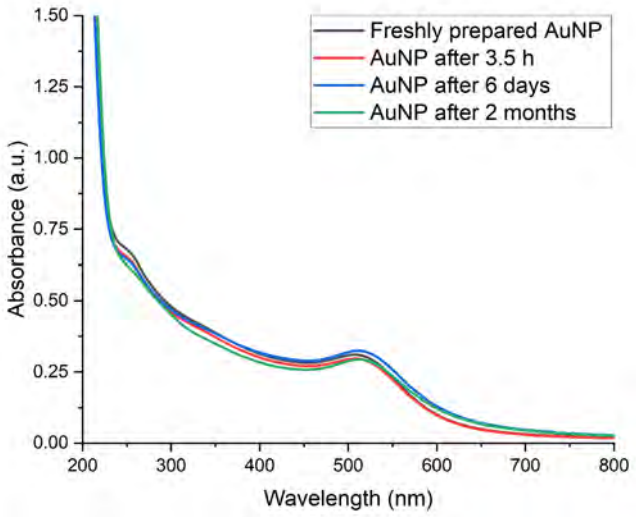

Figure 3. *UV-vis spectra of AuNP used as seeds for the growth of f-GNS. Spectra recorded in water right after the synthesis (black line), after 3.5 h (red line), after 6 days (blue line) and after 2 months from the synthesis.*

The growth of f-GNS on such Au@citrate seeds was achieved by adding, under stirring: $AgNO_3$, ascorbic acid and the AuNP to a solution of $HAuCl_4$ 0.25 mM at room temperature, whose pH was previously fixed at 3. Four different batches of f-GNS were prepared in parallel, changing the addition order and the amount of the reagents, as summarized in Table 1. The first one (f-GNS A), obtained following the protocol as described in the literature,[16] i.e. first the addition of the seed suspension followed by $AgNO_3$ and ascorbic acid, produced a red suspension of spherical nano-objects, whose LSPR absorption band was centered at 514 nm and with an hydrodynamic diameter (d_H) at the DLS of 12 (± 2) nm. Since there was almost no difference from the starting seed suspension, in the second batch (f-GNS B) we first added $AgNO_3$ to the Au^{3+} solution, followed by the fast addition of ascorbic acid and seed suspension (also halving the seed volume), to reduce the nucleation time, aiming to obtain bigger and more anisotropic nano-objects. Anyhow, these changes still produced spherical nanoparticles, whose suspension presented a more intense red color and with a more intense and red-shifted LSPR band (523 nm). The so-obtained nano-objects resulted in a d_H of 20 (± 2) nm. Thus, we further reduced the volume of seeds added in the third batch (f-GNS C) obtaining a blue suspension with an LSPR band centered at 695 nm and a d_H = 98 (± 24) nm, which is compatible with the formation of star-shaped nano-objects. A second UV-vis spectrum and a DLS measurement of f-GNS C were recorded after 24 h from the synthesis, showing a blue shift of the plasmonic band of ca. 40 nm and the reduction of its intensity, while the size measured at the DLS increased to 195 (± 46) nm, suggesting some aggregation of the f-GNS due to their non-stabilized free surface. In the last batch (f-GNS D), the $AgNO_3$ concentration was slightly increased and the obtained GNS showed a LSPR absorption band centered at 684 nm, more intense and sharper than that of f-GNS C, and a size of 98 (± 35) nm. The protocol used in the preparation of this last batch was maintained for all the following syntheses. The UV-vis spectra recorded during the optimization of the synthesis are shown in Figure 4 and the DLS measurements in Figure 5.

Table 1. *Amount of the three reagents added to the $HAuCl_4$ solution (10 mL 0.25 mM, 2.5 µmol) in the four batches prepared to optimize the synthesis of f-GNS.*

Sample ID	$AgNO_3$		Ascorbic acid		Seeds		
	V (µL) and [mM]	µmol	V (µL) and [M]	µmol	V (mL) $HAuCl_4$	µmol Au	Theoretical n of NP with d = 4 nm
f-GNS A	100, 1.5	0.15	50, 0.1	0.5	2	0.328	$1.00 \cdot 10^{14}$ NP
f-GNS B	100, 1.5	0.15	50, 0.1	0.5	1	0.164	$4.99 \cdot 10^{13}$ NP
f-GNS C	100, 1.5	0.15	50, 0.1	0.5	0.1	0.0164	$4.99 \cdot 10^{12}$ NP
f-GNS D	100, 2.2	0.2	100, 0.05	5	0.1	0.0164	$4.99 \cdot 10^{12}$ NP

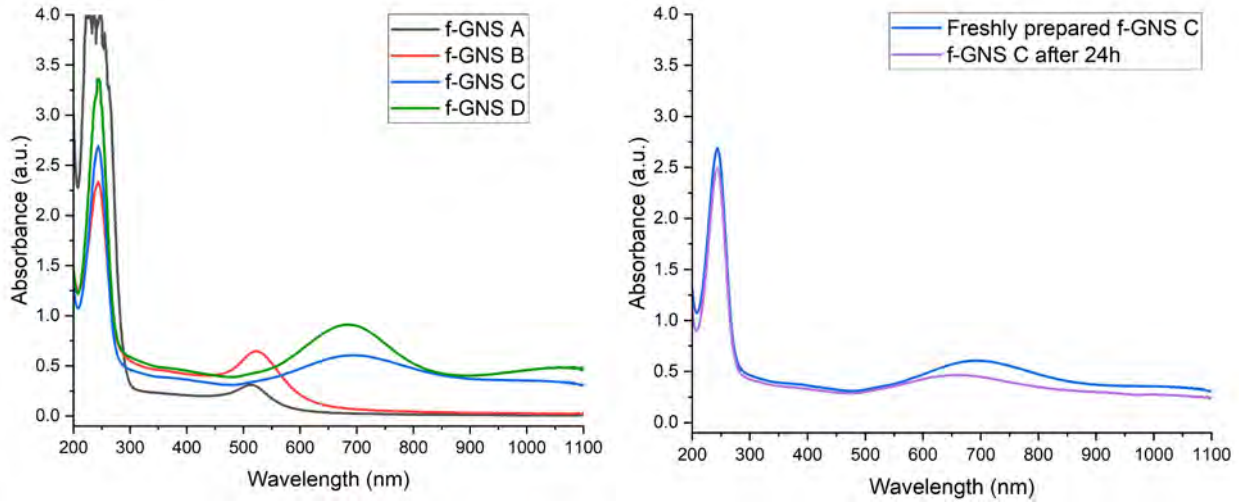

Figure 4. *Left panel: UV-vis spectra of the freshly prepared four batches of f-GNS in water, during the optimization of the synthesis of f-GNS. Right panel: UV-vis spectra of f-GNS C recorded in water right after the synthesis and after 24 h.*

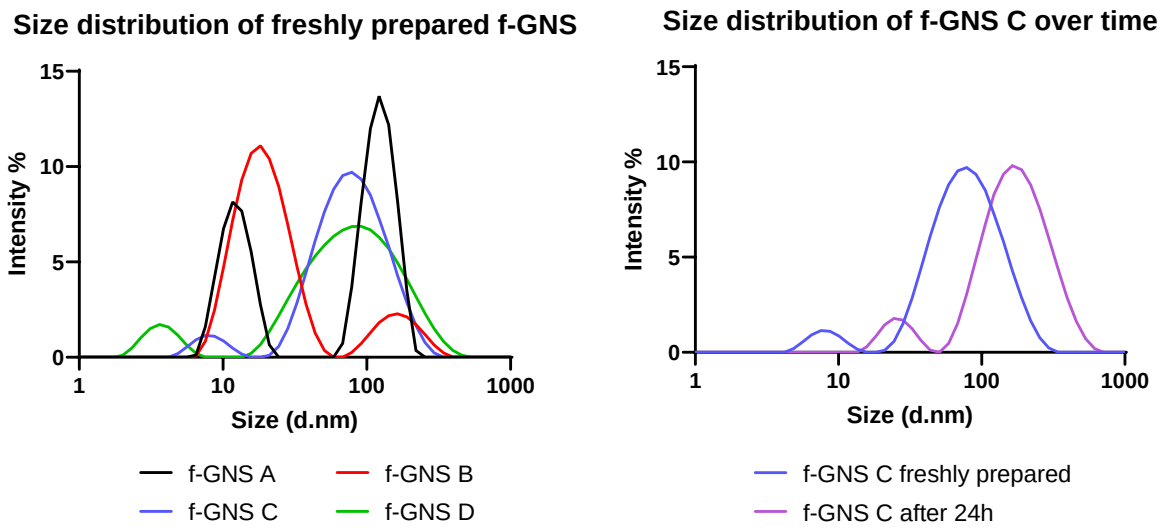

Figure 5*.Left panel: DLS measurements of the freshly prepared four batches of f-GNS during the optimization of the synthesis of f-GNS. Right panel: DLS measurements of f-GNS batch C right after the synthesis and 24h later.*

Decoration of HNT with f-GNS

HNT functionalization was carried out in a two-steps process (see Scheme 2) before their treatment with f-GNS for the decoration of their outer surface, consisting in the external silica surface hydroxylation by a basic etching treatment and the subsequent grafting of 3-aminopropylethoxysilane (APTES). The treatment with NaOH is necessary to increase the number of free -OH groups on the silica surface (HNT-OH), which are naturally present only on silica defects and edges, to maximize the consequent functionalization of the surface with APTES, thus obtaining a sample (HNT-NH_2) in which amino groups are fundamental for the interaction with the gold surface.

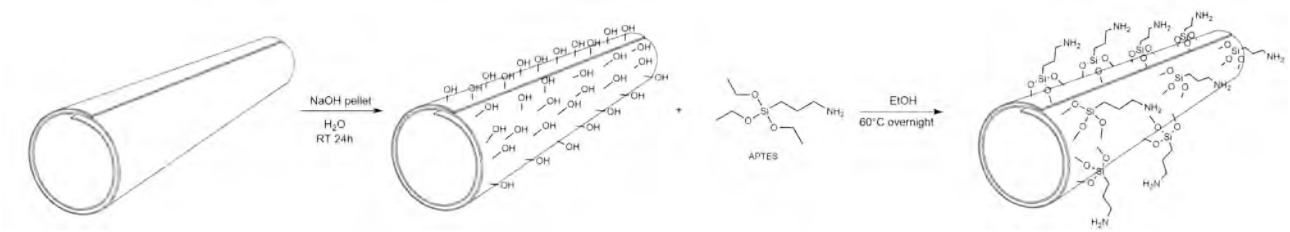

Scheme 2. *Schematic representation of the functionalization steps to obtain HNT-NH_2 prior to their decoration with f-GNS.*

The success of both steps was assessed through ζ-potential measurements: the decrease from -25 (see Ref 19) to -40 mV at pH 7 confirmed that the hydroxylation occurred, while the grafting of APTES was confirmed by the acquisition of an entire ζ-potential vs pH titration (Figure 6) that showed an increase of the surface charge from values between ca. -30 and -50 mV for HNT-OH to more positive ones for HNT-NH_2, ranging from ca. 30 to 0 mV in a pH range from 3 to 11.5. Additionally, while for the hydroxylated samples the ζ-potentials were similar for HNT ALD and HNT USA, when APTES was grafted on the external surface HNT-NH_2 ALD showed more positive values at all the pH, reaching the zero charge at a pH of ca. 11 with 3.4 (± 5.7) mV. On the other hand, HNT-NH_2 USA reached the neutrality at a lower pH: ca. 10 with a measured value of -0.5 (± 5.5) mV. This difference suggested a more efficient functionalization of HNT ALD, which possibly exposed more amino groups on the external surface.[20]

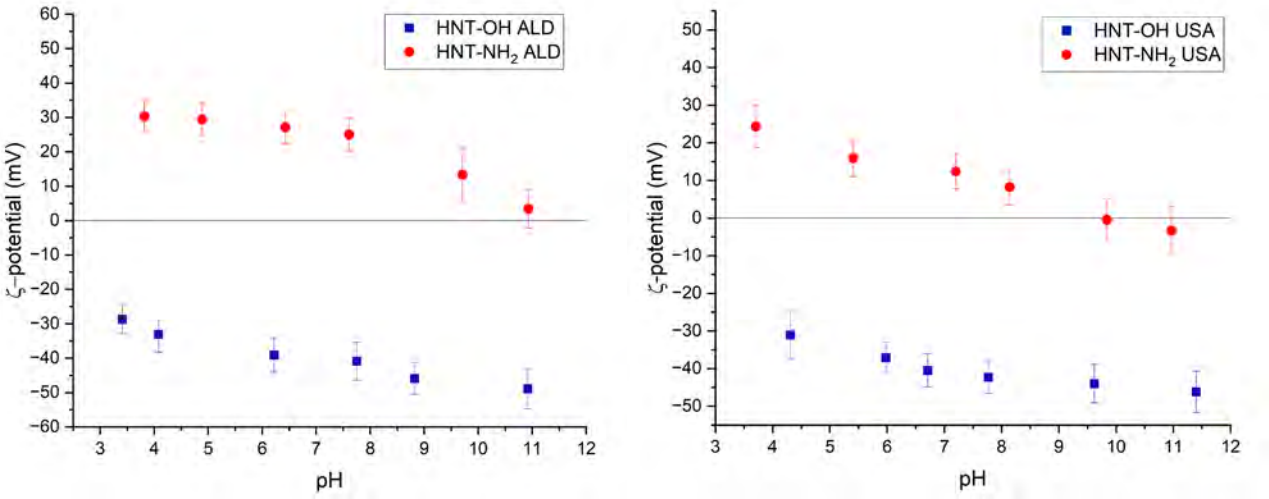

Figure 6. *ζ-potential vs pH titrations of HNT-OH, obtained after the hydroxylation step (blue squares), and of HNT-NH_2, after the grafting of APTES on the external surface (red dots), performed on commercial HNT purchased by Sigma-Aldrich (HNT ALD, left panel) and non-commercial ones extracted from Silver City, Utah, USA (HNT USA, right panel).*

For the decoration of HNT-NH_2 with f-GNS two different approaches were tried, as depicted in Scheme 3: the first consisted in the direct HNT-NH_2 interaction with freshly prepared f-GNS (A), while the second in a first interaction with AuNP, followed by the subsequent growth of f-GNS directly on the HNT surface (B). The protocol followed to decorate HNT-NH_2 with the two kinds of gold nanoparticles (both spheres and stars) was taken and adapted from the literature,[14] consisting of an overnight interaction at room temperature under stirring. For the AuNP, the pH of the suspension was not an important parameter, possessing the citrate molecule at least one negative charge to interact with the positively charged APTES in a wide pH range, while for GNS it was adjusted to ca. 11 prior to the interaction. On the other hand, the second step of approach B, that consisted of the GNS growth on HNT functionalized with AuNP, was inspired by the optimized protocol to synthesize f-GNS in colloidal suspension. All the HNT@f-GNS samples were analyzed through TEM to visualize the best synthetic pathway for the decoration of HNT external surface and to compare the two different samples of HNT employed in this strategy.

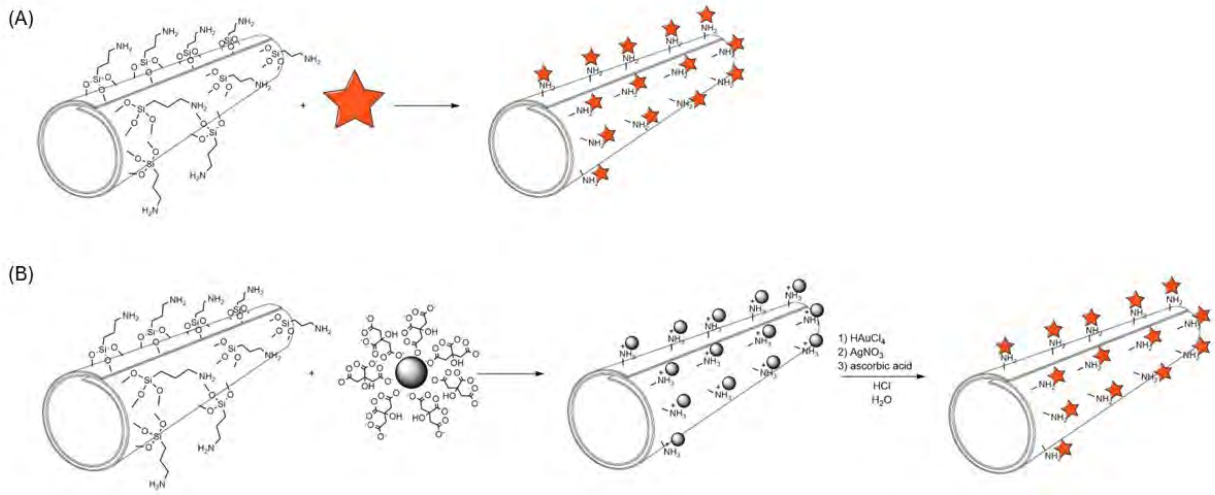

Scheme 3. *Schematic representation of the two strategies used to decorate HNT-NH_2 with f-GNS: by their direct interaction with freshly prepared f-GNS (A) or by their decoration with AuNP stabilized by citrate followed by the f-GNS growth on them.*

The HNT@f-GNS samples prepared with the first approach showed an overall inhomogeneous decoration of HNT (Figure 7), with a great number of undecorated HNT due to the low Au:HNT mass ratio employed (1:68). The f-GNS do not possess a well-defined star shape in most cases and seem to accumulate preferentially in limited portions of the HNT surface.

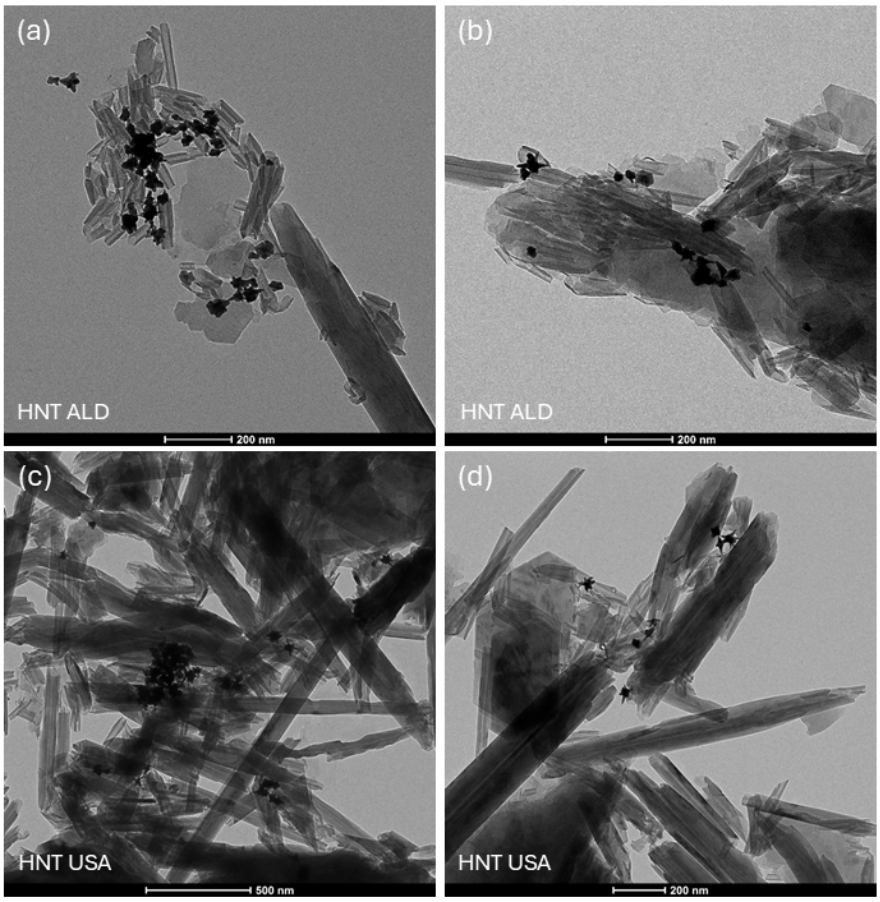

Figure 7. *TEM images of HNT@GNS samples prepared by direct interaction of HNT-NH_2 with freshly prepared f-GNS, using HNT ALD (panels a and b) and HNT USA (panels c and d). Scale bars: 200 nm (panels a, b and d) or 500 nm (panel c).*

In the samples prepared following the second approach, TEM images were recorded after both the decoration with AuNP (Figure 8) and the growth of f-GNS (Figure 10). The pictures of HNT@AuNP show that also in this case AuNP tend to accumulate in specific areas of the nanotubes or interact with kaolin sheets that are quite present in both HNT ALD and HNT USA.

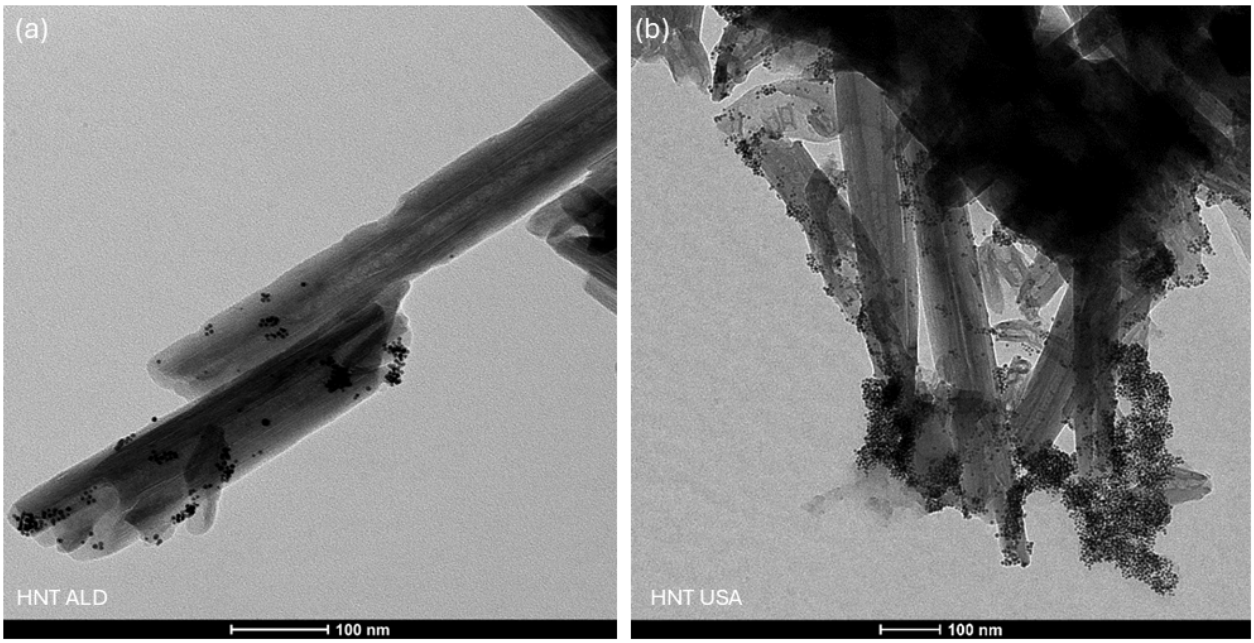

Figure 8. *TEM images recorded on HNT decorated with citrate-stabilized AuNP, employing HNT ALD (a) and HNT USA (b). Scale bar: 100 nm.*

For the following step of GNS growth on HNT@AuNP, two different AuNP:gold amounts in the growing solution were tested, to achieve a final HNT:Au w/w ratio of 1:1.5 and 1:3, respectively, which are both much higher than that tested with the first decoration approach, trying to overcome the inhomogeneity problem. UV-vis absorption spectra of the HNT@f-GNS samples recorded immediately after the decoration and again 3 days later (Figure 9), revealed an overall good stability of the nanocomposite. The plasmonic band of f-GNS, centered at ca. 633 nm for the 1:1.5 sample and at ca. 678 nm for the 1:3 sample, and clearly distinguishable over the scattering of HNT, remained unchanged in both spectra. Additionally, TEM images were recorded also for the 1:3 sample (Figure 10), to visualize the state of the HNT decoration and compare it to the results obtained with the first approach. In this case, HNT resulted indeed more decorated with gold, but again the decoration resulted inhomogeneous, with a lot of gold accumulated in some areas of the HNT sample, leaving an important amount of HNT still “naked”, probably due to the inhomogeneity of their decoration with AuNP in the previous step. The nano-objects obtained with this second approach possessed a much less defined shape, in many cases still pseudo-spherical.

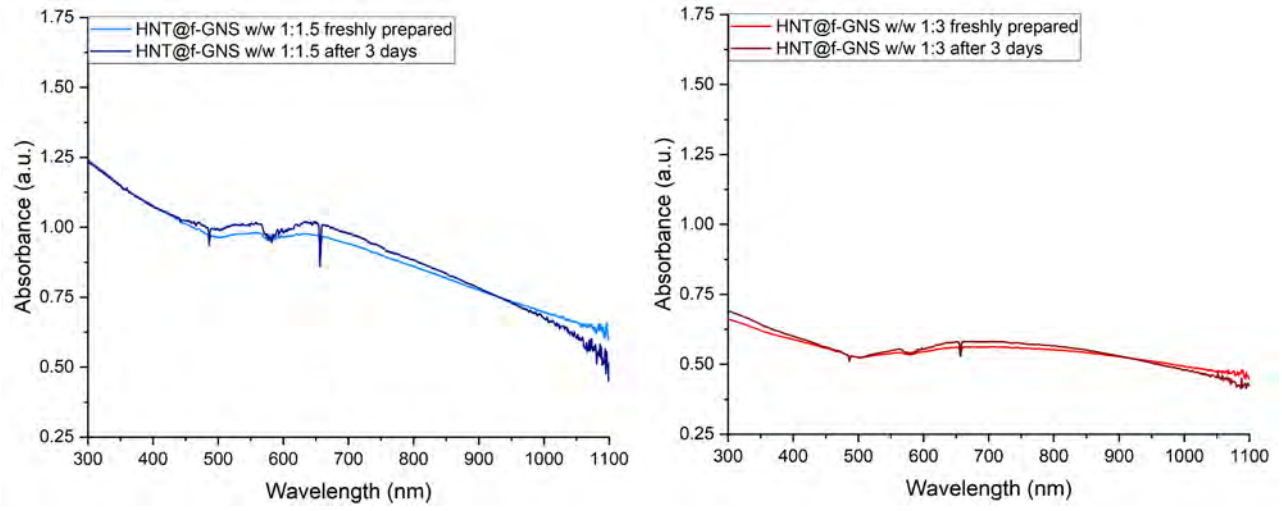

Figure 9. *UV-vis spectra of f-GNS growth on HNT@AuNP using to achieve two different HNT:GNS mass ratios (1:1.5 in the left panel and 1:3 in the right panel), recorded right after the GNS growth (light blue and right red) and after 3 days (dark blue and dark red).*

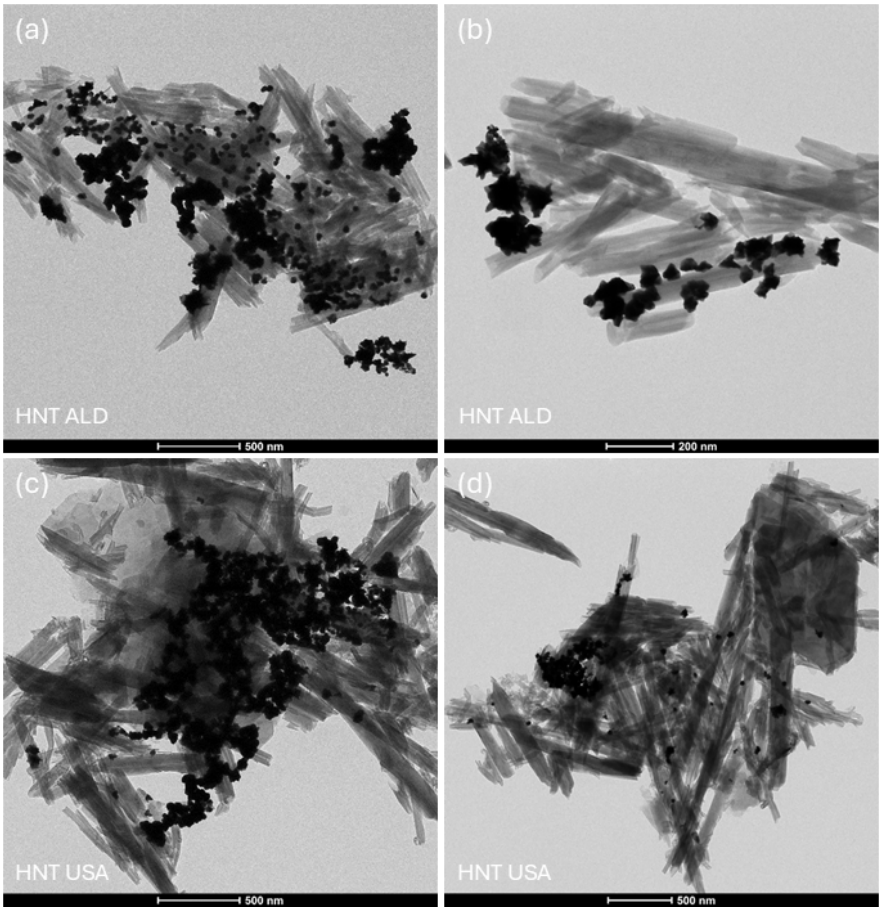

Figure 10. *TEM images of HNT@GNS samples prepared by the growth of f-GNS on HNT@AuNP, using HNT ALD (panels a and b) and HNT USA (panels c and d). Scale bars: 200 nm (panel b) or 500 nm (panels a, c and d).*

Second synthetic strategy: decoration of HNT-NH_2 with GNS@TX-100

Overall, the previous strategy did not result optimal to prepare the HNT@GNS nanocomposites, both in terms of stability and of shape of f-GNS. Thus, we changed the synthesis of GNS, moving to a literature procedure[21] that uses the surfactant Triton X-100 (TX-100) as directing and stabilizing agent through weak interactions with the gold surface, to obtain nanostars with a well-defined shape, on which a ligand exchange can be easily carried out.

Considering the better results obtained, in this second strategy we decided to try only the direct interaction between functionalized HNT and GNS. This last one was carried out similarly, under an overnight magnetic stirring at RT and adjusting the pH of the GNS suspension to ca. 10 to exclude any electrostatic repulsion between the amino groups on HNT surface and the gold. Other than the type of GNS used in this second strategy, the other main difference was the sonication of HNT-NH_2 using an immersion ultrasound system at high power before the interaction with GNS, due to the high aggregation state of HNT observed in the TEM images of the HNT@f-GNS samples, trying to increase the suspensibility of HNT and to obtain a more homogeneous decoration with GNS.

Additionally, even though we considered to functionalize HNT with a different alkoxysilane bearing a thiol group, the 3-mercaptopropyltrimethoxysilane (MPTMS), to exploit the stronger interaction between sulfur and gold, we decided to maintain the already used APTES as linking molecule between the HNT and GNS, as a work from the literature[22] states that in the functionalization of Triton-stabilized AuNP with oligonucleotides, only those functionalized with amino groups where able to penetrate the Triton X-100 layer adsorbed on the NP and interact with the gold surface, while when thiol-functionalized oligonucleotides were employed they did not record any interaction at all, in contrast with the well-known stronger interaction between gold and sulfur. In this second strategy only HNT from Sigma-Aldrich (HNT ALD) were used, since the non-commercial HNT USA used in the first strategy did not provide any advantages over the commercial ones.

This time three different HNT:Au w/w ratios were tested: starting from 60:1, close to the one attempted in the first strategy, we then tried to increase the gold amount to the 30:1 and 10:1 ratios. The produced samples were visualized through TEM images (Figure 11) to get a clear idea of the situation of the produced nanocomposites. The TEM images confirmed that using the ratio with the lowest amount of gold (60:1), the decoration of HNT is almost absent, since only a little part of the HNT appears decorated with GNS. Moreover, it is clear from these images that GNS tend to clusterize in bigger roundish and hollow structures whose tips are barely sketched, possibly due to the time that passed from the GNS synthesis to the HNT decoration (Figure 11). The number of GNS on HNT increases when the HNT:Au ratio is 30:1, but the produced sample shows a satisfying decoration only for the one containing the

highest amount of gold between the three tested (HNT:Au 10:1), in which the decoration of HNT is also more uniform.

However, the samples produced with this second strategy showed again some stability problems, tentatively explained by the weak interaction between the amino group on the HNT surface and the GNS, as suggested macroscopically from the bleaching of the blue color of the suspension after the centrifuge cycles and confirmed by the TEM picture recorded for the 10:1 sample (Figure 11C), in which some of the GNS are detached from the HNT surface. Additionally, the GNS appear still aggregated and do not possess the defined shape that GNS prepared with this synthesis usually show. A possible explanation could be the time that passed from the GNS synthesis to their use to decorate HNT-NH_2.

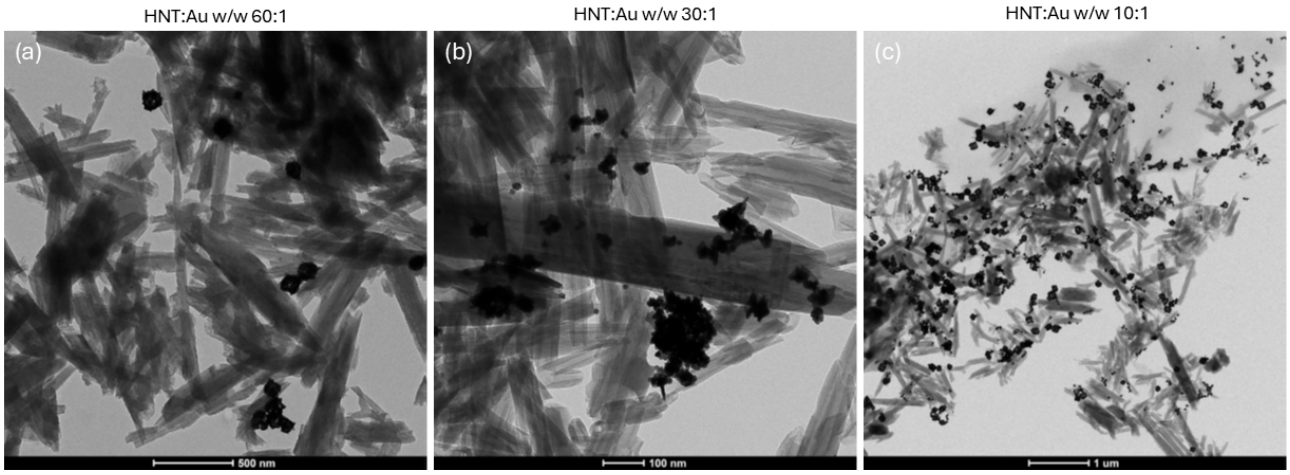

Figure 11. *TEM images of HNT ALD functionalized with APTES and decorated with GNS@TX-100 with three different HNT:Au w/w ratios: 60:1 (panel a, scale bar: 500 nm), 30:1 (panel b, scale bar: 100) and 10:1 (panel c, scale bar 1 μm).*

Nonetheless, the 30:1 and 10:1 samples were analyzed with DRS (diffuse reflectance spectroscopy) to characterize the plasmonic band of GNS over the light scattered by HNT as well as to investigate the spectral range beyond 1100 nm (Figure 12), showing a peak centered at ca. 700 nm. Since the GNS derives from the same batch, the slight difference in their plasmonic band in the two samples derives only from the different aggregation state of GNS on the HNT surface.

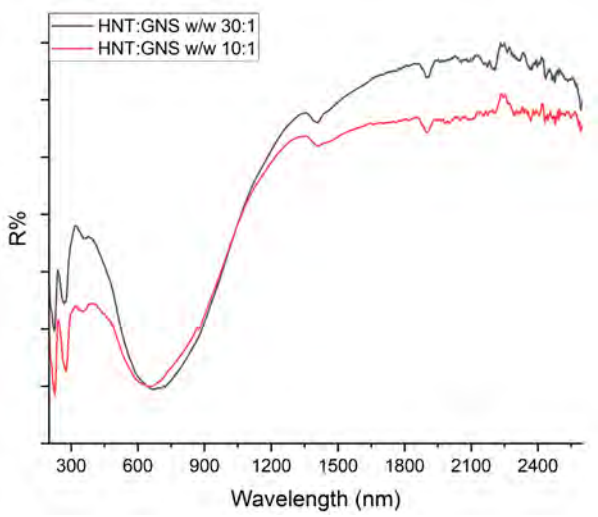

Figure 12. *DRS spectra of HNT-NH_2@GNS samples with a HNT:GNS mass ratio of 30:1 (black line) and 10:1 (red line).*

Moreover, to evaluate the interaction efficiency obtained with this strategy, the amount of Au in these samples was determined by ICP analyses, as it is a fundamental parameter to characterize the photothermal feature of the nanocomposite. The sample, which was previously deposited and dried on a glass support for the photothermal characterization, was carefully removed from the support, weighted, digested overnight with freshly prepared aqua regia, and diluted with milliQ water, and finally, using syringe filters (RC, 0.2 µm), the undigested solid SiO_2 was filtered off. The Au amount obtained with the analysis was compared to the nominal one expected with a quantitative HNT-GNS interaction and calculated from the theoretical yield of the GNS synthesis reported in the literature (75%).[23] The deposited HNT mass was calculated by subtracting the Au mass from the weighted nanocomposite and neglecting those of APTES and TX-100. The HNT/Au experimental ratios are listed in Table 2 and are significantly lower than the nominal ones, mainly due to the low stability of these nanocomposites, as an important part of the GNS detached from the HNT surface during the centrifugation cycles used to clean the nanocomposites from the excess of TX-100 due to the synthesis of GNS. The calculated yields of the interaction are 33.3% for the nominal 60:1 sample, 54.5% for the 30:1 and 33.3% for the 10:1 one, in all three cases too low to consider this strategy a satisfying way to produce the HNT@GNS nanocomposite.

Table 2. *Mass of Au (determined by ICP-MS) and of HNT (calculated by difference with the weighted composite and neglecting the mass of APTES and the possible TX-100) of the deposited samples, weighted, digested and analyzed after the photothermal characterization of the three samples. In the last column the experimental ratio of the two samples are reported.*

Nominal HNT:Au w/w ratio	Au mass (mg)	HNT mass (mg)	Experimental HNT:Au w/w ratio
60:1	0.007	1.26	180:1
30:1	0.022	1.20	55:1
10:1	0.042	1.26	30:1

Third synthetic strategy: decoration of HNT-PVP with GNS@TX-100

In the third and last synthetic strategy that we attempted to prepare the HNT@GNS nanocomposites, we tried to change the linking molecule between HNT and GNS to overcome the stability problem that the samples prepared with the second strategy displayed. This time we used a low molecular weight PVP polymer (PVP10, Mw: 10kDa, polyvinyl pyrrolidone) that could interact with both the HNT[24-26] and GNS and stabilize at the same time the GNS[27-29]. PVP is vastly used for pharmaceutical and biomedical industry thanks to its high solubility in water as well as many organic solvents, its biocompatibility and its capability to associate with many substances with high stability, that makes this polymer largely used in pharmaceutical industry as a binder in drug tablets, also containing an inorganic clay component.[30,31] In the literature PVP was also employed to functionalize single-wall carbon nanotubes to produce biomaterials with potential uses in drug delivery and cancer therapy.[32]

Moreover, we also changed the type of HNT to decorate with GNS, moving to the non-commercial HNT AUS, extracted from Camel Lake in Australia (see the first paragraph of the "Results and discussion" part for the description of their properties). This change aimed to exploit the higher suspensibility of these HNT compared to HNT ALD and HNT USA and their higher homogeneity in terms of length and diameter, to possibly achieve also a better homogeneity in the decoration with GNS.

The HNT AUS were pretreated as done with the other two HNT samples used in the previous strategies for comparison: first hydroxylated to maximize the -OH groups on the external surface and then functionalized with APTES. The left panel of Figure 13 shows the ζ-potential vs pH titration of HNT-OH AUS and HNT-NH_2 AUS. The hydroxylated HNT AUS show a more negative surface charge (ca. -50 mV in all the pH range tested) compared to the two other HNT types, whose ζ-potential curve has been reported in Figure 6, while the ζ-potential measured for the HNT-OH ALD and USA are more pH-dependent (ca. -30 mV at low pH that reaches -50 mV only at basic pH) and, at acidic pH, they both showed a higher similarity to the ζ-potential of pristine HNT. This difference confirms the higher natural density of -OH groups on HNT AUS compared to the other two. At the same time, also the ζ-potential values measured on HNT-NH_2 AUS in the whole pH range show a less positive charge, ranging from ca. 20 mV at pH ca. 3 to ca. -10 at pH ca. 11, that reaches the neutrality at a lower pH compared to the other two batches with a value of 4.6 (± 6.4) mV at pH 8.6. This might be in accordance with the higher density of -OH groups as well, as a higher amount of APTES might be necessary to saturate them. However, this functionalization was carried out just for characterization purposes and the HNT-NH_2 sample was not used in any attempt of HNT decoration with GNS.

The functionalization of HNT with PVP10 was carried out following a literature procedure,[24] suspending the HNT-OH AUS in a solution of PVP10 for 24h under stirring, as schematized in Scheme 4. The success of the functionalization was assessed first by a ζ-potential vs pH titration, that showed less negative

values (ca. -20 mV) in the whole pH range compared to HNT-OH before the functionalization step (see right panel of Figure 13), and then by FT-IR spectroscopy, observing the presence of the peaks assigned to PVP at 1652 (C=O stretching), 1422 (CH_2 bending) and 1286 cm^{-1} (C-N vibrations),[33] which are very intense in the spectrum of PVP powder, clearly visible in the HNT-PVP sample and absent in the HNT-OH, as shown in Figure 14.

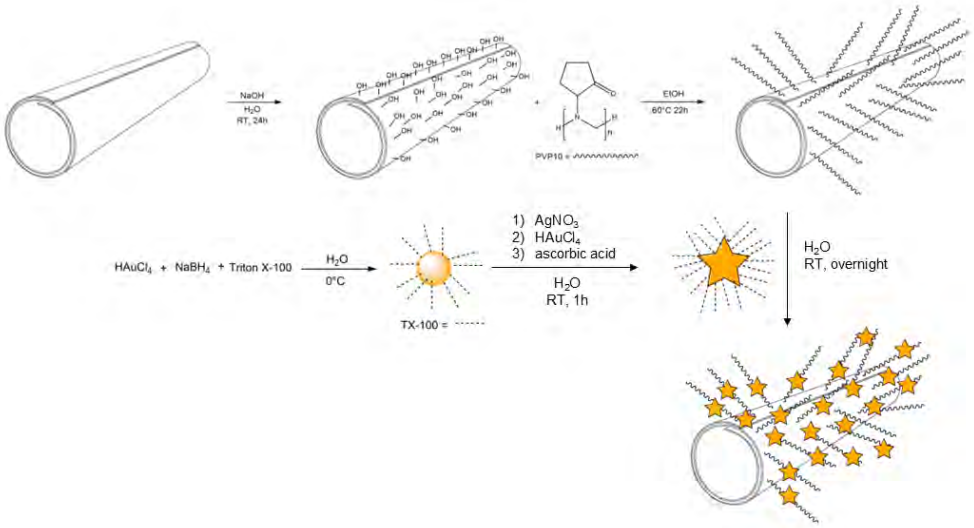

Scheme 4. *Schematic representation of the strategy used to functionalize HNT AUS with PVP10 and their subsequent decoration with GNS@TX-100.*

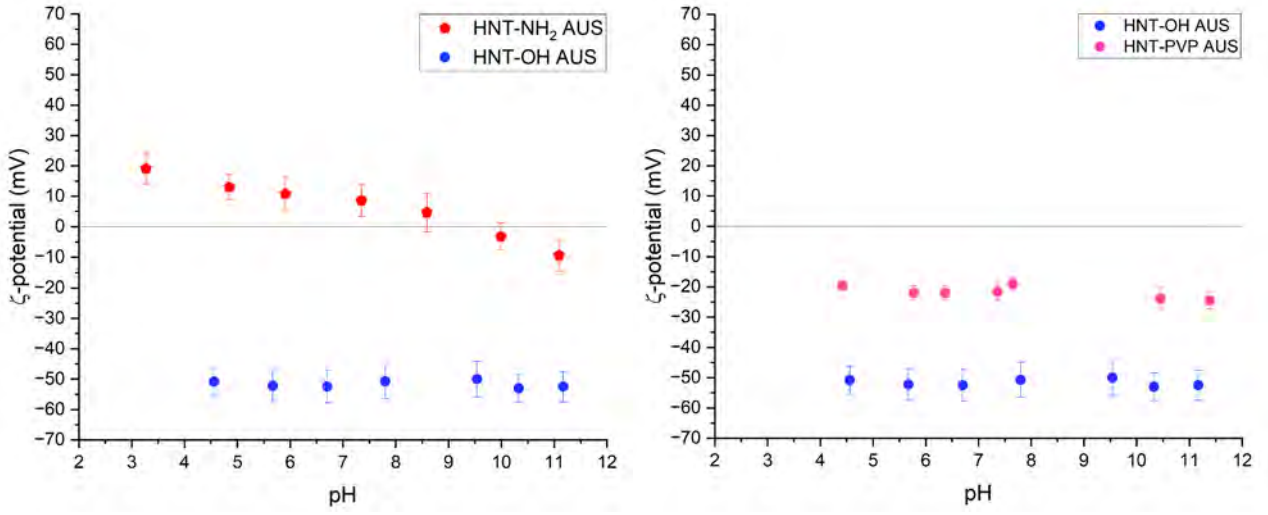

Figure 13. *ζ-potential vs pH titrations of HNT-OH, obtained after the hydroxylation step (blue dots), of HNT-NH_2, after the grafting of APTES on the external surface (red dots on the left panel), and on HNT-PVP after their functionalization with PVP10 (pink dots on the right panel), performed on non-commercial HNT extracted from Camel Lake, Australia (HNT AUS).*

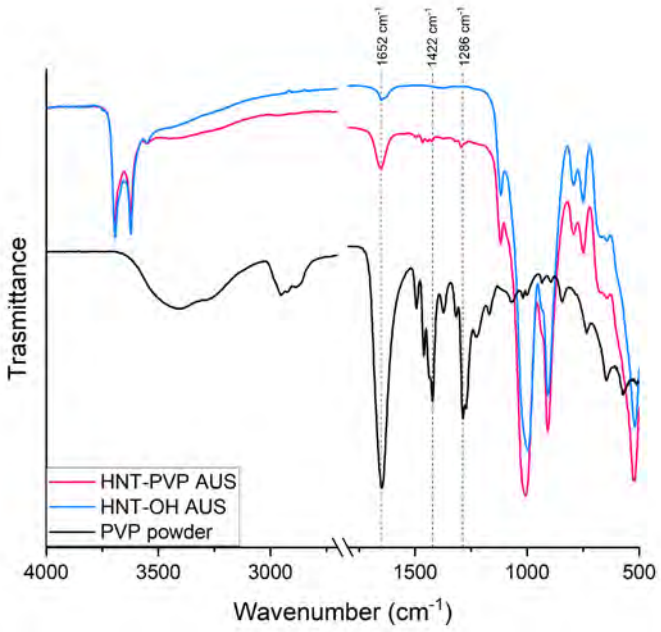

Figure 14. *FT-IR spectra recorded in ATR mode of HNT-OH AUS (blue trace), of HNT functionalized with PVP10 (pink trace) and of PVP10 alone (black trace)*

On the PVP-functionalized HNT the decoration with GNS@TX-100 was carried out following an approach analogue to the one already followed in the previous strategies, which involved the direct interaction between GNS and functionalized HNT. The HNT suspension was sonicated with tip horn ultrasound system prior the interaction and the GNS@TX-100 colloidal solution was added dropwise, leaving the mixture to interact under stirring overnight. Considering the results obtained in the second strategy when three different HNT:Au mass ratios were tested, this time we tested again the higher one already attempted (10:1), and we tried to further increase the gold to the 5:1 ratio.

This third approach seemed more efficient in the HNT decoration already macroscopically: the blue color of the obtained pellet appeared at the naked eye more intense compared to those prepared with the previous strategies, suggesting a higher amount of GNS on the HNT surface. Interestingly, the blue color did not fade out during the washing cycles by centrifugation, differently to what observed with the nanocomposite obtained involving the same GNS and the APTES as linking molecule.

The UV-vis spectra of the nanocomposites prepared with the two ratios (Figure 15) show over the scattering produced by HNT the same plasmonic bands of the freshly prepared GNS@TX-100: a main peak was centered at ca. 850 nm and was assigned to five-branched nanoobjects,[34] whose plasmonic band is heavily dependent on the synthetic conditions and easily changes from one batch to another, and a second one at ca. 630 nm, typical of smaller monocrystalline shrunk GNS.[34]

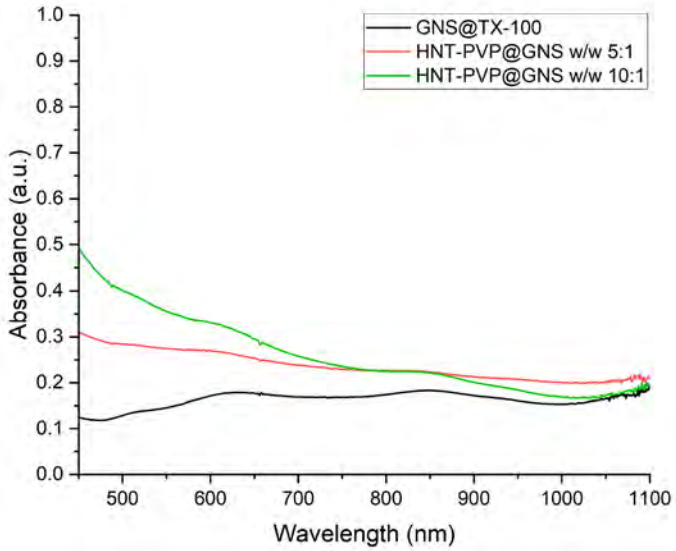

Figure 15. *UV-vis absorption spectra of freshly prepared GNS@TX-100 (black trace), and of the HNT-PVP@GNS samples, prepared with the HNT:Au mass ratios of 10:1 (green trace) and 5:1 (pink trace).*

The TEM images in Figure 16 show an overall good HNT decoration, with an increased homogeneity compared to the samples prepared with the previous strategies. In the 10:1 sample (panel a and c) the GNS seem to localize mainly at the ends of the HNT, as no visible nano-objects in the panels seem to functionalize the external surface. On the other hand, as expected from the higher Au content, the 5:1 sample appears more decorated (panels b and d): some of the GNS are still localized at the ends of the nanotubes, but a lot more are on the external surface. We tentatively explained the GNS tendency to first localize at the entrance of HNT as due to the PVP polymer, which could accumulate preferentially there rather than on the length of the nanotube and thus the interaction with GNS might occur in the areas of the samples containing more PVP.

Anyhow, in both cases the GNS possess a more defined star-like shape compared to those obtained in the previous strategies, with the coexistence of both GNS with long and thin branches and others shrunk, with less and shorter tips, as suggested by their extinction spectrum. Additionally, the images show that GNS aggregation state is minimal and slightly higher for the 5:1 sample.

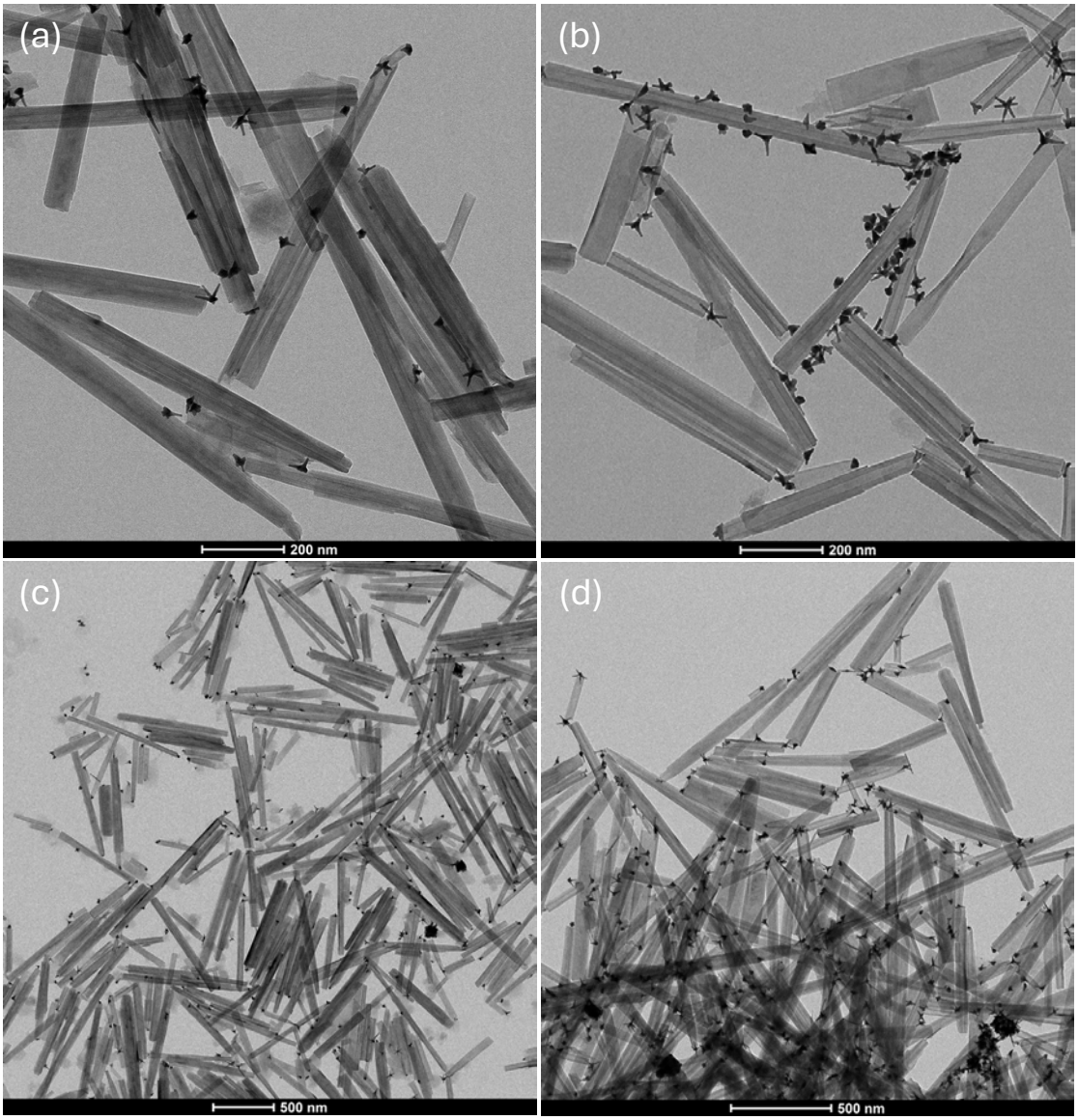

Figure 16. *TEM images of HNT AUS functionalized with PVP10 and decorated with GNS@TX-100 with two different HNT:Au w/w ratios: 10:1 (panels a and c) and 5:1 (panels b and d). Scale bars: 200 nm (panels a and b) or 500 nm (panels c and d).*

The decoration efficiency for these two samples was estimated as well, following a protocol analogous to the one used for the HNT-NH_2@GNS samples. This time the Au concentration obtained with the analysis was compared to the one expected with quantitative HNT-GNS interaction and calculated from the experimental yield of the GNS synthesis (78.8%). We chose not to use this experimental yield for the HNT-NH_2@GNS samples as the GNS used in that case were prepared in a different batch. The decoration yield was calculated as 75.5% for the 10:1 ratio sample and 99.5% for the 5:1 one, which are listed in Table 3, improving considerably the yield obtained with the previous synthetic approach. Analogously to what done for the HNT@GNS nanocomposites prepared with the second strategy, we calculated the experimental HNT:Au mass ratios of these two samples as well, by subtracting the gold mass from the weight of the whole nanocomposite and considering negligible the masses of the PVP10

on the HNT surface and of the residual TX-100 around the GNS. We tentatively explained the higher yield by a geometric point of view: we suppose that due to the curved surface of the HNT and the shape of the GNS, that show a certain number (from 3 to 6) of elongated tips, choosing a polymer rather than a smaller molecule provides more points of contact and thus ensures a more stable linkage between the two components.

Table 3. *Mass of Au (determined with ICP-OES) and of HNT (calculated by difference and considering negligible the masses of PVP10 and TX-100) of the deposited samples, weighted, digested and analyzed after the photothermal characterization of the two samples. In the last column the experimental ratio of the two samples is reported.*

Theoretical HNT:Au w/w ratio	Au mass (mg)	HNT mass (mg)	Experimental HNT:Au w/w ratio
10:1	0.00981	0.17	17:1
5:1	0.0209	0.13	6:1

Photothermal characterization of HNT@GNS

The photothermal characterization of the HNT@GNS nanocomposites was carried out on the five samples produced following the second and the third covering strategies.

As already mentioned above, the samples were deposited on a glass coverslip (previously washed with aqua regia) until a thin opaque layer was observable. The deposited samples were irradiated with a monochromatic laser tunable in wavelength and power, and the generated local heat was measured using a thermocamera. The achieved heating curves were well fitted with a double exponential function reported in equation 1.

$$T(t) = T_0 + \Delta T_1\left(1 - e^{-\frac{t}{\tau_1}}\right) + \Delta T_2\left(1 - e^{-\frac{t}{\tau_2}}\right) \qquad \text{eq. 1}$$

The two τ parameters that appear in the equation describe the thermal relaxation of the sample. The first and faster component (τ_1) represent the heat exchange from the irradiated GNS to the HNT, while the second and slower (τ_2) is the re-equilibration with the laboratory environment and its value is negligible.[21] Thus, since Au is the sole component of the nanocomposite to present photothermal features, only its specific heating (τ_1) is considered in the determination of the thermal capacity of the nanocomposite.

The thermal capacity (C) is calculated as the ratio between the exchanged heat and the temperature variation, as described by equation 2. In particular, assuming that the laser powers involved in this characterization are much lower than the saturation power, i.e. the power at which the saturation condition (60% of its asymptotic value) of the total temperature variation is reached, the linear approximation is valid and thus the exchanged heat is calculated by the direct product between the

laser power and the time that the sample needs to reach the equilibrium temperature (five times the τ parameter).[35] Being C described as the energy supplied to a material to produce a unit change in its temperature, samples with a lower C value possess better photothermal features.

$$C = \frac{5\tau P}{\Delta T} \qquad \text{eq. 2}$$

However, the thermal capacity is an extensive property, hence the mass of the photothermal material is not considered in its calculation. We thus determined the Au mass in each irradiated sample using ICP-OES or ICP-MS (depending on the sample), as already described in the previous section regarding the decoration efficiency of HNT. This way the thermal capacity can be normalized on the Au mass, obtaining the specific heat capacity (C_s), and finally allowing a quantitative comparison between the samples. The following Table 4 summarizes the five HNT@GNS samples involved in the photothermal characterization, and the masses of HNT and Au contained in each sample and their nominal HNT:Au ratio are listed.

Table 4. *Mass of the deposited material on the glass coverslips for the characterization of the photothermal features and of the Au contained in each HNT@GNS sample.*

#	Sample type	Nominal HNT:Au mass ratio	Mass of the deposited sample (mg)	Au mass measured via ICP (mg)
A1	HNT-NH_2@GNS	60:1	1.27	0.0068
A2	HNT-NH_2@GNS	30:1	1.22	0.0222
A3	HNT-NH_2@GNS	10:1	1.30	0.0417
B1	HNT-PVP@GNS	10:1	0.18	0.0098
B2	HNT-PVP@GNS	5:1	0.15	0.0209

The HNT-NH_2@GNS samples (A1-3) were irradiated with two laser powers (200 and 220 mW), while the HNT-PVP@GNS samples (B1-2) were irradiated with three different laser powers (200, 300 and 400 mW). In general, all the samples were irradiated in the NIR, selecting a wavelength close to their LSPR maxima (720 nm for HNT-NH_2@GNS and 850 nm for HNT-PVP@GNS). In Figure 17 the heating curves of all the samples irradiated with the 200 mW power are shown to compare the features of the two different covering strategies, while in Table 5 the photothermal parameters of the measurements are listed, i.e. the emitting wavelength of the laser used to irradiate the two types of HNT@GNS samples, the starting and final temperatures of the samples, and the temperature increases produced by each irradiation.

From the qualitative comparison of all the samples, the temperature increase (ΔT) produced by the HNT-PVP@GNS samples is higher than the one generated when the linking molecule between the HNT and the GNS is APTES (HNT-NH_2@GNS). This preliminary comparison already suggests that the decoration involving PVP produces samples with better photothermal feature, by comparing the HNT-NH_2@GNS 30:1 (A2) and the HNT-PVP@GNS 5:1 (B2) samples (orange and light blue traces in Figure 17

respectively), that contain the same mass of gold, and the HNT-NH_2@GNS 60:1 (A1) with the HNT-PVP@GNS 10:1 (B1) one, in which the gold amount is similar, as shown in Table 4.

The calculated thermal capacities appear quite similar to one another, even though a bit lower for the PVP-functionalized samples, but notably the parameters of the APTES-functionalized samples are measured on a mass ten times higher than the others, which is not considered in the calculation of C. Thus, if we had measured these features on a similar amount of sample, we would have expected a thermal capacity of the HNT-NH_2@GNS samples about ten times higher than the values listed. On the other hand, when the specific heat capacities are taken into account, to get a good comparison between the two sets of samples, those with the same amount of gold must be considered: the A2 sample possesses a C_s ca. 1.5 times higher than B2, indicating worse photothermal properties of the first nanocomposite than the second. From this comparison we can conclude that the third strategy (involving PVP) allowed the production of better nanocomposites for the light induced generation of heat by GNS.

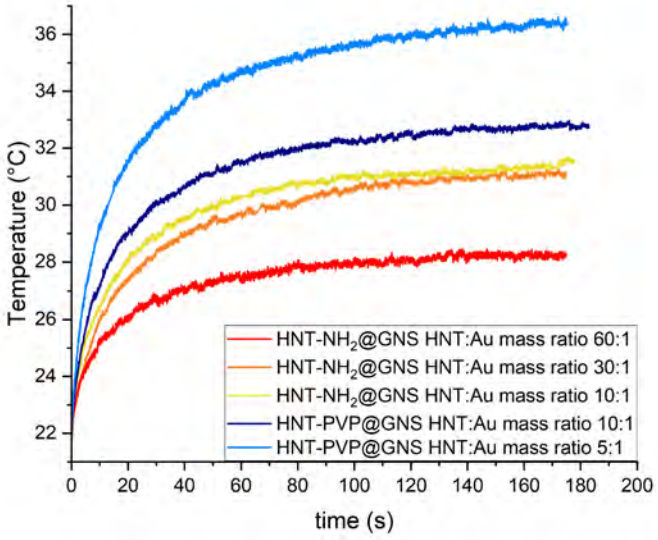

Figure 17. *Heating curves (temperature vs time) of all the five HNT@GNS nanocomposites produced with the second (red, orange and yellow lines. HNT:Au w/w ratios of 60:1, 30:1 and 10:1, respectively) and third (blue and light blue lines. HNT:Au w/w ratios of 10:1 and 5:1, respectively) synthetic approach and irradiated with a monochromatic laser (λ= 720 nm for the HNT-NH_2@GNS samples and λ= 850 nm for the HNT-PVP@GNS ones) using 200 mW power.*

Table 5. *Photothermal parameters recorded on five different HNT@GNS samples (HNT-NH_2@GNS with the HNT:GNS w/w ratios of 60:1, 30:1 and 10:1 and HNT-PVP@GNS with the HNT:GNS w/w ratios of 10:1 and 5:1), irradiated with a laser power of 200 mW.*

Sample type	HNT:Au mass ratio	Irradiation λ (nm)	Initial T_1 (°C)	Final T_1 (°C)	ΔT (°C)	C (mJ/K)	C_s (mJ/K·mg)
HNT-NH_2@GNS	60:1	720	22.0	28.3	6.3	596	$9.31 \cdot 10^4$
HNT-NH_2@GNS	30:1	720	21.6	31.2	9.6	637	$2.68 \cdot 10^4$
HNT-NH_2@GNS	10:1	720	22.2	31.3	9.1	534	$1.28 \cdot 10^4$
HNT-PVP@GNS	10:1	850	21.7	32.8	11.1	420	$4.28 \cdot 10^4$
HNT-PVP@GNS	5:1	850	21.6	36.4	14.8	342	$1.64 \cdot 10^4$

After comparing the two sets of samples, we focused singularly on the various HNT:Au ratios of the nanocomposites prepared with both strategies. In the following Figure 18 the heating curves recorded on the HNT-NH_2@GNS samples using the two laser powers 200 and 230 mW are reported, while in Table 6 all the parameters derived from each fitting, the calculated thermal capacity (C) and specific heat capacity (C_s) are listed. The large discrepancy between the C values obtained from the heating curves at 200 and 230 mW indicates a saturation of the photothermal response in these nanocomposites. In other words, the measured ΔT no longer increases proportionally with the incident laser power. Thus, only the C values obtained under 200 mW irradiation were used to calculate the specific heat and to compare the nanocomposites prepared by the two synthetic strategies. The photothermal performance shows a 3.5-fold enhancement when moving from the lowest- to the intermediate-gold sample, followed by an additional 2-fold increase between the intermediate sample and the one with the highest gold content. This result is consistent with the experimental HNT:Au mass ratios of these samples determined via ICP-MS (respectively 180:1 for the nominal 60:1, 55:1 for the nominal 30:1 and 30:1 for the nominal 10:1), which resulted a lot lower in terms of gold content, possibly due to the low stability of the nanocomposite consequently to the mechanical stress during the centrifugation cycles when using the APTES linking molecule.

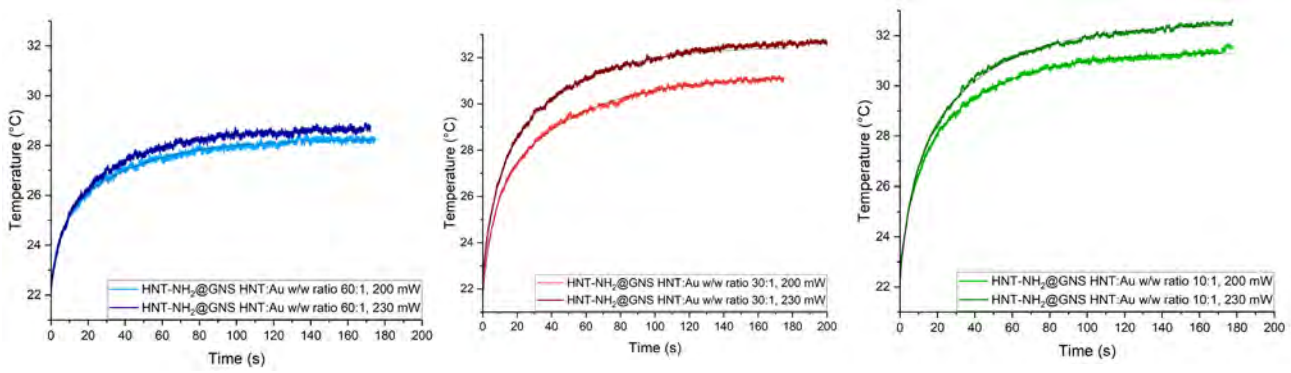

Figure 18. *Heating curves (temperature vs time) of the three HNT-NH_2@GNS nanocomposites produced with a HNT:Au w/w ratio of 60:1 (blue traces), 30:1 (red traces) and 10:1 (green traces), irradiated with a monochromatic laser (λ= 720 nm) with 200 mW (light traces) and 230 mW (dark traces) powers. The black lines are the fitted curves.*

Table 6. *Photothermal parameters recorded on the three HNT-NH_2@GNS nanocomposites, irradiated with two different laser power (200 and 230 mW), emitting a monochromatic light (λ= 720 nm).*

Nominal HNT:Au mass ratio	Laser power (mW)	ΔT (°C)	τ_1 (s)	τ_2 (s)	C (mJ/K)	C_s (mJ/K·mg)
60:1	200	6.3	3.98	37.4	596	$9.31 \cdot 10^4$
60:1	230	6.7	4.15	33.6	718	-
30:1	200	9.6	5.72	45.8	637	$2.68 \cdot 10^4$
30:1	230	10.4	6.73	46.7	743	-
10:1	200	9.1	4.9	35.3	534	$1.28 \cdot 10^4$
10:1	230	10.3	6.4	39.9	712	-

Moving to the HNT-PVP@GNS samples, their heating curves recorded using the three different laser powers (200, 300 and 400 mW) are reported in Figure 19 and the derived photothermal parameters in Table 7. The specific heat capacity of the 5:1 ratio sample shows a ca. 3-fold increase in the photothermal features of this sample, consistent with the higher Au content and with the experimental HNT:Au ratio calculated for the two samples from the ICP-OES gold determination, listed in Table 5 (17:1 vs 6:1). The photothermal features of HNT-PVP@GNS nanocomposite with the HNT:Au 10:1 mass ratio is comparable to those of a similar HNT-gold nanorod composite reported in the literature, while for the one with the 5:1 ratio they resulted even superior.[36]

Thus, given the lower specific heat capacity and the nearly quantitative yield in the interaction between functionalized HNT and GNS, we selected this mass ratio as optimal one for the subsequent drug loading into the nanotubes. Nevertheless, higher gold concentrations have not been tested yet, so it remains to be determined whether the interaction efficiency already reaches saturation at the 5:1 ratio or whether the photothermal performance of the nanocomposite could be further enhanced.

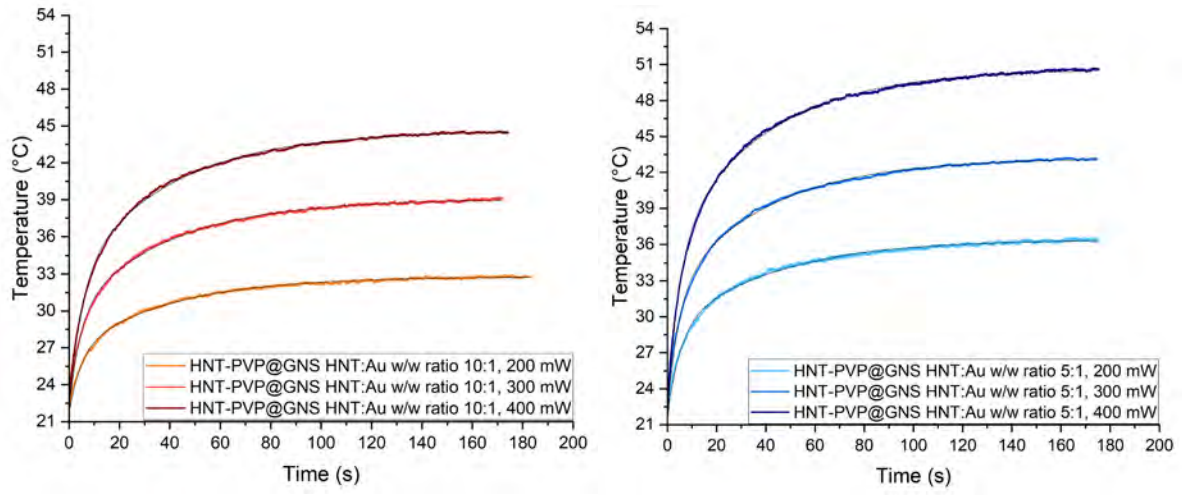

Figure 19. *Heating curves (temperature vs time) of the three HNT-NH_2@GNS nanocomposites produced with a HNT:Au w/w ratio of 60:1 (blue traces), 30:1 (red traces) and 10:1 (green traces), irradiated with a monochromatic laser (λ= 720 nm) with 200 mW (light traces) and 230 mW (dark traces) powers. The black lines are the fitted curves.*

Table 7. *Photothermal parameters recorded on the two HNT-PVP@GNS nanocomposites, irradiated with three different laser power (200, 300 and 400 mW), emitting a monochromatic light (λ= 8500 nm).*

HNT:Au mass ratio	Laser power (mW)	ΔT (°C)	τ_1 (s)	τ_2 (s)	C (mJ/K)	C_s (mJ/K·mg)
10:1	200	11.1	4.65	38.3	420	$4.28 \cdot 10^4$
10:1	300	17.1	4.45	39.0	392	$3.99 \cdot 10^4$
10:1	400	22.8	4.81	38.5	423	$4.31 \cdot 10^4$
5:1	200	14.8	5.06	41.0	342	$1.64 \cdot 10^4$
5:1	300	21.3	4.49	39.1	317	$1.52 \cdot 10^4$
5:1	400	28.6	4.85	38.4	339	$1.62 \cdot 10^4$

Loading of HNT with mitoxantrone

Preliminary tests to load the mitoxantrone (MTX) drug into pristine and PVP-functionalized HNT were carried out to find the best loading conditions in terms of pH and loading strategy before moving to the HNT-PVP@GNS samples.

It is known that HNT present different chemical compositions in the inner lumen and outer surface, being the first positively charged due to protonation of AlOH groups and the second negatively charged at pH higher than 2. Based on a quantitative study from the literature,[37] we schematized their speciation curves (Figure 20) for a more precise estimation of the overall HNT charge at different pH values and to hypothesize the kind of interaction that occurs with MTX.

SiOH groups on the external surface of HNT result protonated (in their neutral form) at pH 2, while they start deprotonating in the 2-6 pH range until fully deprotonated (one negative charge per group) is reached at about pH 6.5 (pK_a= 4.1 when suspended in a solution with an ionic strength of 0.041 mol/dm^3)[37]. At the same time, for the AlOH groups of the inner lumen three different protonation states are possible: $AlOH_2^+$, AlOH and AlO^-. The AlOH groups are fully protonated until ca. pH 6, when they gradually deprotonate to the other two forms in the 6-11 pH range. These deprotonations are highly dependent on the ionic strength of the solution (pK_{a1}= 6.92 and pK_{a2}= 9.63 when the ionic strength is 0.041 mol/dm^3 and pK_{a1}= 7.67 and pK_{a2}= 10.08 with an ionic strength of 0.428 mol/dm^3, calculated using the Högfeldt protonation model).[37]

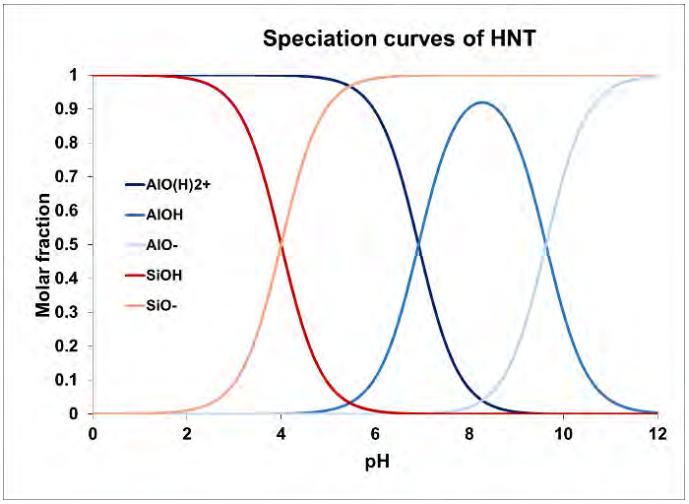

Figure 20. *Speciation curves of pristine HNT based on the pK_a values of AlOH and SiOH groups present respectively in their inner lumen and outer surface and on a study from the literature.*[37]

On the other hand, mitoxantrone, whose structure is shown in Scheme 1, possesses two pK_a in the 8.3-8.6 range[38] corresponding to the protonation of its two amine groups. Thus, we attempted to load the drug at two different pH values, 7.8 and 10, to test two different protonation states of MTX. At the lower pH tested, the drug is almost fully protonated while the HNT is likely slightly negatively charged as the

external surface exposes fully deprotonated SiO^- groups and the inner lumen a prevalence of neutral AlOH groups as well as their partial protonated state $AlOH_2^+$. Conversely, at pH 10 mitoxantrone is in its neutral form, while we expect the HNT to be fully deprotonated, with the inner lumen presenting partially neutral AlOH and negative AlO^- groups.

The drug loading was carried out using two different approaches. In the first the HNT powder was dispersed in a saturated drug solution and subjected to dynamic vacuum/N_2 cycles,[39,40] a widely used literature method to promote loading of the drug into the inner lumen by air and possibly water removal.[41] In parallel, loading by simple diffusion at room pressure at pH 7.8 was carried out for comparison. After their loading, all the samples turned their color from white to blue, with the color being more intense for the pristine HNT than for those functionalized with PVP. The loaded HNT samples were analyzed by ATR-FTIR spectroscopy (Figures 21 and 22). In all the samples, three peaks at 1564, 1463 and 1349 cm^{-1} assigned to mitoxantrone were visible, confirming the presence on HNT. Additionally, two of the most intense peaks assigned to the PVP polymer (at 1652 and 1286 cm^{-1}) were recognizable in all the samples containing it, suggesting that the loading of the drug does not disrupt the HNT-PVP interaction.

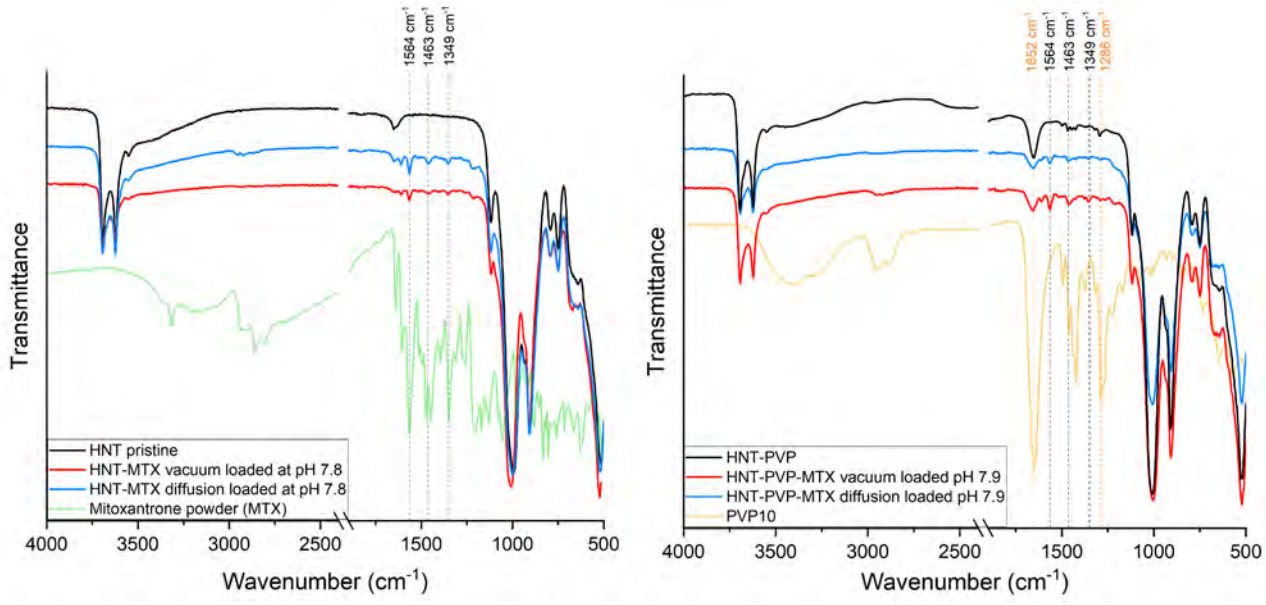

Figure 21. *Left panel: ATR-FTIR spectra of pristine HNT (black trace), of mitoxantrone powder (green trace) and of pristine HNT loaded at pH 7.8 by dynamic vacuum (red trace) or by diffusion (blue trace). Right panel: ATR-FTIR spectra of HNT-PVP (black trace), of PVP10 powder (yellow trace) and of HNT-PVP loaded at pH 7.9 by dynamic vacuum (red trace) or by diffusion (blue trace). In both spectra the peaks assigned to MTX (1564, 1463 and 1349 cm^{-1}) are marked in black, while those assigned to PVP (1652 and 1286 cm^{-1}) are marked in orange only in the second spectrum.*

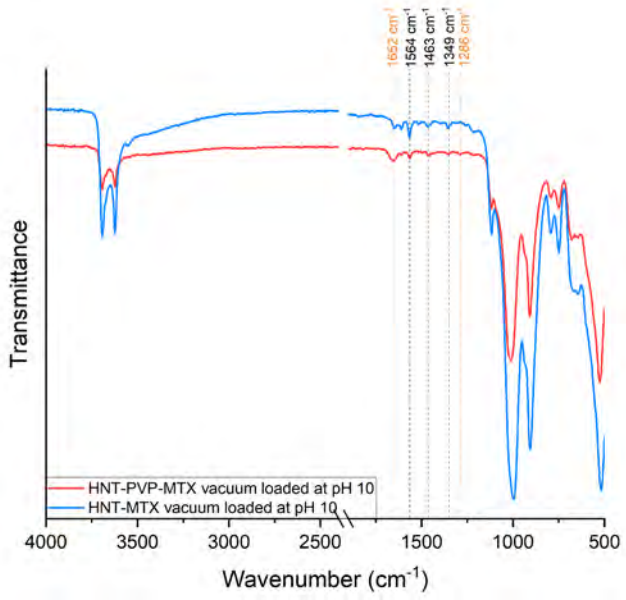

Figure 22. *ATR FT-IR spectra of pristine HNT (blue trace), and of HNT-PVP (red trace) vacuum loaded at pH 10. The dashed lines marks peaks assigned to MTX (1564, 1463 and 1349 cm^{-1}) in black and those assigned to PVP (1652 and 1286 cm^{-1}) in orange.*

Additionally, thermogravimetric analyses (TG-DTG, Figure 23) were carried out on the loaded samples under air flux, as well as on pristine HNT, HNT-PVP and mitoxantrone alone, to quantify the drug loaded in the HNT and, hence, the loading efficiency of the different attempted strategies. The temperature at the inflection points of the TGA weight losses are listed in Table 8.

Table 8. *Temperature at the inflection point of the three peaks visible in the DTG curves of all the samples.*

Sample	Weight loss 1	Weight loss 2	Weight loss 3
HNT pristine	/	471 °C	/
HNT-PVP	305 °C	473 °C	/
HNT pristine diffusion loaded at pH 7.8	322 °C	464 °C	583 °C
HNT pristine vacuum loaded at pH 7.8	238-312 °C	474 °C	/
HNT pristine vacuum loaded at pH 10	248 °C	477 °C	579 °C
HNT-PVP diffusion loaded at pH 7.9	316 °C	471 °C	577 °C
HNT-PVP vacuum loaded at pH 7.9	317 °C	470 °C	580 °C
HNT-PVP vacuum loaded at pH 10	320 °C	473 °C	576 °C

In Figure 23A all the TG curves are reported for comparison. The three curves of the loaded HNT-PVP samples are superimposable, suggesting a similar MTX loading, while for the loaded pristine HNT a higher variability is recorded. The sample loaded by diffusion seems to contain the higher amount of MTX, while the one loaded by vacuum at pH 7.8 the least and the vacuum-loaded at pH 10 seems to show an intermediate quantity.

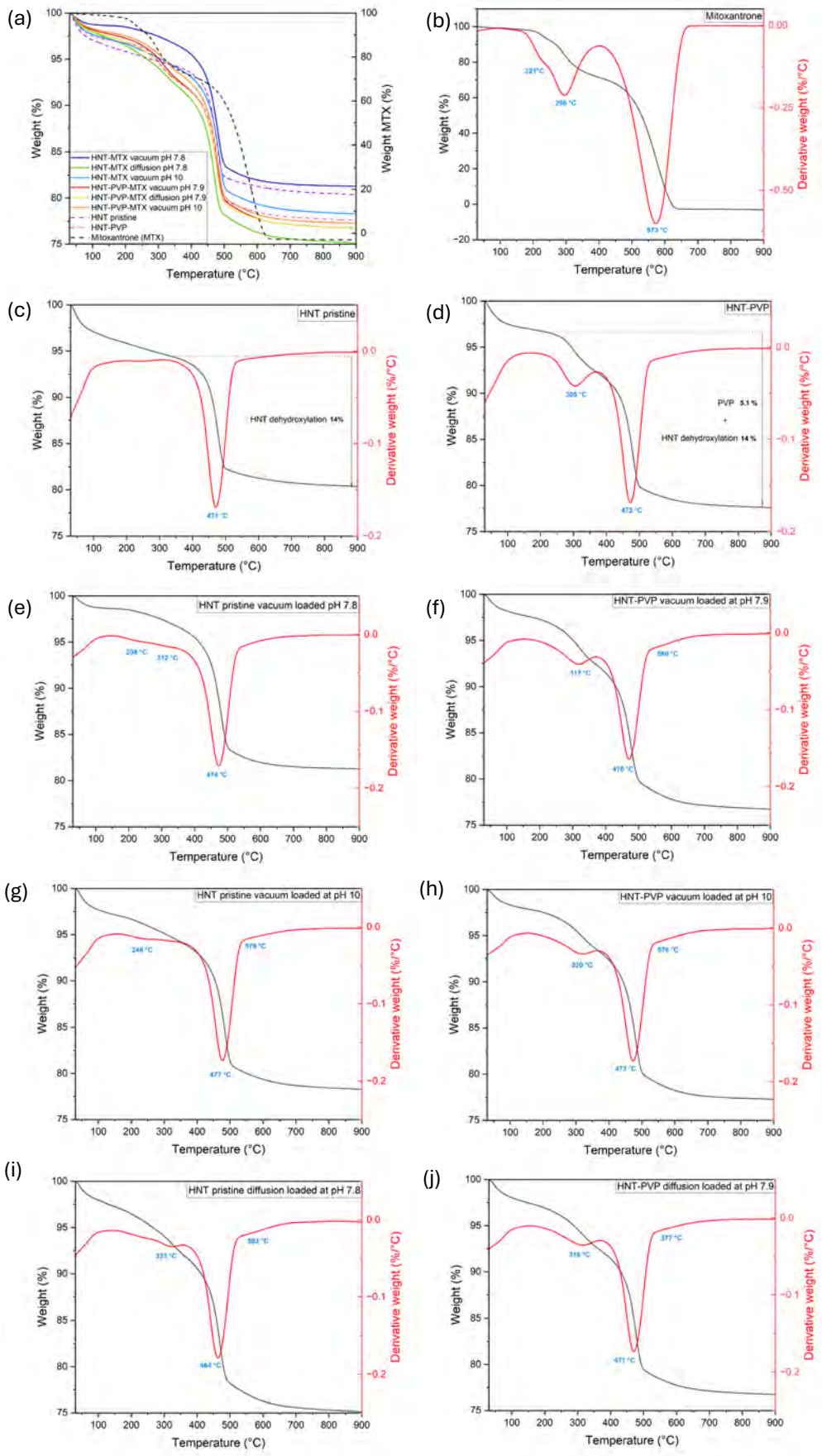

Figure 23. *(a) Full lines: TGA of pristine HNT or PVP-functionalized HNT loaded with mitoxantrone (MTX). Dashed lines: TGA of the unloaded pristine HNT, HNT-PVP and of the MTX alone. (b) TGA and DTGA of MTX. (c, e, g, i) TGA and DTGA of pristine HNT loaded with MTX. (d, f, h, j) TGA and DTGA of HNT-PVP loaded with MTX.*

The analysis of the TG/DTG curves was not trivial, since the weight losses caused by the dehydroxylation of HNT, the degradation of PVP and of mitoxantrone partially overlapped. The DTG curve of mitoxantrone (Figure 23B) showed two peaks: a main weight loss with an inflection point at 573 °C and a second one at 296 °C with a shoulder at 221 °C. Analogously, TGA curves of PVP in air reported in the literature show that the PVP polymer decomposes in two steps when alone[42,43] with a minor weight loss between 300-370 °C and a major one at ca. 400 °C.[33,44] Similarly, TGA curves of PVP on silica nanoparticles showed a sharp weight loss between 300-600 °C.[44] Moreover, the thermal degradation curve found in the literature of HNT extracted from Camel Lake mines, the same as those named in this work as HNT AUS, showed a minor weight loss due to the evaporation of interstitial water, followed by a steep step due to their dehydroxylation at ca. 500 °C (data measured under nitrogen flux).[45]

To confirm these data, we recorded a TG curve of our batch of pristine HNT AUS in the same conditions as the loaded samples (Figure 23C), that, apart from the initial weight loss due to water evaporation, showed one weight loss with a T_{onset} of ca. 400 °C with an inflection point at 471 °C, which accounted for the loss of 14% of the weight. Thus, we assumed this value as constant for all the samples, to discriminate the contribution of PVP and MTX in the more complex nanocomposites.

The weight loss contribution of PVP was determined on the HNT-PVP sample (Figure 23D), by subtracting the 14% associated with dihydroxylation from the total weight loss. This accounted for 5.1%, which was then assumed to be constant for all the PVP-containing samples (Figures 23F, H, J). In Table 9 the MTX weight % measured for all the samples are listed.

Table 9. *Drug content estimated from the TG-DTG curves for each HNT or HNT-PVP loaded sample, assuming a fixed weight loss of 14% due to the HNT dihydroxylation, and a fixed PVP content of 5.1% for all the HNT-PVP samples.*

Sample	Mitoxantrone weight %
HNT pristine diffusion loaded at pH 7.8	8.2
HNT pristine vacuum loaded at pH 7.8	3.3
HNT pristine vacuum loaded at pH 10	4.7
HNT-PVP diffusion loaded at pH 7.9	1.5
HNT-PVP vacuum loaded at pH 7.9	1.9
HNT-PVP vacuum loaded at pH 10	1.6

From these analyses we hypothesize that the mitoxantrone interacts with the SiO^- groups present on the external surface of pristine HNT, which are deprotonated starting from ca. pH 6 and thus in all the loading conditions that we attempted. If this kind of interaction was taking place, the loading efficiency of pristine HNT under vacuum and diffusion conditions should be comparable. Instead, the marked difference in the amount of loaded MTX was tentatively attributed to the different interaction kinetics: the less efficient vacuum loading was carried out for only 1h, while diffusion loading proceeded overnight.

Moreover, comparing the two vacuum-loaded pristine HNT samples, the higher loading efficiency achieved at pH 10 suggests that the neutral form of the drug enters the inner lumen more readily than at pH 7.8, where repulsion occurs between the partially protonated inner lumen and the protonated drug.

Moving to the PVP-functionalized HNT, the achieved loading efficiencies are similar for all the three samples and lower than those obtained with the pristine HNT. The absence of significant difference between the diffusion and vacuum loaded PVP-functionalized samples confirms that for the pristine HNT the interaction occurs mainly with the external surface, since PVP binds to the external -OH groups hindering their possible interaction with MTX.

Release of mitoxantrone from HNT

After the loading of mitoxantrone on both pristine HNT and HNT-PVP, a preliminary release study was attempted at room temperature from all the loaded samples by suspending the samples in acetate buffer at pH 4.65, to mimic the acidic conditions of lysosomes (pH ca. 4.5-5.0).[46] Indeed, the loaded samples might experiment these condition when taken up by tumoral cells, according to the pathways proposed in the literature for various loaded and functionalized HNT.[47-49] Additionally, the pH of malignant tumor microenvironments is usually decreased (from 5.5 to 6.8)[50] compared to the physiological pH of healthy tissues, due to the lack of a hierarchical structure in tumoral bloody vessels and the consequently low blood flow, which generates hypoxic microenvironments in which the glycolysis is increased and the pH is decreased (due to the increase of lactate generation).[51]

On HNT-PVP vacuum loaded at pH 10, two additional release studies of MTX were carried out: the first was carried out in phosphate buffer at physiological pH (7.45), to determine whether the release might differ when the loaded HNT are located outside the lysosomes and in healthy cells and tissues, while the second one at 40 °C and pH 4.65 to mimic the temperature reached by the HNT-PVP@GNS nanocomposites when irradiated with the 300 mW laser (see the Photothermal characterization of HNT@GNS section). Notably, all these release studies were performed on samples not decorated with the GNS yet, to determine the best loading and release conditions before moving on to the samples decorated with the GNS.

Similarly to the protocol for drug release studies from HNT adopted in the literature[52] and previously used by our group,[53] the loaded HNT were suspended in milliQ water in a glass centrifuge tube and magnetically stirred for a defined period at either RT or 40 °C. The suspension was then centrifuged to separate the supernatant containing the released drug from the pellet.

The blue supernatant was then analyzed by UV-vis spectroscopy[viii] to determine the concentration of solubilized MTX. Finally, the released drug % was calculated using the MTX mass % determined by TGA (Table 9). The overall protocol is schematized in Scheme 5.

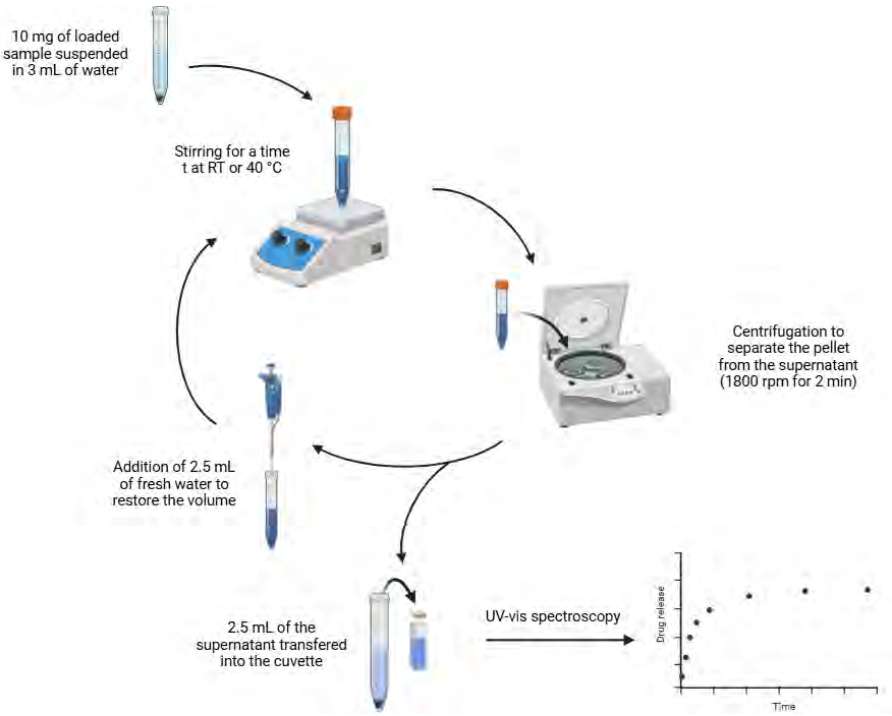

Scheme 5. *Schematic representation of the protocol followed to determine the mitoxantrone release kinetics from the loaded HNT or HNT-PVP. Figure prepared using Biorender.*

Several fitting models commonly used in the drug delivery field - particularly for tubular nanocarriers such as HNT - were applied to fit the MTX release profiles from each sample. These include the zero-, first-order, Higuchi, Weibull and Korsmeyer-Peppas models, whose mathematical expressions are reported in Table 10.[54,55] The zero-order model assumes a slow, constant, and purely time-dependent release rate, with a constant dosage area, such that any equilibrium is reached during the release. In contrast, the first-order model describes a release rate that depends on the drug concentration remaining in the carrier. The Weibull model is instead a descriptive model that considers one burst release followed by a slower and prolonged one, and in which the total drug release is influenced by the effective surface area of the carrier. Its equation is defined by the parameters *a* and *b*, respectively depending on the time of the process and on the shape of the curve (exponential when $b = 1$, parabolic when $b < 1$ and S-shaped when $b > 1$). Lastly, the Higuchi and the Korsmeyer-Peppas models are both semi-empirical models that explain drug release as a diffusion process based on Fick's law. In particular, the Higuchi model assumes a one-dimensional drug diffusion in which the final drug concentration is higher than its solubility and ignores the swelling and the dissolution of the matrix, while the Korsmeyer-Peppas model allows to explain different mechanisms (like the diffusion of water

[viii] ε (608 nm) = 19200 M^{-1} cm^{-1} in water, datum from Ref. 58

into the matrix, the matrix swelling or its dissolution) and is employable when various mechanisms are involved. The value of the parameter *n* allows to discriminate whether the drug release is Fickian or non-Fickian: for cylindrical matrixes like the HNT, the release depends mainly on the Fickian diffusion when $n \leq 0.45$, on the non-Fickian when $0.45 < n < 0.89$, on the matrix relaxation when $n = 0.89$ and on the polymer swelling when $n > 0.89$.[54] A non-Fickian or anomalous release indicates that the process is controlled by a combination of diffusion and factors as polymer swelling, erosion or conformation relaxation. In this case the degree by which these factors influence the release can be calculated employing the Peppas-Sahlin model, whose expression is reported in equation 3 (where k_d is a constant depending on the Fickian diffusion and k_{nd} on the other release mechanism due to the polymer).[55]

$$C_t/C_{max} = k_d \cdot t^n + k_{nd} \cdot t^{2n} \qquad \text{eq. 3}$$

Table 10. *Mathematical equations for the drug release kinetics models tentatively employed to fit the release curves of MTX from HNT and HNT-PVP.*

Drug release kinetics fitting model	Mathematical equation	Fitting curves[ix]
Zero-order	$C_t = C_{max} + k_0 \cdot t$	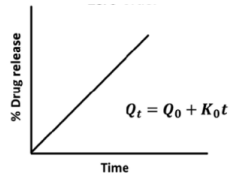
First-order	$lnC_t = lnC_{max} - k_1 \cdot t$	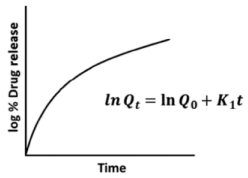
Higuchi	$C_t = k_H \cdot t^{1/2}$	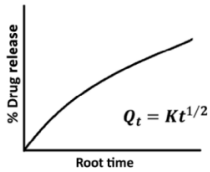
Weibull	$C_t/C_{max} = 1 - e^{(-b \cdot t^a)}$	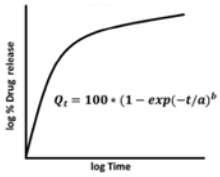
Korsmeyer-Peppas	$C_t/C_{max} = k_{KP} \cdot t^n$	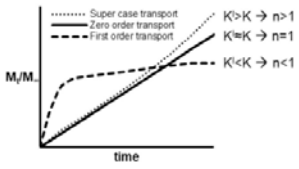

[ix] The curves of the zero-, first-order, Higuchi and Weibull models are from Ref. 59, while the curve of the Korsmeyer-Peppas model is taken from Ref. 60

In Table 11 the R^2 calculated from the fits of the release curves using the already described models are listed, showing that all the samples are best described by the Weibull and the Korsmeyer-Peppas models. Thus, the experimental data collected in the release study at RT and pH 4.65, fitted using the Korsmeyer-Peppas model are reported in Figure 24. Additionally, in Table 12 the parameters derived from these two fits are listed, allowing to hypothesize and describe the type of release. These results are consistent with various release studies of drugs from functionalized HNT reported in the literature, usually best fitted with the Korsmeyer-Peppas model and suggest a first burst release followed by a second slower release process, whose rate differs between each sample, until the various release efficiencies are reached. In particular, the Korsmeyer-Peppas fits indicate that for all the samples the drug release is governed by Fickian diffusion (being the n values always lower than 0.45, as reported in Table 12) and that in the samples functionalized with the PVP, the polymer is not directly involved in the release mechanism. Additionally, in the Weibull fit the values of the *b* parameter indicate a parabolic release for all the samples, and the higher *a* parameter in the MTX release from the pristine HNT (at least one order of magnitude higher than the PVP-functionalized samples) indicates that the drug release is slower and is linked to the lower amount of released MTX, under 6% after 48 h for all the three samples. This result is consistent with the hypothesis of a strong interaction between the drug and the SiO^- groups on the external surface of HNT, that possibly prevents the release of most of the drug. In agreement to this hypothesis, the released MTX from the pristine HNT might be the part of the loaded drug effectively introduced into the inner lumen of HNT during the loading, thus being less of 10% of the total loaded mass. Conversely, the loaded HNT-PVP samples showed a higher ratio of released drug, that seems faster for the sample loaded at pH 10, reaching much higher release efficiencies (between 35-55% at RT), due to the presence of PVP on the external surface of HNT that hinders or reduces its strong interaction with the drug. PVP is indeed known to delay the drug release when used as a coating agent in drug delivery systems.[31]

Table 11. *Results of the fitting of the mitoxantrone release from HNT or HNT-PVP loaded with the various strategies attempted using the most commonly used models in pharmaceutics.*

Sample	Loading method	Loading pH	Release T and pH	Fitting model	R^2
Pristine HNT	diffusion	7.8	RT, 4.65	Zero-order	0.48520
				First-order	-1.19710
				Higuchi	0.34701
				Weibull	**0.94815**
				Korsmeyer-Peppas	**0.93878**
Pristine HNT	vacuum/N_2 cycles	7.8	RT, 4.65	Zero-order	0.58900
				First-order	0.54100
				Higuchi	0.54100
				Weibull	**0.97401**
				Korsmeyer-Peppas	**0.97341**
Pristine HNT	vacuum/N_2 cycles	10	RT, 4.65	Zero-order	0.63049
				First-order	-0.39447
				Higuchi	0.59836
				Weibull	**0.97995**
				Korsmeyer-Peppas	**0.97971**
HNT-PVP	diffusion	7.9	RT, 4.65	Zero-order	0.41328
				First-order	-
				Higuchi	0.01149
				Weibull	**0.96772**
				Korsmeyer-Peppas	**0.96233**
HNT-PVP	vacuum/N_2 cycles	7.9	RT, 4.65	Zero-order	0.23703
				First-order	-2.80393
				Higuchi	-0.84447
				Weibull	**0.98032**
				Korsmeyer-Peppas	**0.97820**
HNT-PVP	vacuum/N_2 cycles	10	RT, 4.65	Zero-order	0.33560
				First-order	-
				Higuchi	-0.37119
				Weibull	**0.97966**
				Korsmeyer-Peppas	**0.97391**
HNT-PVP	vacuum/N_2 cycles	10	RT, 7.45	Zero-order	0.66683
				First-order	-0.59022
				Higuchi	0.76359
				Weibull	**0.96329**
				Korsmeyer-Peppas	**0.96328**
HNT-PVP	vacuum/N_2 cycles	10	40 °C, 4.65	Zero-order	0.48394
				First-order	0.34364
				Higuchi	-0.02744
				Weibull	**0.98948**
				Korsmeyer-Peppas	**0.99660**

Table 12. *Parameters derived from the two best models used to fit the MTX release from HNT and HNT-PVP samples (Weibull and Korsmeyer-Peppas fittings).*

Sample	Loading method	Loading pH	Release T and pH		Weibull		Korsmeyer-Peppas	
					a	b	k_{KP}	n
Pristine HNT	diffusion	7.8	RT	4.65	92.37	0.20	1.09	0.20
Pristine HNT	vacuum/N_2 cycles	7.8	RT	4.65	97.56	0.23	1.04	0.23
Pristine HNT	vacuum/N_2 cycles	10	RT	4.65	195.57	0.24	0.51	0.24
HNT-PVP	diffusion	7.9	RT	4.65	7.80	0.20	13.32	0.16
HNT-PVP	vacuum/N_2 cycles	7.9	RT	4.65	3.39	0.11	26.80	0.08
HNT-PVP	vacuum/N_2 cycles	10	RT	4.65	4.06	0.18	24.75	0.12
			RT	7.45	16113.78	0.29	0.29	0.01
			40 °C	4.65	5.17	0.29	24.90	0.16

The release curves of two additional release experiments carried out on the HNT-PVP sample vacuum loaded at pH 10 are shown in Figure 25. By increasing the pH of the release from 4.65 to 7.45 at RT, the loaded MTX is no longer released from the HNT. On the other hand, at pH 4.65, when the temperature is increased to 40 °C, the release efficiency of the drug is almost doubled compared to the release at the same pH at RT (from 55% to 91% after 48 h) and after the first burst release visible for all the samples, the amount of released MTX visibly increases over time (as the *a* parameter of the Weibull fit that defines the timescale of the release, decreases). These results are consistent with a release study appeared in the literature[8] on mitoxantrone-loaded carbon nanotubes (CNT): the authors found that MTX release is based on a Fickian diffusion, being more effective at acid pH (5.5) compared to the physiological one and is further increased when the temperature passes from 37 °C to 50 °C. Moreover, another release study of doxorubicin from a CNT-polymer hybrid carrier,[56] carried out at two different pH values (5.3 and 7.4) and at two distinct temperatures (37 °C and 40 °C), observed a more efficient drug release when the pH is decreased and when the temperature is increased, explained by the facilitated swelling capability of the polymer and the weaker hydrogen bonding interaction between the polymer and the drug at acid pH.

Overall, considering both the loading results obtained with the TG analyses and the release data, the most suitable conditions for loading MTX into the HNT-PVP@GNS nanocomposites appeared to be the vacuum loading at pH 10. Although the presence of PVP reduces the total amount of loaded drug, it also weakens its strong interaction with the HNT surface, thereby enabling a more efficient release, particularly at 40° C. Our preliminary results are quite promising for the release of mitoxantrone from the HNT-PVP@GNS nanocomposite triggered by the temperature increase due to the photothermal features of the GNS. The loading and release of mitoxantrone from the HNT-PVP@GNS nanocomposite will be evaluated in the near future to test the performance of the complete system.

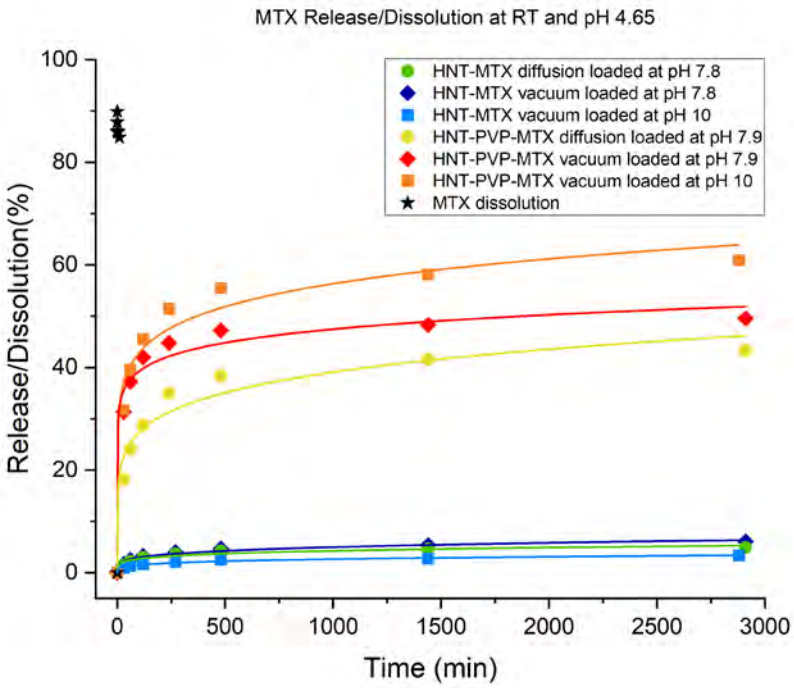

Figure 24. *Experimental release plots of mitoxantrone at pH 4.65 and RT from HNT or HNT-PVP loaded with various strategies. Respectively the dots represent the samples loaded by diffusion at pH 7.8-7.9 (green for pristine HNT and yellow for HNT-PVP), and the squares the samples vacuum loaded (blue for pristine HNT at pH 7.8, light blue for pristine HNT at pH 10, red for HNT-PVP at pH 7.9 and orange for HNT-PVP loaded at pH 10). The black stars represent the MTX dissolution at pH 4.65 and RT. All the release plots were fitted using the Korsmeyer-Peppas model.*

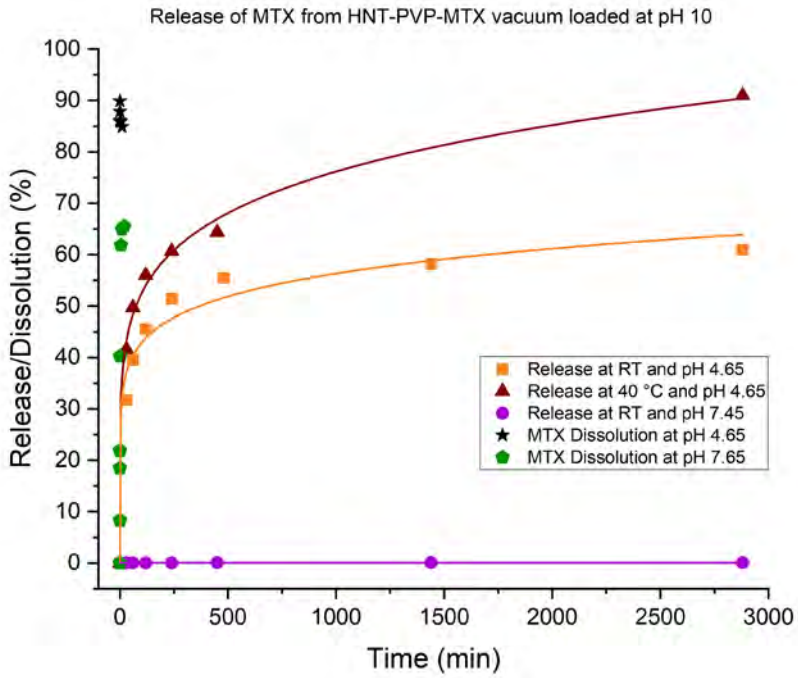

Figure 25. *Experimental release plots of mitoxantrone from HNT-PVP vacuum loaded at pH 10 at various temperatures and pH values. The drug is released at RT and pH 4.65 (orange squares), at RT and pH 7.45 (purple circles) and at 40 °C and pH 4.65 (brown triangles). The black stars represent the MTX dissolution at pH 4.65 and RT, while the green pentagons the MTX dissolution at pH 7.45 and RT. All the release plots were fitted using the Korsmeyer-Peppas model.*

Conclusions

The aim of this work was the preparation of an HNT-GNS nanocomposite material, to combine the HNT properties as drug delivery carriers with the therapeutic feature of GNS based on the photothermal effect, i.e. the generation of local heat when the GNS is irradiated by a suitable NIR light source. The purpose of HNT decoration was to obtain a dual therapeutic agent, by loading the HNT inner lumen with a proper antitumoral drug, whose release could be triggered by the photothermal effect of the GNS. Moreover, the drug action could be further enhanced locally by the PTT promoted by the same GNS on the HNT surface.

A great part of my work consisted in the development of an efficient HNT decoration strategy. To achieve it, three different protocols were attempted, by varying both the synthesis of GNS and the linking molecule between them and the HNT. In the first attempt HNT were functionalized with the amino-alkoxysilane APTES and subsequently treated with GNS without any surfacting agent (f-GNS) that possessed a free and available surface for the interaction with APTES. The so obtained HNT-NH_2@f-GNS nanocomposites resulted poor in terms of homogeneity and efficiency of the decoration and of the f-GNS stability. For this reason, as a first attempt, we considered a different GNS synthesis, moving to GNS@TX-100, stabilized by an excess of the surfactant Triton X-100, which interacts weakly with the gold surface and thus can be easily exchanged with other ligands. However, changing the GNS was not enough to improve the homogeneity of HNT decoration and the stability of the HNT-NH_2@GNS nanocomposite, since the GNS seemed to self-aggregate in roundish hollow structures and detach from the HNT surface upon mechanic stress, i.e. the centrifugation cycles used to wash HNT@GNS from the excess of TX-100. In this second strategy we additionally tried to increase the Au:HNT ratio involved in the interaction and we observed that a satisfying grade of decoration was achieved when the HNT excess was reduced from 60:1 to 10:1 (considering the HNT:Au ratio). For this reason, in the third strategy that we attempted, we decided to increase further the gold amount, by testing the 10:1 and the 5:1 HNT:Au ratios. Moreover, the main difference introduced at this point consisted in the linking molecule passing from molecular APTES to the PVP polymer with low molecular weight (10 kDa, PVP10). These HNT-PVP@GNS nanocomposites finally showed satisfying stability and decoration grade and an almost quantitative interaction efficiency, in particular for the 5:1 ratio (99.5% yield), in which GNS are visible not only at the nanotube edges, but also on the external HNT surface.

Once optimized the decoration strategy, the photothermal properties of the HNT-PVP@GNS nanocomposites were evaluated and compared with those of the HNT-NH_2@GNS ones. For this aim, a small amount of nanocomposite was deposited and dried on a glass support and irradiated using a monochromatic laser (with a wavelength close to the LSPR peak of the GNS) with low and tunable power, measuring the local temperature increase generated by the nanocomposite using a

thermocamera. Overall, the HNT-NH_2@GNS nanocomposite possessed worse photothermal performances compared to the HNT-PVP@GNS one: by the comparison of one sample of each type with the same Au amount (based on ICP analyses) and irradiated with 200 mW power, the temperature increased of just 9.1 °C for the deposited HNT-NH_2@GNS sample vs 14.8 °C for the HNT-PVP@GNS one, whose specific heat capacity (C_s) was calculated 1.5 times lower. This means that fixing the gold amount of the sample, the HNT-PVP@GNS nanocomposites have photothermal features 1.5 times higher than the HNT-NH_2@GNS ones. Moreover, the performances of the HNT-PVP@GNS samples at various HNT:GNS ratios were compared, also increasing the laser power (200, 300 and 400 mW), measuring a 3-fold increase in the C_s parameter for the 5:1 ratio compared to the 10:1, consistent with the higher decoration efficiency reached with the sample with the highest amount of gold. However, the photothermal features of the 10:1 nanocomposite resulted comparable to examples of HNT-anisotropic gold nanoparticles reported in the literature, while those of the 5:1 sample resulted even superior. For this reason we chose the 5:1 ratio as the optimal one, even though in the near future we will attempt to further increase the GNS amount to see whether we already reached a saturation in the decoration efficiency or if the photothermal properties of the HNT-PVP@GNS nanocomposite can be further improved, both by the direct interaction of HNT-PVP with an higher volume of GNS and by a second interaction between HNT-PVP@GNS and GNS@TX-100, trying to form a second GNS layer in the HNT decoration. A PVP polymer with higher molecular weight will be employed as well to functionalize HNT surface. We also would like to characterize the features of these samples also in suspension, to mimic *in vitro* and *in vivo* situations in which the nanocomposite is suspended inside tumoral cells and tissues, to determine whether their photothermal efficiency is similar to what observed on the deposited samples.

Finally, we carried out preliminary loading and releasing tests, by loading into pristine HNT or PVP-functionalized HNT the mitoxantrone molecule (MTX). Three different loading strategies were attempted: by diffusion and by vacuum/N_2 cycles at two different pH (7.8 and 10), producing a total of 6 samples. The mitoxantrone loading % was then measured by TGA, showing higher loading % when MTX is loaded in pristine HNT, especially by diffusion, and lower when the HNT is functionalized with PVP, with comparable % using all the three strategies. However, we hypothesize that MTX might interact with the free SiO^- groups on the external surface of pristine HNT, causing the higher loading % that we measured. On the other hand, when loaded into HNT-PVP, the PVP polymers hinder this interaction and the loaded MTX might be preferentially located into the inner lumen (the higher loaded % was indeed measured for one of the vacuum loaded samples). The MTX release from the loaded samples was tested at pH 4.65, to mimic the acidic pH present in late endosomes and lysosomes (involved in the endocytic internalization mechanisms of such nanoparticles) and in tumoral tissues. Even though for all the samples the release was much slower compared to the drug dissolution at the same pH, MTX was

released more efficiently from PVP-functionalized HNT (reaching after 48 h the release of 35-55% of the loaded drug), while from the pristine HNT the released drug after 48 h remained below 6%, confirming the hypothesis of the strong interaction between SiO^- groups and the protonated drug for these samples. The efficiency of MTX release at acidic pH was further increased to 90% by heating the system at the same temperature reached by the HNT-PVP@GNS sample when irradiated, reaching a promising result for the light-triggered drug release from the HNT-PVP@GNS nanocomposite. Additionally, the drug was not released at all from the loaded HNT-PVP when the pH was increased to 7.45. In the next future, the MTX loading into HNT-PVP@GNS will be attempted, as well as its release triggered by irradiation, to test the efficacy of the overall system before moving to *in vitro* tests with tumoral cells.

Additionally, another decoration strategy that will be tested consists of a first GNS functionalization with PVP to remove the excess of Triton X-100 before their interaction with HNT and exclude the possibility of any competition during their interaction with GNS.

Experimental

Materials and instruments

Ultrapure milli-Q water (Millipore, resistivity=18 $M\Omega cm^{-2}$) was used for the preparation of the aqueous solutions. UV-vis spectra were acquired on an Agilent (model 8543) single beam spectrophotometer equipped with a diode array detector using a quartz cuvette with a 1 cm path length at room temperature. The size distributions by dynamic light scattering and zeta potentials were determined using a Malvern ZetaSizer Nano ZS (Malvern Instruments Ltd.) at 25 °C, using as dispersants milliQ water. Each sample was measured 3 times, and the size results are the average of at least 10 runs for each replicate measurement. TEM pictures were recorded on a FEI Tecnai G2 F20 instrument. ATR-FTIR spectra were recorded on a PerkinElmer Frontier instrument equipped with an ATR accessory with a diamond/ZnSe crystal. The IR spectra were registered between 4000 and 400 cm^{-1}. Thermogravimetric analyses (TGA) were carried out in air atmosphere and in the 30-900 °C temperature range with a heating rate of 5 °C · min^{-1}, using a Mettler-Toledo thermogravimetric balance (TGA/DSC 2 Star® System) on ca. 10 mg of samples. The Au in HNT-NH_2@GNS samples was determined by ICP-MS (AGILENT 7850 ICP-MS), diluting the samples 1:10 in a 1.2 M HCl solution in milliQ water prior to the measurement. To check nebulization efficiency, a solution 200 ppb of an internal standard solution (^{75}As, ^{78}Se, ^{95}Mo) was introduced before the nebulizer in the sample flow. The Au in the HNT-PVP@GNS samples was determined by ICP-OES analysis on a Perkin–Elmer Optima 8300 instrument.

Hydroxylation of HNT (HNT-OH)

Both commercial HNT purchased from Sigma-Aldrich (HNT ALD) and two non-commercial batches, one extracted from Northstar Mine, Utah (HNT USA) and the other from Camel Lake, Australia (HNT AUS) were pre-treated with NaOH before their use, to maximize the exposure of -OH groups on the external surface of HNT and thus increase the efficiency in their functionalization.

Following a literature procedure, [57] the HNT powder (1 g) was suspended in 50 mL of milliQ water and 30 mg of NaOH pellet were added, leaving the mixture reacting at RT for 24h. The suspension was then centrifuged at 7000 rcf for 10 min and washed with fresh water until the pH of 7 was reached. One last wash with EtOH was performed and the obtained hydroxylated HNT (HNT-OH) were dried overnight under vacuum with mechanical pump at RT. The success of this step was ascertained through ζ-potential measurements.

The non-commercial batch of HNT extracted from Camel Lake, South Australia (HNT AUS) does not require this step since they are naturally rich in -OH groups.

Functionalization of HNT external surface with 3-aminopropylethoxysilane (HNT-NH_2)

300 mg of HNT-OH (ALD, USA and AUS) were suspended in 15 mL of EtOH 96% and 6 mL of an ethanolic solution of 3-aminopropylethoxysilane (APTES), containing 60 µL of the reagent, was added under stirring. The suspension was heated to 60°C, carrying out the reaction overnight. The functionalized HNT exposing amino groups (HNT-NH_2) were then centrifuged at 7000 rcf for 10 min, washed 3 times with EtOH 96%, and finally dried under vacuum at RT for 6 h. Also this functionalization was carried out following a literature procedure.[15]

Functionalization of HNT AUS with PVP10 (HNT-PVP)

The functionalization was carried out following a literature procedure[24]. 300 mg of HNT-OH AUS were suspended in a solution of PVP10 (0.75 mM, obtained dissolving 150.5 mg of polymer in 20 mL of milliQ water). The suspension was stirred for 24h at RT, after which it was centrifuged (6000 rpm for 2 min), washed twice with fresh water and dried under vacuum.

Preparation of surfactant-free gold nanostars (f-GNS)

Surfactant-free GNS were prepared in a two steps seed-growth synthesis, starting from the preparation of spherical gold nanoparticles (AuNP) with a mean size smaller than 10 nm, to be used as seeds for the growth of star-shaped nano-objects in the second part of the procedure.

AuNP were prepared following a literature method.[18] To 30 mL of a solution of sodium citrate 2.2 mM, 20 µL of tannic acid 2.5 mM and 200 µL of K_2CO_3 0.15 M were added. The solution was heated to 70 °C and 395 µL of $HAuCl_4$ 12.7 mM were finally added, obtaining a dark grey solution whose color shifted to orange-red after few minutes, indicating the formation of low-size AuNP, whose growth is stopped cooling the mixture with an ice bath. The so-prepared AuNP were characterized with UV-vis spectroscopy and DLS measurements (filtering them with a 0.2 µm cellulose siringe filter prior to such measurements) and stored at 4°C before their use.

Before the synthesis of f-GNS and each synthetic step involving them, the lab glassware was treated with aqua regia for 15 min, followed by 3 washing cycles with milliQ-H_2O and sonication for 3 min.

The procedure followed for the growth of f-GNS was adapted from the literature,[16] with a variation in the ratio of the reagents and their order of addition. To a 10 mL of a $HAuCl_4$ solution 0.25 mM, containing 100 µL of HCl 0.1M, under vigorous stirring are first added 100 µL of $AgNO_3$ 2.0 mM and then simultaneously 50 µL of gold seeds and 100 µL of ascorbic acid 50 mM. The appearance of the blue

color indicated the formation of GNS, that were characterized by UV-vis spectroscopy and DLS measurements.

Preparation of GNS stabilized with Triton X-100 (GNS@TX-100)

Analogously to the f-GNS procedure reported in the previous section, also for this synthesis and all the synthetic steps involving GNS@TX-100, the lab glassware was treated with aqua regia for 15 min, followed by 3 washing cycles with milliQ-H_2O and sonication for 3 min.

Gold nanostars (GNS@TX-100) were prepared as described in the experimental section of the chapter "Decoration of gold nanostars with a polyamidoamine-Ru(II) complex to increase $^1O_2$ generation in Photodynamic Therapy" following with the same literature procedure[21] with slight variations. First the gold seeds were prepared by adding to a 0.2 M Triton X-100 solution (5 mL), 5 mL of a 0.5 mM of $HAuCl_4$ and 600 µL of a 0.01 M $NaBH_4$ ones. The resulting solution was gently hand-shaked and its color turned to orange-brune. The reagents were kept at 0 °C in an ice bath for 1.5 h before the seed preparation. Then GNS were growth from the seeds, by adding to a 0.2 Triton X-100 solution (15 mL) 750 µL of $AgNO_3$ 4 mM, 15 mL of $HAuCl_4$ 1 mM, 510 µL of ascorbic acid 0.0788 M and 36 µL of the seed solution in this order, at RT and under stirring. After 1h the GNS@TX-100 were obtained, as confirmed by the blueish-grayish color of the solution, depending on the dimensions of the obtained nano-objects. Both the seeds and the $HAuCl_4$ solutions were kept at 0 °C for 2h before the GNS growth step. The prepared GNS were characterized with UV-vis spectroscopy before their use.

To determine the yield of the synthesis, an aliquot of the fresh prepared GNS@TX-100 was centrifugated at 20817 rcf for 15 minutes and washed various time with H_2O. The residual pellet was dried overnight at 50 °C and weighed, calculating a concentration of 0.079 mg/mL. The calculated yield (79.9%) is in accordance with the literature data reported for this kind of synthesis (75%)[58].

Decoration of HNT-NH_2 with f-GNS (HNT@f-GNS)

Two different strategies were followed for the decoration of HNT-NH_2 with the surfactant-free GNS. The first consisted of their direct decoration, inspired by a literature procedure.[14] To a suspension of HNT-NH_2 (33 mg for 1 mL of milliQ water), 10 mL of freshly prepared f-GNS were added and the pH was adjusted to ca. 10. The mixture was left under stirring at RT overnight, after which the blue pellet was centrifuged at 180 rcf for 15 min. The Au:HNT w/w ratio calculated for this synthesis is 1:67.

The second strategy consisted in the decoration of HNT-NH_2 with AuNP, followed by the growth of GNS on the seed directly on HNT's surface. For the decoration with AuNP we adopted the same protocol used in the first strategy, while for the growth of GNS the procedure was analogous to the one used for the synthesis of f-GNS in suspension, described in the previous section. At the end of the growth, which was indicated by the changing of the color of the pellet from red to blue, the pellet was centrifuged at 180 rcf for 10 min.

Decoration of HNT-NH_2 with GNS@TX-100 (HNT-NH_2@GNS)

A suspension of HNT-NH_2 ALD (30 mg for 5 mL of milliQ water) was sonicated for 20 s using an immersion ultrasonic system. Then a defined volume of GNS@TX-100 was added dropwise to the

stirring suspension , to achieve the three different HNT:Au w/w ratios 60:1, 30:1 and 10:1. The pH of the mixture was adjusted to ca.10 and the interaction was carried out at RT under stirring for ca. 16-20 h, after with the blue suspension was centrifuged (10 min at 360 rcf), washed three times with fresh milliQ water and concentrated to 1.5 mL.

Decoration of HNT-PVP with GNS@TX-100 (HNT-PVP@GNS)

A suspension of HNT-PVP AUS in 5 mL of milliQ water (the mass suspended depends on the HNT:Au ratio chosen for the decoration) was sonicated for 30 s using an immersion ultrasound system. 15 mL of GNS@TX-100 were then added dropwise to reach a final volume of 20 mL and the two different HNT:Au mass ratios of 10:1 and 5:1. The interaction was carried out overnight at RT under magnetic stirring. The following day the suspension was centrifuged at 117 rcf for 10 min and washed three times with fresh milliQ water, centrifuging at 470 rcf for 10 min after each wash, concentrating and collecting the blue pellet.

Preparation of samples for photothermal measurements and for ICP-OES and ICP-MS analysis

The HNT@GNS pellets were suspended in 1.5 mL of milliQ water using the vortex and a few drops of the suspensions were deposited and layered on glass coverslips (previously treated with aqua regia for 15 min and washed three times with fresh milliQ water through sonication cycles). Each layer was carefully dried before the addition of the next, until an opaque spot of each HNT@GNS sample was obtained.

For the photothermal characterization of the nanocomposites, the solid spots were irradiated using a monochromatic laser with tunable wavelength (fixed at 720 nm for the HNT-NH_2@GNS samples and at 850 nm for the HNT-PVP@GNS ones) and power (employed 200 mW and 230 mW for the HNT-NH_2@GNS samples and 200 mW, 300 mW and 400 mW for the HNT-PVP@GNS ones). The temperature increase with irradiation for each sample was measured using a FLIR E40 thermal camera with FLIR Tools+ dedicated software for data acquisition and analysis.

For the determination of Au, the deposited samples were carefully removed from the glass, weighted and digested overnight with 0.7 or 0.75 mL of fresh aqua regia. The following day the digested samples were diluted to 10 mL with fresh milliQ water and filtered using syringe filters with a porosity of 0.2 µm, washing the filter repeatedly with milliQ water to recover all the sample from the dead volume. Two blanks were prepared using only aqua regia.

Loading of mitoxantrone into pristine HNT and HNT-PVP

50 mg of HNT or HNT-PVP were suspended in 2 mL of milliQ water and sonicated for 15 min using a ultrasound bath. The pH of the suspension was measured and adjusted to either 7.8 or 10 with NaOH. 2 mg of mitoxantrone powder were then dissolved in 2 mL of milliQ water and added dropwise to the suspension, washing twice the residual MTX with 0.2 mL of fresh H_2O.

For the samples loaded under vacuum, vacuum/N_2 cycles were carried out by first leaving the samples under vacuum for 30 min, followed by 5 min at room pressure and additional 30 min under vacuum, keeping the suspension under magnetic stirring for the whole loading process. For the samples loaded by diffusion, the suspension was simply left under magnetic stirring at room pressure overnight.

The suspension was then centrifuged three times at 1800 rpm for 2 min, changing the supernatant with fresh water after each cycle to remove any unloaded MTX. The blue pellet was finally recovered and dried at 60 °C for 3 days.

Release study of mitoxantrone from HNT and HNT-PVP

10 mg of HNT-MTX or HNT-PVP-MTX were suspended in 3 mL of acetate buffer (pH 4.65) or phosphate buffer (pH 7.45) in glass tubes. The suspension was magnetically stirred and before recording each timepoint, it was centrifuged at 1800 rpm for 2 min. 2.5 mL of the blue supernatant were then taken to record the UV-vis spectra and replaced with 2.5 mL of fresh buffer to maintain the drive force of the MTX release. The absorbance of 608 nm was recorded and used to determine the concentration of MTX in solution (ε (608 nm) = 19200 M^{-1} cm^{-1} in water)[59], from which the total released drug was calculated. Timepoints recorded: 0 min, 30 min, 1 h, 2 h, 4 h, 8 h, 24 h and 48 h.

To carry out the release experiment at 40 °C the glass tube was heated with an oil bath and the temperature measured by a thermocouple.

The MTX dissolution experiments in the same acetate or phosphate buffers were carried out dissolving 0.9 mg of MTX powder in 9 mL of buffer, keeping the solution under magnetic stirring. To record each timepoint, 2 mL of supernatant were taken to record UV-vis spectra and replaced with fresh buffer. Timepoints recorded: 0 s, 10 s, 20 s, 30 s, 1 min, 5 min, 10 min and 20 min (this last one only for the experiment at pH 7.45)

References

(1) Evison, B. J.; Sleebs, B. E.; Watson, K. G.; Phillips, D. R.; Cutts, S. M. Mitoxantrone, More than Just Another Topoisomerase II Poison. *Med. Res. Rev.* **2016**, *36* (2), 248–299. https://doi.org/10.1002/med.21364.

(2) S., P.; Kumar, H.; Rawal, V. B.; Ajmeer, R.; Jain, V. Overview of Mitoxantrone - A Potential Candidate for Treatment of Breast Cancer. *International Journal of Applied Pharmaceutics* **2022**, 10–22. https://doi.org/10.22159/ijap.2022v14i2.43474.

(3) Barar, J.; Kafil, V.; Majd, M. H.; Barzegari, A.; Khani, S.; Johari-Ahar, M.; Asgari, D.; Cokous, G.; Omidi, Y. Multifunctional Mitoxantrone-Conjugated Magnetic Nanosystem for Targeted Therapy of Folate Receptor-Overexpressing Malignant Cells. *J. Nanobiotechnology* **2015**, *13* (1), 26. https://doi.org/10.1186/s12951-015-0083-7.

(4) Zhang, P.; Ling, G.; Pan, X.; Sun, J.; Zhang, T.; Pu, X.; Yin, S.; He, Z. Novel Nanostructured Lipid-Dextran Sulfate Hybrid Carriers Overcome Tumor Multidrug Resistance of Mitoxantrone Hydrochloride. *Nanomedicine* **2012**, *8* (2), 185–193. https://doi.org/10.1016/j.nano.2011.06.007.

(5) Truong, N. P.; Whittaker, M. R.; Mak, C. W.; Davis, T. P. The Importance of Nanoparticle Shape in Cancer Drug Delivery. *Expert Opin. Drug Deliv.* **2015**, *12* (1), 129–142. https://doi.org/10.1517/17425247.2014.950564.

(6) Aydın, B.; Bozoğlu, S.; Karatepe, N.; Güner, F. S. Synthesis of Bovine Serum Albumin-Coated Magnetic Single-Walled Carbon Nanotubes as a Delivery System for Mitoxantrone. *ACS Omega* **2025**, *10* (1), 102–113. https://doi.org/10.1021/acsomega.3c09608.

(7) Aydın, B.; Bozoğlu, S.; Karatepe, N.; Güner, F. S. Folic Acid-Conjugated Magnetic Carbon Nanotube Nanocarriers for Targeted Delivery of Mitoxantrone. *Nanotechnology* **2025**, *36* (30), 305701. https://doi.org/10.1088/1361-6528/aded95.

(8) Aydın, B.; Güner-Yılmaz, Ö. Z.; Yılmaz, A.; Kilic-Cevirgel, S.; Karaoglu, I. C.; Bozoglu, S.; İzbudak, B.; Kurkcuoglu, O.; Bal-Öztürk, A.; Karatepe, N.; Güner, F. S. Mitoxantrone Release from Fmoc-Protected Amino Acids Coated Magnetic Carbon Nanotubes: Computational and Experimental Study for Cancer Treatment. *J. Drug Deliv. Sci. Technol.* **2024**, *101*, 106291. https://doi.org/10.1016/j.jddst.2024.106291.

(9) Risi, G.; Bloise, N.; Merli, D.; Icaro-Cornaglia, A.; Profumo, A.; Fagnoni, M.; Quartarone, E.; Imbriani, M.; Visai, L. Invitro Study of Multiwall Carbon Nanotubes (MWCNTs) with Adsorbed Mitoxantrone (MTO) as a Drug Delivery System to Treat Breast Cancer. *RSC Adv.* **2014**, *4* (36), 18683–18693. https://doi.org/10.1039/C4RA02366H.

(10) Wu, Y.-P.; Yang, J.; Gao, H.-Y.; Shen, Y.; Jiang, L.; Zhou, C.; Li, Y.-F.; He, R.-R.; Liu, M. Folate-Conjugated Halloysite Nanotubes, an Efficient Drug Carrier, Deliver Doxorubicin for Targeted Therapy of Breast Cancer. *ACS Appl. Nano Mater.* **2018**, *1* (2), 595–608. https://doi.org/10.1021/acsanm.7b00087.

(11) Glotov, A.; Vutolkina, A.; Pimerzin, A.; Vinokurov, V.; Lvov, Y. Clay Nanotube-Metal Core/Shell Catalysts for Hydroprocesses. *Chem. Soc. Rev.* **2021**, *50* (16), 9240–9277. https://doi.org/10.1039/D1CS00502B.

(12) Keeling, J. L.; Self, P. G.; Raven, M. D. *Exploration Halloysite in Cenozoic Sediments along the Eucla Basin Margin*; 2010; Vol. 59.

(13) Pasbakhsh, P.; Churchman, G. J.; Keeling, J. L. Characterisation of Properties of Various Halloysites Relevant to Their Use as Nanotubes and Microfibre Fillers. *Appl. Clay Sci.* **2013**, *74*, 47–57. https://doi.org/10.1016/j.clay.2012.06.014.

(14) Zieba, M.; Hueso, J. L.; Arruebo, M.; Martínez, G.; Santamaría, J. Gold-Coated Halloysite Nanotubes as Tunable Plasmonic Platforms. *New Journal of Chemistry* **2014**, *38* (5), 2037–2042. https://doi.org/10.1039/c3nj01127e.

(15) Kornilova, A. V.; Kuralbayeva, G. A.; Stavitskaya, A. V.; Gorbachevskii, M. V.; Karpukhina, O. V.; Lysenko, I. V.; Pryadun, V. V.; Novikov, A. A.; Vasiliev, A. N.; Timoshenko, V. Y. Gold Nanoparticles Immobilized on Halloysite Nanotubes for Spatially-Temporally Localized Photohyperthermia. *Appl. Surf. Sci.* **2021**, *566*. https://doi.org/10.1016/j.apsusc.2021.150671.

(16) Yuan, H.; Khoury, C. G.; Hwang, H.; Wilson, C. M.; Grant, G. A.; Vo-Dinh, T. Gold Nanostars: Surfactant-Free Synthesis, 3D Modelling, and Two-Photon Photoluminescence Imaging. *Nanotechnology* **2012**, *23* (7). https://doi.org/10.1088/0957-4484/23/7/075102.

(17) Vega, M. M.; Bonifacio, A.; Lughi, V.; Marsi, S.; Carrato, S.; Sergo, V. Long-Term Stability of Surfactant-Free Gold Nanostars. *Journal of Nanoparticle Research* **2014**, *16* (11). https://doi.org/10.1007/s11051-014-2729-z.

(18) Piella, J.; Bastús, N. G.; Puntes, V. Size-Controlled Synthesis of Sub-10-Nanometer Citrate-Stabilized Gold Nanoparticles and Related Optical Properties. *Chemistry of Materials* **2016**, *28* (4), 1066–1075. https://doi.org/10.1021/acs.chemmater.5b04406.

(19) Hamza, H.; Ferretti, A. M.; Innocenti, C.; Fidecka, K.; Licandro, E.; Sangregorio, C.; Maggioni, D. An Approach for Magnetic Halloysite Nanocomposite with Selective Loading of Superparamagnetic Magnetite Nanoparticles in the Lumen. *Inorg. Chem.* **2020**, *59* (17), 12086–12096. https://doi.org/10.1021/acs.inorgchem.0c01039.

(20) Liu, C.; Han, Y.; Wang, Z.; Zhang, L.; Yang, W. Preparation of (3-Aminopropyl)Triethoxysilane-Modified Silica Particles with Tunable Isoelectric Point. *Langmuir* **2024**, *40* (24), 12565–12572. https://doi.org/10.1021/acs.langmuir.4c01027.

(21) Dacarro, G.; Pallavicini, P.; Bertani, S. M.; Chirico, G.; D'Alfonso, L.; Falqui, A.; Marchesi, N.; Pascale, A.; Sironi, L.; Taglietti, A.; Zuddas, E. Synthesis of Reduced-Size Gold Nanostars and Internalization in SH-SY5Y Cells. *J. Colloid Interface Sci.* **2017**, *505*, 1055–1064. https://doi.org/10.1016/J.JCIS.2017.06.102.

(22) Yang, J.; Lee, J. Y.; Too, H.-P.; Chow, G.-M.; Gan, L. M. Triton X-100-Assisted Assembly of 5-Nm Au Nanoparticles by DNA Hybridization. *Chem. Lett.* **2005**, *34* (3), 354–355. https://doi.org/10.1246/cl.2005.354.

(23) Pallavicini, P.; Donà, A.; Casu, A.; Chirico, G.; Collini, M.; Dacarro, G.; Falqui, A.; Milanese, C.; Sironi, L.; Taglietti, A. Triton X-100 for Three-Plasmon Gold Nanostars with Two Photothermally Active NIR (near IR) and SWIR (Short-Wavelength IR) Channels. *Chemical Communications* **2013**, *49* (56), 6265. https://doi.org/10.1039/c3cc42999g.

(24) Liu, M.; Zhang, Y.; Zhu, E.; Jin, P.; Wang, K.; Zhao, J.; Li, C.; Yan, Y. Facile Synthesis of Halloysite Nanotubes-Supported Acidic Metal-Organic Frameworks with Tunable Acidity for Efficient Fructose Dehydration to 5-Hydroxymethylfurfural. *ChemistrySelect* **2017**, *2* (32), 10413–10419. https://doi.org/10.1002/slct.201702137.

(25) Sun, J.-T.; Li, J.-W.; Tsou, C.-H.; Pang, J.-C.; Chung, R.-J.; Chiu, C.-W. Polyurethane/Nanosilver-Doped Halloysite Nanocomposites: Thermal, Mechanical Properties, and Antibacterial Properties. *Polymers (Basel)*. **2020**, *12* (11), 2729. https://doi.org/10.3390/polym12112729.

(26) Farhanian, S.; Hatami, M. Thermal and Morphological Aspects of Silver Decorated Halloysite Reinforced Polypropylene Nanocomposites. *J. Therm. Anal. Calorim.* **2017**, *130* (3), 2069–2078. https://doi.org/10.1007/s10973-017-6630-8.

(27) Mishra, A.; Inaam, R.; Okamoto, S.; Shibata, T.; Santra, T. S.; Nagai, M. Visible Pulsed Laser-Assisted Selective Killing of Cancer Cells with PVP-Capped Plasmonic Gold Nanostars. *Micromachines (Basel)*. **2023**, *14* (6), 1173. https://doi.org/10.3390/mi14061173.

(28) Wagner, M.; Herrero-Ruiz, A.; Verde-Sesto, E.; Asenjo-Sanz, I.; Liz-Marzán, L. M. Influence of Poly(Vinylpyrrolidone) Synthesis Conditions on the Formation of Gold Nanostars. *Chemistry of Materials* **2025**, *37* (2), 644–654. https://doi.org/10.1021/acs.chemmater.4c02513.

(29) Fernández-Lodeiro, C.; Fernández-Lodeiro, J.; Fernández-Lodeiro, A.; Nuti, S.; Lodeiro, C.; LaGrow, A.; Pérez-Juste, I.; Pérez-Juste, J.; Pastoriza-Santos, I. Synthesis of Tuneable Gold Nanostars: The Role of Adenosine Monophosphate. *J. Mater. Chem. C Mater.* **2023**, *11* (37), 12626–12636. https://doi.org/10.1039/D3TC01567J.

(30) Ali, M.; Mir, S.; Atanase, L. I.; Abid, O.-U.-R.; Kazi, M. Chitosan–PVA–PVP/Nano-Clay Composite: A Promising Tool for Controlled Drug Delivery. *RSC Adv.* **2024**, *14* (22), 15777–15790. https://doi.org/10.1039/D4RA02959C.

(31) Teodorescu, M.; Bercea, M. Poly(Vinylpyrrolidone) – A Versatile Polymer for Biomedical and Beyond Medical Applications. *Polymer - Plastics Technology and Engineering* **2015**, *54* (9), 923–943. https://doi.org/10.1080/03602559.2014.979506.

(32) Abbaszadeh, F.; Moradi, O.; Norouzi, M.; Sabzevari, O. Improvement Single-Wall Carbon Nanotubes (SWCNTs) Based on Functionalizing with Monomers 2-Hydroxyethylmethacryate (HEMA) and N-Vinylpyrrolidone (NVP) for Pharmaceutical Applications as Cancer Therapy. *Journal of Industrial and Engineering Chemistry* **2014**, *20* (5), 2895–2900. https://doi.org/10.1016/j.jiec.2013.11.025.

(33) Koczkur, K. M.; Mourdikoudis, S.; Polavarapu, L.; Skrabalak, S. E. Polyvinylpyrrolidone (PVP) in Nanoparticle Synthesis. *Dalton Transactions* **2015**, *44* (41), 17883–17905. https://doi.org/10.1039/C5DT02964C.

(34) Sardo, C.; Bassi, B.; Craparo, E. F.; Scialabba, C.; Cabrini, E.; Dacarro, G.; D'Agostino, A.; Taglietti, A.; Giammona, G.; Pallavicini, P.; Cavallaro, G. Gold Nanostar–Polymer Hybrids for SiRNA Delivery: Polymer Design towards Colloidal Stability and in Vitro Studies on Breast Cancer Cells. *Int. J. Pharm.* **2017**, *519* (1–2), 113–124. https://doi.org/10.1016/J.IJPHARM.2017.01.022.

(35) Paściak, A.; Pilch-Wróbel, A.; Marciniak, Ł.; Schuck, P. J.; Bednarkiewicz, A. Standardization of Methodology of Light-to-Heat Conversion Efficiency Determination for Colloidal Nanoheaters. *ACS Appl. Mater. Interfaces* **2021**, *13* (37), 44556–44567. https://doi.org/10.1021/acsami.1c12409.

(36) Zhang, J.; Luo, X.; Wu, Y.-P.; Wu, F.; Li, Y.-F.; He, R.-R.; Liu, M. Rod in Tube: A Novel Nanoplatform for Highly Effective Chemo-Photothermal Combination Therapy toward Breast Cancer. *ACS Appl. Mater. Interfaces* **2019**, *11* (4), 3690–3703. https://doi.org/10.1021/acsami.8b17533.

(37) Bretti, C.; Cataldo, S.; Gianguzza, A.; Lando, G.; Lazzara, G.; Pettignano, A.; Sammartano, S. Thermodynamics of Proton Binding of Halloysite Nanotubes. *Journal of Physical Chemistry C* **2016**, *120* (14), 7849–7859. https://doi.org/10.1021/acs.jpcc.6b01127.

(38) Raghunand, N.; Mahoney, B. P.; Gillies, R. J. Tumor Acidity, Ion Trapping and Chemotherapeutics. *Biochem. Pharmacol.* **2003**, *66* (7), 1219–1229. https://doi.org/10.1016/S0006-2952(03)00468-4.

(39) Lisuzzo, L.; Cavallaro, G.; Pasbakhsh, P.; Milioto, S.; Lazzara, G. Why Does Vacuum Drive to the Loading of Halloysite Nanotubes? The Key Role of Water Confinement. *J. Colloid Interface Sci.* **2019**, *547*, 361–369. https://doi.org/10.1016/j.jcis.2019.04.012.

(40) R. Price, B. P. G. Y. L. R. In-Vitro Release Characteristics of Tetracycline HCl, Khellin and Nicotinamide Adenine Dineculeotide from Halloysite; a Cylindrical Mineral. *J. Microencapsul.* **2001**, *18* (6), 713–722. https://doi.org/10.1080/02652040010019532.

(41) Lvov, Y.; Wang, W.; Zhang, L.; Fakhrullin, R. Halloysite Clay Nanotubes for Loading and Sustained Release of Functional Compounds. *Advanced Materials* **2016**, *28* (6), 1227–1250. https://doi.org/10.1002/adma.201502341.

(42) Yu, M.; Wang, Q.; Zhang, M.; Deng, Q.; Chen, D. Facile Fabrication of Raspberry-like Composite Microspheres for the Construction of Superhydrophobic Films and Applications in Highly Efficient Oil–Water Separation. *RSC Adv.* **2017**, *7* (63), 39471–39479. https://doi.org/10.1039/C7RA07250C.

(43) Koczkur, K. M.; Mourdikoudis, S.; Polavarapu, L.; Skrabalak, S. E. Polyvinylpyrrolidone (PVP) in Nanoparticle Synthesis. *Dalton Transactions* **2015**, *44* (41), 17883–17905. https://doi.org/10.1039/C5DT02964C.

(44) Yang, W.; Yang, Z. PVP-Induced Synthesis of Silica Nanoparticles with Tailored Size for PH-Controlled Drug Release. *Materials Highlights* **2021**, *2* (3), 52. https://doi.org/10.2991/mathi.k.210414.001.

(45) Ramadass, K.; Sathish, C. I.; Johns, A.; Ruban, S. J.; Singh, G.; Lakhi, K. S.; Almajid, A. M.; Belperio, T.; Vinu, A. Characterization and Hydrogen Storage Performance of Halloysite Nanotubes. *J. Nanosci. Nanotechnol.* **2019**, *19* (12), 7892–7898. https://doi.org/10.1166/jnn.2019.16751.

(46) Zeng, J.; Shirihai, O. S.; Grinstaff, M. W. Modulating Lysosomal PH: A Molecular and Nanoscale Materials Design Perspective. *JoLS, Journal of Life Sciences* **2020**. https://doi.org/10.36069/JoLS/20201204.

(47) Rozhina, E.; Panchal, A.; Akhatova, F.; Lvov, Y.; Fakhrullin, R. Cytocompatibility and Cellular Uptake of Alkylsilane-Modified Hydrophobic Halloysite Nanotubes. *Appl. Clay Sci.* **2020**, *185*, 105371. https://doi.org/10.1016/j.clay.2019.105371.

(48) Biddeci, G.; Spinelli, G.; Massaro, M.; Riela, S.; Bonaccorsi, P.; Barattucci, A.; Di Blasi, F. Study of Uptake Mechanisms of Halloysite Nanotubes in Different Cell Lines. *Int. J. Nanomedicine* **2021**, *Volume 16*, 4755–4768. https://doi.org/10.2147/IJN.S303816.

(49) Liao, J.; Peng, S.; Long, M.; Zhang, Y.; Yang, H.; Zhang, Y.; Huang, J. Nano-Bio Interactions of Clay Nanotubes with Colon Cancer Cells. *Colloids Surf. A Physicochem. Eng. Asp.* **2020**, *586*, 124242. https://doi.org/10.1016/j.colsurfa.2019.124242.

(50) Lin, B.; Chen, H.; Liang, D.; Lin, W.; Qi, X.; Liu, H.; Deng, X. Acidic PH and High-H2O2 Dual Tumor Microenvironment-Responsive Nanocatalytic Graphene Oxide for Cancer Selective Therapy and Recognition. *ACS Appl. Mater. Interfaces* **2019**, *11* (12), 11157–11166. https://doi.org/10.1021/acsami.8b22487.

(51) Hosonuma, M.; Yoshimura, K. Association between PH Regulation of the Tumor Microenvironment and Immunological State. *Front. Oncol.* **2023**, *13*. https://doi.org/10.3389/fonc.2023.1175563.

(52) Hemmatpour, H.; Haddadi-Asl, V.; Burgers, T. C. Q.; Yan, F.; Stuart, M. C. A.; Reker-Smit, C.; Vlijm, R.; Salvati, A.; Rudolf, P. Temperature-Responsive and Biocompatible Nanocarriers Based on Clay Nanotubes for Controlled Anti-Cancer Drug Release. *Nanoscale* **2023**, *15* (5), 2402–2416. https://doi.org/10.1039/d2nr06801j.

(53) Hamza, H.; Schifano, V.; Colciago, G.; Ortenzi, M. A.; Ferretti, A. M.; Di Carlo, G.; Dozzi, M. V.; Vago, R.; Tessore, F.; Maggioni, D. Halloysite Nanotubes as a Vector for Hydrophobic Perfluorinated Porphyrin-Based Photosensitizers for Singlet Oxygen Generation. *Nanoscale* **2025**, *17* (32), 18935–18947. https://doi.org/10.1039/D5NR01078K.

(54) Askarizadeh, M.; Esfandiari, N.; Honarvar, B.; Sajadian, S. A.; Azdarpour, A. Kinetic Modeling to Explain the Release of Medicine from Drug Delivery Systems. *ChemBioEng Reviews* **2023**, *10* (6), 1006–1049. https://doi.org/10.1002/cben.202300027.

(55) Husain, T.; Shoaib, M. H.; Ahmed, F. R.; Yousuf, R. I.; Farooqi, S.; Siddiqui, F.; Imtiaz, M. S.; Maboos, M.; Jabeen, S. Investigating Halloysite Nanotubes as a Potential Platform for Oral Modified Delivery of Different Bcs Class Drugs: Characterization, Optimization, and Evaluation of Drug Release Kinetics. *Int. J. Nanomedicine* **2021**, *16*, 1725–1741. https://doi.org/10.2147/IJN.S299261.

(56) Depan, D.; Misra, R. D. K. Hybrid Nanostructured Drug Carrier with Tunable and Controlled Drug Release. *Materials Science and Engineering: C* **2012**, *32* (6), 1704–1709. https://doi.org/10.1016/j.msec.2012.04.045.

(57) Zeng, S.; Reyes, C.; Liu, J.; Rodgers, P. A.; Wentworth, S. H.; Sun, L. Facile Hydroxylation of Halloysite Nanotubes for Epoxy Nanocomposite Applications. *Polymer (Guildf).* **2014**, *55* (25), 6519–6528. https://doi.org/10.1016/j.polymer.2014.10.044.

(58) Pallavicini, P.; Donà, A.; Casu, A.; Chirico, G.; Collini, M.; Dacarro, G.; Falqui, A.; Milanese, C.; Sironi, L.; Taglietti, A. Triton X-100 for Three-Plasmon Gold Nanostars with Two Photothermally Active NIR (near IR) and SWIR (Short-Wavelength IR) Channels. *Chemical Communications* **2013**, *49* (56), 6265–6267. https://doi.org/10.1039/c3cc42999g.

(59) Hajihassan, Z.; Rabbani-Chadegani, A. Studies on the Binding Affinity of Anticancer Drug Mitoxantrone to Chromatin, DNA and Histone Proteins. *J. Biomed. Sci.* **2009**, *16* (1), 31. https://doi.org/10.1186/1423-0127-16-31.

(60) Chaudhari, V. S.; Kushram, P.; Bose, S. Drug Delivery Strategies through 3D-Printed Calcium Phosphate. *Trends Biotechnol.* **2024**, *42* (11), 1396–1409. https://doi.org/10.1016/j.tibtech.2024.05.006.

(61) Wu, I. Y.; Bala, S.; Škalko-Basnet, N.; di Cagno, M. P. Interpreting Non-Linear Drug Diffusion Data: Utilizing Korsmeyer-Peppas Model to Study Drug Release from Liposomes. *European Journal of Pharmaceutical Sciences* **2019**, *138*, 105026. https://doi.org/10.1016/j.ejps.2019.105026.

Halloysite nanotubes as a vector for hydrophobic perfluorinated porphyrin-based photosensitizers for singlet oxygen generation.

Adapted from: Hamza H., Schifano V., Colciago G., Ortenzi M. A., Ferretti A. M., Di Carlo G., Dozzi M. V., Vago R., Tessore F. and Maggioni D., *Nanoscale* 2025,17, 18935-18947

Introduction

Porphyrins in photodynamic therapy

Porphyrins are a class of tetrapyrrolic macrocycles with an extended 18-electron π-conjugated system that results in strong absorptions in the visible light spectrum. Their structure can be designed with specific functionalities to tune their chemical-physical properties and electronic features, allowing their use in a wide range of applications, including biomedicine, in which they are employed for diagnostic purposes in tumor imaging.[1,2]

Moreover, porphyrins are widely employed for photodynamic therapy (PDT) and, together with other macrocyclic tetrapyrrolic structures, constitute the majority of photosensitizers employed in PDT.[1,3] Because of their visible light absorption and the possibility to tune it toward the therapeutic window, which enable deep tissue penetration, their ability to generate reactive oxygen species (ROS) upon light irradiation, their low dark cytotoxicity and preferential uptake by tumoral cells, porphyrins result particularly suitable as photosensitizers (PS) in PDT.[4]

PDT porphyrin-based photosensitizers can be divided into three generations. The first generation, commercially named Photofrin, has seen limited use due to long half-life, chemical impurity, low attenuation coefficients, and excessive accumulation onto the skin, although being effective PS. Thus, the second generation ones were developed to overcome these drawbacks. However, they lacked the desired water solubility and did not result suitable for light penetration into deep tumors. This resulted in the development of third generation ones with increased cancer cell-specific accumulation.[1,2]

In this work, we used as PS the perfluorinated and apolar porphyrin 5,10,15,20-tetrakis(pentafluorophenyl)porphyrin (H_2TPPF_{20}) and its Zn(II) complex ($ZnTPPF_{20}$), whose structures are shown in Scheme 1. Their photosensitizing abilities are known in the literature, although being tested in water only upon further functionalization with polar groups to improve their solubility.[5,6]

The objective of this work is the development of appropriately modified HNT for the possible *in situ* delivery of these two apolar porphyrins for their use in PDT, used as models for apolar drugs that face solubility challenges in aqueous environments.

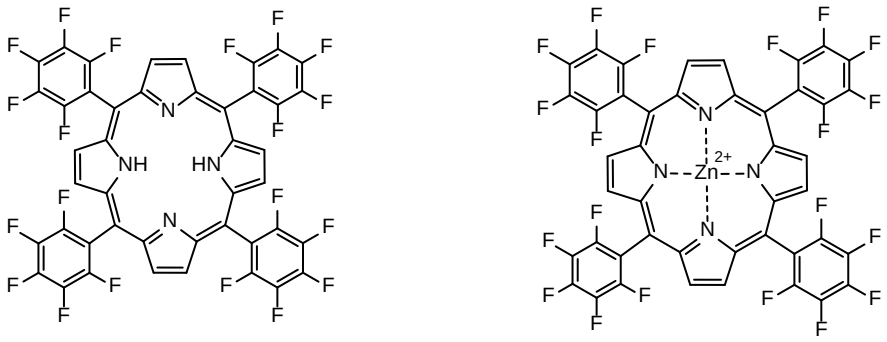

Scheme 1. *Structures of the freebase H_2TPPF_{20} porphyrin and its Zn(II) complex used in our work.*

Results and discussion

The work consisted in the loading of the apolar porphyrin H_2TPPF_{20} and its Zn(II) complex into Halloysite nanotubes (HNT), through N_2/vacuum cycles (analogously to the loading of mitoxantrone into HNT carried out in the previous chapter "Decoration of halloysite nanotubes with gold nanostars to obtain a dual therapeutic carrier exploiting Photothermal Therapy") and the characterization of the obtained samples with a wide range of analytical techniques techniques - attenuated total reflectance infrared (ATR-IR), diffuse reflectance (DRS) and photoluminescence spectroscopies - to investigate the material thoroughly, particularly the location of PS within the HNT. Additionally, the loading capacity of HNT was investigated employing thermogravimetric analyses (TGA). The two porphyrins were loaded into pristine HNT or HNT functionalized in their inner lumen with tetradecylphosphonic acid (TDP) to increase their apolar character and facilitate the loading of the two lipophilic compounds. For comparison, two samples obtained by grinding H_2TPPF_{20} and $ZnTPPF_{20}$ with pristine HNT were prepared, as for these samples we expected the two porphyrins to localize outside the HNT.

Moreover, their release kinetics from HNT and HNT-TDP in a THF:H_2O 1:1 mixture was studied using UV-vis spectroscopy and a capping of the loaded samples with dextrin was carried out to delay the release of the photosensitizers.

The ability of H_2TPPF_{20} and $ZnTPPF_{20}$ in sensitizing $^1O_2$ conversion from molecular oxygen in PDT was then investigated in a polar organic solvent (EtOH) in which we would expect a partial aggregation of the photosensitizers (PS).

Finally, the uptake of the HNT-TDP-H_2TPPF_{20}-Dextrin, chosen as it contained one of the highest amounts of porphyrin and exhibited the slowest release kinetic profile, by three tumoral cell lines (prostate cancer, PC3 and bladder cancer, 5637 and UMUC3) was studied, revealing similar accumulation in the cytosol for all three cell lines. Finally, PDT treatment on the three cell lines treated with either pristine

HNT or HNT-TDP-H_2TPPF_{20}-dextrin were carried out, by irradiating the samples with a low intensity lamp emitting in the visible-NIR range (400-800 nm).

Inside the project I've dealt with the study of the photoluminescence of the two unloaded compounds to explore whether the shape of their emission bands, both in solution and at the solid state, might give some insight into their main localization within HNTs when loaded. Moreover, I've estimated $^1O_2$ generation by the two species in EtOH upon irradiation with a lamp emitting in the visible range and carried out the biological investigation of the HNT-TDP-H_2TPPF_{20}-dextrin sample on the three cell lines.

Photoluminescence spectroscopy of H_2TPPF_{20} and $ZnTPPF_{20}$

The emission of the two unloaded porphyrin samples (H_2TPPF_{20} and $ZnTPPF_{20}$) in solution were carried out in THF and in a THF:H_2O 8:2 mixture, as pure THF completely solubilizes the two compounds, dissolved as free molecules, while in the mixture we expected some aggregation, in a situation more similar to what would occur when the compounds are internalized into the HNT inner lumen.[7] Moreover, their photoluminescence spectra were also recorded on powders of the two compounds. All these spectra are shown in the last three bottom traces of Figure 1, together with the solid state emission spectra recorded on the loaded samples (both with HNT and HNT-TDP) and the porphyrins mechanically ground with HNT.

The THF spectrum of H_2TPPF_{20} showed three main emission bands at 639, 659 and 706 nm, with a slightly perceivable shoulder at ca. 690 nm. When the non-solvent was added to reach the THF:H_2O ratio, keeping the porphyrin concentration constant, the emission band at 639 nm almost disappeared due to the almost complete quenching of that transition. Moreover, the band at 659 nm red shifted to 664 nm and the intensity of the one at 706 nm significantly reduced, due to the formation of J-aggregates.[7] Moving to the solid compound, the relative intensities of the two bands changed.

Analogously, the emission spectrum of $ZnTPPF_{20}$ in THF showed a main Q band at 644 nm and one with lower Q one at 589 nm, while in the THF:H_2O mixture a shoulder at 633 nm appeared, attributed to a partial aggregation. This shoulder indeed became predominant in the spectrum recorded on the solid compound, together with the appearance of a broad band at 690 nm.

The spectra of vacuum-loaded HNT with H_2TPPF_{20} and the HNT ground with H_2TPPF_{20} resembled that of the solid freebase porphyrin, while when H_2TPPF_{20} was loaded into HNT functionalized with TDP in their inner lumen, the intensity of the band at 663 nm increased and the one at 706 nm decreased, gaining a pattern almost superimposable to the spectrum recorded in THF:H_2O 8:2, with the difference of an additional shoulder at ca. 660 nm, the same wavelength of one of the emission bands in pure THF, suggesting a lower aggregation state of the compound into the functionalized HNT (HNT-TDP).

On the other hand, the emission spectra recorded on the loaded $ZnTPPF_{20}$ into both pristine HNT and HNT functionalized with TDP changed significantly compared to those recorded both in solution and on the $ZnTPPF_{20}$ powder, resembling the profile recorded in the THF:H_2O mixture. However, in both the loaded samples the main emission band resulted red shifted to 654 nm and the shoulder at 589 nm, also present in the profiles recorded in solution and assigned to the lower energy Q transition, reappeared. Additionally, when loaded into pristine HNT, also a minor band at 704 nm is slightly visible. Differently, the profile of the ground $ZnTPPF_{20}$ and HNT is much more similar to the one recorded on the solid compound. The differences in the loaded samples with both the solid and the ground ones and the resemblance with the spectra recorded in solution suggested a more dispersed condition in loaded $ZnTPPF_{20}$ samples, especially into TDP-functionalized HNT.

Notably, the emission spectra were recorded at two or three distinct wavelengths, as shown in Figure 2 for the spectra of solid H_2TPPF_{20} and $ZnTPPF_{20}$. In any case, despite the excitation wavelength, the emission profile remained unchanged as expected according to Kasha's rule.

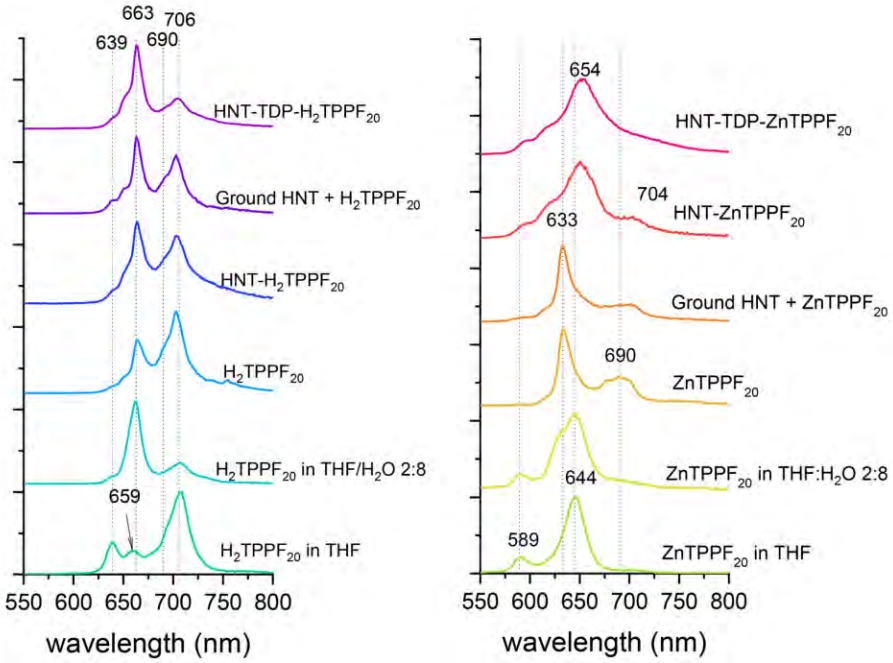

Figure 1. *Normalized emission spectra of H_2TPPF_{20} (left panel) or $ZnTPPF_{20}$ (right panel) recorded on a THF solution, in a THF:H_2O 8:2 mixture, on the pristine solid compounds, on the compounds ground with pristine HNT and on the compounds loaded into HNT-TDP or pristine HNT (from the bottom to the top).*

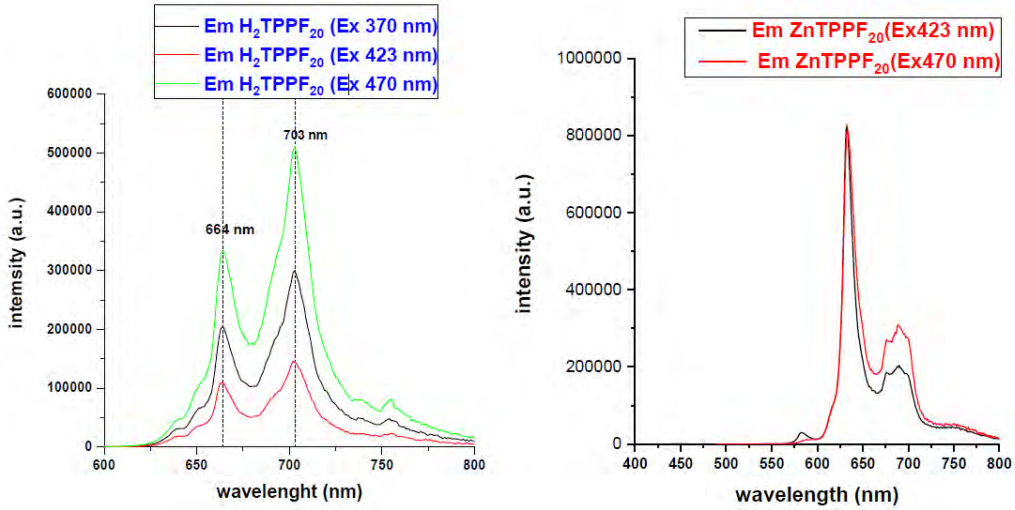

Figure 2. *Solid state emission spectra of H_2TPPF_{20} (left panel, λ_{ex}= 370, 423, and 470 nm) and Zn-$TPPF_{20}$ (λ_{ex}= 423, and 470 nm) respectively.*

In cuvette $^1O_2$ generation by H_2TPPF_{20} and $ZnTPPF_{20}$ with irradiation

Although the ability of H_2TPPF_{20} and $ZnTPPF_{20}$ to act as photosensitizers (PS) for $^1O_2$ generation is well known, in the literature[8,9] their quantum yield for singlet oxygen generation (Φ_Δ) were determined only in apolar solvents due to their limited solubility. Thus, we investigated whether the aggregation that occurs in polar solvents might quench the production of $^1O_2$ due to the partial quenching of their emitting features. The estimation of Φ_Δ was carried out in ethanol, by employing 1,5-dihydroxynaphthalene (DHN) as indirect reporter for $^1O_2$ generation. DHN is vastly used in the literature[10-12] as a scavenger for $^1O_2$, since it is photo-oxidized promptly, efficiently and selectively to 5-hydroxy-1,4-naphthalenedione (Juglone) by singlet oxygen, following the mechanism proposed in Scheme 2.[13]

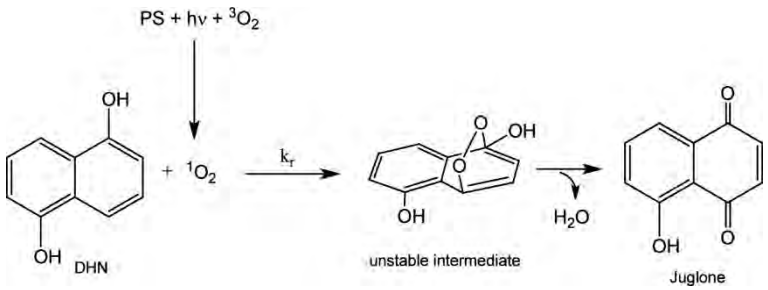

Scheme 2. *Schematization of the photo-oxidation of DHN to Juglone by $^1O_2$.*

H_2TPPF_{20} and $ZnTPPF_{20}$ were added to a DHN solution in EtOH, to reach a final PS:DHN molar ratio 1:10, and the mixture was saturated with O_2 by bubbling it for ca. 3 min. This way the conversion of DHN to Juglone follows a pseudo-first order kinetics (described by equation 1), by applying the steady-state approximation to $^1O_2$, and the kinetic constant (k_{obs}) and the initial rate (v_0) are calculated according to equations 2 and 3.

$$v_0 = k_{obs}[^1O_2][DHN] \quad \text{eq. 1}$$

$$v_0 = -\frac{d[DHN]}{dt} = k_{obs}[DHN] \quad \text{eq. 2}$$

$$ln\frac{[DHN]_t}{[DHN]_0} = ln\frac{A_t}{A_0} = k_{obs} \cdot t \quad \text{eq. 3}$$

The PS+DHN mixtures saturated in O_2 were irradiated with a LED lamp emitting in the visible range (whose emission profile is shown in Figure 3) and UV-spectra of the mixture were recorded over the irradiation time (Figure 4) to monitor the decrease of DHN absorption bands (in particular the one at 317 nm) and the increase of the one at 423 nm attributed to Juglone. The values of $ln(A_t/A_0)$, with A_t the absorbance at 317 nm after t min of irradiation, and A_0 the absorbance at the same wavelength before irradiation, decrease linearly over time (last panel of Figure 4). The k_{obs} values were obtained from the slope of this plot for the reaction, each employing H_2TPPF_{20}, $ZnTPPF_{20}$ or methylene blue (MB) as PS. Then v_0 was calculated from the product between k_{obs} and the concentration of DHN.

Finally, Φ_Δ was calculated according to equation 4. In the equation, the apex "std" refers to the values experimentally calculated for MB, while Φ_Δ^{std} is its tabulated $^1O_2$ quantum yield in ethanol taken from the literature (Φ_Δ^{std}= 0.5).[14]

$$\Phi_\Delta = \Phi_\Delta^{std}\frac{v_0 \cdot I^{std}}{v_0^{std} \cdot I} \quad \text{eq. 4}$$

In equation 4, I denotes the photons absorbed by the photosensitizer, whiche were estimated through a numerical integration of equation 5 at all the wavelengths at which the light source emits.

$$I = \sum_{\lambda_i}^{\lambda_f} I_{source}(1 - 10^{A(\lambda)}) \quad \text{eq. 5}$$

The k_{obs}, v_0 and Φ_Δ calculated for H_2TPPF_{20} and $ZnTPPF_{20}$ are listed in Table 1, confirming that the two porphyrins, although partially aggregated in ethanol, were still able to interact with molecular oxygen and, through an energy transfer, produce the cytotoxic singlet oxygen when irradiated with a visible low-intensity light.

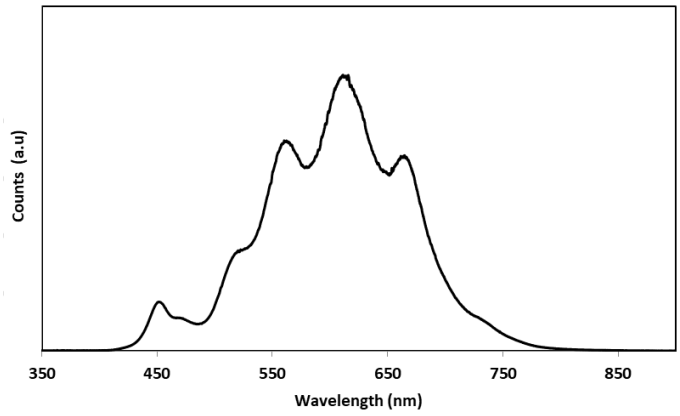

Figure 3. *Emission profile of the LED lamp employed for the in-cuvette determination of the $^1O_2$ generation by the two photosensitizers in ethanol.*

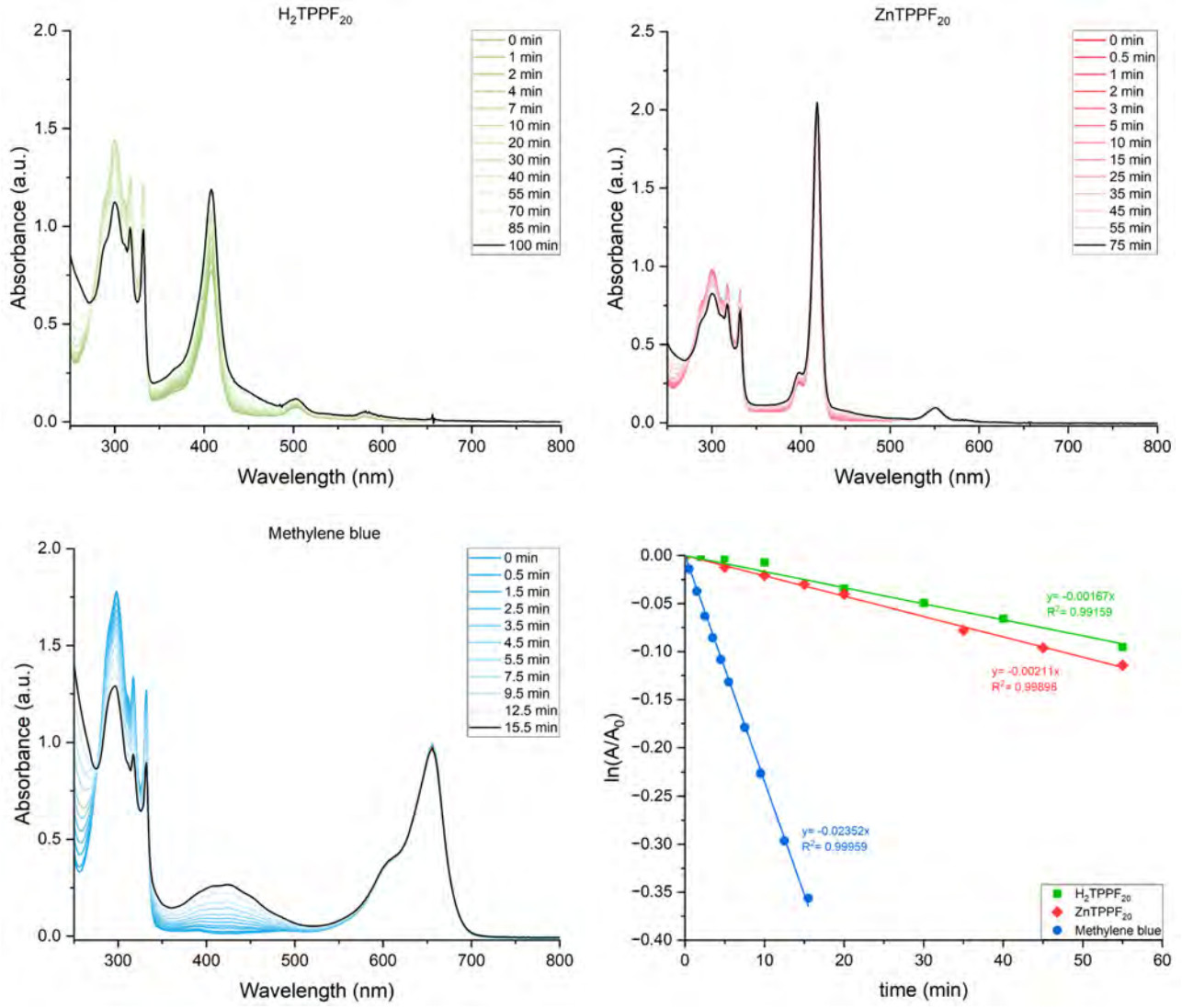

Figure 4. *Evolution of UV–vis absorption spectra of ethanol solutions containing a mixture of DHN ($1.74 \cdot 10^{-4}$ M) and either H_2TPPF_{20} ($2.17 \cdot 10^{-5}$ M) (red traces), $ZnTPPF_{20}$ ($8.09 \cdot 10^{-6}$ M) (blue traces) or methylene blue ($5.00 \cdot 10^{-6}$ M) irradiated for several minutes with the monochromatic UV LED emitting at 400 nm. The last panel shows a comparison of the semilogarithmic plots of DHN consumption as a function of the irradiation time registered for the investigated sensitizers, with A_t and A_0 indicating the DHN absorbance at 317 nm registered at irradiation times t and 0, respectively.*

Table 1. *Experimental kinetic constant (k_{obs}), initial rate (v_0) of the photo-oxidation of DHN to Juglone and the estimated quantum yield for $^1O_2$ generation (Φ_Δ) of $H_2TPPF20$ and $ZnTPPF_{20}$ in ethanol when irradiated with the LED light source. In the last row the same parameters calculated for methylene blue (MB), used as standard.*

Species	k_{obs} (min^{-1})	v_0 ($M\ min^{-1}$)	Φ_Δ
H_2TPPF_{20}	0.00167	$2.96 \cdot 10^{-7}$	0.22
$ZnTPPF_{20}$	0.00211	$3.65 \cdot 10^{-7}$	0.34
MB	0.02352	$3.80 \cdot 10^{-6}$	0.50[x]

[x] Literature data from Ref. 14

Internalization studies using confocal microscopy

Before studying the cytotoxicity of the sample loaded with porphyrin, the uptake kinetic of pristine HNT was investigated on three different cell lines (prostate cancer, PC3 and two bladder cancer cells, 5637 and UMUC3) that resemble different grades and stages of the disease. Cells were treated with 10 µg mL^{-1} of pristine HNT for either 4 or 24 h. In order to visualize HNT localization, microscopy images in both reflectance and in fluorescence modes were recorded after staining the cells with Hoechst and phalloidin to mark the nuclei and the cytoskeleton, respectively. The images recorded on treated PC3 cells, shown in Figure 5, revealed that no HNT were internalized by the cells after the shortest incubation time, while after 24 h accumulation at the cellular level became easily observable. The microscopy images recorded on the three cell lines after 24 h of incubation showed that HNT accumulated in the cytosol without any significant differences in internalization among the cell lines (Figure 6).

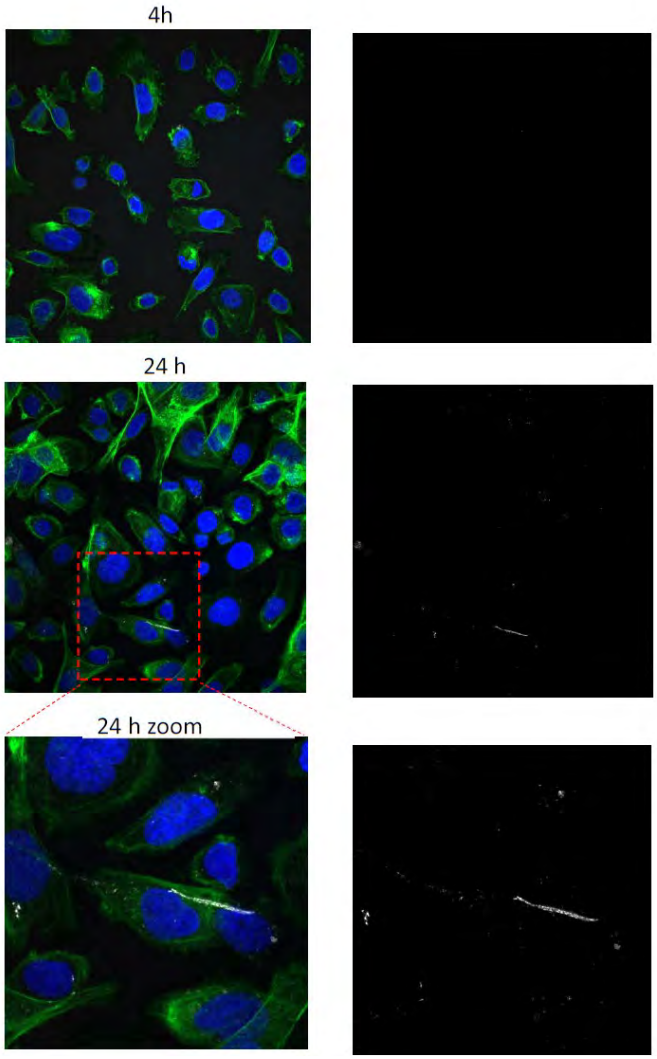

Figure 5. *Microscopy pictures of PC3 cells treated with 10 µg mL^{-1} of pristine HNT for 4h (first raw) and 24 h (middle panel). Cells were stained with Hoechst dye to visualize the nuclei (blue channel) and Alexa Fluor 488 Phalloidin to visualize the cytoskeleton (green channel). In the grey channel the light reflected by HNT is recorded. The left column shows the overlay of the three channels, while right column shows the reflected light channel only. All the images are the superposition of several images acquired along the optical axis (z-stack).*

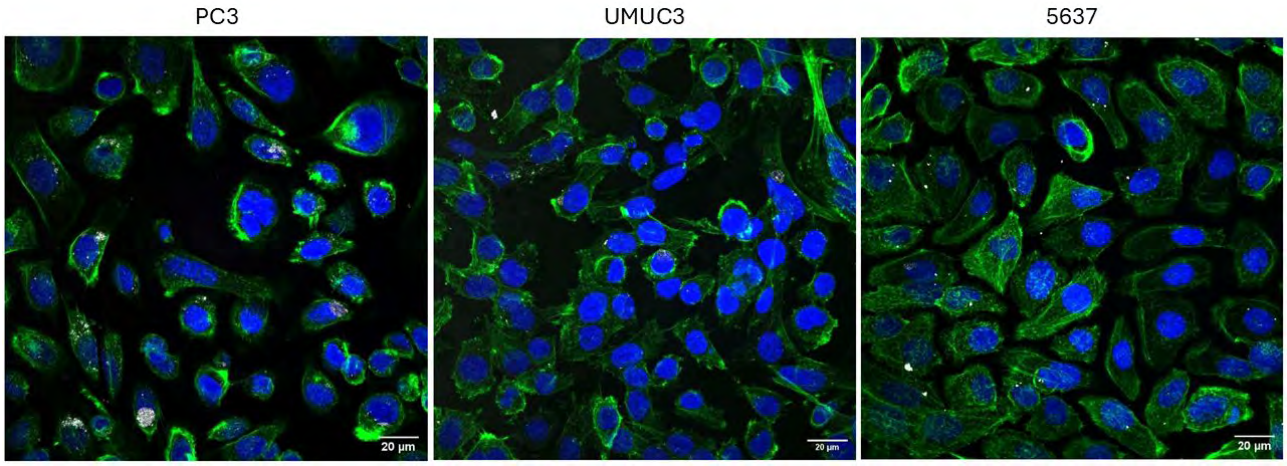

Figure 6. *Microscopy pictures of PC3 (left panel), UMUC3 (middle panel) and 5637 (right panel) cells treated with 10 µg mL^{-1} of pristine HNT for 24 h. Hoechst stain was used to visualize the nuclei (blue channel), Alexa Fluor 488 Phalloidin was used to mark actin to visualize the cytoskeleton (green channel), while reflected light marked the HNT location (grey channel). The three pictures are an overlay of the three channels and the superposition of several images acquired along the optical axis (z-stack).*

Similar samples were prepared by incubating the three cell lines with HNT-TDP-H_2TPPF_{20}-Dextrin. This loaded sample was chosen among the others due to the highest porphyrin content measured with TGA, which is a consequence of the inner lumen functionalization with TDP, and the slowest porphyrin kinetics due to the HNT capping with dextrin. Cells were treated with 10 µg mL^{-1} of the loaded HNT for 24 h and stained only with phalloidin, as the emission tail from Hoechst interfered with the porphyrin emission in the red channel. From the pictures recorded, shown in Figure 7, it is clear that the emission signal of the porphyrin is effectively co-localized with the reflectance signal of the HNT, confirming the success in employing the so-modified HNT as carrier to deliver the PS into cells.

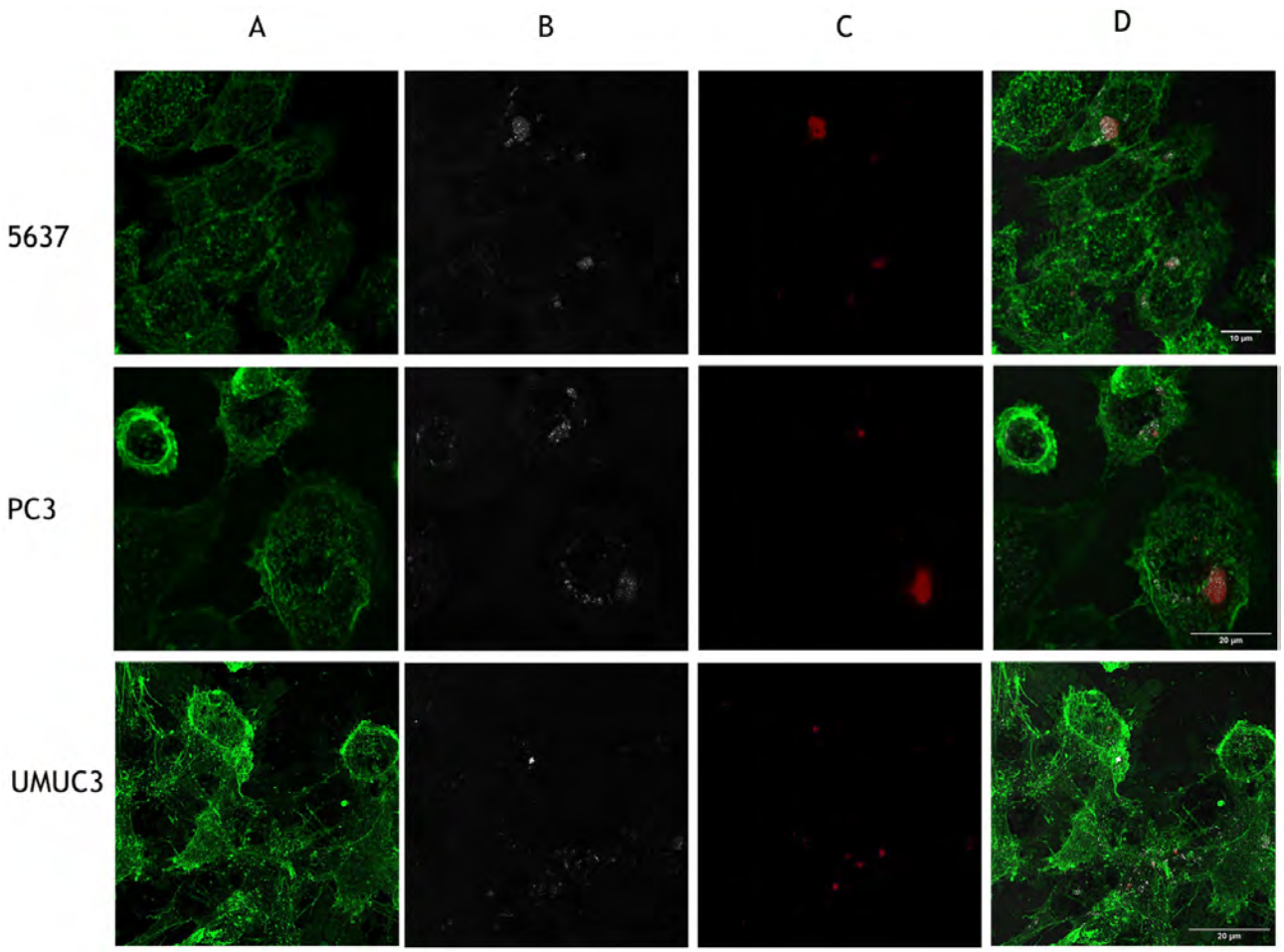

Figure 7. *Confocal microscopy images of 5637, PC3, and UMUC3 cells treated with HNT-TDP-H2TPPF20-Dextrin for 24 hours. The columns show the staining with phalloidin to visualize the cell cytoskeleton in the green channel (A), the reflected light to localize HNT in the grey channel (B) and the emission of H_2TPPF_{20} in the red channel (C). Column D shows the overlay of the three channels. All the images are the superposition of several images acquired along the optical axis (z-stack). Scale bars: 10 μm (first row) and 20 μm (second and third rows).*

Photocytotoxicity of the porphyrin-loaded HNT

Finally, the photocytotoxicity of HNT-TDP-H_2TPPF_{20}-Dextrin was evaluated on the same three tumoral cell lines (PC3, 5637, UMUC3) irradiating the samples with a commercial lamp emitting in the visible range (with an intensity of 1.3 mW/cm^2 and whose emission profile is shown in Figure 8). The cytotoxicity of the loaded sample was compared to that of pristine HNT.

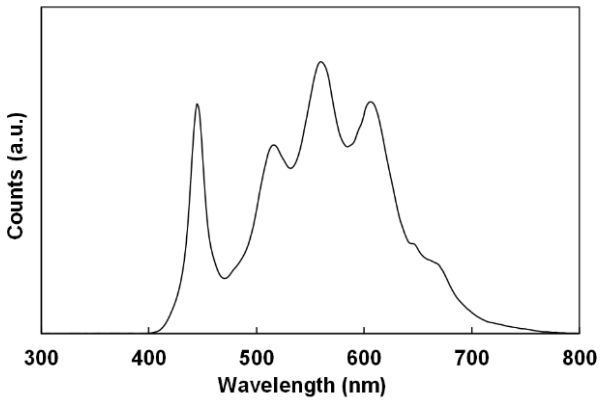

Figure 8. *The emission profile of the commercial lamp used to irradiate cells treated with pristine HNT and HNT-TDP-H_2TPPF_{20}-Dextrin in the photocytotoxicity test.*

The protocol followed in the photocytotoxicity experiment is schematized in Scheme 3. Each cell line, seeded in two 96-well plates, was treated with either pristine or loaded HNT suspended in the cell culture medium for 24 h with increasing concentrations in the 0.01-100 μg mL^{-1} range, after which the medium was replaced with fresh one to remove the compound that was not taken up by cells. One plate of cells was irradiated for 45 min, while the other was kept in the dark outside the incubator for the same time, to keep the same conditions but irradiation the same between the two plates. After 48 h of additional incubation, the MTT assay was carried out to evaluate the photocytotoxicity of the loaded HNT and compare it with the effect of pristine HNT on the three different cell lines.

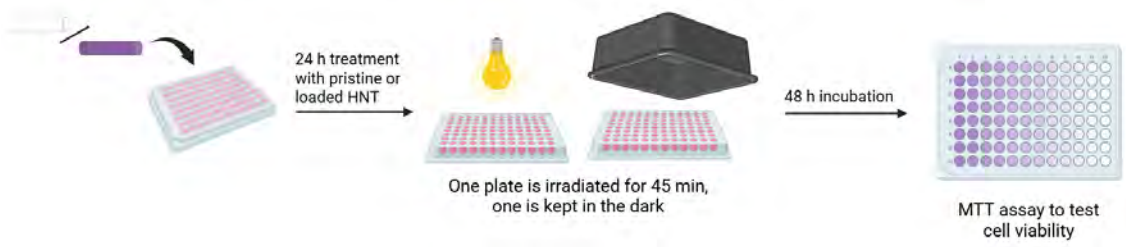

Scheme 3. *Schematic representation of the general protocol followed in the photocytotoxicity experiments. Picture made using Biorender software.*

Pristine HNT showed the same non-toxic behavior in the dark for all three cell lines until a dose of 10 μg mL^{-1}, at which some small dark toxicity is visible on 5637 and UMUC3 cells. Under irradiation the cytotoxicity of HNT remained unchanged for PC3 and UMUC3 cells, while 5637 cells revealed to be more sensitive to HNT presence, exhibiting a consistent reduction of viability even at lower HNT concentrations and showing a small difference in cell viability under irradiation compared to the dark conditions. The higher sensitivity of 5637 cells compared to UMUC3 is consistent to what already observed in other studies in literature.[15] The cytoxicity of pristine HNT is shown in the upper row of Figure 9.

For all three cell lines, cells treated with HNT-TDP-H_2TPPF_{20}-Dextrin showed different behaviors in comparison to treatment with HNT alone (bottom row of Figure 9). Similarly to the response towards HNT, 5637 cells showed again to be more sensitive than the other two cell types and, in this case, a significant reduction of cell viability was detected starting from the 1 μg mL^{-1} dose. By comparing cell viability curves in the dark and after light irradiation we estimated the EC_{50} values, shown in Table 2, which represent the effective concentration required to reduce cell viability to 50% in the dark and after irradiation, respectively.

In Figure 10 the toxicity capabilities of HNT and porphyrin-loaded HNT under irradiation were compared, from which the role played by H_2TPPF_{20} in favoring the singlet oxygen production is clearly visible, inducing an overall higher toxicity, especially at the highest dose (100 μg mL^{-1}) for PC3 and UMUC3 cells.

These preliminary data confirmed a cytotoxic effect of the investigated nanocomposites, which is enhanced when the cells are exposed to irradiation, thus underscoring the critical role of the photosensitizer.

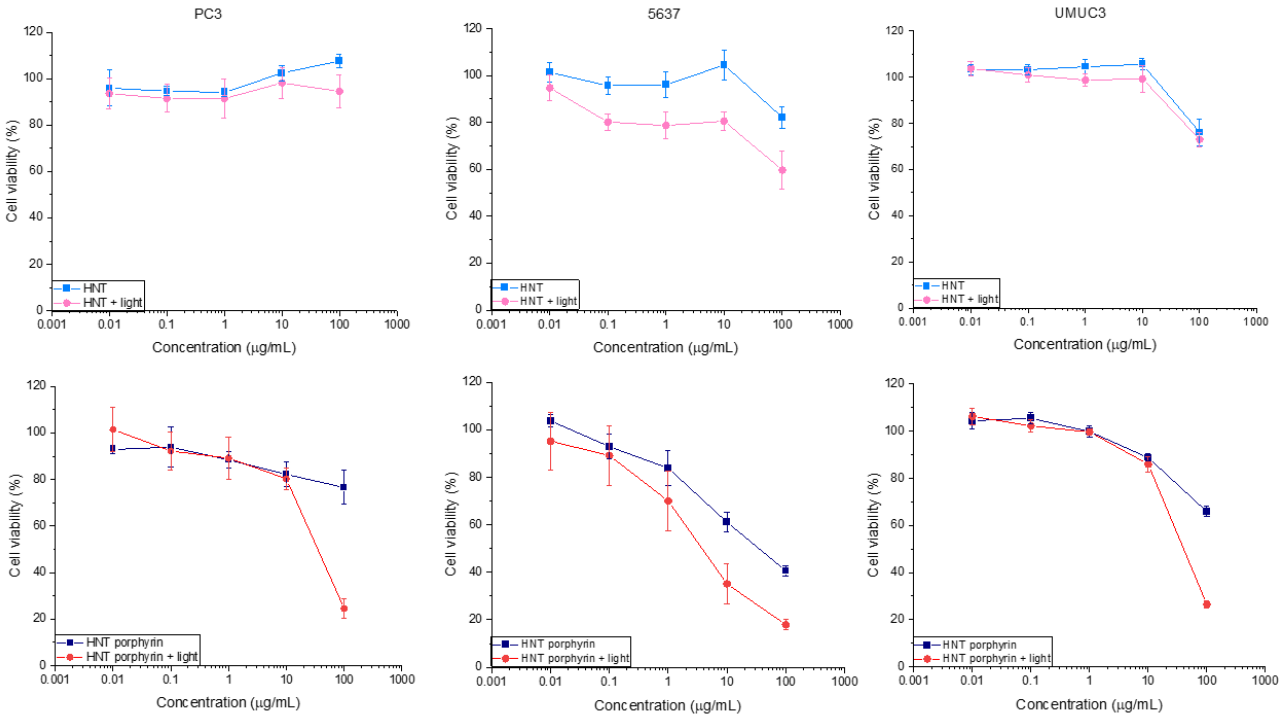

Figure 9. *Dose–response plots for PC3 (left column), 5637 (middle column) and UMUC3 (right column) cells treated with pristine HNT (upper row) or HNT-TDP-H_2TPPF_{20}-Dextrin (bottom row) in the dark (blue and light blue traces) and under 45 min of irradiation (red and pink traces).*

Table 2. *Cytotoxicity of the HNT-TDP-H_2TPPF_{20}-Dextrin nanocomposite toward PC3, 5637, and UMUC3 cells in the dark and after 45 min of irradiation, expressed in terms of EC_{50} (dark and light).*

Cell line	Dark EC_{50}	Light EC_{50}	PI[xi]
PC3	> 100 μg mL^{-1}	50 μg mL^{-1}	> 2
5637	35 μg mL^{-1}	3.5 μg mL^{-1}	10
UMUC3	> 100 μg mL^{-1}	50 μg mL^{-1}	> 2

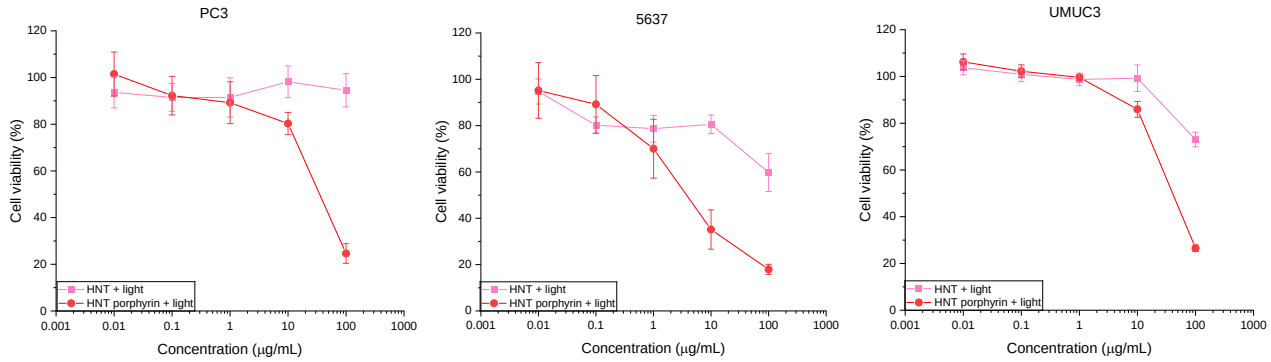

Figure 10. *Dose–response plots for PC3 (left column), 5637 (middle column) and UMUC3 (right column) cells treated with pristine HNT (pink traces) or HNT-TDP-H_2TPPF_{20}-Dextrin (red traces) irradiated for 45 min.*

Conclusions

The present work aimed at the development and characterization of HNT-based nanocarriers for potential PDT applications, by loading two perfluorinated porphyrins, H_2TPPF_{20} and $ZnTPPF_{20}$, into pristine or TDP-modified HNT, used to functionalize HNT in order to facilitate the loading of the PS into their inner lumen. The well-established ability of the two porphyrins to react with O_2 and generate cytotoxic singlet oxygen for PDT was ascertained in a polar solvent such as ethanol, where the perfluorinated porphyrins were still able to produce $^1O_2$ even when possessing a certain degree of aggregation.

Additionally, the loaded HNT samples were covered with dextrin to better suspend HNT in water media and slightly delay the release of guest molecules from the nano-carriers.

To validate our approach, we thoroughly examined the spectroscopic and thermogravimetric properties of the loaded samples, also compared with H_2TPPF_{20} and $ZnTPPF_{20}$ in their pristine form and mechanically mixed with HNT, as any interaction in the ground samples would only occur with the silica-based external part of the nanoclay.

Finally, three cell lines including one prostate cancer (PC3) and two bladder cancer (5637 and UMUC3) lines resembling different grades and stages of the tumor were treated with the HNT-TDP-H_2TPPF_{20}-Dextrin sample, showing accumulation the loaded sample after 24 h of treatment in the cytosol, being

[xi] Phototherapeutic index, measured as the ratio between dark EC_{50} and light EC_{50}

the emission of the porphyrin co-localized with the reflectance signal of HNT. The HNT-TDP-H_2TPPF_{20}-Dextrin showed no cytotoxicity toward the same three cell lines in the dark and a certain photocytotoxicity after irradiation, with light EC_{50} values of 50 μg mL^{-1} toward PC3 and UMUC3 cells and 3.5 μg mL^{-1} toward 5367 cells.

Experimental

Materials and instruments

Ultrapure water (Milli-Q, Millipore, resistivity = 18 MΩcm^{-2}) was used for the preparation of the aqueous solutions. Commercial reagents were used without further purification. UV–vis absorption spectra were acquired on a single beam Agilent model 8543 spectrophotometer equipped with a diode array detector using a 1 cm path length quartz cuvette at room temperature. Emission spectra were acquired by using an Edinburgh FLS980 spectrofluorimeter equipped with a 450 W xenon arc lamp. Emission spectra were corrected for source intensity (lamp and grating) and emission spectral response (detector and grating) by standard correction curves. The estimated experimental errors are 2 nm on the PL bands maxima. In the $^1O_2$ generation in cuvette samples were irradiated with a Megamanlamp ® PAR16 GU10 LR0707-SP LED light, while for the photocytotoxicity experiments cells were irradiated with an YIQUIBRO® LED Flood Light. The cell viability was assessed by measuring the absorbance at 570 nm on a micro plate reader Mithras LB940-Berthold. Cell images were acquired using Nikon A1 laser scanning confocal microscope using a 63x oil immersion objective (NA 1.4). Phalloidin was excited using the 488 nm laser line and the emitted signal was collected using a 525/25 emission filter. Porphyrin was excited using the 405 nm laser line and the emitted signal was collected using a 700/75 emission filter. Nanotubes images were acquired in the reflection mode. Z-stack images were acquired at 0.25 μm intervals.

Estimation of the molar extinction coefficient of H_2TPPF_{20} and $ZnTPPF_{20}$ in THF

A stock solution of the photosensitizer was prepared by dissolving 1.0 mg of H_2TPPF_{20} or $ZnTPPF_{20}$ in 250 μL of pure THF and then added with a mixture 1:1 H2O:THF to a total volume of 5 mL ($2 \cdot 10^{-1}$ mM). Then, from this stock solution, diluted solutions were subsequently prepared at different concentrations in the 10^{-1} – $5 \cdot 10^{-5}$ mM range. For each concentration, a UV-vis spectrum was recorded and the molar extinction coefficient of the Soret band was determined from the slope obtained by plotting the absorbance at 410 nm vs molar concentration. ε(410 nm) = 327312 $M^{-1}cm^{-1}$ for H_2TPPF_{20} and 767773 $M^{-1}cm^{-1}$ for $ZnTPPF_{20}$.

In cuvette $^1O_2$ generation by H_2TPPF_{20} and $ZnTPPF_{20}$ with irradiation

A solution of H_2TPPF_{20} was prepared by dissolving 0.200 mg of the free base porphyrin in 2 mL by of EtOH ($5.1 \cdot 10^{-4}$ M). 250 μL of a DHN solution in EtOH ($1.64 \cdot 10^{-3}$ M) was transferred in a cuvette, diluted with 2 mL of EtOH, and added with 100 μL of the H_2TPPF_{20} solution to obtain a final concentration $1.74 \cdot 10^{-4}$ M of DHN and $2.17 \cdot 10^{-5}$ M of the porphyrin. Before irradiation, the solution was saturated with O_2 by bubbling directly in the cuvette for ca. 3 min.

The solution was then irradiated through a LED light source and UV-vis spectra were collected every 1-2 min for the first points, then at the following time points: 10, 20, 30, 40, 55, 70 and 85 min. The same procedure was followed for the photoreaction employing $ZnTPPF_{20}$ as PS dissolving 0.2 mg of $ZnTPPF_{20}$ in 2.0 mL of pure EtOH (1.9×10^{-4} M).

Preparation of samples for confocal microscopy

Cells were seeded in 24-well plates with a density of 10^5 cells/well and grown overnight on glass coverslips, after which they were treated with 10 μg mL^{-1} of pristine HNT or HNT-TDP-H_2TPPF_{20}-Dextrin for either 4 or 24 h, washed with PBS and fixed using 4 % paraformaldehyde for 30 min. After extensive PBS washing to remove the excess of paraformaldehyde, cells were incubated with Alexa Fluor 488 Phalloidin and Hoechst 33342 Trihydrochloride, Trihydrate in 0.1 % donkey serum and 0.1 % Triton in PBS for 30 min at room temperature. After extensive washing with PBS, coverslips with stained cells were mounted on a microscope slide. Fluorescent images were analyzed using ImageJ (FIJI) software.

Photocytotoxicity assay (MTT assay)

Cells were seeded in 96-well plates with a density of 5000 cells/well and incubated with logarithmic concentrations of pristine HNT or HNT-TDP-H_2TPPF_{20}-Dextrin in the 0.01-100 μg mL^{-1} range. After 24 h, cells were irradiated for 45 min and incubated additional 48 h at 37 °C. Then, 3-(4,5-dimethylthiazol-2-yl)-2,5-diphenyltetrazolium bromide (MTT) (5 mg/mL in PBS) was added (0.5 mg/mL working concentration). After 1 h incubation at 37 °C, the supernatants were removed, and 100 μL of DMSO were added to each well to dissolve the formazan crystals. Cell viability was assessed by measuring the absorbance at 570 nm and expressed as a percentage of the untreated control. Experiments were performed in quadruplicate and data were shown as the mean ± SD

References

(1) Tsolekile, N.; Nelana, S.; Oluwafemi, O. S. Porphyrin as Diagnostic and Therapeutic Agent. *Molecules* **2019**, *24* (14), 2669. https://doi.org/10.3390/molecules24142669.

(2) Ethirajan, M.; Chen, Y.; Joshi, P.; Pandey, R. K. The Role of Porphyrin Chemistry in Tumor Imaging and Photodynamic Therapy. *Chem. Soc. Rev.* **2011**, *40* (1), 340–362. https://doi.org/10.1039/B915149B.

(3) Benov, L. Photodynamic Therapy: Current Status and Future Directions. *Medical Principles and Practice* **2015**, *24* (1), 14–28. https://doi.org/10.1159/000362416.

(4) Goswami, L. N.; White, W. H.; Spernyak, J. A.; Ethirajan, M.; Chen, Y.; Missert, J. R.; Morgan, J.; Mazurchuk, R.; Pandey, R. K. Synthesis of Tumor-Avid Photosensitizer−Gd(III)DTPA Conjugates: Impact of the Number of Gadolinium Units in T 1 /T 2 Relaxivity, Intracellular Localization, and Photosensitizing Efficacy. *Bioconjug. Chem.* **2010**, *21* (5), 816–827. https://doi.org/10.1021/bc9005305.

(5) Castro, K. A. D. F.; Biazzotto, J. C.; Tomé, J. P. C.; da Silva, R. S.; Lourenço, L. M. O. In Vitro Anti-Tumoral Activity of Two Versatile Cationic Porphyrins on Melanoma Cells. *J. Porphyr. Phthalocyanines* **2023**, *27* (01n04), 712–718. https://doi.org/10.1142/S1088424623500827.

(6) Samaroo, D.; Vinodu, M.; Chen, X.; Drain, C. M. Meso-Tetra(Pentafluorophenyl)Porphyrin as an Efficient Platform for Combinatorial Synthesis and the Selection of New Photodynamic Therapeutics Using a Cancer Cell Line. *J. Comb. Chem.* **2007**, *9* (6), 998–1011. https://doi.org/10.1021/cc070067j.

(7) Aljabri, M. D.; La, D. D.; Jadhav, R. W.; Jones, L. A.; Nguyen, D. D.; Chang, S. W.; Tran, L. D.; Bhosale, S. V. Supramolecular Nanomaterials with Photocatalytic Activity Obtained via Self-Assembly of a Fluorinated Porphyrin Derivative. *Fuel* **2019**, *254*, 115639. https://doi.org/10.1016/j.fuel.2019.115639.

(8) Foletto, P.; Correa, F.; Dornelles, L.; A. Iglesias, B.; H. da Silveira, C.; A. Nogara, P.; T. da Rocha, J. B.; F. Faustino, M. A.; D. Rodrigues, O. E. A New Protocol for the Synthesis of New Thioaryl-Porphyrins Derived from 5,10,15,20-Tetrakis(Pentafluorophenyl)Porphyrin: Photophysical Evaluation and DNA-Binding Interactive Studies. *Molecules* **2018**, *23* (10), 2588. https://doi.org/10.3390/molecules23102588.

(9) Cavaleiro, J. A. S.; Görner, H.; Lacerda, P. S. S.; MacDonald, J. G.; Mark, G.; Neves, M. G. P. M. S.; Nohr, R. S.; Schuchmann, H.-P.; von Sonntag, C.; Tomé, A. C. Singlet Oxygen Formation and Photostability of Meso-Tetraarylporphyrin Derivatives and Their Copper Complexes. *J. Photochem. Photobiol. A Chem.* **2001**, *144* (2–3), 131–140. https://doi.org/10.1016/S1010-6030(01)00540-8.

(10) Takizawa, S.; Aboshi, R.; Murata, S. Photooxidation of 1,5-Dihydroxynaphthalene with Iridium Complexes as Singlet Oxygen Sensitizers. *Photochemical & Photobiological Sciences* **2011**, *10* (6), 895–903. https://doi.org/10.1039/c0pp00265h.

(11) Ohshita, J.; Hayashi, Y.; Murakami, K.; Enoki, T.; Ooyama, Y. Single Oxygen Generation Sensitized by Spiro(Dipyridinogermole)(Dithienogermole)s. *Dalton Transactions* **2016**, *45* (39), 15679–15683. https://doi.org/10.1039/C6DT02767A.

(12) Öztürk, E.; Eserci, H.; Okutan, E. Perylenebisimide-Fullerene Dyads as Heavy Atom Free Triplet Photosensitizers with Unique Singlet Oxygen Generation Efficiencies. *J. Photochem. Photobiol. A Chem.* **2019**, *385*, 112022. https://doi.org/10.1016/j.jphotochem.2019.112022.

(13) Luiz, M.; Soltermann, A. T.; Biasutti, A.; Garcia, N. A. A Kinetic Study on Singlet Molecular Oxygen (O2 (1Δg)) Generation and Quenching by Dihydroxynaphthalenes. *Can. J. Chem.* **1996**, *74* (1), 49–54. https://doi.org/10.1139/v96-006.

(14) Wilkinson, F.; Helman, W. P.; Ross, A. B. Quantum Yields for the Photosensitized Formation of the Lowest Electronically Excited Singlet State of Molecular Oxygen in Solution. *J. Phys. Chem. Ref. Data* **1993**, *22* (1), 113–262. https://doi.org/10.1063/1.555934.

(15) Notarbartolo, M.; Massaro, M.; de Melo Barbosa, R.; Emili, C.; Liotta, L. F.; Poma, P.; Raymo, F. M.; Sànchez-Espejo, R.; Vago, R.; Viseras-Iborra, C.; Riela, S. Exploring the Cellular Uptake of Hectorite Clay Mineral and Its Drug Carrier Capabilities. *Colloids Surf. B Biointerfaces* **2022**, *220*, 112931. https://doi.org/10.1016/j.colsurfb.2022.112931.

PART TWO:

MOLECULAR ORGANIC AND ORGANOMETALLIC COMPOUNDS

A luminescent Ir-PNA bioconjugate as photosensitizer for $^1O_2$ production in PDT: toward a potential dual therapeutic agent.

Adapted from: Dell'Acqua R. M., Schifano V., Dozzi V. M., D'Alfonso L., Panigati M., Rusmini P., Piccolella M., Poletti A., Cauteruccio S. and Maggioni D., Inorg. Chem. 2025, 64, 14, 6898–6911

Introduction

Cyclometalated Ir complexes as PS for $^1O_2$ production

In the last two decades, cyclometalated Ir(III) complexes have attracted increasing attention, at the beginning as cellular imaging agents, with the development of two cationic Ir (III) complexes emitting in the green and red regions that were shown to be internalized by cells and accumulate in the cytoplasm.[1] More recently, these complexes have emerged as promising photosensitizers for $^1O_2$ production, owing to their long excited-state lifetimes, large Stokes shifts, accessibility of triplet excited states, high intersystem crossing (ISC) efficiency, high quantum yields for ROS generation, and excellent thermal and photo-stability under physiological conditions.[2,3] However, Ir (III) complexes generally possess low solubility in aqueous media due to their rigidity and strong π-π stacking, limiting their internalization efficiency by cells, and absorb UV or blue light, limiting the penetration of light through tissues and resulting in photodamage, which is a possible obstacle for practical clinical applications. Moreover, they also possess non-negligible cytotoxicity.[2] Thus, recent studies have worked on overcoming these drawbacks and effectively exploit the excellent features of this kind of complexes as PS for PDT. Their solubility in water can be improved, for instance, by their conjugation to hydrophilic polymers[4] and/or positively charged moieties, such as poly(L-lysine),[5] to encapsulate the complexes into suitable nanometric carriers and reduce their toxicity.

Two different strategies have been employed to red shift Ir complexes absorption toward the NIR. One consists in the extension of the π-conjugation of ligands. In a recent work[6] a donor–acceptor–donor fluorescent chromophore was used to prepare an iridium(III) complex with high ROS generation efficiency upon irradiation at 808 nm. On the other hand, the second strategy relies on two-photon excitation (TPE) of the Ir complexes. TPE consists of the absorption of two NIR photons to populate a given excited state of the corresponding one-photon transition in the UV-vis. This strategy, other than allowing a deeper penetration of light, reduces the damage area caused by the irradiation compared to one-photon, being TPE triggered by high illumination intensity with a small volume.[2] Byant and coworkers[7] prepared two cyclometalated Ir complexes with high TP absorption that localized in mitochondria and lysosomes in live cells, photosensitizing cell death by apoptosis when excited with one-photon 405 nm light as well as under TPE at 760 nm.

Additionally, the conjugation of these complexes to targeting vehicles, such as peptides[8] and proteins,[9] or oligonucleotides,[10] other than improving some of their drawbacks might also add new pharmacological properties in synergy with PDT for applications in theranostic and as organelle-targeted photosensitizers.[11]

Peptide Nucleic Acids (PNAs)

Peptide Nucleic Acids (PNAs) are synthetic mimics of DNA, developed by Nielsen and co-workers[12] in 1991 and consisting of *N*-(2-amino-ethyl)glycine units covalently linked to nucleobases through a carboxymethyl spacer, in a structure analogous to DNA and RNA, with the pseudopeptide backbone replacing the sugar-phosphate one (Figure 1). This allows a strong and sequence-specific binding to complementary DNA and RNA strands, following the Watson-Crick hydrogen bonding rules, forming PNA/DNA or PNA/RNA duplexes with a higher stability compared to DNA/DNA and DNA/RNA ones due to the uncharged backbone of PNA and thus the absence of any electrostatic repulsions. For this reason, the duplexes with PNA chains are stable at higher temperatures and unaffected by the ionic strength pf the medium. The greater stability of the duplexes is reflected by a higher thermal melting temperature (T_m), i.e. the temperature at which 50% of the DNA strands results separated in a single strand or denaturated. The two strands of these DNA/PNA duplexes can be bound in either antiparallel (with the N-terminus of the PNA facing the 3'-end of the DNA strand) or parallel orientation, although the first one is the most favorable, due to the achirality of the PNA backbone.[13,14] Additionally, it is possible for PNAs to form triplexes with double stranded DNA with a very high T_m, depending on the length of the oligomers (10 °C increase in T_m per base). The formation of this kind of triplex is observed in homopyrimidine PNAs or PNAs with a high pyrimidine/purine ratio and consists in a triplex invasion complex in which one PNA binds the DNA by antiparallel paring and another PNA binds the PNA-DNA duplex by Hoogsteen binding, while $(DNA)_3$ hybrids might result unstable under certain circumstances. However, the formation of such triplets is quite slow.[13,15]

Moreover, PNA probes are very sequence-specific, providing better discrimination of single-point mismatches compared to DNA or RNA. Their "unnatural" backbone also allows a high resistance toward enzymatic degradation by proteases, peptidases and nucleases and higher chemical stability than DNA or RNA fragments both toward elevated temperatures and in a wide pH range.[13,14]

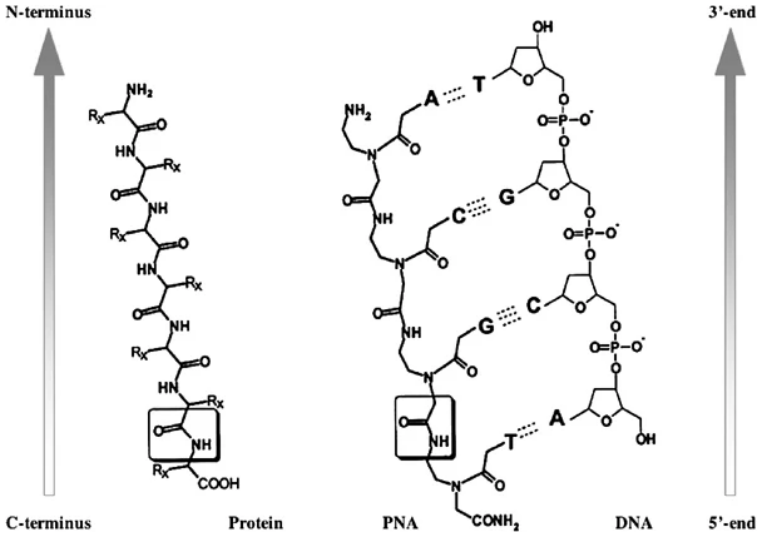

Figure 1. *General structure of PNA, compared to those of proteins and DNA. On the right part of the picture the formation of a duplex between PNA and a complementary single DNA strand is schematized, through the antiparallel interaction of the N-terminus of the PNA with the 3'-end of the DNA strand. From Ref. 16*

PNAs have acquired a great interest over the years as antigene and antisense agents for antibacterial, antiviral and anticancer applications and as biosensors (Figure 2). In antigene therapy DNA-based triplex-forming oligonucleotides are used to silence gene expression at the transcription step, while antisense strategy is based on the binding of oligonucleotides to a complementary mRNA sequence of the target gene, reducing or blocking the production of the associated protein. The antigene activity of PNAs is promoted by their tight binding to a DNA target, causing strand invaded triplexes or strand displacements that efficiently block transcriptional elongation and the binding of transcriptional factors. Analogously, the antisense activity is based on the strong interaction of PNAs with mRNA, independent from the RNA secondary structure, causing steric hinderance of RNA processing, transport into the cytoplasm or translation in a both sequence-specific and dose-dependent way.[14,16]

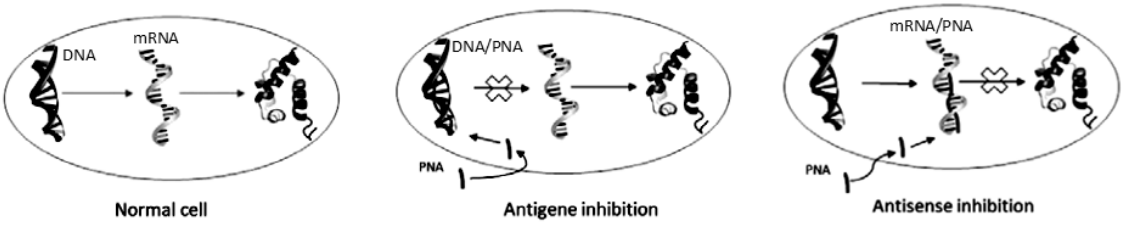

Figure 2. *Schematization of antigene and antisense strategies employing PNAs. Adapted from Ref. 17*

Nonetheless, PNAs show some drawbacks compared to native nucleic acids, mainly linked to their neutral backbone. PNA has low solubility in water, also related to its length and to the purine/pyrimidine ratio and tends to aggregate depending on the sequence of the oligomer. Although some protocols for cellular delivery exist, the cell permeability of PNA itself is very low. These disadvantages constitute an important obstacle for the effective use of PNA in therapy and can be overcome by the conjugation of various moieties at the end of the PNA chain, to improve chemical-physical properties of PNAs.[13]

Synthesis of PNAs

PNAs are synthetized easily using well-established automated or manual synthetic procedures supported on solid phase, that allow a relatively large-scale production of PNA oligomers in high yield and purity. Liquid phase syntheses also can be used, although less common.

Solid phase synthesis of PNAs consists in the assembly of protected monomers on a solid polymeric support, usually polystyrene, with a N-protected amino acid attached on its C-terminus through a cleavable linker. In general, the first consists in the loading of the first monomer on the resin using a proper coupling agent (HATU is the most commonly employed), followed by its deprotection on the N-terminus and the coupling of the other N-protected monomers (one by one) to elongate the PNA chain. The elongation step is critical for the overall yield and purity of the final PNA. Once reached the desired length of the sequence, the last step is the cleavage of the PNA chain from the resin. Usually, PNA oligomers prepared with solid phase synthesis do not exceed 16 bases, since this length already provides a high affinity for DNA and RNA avoiding the self-aggregation of PNA on the resin causing lower yields. PNA can be purified by reverse phase HPLC using conditions like those employed for the purification of small peptides.[13,17]

Various combinations of protecting groups are used in the PNA synthesis. The most common are the Boc/Cbz and the Fmoc/Bhoc since monomers protected with these groups are commercially available, although monomers can be easily synthetized from inexpensive reagents.[13] The synthesis followed in this work is a Fmoc/Bhoc manual solid phase synthesis, as schematized in Scheme 1.[18]

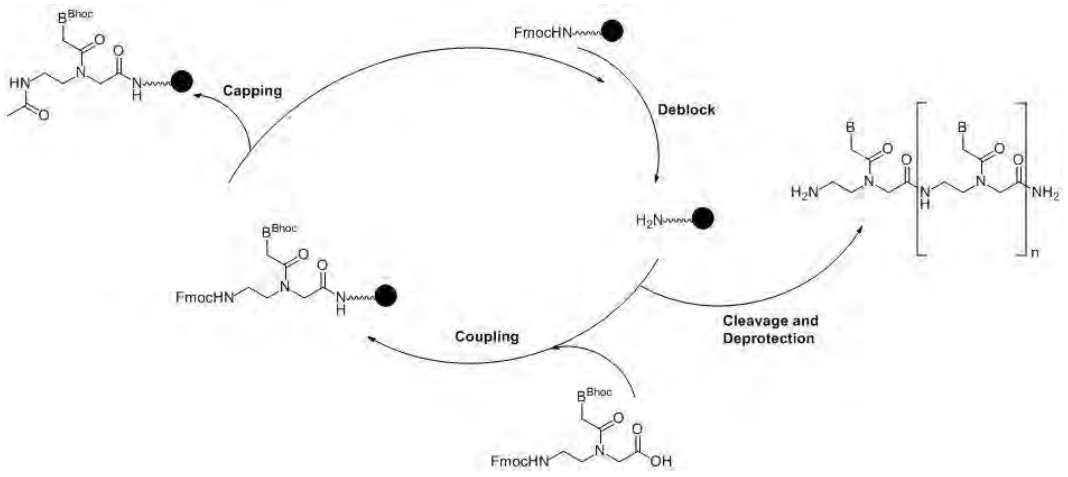

Scheme 1. *General procedure for the Fmoc/Bhoc solid phase synthesis of PNA chains.*

PNA-Transition metal complexes

Between the various approaches developed to address the low solubility and the low cellular penetration of PNAs, their covalent conjugation to luminescent organometallic complexes represents

a useful strategy because, other that improving the drawbacks that limit the use of PNAs for *in vitro* and *in vivo* applications, it also adds additional features to PNAs depending on the nature of the metal complex.[19,20] In the literature, various examples of PNA conjugates with Fe(II), Pt(II), Re(I) and Ru(II) complexes are reported for a wide variety of biomedical applications.

For instance, many metal-containing PNAs were developed for DNA electrochemical, fluorescent, radioactive and magnetic detection, exploiting the high stability of PNA/DNA duplexes and mismatch discrimination. PNA-ferrocenes conjugates were synthetized labelling the N-terminus of dodecamer PNAs via click chemistry to obtain biosensors for the identification of two different DNA target sequences in a single square wave voltammetry measurement on crude bacterial RNA extracts from *P. putida* and *E. coli*, due to selective and clear changes in peak current and potential.[21] Emissive binuclear Re-PNA conjugates were employed for antigene therapy to target cancer-associated microRNA-221, showing a low cellular uptake by human breast cancer cells (MDA-MB-221) but a high inhibitory effect toward its expression.[22] Another clinically relevant PNA sequence, 16-mer, complementary to the translation start region of the N-myc oncogene messenger RNA, was labelled with the *fac*-$[^{99m}Tc(CO)_3]^+$ moiety. Experiments carried out on human neuroblastoma cells (SH-SY5Y), which express N-myc, showed a good internalization/retention of the radioactive conjugate (After 4 h at 37 °C 7 % of the activity was recorded into the cells, 60 % of which was still present after 6 h).[23]

In another study, a PNA sequence was conjugated with a Ru(II) complex to target pBR322 plasmid DNA from *e. coli*. This Ru-PNA conjugate showed a more efficient formation of an invasion complex with DNA, under conditions at which unmodified PNA did not, obtaining a DNA/PNA duplex stabilized by the presence of the Ru complex and sensitive to single-base mismatches.[24]

Nevertheless, none of these metal-PNA conjugates have been explored as photosensitizers for PDT, despite some of them having the potential to exhibit all the necessary characteristics for ROS production under appropriate light irradiation. Nonetheless, there are some examples of PNA conjugates with organic photosensitizers. A PNA-Rose Bengal conjugate was prepared as a sequence-specific photoinduced DNA modulator activated with visible light, in which the generation of $^1O_2$ by rose bengal, leads to the formation of DNA/PNA duplex adducts.[25] The PS chlorin e6 (Ce6) in another work was conjugated to a PNA sequence complementary to the cancer specific miRNA. In the presence of miR-21in cancer cells Ce6-PNA drug gets hybridized with miR-21, released from dextrane-coated grafene oxide nanocolloids and the PS activated by NIR irradiation.[26]

Thus, this work aims to synthesize and characterize a novel PNA conjugate, consisting of a PNA tetramer with a standard sequence covalently functionalized with a luminescent bis-cyclometalated Ir(III) complex, able to generate singlet oxygen upon irradiation. The conjugation of PNA with the emissive

Ir(III) complex could offer the advantages already mentioned: enabling the tracking of PNA fate in cells through fluorescence microscopy, overcoming the low cell permeability of PNA and can create a synergistic effect, combining the precise genetic targeting capability of the PNA with the therapeutic action of PDT.

Results and discussion

Preparation of the Ir-PNA bioconjugate

For the preparation of the Ir-PNA bioconjugate, two complementary synthetic strategies were designed and attempted, both based on the reaction between a carboxylic and an amino group to form an amine, as schematized in Scheme 2. The first one consisted of a reaction between the PNA chain as-prepared, exposing a -NH_2 (deprotected from Fmoc using a solution of piperidine) and the phenanthroline ligand of an Ir (III) complex functionalized to bear the carboxylic group (Ir-COOH). On the other hand, the second strategy involved the functionalization of the PNA tetramer with succinic acid to bear the terminal carboxylic group, that this time was coupled with the same Ir (III) complex bearing a terminal amine (Ir-NH_2). Both coupling strategies allowed to prepare the Ir-PNA with the same efficiency.

The coupling between the Ir complex and the PNA tetramer was carried out on resin supported PNA-NH_2-Fmoc or PNA-COOH, prepared according to Fmoc/Bhoc solid phase synthesis as reported in the literature[18] and already discussed in the Introduction section about PNAs. O-(7-aza-1H-benzotriazole-1-yl)-N,N,N,N-tetramethyluronium hexafluorophosphate (HATU) and N-ethyldiisopropylamine (DIPEA) were used in the coupling as condensing agent and base respectively and, as final step, the Ir-PNA conjugate was detached from the resin with a TFA/*m*-cresol mixture, deprotecting the nucleobases of the PNA chain at the same time.

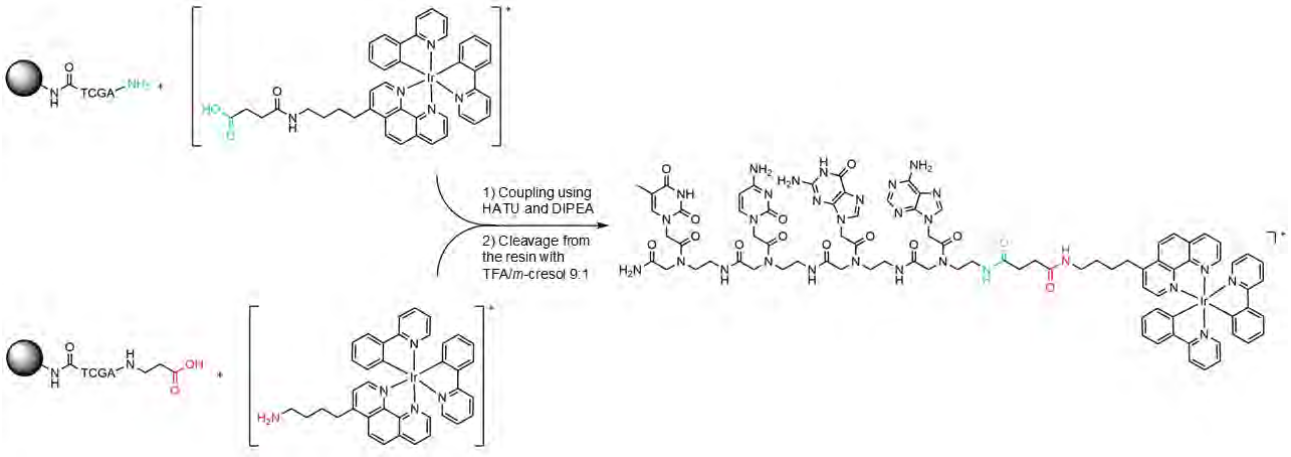

Scheme 2. *The two coupling strategies between the Ir (III) complex and the PNA tetramer employed to synthetize the Ir-PNA bioconjugate.*

Synthesis of phen-NH_2

The two substituted phenanthroline ligands (phen-NH_2 and phen-COOH) employed in the two strategies were prepared starting from the functionalization of 4-methyl-1,10-phenanthroline (phen-Me) with a pendant exposing the terminal amino group to obtain 4-(1,10-phenanthrolin-4-yl)butan-1-amine (phen-NH_2), following a synthetic strategy already employed from our research group in a past work[27] and schematized in Scheme 3.

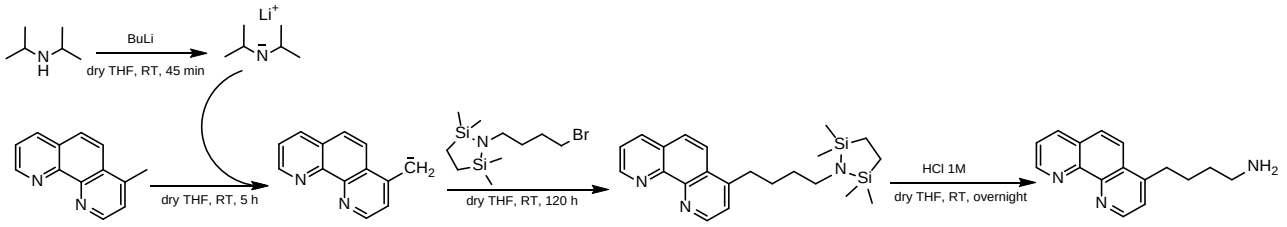

Scheme 3. *Synthesis of phen-NH_2 starting from 4-methyl-1,10-phenanthroline.*

However, before the addition of HCl to deprotect the terminal amine group, a side reaction occurs (Scheme 4) between the protected product and LDA (lithium diisopropylamide), generating a secondary carbanion on the same C in α position to the aromatic ring of phenanthroline. This carbanion further reacts with the protected bromopropylamine, generating as byproduct a phenanthroline substituted with two amine pendants, phen-bisNH_2, that together with unreacted phen-Me and phen-NH_2 constitutes the crude product of the reaction.

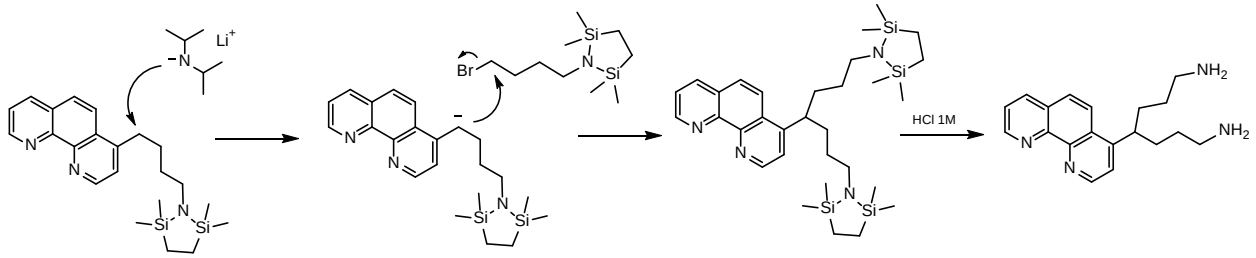

Scheme 4. *Side reaction occurring during the synthesis of phen-NH_2 between the protected product and LDA and the protected bromopropylamine, producing the byproduct phen-bisNH_2.*

Thus, we attempted two different strategies to isolate phen-NH_2 from the byproducts. The first consisted of three subsequent extractions from a water solution of the mixture using CH_2Cl_2 and varying the pH, exploiting the different pK_a values of the three molecules: the first at pH 6, to extract the neutral phen-Me (pk_a= 4.5), being all the other species protonate at this pH value, a second one in a pH range between 9.5-10 to extract phen-NH_2 (pK_{a1}= 4.5, pK_{a2}= 10.2)[4] and the last one at pH 11 to extract the neutral phen-bisNH_2 (pK_{a1}= 4.5, pK_{a2}= 10.2, pK_{a3}= 10.5). The speciation curves of the three molecules are shown in Figure 3. For all three, the first deprotonation is attributed to the phenanthroline moieties, while the other two to the amino pendants. Although we managed to separate phen-Me from the mixture, the strategy did not result optimal for the separation of phen-NH_2 and phen-bisNH_2 due to the too similar

pK_a values of the amino pendants and the difficulties in controlling the pH precisely, as the ^1H NMR spectrum recorded on the organic phases extracted between 9.2 and 10 still showed the presence of both species (Figure 4).

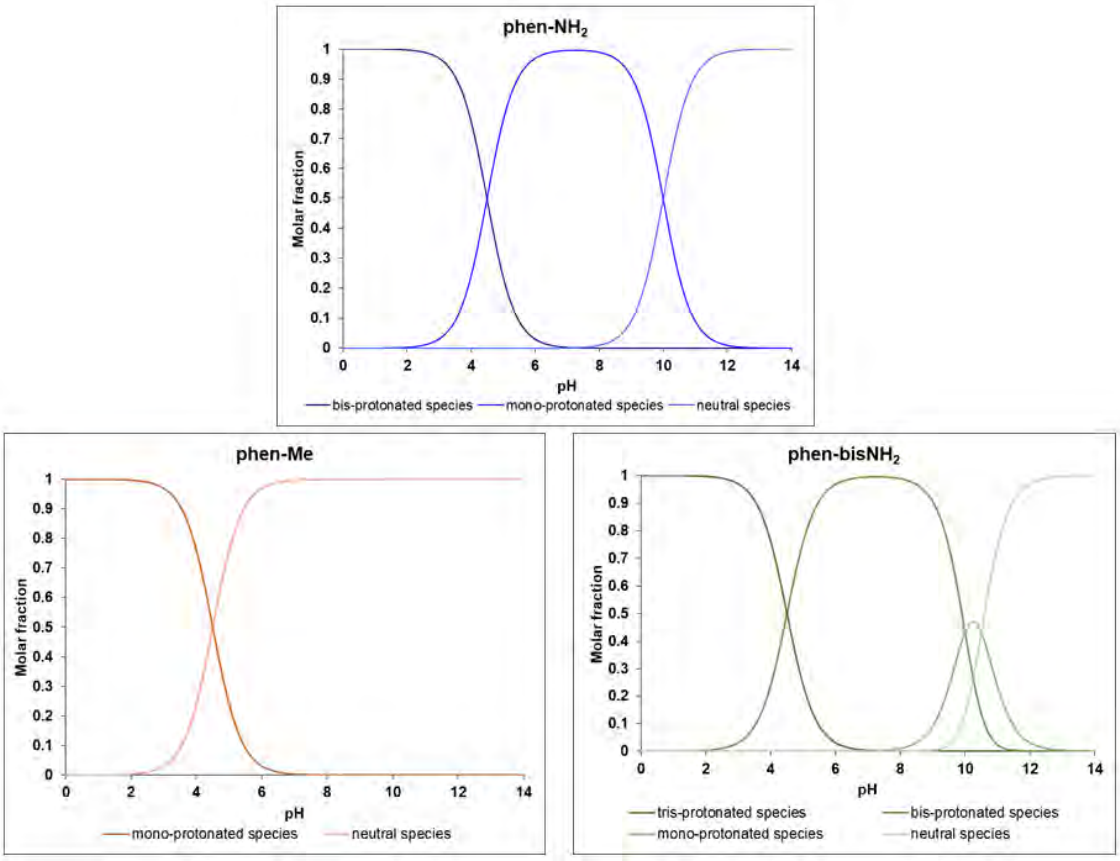

Figure 3. *Speciation curves of the three components of the crude product of the synthesis of phen-NH_2: phen-NH_2 (blue trace), phen-Me (orange trace) and phen-bisNH_2 (green trace).*

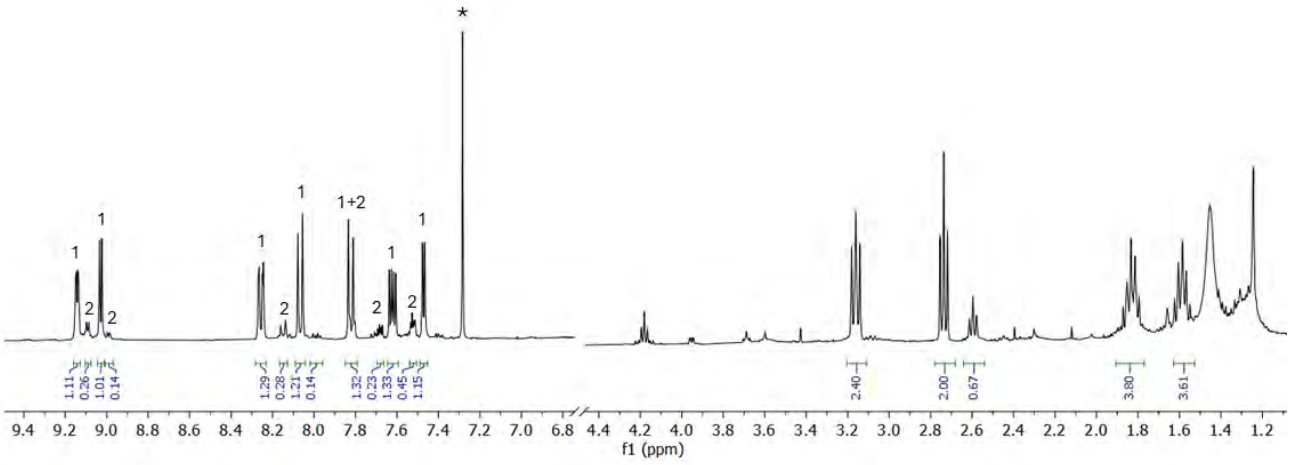

Figure 4. *^1H NMR (9.4 T, 300 K, $CDCl_3$) of the organic phases extracted in the pH range 9.2-10. The 1 mark the signals in the aromatic region assigned to phen-NH_2, 2 to phen-bisNH_2 and * the residual solvent.*

The second attempt in the separation of phen-NH_2 from the byproduct involved gravimetric chromatography, prior protection of the amine groups of both molecules with t-Boc following a literature procedure[28] schematized in Scheme 5.

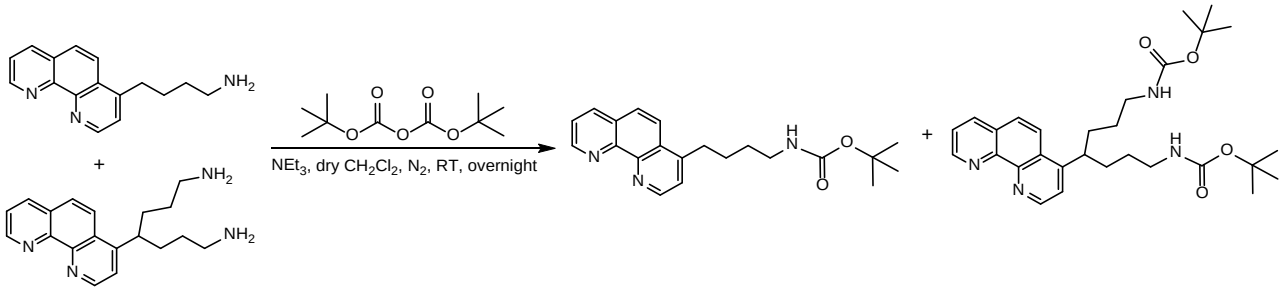

Scheme 5. *Protection of the terminal amines of phen-NH_2 and phen-bis-NH_2 using tBoc.*

A TLC of the crude product (using CH_2Cl_2:MeOH 9:1 as eluting mixture) showed three different spots: one with R_f= 0.95, assigned to the protected phen-NH_2, a second one with R_f= 0.47, assigned to a mixture of unprotected phen-NH_2 and mono-protected phen-bisNH_2 and a third one (R_f= 0) attributed to the unprotected phen-bisNH_2. The protected phen-NH_2 was thus successfully isolated by chromatography from the crude mixture, as confirmed by ^{1}H NMR (Figure 5). The protected phen-NH_2 resulted contained in the first fractions, while the second product collected resulted in a mixture of phen-NH_2 and phen-bisNH_2, confirming the attributions of the TLC spots.

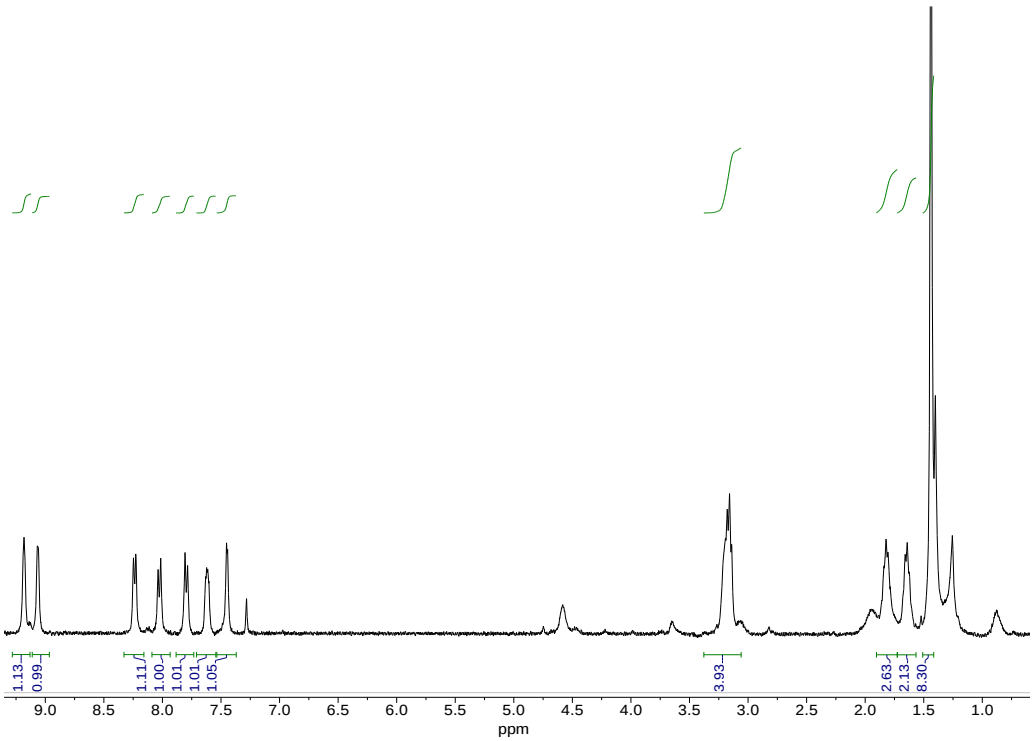

Figure 6. *^{1}H NMR (9.4 T, 300 K, $CDCl_3$) of phen-NH_2 isolated with a gravimetric chromatography using CH_2Cl_2:MeOH 9:1 as eluting mixture (fractions 3-5).*

Synthesis of phen-COOH

The phen-NH_2 ligand was then further reacted with succinic anhydride to obtain 4-((4-(1,10-phenanthrolin-4-yl)butyl)- amino)-4-oxobutanoic acid (phen-COOH), partially following a literature procedure[29] involving the deprotonation of the terminal amine with triethylamine (TEA) to allow the nucleophilic opening of the ring of succinic anhydride (Scheme 6).

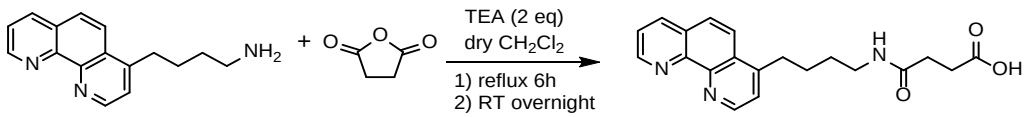

Scheme 6. *Preparation of the phen-COOH ligand reacting phen-NH_2 with succinic anhydride.*

The product was characterized by NMR spectroscopy confirming the success in the preparation of phen-COOH, from the presence of a large signal in the ^{1}H spectrum attributed to the proton of the carboxylic group, visible since we recorded the spectrum in an aprotic solvent mixture (Figure 6), and from a ^{1}H-^{1}H scalar correlation observed in a 2D COSY experiment (Figure 7) between the amide proton at 7.45 ppm and the aliphatic -CH_2 proton in α position.

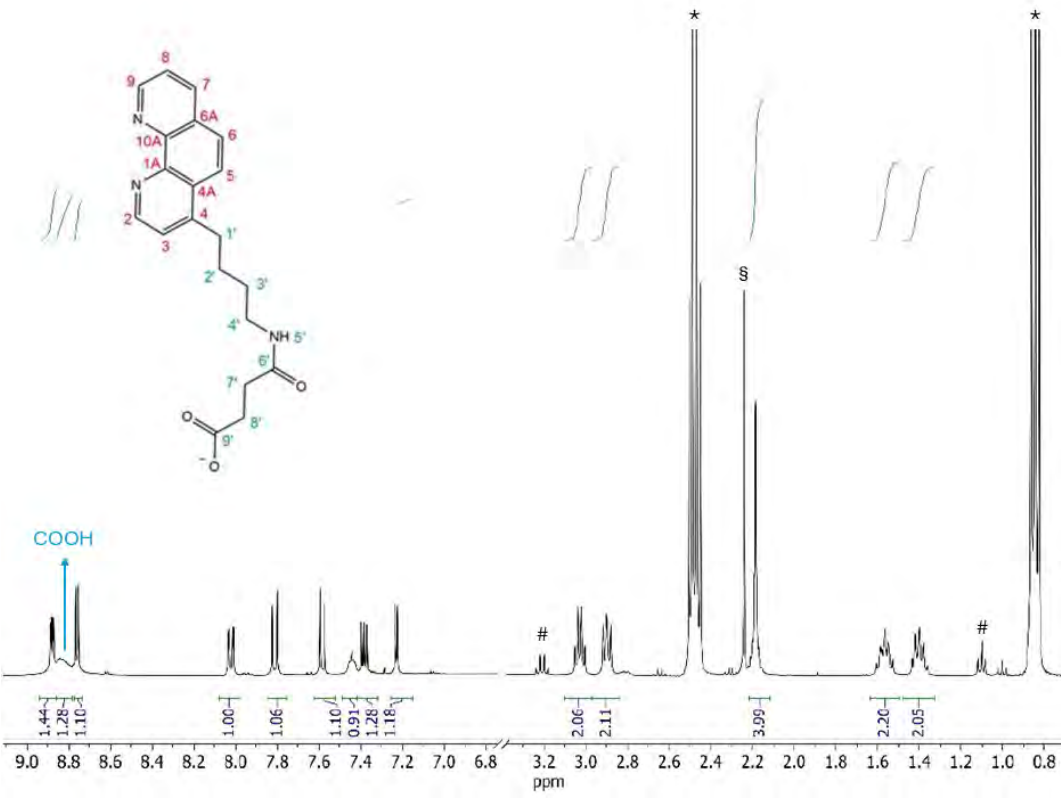

Figure 6. *^{1}H NMR (9.4 T, 300 K, CH_2Cl_2/$CDCl_3$) of crude phen-COOH. The * mark the signals assigned to TEA, # those of the protonated TEA and § the succinate residue.*

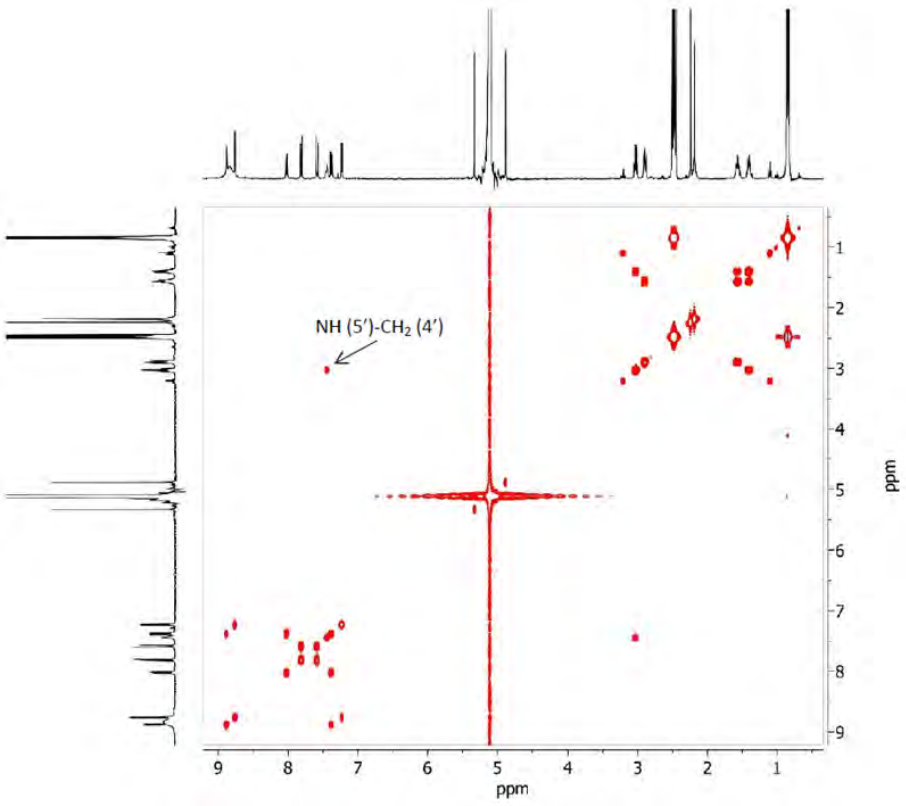

Figure 7. *^{1}H-^{1}H NMR COSY experiment (9.4 T, 300 K, CH_2Cl_2/$CDCl_3$) of crude phen-COOH.*

Preparation of the Ir precursor $[Ir(ppy)_2Cl]_2$

The two Ir(III) complexes employed in the coupling with the PNA chain were synthetized starting from a binuclear Ir precursor, in which each metal ion coordinates two phenylpyridine (ppy) ligands and two μ-Cl. The reaction was carried out according to the literature,[30-32] following a procedure schematized in Scheme 7.

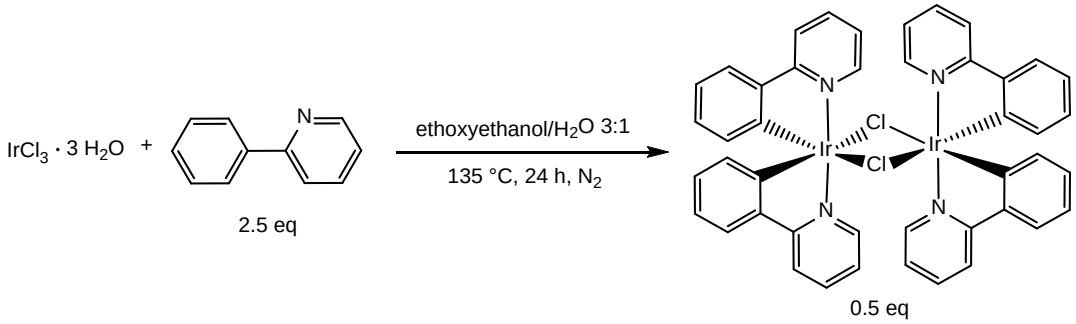

Scheme 7. *Synthesis of the binuclear Ir precursor $[Ir(ppy)_2Cl]_2$.*

Chloro-bridged binuclear complexes are vastly used in literature as precursors for luminescent Ir(III) complexes employed in a wide range of applications, such as photocatalysts, sensors and biologically active species.[33,34] The reason behind the use of ppy for the Ir coordination is the more readily metalation of a C^N compared to analogous N^N ligands (bpy, bipyridine) due the reduced reactivity of

a pyridine ring toward metalation, while the complexation of the phenyl ring might be considered as an electrophilic attack of the metal toward the electron-rich deprotonated C. Additionally, this kind of ligand is more suitable in the formation of chloro-bridges dinuclear species, due to the larger σ donation through the M-C bond compared to the M-N that produces an increased electron density at the metal center, while ligands as bpy and phen tend to form mononuclear species under similar synthetic conditions.[32]

The ^{1}H NMR spectrum of the product, recovered after filtration, showed the isolation on the sole binuclear complex (Figure 8), in which the chemical shifts of the ppy are different from those reported in the literature both in CD_2Cl_2[35] and in $CDCl_3$[36], further confirming the successful metalation of ppy.

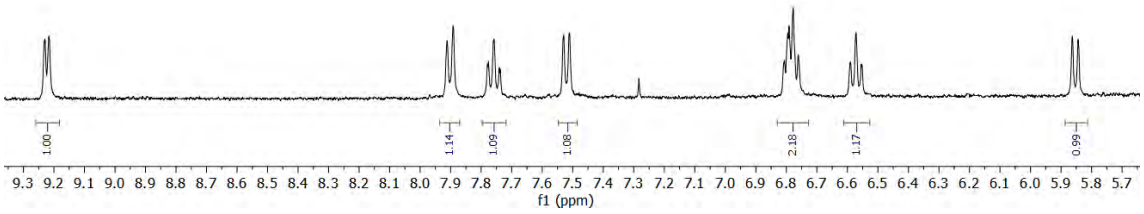

Figure 8. *^{1}H NMR (9.4 T, 300 K, $CH_2Cl_2/CDCl_3$) of the filtered $[Ir(ppy)_2Cl]_2$ bimetallic Ir precursor.*

However, the yield of this kind of binuclear Ir complexes is lower than when other transition metals (as Rh) are used, due to the formation of mononuclear byproducts.[32] For this reason, after the isolation of $[Ir(ppy)_2Cl]_2$ from the crude mixture, we attempted to further move the reaction toward the formation of the bimetallic product, inspired from a literature study that exploit MW heating to increase the yields of these reactions.[34] The supernatant recovered after the filtration of the product was analyzed by NMR to confirm the absence of the bimetallic product and the presence of undefined mononuclear species. However, after 40 minutes of MW heating in a sealed vessel the dimer product was not further formed in the mixture (Figure 9), possibly due to the absence of the volatile HCl in the vessel after filtering the product of the reaction carried out refluxing or due to consumption during the previous reaction through its side reaction with alcohol.[37] The presence of HCl, produced during the cyclometallation, of other Lewis's acids resulted indeed essential in shifting the equilibrium toward the formation of the binuclear species.[38]

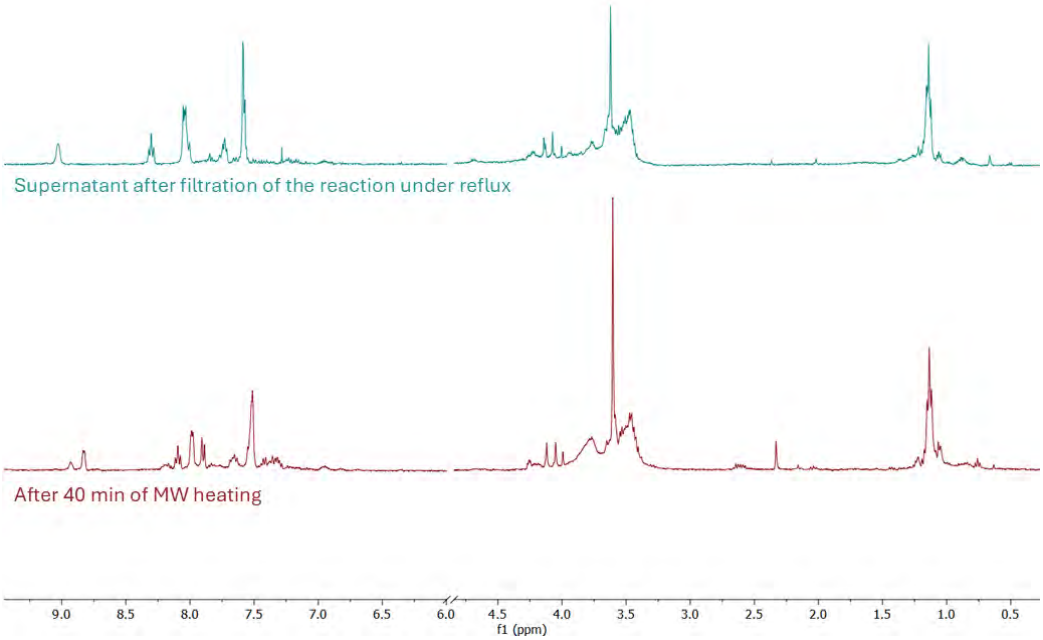

Figure 9. *^{1}H NMR (9.4 T, 300 K, D_2O) of the supernatant recovered after filtration of the binuclear product (blue trace) and of the same mixture after 40 min heating by MW irradiation (red trace).*

Synthesis of the Ir complexes (Ir-COOH and Ir-NH_2)

The two phenanthroline ligands phen-NH_2 and phen-COOH were employed in the preparation of the two Ir complexes used in each of the two strategies to prepare the Ir-PNA conjugate, refluxing the substituted phenanthrolines with the binuclear $[Ir(ppy)_2Cl]_2$ in a THF:H_2O mixture, obtaining respectively Ir-NH_2 (schematized in Scheme 8) and Ir-COOH (Scheme 9).

The protocol followed to prepare Ir-NH_2 was slightly different from a procedure previously used by our group to prepare the same complex.[4] The variations introduced in this work allowed us to increase the yield from 69% to 94% and the product, analyzed with ^{1}H NMR (Figure 10) resulted equal to the complex already prepared before.

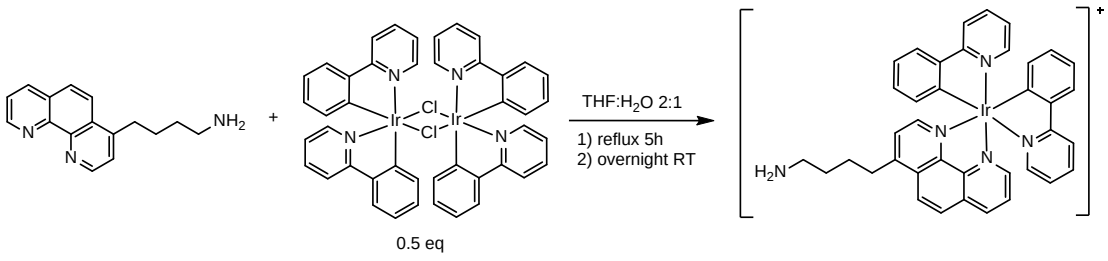

Scheme 8. *Synthesis of the Ir-NH_2 complex.*

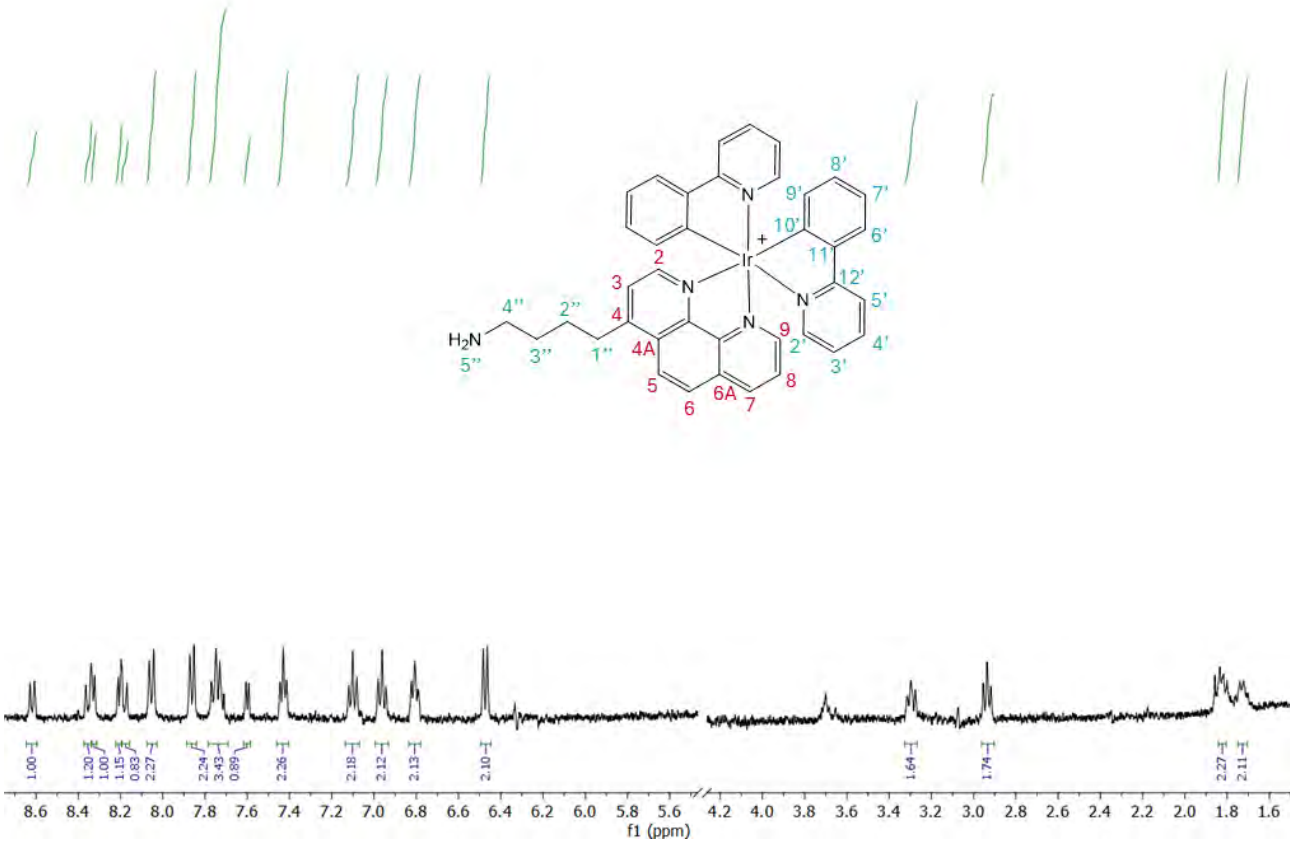

Figure 10. *^{1}H NMR (9.4 T, 300 K, D_2O) of the Ir-NH_2 complex.*

On the other hand, the Ir-COOH complex was prepared similarly to Ir-NH_2, further increasing the THF content due to solubility issues of the reagents, obtaining a slightly higher yield compared to that of Ir-NH_2 (96%). The isolated complex was fully characterized by NMR spectroscopy (in Figure 11 is reported only the ^{1}H experiment) and MS-ESI^{+} (Figure 12), confirming the success in the complex preparation as a zwitterion, where the remaining positive charge of Ir(III) results neutralized by the deprotonated carboxylate terminal group.

The attribution of the proton signals of the complex was not trivial, due to the high numerosity of signals in the spectrum. A NOE cross peak between CH_2 (1'') and CH_2 (2'') in the ^{1}H-^{1}H NOESY spectrum allowed the identification of the protons CH (3) and CH (5) of the phenathroline ligand. CH (2) and CH (6) were identified through the scalar correlation in a ^{1}H-^{1}H COSY experiment with CH (3) and CH (5) respectively, as well as the development of a NOE. Scalar and dipolar correlations in ^{1}H-^{13}C HMBC experiments were exploited to attribute signals of CH(8) and CH(7), once attributed the signal at 8.76 ppm to CH (9) and the CH_2 (3'') and CH_2 (4'') were assigned consequently. From the signal at 8.14 ppm, attributed to CH(2') of the ppy ligandall the other protonic signals of the ligand were assigned through a ^{1}H-^{13}C HMBC experiment, except for the protons a CH (5') and CH (6') identified from a dipolar correlation in the ^{1}H-^{1}H NOESY spectrum.

The MS-ESI$^+$ spectrum shows the molecular peak of the complex at 852.68 m/z as the main signal, while the less intense peaks at 890.35 m/z and 874.48 m/z are assigned to the complex with the addition of a K^+ and a Na^+ respectively, while the one at 752.61 m/t to a fragmentation of the amide bond, causing the loss of a $C(O)CH_2CH_2COOH$ fragment.[39]

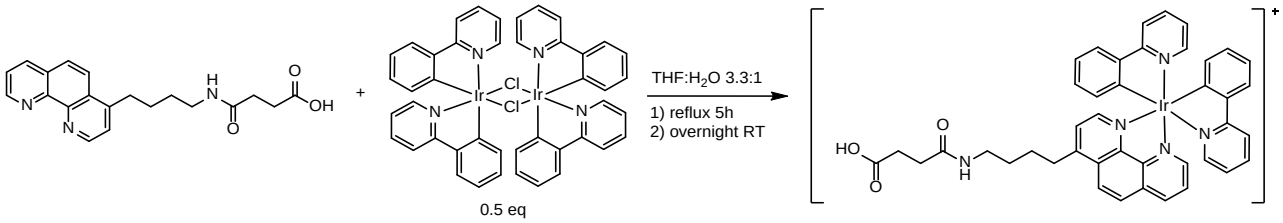

Scheme 9. *Synthesis of the Ir-COOH complex.*

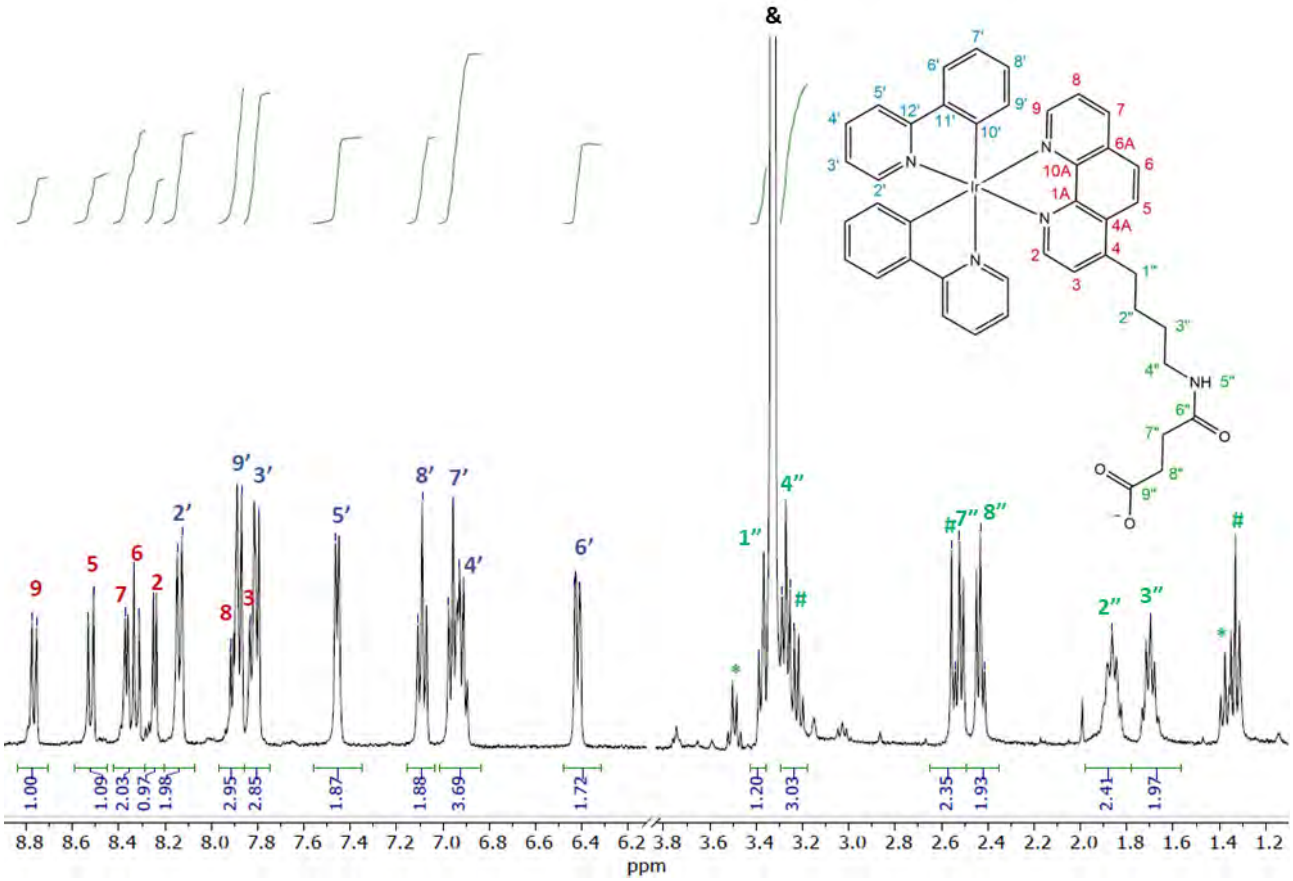

Figure 11. *^{1}H NMR (9.4 T, 300 K, MeOD) of the Ir-COOH complex. # marks triethylammonium succinate, * triethylammonium chloride, and & the residual solvent.*

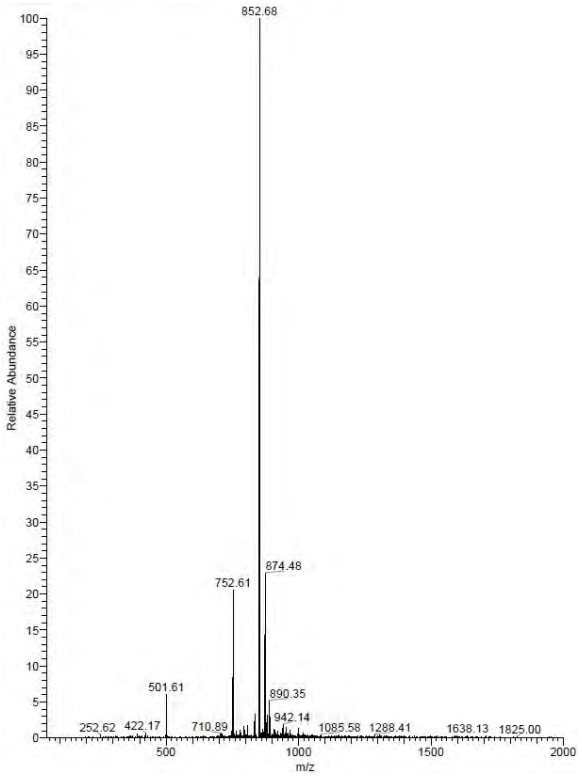

Figure 12. *MS-ESI$^+$ spectrum of Ir-COOH.*

Chemical stability of Ir-NH_2 under cleavage conditions

Before coupling the two Ir complexes to the PNA tetramer, the stability of Ir-NH_2 under the cleavage conditions of PNA from the resin was tested. The UV-vis spectra of the complex dissolved in a mixture of TFA:*m*-cresol 9:1 were recorded over 1.5 h, the time required to cleave the Ir-PNA conjugate from the resin. Figure 13 shows that the MLCT bands of the complex remained unvaried in all the spectra, confirming its stability in these conditions, in agreement with what reported in the literature for similar cyclometalated Ir(III) complexes.[8] We thus assumed the same high stability for Ir-COOH as well.

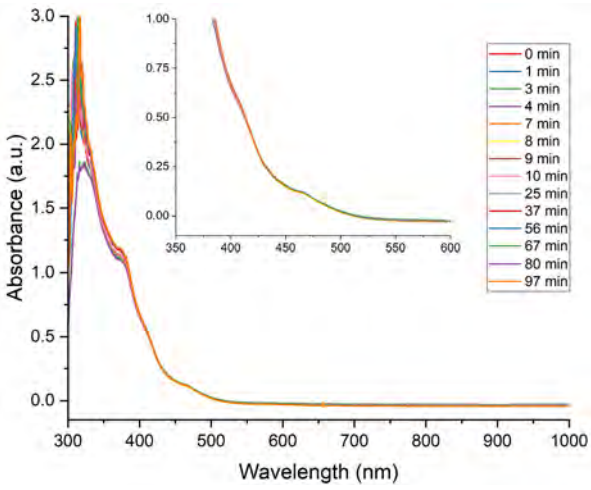

Figure 13. *UV-vis spectra of Ir-NH_2 in a mixture of TFA/m-cresol 9:1 recorded over 1.5 h at RT. The inset shows a magnification of the MLCT bands of the complex.*

Photophysical characterization of Ir-COOH and Ir-PNA

The absorption and emission spectra of Ir-COOH, Ir-PNA, as well as the absorption spectrum of the PNA tetramer, are shown in right panel of Figure 14, while in Table 1 their photophysical features are listed.

The UV-vis absorption spectrum of Ir-COOH displays intense absorption bands in the ultraviolet region at ca. 220-300 nm, assigned to spin-allowed π-π*ligand centred ^{1}LC transitions, depending the bands between 220-250 nm mainly on ppy-centred transitions, while those between 250-290 nm on the phenanthroline ligand, accordingly to the literature data[40,41]. Other than these, the two MLCT bands in the visible range (350-420 nm) are mainly attributed to the spin-allowed ^{1}MLCT transition from filled t_{2g} orbitals of Ir(III) to a vacant π* orbital of the phenanthroline ligand. However, being the HOMO of Ir(III) cyclometalated compounds significantly delocalized over the C^N ligands, with a large participation also of the Ir–C^- σ bond orbital, due to its high covalent character, the absorption bands in this region might also be attributed to ^{1}SBLCT (σ bond to ligand charge transfer).[41,42] Finally the absorption bands at ca. 470 nm are assigned to spin-forbidden CT transitions, visible in the spectrum due to the large spin–orbit coupling induced by the iridium center. The absorption profile of Ir-NH_2 (left panel of Figure 14) is completely superimposable, confirming that the functionalization of the pendant of the phenanthroline does not influence the absorption bands of the complexes due to the presence of the aliphatic chain that hampers any electronic conjugation. For the same reason, the conjugation of the complexes to the PNA chain does not affect their MLCT bands. The only visible differences are in the UV region, where a new band at 210 nm appears due to the PNA backbone transitions and the band at 260 nm intensifies due to the LC transitions of the purine bases.

Both Ir-COOH and Ir-PNA display photoluminescence emission bands in the yellow-orange range of the visible spectrum, attributable to ^{3}MLCT transitions. The maximum emission wavelength blue shifts from 590 nm to 582 nm when the Ir complex is conjugated with the PNA chain, while both the lifetime (τ) and the photoluminescence quantum yield (Φ) increase.

Table 1. *Photophysical data for the Ir-COOH complex and the Ir-PNA conjugate, measured in aerated MeOH solution at RT (λ_{exc}= 405 nm).*

Species	λ_{abs} (nm)	λ_{em} (nm)	τ (ns)	Φ (%)	k_r (s^{-1})[xii]	k_{nr} (s^{-1})[i]
Ir-COOH	377 (MLCT) 415 (MLCT)	590	33.0 (10%) 69.2 (90 %)	3.4	$4.9\cdot10^5$	$13.9\cdot10^6$
Ir-PNA	377 (MLCT) 415 (MLCT)	582	13.5 (6%) 80.3 (94%)	3.9	$4.8\cdot10^5$	$12.0\cdot10^6$

[xii] The radiative (k_r) and non-radiative (k_{nr}) decay constants of the excited states were calculated on the most significant lifetime component

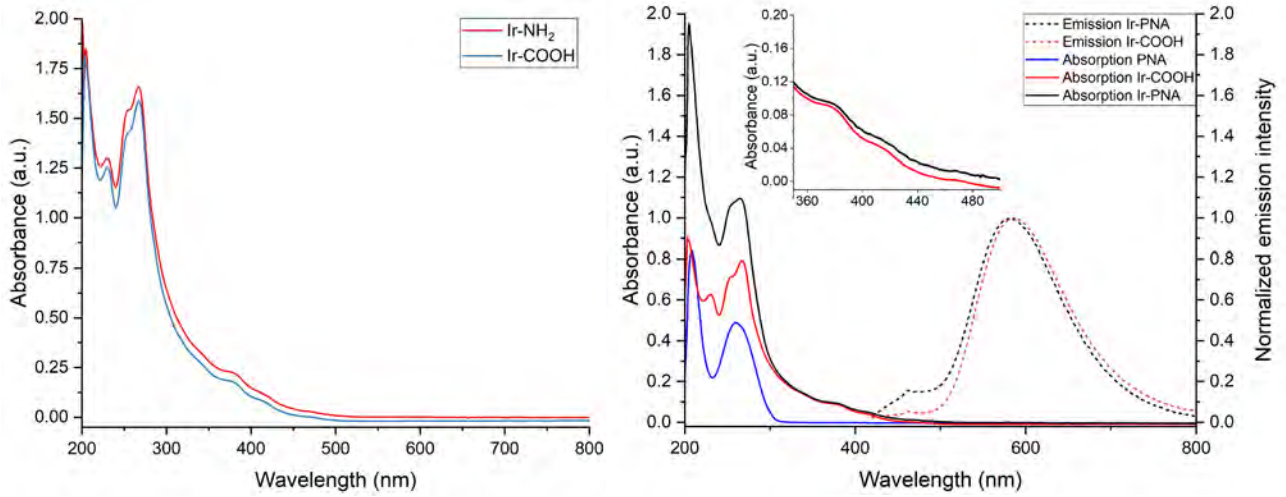

Figure 14. *Left panel: UV-vis absorption spectra of Ir-NH_2 (red trace) and Ir-COOH (blu trace) complexes, recorded in aerated MeOH solutions at RT. Right panel: UV-vis absorption (full lines) and emission (dashed lines, λ_{exc}= 405 nm) of Ir-COOH (red traces), Ir-PNA (black traces) and PNA tetramer (blue trace) recorded in aerated MeOH solutions at RT. The inset shows a magnification of the MLCT bands centered at 377 and 415 nm.*

UV-vis absorption (left panel of Figure 15) and emission (right panel of Figure 15) spectra of Ir-COOH were additionally recorded in various solvents with progressive polarity (in order: CH_2Cl_2, CH_3CN, and H_2O) and compared to the literature data[4] of Ir-NH_2 recorded in the same solvents. The progressive blue shift of the absorption bands in the visible range when the solvent polarity increases confirms their CT character.

Analogously, the CT character of the emission is confirmed by the maximum emission wavelength recorded in CH_2Cl_2 for both Ir-COOH and Ir-NH_2 (respectively 571 and 574 nm), slightly blue shifted compared to that of an analogous complex with the unsubstituted phenanthroline in the same solvent (582 nm)[43] due the weak electron donor ability of the aliphatic substituent. This wavelength red shifts when the polarity of the solvent increases for both Ir-COOH and Ir-NH_2 (Table 2), in agreement to the common trend of excited states having charge transfer character. Although this shift is usually associated with a progressive decrease of the photoluminescent quantum yield and a shortening of lifetimes, in agreement with the energy gap law, it is not observed in the Φ values of both complexes, while it results true only considering the shorter component of τ. This behavior suggests that Ir-COOH might partially nanoaggregate in polar solvents such as MeOH and water, as already observed for Ir-NH_2 complex,[4] that might govern their emission.

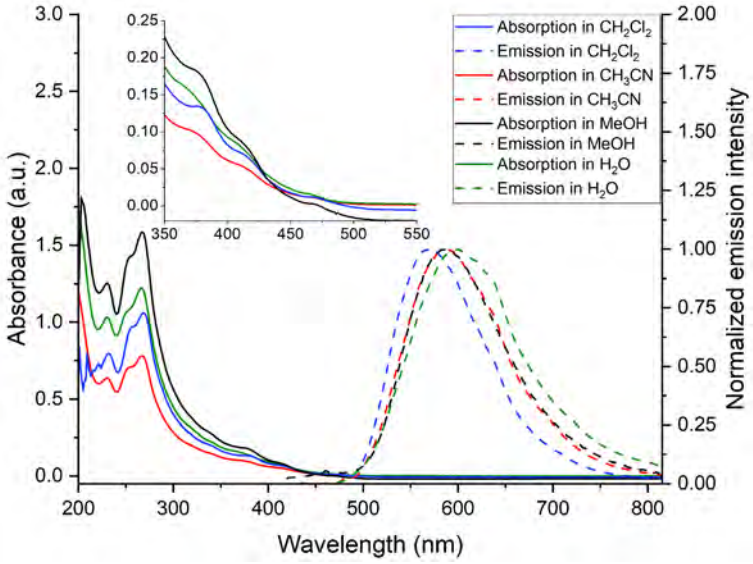

Figure 15. *Left panel: Absorption spectra (left panel) and emission spectra (right panel) of the Ir-COOH complex in CH_2Cl_2 (blue trace), CH_3CN (red trace), MeOH (black trace) and H_2O (green trace) recorded at RT in aerated conditions.*

Table 2. *Photophysical data for the Ir-COOH complex and Ir-NH_2 in CH_2Cl_2, CH_3CN, MeOH and H_2O, measured in aerated solutions at RT (λ_{exc}= 420 nm for Ir-COOH and 400 nm for Ir-NH_2).*

Complex	Solvent	λ_{abs} (nm)	λ_{em} (nm)	τ (ns)	Φ (%)	k_r (s^{-1})[i]	k_{nr} (s^{-1})[i]
Ir-COOH	CH_2Cl_2	381 415 472	571	128.3	8.4	$6.5\cdot10^5$	$7.1\cdot10^6$
	CH_3CN	374 415 470	585	56.9	2.7	$4.7\cdot10^5$	$1.7\cdot10^7$
	MeOH	377 415 470	590	33.0 (10%) 69.2 (90 %)	3.4	$4.9\cdot10^5$	$1.4\cdot10^7$
	H_2O	374 412 469	600	31.8 (3%) 113.4 (97%)	5.1	$4.5\cdot10^5$	$8.4\cdot10^6$
Ir-NH_2[xiii]	CH_2Cl_2	382 417	574	153	5.2	$3.4\cdot10^5$	$6.2\cdot10^6$
	CH_3CN	376 414	591	56	1.7	$3.1\cdot10^5$	$1.8\cdot10^7$
	H_2O	378 417	604	2 (2%) 116 (98%)	3.3	2.8	$8.3\cdot10^6$

To confirm this hypothesis, DLS size measurements of Ir-COOH were carried out in H_2O:CH_3CN mixtures with various ratios ranging from pure water to 3:7 (Figure 16) and its photophysical features were recorded in the same mixtures (Table 3). A progressive red shift of the emission maximum is observed with the increase of the water content in the mixture, while both fluorescence quantum yield and lifetime increase, the latter becoming progressively biexponential. Notably, in pure water a slight shortening of the main lifetime component and of Φ is observed, suggesting that water acts as a

[i] The radiative (k_r) and non-radiative (k_{nr}) decay constants of the excited states were calculated on the most significant lifetime component

[xiii] Data taken from Ref. 4

quencher, as confirmed by the 2-fold increase in the k_{nr} constant and in agreement with what reported in the literature for other fluorophores.[44] The DLS measurement show the appearance of larger populations when the content of water is increased, together with a intensification of the signal of scattered photons. In the size measurements by numbers appear clear that the dimension and the quantity of the nanoaggregates increases when the mixture becomes more polar. However, the biexponential character of τ suggests that they never account for the entire amount of compound present in the solution.

Table 3. *Photoluminescence data of Ir-COOH measured at room temperature in aerated mixtures of acetonitrile and water (1.1 x 10-5 M, λ_{ex} = 410 nm) and hydrodynamic diameter (d_H) measured by DLS. In pure acetonitrile and in H_2O:CH_3CN 9:1 the scattering signal was too low to be detected.*

H_2O:CH_3CN v/v ratio	λ_{em} (nm)	τ (ns)	Φ (%)	k_r (s^{-1})	k_{nr} (s^{-1})	d_H (nm)
10:0	600	31.8 (3%) 113.4 (97%)	5.1	$4.5 \cdot 10^5$	$8.4 \cdot 10^6$	1280 ± 476
9:1	598	26 (0.7%) 185 (99.3%)	8.4	$4.5 \cdot 10^5$	$4.9 \cdot 10^6$	712 ± 326
7:3	595	38(1%) 199 (99%)	9.3	$4.7 \cdot 10^5$	$4.5 \cdot 10^6$	105 ± 83
5:5	592	31 (1.3%) 138 (98.7%)	6.5	$4.7 \cdot 10^5$	$6.8 \cdot 10^6$	1.5 ± 0.4 295 ± 115
3:7	591	58 (4.6%) 103 (95.4%)	5.0	$4.8 \cdot 10^5$	$9.2 \cdot 10^6$	1.7 ± 0.7 255 ± 160
1:9	591	71.5	3.3	$5.6 \cdot 10^5$	$1.3 \cdot 10^7$	-
0:10	585	56.9	2.7	$4.7 \cdot 10^5$	$1.7 \cdot 10^7$	-

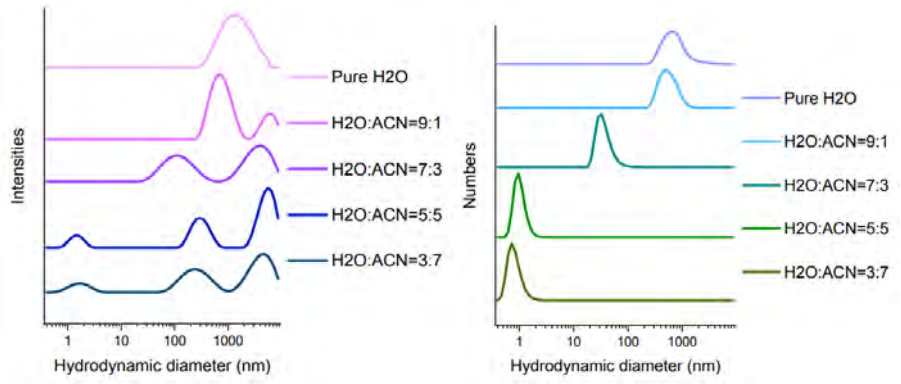

Figure 16. *DLS size measurements of Ir-COOH in H_2O:CH_3CN mixtures with decreasing polarity (from pure H_2O, the content of CH_3CN is increased to the ratios 9:1, 7:3, 5:5 and finally 3:7). The size distributions are shown by intensities (left panel) and by numbers (right panel).*

A DLS size measurement performed in MeOH solution at the same concentration as the photophysical characterization shows the presence of two populations (one attributed to the free molecule and one to the nanoaggregates at ca. 300 nm) in this solvent as well, as shown in Figure 17. Analogously, we expect this tendency to be further increased in Ir-PNA by the presence of the hydrophobic PNA chain, explaining the blue shift in the emission wavelength and the increase in Φ and τ already mentioned before. Thus,

we attributed the short component (33.0 and 13.5 ns for Ir-COOH and Ir-PNA, respectively) of τ to the free molecules, more affected by the presence of oxygen and more exposed to the polar solvent, while the longer component (69.2 and 80.3 ns for Ir-COOH and Ir-PNA, respectively) to the nanoaggregates.

Notably, the presence of these nanoaggregates was not visible in NMR spectra of Ir-COOH, that showed only the sharp signals of the non-aggregated fraction, being NMR spectroscopy silent to aggregates larger than 50 nm.

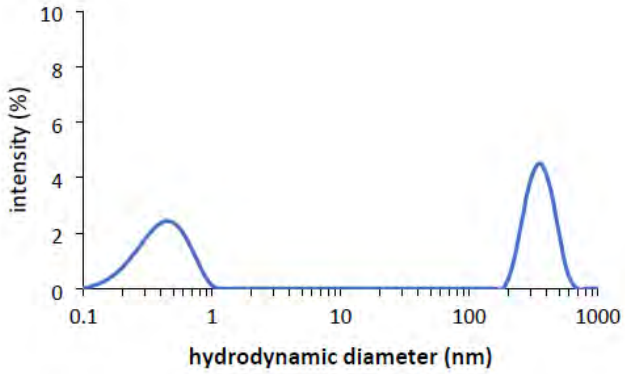

Figure 17. *DLS size measurements of Ir-COOH in MeOH at the same concentration used for the photoohysical characterization.*

Photostability of Ir-COOH and Ir-PNA

Two different lamps were employed to irradiate Ir-COOH and Ir-PNA in the $^1O_2$ generation experiments *in cuvette* and *in vitro* with HeLa cells (see the next two sections): the first one is a monochromatic LED emitting at 400 nm (with an emission intensity of 15.2 mW/cm^2), while the second is a low-intensity (5.2 mW/cm^2) commercial polychromatic lamp emitting in the 200-800 nm range. The emission profiles of the two irradiation sources are shown in Figure 18.

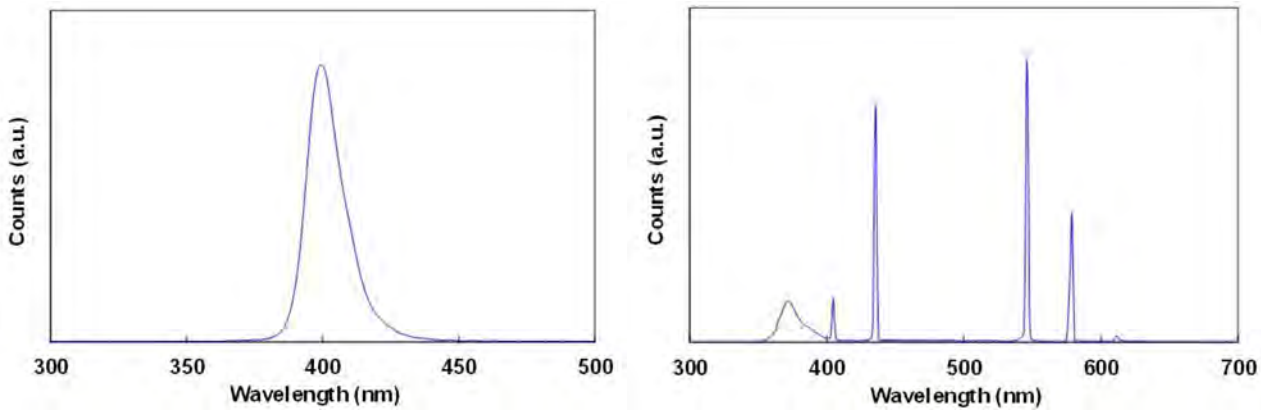

Figure 18. *Emission profiles of the UV-LED (left panel) and of the UV commercial lamp (right panel).*

First, the photostability of both compounds was assessed in O_2-saturated solutions at the same concentration used for the evaluation of $^1O_2$ production, irradiated with the UV LED for 20-30 min and

measuring the absorption spectra of the solutions every few minutes over all the irradiation time. The spectra shown in Figure 19 confirms the high photostability of both Ir-COOH and Ir-PNA and that the $^1O_2$ produced during the irradiation affected neither the Ir complex, nor the PNA chain.

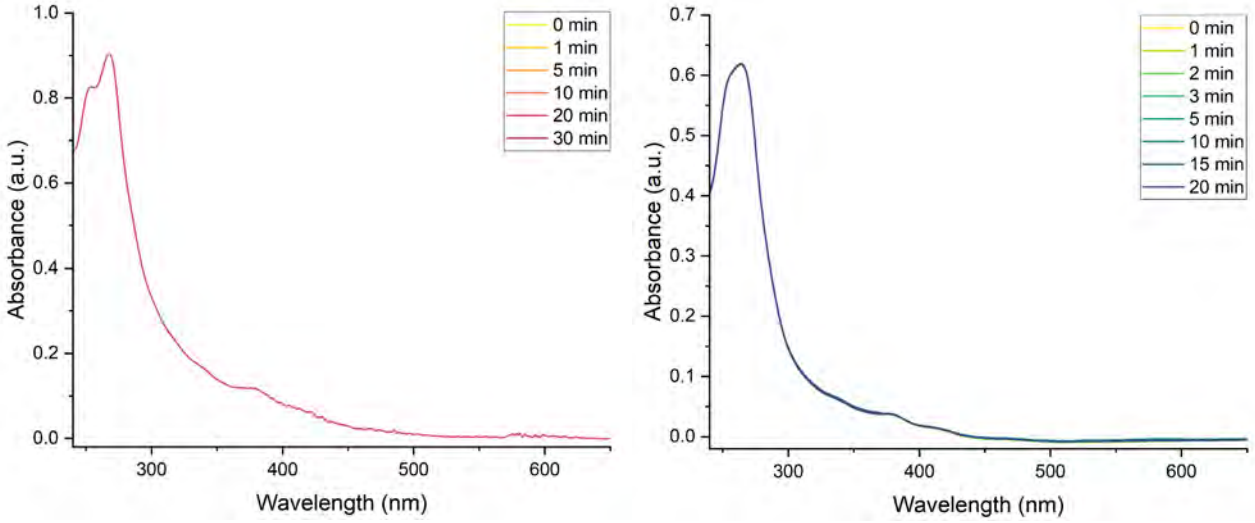

Figure 19. *UV-vis absorption spectra of Ir-COOH (left panel) and Ir-PNA (right panel) dissolved in MeOH and MeOH:CH_2Cl_2 9:1 respectively. The solutions were saturated with O_2 and irradiated with the UV LED for 20/30 min, recording spectra every few minutes.*

In cuvette $^1O_2$ generation by Ir-COOH and Ir-PNA with irradiation

To evaluate the ability of Ir-COOH and Ir-PNA to produce $^1O_2$ when irradiated, we employed 1,5-dihydroxynaphthalene (DHN) as an indirect reporter, consistently to what was done before for Ir-NH_2.[4] DHN is vastly used in the literature[45-47] as a scavenger for $^1O_2$, since it is photo-oxidized promptly, efficiently and selectively to 5-hydroxy-1,4-naphthalenedione (Juglone) by singlet oxygen, following the mechanism proposed in Scheme 10.[48] From the kinetics constant of the conversion of DHN to Juglone, k_r, it is thus possible to calculate the quantum yield for $^1O_2$ production of the photosensitizer (Φ_Δ), an index of the goodness of the compound to sensitize the conversion of molecular oxygen to $^1O_2$ when irradiated.

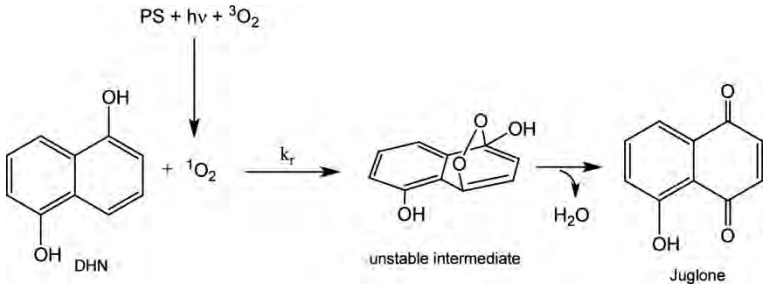

Scheme 10. *Schematization of the photo-oxidation of DHN to Juglone by $^1O_2$.*

A mixture of the photosensitizer and DHN with a 1:10 PS:DHN molar ratio in CH_2Cl_2:MeOH 9:1 was saturated with O_2 and irradiated with the UV LED at 400 nm, whose emission profile is shown in the left

panel of Figure 18, recording UV-vis spectra over the irradiation time (Figure 20). The decreasing bands assigned to DHN (300, 316 nm and 331 nm) were monitored over time, as well as the increasing one assigned to Juglone (430 nm). In particular, from the decreasing absorbance at 316 nm, the kinetic constant (k_{obs}) and the initial rate (v_0) of the conversion of DHN to Juglone were determined, by applying the steady-state approximation to the reactive $^1O_2$ and describing the equation rate of the reaction using the pseudo-first order kinetics (equations 1 and 2). Thus, k_{obs} indirectly monitors the $^1O_2$ produced by the photosensitizer. The k_{obs} values were calculated according to equation 3, from the slope of the linear fitting obtained by plotting the logarithm of the ratio between the absorbance of DHN after an irradiation time t and the initial absorbance of DHN before the irradiation vs the irradiation time.

$$v_0 = k_r[^1O_2][DHN] \quad \text{eq. 1}$$

$$v_0 = -\frac{d[DHN]}{dt} = k_{obs}[DHN] \quad \text{eq. 2}$$

$$ln\frac{[DHN]_t}{[DHN]_0} = ln\frac{A_t}{A_0} = k_{obs} \cdot t \quad \text{eq. 3}$$

The quantum yield of $^1O_2$ generation is determined according to equation 4[49]:

$$\Phi_\Delta = \Phi_\Delta^{std}\frac{v_0 \cdot I^{std}}{v_0^{std} \cdot I} \quad \text{eq. 4}$$

Where *I* represents the light absorbed by the photosensitizer (described by equation 5), expressed as moles of photons per minute, and in this case, having considered the emission of the UV LED monochromatic, it was calculated only at the 400 nm wavelength. On the contrary, for a polychromatic lamp it consists in the sum of the light absorbed at all the wavelengths at which the lamp emits, according to equation 6.

$$I = I_{source\ (400\ nm)}(1 - 10^{A(400\ nm)}) \quad \text{eq. 5}$$

$$I = \sum_{\lambda_i}^{\lambda_f} I_{source}(1 - 10^{A(\lambda)}) \quad \text{eq. 6}$$

Being I_{source} the light emitted by the light source at the wavelength λ (in the λ_i-λ_f range) and A(λ) the absorbance of the photosensitizer at such wavelength.

The *std* apex in equation 4 marks the values for the adopted standard, which in our case corresponds to the $Ir(ppy)_3$ complex, whose generation of $^1O_2$ in CH_2Cl_2/methanol 9:1 is known and fixed to $\Phi_\Delta = 0.50$.[45]

The experimental k_{obs} and v_0 values of Ir-COOH, Ir-PNA and $Ir(ppy)_3$ and the relative Φ_Δ, calculated for Ir-COOH and Ir-PNA based on the literature Φ_Δ value for $Ir(ppy)_3$ are listed in Table 4.

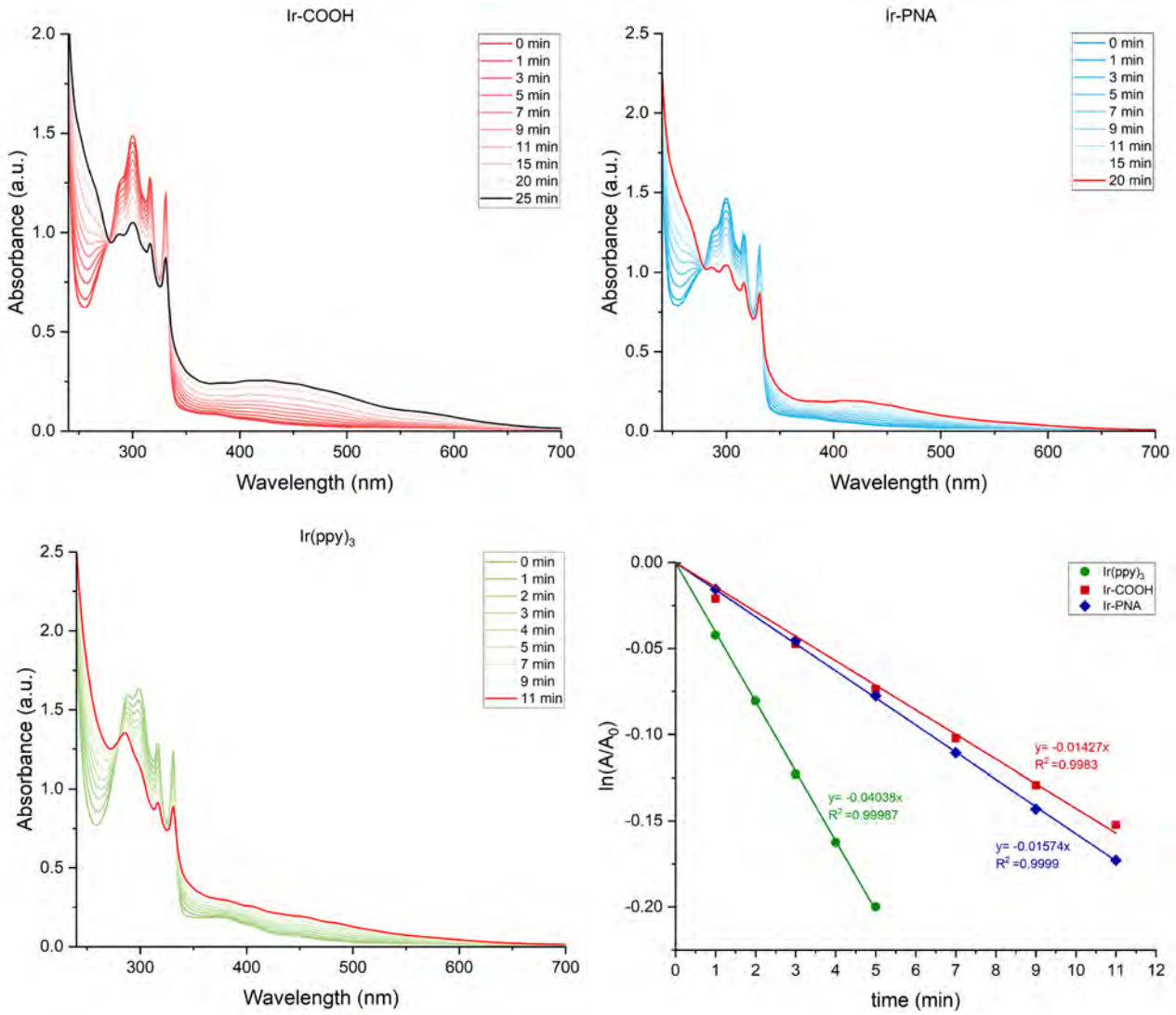

Figure 20. *Evolution of UV–vis absorption spectra of CH_2Cl_2:methanol 9:1 solutions containing a mixture of DHN ($1.7 \cdot 10^{-4}$ M) and either Ir-COOH ($1.27 \cdot 10^{-5}$ M) (red traces), Ir-PNA ($1.12 \cdot 10^{-5}$ M) (blue traces) or Ir(ppy)$_3$ ($1.18 \cdot 10^{-5}$ M) irradiated for several minutes with the monochromatic UV LED emitting at 400 nm. The last panel shows a comparison of the semilogarithmic plots of DHN consumption as a function of the irradiation time registered for the investigated sensitizers, with A_t and A_0 indicating the DHN absorbance at 318 nm registered at irradiation times t and 0, respectively.*

Table 4. *Experimental kinetic constant (k_{obs}), initial rate (v_0) of the photo-oxidation of DHN to Juglone and the estimated quantum yield for $^1O_2$ (Φ_Δ) of Ir-COOH and Ir-PNA in CH_2Cl_2:MeOH when irradiated with the UV LED emitting at 400 nm.*

Species	k_{obs} (min^{-1})	v_0 ($M\ min^{-1}$)	I at 400 nm ($mol\ min^{-1}$)	ΦΔ
Ir-COOH	0.01427	$2.44 \cdot 10^{-6}$	$2.83 \cdot 10^{-7}$	0.44
Ir-PNA	0.01574	$2.60 \cdot 10^{-6}$	$2.48 \cdot 10^{-7}$	0.54
Ir(ppy)$_3$	0.04038	$6.82 \cdot 10^{-6}$	$7.00 \cdot 10^{-7}$	0.50[xiv]

Additionally, we evaluated the same photoreaction by irradiating the photosensitizer in the same solvent mixture using the commercial lamp (right panel of Figure 18), since the UV LED was not suitable for the PDT treatment on cells (see next section) due to geometric issues. The UV-vis spectra recorded during

[xiv] Literature data from Ref. 45

the irradiation using the three Ir complexes as photosensitizers for $^1O_2$ production and the corresponding plots to calculate the k_{obs} values are shown in Figure 21.

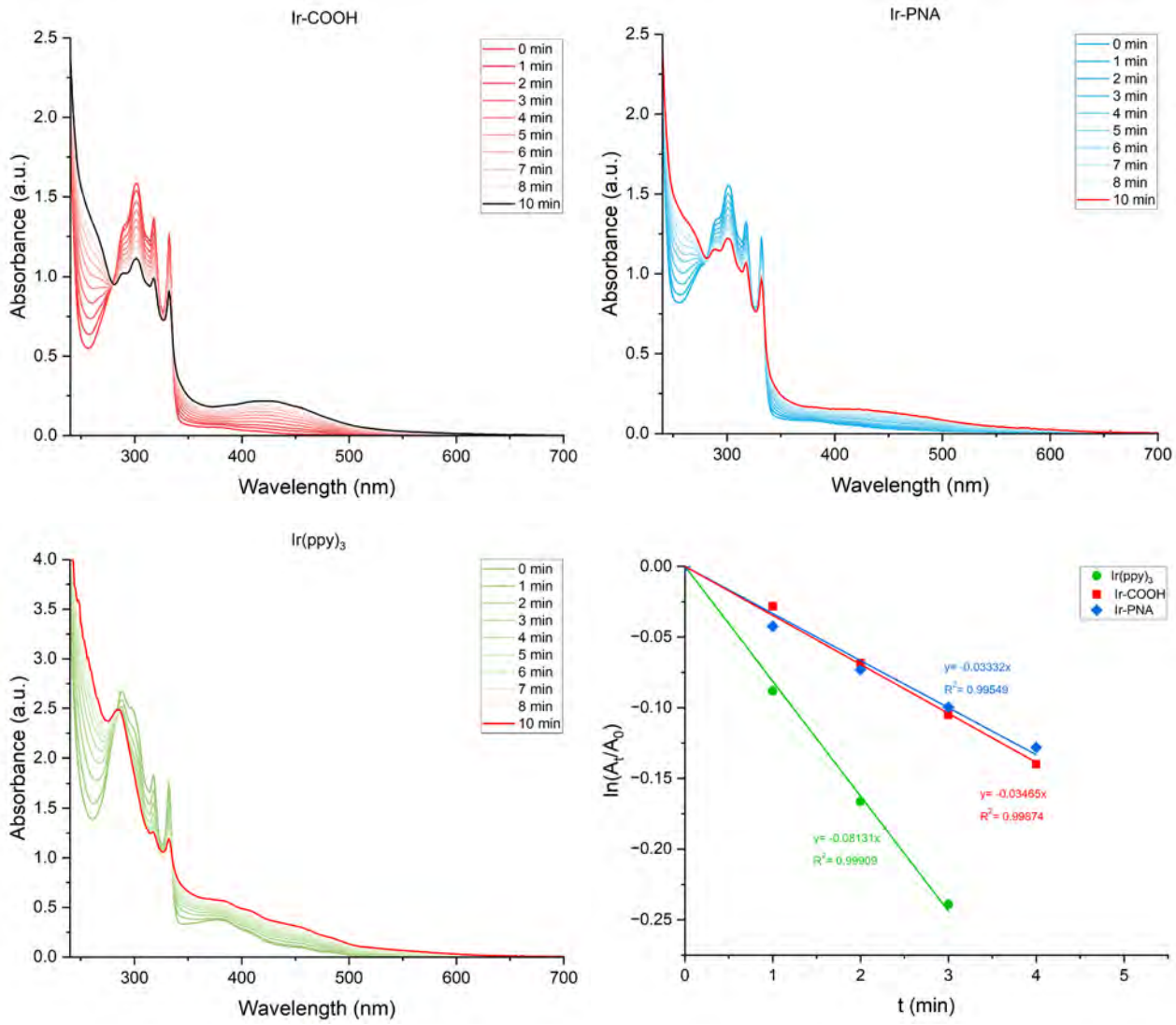

Figure 21. *Evolution of UV–vis absorption spectra of CH_2Cl_2:methanol 9:1 solutions containing a mixture of DHN ($1.8 \cdot 10^{-4}$ M) and either Ir-COOH ($1.3 \cdot 10^{-5}$ M) (red traces), Ir-PNA ($1.12 \cdot 10^{-5}$ M) (blue traces) or Ir(ppy)$_3$ ($2 \cdot 10^{-5}$ M) irradiated for several minutes with the commercial UV lamp emitting in the 200-800 nm range. The last panel shows a comparison of the semilogarithmic plots of DHN consumption as a function of the irradiation time registered for the investigated sensitizers, with A_t and A_0 indicating the DHN absorbance at 316 nm registered at irradiation times t and 0, respectively.*

Biological investigation

Photocytotoxicity of Ir-COOH and Ir-PNA

Due to the limited solubility of both Ir-COOH and Ir-PNA in water we used MeOH as vehicle for the biological investigation, by preparing concentrated solutions of the two compounds and diluting 1000x with cell culture medium. Thus, we carried out a first experiment treating HeLa cells with increasing amounts of methanol (1-4 µL to be diluted to 250 µL), confirming that the vehicle solvent was not cytotoxic for the cells in the concentrations we intended to use to solubilize Ir-COOH and Ir-PNA (Figure 22).

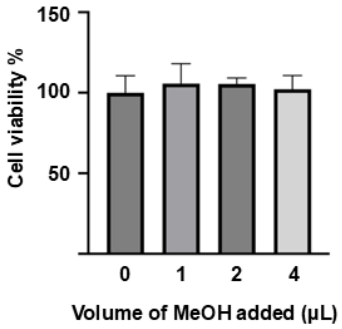

Figure 22. *Viability assay of untreated cells or treated with 1, 2 or 4 µL of MeOH. The graph represents the mean relative absorbance (Abs ± SD for 4 independent samples).*

Firstly, we optimized the irradiation time to confirm that the irradiation with the lamp was not harmful for the cells *per se* and that any photo-cytotoxicity observed in the subsequent PDT treatment employing Ir-COOH and Ir-PNA would only depend on the generation of $^1O_2$ by the two compounds. Untreated HeLa cells, seeded in 24-well plates, were irradiated for either 10, 20 or 30 minutes, while the second plate was covered and kept in the dark, outside of the incubator for the same amount of time, i.e. in the very same conditions as the irradiated plate. The irradiation was carried out with the commercial lamp whose emission profile is shown in the right panel of Figure 18 and temperature of the irradiated plate was monitored during all the irradiation time to remain at ca. 37 °C to prevent overheating caused by the lamp. The results of this preliminary experiment are shown in Figure 23, showing that none of the attempted irradiation times resulted toxic for the cells, their viability being

always higher than 90%, without any difference between the irradiated plate and the respective non-irradiated one.

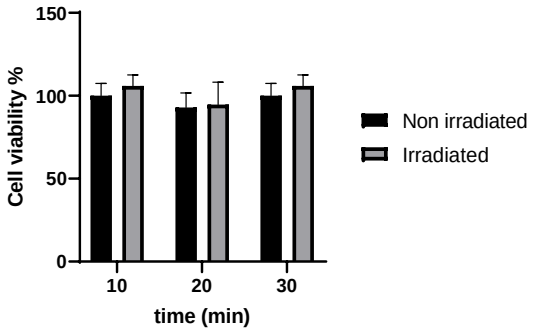

Figure 23. *Viability assay of untreated cells irradiated for 10, 20 or 30 min (black bars) or kept in the dark outside of the incubator for the same time (grey bars). The graph represents the mean relative absorbance (Abs ± SD for 4 independent samples).*

Having ascertained that neither 4 µL of methanol nor 30 min of irradiation toxic for the cells and the photostability of both Ir-COOH and Ir-PNA, their photocytotoxicity toward HeLa cells was determined, following the protocol schematized in Scheme 11. HeLa cells, seeded in two 48-well plates, were treated with methanolic solutions of Ir-COOH and Ir-PNA, diluted with cell culture medium to reach concentrations in the 1-50 µM range. After 24 h of treatment, the medium was replaced with fresh one to remove the compound that was not taken up by cells. At this point one plate was irradiated outside of the incubator for 30 min, while the other was kept in the dark outside the incubator, as described above. The two plates were then additionally incubated for 6 h and, lastly, the cell viability was assessed by an MTT assay.

Scheme 11. *Schematic representation of the general protocol followed in the photocytotoxicity experiments. Picture made using Biorender software.*

In Figure 24 the results of photocytotoxicity experiments are shown. Cells treated with Ir-PNA showed high viability in the dark (>90%) at all the concentrations tested, while for Ir-COOH a certain dose-dependent cytotoxicity starting from the 10 µM concentration was detected. Analogously, in our previous work,[4] Ir-NH_2, displayed higher cytotoxicity in the dark toward HeLa cells in comparison to the corresponding conjugate with a PAA polymer.

In both cases, the irradiation induced stronger cytotoxicity that resulted higher for cells treated with Ir-COOH than with Ir-PNA. The dose–response curves for the two compounds, thus, were nonlinearly

fitted with a sigmoidal function to calculate dark and light EC_{50} values (i.e. the dose of drug required to reduce the cell viability to 50%), reported in Table 5, together with the corresponding phototherapeutic index (PI). The light EC_{50} calculated for Ir-PNA, ca. 5 times higher than the one of Ir-COOH, indicated a higher photo-cytotoxicity of the Ir complex when not conjugated to the PNA chain, in contrast with the results obtained in the experiments carried out in cuvette. However, it is noteworthy to highlight that the higher quantum yield of $^1O_2$ production in those experiments was calculated from experiments carried out in an apolar environment. On the other hand, the lower EC_{50} of Ir-PNA might be attributed to its low solubility in water and to its tendency to aggregate in vesicle-like structures, as observed in the two-photon microscopy pictures shown and discussed in the following section, that might trap the singlet oxygen produced during irradiation and hinder it from effectively reaching target biomolecules. Additionally, the higher cytotoxicity of Ir-COOH after the irradiation might possibly be seen as the sum of the $^1O_2$ generation with the intrinsic cytotoxicity that the complex already showed in the dark.

Nonetheless, the PI values calculated from the dark and light EC_{50} of the two compounds are lower than the values reported in the literature[7,50,51] for similar cyclometalated Ir complexes, even though it is not easy to carry out an accurate comparison with the literature data, as the standardization of variables involved in the study would be necessary, such as the light dose (in terms of irradiation time, power of the lamp, and the spectral overlap between the emission profile of the lamp and the absorption spectrum of the photosensitizer) and the incubation time of the treated cells, both before and after irradiation.

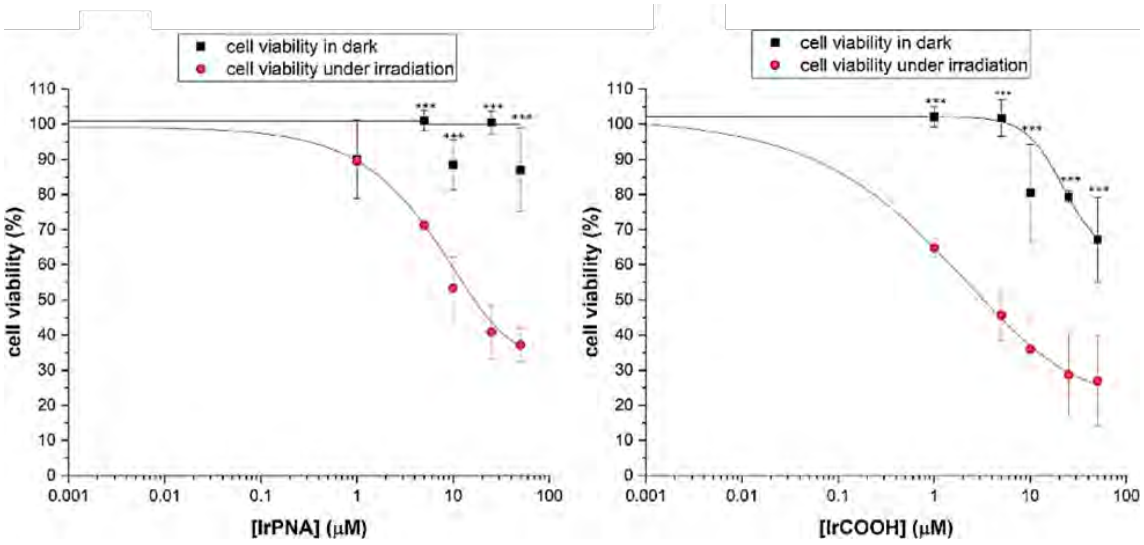

Figure 24. *Dose–response plots for HeLa cells treated with the Ir-PNA conjugate (left panel) and the Ir-COOH complex (right panel) in the 1-50 μM concentration range, both in the dark (black curves) and under UV irradiation. One-way ANOVA corrected for multiple comparison by Sidak's post hoc analysis was performed, ***p < 0.001. The dots in each graph represent the mean relative absorbance (Abs± SD for n= 4 independent samples).*

Table 5. *Cytotoxicity of Ir-COOH and Ir-PNA toward HeLa cells in the dark and after 30 min of irradiation, expressed in terms of EC_{50} (dark and light).*

Species	Dark EC_{50}	Light EC_{50}	PI[xv]
Ir-COOH	> 50 μM	3.5 μM	> 14.3
Ir-PNA	> 50 μM	18 μM	> 2.8

Additionally, we also carried out a cytotoxicity experiment without any irradiation of Ir-COOH and Ir-PNA on a non-cancerous cell line. We employed for this experiment NCS-34 cells, a hybrid cell line produced by the fusion of motor neuron enriched embryonic mouse spinal cord cells with mouse neuroblastoma. The cells were treated for 24 h with increasing concentrations of Ir-COOH, Ir-PNA and of the PNA tetramer (1-10 μM), using in all three cases methanol as vehicle to dissolve the three compounds, as described above. As shown in Figure 25, none of the compounds resulted cytotoxic toward this cell line in the concentration range tested. Nonetheless, it is difficult to make a comparison with the viability in the dark measured on HeLa cells treated with the same compounds, due to the large error bars associated with the cells treated with the 10 μM concentration, especially of Ir-COOH.

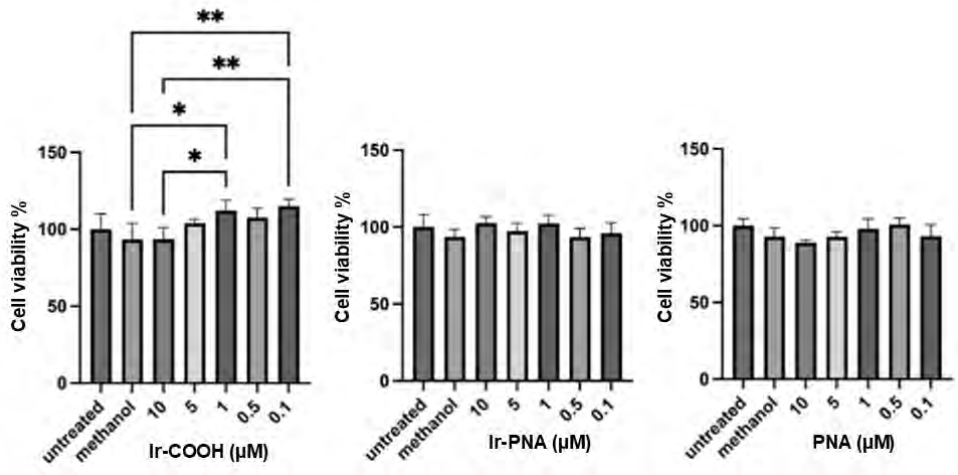

Figure 25. *Viability of NSC-34 cells after the treatment with various concentrations of Ir-COOH (left panel), Ir-PNA (middle panel) and the PNA tetramer (right panel) in the 1-10 μM range, using MeOH as vehicle. The first two columns of each panel show untreated cells and cells treated with the same volume of methanol. One-way ANOVA corrected for multiple comparison by Sidak's post hoc analysis was performed. The graphs represent the mean relative absorbance (Abs± SD for n= 4 independent samples).*

Internalization study of Ir-COOH and Ir-PNA using two-photon microscopy

Finally, two-photon microscopy pictures of HeLa cells treated with Ir-COOH and Ir-PNA were recorded to visualize differences in their uptake and location inside the cells. MeOH was used again as vehicle, having confirmed that its concentration after dilution in cell culture medium does not affect the viability of the cells. HeLa cells were treated with 25 μM solutions of the two compounds and incubated for 21

[xv] Phototherapeutic index, measured as the ratio between dark EC_{50} and light EC_{50}

h, after which live cells were visualized under the microscope, employing two-photon excitation (TPE) at 720 nm to excite the two Ir complexes. The pictures recorded at two different magnifications are shown in Figure 26. In all the panels the autofluorescence of the cells is visible in the blue channel (450-510 nm), marking their cytosol and attributed to the TPE of NADH, whose absorption takes place in the UV range with a maximum at 360 nm and emitting at 460 nm.[52] Additionally, cells treated with Ir-COOH and Ir-PNA show another emission in both the green (485-585 nm) and the red (560-640 nm) channels, consistent with their broad emission band. To confirm that the two compounds effectively localize inside the cells, the pictures with the highest magnification were recorded using z-scans (i.e. recording and overlaying multiple pictures over the z axis to comprehensively visualize the cell).

Ir-COOH and Ir-PNA resulted to be internalized by the cells with different efficiencies, as the emission of Ir-PNA is visible in all the cells within the frame while only part of those treated with Ir-COOH show its emission. This difference implies that the internalization process might be easier for the positively charged Ir-PNA conjugate compared to Ir-COOH, which at physiological pH results in its zwitterionic form (with the residual positive charge of the metal center balanced by the terminal COO^-). Consistently, in our previous work,[4] also Ir-NH_2 was efficiently internalized by HeLa cells, possibly due to its positive charge. Moreover, the higher lipophilic character of Ir-PNA could facilitate its internalization as well.

Nevertheless, Ir-PNA appeared to aggregate inside the cells, mainly accumulating in the cytosol and in the nuclei, possibly due to its lipophilicity and thus its limited solubility in water. Differently, the Ir-COOH complex, when internalized, showed a more homogeneous distribution at the cytoplasm level without any emission coming from the nuclei. Further studies will be dedicated to better characterize the internalization mechanisms of Ir-PNA, together with co-localization studies. However, it is noteworthy that we carried out this measurement exploiting TPE of Ir-PNA and Ir-COOH, paving the way for future $^1O_2$ generation studies employing a NIR light source instead of the UV-vis one used in this work.

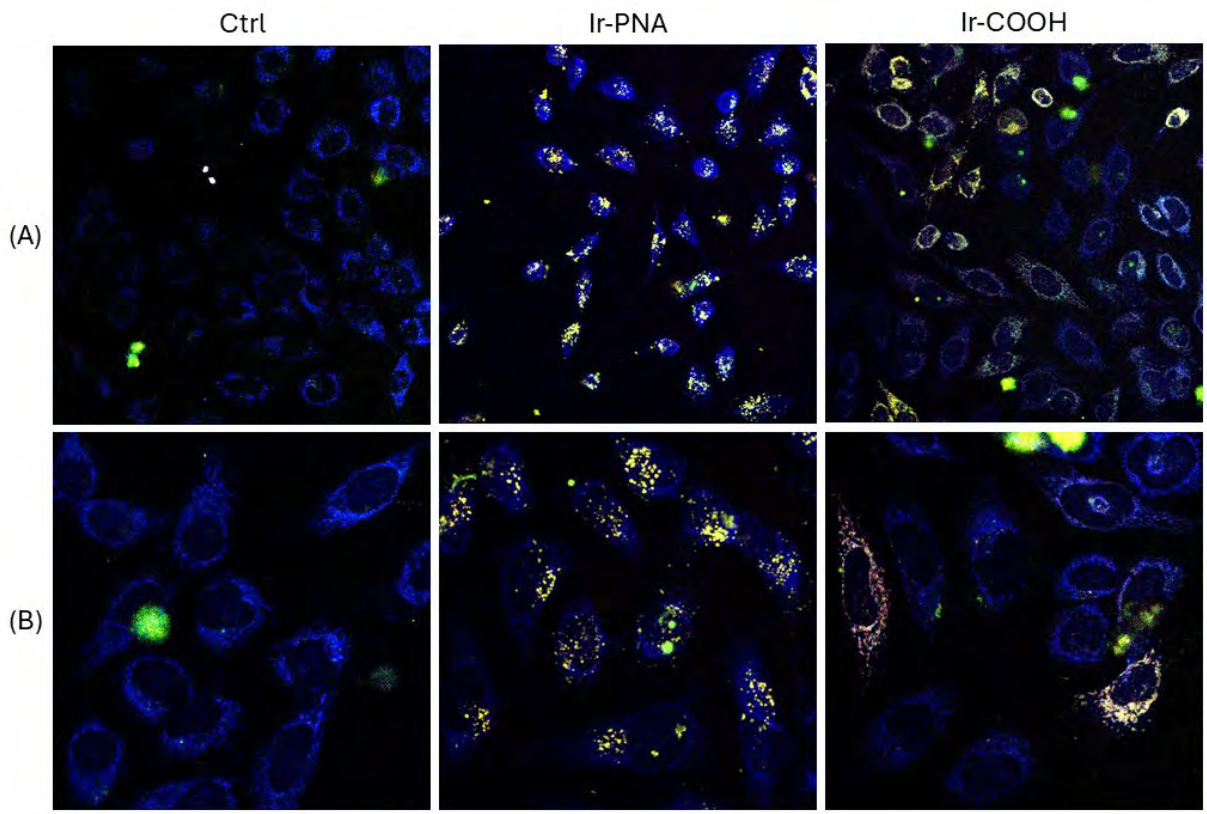

Figure 26. *TP microscopy images of HeLa cells only treated with MeOH (control, in the first column), treated with a 25 μM methanolic solution of Ir-PNA (in the second column) or Ir-COOH (third column) exciting with a TP 720 nm laser and recording the emission at 450-510 nm (blue channel), 485-585 nm (green channel) and 560-640 nm (red channel). Pictures were recorded at two distinct magnifications: 100x, 300 × 300 μm^2 field of view (row a) and 50x, 150 × 150 μm^2 field of view (row b). The z-scan images were acquired on the optical axis at 1 μm intervals.*

Conclusions

This project aimed at the preparation of a bioconjugate made of a cyclometalated Ir(III) complex and a PNA chain, to obtain a dual therapeutic agent based first on the ability of the complex to sensitize the formation of $^1O_2$ from molecular oxygen in PDT and to possibly combine it with an antigene/antisense strategy promoted by a specific PNA sequence. However, in this preliminary work, we focused mainly on the preparation of a model bioconjugate as a proof of concept, by preparing a PNA tetramer with a standard sequence and attempting two different coupling strategies to obtain Ir-PNA. We focused a wide part of the work also on developing a synthetic strategy to prepare an Ir complex bearing a terminal carboxylic group (Ir-COOH) to be employed in one of the conjugation strategies. Moreover, we fully characterized the photophysical features of the Ir-PNA compound and compared them with those of the Ir complex before its conjugation with the PNA sequence. The maximum emission wavelength of Ir-PNA resulted slightly blue shifted compared to the Ir-COOH complex (from 590 nm to 582 nm) and the photoluminescence quantum yield (Φ) increased (3.4% for Ir-COOH vs 3.9% for Ir-PNA, respectively), possibly due to the more apolar surroundings promoted by the presence of the lipophilic PNA chain. The lifetimes (τ) of both compounds resulted well-fitted by a biexponential fit, suggesting that the

compounds might partially aggregate in this solvent. We thus carried out a study on Ir-COOH, by measuring its photophysical features in various solvents, showing that, increasing the polarity, the red shift in the emission wavelength of the complex is not associated with the decrease of the Φ in those solvents in which the τ were biexponential and that the expected decrease in τ was true only considering its shorter component. This trend was the same observed by our group in a previous work on an analogous Ir(III) cyclometalated complex. DLS size measurements of Ir-COOH, carried out in solvent mixtures with increasing polarity confirmed the presence of nanoaggregates, whose size and amount depended on the solvent polarity, that governed the photophysical features of the compounds. The coexistence of the free molecule with the nanoaggregates was detected in MeOH as well.

Other than the synthesis and characterization, we especially focused on the PDT features of the bioconjugate, by comparing the singlet oxygen generation features and its behavior when used to treat cells to those of Ir-COOH. The $^1O_2$ generation under irradiation of the Ir-COOH complex was not affected by its conjugation to the PNA chain, after which, on contrary, seem to be produced more efficiently in a non-polar environment (Φ_Δ= 0.44 for Ir-COOH vs 0.54 for Ir-PNA in CH_2Cl_2:MeOH 9:1). Moreover, the presence of the PNA chain also affected the uptake of the Ir complex by HeLa cells and its localization inside. The enhanced uptake visualized for Ir-PNA might be due to a combination of the residual positive charge of the conjugate, that is known to facilitate the internalization of compounds by the cells, in comparison with the global neutral charge of Ir-COOH, that at physiological pH results in its zwitterionic form. Also, the higher lipophilicity brought by the PNA chain might possibly be another reason for its more efficient uptake. However, the conjugation of the PNA to the Ir complex also increases the internalization of the PNA chain, usually poor due to the neutral charge of their backbone. Nevertheless, inside the cells Ir-PNA appeared to aggregate in vesicle-like structures both in the cytosol and in the nuclei, possibly due to its lipophilicity and thus its limited solubility in water, while Ir-COOH when internalized, resulted more homogeneously distributed but only in the cytoplasm.

The *in vitro* PDT treatment on HeLa cells showed a dose dependent photocytotoxicity of both Ir-PNA and Ir-COOH, with a EC_{50} value after irradiation about five times lower for the latter (3.5 μM for Ir-COOH vs 18 μM), indicating its more efficient photo-induced cell death. This result, that at a first sight might be seen in contrast to the higher Φ_Δ obtained for Ir-PNA in the *in-cuvette* study, might be attributed to the low solubility in water of Ir-PNA and to its tendency to aggregate in vesicle-like structures inside the cells, that might trap and hider the produced $^1O_2$ from reaching target biomolecules. Additionally, it is noteworthy that Ir-PNA appeared cytotoxic only after irradiation, a fundamental feature when it comes to PS for PDT, while dose-dependent cytotoxicity in the dark was recorded for Ir-COOH. This dark cytotoxicity is consistent with what our group has previously observed on HeLa cells treated with an analogous Ir(III) cyclometalated complex.

To sum up, even if it is still a preliminary work, this study marks the first example of a conjugate between an iridium complex and a PNA tetramer, and although the literature contains notable examples of studies on PNA-metal complex conjugates, none have exploited them as PS for PDT. Overall, the Ir complex appears to transfer its beneficial properties to the conjugate by helping PNA to enter cells, while the PNA seems to mitigate the negative characteristics of the complex in terms of dark cytotoxicity. Moreover, Ir-PNA conjugated was successfully excited employing a TPE at 720 nm for its uptake study with TP microscopy, paving the way for a future study on two-photon $^1O_2$ generation to shift its absorption to the NIR spectral range at which light has the deepest penetration through tissues, increasing this way the *in vivo* efficiency of PDT.

Based on these results, the next step of the work will be to select an appropriate PNA sequence capable of acting as an antisense agent, and after conjugating it with the Ir-COOH complex, testing the corresponding Ir-PNA conjugate on different cell lines to study the potential synergistic effect between the antisense strategy and PDT in inducing the death of tumoral cells with respect to the two separate components.

Experimental

Materials and instruments

Ultrapure water (Milli-Q, Millipore, resistivity = 18 MΩcm^{-2}) was used for the preparation of the aqueous solutions. Commercial reagents were used without further purification. THF and CH_2Cl_2 were distilled respectively from sodium/benzophenone and from P_2O_5 just before their use. NMR experiments were acquired on a Bruker DRX400 spectrometer equipped with a Bruker 5 mm BBI Z-gradient probe head with a maximum gradient strength of 53.5 G/cm (π/2 pulse: 1 H 8.5 μs, 13C 13 μs) operating at 400.13 and 100.62 MHz for 1 H and 13C NMR, respectively. The ESI+ MS analyses were recorded with a Thermo Fisher LCQ Fleet ion trap mass spectrometer. Elemental C, H, and N analyses were performed on a PerkinElmer CHN 2400 instrument. High-resolution electrospray ionization mass spectrometry (HR-ESI+ MS) analyses were acquired in a positive polarity with a Synapt G2-Si QToF instrument (Waters) interfaced through a ZsprayTM ESI-probe for electrospray ionization (Waters). Data were processed with a MassLynxTM v4.2 software (Waters). UV–vis absorption spectra were acquired on a single beam Agilent model 8543 spectrophotometer equipped with a diode array detector using a 1 cm path length quartz cuvette at room temperature. Emission spectra were acquired by using an Edinburgh FLS980 spectrofluorimeter equipped with a 450 W xenon arc lamp. Emission spectra were corrected for source intensity (lamp and grating) and emission spectral response (detector and grating) by standard correction curves. The estimated experimental errors are 2 nm on the PL bands maxima. Time-resolved measurements were performed using the time-correlated singlephoton counting (TCSPC) option on the FLS980. The pulsed excitation source, an LED at 404 nm, was mounted directly on the sample chamber, and the emission was collected by a multichannel plate MCP-PMT Hamamatsu H10720–01 single photon-counting detector. The photons collected at the detector were correlated by a time-to-amplitude converter (TAC) to the excitation pulse. The data analysis was performed using the commercially available F980 software (Edinburgh Instruments). The goodness of the data fitting was

assessed by minimizing the reduced chi-squared function (χ^2). The uncertainty on fluorescence lifetimes is estimated to be ±0.05 ns. Photoluminescence quantum yields (Φ) were collected for an optically diluted solution (<10^{-5} M) using wavelength scanning with a Hamamatsu C11347−11 Quantaurus-QY absolute PL quantum yield spectrometer, equipped with a xenon light source (150 W), a monochromator, and a Spectralon integrating sphere, and employing the commercially available U6039−05 PLQY measurement software (Hamamatsu Photonics Ltd., Shizuoka, Japan). The photoluminescence quantum yields were measured by exciting the samples between 350 and 430 nm. Two-photon excitation (TPE) fluorescence microscopy experiments were conducted using a 720 nm excitation beam generated by a mode-locked Ti:sapphire laser (Mai Tai HP, Spectra Physics). The laser emits pulses with a duration of 120 fs full width at half-maximum and a repetition frequency of 80 MHz, delivering 20 mW of power at the sample plane. The optical setup comprises a confocal scanning head (M610 scanning mirrors module, ISS) integrated onto an upright optical microscope (BX51, Olympus), equipped with a high working distance objective (XLPlan, NA = 1.05, wd = 2 mm, 25x water immersion, Olympus). Fluorescence signals, collected in epifluorescence geometry by the same objective, were directed to a nondescanned detection unit and then transmitted to three Hamamatsu analog output photomultipliers (HC125−02, Hamamatsu). Sample emissions were filtered using 480/30, 535/50, and 600/40 band-pass filters to eliminate scattering contributions. Fluorescence data were processed by using the ISS Vista Vision Suite software (ISS). The microscopy images presented in this paper are the result of 4 averaged scans, with a residence time of 10 μs per pixel. The field of view for the 512 × 512 pixel images ranged from 300 to 50 μm^2, depending on the zoom factor employed. Z-scan images were acquired at 1 μm intervals. The photochemical stability test and photoreaction with DHN in the presence of investigated systems were monitored by employing a Jasco V-650 spectrophotometer. The experiments were performed by directly irradiating a 3 mL quartz cuvette with a monochromatic LED light with a maximum emission centered at 400 nm (BRIDGELUX, USA). The average full emission intensity reaching the cuvette corresponded to ca. 15.2 mW/cm^2, as regularly checked with a Thorlabs PM200 optical power meter equipped with a thermal Thorlabs S302C power sensor. For the MTT tests, formazan formation was measured spectrophotometrically using the microplate reader (PerkinElmer, EnSpire, Waltham, MA, USA). The phototoxicity tests on HeLa cells were carried out by using a low-intensity and mainly UV-light-emitting polychromatic irradiation source, with an average intensity emission of ca. 5.2 mW/cm^2 in the 200−800 nm range.

Attempt to isolate phen-NH_2 by extractions

The first attempt in the isolation of phen-NH_2 consisted in extractions at variable pH. The mixture containing phen-NH_2, phen-bisNH_2 and phen-Me was first dissolved in 10 mL of acid H_2O, then increasing the pH to ca. 6 with NaOH before the first extraction. Phen-Me was extracted from the mixture using CH_2Cl_2 (3 x 5 mL), the organic phases collected and the solvent evaporated. The pH of the aqueous solution was then increased to 9.18. Extractions with CH_2Cl_2 were carried out at this pH (3 x 5 mL), other two at pH 9.73 and additional two at pH 9.95. All these organic phases were collected and the solvent evaporated. Finally, the pH was further increased to 10.55, extracting twice with CH_2Cl_2 and the three times after increasing the pH to 11.05.

Protection of terminal amines of phen-NH_2 and phen-bisNH_2 with t-Boc

A mixture containing phen-NH_2 and phen-bisNH_2 (48.2 mg) was dissolved in 4 mL of dry CH_2Cl_2 and 87 µL of Et_3N were added (0.624 mmol, 4 eq calculated considering all the mixture as phen-bisNH_2) under N_2 protection. After 30 min stirring at RT, 86 µL of t-Boc were added (0.375 mmol, 2.4 eq considering all the mixture as phen-bisNH_2) and the mixture was left reacting overnight at RT under inert N_2 atmosphere. The following day the reaction solvent was evaporated and the solid first suspended three times in ethyl acetate to remove the Et_3N and finally washed with 2 mL of CH_2Cl_2. A TLC of the solid showed three spots with R_f= 0.95, 0.47 and 0 respectively (eluted with CH_2Cl_2:MeOH 9:1).

Isolation of phen-NH-Boc by gravimetric chromatography

The column was packed with 3.2 g of SiO_2 and the mixture containing the protected phen-NH_2 and phen-bisNH_2 were separated using an initial eluting mixture of CH_2Cl_2:MeOH 9:1, increasing the amount of MeOH first to the 8:2 and then to the 7.5:2.5 ratios. The fractions containing the substituted phenanthrolines were determined under UV light by depositing a spot of each on a TLC foil. The ^{1}H NMR spectra showed that fractions 3-5 contain phen-NHBoc, while fractions 6-10 a mixture of phen-NH_2 and phen-bisNH_2-monoBoc.

Synthesis of phen-COOH

19.5 mg of succinic anhydride (0.195 mmol) were dissolved in 2 mL of dry CH_2Cl_2 under N_2 inert atmosphere. Phen-NH_2 (49.1 mg, 0.195 mmol) and Et_3N (55 µL, 0.391 mmol, 2 eq) were added and the mixture was refluxed at 45 °C for 6 h. The next day, the mixture presented a small amount of a light brown sticky solid at the bottom of the flask and a light yellow clear supernatant solution. The solid was washed twice with CH_2Cl_2 at 40 °C, the supernatants containing the crude product combined and characterized by NMR in CH_2Cl_2/$CDCl_3$. ^{1}H NMR (9.4 T, 300 K, CH_2Cl_2/$CDCl_3$): δ 8.88 (1H, CH(9) dd, J = 4.5 Hz, 1.9 Hz), 8.7 (1H, CH(2) d, J = 4.7 Hz), 8.0 (1H, CH(7) dd, J = 8.2 Hz, 1.9 Hz), 7.8 (1H, CH(5) d J = 9.2 Hz), 7.6 (1H, CH(6)d J = 9.2 Hz), 7.3 (1H, CH(8) dd J = 8.2 Hz, 4.5 Hz), 7.2 (1H, CH(3) d J = 6.6 Hz), 7.45 (1H, CONH(5')), 3.0 (2H, CH2(4') m), 2.9 (2H, CH2(1') t J = 19.2 Hz), 2.2 (4H, CH2(7' and 8') m), 1.5 (2H, CH2(2') m), 1.4 (2H, CH2(3') m). ^{13}C NMR ((9.4 T, 300 K, CH_2Cl_2/$CDCl_3$): δ 178.4 (COO(9')), 173.5 (CONH(6')), 149.8 (CH(9)), 149.5 (CH(2)), 148.4 (Cq(1a)), 146.4 (Cq(10a)), 145.9 (Cq(4a)), 135.6 (CH(7)), 128.2 (Cq(6a)), 127.5 (Cq(4)), 125.9 (CH(6)), 122.8 (CH(3)), 122.6 (CH(8)), 122.2 (CH(5)), 38.4 (CH2(4')), 32.9 (CH2(7' and 8')), 31.8 (CH2(1')), 29.4 (CH2(3')), 27.5 (CH2(2')).

After the NMR characterization, Et_2O was added to the supernatants, causing the precipitation of a whitish solid. The dried residue was finally washed with CH_2Cl_2/Et_2O and vacuum-dried. Yield 49.6%. Elemental Analysis: C, 62.52%; H, 6.62%; N, 10.74% (calculated for $(C_{20}H_{21}N_3O_3)$-$(C_4O_4H_6)_{0.45}(C_6H_{15}NCl)_{0.6}$: C, 62.70%; H, 6.77%; N, 10.36%).

Synthesis of $[Ir(ppy)_2Cl]_2$

The Ir precursor $[Ir(ppy)_2Cl]_2$ was prepared partially following a combination of some literature procedures.[30-32] N_2 was fluxed in the solvent mixture, containing 7.5 mL of H_2O and 23 mL of ethoxyethanol, for 40 min before the reaction. 300.8 mg of $IrCl_3 \cdot 3H_2O$ (0.853 mmol) were suspended in the solvent mixture and, with the addition of 310 µL of ppy (2.127 mmol, 2.5 eq), the black suspension

turns brown and then greenish and yellow after heating. The mixture was refluxed at 135 °C for 24 h, cooled down to RT and filtered in N_2 inert atmosphere. The yellow solid was washed with 50 mL of absolute ethanol and 10 mL of diethyl ether and finally recovered from the filter by dissolution with 27 mL of CH_2Cl_2 and vacuum-dried, obtaining 251.6 mg of yellow powder. Yield 55.1%.

The supernatant recovered after filtration was heated with MW irradiation in an attempt to move the equilibrium toward the bimetallic product through two heating cycles at 150 °C in a sealed vessel (10 min + 30 min) for a total of 40 min, but no further product was obtained.

Synthesis of Ir-NH_2

Ir-NH_2 was prepared by slightly varying a procedure already used by our research group.[2] The Ir precursor $[Ir(ppy)_2Cl]_2$ (88.6 mg, 0.0827 mmol) was suspended in 20 mL of freshly distilled THF, obtaining a yellow suspension in which 40.8 mg of phen-NH_2 (0.163 mmol, 2 eq) were added, completely dissolved after the addition of 10 mL of H_2O. The mixture was heated at 70 °C under N_2 inert atmosphere, and after a few minutes, the cloudy yellow suspension turned completely clear. Once the set temperature was reached, it turned emerald green, denoting a slight defect of ligand. After heating the mixture for 5 h, a nominal slight excess of phen-NH_2 (3.2 mg, 0.0127 mmol, 0.15 eq) was added, turning the color to yellow-greenish. The reaction mixture was left under stirring at 70 °C for another 2 h and then at room temperature overnight. The clear yellow-greenish solution, which under UV lamp irradiation showed a yellow-orange emission, was evaporated by vacuum to dryness. The obtained fine solid was dissolved in a few mL of dry THF and treated twice with an excess of diethyl ether, obtaining a fine yellow precipitate. Yield 94% (124 mg). ^{1}H NMR (D_2O, 300 K, 9.4 T): δ phen-NH_2 ligand 8.62 (1H, CH(9)), 8.35 (1H, CH(5)), 8.32 (1H, CH(7)), 8.20 (1H, CH(2)), 8.18 (1H, CH(6)), 7.72 (1H, CH(8)), 7.60 (1H, CH(3)), 3.30 (2H, CH(δ)), 2.93 (2H, CH2(α)), 1.83 (2H, CH2(γ)), 1.73 (2H, CH2(β)); δ phenylpyridine ligands 8.1 (2H, CH(6')), 7.86 (2H, CH(3")), 7.74 (2H, CH(5')), 7.43 (2H, CH(3')), 7.1 (2H, CH(4")), 6.96 (2H, CH(5")), 6.81 (2H, CH(4')), 6.47 (2H, CH(6")).

Synthesis of Ir-COOH

The Ir precursor $[Ir(ppy)_2Cl]_2$ was added (48.1 mg, 0.045 mmol, 0.43 equiv) was added to a suspension of phen-COOH (37 mg, 0.105 mmol) in freshly distilled THF (20 mL) at room temperature under stirring and N_2 inert atmosphere. The mixture was first heated at 70 °C, but neither the Ir precursor nor the functionalized phenanthroline was soluble, even refluxing. Hence, after 30 min at 70 °C, the mixture was cooled down at room temperature and 6 mL of H_2O were added. Immediately the heterogeneous mixture became more homogeneous, and after a few minutes at 70 °C the mixture turned clear and yellow. The mixture was left under stirring at 70 °C for ca. 5 h and then was left overnight at room temperature. The obtained clear yellow mixture, which under UV lamp irradiation showed a yellow-orange emission, was evaporated by vacuum to dryness, and the residue was redissolved in a few mL of dry THF and treated twice with an excess of Et_2O to give a fine yellow precipitate. Yield 96.3% (80.2 mg, of which 3.1 mg are triethylammonium succinate). ^{1}H NMR (MeOD, 300 K, 9.4 T): δ phen-COOH ligand 8.76 (1H, CH(9) dd, J = 8.2 Hz, 1.9 Hz), 8.52 (1H, CH(5) d, J = 9.2 Hz), 8.37 (1H, CH(7) dd, J = 5.3 Hz, 1.9 Hz), 8.32 (1H, CH(6) d, J = 9.2 Hz), 8.24 (1H, CH(2) d, J = 5.6 Hz), 7.90 (1H, CH(8) dd J = 8.2 Hz, 5.3 Hz), 7.79 (1H, CH(3) d, J = 5.6 Hz), 3.36 (2H, CH2(1") t, J = 8.9 Hz), 3.29 (2H, CH2(4") t, J = 6.8 Hz), 2.54 (2H, CH2(8") t, J = 7.0 Hz), 2.43 (2H, CH2(7") t, J = 7.0 Hz), 1.86 (2H, CH2(3") m), 1.70 (2H, CH2(2")

m); δ phenylpyridine ligands 8.13 (1H, CH(2') psd, J = 8.2 Hz), 7.87 (1H, CH(9') psd J = 7.9 Hz), 7.81 (1H, CH(3') pst, J = 7.7 Hz), 7.45 (1H, CH(5') psd, J = 5.9 Hz), 7.10 (1H, CH(8') pst, J = 7.5 Hz), 6.95 (1H, CH(7') pst, J = 7.7 Hz), 6.91 (1H, CH(4') pst, J = 6.4 Hz), 6.41 (1H, CH(6') dd, J = 7.4, 2.8 Hz). ^{13}C NMR (MeOD, 300 K, 9.4 T): δ phen-COOH ligand 176.2 (COO(9")), 173.8 (CONH(6")), 153.1 (Cq(4)), 150.9 (Cq(6a)), 150.6 (CH(7)), 149.9 (CH(2)), 147.2 (Cq(10a)), 138.2 (CH(9)), 131.7 ((Cq(1a)), 130.6 (Cq(4a)), 127.9 (CH(6)), 126.4 (CH(3)), 124.7 (CH(8)), 124.6 (CH(5)), 38.3 (CH2(4")), 31.4 (CH2(1")), 31.3 (CH2(7")), 30.5 (CH2(8")), 29.0 (CH2(2")), 27.2 (CH2(3")). δ phenylpyridine ligands 168.1 (Cq(12')), 150.2 (Cq(11')), 148.6 (CH(5')), 144.3 (Cq(10')), 138.3 (CH(3')), 131.7 (CH(6')), 130.2 (CH(7')), 124.6 (CH(9')), 123.0 (CH(4')), 122.4 (CH(8')), 119.6 (CH(2')).

Estimation of the molar extinction coefficient of Ir-COOH in MeOH

7.57 mg of Ir-COOH were transferred in a NMR tube and dissolved in 550 µL of MeOD (measured by weight, 442.6 mg). Four solutions with various concentrations ($4.06 \cdot 10^{-5}$, $5.89 \cdot 10^{-5}$, $1.17 \cdot 10^{-4}$ and $1.75 \cdot 10^{-4}$ M) were prepared from this stock solution. The absorbances at 377 and 415 nm were plotted against the concentration of the solutions and the ε at those wavelengths were calculated from the slope. ε(377 nm)= 5102 M^{-1} cm^{-1}, ε(415 nm)= 2517 M^{-1} cm^{-1}. The estimated experimental errors are 2 nm on the absorption maxima and 5% on the molar absorption coefficients.

Estimation of the molar extinction coefficient of adenine in MeOH

1.9 mg of adenine were dissolved in 10 mL od MeOH and diluted 1:30 by first adding to 0.625 mL (371.7 mg) of the solution 1.875 mL (1.4126 g) of fresh MeOH and then to 0.1 mL of this diluted solution (58.6 mg) 2.9 mL (2.2273 g) of MeOH. From the absorbance of this solution at 260 nm we calculated the molar extinction coefficient of the nucleobase. Being the calculated value, 13.8 mM^{-1} cm^{-1}, almost identical to the value reported in the literature in water (13.7 mM^{-1} cm^{-1})[3], we did not calculated the values for the other three nucleobases contained in the PNA chain and considered their literature data in water in the estimation of the molar extinction coefficient of the PNA tetramer (composed of one adenine, one cytosine, one guanine and one tymin): ε(260 nm)= 40.6 mM^{-1} cm^{-1}.

Stability of Ir-NH_2 in cleavage conditions

A small amount of the Ir-NH_2 complex was dissolved in 3 mL of a TFA:*m*-cresol 9:1 mixture, and the solution was monitored by UV–vis spectroscopy over a period of 1.5 h, mimicking the contact time and the conditions used during the cleavage of the Ir-PNA from the resin.

Photostability of Ir-COOH and Ir-PNA

The Ir-COOH complex and the Ir-PNA conjugate, both dissolved in methanol, were diluted to 2.5 mL by using a CH_2Cl_2:methanol mixture (9:1) in a quartz cuvette to reach the same concentration employed during their photoreaction with DHN ($2.3 \cdot 10^{-5}$ M for Ir-COOH and $6.5 \cdot 10^{-6}$ M for Ir-PNA). The solutions were irradiated with a monochromatic LED light (400 nm, 15.2 mW/cm^2) for increasing times ranging from 1 to 25 min. Multiple UV-vis spectra were recorded over time to ascertain the photostability of the two compounds.

In cuvette $^1O_2$ generation by Ir-COOH and Ir-PNA with irradiation

In a quartz cuvette, 15 µL of a $1.68 \cdot 10^{-3}$ M methanol solution of Ir-PNA adduct were diluted to 2.25 mL with a CH_2Cl_2:methanol 9:1 mixture. A UV-vis spectrum was recorded and 250 µL of a $1.44 \cdot 10^{-3}$ M solution of DHN in the same solvent mixture were added, to obtain a final Ir-PNA concentration of $1.12 \cdot 10^{-5}$ M and final DHN concentration of $1.44 \cdot 10^{-3}$ M (1:10 PS:DHN molar ratio). Another spectrum was recorded and subsequently, the solution was saturated with O_2 by bubbling it for 5 min and exposed to monochromatic LED light (400 nm, 15.2 mW/ cm^2) for durations ranging from 30 s to 25 min. Thus, the variations in DHN and Juglone absorption bands were monitored using UV–vis spectroscopy. Alternatively, for the irradiation with a low-intensity commercial lamp (5

The solutions for the experiments carried out on Ir-COOH and $Ir(ppy)_3$ were prepared analogously, by diluting to 2.25 mL 120 µL of a solution of Ir-COOH $1.87 \cdot 10^{-4}$ M in methanol and 100 µL of $Ir(ppy)_3$ $2.29 \cdot 10^{-4}$ M in CH_2Cl_2 and obtaining respectively final 10^{-5} M and $1.02 \cdot 10^{-5}$ M concentrations of the two PS.

Photocytotoxicity assay (MTT viability assay)

For cell viability assay, HeLa cells were seeded at 25,000 cells/well in 48-well plates. After 24 h of incubation at 37 °C in 5% CO_2 atmosphere, the wells were emptied and the old culture medium replaced with 250 µL of either fresh medium, fresh medium containing 4 µL of MeOH per well or solutions of Ir-COOH and Ir-PNA, first solubilized in methanol and then diluted with the cell culture medium to reach 1, 5, 10, 25 and 50 µM doses. After 24 h of treatment one plate of cells was exposed to light for 30 min, while the other was kept in the dark outside of the incubator for the same time. Then, after 6 h of incubation at 37 °C, the medium was replaced with 300 µL of 3-(4,5-di methyl thiazol-2-yl)-2,5-diphenyltetrazolium bromide (MTT) solution and the cells incubated for 30 min at 37 °C with 5% CO_2. The wells were emptied and 500 µL of 2-propanol were added to each well to dissolve the formed formazan crystals, which were measured spectrophotometrically at 570 nm using the microplate reader. Four replicas were prepared for each condition and the average absorbance values and standard deviation were calculated. The cell viability % was then calculated and normalized by the value obtained for the untreated cells kept in the dark. Light EC_{50} values were obtained by analyzing the fitting curves using the vertical cursor instrument for reading the data at 50% of cell viability.

Preparation of samples for Two-photon Microscopy

HeLa cells were seeded at 200,000 cells/well in 6-well plates and treated with 25 µM Ir-COOH or Ir-PNA, using methanol as vehicle control (4 µL) for 21 h, after which live cells were visualized with TP-microscopy.

References

(1) Yu, M.; Zhao, Q.; Shi, L.; Li, F.; Zhou, Z.; Yang, H.; Yi, T.; Huang, C. Cationic Iridium(III) Complexes for Phosphorescence Staining in the Cytoplasm of Living Cells. *Chemical Communications* **2008**, No. 18, 2115. https://doi.org/10.1039/b800939b.

(2) Zhang, L.; Ding, D. Recent Advances of Transition Ir(III) Complexes as Photosensitizers for Improved Photodynamic Therapy. *VIEW* **2021**, *2* (6). https://doi.org/10.1002/VIW.20200179.

(3) Bermejo-Casadesús, C.; Gonzalo-Navarro, C.; Organero, J. A.; María Rodríguez, A.; Santos, L.; Zafon, E.; Lima, J. C.; Moro, A. J.; Iglesias, M.; Tavares, P.; Martínez, D.; Manzano, B. R.; Massaguer, A.; Durá, G. New Encapsulated Bis-Cyclometalated Ir(III) Complexes with Very Potent Anticancer PDT Activity. *Inorg. Chem. Front.* **2025**, *12* (22), 7304–7332. https://doi.org/10.1039/D5QI00775E.

(4) Maggioni, D.; Galli, M.; D'Alfonso, L.; Inverso, D.; Dozzi, M. V.; Sironi, L.; Iannacone, M.; Collini, M.; Ferruti, P.; Ranucci, E.; D'Alfonso, G. A Luminescent Poly(Amidoamine)-Iridium Complex as a New Singlet-Oxygen Sensitizer for Photodynamic Therapy. *Inorg. Chem.* **2015**, *54* (2), 544–553. https://doi.org/10.1021/ic502378z.

(5) Kritchenkov, I. S.; Zhukovsky, D. D.; Mohamed, A.; Korzhikov-Vlakh, V. A.; Tennikova, T. B.; Lavrentieva, A.; Scheper, T.; Pavlovskiy, V. V.; Porsev, V. V.; Evarestov, R. A.; Tunik, S. P. Functionalized Pt(II) and Ir(III) NIR Emitters and Their Covalent Conjugates with Polymer-Based Nanocarriers. *Bioconjug. Chem.* **2020**, *31* (5), 1327–1343. https://doi.org/10.1021/acs.bioconjchem.0c00020.

(6) Zhao, J.; Yan, K.; Xu, G.; Liu, X.; Zhao, Q.; Xu, C.; Gou, S. An Iridium (III) Complex Bearing a Donor–Acceptor–Donor Type Ligand for NIR-Triggered Dual Phototherapy. *Adv. Funct. Mater.* **2021**, *31* (11). https://doi.org/10.1002/adfm.202008325.

(7) McKenzie, L. K.; Sazanovich, I. V.; Baggaley, E.; Bonneau, M.; Guerchais, V.; Williams, J. A. G.; Weinstein, J. A.; Bryant, H. E. Metal Complexes for Two-Photon Photodynamic Therapy: A Cyclometallated Iridium Complex Induces Two-Photon Photosensitization of Cancer Cells under Near-IR Light. *Chemistry - A European Journal* **2017**, *23* (2), 234–238. https://doi.org/10.1002/chem.201604792.

(8) Novohradsky, V.; Zamora, A.; Gandioso, A.; Brabec, V.; Ruiz, J.; Marchán, V. Somatostatin Receptor-Targeted Organometallic Iridium(III) Complexes as Novel Theranostic Agents. *Chemical Communications* **2017**, *53* (40), 5523–5526. https://doi.org/10.1039/C7CC01946G.

(9) Linero-Artiaga, A.; Servos, L.-M.; Papadopoulos, Z.; Rodríguez, V.; Ruiz, J.; Karges, J. Conjugation of a Cyclometalated Ir(III) Complex to Human Serum Albumin for Oncosis-Mediated Photodynamic Therapy. *Inorg. Chem. Front.* **2025**, *12* (22), 7068–7082. https://doi.org/10.1039/D5QI01287B.

(10) Ito, Y.; Mizuno, K.; Domoto, K.; Hari, Y. Synthesis and Hybridization Properties of Iridium(III) Polypyridyl Complex-Conjugated Oligonucleotide. *Nucleosides Nucleotides Nucleic Acids* **2020**, *39* (1–3), 69–81. https://doi.org/10.1080/15257770.2019.1690150.

(11) Wu, Y.; Li, S.; Chen, Y.; He, W.; Guo, Z. Recent Advances in Noble Metal Complex Based Photodynamic Therapy. *Chem. Sci.* **2022**, *13* (18), 5085–5106. https://doi.org/10.1039/D1SC05478C.

(12) Nielsen, P. E.; Egholm, M.; Berg, R. H.; Buchardt, O. Sequence-Selective Recognition of DNA by Strand Displacement with a Thymine-Substituted Polyamide. *Science (1979).* **1991**, *254* (5037), 1497–1500. https://doi.org/10.1126/science.1962210.

(13) Porcheddu, A.; Giacomelli, G. *Peptide Nucleic Acids (PNAs), A Chemical Overview*; 2005; Vol. 12.

(14) Gupta, A.; Mishra, A.; Puri, N. Peptide Nucleic Acids: Advanced Tools for Biomedical Applications. *Journal of Biotechnology*. Elsevier B.V. October 10, 2017, pp 148–159. https://doi.org/10.1016/j.jbiotec.2017.07.026.

(15) Koppelhus, U.; Nielsen, P. E. *Cellular Delivery of Peptide Nucleic Acid (PNA)*; 2003; Vol. 55. www.elsevier.com/locate/addr.

(16) Pellestor, F.; Paulasova, P. The Peptide Nucleic Acids (PNAs), Powerful Tools for Molecular Genetics and Cytogenetics. *European Journal of Human Genetics*. September 2004, pp 694–700. https://doi.org/10.1038/sj.ejhg.5201226.

(17) Sharma, C.; Awasthi, S. K. Versatility of Peptide Nucleic Acids (PNAs): Role in Chemical Biology, Drug Discovery, and Origins of Life. *Chemical Biology and Drug Design*. Blackwell Publishing Ltd January 1, 2017, pp 16–37. https://doi.org/10.1111/cbdd.12833.

(18) Riela, S.; Borrego-Sánchez, A.; Cauteruccio, S.; de Melo Barbosa, R.; Massaro, M.; Sainz-Díaz, C. I.; Sánchez-Espejo, R.; Viseras-Iborra, C.; Licandro, E. Exploiting the Interaction between Halloysite and Charged PNAs for Their Controlled Release. *J. Mater. Chem. B* **2023**, *11* (28), 6685–6696. https://doi.org/10.1039/D3TB00637A.

(19) Cauteruccio, S.; Licandro, E.; Panigati, M.; D'Alfonso, G.; Maiorana, S. Modifying the Properties of Organic Molecules by Conjugation with Metal Complexes: The Case of Peptide Nucleic Acids and of the Intrinsically Chiral Thiahelicenes. *Coord. Chem. Rev.* **2019**, *386*, 119–137. https://doi.org/10.1016/j.ccr.2019.02.002.

(20) Gasser, G.; Sosniak, A. M.; Metzler-Nolte, N. Metal-Containing Peptide Nucleic Acid Conjugates. *Dalton Transactions*. July 7, 2011, pp 7061–7076. https://doi.org/10.1039/c0dt01706j.

(21) Hüsken, N.; Gębala, M.; Schuhmann, W.; Metzler-Nolte, N. A Single-Electrode, Dual-Potential Ferrocene–PNA Biosensor for the Detection of DNA. *ChemBioChem* **2010**, *11* (12), 1754–1761. https://doi.org/10.1002/cbic.200900748.

(22) Cauteruccio, S.; Panigati, M.; Veronese, L.; Zaffaroni, N.; Folini, M.; Licandro, E. Luminescent Dinuclear Rhenium(I) PNA Conjugates for MicroRNA-21 Targeting: Synthesis, Chemico-Physical and Biological Characterization. *J. Organomet. Chem.* **2019**, *887*, 32–39. https://doi.org/10.1016/j.jorganchem.2019.02.020.

(23) Xavier, C.; Giannini, C.; Gano, L.; Maiorana, S.; Alberto, R.; Santos, I. Synthesis, Characterization, and Evaluation of a Novel 99mTc(CO)3 Pyrazolyl Conjugate of a Peptide Nucleic Acid Sequence. *JBIC Journal of Biological Inorganic Chemistry* **2008**, *13* (8), 1335–1344. https://doi.org/10.1007/s00775-008-0419-y.

(24) Hibino, M.; Aiba, Y.; Watanabe, Y.; Shoji, O. Peptide Nucleic Acid Conjugated with Ruthenium-Complex Stabilizing Double-Duplex Invasion Complex Even under Physiological Conditions. *ChemBioChem* **2018**, *19* (15), 1601–1604. https://doi.org/10.1002/cbic.201800256.

(25) Shemesh, Y.; Yavin, E. PNA–Rose Bengal Conjugates as Efficient DNA Photomodulators. *Bioconjug. Chem.* **2015**, *26* (9), 1916–1922. https://doi.org/10.1021/acs.bioconjchem.5b00406.

(26) Lee, J.; Kim, S.; Na, H.; Min, D. MicroRNA-Responsive Drug Release System for Selective Fluorescence Imaging and Photodynamic Therapy In Vivo. *Adv. Healthc. Mater.* **2016**, *5* (18), 2386–2395. https://doi.org/10.1002/adhm.201600328.

(27) Maggioni, D.; Fenili, F.; D'Alfonso, L.; Donghi, D.; Panigati, M.; Zanoni, I.; Marzi, R.; Manfredi, A.; Ferruti, P.; D'Alfonso, G.; Ranucci, E. Luminescent Rhenium and Ruthenium Complexes of an Amphoteric Poly(Amidoamine) Functionalized with 1,10-Phenanthroline. *Inorg. Chem.* **2012**, *51* (23), 12776–12788. https://doi.org/10.1021/ic301616b.

(28) Huang, A. Y.-T.; Tsai, C.-H.; Chen, H.-Y.; Chen, H.-T.; Lu, C.-Y.; Lin, Y.-T.; Kao, C.-L. Concise Solid-Phase Synthesis of Inverse Poly(Amidoamine) Dendrons Using AB2 Building Blocks. *Chemical Communications* **2013**, *49* (51), 5784. https://doi.org/10.1039/c3cc40661j.

(29) Comstock, L. R.; Rajski, S. R. Methyltransferase-Directed DNA Strand Scission. *J. Am. Chem. Soc.* **2005**, *127* (41), 14136–14137. https://doi.org/10.1021/ja054128y.

(30) Carmo dos Santos, N. A.; Natali, M.; Badetti, E.; Wurst, K.; Licini, G.; Zonta, C. Cobalt, Nickel, and Iron Complexes of 8-Hydroxyquinoline-Di(2-Picolyl)Amine for Light-Driven Hydrogen Evolution. *Dalton Transactions* **2017**, *46* (47), 16455–16464. https://doi.org/10.1039/C7DT02666H.

(31) Sauvageot, E.; Lafite, P.; Duverger, E.; Marion, R.; Hamel, M.; Gaillard, S.; Renaud, J.-L.; Daniellou, R. Iridium Complexes Inhibit Tumor Necrosis Factor-α by Utilizing Light and Mixed Ligands. *J. Organomet. Chem.* **2016**, *808*, 122–127. https://doi.org/10.1016/j.jorganchem.2016.02.001.

(32) Sprouse, S.; King, K. A.; Spellane, P. J.; Watts, R. J. *Photophysical Effects of Metal-Carbon Bonds in Ortho-Metalated Complexes of Ir(III) and Rh(III)*; 1984; Vol. 106. https://pubs.acs.org/sharingguidelines.

(33) Sauvageot, E.; Marion, R.; Sguerra, F.; Grimault, A.; Daniellou, R.; Hamel, M.; Gaillard, S.; Renaud, J.-L. Iridium(Iii) Dipyridylamine Complexes: Synthesis, Characterization and Catalytic Activities in Photoredox Reactions. *Organic Chemistry Frontiers* **2014**, *1* (6), 639. https://doi.org/10.1039/c4qo00059e.

(34) Orwat, B.; Oh, M. J.; Zaranek, M.; Kubicki, M.; Januszewski, R.; Kownacki, I. Microwave-Accelerated C,N-Cyclometalation as a Route to Chloro-Bridged Iridium(III) Binuclear Precursors of Phosphorescent Materials: Optimization, Synthesis, and Studies of the Iridium(III) Dimer Behavior in Coordinating Solvents. *Inorg. Chem.* **2020**, *59* (13), 9163–9176. https://doi.org/10.1021/acs.inorgchem.0c01071.

(35) Mastalir, M.; Stöger, B.; Pittenauer, E.; Allmaier, G.; Kirchner, K. Air-Stable Triazine-Based Ni(II) PNP Pincer Complexes As Catalysts for the Suzuki–Miyaura Cross-Coupling. *Org. Lett.* **2016**, *18* (13), 3186–3189. https://doi.org/10.1021/acs.orglett.6b01398.

(36) Chen, W.-C.; Hsu, Y.-C.; Shih, W.-C.; Lee, C.-Y.; Chuang, W.-H.; Tsai, Y.-F.; Chen, P. P.-Y.; Ong, T.-G. Metal-Free Arylation of Benzene and Pyridine Promoted by Amino-Linked Nitrogen Heterocyclic Carbenes. *Chemical Communications* **2012**, *48* (53), 6702. https://doi.org/10.1039/c2cc32519e.

(37) Gerrard, W.; Madden, R. W.; Tolcher, P. Interaction of Alcohols with Hydrogen Halides. *Journal of Applied Chemistry* **1955**, *5* (1), 28–34. https://doi.org/10.1002/jctb.5010050104.

(38) Tamura, Y.; Hisamatsu, Y.; Kazama, A.; Yoza, K.; Sato, K.; Kuroda, R.; Aoki, S. Stereospecific Synthesis of Tris-Heteroleptic Tris-Cyclometalated Iridium(III) Complexes via Different Heteroleptic Halogen-Bridged Iridium(III) Dimers and Their Photophysical Properties. *Inorg. Chem.* **2018**, *57* (8), 4571–4589. https://doi.org/10.1021/acs.inorgchem.8b00323.

(39) Silverstein, R. M.; Webster, F. X.; Kiemle David J. *Spectrometric Identification of Organic Compounds*, Seventh Edition.; Wiley, 2005.

(40) Neve, F.; La Deda, M.; Crispini, A.; Bellusci, A.; Puntoriero, F.; Campagna, S. Cationic Cyclometalated Iridium Luminophores: Photophysical, Redox, and Structural Characterization. *Organometallics* **2004**, *23* (24), 5856–5863. https://doi.org/10.1021/om049493x.

(41) Dragonetti, C.; Falciola, L.; Mussini, P.; Righetto, S.; Roberto, D.; Ugo, R.; Valore, A.; De Angelis, F.; Fantacci, S.; Sgamellotti, A.; Ramon, M.; Muccini, M. The Role of Substituents on Functionalized 1,10-Phenanthroline in Controlling the Emission Properties of Cationic Iridium(III) Complexes of Interest for Electroluminescent Devices. *Inorg. Chem.* **2007**, *46* (21), 8533–8547. https://doi.org/10.1021/ic700414z.

(42) Lepeltier, M.; Kwok-Ming Lee, T.; Kam-Wing Lo, K.; Toupet, L.; Le Bozec, H.; Guerchais, V. Synthesis, Structure, and Photophysical and Electrochemical Properties of Cyclometallated Iridium(III) Complexes with Phenylated Bipyridine Ligands. *Eur. J. Inorg. Chem.* **2005**, *2005* (1), 110–117. https://doi.org/10.1002/ejic.200400418.

(43) Lowry, M. S.; Hudson, W. R.; Pascal, R. A.; Bernhard, S. Accelerated Luminophore Discovery through Combinatorial Synthesis. *J. Am. Chem. Soc.* **2004**, *126* (43), 14129–14135. https://doi.org/https://doi.org/10.1021/ja047156+.

(44) Maillard, J.; Klehs, K.; Rumble, C.; Vauthey, E.; Heilemann, M.; Fürstenberg, A. Universal Quenching of Common Fluorescent Probes by Water and Alcohols. *Chem. Sci.* **2021**, *12* (4), 1352–1362. https://doi.org/10.1039/D0SC05431C.

(45) Takizawa, S.; Aboshi, R.; Murata, S. Photooxidation of 1,5-Dihydroxynaphthalene with Iridium Complexes as Singlet Oxygen Sensitizers. *Photochemical & Photobiological Sciences* **2011**, *10* (6), 895–903. https://doi.org/10.1039/c0pp00265h.

(46) Ohshita, J.; Hayashi, Y.; Murakami, K.; Enoki, T.; Ooyama, Y. Single Oxygen Generation Sensitized by Spiro(Dipyridinogermole)(Dithienogermole)s. *Dalton Transactions* **2016**, *45* (39), 15679–15683. https://doi.org/10.1039/C6DT02767A.

(47) Öztürk, E.; Eserci, H.; Okutan, E. Perylenebisimide-Fullerene Dyads as Heavy Atom Free Triplet Photosensitizers with Unique Singlet Oxygen Generation Efficiencies. *J. Photochem. Photobiol. A Chem.* **2019**, *385*, 112022. https://doi.org/10.1016/j.jphotochem.2019.112022.

(48) Luiz, M.; Soltermann, A. T.; Biasutti, A.; Garcia, N. A. A Kinetic Study on Singlet Molecular Oxygen (O2 (1Δg)) Generation and Quenching by Dihydroxynaphthalenes. *Can. J. Chem.* **1996**, *74* (1), 49–54. https://doi.org/10.1139/v96-006.

(49) Balzani, Vincenzo.; Carassiti, Vittorio. *Photochemistry of Coordination Compounds, by V. Balzani and V. Carassiti*; Academic Press, 1970.

(50) Martínez-Alonso, M.; Jones, C. G.; Shipp, J. D.; Chekulaev, D.; Bryant, H. E.; Weinstein, J. A. Phototoxicity of Cyclometallated Ir(III) Complexes Bearing a Thio-Bis-Benzimidazole Ligand, and Its Monodentate Analogue, as Potential PDT Photosensitisers in Cancer Cell Killing. *JBIC Journal of Biological Inorganic Chemistry* **2024**, *29* (1), 113–125. https://doi.org/10.1007/s00775-023-02031-z.

(51) McKenzie, L. K.; Bryant, H. E.; Weinstein, J. A. Transition Metal Complexes as Photosensitisers in One- and Two-Photon Photodynamic Therapy. *Coord. Chem. Rev.* **2019**, *379*, 2–29. https://doi.org/10.1016/j.ccr.2018.03.020.

(52) Buryakina, T. Yu. Metabolism of HeLa Cells Revealed through Autofluorescence Lifetime upon Infection with Enterohemorrhagic Escherichia Coli. *J. Biomed. Opt.* **2012**, *17* (10), 101503. https://doi.org/10.1117/1.JBO.17.10.101503.

(53) Wehland, J.-D. Hybrids of SNARE Transmembrane Domains and Artificial Recognition Motifs as Membrane Fusion Inducing Model Peptides, 2018. https://doi.org/10.13140/RG.2.2.35451.67366.

Preparation of a luminescent molecule containing a biguanide moiety to investigate the antitumoral action of metformin.

Introduction

Metformin

Metformin (N,N-dimethylbiguanide) is an antihyperglycemic drug, currently the first-line treatment for Type II diabete. It was first synthetized and tested in 1950s together with other two biguanide-derivative drugs, phenformin and buformin, then they were distributed in early 1960s. However, the other two drugs were removed from the marked due to high risk of lactic acidosis and increased cardiac mortality, while the incidence associated to metformin is much lower and the drug is considered safe and effective both as monotherapy and combined with insulin or other antidiabetics.[1,2] The structures of the three drugs are shown in Scheme 1.

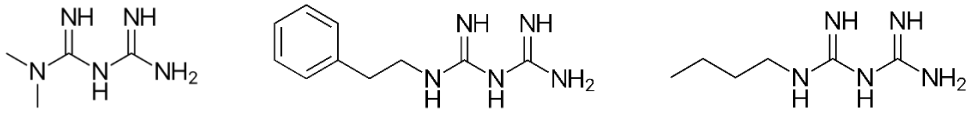

Scheme 1. *Structures of metformin (on the left), phenformin (in the middle) and buformin (on the right).*

Being hydrophilic and mostly in its protonated form in physiological conditions, it is taken up through an active mechanism mediated by organic carries rather than passive diffusion. However, the exact mechanisms of the antidiabetic activity of metformin are not completely clear, possibly targeting the gut microbioma,[3] despite having been deeply studied since its diffusion. It is stated that the molecule is involved in the inhibition of cellular respiration, targeting the complex I of the respiratory chain (NADH:ubiquinone oxidoreductase) and inducing a decrease in the cellular ATP concentration. The increase in AMP/ATP and ADP/ATP ratios activated AMPK (AMP-activated protein kinase), a sensor of the energy homeostasis of the cells that start a wide array of cellular responses to compensate, protect and spare energy. Moreover, metformin inhibits directly mitochondrial glycerophosphate dehydrogenase (mGPD), blocking glycerophosphate shuttle, increasing NADH cytosolic concentration and impairing incorporation of lactate into glucose. These two mechanisms, schematized in Figure 1, exert a major role in the suppression of hepatic gluconeogenesis by the drug, its primary action against Type II diabetes together with the increase in insulin suppression of endogeneous glucose production. Others are the reduction of intestinal glucose absorption and the improvement of glucose uptake by peripheral tissues, such as skeletal muscles and adipose tissue.[1,4,5]

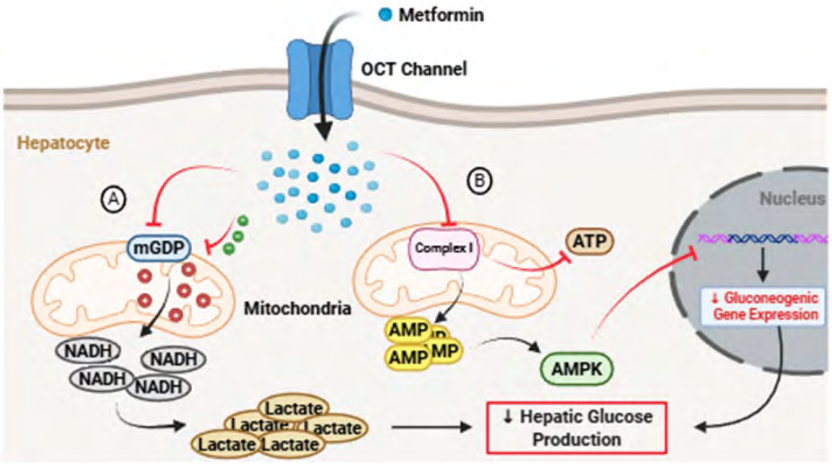

Figure 1. *Schematization of the mechanisms involved in decreasing hepatic glucose production, the main anti Type II diabetes action of metformin. From Ref. 6*

Additionally, the activity of metformin has been discovered not to be limited to Type II diabetes treatment, having shown benefits, depending on the regulation of the glucose metabolism via AMPK, for various diseases, including obesity, liver, cardiovascular and kidney diseases and against aging. Being the liver the main target organ of metformin, the AMPK activation results in the reduction of fatty acid oxidation and suppression of fatty acid synthesis, reducing the incidence of fatty liver diseases. The drug is also involved in the treatment of cardiovascular diseases: it inhibits alpha-carbonyl-mediated modification of apolipoproteins, improving cholesterol transport. It also improves endothelial oxidative stress and attenuates hyperglycemia-induced inflammation and improves the myocardial energy status, reducing the cardiovascular risk and the occurrence of such diseases. The regulation of glucose, the decrease in cell inflammation and oxidative stress might also be associated with a protection role toward kidneys, as reported by studies that showed an improvement of kidney fibrosis and the restoration of kidney function and structure with oral administration of metformin. All these effects generate beneficial consequences against aging (the improvement of aging-associated diseases and the decrease of DNA damage) and obesity (as potential therapy for metabolic disfunctions and weight loss) as well.[5]

In the last years, epidemiological studies have revealed a protective effect of metformin on diabetic,[7,8] as well on non-diabetic patients[9,10] in terms of reduction of cancer incurrence and mortality. Evidence on the inhibition of growth, survival and metastasis of several types of tumors, including breast, liver, bone, pancreas, endometrial, colorectal and lung are reported in the literature.[11] Metformin has also been found to reduce side effects and increase sensitivity to radiotherapy, chemotherapy and immunotherapy.[12]

The antitumoral properties of metformin can be divided into indirect effects, depending on blood glucose and insulin levels, and direct effects, depending on the direct interaction with cancer cells. The

direct effects are partly AMPK-dependent: its activation leads to the inhibition of mTOR complex I, blocking the ATP-consuming processes. Metformin is also associated with an AMPK-independent inhibition of mTOR signaling, that disturbs and suppresses protein synthesis and cell growth and proliferation. The suppression of mitochondrial complex I limits the electron flow to mitochondrial complex III, in which ROS are generated, preventing their production and reducing DNA damage. The activation of autophagy and apoptosis through an AMPK-independent pathway was also proposed in the suppression of cancer, as well as the modification of the tumor microenvironment through the regulation of angiogenesis, fibroblasts, tumor-associated macrophages and immunosuppression.[5,12]

However, the exact antitumoral mechanisms of metformin remain uncertain, although many have been proposed, and the topic is still object of investigation. In this landscape, the final aim of this ongoing project is to investigate the interaction of a luminescent molecule bearing a terminal biguanide to mimic metformin with tumoral cells, employing techniques such as confocal and fluorescence microscopy, to gain a deeper understanding of the antitumoral mechanisms promoted by the drug. In particular, we are currently focusing on developing an efficient synthetic strategy to prepare this molecule in large amount and with the high purity necessary for the subsequent biological investigation.

Synthetic strategies to prepare biguanides

In the literature, various synthetic strategies for the preparation of biguanides have been reported, most of them starting from amines. This category includes reactions employed when biguanides were first discovered, which are still largely popular nowadays. Two examples are the reaction of cyanoguanidine with ammonia or with primary amines in the presence of Cu^{2+} salts (i.e. $CuSO_4$ and $CuCl_2$) and the direct fusion of cyanoguanidine with amine salts. Other than these two, one of the most widely used strategies for the synthesis of biguanides involves the reaction of primary or secondary amines with the nitrile group of 1-cyanoguanidine under acid catalysis. This transformation is typically carried out in polar solvents such as alcohols, water or acetonitrile at high temperatures. Under these conditions, proton exchanges processes promote the activation of the cyanoguanidine toward nucleophilic attack of the free amine, as schematized in Scheme 2A. In the absence of such activation, the reaction would proceed too slow.[13,14] HCl is usually employed for this aim, also because it is usually already present in the precursor hydrochloride amines, working at ca. pH 2.6.[15] However, HCl in some cases might be too harsh, generating undesired side reactions that involve the terminal amine of the cyanoguanidine (Scheme 2B). Thus, other Lewis acids are often used as activating agents for this kind of reaction, i.e. $FeCl_3$[16] or chlorotrimethylsilane (TMSCl)[17].

Another optimization for these reactions that have received growing attention lately is the microwave (MW) heating, either associated with acid catalysis by HCl[18] or with the use of TMSCl[19] to activate the nitrile function of the cyanoguanidine. The use of MW remarkably accelerates the rate of the reaction over conventional heating, allowing to reduce the long reaction times required to prepare biguanides from several hours to 15-30 min, even though it is unclear whether the role of microwaves is thermal or not.[13,20]

Moreover, disubstituted biguanides can be obtained by the addition of amines to the cyano group of substituted cyanoguanidine, employing conditions similar to those used for unsubstituted cyanoguanidines.[13]

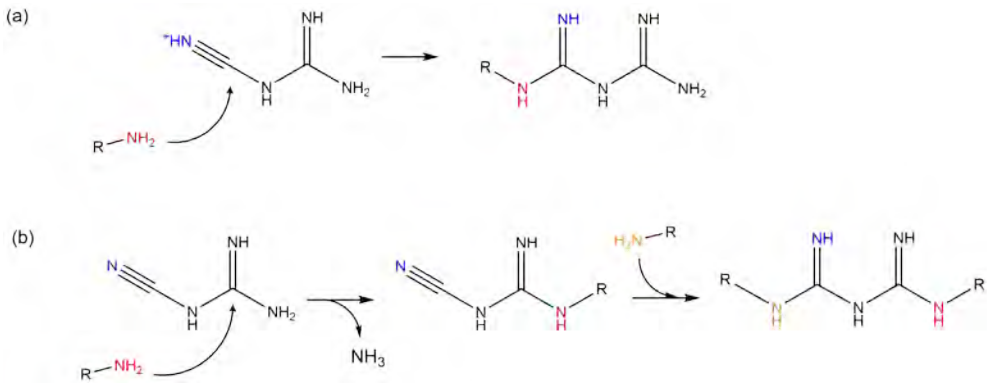

Scheme 2. *Schematization of the nucleophilic attack of primary amines to the activated nitrile group (a) and of the possible side reaction with the guanidine moiety (b) of 1-cyanoguanidine.*

An alternative to the reactions described above consists in the double addition of amines to the two C≡N group of sodium dicyanamide, to obtain biguanides either by two subsequent steps reacting two different amines or employing 2 equivalents of the same amine to obtain a symmetric product. This reaction can be performed both on aromatic or aliphatic amines, but the conditions necessary in this second case are harsher, usually requiring high temperatures and long reaction times.[13]

The synthesis of biguanides starting from amines can be carried out with milder conditions by using a biamidine-transfer reagent. This strategy involves a biamidine moiety linked to a leaving group to allow the transfer by an addition–elimination process. Benhida and coworkers[21] proposed a method carried out in either water or pyridine, affording smooth transformation of various amines into the corresponding biguanides with high yields.

Finally, the second typology of reactions uses guanidine as starting point. This strategy is suitable for the preparation of highly substituted biguanides and involves the addition of guanidine to the carbodiimide upon heating in a polar and protic solvent, such as DMF, toluene or hexane at temperatures between 25–100 °C, although in general higher temperatures seem to greatly accelerate

the reaction. This method was further optimized using solvent-free conditions under microwave irradiation or reflux conditions in butanol.[13,15]

Results and discussion

To prepare the luminescent metformin-like derivative, the synthetic pathway schematized in Scheme 3 was developed. This strategy exploits the high reactivity of the -SH group toward the double bond of a maleimide to link the biguanide moiety to the luminescent fluorescein fragment. The first step involved the preparation of the biguanide, through a reaction between cystamine dihydrochloride and 1-cyanoguanidine to form intermediate **1**, followed by the reduction of the disulfuric bond with $NaBH_4$. Once obtained the reduced intermediate **2**, the last step consists in a Michael reaction with the luminescent fluorescein, appropriately functionalized with a maleimide group (compound **3b**). All the synthetic steps have been carried out under an N_2 atmosphere and followed with NMR spectroscopy.

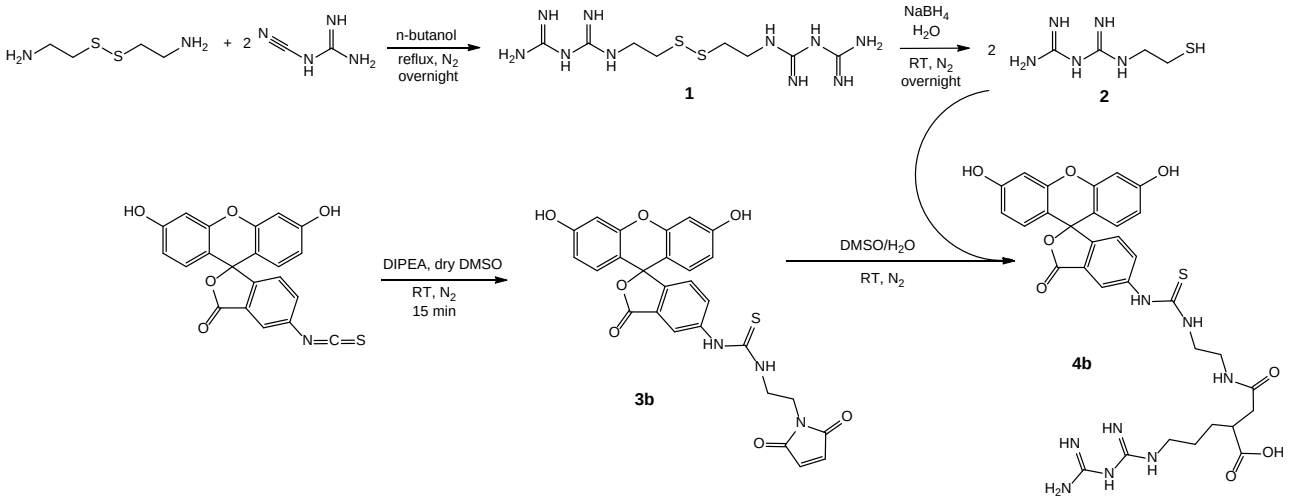

Scheme 3. *The comprehensive synthetic path followed to obtain S-S bis-biguanide (**1**) and the reduced biguanide-SH (**2**), the rhodamine-maleimide adduct (**3b**) and the final fluorescein-biguanide product (**4b**).*

An alternative pathway that will be tested as a future perspective consists of a first reaction between a bis-amine with a long aliphatic chain (such as cadaverine) mono-protected on one of the two amines with a Fmoc group, and cyanoguanidine to form the biguanide group. Then the reaction with fluorescein isothiocyanate will be carried out as final step, in which the basic environment needed for this reaction will remove the Fmoc protection from the amine, allowing the formation of the thiourea and yielding the fluorescent biguanide.

Preparation of S-S bis-biguanide (1)

The first goal in the synthesis of the metformin derivative was the preparation of a molecule containing a terminal biguanide, analogous to the part of metformin that we hypothesize to be involved in its antitumoral behavior.

Based on previous work carried out by our group to prepare similar biguanide moieties by reacting aliphatic amines with 1-cyanoguanidine, in this work we opted for HCl, as it should give the best results for the kind of reagents employed. For the preparation of S-S bis-biguanide intermediate (**1**), we started from the commercial and inexpensive cystamine hydrochloride, a symmetric bis-amine containing a disulfur bond easily reduced in the subsequent synthetic step to obtain two equivalent molecules exposing both the biguanide and a -SH group.

Unfortunately, the reactivity of primary alkyl amines toward 1-cyanoguanidine is very high and not limited to the C≡N group, as it might lead to undesired subproducts derived from their reaction with the guanidine end of cyanoguanidine, that in some cases might further react with another equivalent of the amine, yielding to a symmetrical product with one biguanide in the middle of the molecule (Scheme 2B).[19] Hence, the right reaction temperature and the amount of protons employed in the reaction should be carefully investigated.

We attempted four different strategies to synthesize product **1** by varying the solvent (and consequently the reflux temperature at which the reaction was carried out) and the equivalents of HCl employed.

The first attempt was carried out in H_2O by adding to the reaction mixture 5 equivalents of HCl and refluxing overnight (for a total of 7 equivalents, considering the additional 2 eq from the amine dihydrochloride), as shown in Scheme 4, taking inspiration from literature reports, obtaining an oil and not a precipitate. The washed product was analyzed by ^{1}H NMR (Figure 2), showing two sets of signals: an intense couple of triplets at 2.76 and 2.88 ppm containing 95% of the CH_2 signals, together with a second and less intense triplet couple centered at 2.85 and 3.49 ppm (5%). The formation of a product resembling a biguanide is suggested by a ^{13}C NMR experiment (Figure 3), which showed two signals at 161.9 and 167.5 ppm. An additional ^{1}H-^{15}N HMBC experiment (Figure 4) suggested that the most intense protonic signals might be attributed to the aliphatic protons of unreacted cystamine, as they both correlate to a nitrogen signal at 21.8 ppm (using NH_4OH as reference), in the usual range of aliphatic amino groups.[22] The other correlation visible in this experiment occurs between the less intense set of protons and a N signal at 122.2 ppm, which could correspond to a nitrogen signal of the biguanide.

However, the other ^{15}N signals are not intense enough to provide information on whether the less intense set of protonic signals might be due to the desired biguanide product.

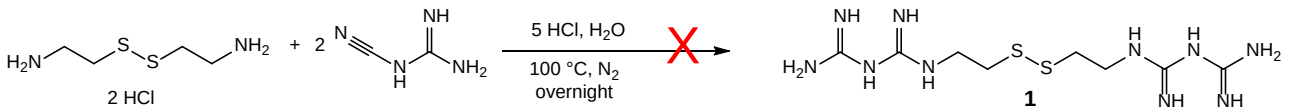

Scheme 4. *First attempt to prepare the product* ***1*** *(S-S bis-biguanide), employing 7 equivalents of HCl and carrying out the reaction in* H_2O.

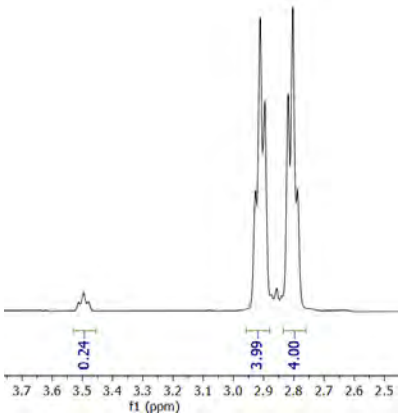

Figure 2. *^{1}H NMR (9.4T, 300 K, D_2O) of the product obtained in H_2O with 7 eq of HCl.*

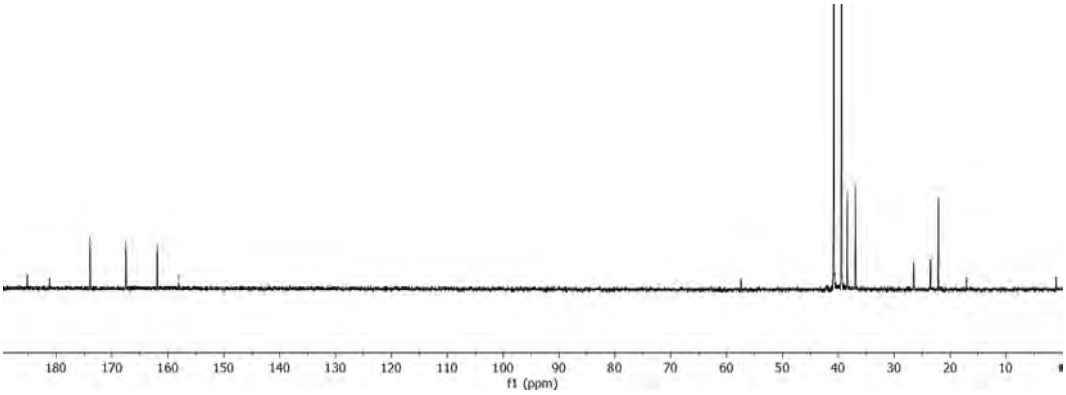

Figure 3. *^{13}C NMR (9.4T, 300 K, D_2O) of the product obtained in H_2O with 7 eq of HCl.*

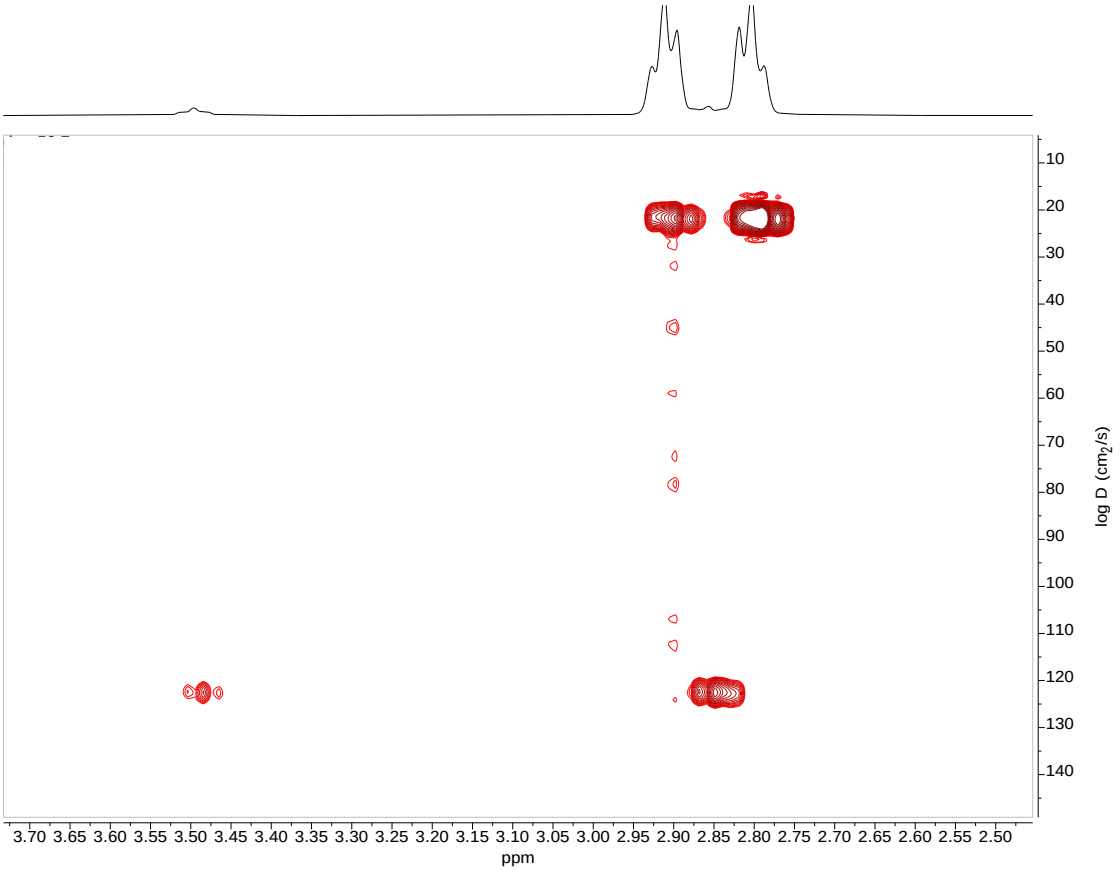

Figure 4. *^{1}H-^{15}N bidimensional HMBC NMR experiment (9.4T, 300 K, D_2O) of the product obtained in H_2O with 7 eq of HCl. The ^{15}N spectrum was recorded using NH_4OH as reference.*

It should be noted that the protons in this type of reaction can both activate the nitrile group of the cyanoguanidine and reduce the nucleophilic character of the amine, preventing the nucleophilic attack from occurring. For this reason, it is very important to choose the right amount of HCl to activate cyanoguanidine without reducing the reactivity of the amine. In this first attempt pH possibly was too low, drastically decreasing the nucleophilic character of the primary amines of cystamine.

Thus, in the second attempt to the synthesis we reduced the equivalents of HCl from 7 to 4, changing at the same time the solvent from water to MeOH, since in the literature this kind of reaction many times is carried out using alcohols as solvents. This way the reaction temperature was reduced from 100 °C to 70 °C (Scheme 5). The two additional equivalents of HCl were added to improve the solubility of the reagents in this solvent.

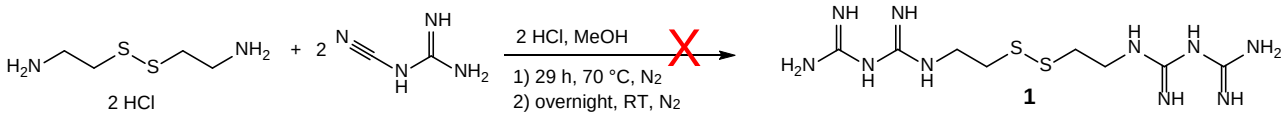

Scheme 5. *Second attempt to prepare the product **1** (S-S bis-biguanide), employing 4 equivalents of HCl and carrying out the reaction in MeOH.*

After the reaction, the solid crude product was washed and filtered, separating the supernatant from a white solid that was recognized as unreacted cystamine. On the other hand, the ^{1}H-^{13}C HMBC experiment recorded on the supernatant after the work-up (Figure 5) clearly showed that a mixture of products was obtained. The ^{13}C signals attributed to the unreacted 1-cyanoguanidine were still visible (at 118.6 and 163.6 ppm, respectively attributed to the nitrile and the guanidine carbon atoms). Other than these, two pairs of signals were visible in the range attributed to quaternary carbons that lie at higher fields with respect to the usual chemical shift of biguanide moieties (153.3 and 155.6 ppm vs 154.8 and 156.1 ppm). Contemporarily in the ^{1}H spectrum different singlet around 3.7-3.9 ppm where present and a direct heteronuclear 2D NMR experiment (^{1}H-^{13}C HSQC-dept, not shown) confirmed that these signals were due to methyl groups. Moreover, the two triplets visible in the protonic spectrum (Figure 6) correlate only one to each other in both the ^{1}H-^{13}C HMBC and HSQC experiments and thus are assigned to some additional unreacted cystamine that remained dissolved in the supernatant. Nonetheless, the two large signals at 6.60 and 6.96 ppm are consistent with =NH protons of biguanides and might be attributed to the unreacted cyanoguanidine as well to the biguanide-like group of the byproduct. All the experimental evidences, together with some correlations between these quaternary ^{13}C signals and the above cited singlets, suggest that the desired product did not formed, and undefined byproducts possibly deriving from the reaction of MeOH with cyanoguanidine together with the starting cystamine were the only species present at the end of the reaction.

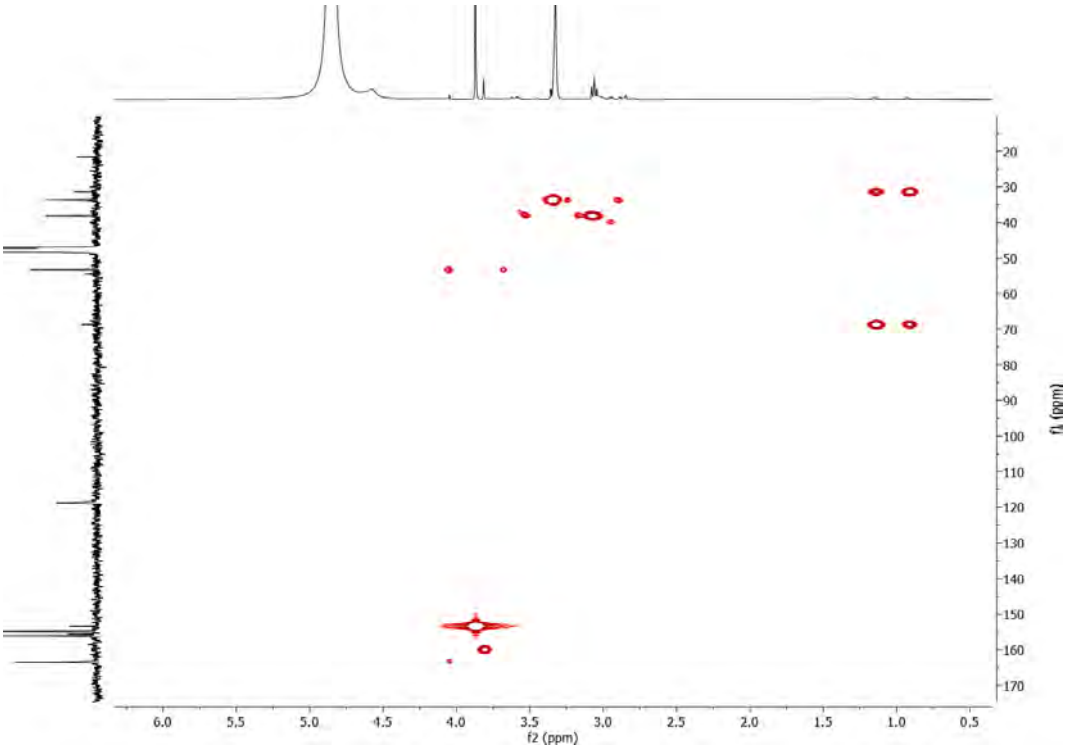

Figure 5. *^{1}H-^{13}C HMBC NMR experiment (9.4T, 300 K, MeOD) of the product of the reaction carried out in MeOH with 4 eq of HCl, recorded after the work up steps to remove the unreacted cystamine.*

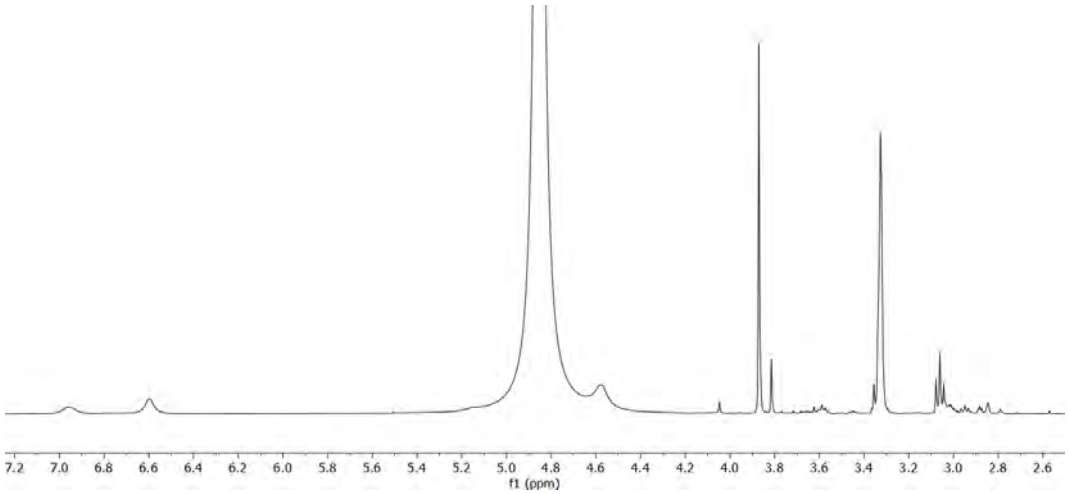

Figure 6. *^{1}H NMR (9.4T, 300 K, MeOD) of the product of the reaction carried out in MeOH with 4 eq of HCl, recorded after the work up steps to separate the unreacted cystamine.*

Given the results of the reaction carried out in MeOH, we changed the solvent of the reaction to *n*-butanol to increase the temperature of the reaction from 70 °C to 130 °C. This choice was inspired by the literature, as various examples of reactions carried out in this solvent to prepare biguanides are reported.[23,24] In particular, in a work from Fu et al.[25] the authors use the same cystamine hydrochloride that we chose as starting point in our synthetic pathway, but forming the biguanide moiety only on one of the amine groups of the diamine. Thus, our third attempt in the preparation of the S-S bis-biguanide molecule was inspired by this work, increasing the equivalents of cyanoguanidine to 2 and modifying some parameters not specified by the authors, as schematized in Scheme 6.

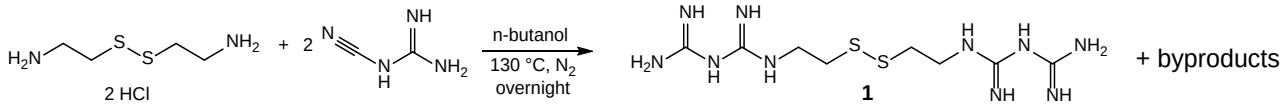

Scheme 6. *Third attempt to prepare the product **1** (S-S bis-biguanide), employing 2 equivalents of HCl and carrying out the reaction in n-BuOH.*

The NMR spectra recorded on the crude product suggested the formation of the desired S-S bis-biguanide, from the couple of ^{13}C signals at 159.0 and 160.6 ppm in the ^{1}H-^{13}C HMBC experiment shown in Figure 7, and the long-range correlation of one of these two with the proton signal at 3.58 ppm. The attributions shown in the figure were confirmed by an additional short-range ^{1}H-^{13}C HSQC experiment. Aside from this couple of signals and those of the two solvents, in the ^{13}C spectrum two signals assigned to the unreacted cyanoguanidine (at 118.5 and 163.5 ppm) are visible, together with another set of signals assigned to a byproduct. The assignment of these signals was not trivial: the intense signal at 157.3 ppm was attributed to a symmetric biguanide group, while the presence of only two multiplets in the protonic spectrum (Figure 8) suggests that the overall byproduct should be symmetric as well and the aliphatic -CH_2 similar to those of S-S bis-biguanide **1**, since in both experiments they possess very similar chemical shifts. Thus, we have tentatively ascribed the byproduct as the molecule shown in

Scheme 7, that might be generated by the side reaction involving the guanidine group of the cyanoguanidine instead of the nitrile one, as previously described in Scheme 2b, and the consequent reaction of the free C≡N of this intermediate with free or partially reacted cystamine.

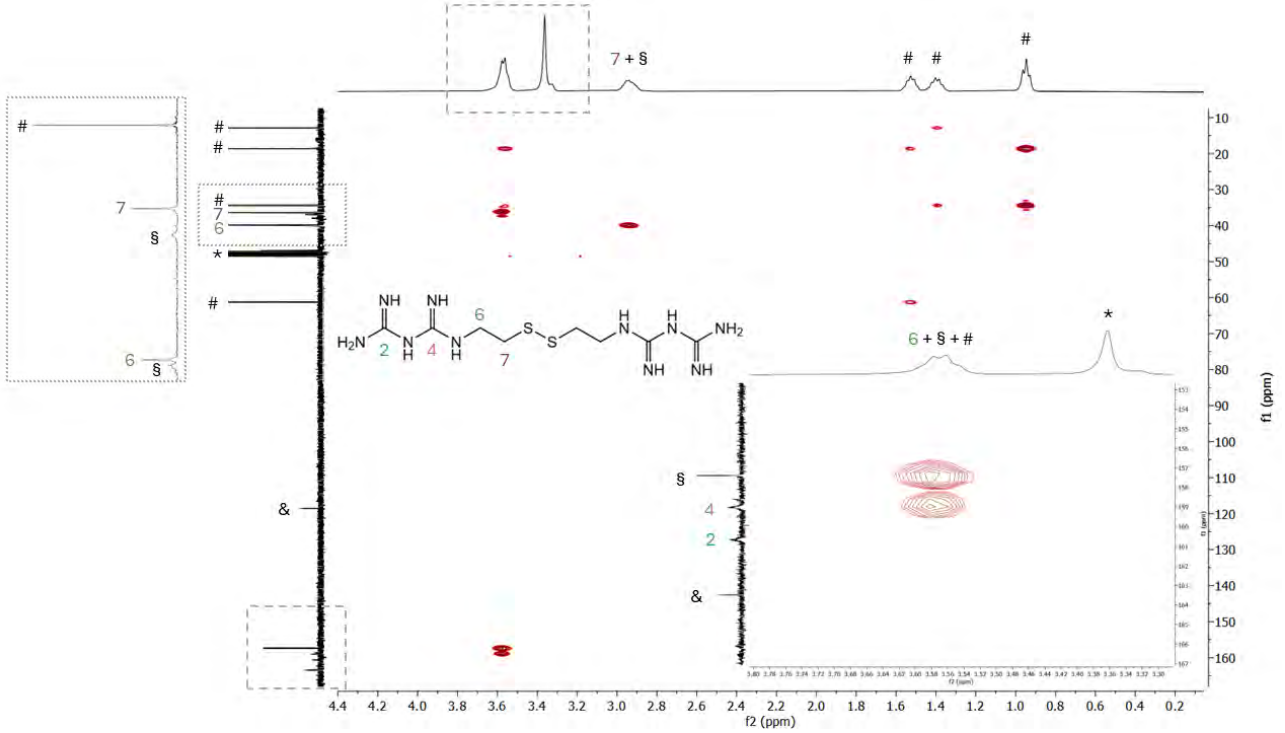

Figure 7. *^{1}H-^{13}C HMBC NMR experiment (9.4T, 300 K, MeOD) of the product of the reaction carried out in n-BuOH with 2 eq of HCl. The § marks the signals assigned to the byproduct, & those of the unreacted cyanoguanidine and * and # respectively the residual MeOH and n-butanol.*

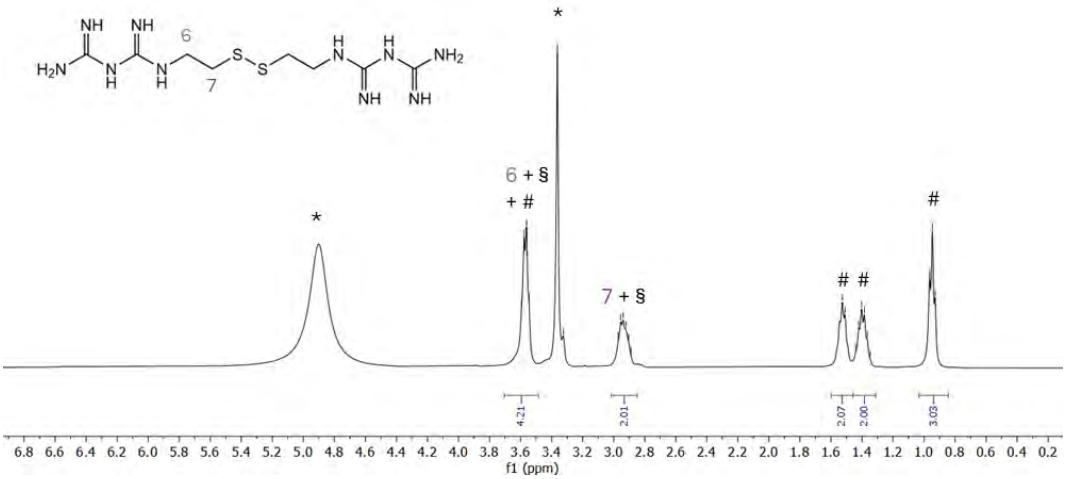

Figure 8. *^{1}H NMR (9.4T, 300 K, MeOD) of the product of the reaction carried out in n-BuOH with 2 eq of HCl. The * and # mark respectively the residual MeOH and n-butanol, while § the aliphatic signals of the byproduct, accidentally overlapped with the aliphatic signals of the product.*

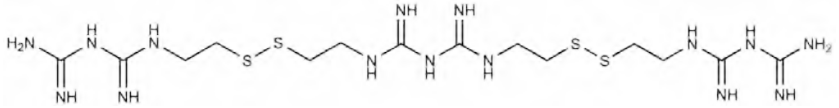

Scheme 7. *Hypothesized structure of a possible byproduct formed during the reaction.*

Another attempt at the synthesis (Scheme 8) was carried out by increasing the equivalents of HCl employed in the reaction to 4, to improve the poor solubility of the reagents in butanol. Contemporarily we lowered the reaction temperature from 130 to 110 °C in an attempt to reduce the amount of byproduct by trying to limit the extent of the side reaction through protonation of the guanidine moiety of cyanoguanidine.

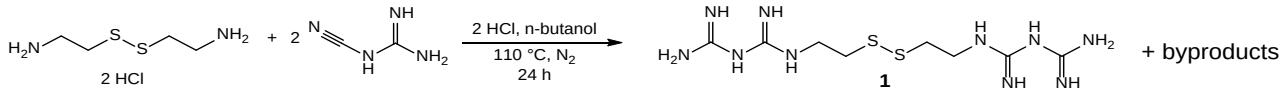

Scheme 8. *Fourth attempt to prepare the product **1** (S-S bis-biguanide), employing 4 equivalents of HCl and carrying out the reaction in n-BuOH.*

The NMR experiments carried out on the crude product showed the formation of a mixture of various compounds. The ^{1}H-^{13}C HMBC spectrum in Figure 9 shows, aside from the signals of the various solvents used during the reaction and the work-up, the same couple of signals at 159.0 and 160.6 ppm already present in the product mixture of the third reaction attempt and assigned to the biguanide group of the desired S-S bis-biguanide, confirming that the increase of the amount of HCl was beneficial. Analogously, the correlation peak in the same heterocorrelate 2D experiment assigned to a symmetrical biguanide of the possible byproduct is still visible, even though the intensity of the ^{13}C signals is too low to see it directly from the 1D $^{13}C\{^{1}H\}$. Other than these two, a third correlation is noticeable between a carbon slightly more up-shielded and a weak ^{1}H triplet at 3.45 ppm, indicating the presence of a new additional but minor subproduct. This hypothesis is supported by the number of signals in both the aliphatic region of the ^{13}C and ^{1}H spectra. While it is difficult to draw conclusions from the latter, the unassigned carbon signals in Figure 9 may be attributed either to a second, possibly asymmetrical byproduct, or to a symmetrical byproduct and unreacted cystamine.

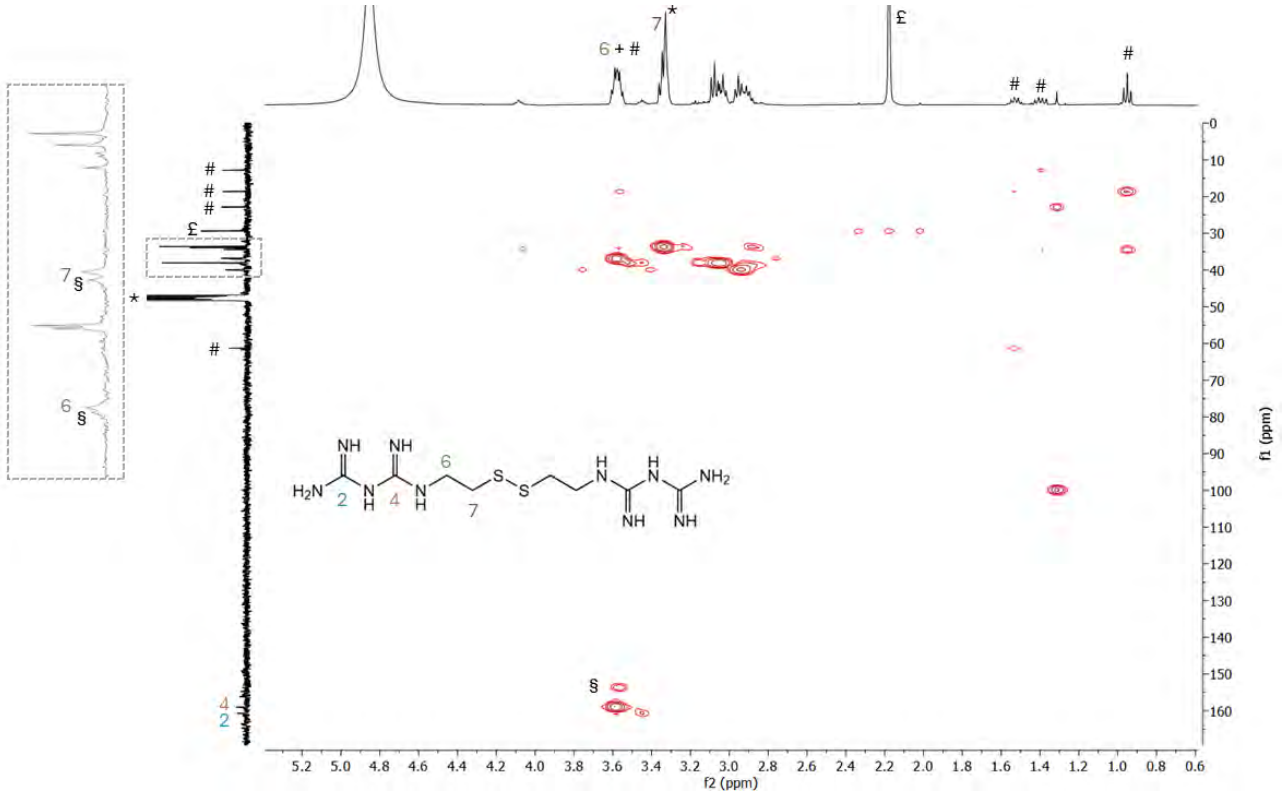

Figure 9. *^{1}H-^{13}C HMBC NMR experiment (9.4T, 300 K, MeOD) of the product of the reaction carried out in n-BuOH with 4 eq of HCl. The § marks the C signals assigned to the byproduct shown in Scheme 7, while *, # and £ respectively those of the residual MeOH, n-butanol and acetone.*

To sum up, in the preparation of the S-S bis-biguanide product a high reaction temperature resulted fundamental to successfully form the biguanide moiety, achieved employing n-butanol as solvent. However, the solubility of the highly polar reagents in this solvent is quite low even upon heating, significantly slowing down the reaction kinetics. We thus tried to increase the amount of HCl employed to catalyze the reaction, from the 2 eq provided by the hydrochloride diamine to a total of 4 eq, to better solubilize the reagents, slightly increasing the reaction time from 16 to 24 h. Nonetheless, this seemed to result in a less clean product, caused either by the formation of more byproducts or by an uncomplete conversion, in agreement to what described in the literature about the protons added during the reaction, that both activate the C≡N group of the cyanoguanidine and protect the free amines by protonation.

However, even though we managed to form our desired product, it was only in a mixture with byproducts, possibly due to the side reaction between the amine and the guanidine moiety of cyanoguanidine. As it will be described in the next section “Separation of S-S bis-biguanide from the product mixture”, the separation of S-S bis-biguanide from the byproducts is not trivial, possessing the molecules very similar groups and polarities, and up to date, we did not find an efficient strategy to obtain an isolated product.

To overcome this undesired side reaction with the guanidine moiety, we proposed a different but similar approach inspired by a work from the literature,[24] involving the reaction of cystamine hydrochloride with 2 eq of sodium dicyanamide to obtain a symmetric molecule exposing two nitrile groups to react with ammonium chloride.

In the future we will also try to exploit microwaves irradiation as heating source, once the optimal parameters in terms of solvent and HCl equivalents have been established, a strategy quite commonly employed to improve yields and reduce reaction times in the synthesis of biguanides.[13,15,19]

Separation of S-S bis-biguanide from the product mixture

The reaction employed to synthetize the S-S bis-biguanide afforded the desired product in a mixture with byproducts; therefore, an efficient purification step to remove these undesired compounds became essential. However, as already mentioned, the purification of this class of molecules is not trivial, since they all possess similar and highly polar functional groups, making their separation challenging. Our first attempt relied on purification by precipitation, a method commonly reported in the literature for isolating compounds of this type. Fu et al.[25] state that upon cooling butanol, a solid precipitates, from which the product can be isolated simply by washing with cold methanol. In contrast, in our case we observed the formation of a yellowish solid already during the heating stage, which we attributed to the formation of the desired product. We separated the warm butanol, cooled it down and evaporated, isolating the solid that precipitated when the temperature of the solvent come back to room temperature. The ^{1}H NMR spectra of the solid formed during the reaction and of the one precipitated from cold butanol (Figure 10) suggest that both fractions contained the same mixture of the S-S bis-biguanide and the byproduct, albeit in different relative amounts. However, the solid proved to be soluble in methanol, preventing its use as a washing solvent for product purification.

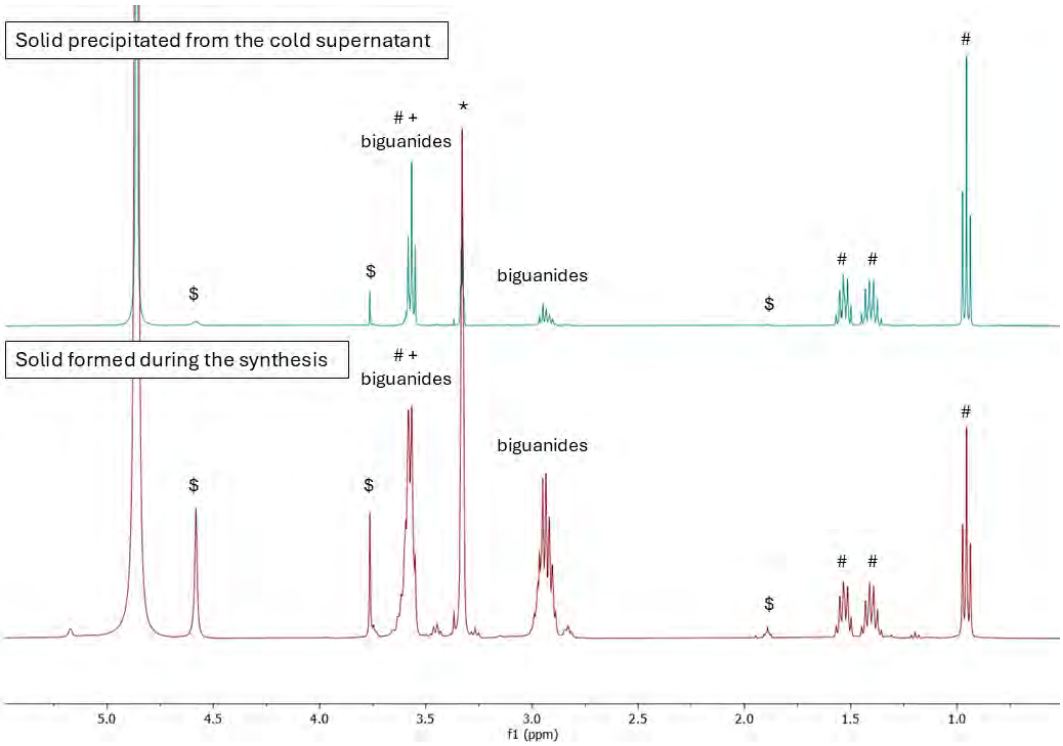

Figure 10. *^{1}H NMR (9.4T, 300 K, MeOD) of the solid precipitated from cold supernatant and soluble in hot butanol (upper panel, blue spectrum) and of the solid formed in hot butanol during the reaction (lower panel, red spectrum). The # and * mark respectively the residual butanol and methanol, while $ an undefined subproduct not containing any biguanide moiety.*

Subsequently, solubility tests were carried out at room temperature: the mixture resulted fully soluble in water, partially in MeOH and acetone, with the precipitation of a solid as the supernatant turned yellowish, and insoluble in acetonitrile and dichloromethane. The solid precipitated from MeOH was separated from the supernatant and analyzed by NMR spectroscopy, showing that even though the sample seemed a bit cleaner than the crude mixture, the S-S bis-biguanide was not separated by most of the byproducts. Nonetheless, the product was successfully and partially isolated from the byproducts, which were precipitated using acetone. The ^{1}H NMR spectrum of the soluble fraction (right panel of Figure 11) mainly shows signals attributed to the S-S bis biguanide and to a species that can be attributed to unreacted cyanoguanidine. However, the undefined multiplicity of the -CH_2 signals in the proton spectrum suggests that additional, undefined byproducts may still be present in this aliquot. Conversely, the solid fraction appeared to contain predominantly the byproduct depicted in Scheme 7,

possibly as a mixture with other byproducts, which may also include residual amounts of the S-S bis-biguanide.

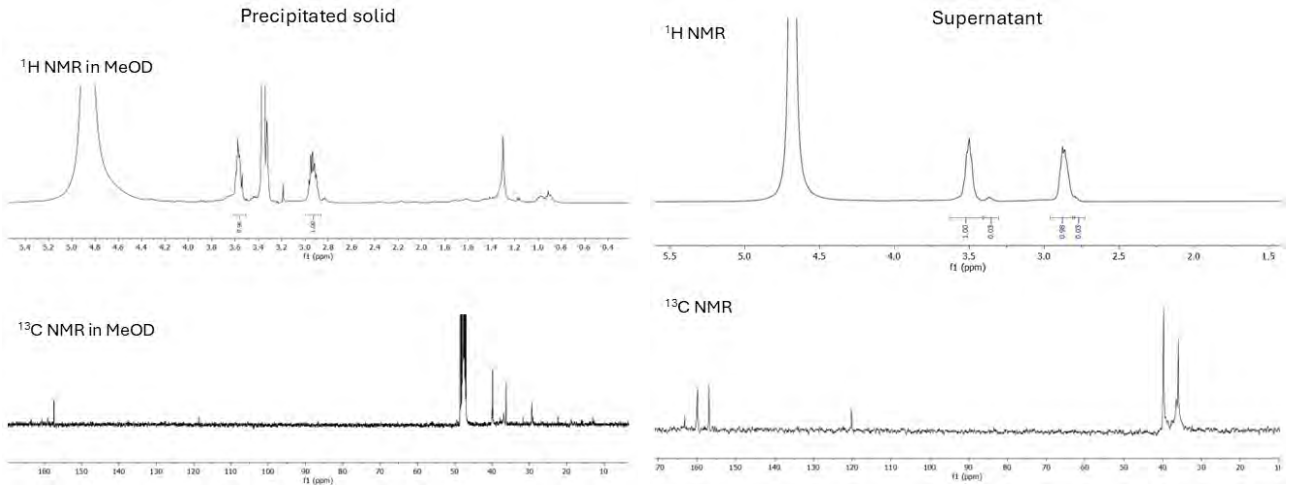

Figure 11. *^{1}H (upper panels) and ^{13}C (lower panels) NMR (9.4T, 300 K, D_2O or MeOD) of the solid precipitated from H_2O with acetone (left spectra) and of the soluble part (right spectra).*

The product recovered in the supernatant after the precipitation of the byproducts with acetone, was then analyzed through UPLC-MS, using H_2O:CH_3CN 1:9 as eluting mixture. The chromatogram (Figure 12) indicates that indeed the product is still in a mixture, but only in the mass spectrum of peak ***a*** the molecular signal of the S-S bis-biguanide is detected (at 321.14 m/z, highlighted in green in Figure 13a), together with other signals (in orange) attributed to the possible fragmentations shown in Scheme 9, coherently to those found in the literature for biguanides-containing molecules.[26,27] In proximity of the S-S bond, two types of fragmentations are possible: one is produced by the cleavage of the C-S bond with a residual positive charge sulfur atom, stabilized by an intramolecular rearrangement that produces a cyclic ion (as seen in the signals at 151.02 m/z, 193.04 m/z, 129.09 m/z and 86.07 m/z, not visible in this mass spectrum but present in Figures 14b and 16a). The signal at 118.04 m/z, on the other hand, might be attributed to the cleavage of the S-S bond without the occurrence of any rearrangement, producing a RS^+ fragment.[28]

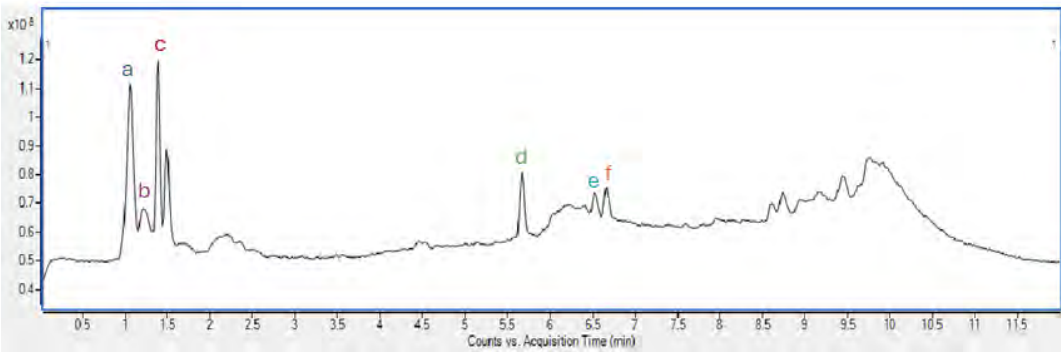

Figure 12. *UPLC chromatogram of the mixture containing the S-S bis-biguanide product, eluted with a H_2O:CH_3CN 1:9 mixture. The y axis shows the total charge measured.*

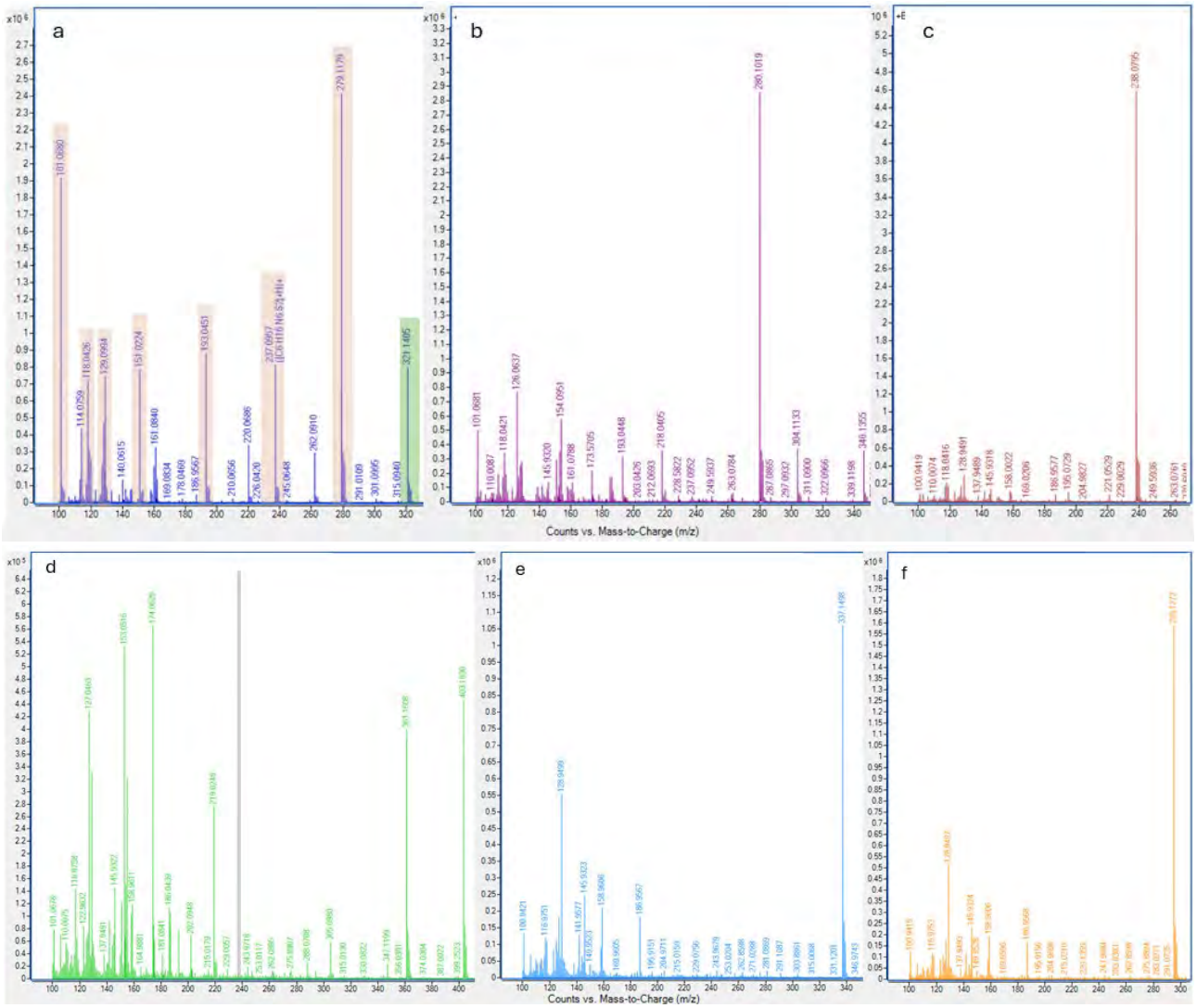

Figure 13. *MS-ESI⁺ of the major peaks isolated with UPLC, as marked in Figure 12. In all the panels the y axis shows the total charge measured.*

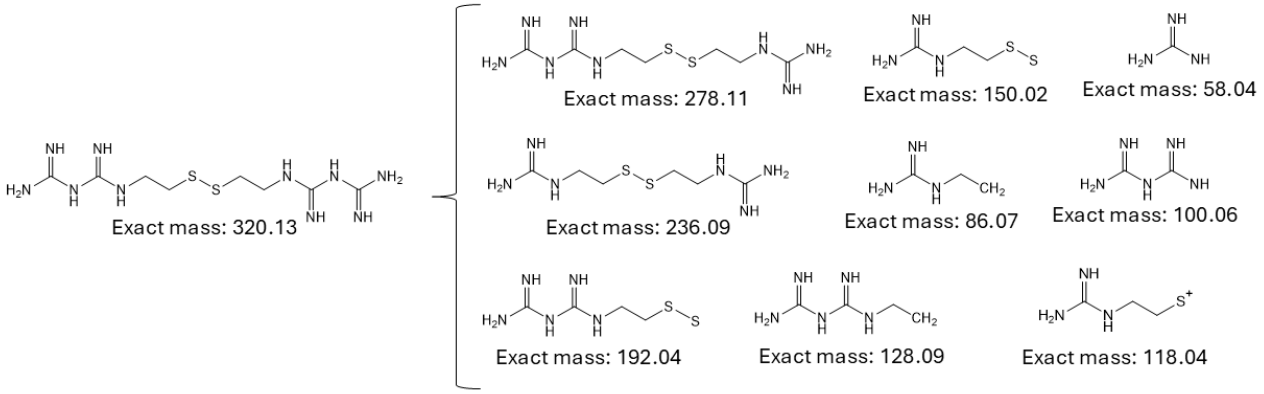

Scheme 9. *Exact mass of S-S bis-biguanide and all its possible fragmentations found in the MS-ESI⁺ spectra as M+1 signals.*

To achieve a better separation of the peak containing the S-S bis-biguanide product from the others, we changed the elution mixture using a gradient starting with an initial CH_3CN:H_2O 98:2 + 0.5% of formic

acid that reached the 30:70 ratio after 15 min. We managed this way to isolate the peak containing the product (peak b, with a retention time of ca. 2 min) as shown in Figure 14.

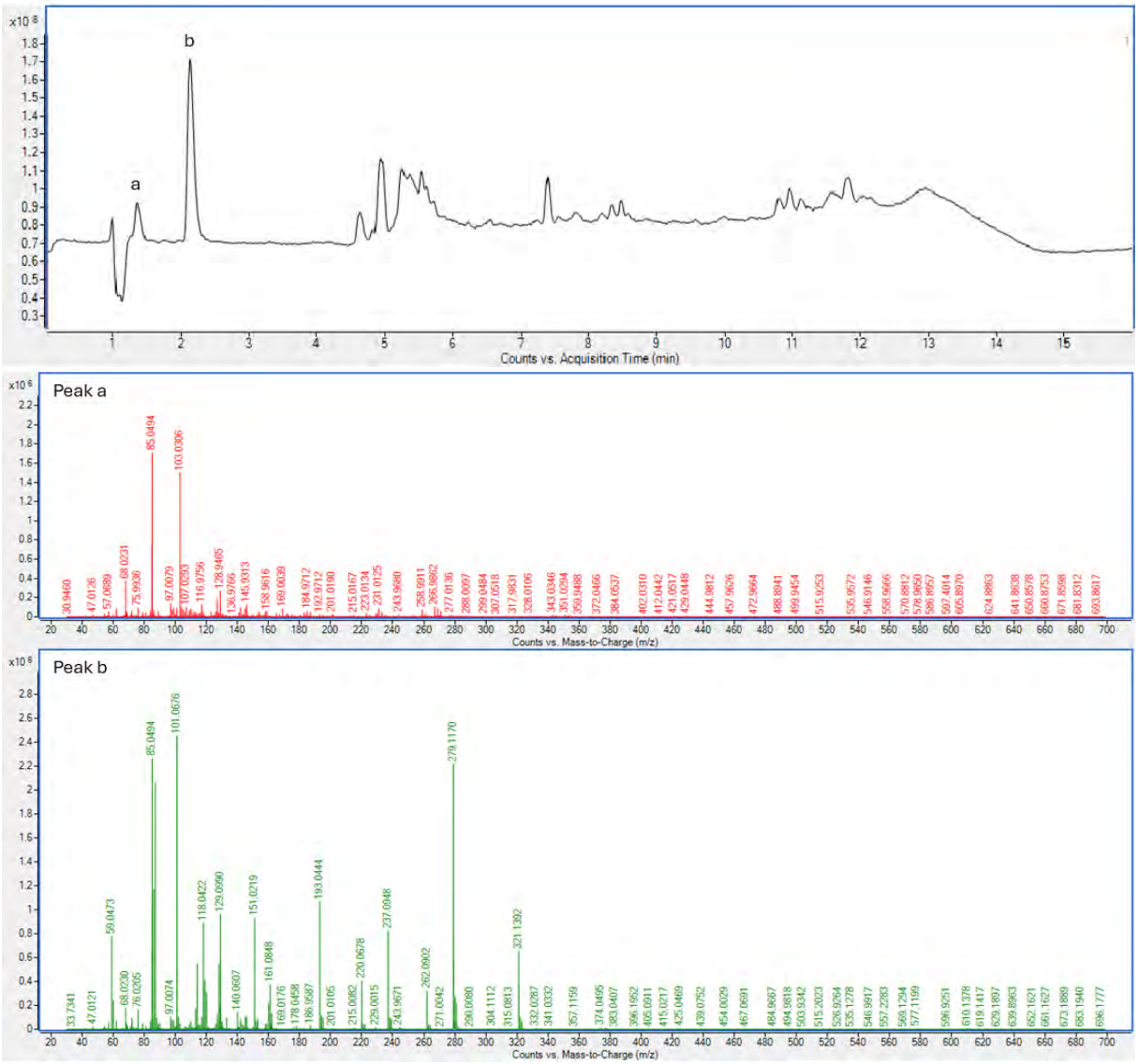

Figure 14. *Upper panel: UPLC chromatogram of the mixture containing the S-S bis-biguanide product, eluted with mixture starting with the initial H_2O:CH_3CN 2:98 composition, that reached the 70:30 ratio after 15 min. Panels a and b show the MS-ESI$^+$ of the first two peaks isolated with UPLC. The mass spectra indicates that only peak b contains the S-S bis-biguanide.*

The separation of the peak containing S-S bis-biguanide was also followed using a photodiode array (PDA) detector. Since neutral biguanides possess a maximum absorption band at 240 nm, shifted to 210 nm when protonated and assigned to the π-π* transition,[29] the eluted sample was monitored using a UV detector at 240 nm. The chromatogram (Figure 15) showed a single peak with a retention time of 2 min, possibly the sole to contain a molecule with biguanide moieties.

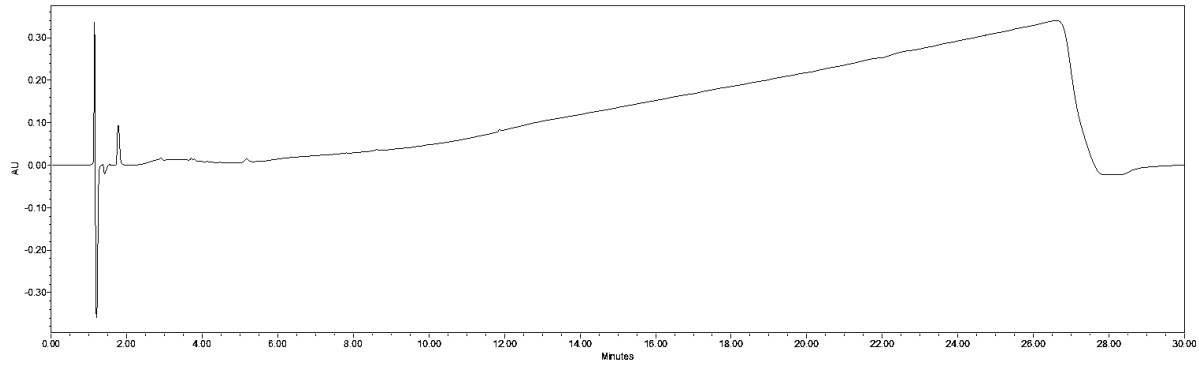

Figure 15. *UPLC-PDA chromatogram using a UV detector at 240 nm. The run was carried out with an initial eluting mixture of $CH_3CN:H_2O$ 98:2 + 0.5% formic acid, with a gradient to reach the composition of $CH_3CN:H_2O$ 30:70 + 0.5% formic acid after 25 min. The initial gradient was restored before starting another run. The peak with a retention time of 2 min was isolated and analyzed with MS-ESI$^+$ through direct injection, confirming its attribution to S-S bis-biguanide product.*

Based on the preliminary results obtained with UPLC, we tried to separate the S-S bis-biguanide from the mixture with HPLC equipped with a semi-preparative column using an eluting mixture with the same gradient as in the UPLC experiments, with an UV detector at 220 and 260 nm wavelengths being the instrument not provided with a detector at 240 nm. We separated two different peaks with similar retention times (ca. 8 and 11 min) which showed an intense absorption at both the two wavelengths, which were then analyzed separately using UPLC-MS (Figure 16). In the mass spectrum of the first peak, with a retention time of 1.5 min, consistent with the preliminary runs, the molecular peak of the S-S bis-biguanide is still not visible, but it shows all the m/z peaks associated with the fragmentations of the product (Scheme 9). Conversely, the second peak separated by HPLC, further separates during the UPLC run in a peak (2a) with 1.5 min retention, whose mass spectrum showed the same m/z signals as peak 1, possibly in a mixture, and a second one (2b) with a retention time of 5.5 min attributed to a byproduct. Nonetheless, a 2D ^1H-^{13}C HMBC NMR spectrum recorded on peak 1 (Figure 17) suggested that we might have isolated the byproduct rather than S-S bis-biguanide. In the MS spectrum of peak 1 there is one signal, at 220 m/z, that can be assigned to the fragmentation shown in Scheme 10 and thus might support this hypothesis. More investigations on the isolation of this molecule are necessary to get a further confirmation and to develop an efficient method to obtain a high amount of this molecule with a good purity to continue the synthetic pathway and prepare the luminescent metformin derivative.

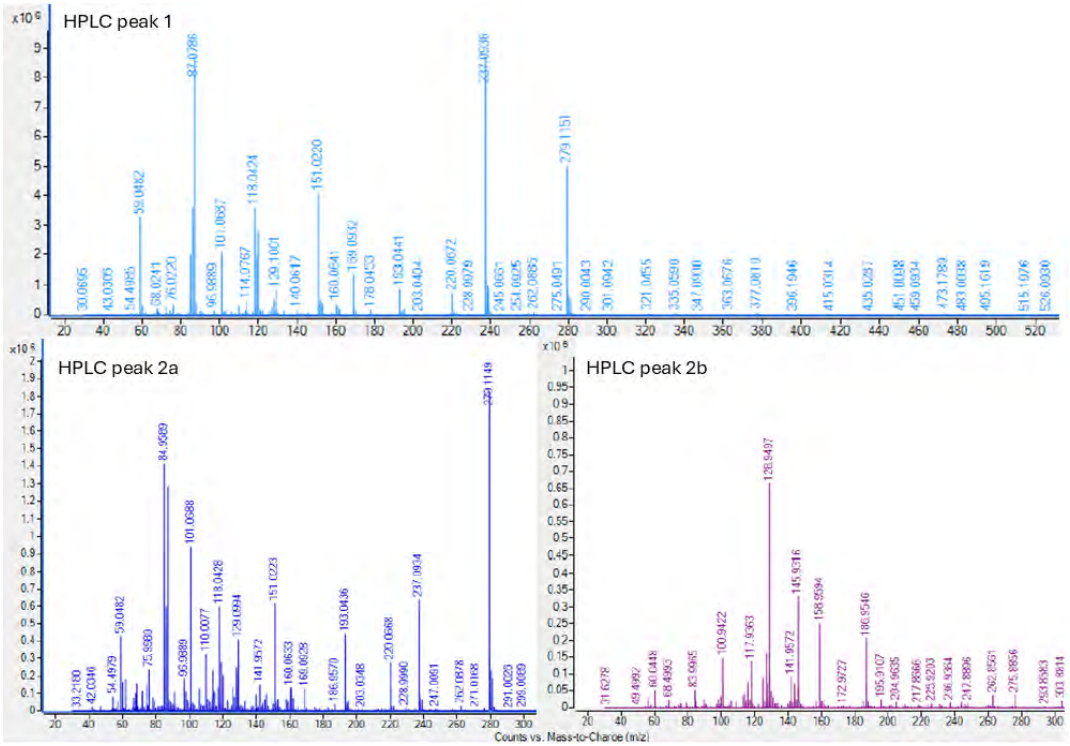

Figure 16. *MS-ESI$^+$ spectrum (fragmentation with a 175.0 V source) recorded on the two aliquots separated with semi-preparative HPLC. Before recording the spectrum an additional UPLC run was performed to check the retention times with those of the previous tests. The label "HPLC peak 1" is related to the peak with a retention time of 8 min in HPLC and of 1.5 min in UPLC, "HPLC peak 2a" of 11 min at HPLC and 1.5 min at UPLC, while "HPLC 2b" of 11 min at HPLC and 5.5 min at UPLC.*

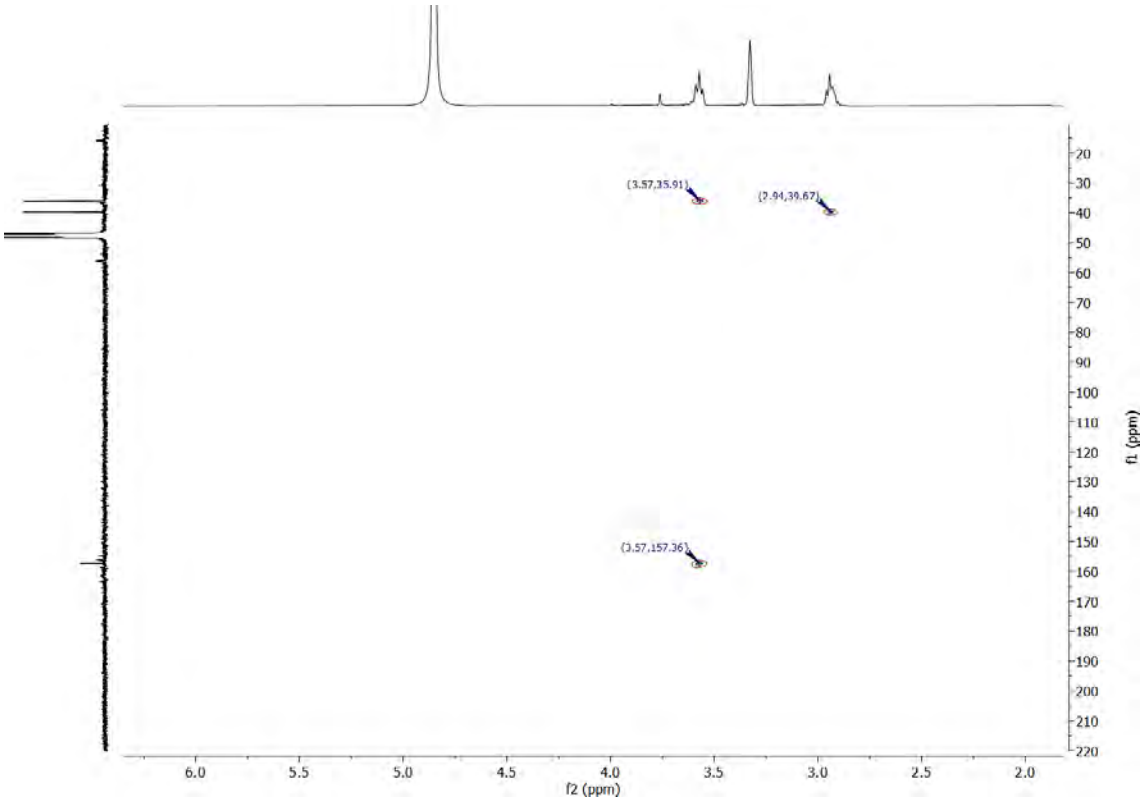

Figure 17. *^{1}H-^{13}C HMBC NMR experiment (9.4T, 300 K, MeOD) of the first peak isolated with HPLC.*

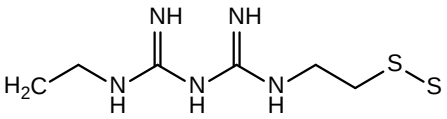

Exact mass: 219.06

Scheme 10. *Fragmentation of the symmetric byproduct possibly assigned to the peak at 220.06 m/z in the MS spectrum of the first peak isolated with HPLC, shown in Figure 16.*

Preparation of biguanide-SH (2) by reduction of the disulfide bridge

In parallel with the attempts to separate the S-S bis-biguanide product from the mixture, we tentatively carried out some of the following steps to prepare the final luminescent molecule on unpurified product **1**, as a proof of concept to test the goodness of the whole synthetic pathway.

The second step consisted in the reduction of the disulfide bond to obtain two equivalents of a molecule exposing the biguanide group at one end the bearing a thiol in the other. In the biochemical field, dithiothreitol (DTT) is extensively used as reductive agent for S-S bonds in peptides, aminoacids and compounds containing amines because of its high selectivity.[30,31] The reaction, which involves the cyclization of DTT forming a very stable intramolecular S-S bond, undergoes only at physiological or basic pH, and it is stopped through acidification to pH 3. The oxidized form of DTT might then be easily removed from the reaction mixture by extraction with ethyl acetate.[32]

The reduction of the S-S bis-biguanide, schematized in Scheme 11, was carried out only on a small aliquot of the mixture containing the product **1**, in an NMR tube to be easily followed by ^{1}H NMR spectroscopy. In Figure 18 the spectra of the S-S bis-biguanide recorded before and after the addition of DTT and after 30 min heating at 50 °C are stacked, showing a partial reduction of the disulfide bond of S-S bis-biguanide.

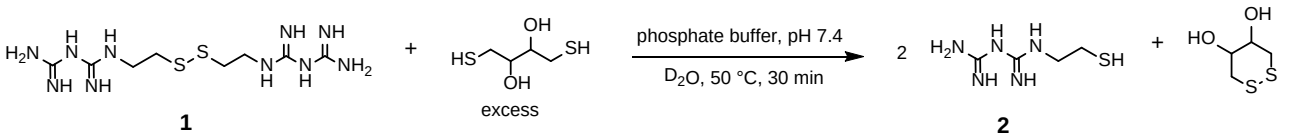

1 **2**

Scheme 11. *Reduction of the disulfide bond of S-S bis-biguanide (**1**) with DTT to obtain the biguanide-SH product (**2**).*

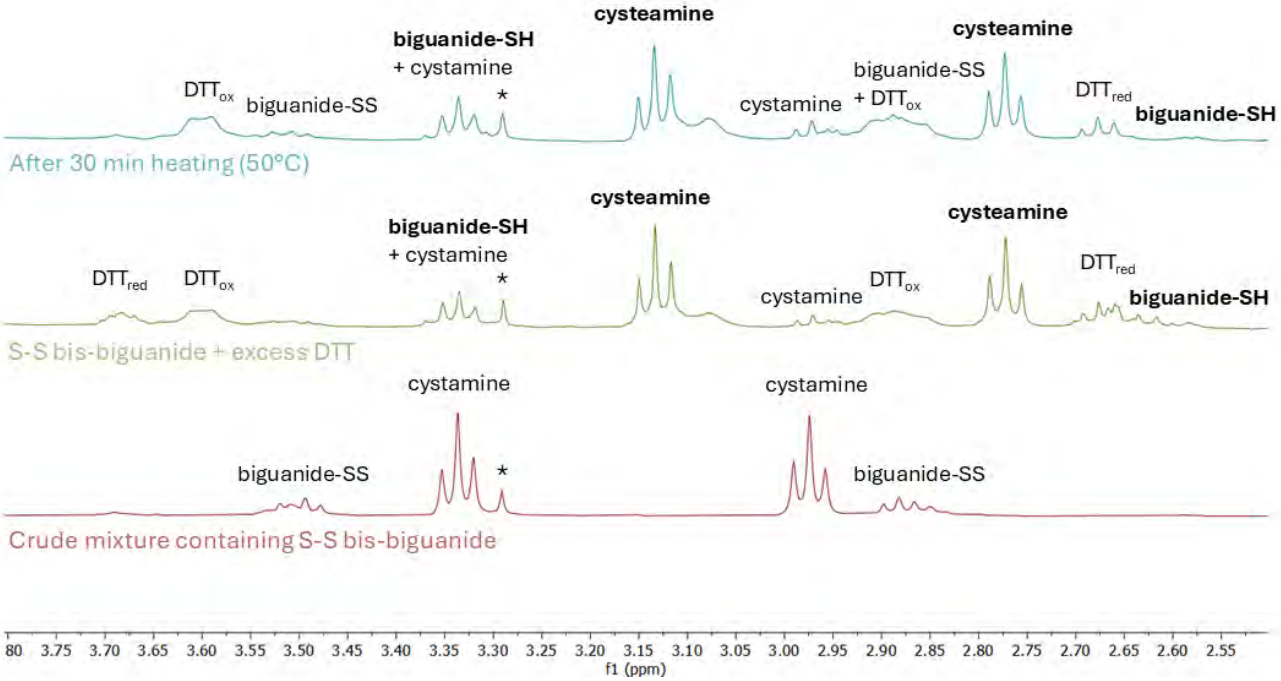

Figure 18. *Stacking of ^{1}H NMR spectra (9.4T, 300 K, D_2O) of the crude mixture containing the S-S bis-biguanide recorded before (red trace) and after (green trace) the addition of DTT and after 30 min heating at 50 °C (blue trace). In bold are highlighted the reduced species in the crude mixture, while the * marks the residual MeOH derived from the mixture containing the S-S bis-biguanide.*

Possibly, a higher excess of DTT would be necessary to fully reduce the S-S bis-biguanide, being this reducing agent usually used in 20-fold excess. For this reason, we moved to the stronger reductant $NaBH_4$, carrying out the reaction (Scheme 12) on a small aliquot of product **1**, in D_2O in an NMR tube as before to easily follow the reaction by ^{1}H NMR spectroscopy.

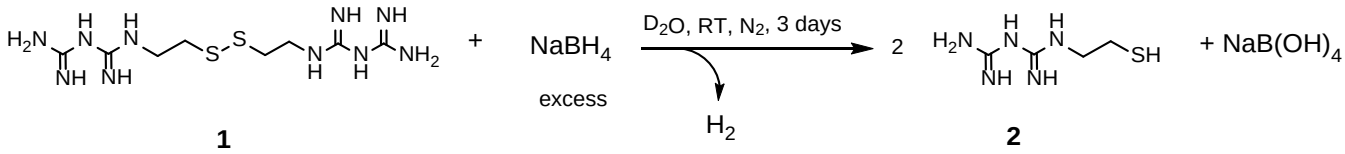

1 **2**

Scheme 12. *Reduction of the disulfide bond of S-S bis-biguanide (**1**) with $NaBH_4$ to obtain the biguanide-SH product (**2**).*

The ^{1}H NMR spectra recorded before and at the end of the reaction (Figure 19) confirmed the success of the reduction of disulfide bridge, with a shift of the two -CH_2 signals from 3.48 and 2.85 ppm to 3.18 and 2.56 ppm. Being $NaBH_4$ a reducing agent without selectivity toward the S-S bond,[32] we recorded two additional ^{1}H-^{13}C HMBC (Figure 20) and HSQC experiments on the product, confirming that the biguanide moiety remained untouched after the reaction due to persistence of the long-range correlation between the proton at 3.18 ppm and the C=N carbon at 158.9 ppm. Moreover, a ^{1}H-^{15}N HMBC experiment (Figure 21) showed a correlation of both aliphatic protons with a N signal at 86.9 ppm, a chemical shift associated in the literature to one of the -NH of biguanides,[33] as assigned in the figure, further confirming that the biguanide was not reduced nor cleaved by $NaBH_4$.

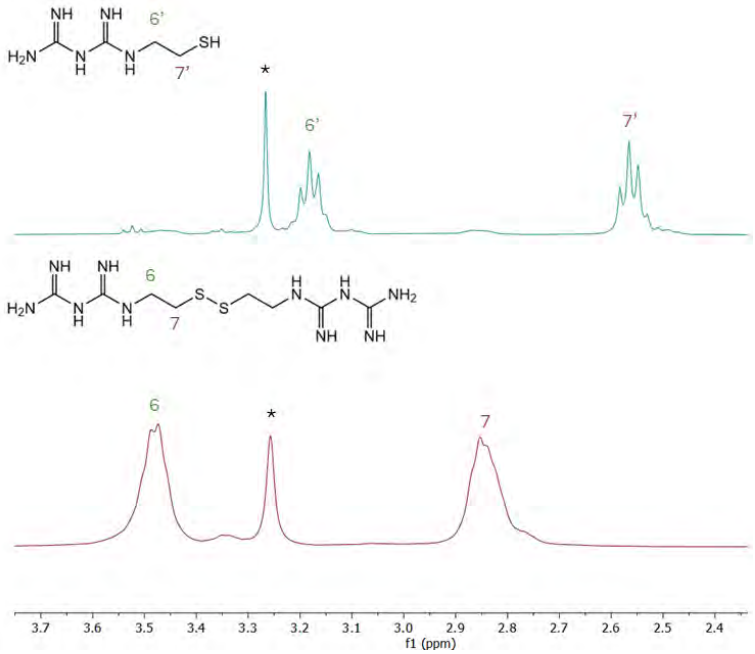

Figure 19. *Stacking of ^{1}H NMR spectra (9.4T, 300 K, D_2O) of the S-S bis-biguanide before the reduction of the disulfide bond with $NaBH_4$ (red trace) and of the biguanide-SH at the end of the reaction (blue trace).*

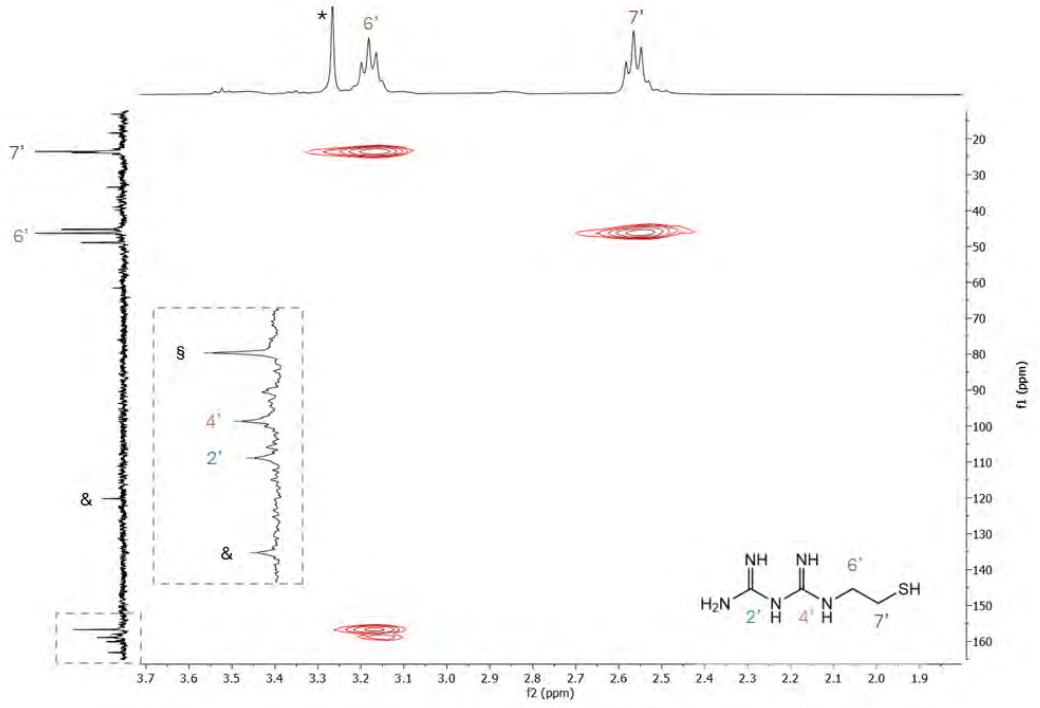

Figure 20. *^{1}H-^{13}C HMBC NMR experiment (9.4T, 300 K, D_2O) of the biguanide-SH after the reduction of the disulfide bond with $NaBH_4$. The * marks the residual MeOH, while § the byproduct, as discussed in the previous section and & the residual cyanoguanidine, already present in the reagent mixture containing the S-S bis-biguanide.*

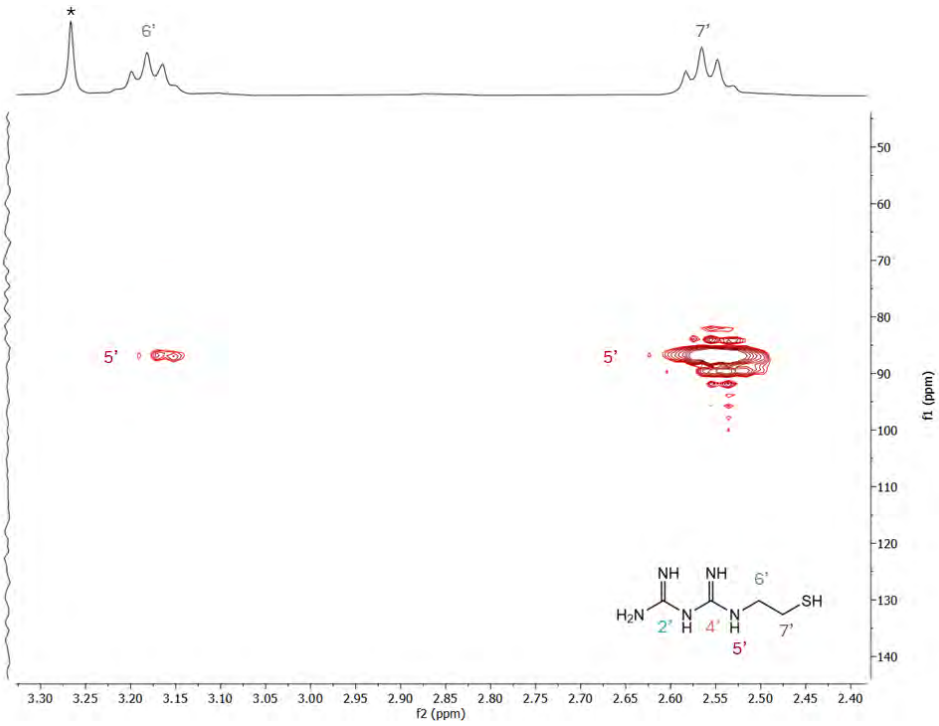

Figure 21. *^{1}H-^{15}N HMBC NMR experiment (9.4T, 300 K, D_2O) of the biguanide-SH after the reduction of the disulfide bond with $NaBH_4$. Spectrum recorded using NH_4OH as reference.*

Conjugation of biguanide-SH to the fluorescent adduct (4)

The final step of the synthetic pathway involved the coupling of the biguanide-SH to a functionalized fluorescent molecule to obtain the luminescent product bearing a terminal biguanide, aimed at investing the interaction of this group with tumoral cells exploiting techniques such as confocal microscopy. N-(2-aminoethyl)maleimide was selected as linker between the two molecules, being functionalized maleimides vastly used in the literature for various applications including the labelling of biomolecules containing thiols with fluorescent moieties. This is due to the high selectivity of the double bond of the maleimide toward -SH groups through Michael addition between pH 6.5 and 7.5 that proceeds at a rate ca. 1000 times higher than the reaction with amines. Conversely, at higher pH values, some cross-reactivity with amino groups takes place.[34] The terminal amine of the substituted maleimide was reacted with the isothiocyanate group of the rhodamine isothiocyanate (RITC), affording the partial formation of the rhodamine-maleimide adduct (**3a**). Due to a partial degradation of the isothiocyanate moiety of RITC and the partial opening of the maleimide ring during the reaction, we attempted it again moving to a just purchased fluorescein isothiocyanate (FITC) as the luminescent molecule and changing some reaction parameters to overcome the problems occurred in the reaction with RITC, successfully yielding to the fluorescein-maleimide adduct (**3b**). Unfortunately, for time issues we did not carry out the last synthetic step of the pathway to prepare the final product **4b**.

Beside the high reactivity of the maleimide double bond toward thiols, another reason behind the choice of the maleimide linker was that the thiourea group originating from the reaction between the isothiocyanate and the amine moieties resulted more stable compared to the dithiocarbamate originating from the reaction with a thiol moiety and that in literature the formation of dithiocarbamate was reported to quench the emission of FITC.[35]

For the first synthetic step, schematized in Scheme 13, we followed a procedure previously used by our research group,[36] employing as one of the reagents N-(2-aminoethyl) maleimide prepared by our group accordingly to two literature procedures for the mono-protection of diethylamine[37] and its consequent reaction with maleimide[38].

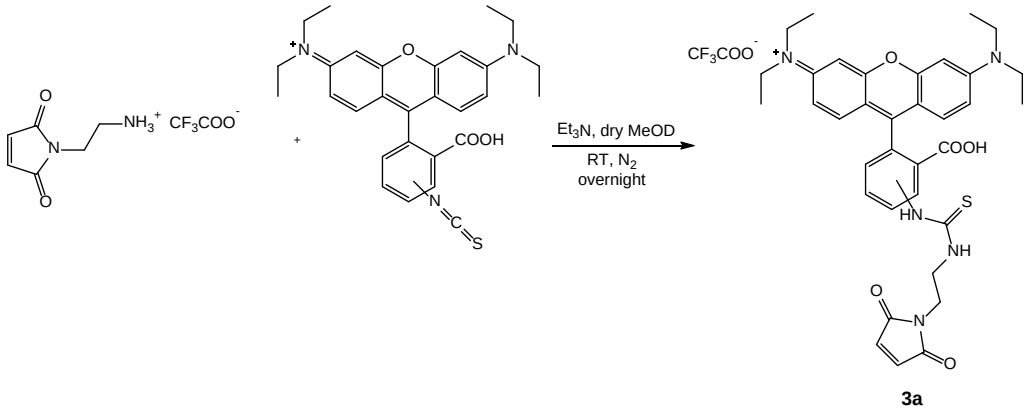

Scheme 13. *Preparation of the rhodamine-maleimide adduct (**3a**) by reacting rhodamine isothiocyanate with N-(2-aminoethyl) maleimide.*

The reaction between RITC (mixture of isomers) and N-(2-aminoethyl) maleimide was monitored by ^{1}H NMR spectroscopy, from the shift of triplet at 3.83 ppm, assigned to the proton in α position to the -NH_2 of N-(2-aminoethyl) maleimide to 3.57 ppm, together with the very slight shift of the vinyl protons of the maleimide moiety from 6.92 to 6.93 ppm. Despite the efforts to preserve maleimide group towards hydrolysis, the concomitant appearance of an AB system (doublets centered at 6.24 and 6.58 ppm) confirmed the partial opening of the maleimide ring. The opening of the maleimide group due to the hydrolysis of the amide bond occurs in the presence of H_2O and proceeds faster at higher pH, resulting in the formation of the maleamic acid, which is unreactive toward thiols (Scheme 14).[39]

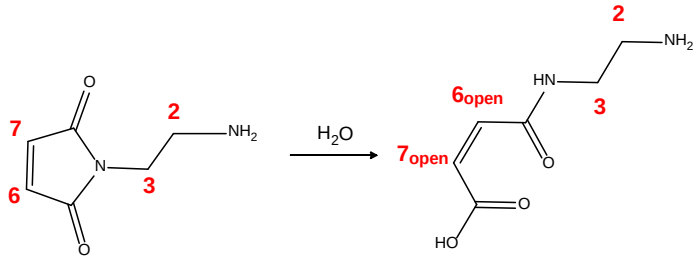

Scheme 14. *Opening of the maleimide ring by H_2O at basic pH.*

According to this attribution, the last spectrum recorded after 28 h suggested that the product was not formed quantitatively, since the triplet at 3.83 ppm and the singlet at 6.92 ppm are is still visible, even after 48 h, where the ^{1}H spectrum remained unchanged (datum not shown). The ^{1}H NMR spectra recorded over time are shown in Figure 22.

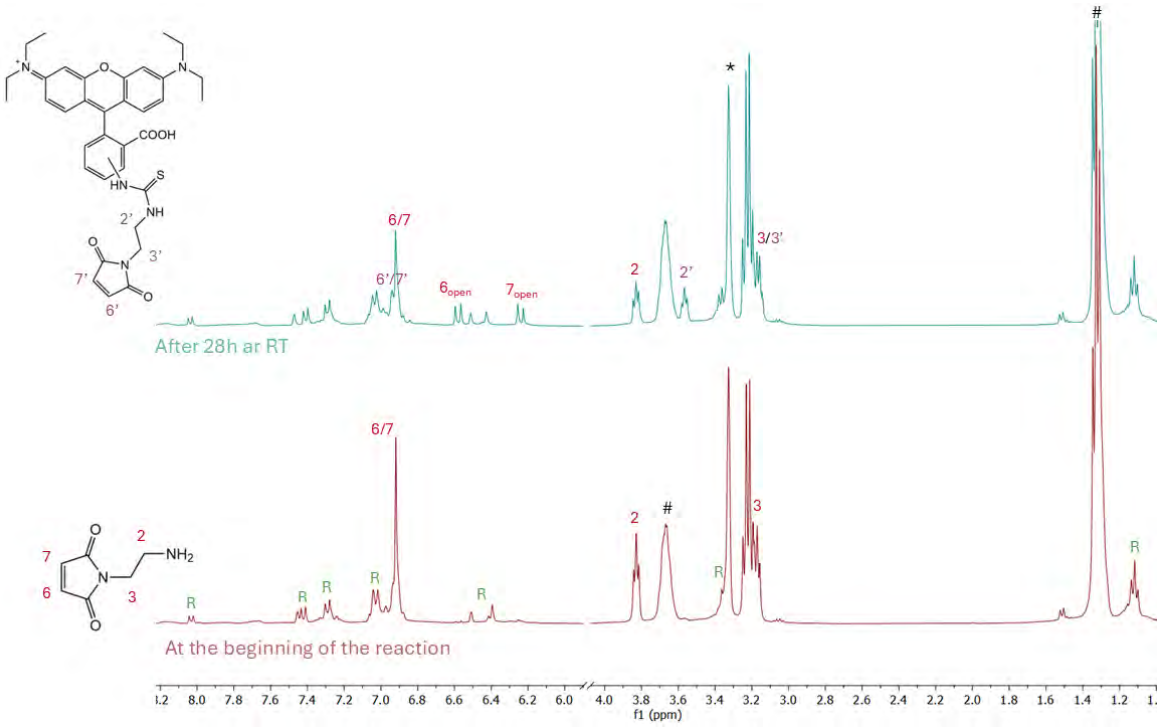

Figure 22. *^{1}H NMR spectra (9.4T, 300 K, MeOD) recorded over time at the beginning of the reaction (red trace) and after 28 h (blue trace) for the formation of of the rhodamine-maleimide adduct (**3a**). The # mark the NEt_3 signals, * the solvent, while the R the rhodamine moiety signals.*

Based on literature attributions,[34] in the ATR-FTIR spectra recorded on RITC before and at the end of the reaction (Figure 23), we attributed the broad band at 2020 cm^{-1} to the asymmetric stretching mode of N=C=S, which completely vanished after the reaction. Moreover, the band at 1644 cm^{-1}, due to the C=N stretching, considerably decreased, while the band at 1200 cm^{-1} that increased after the reaction is attributable to the thiourea formation.

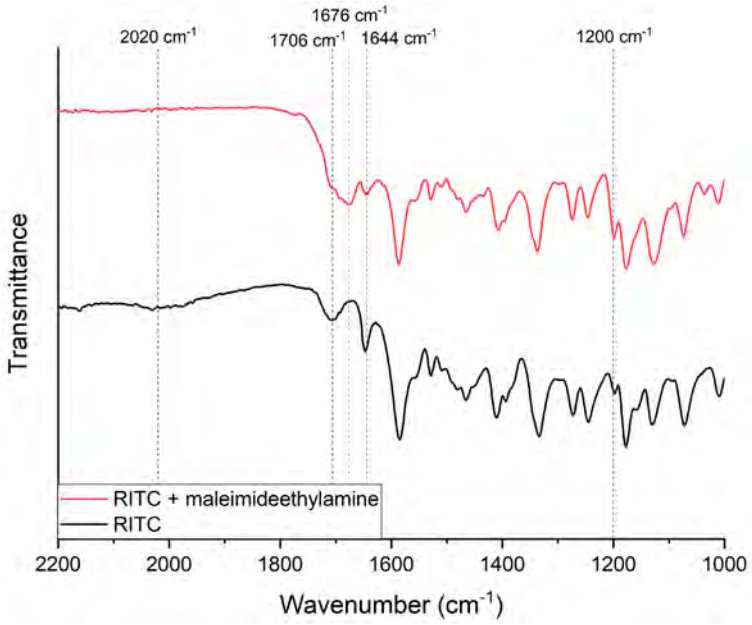

Figure 23. *Selected region of ATR-FTIR spectra of RITC (black trace) and of the rhodamine-maleimide product (red trace).*

Unfortunately, the broad and weak FTIR band at 2020 cm^{-1} in the starting RITC spectrum indicated that the isothiocyanate group of the reagent partially degraded, and this was the main reason we ascribed the incomplete reaction of the maleimide amine observed by ^{1}H NMR. For this reason, we attempted the same reaction again, employing FITC instead of RITC. In addition, to avoid the hydrolysis of the maleimide ring, we changed the solvent of the reaction to dry DMSO and employed the weaker base N-ethyldiisopropylamine (DIPEA) to increase the pH without producing the conditions necessary to open the ring. The procedure of the reaction between 2-(aminoethyl)maleimide and FITC is shown in Scheme 15.

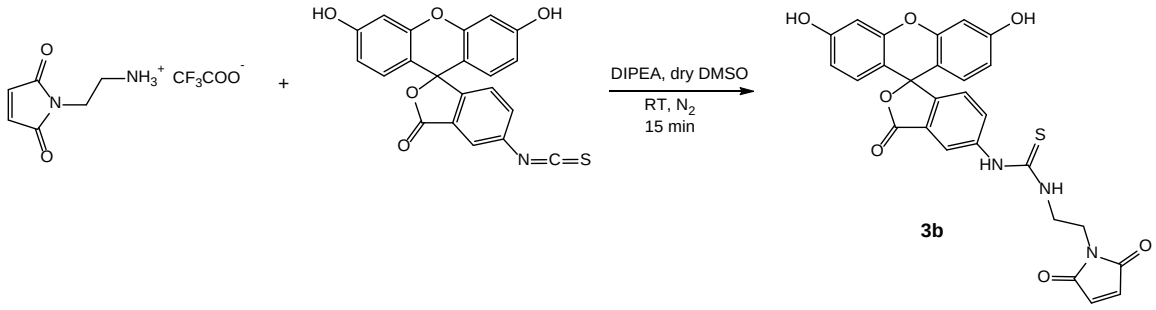

Scheme 15. *Preparation of the rhodamine-maleimide adduct (**3b**) by reacting fluorescein isothiocyanate with N-(2-aminoethyl) maleimide.*

The FTIR spectrum of FITC shows the asymmetric stretching mode of –N=C=S at 2129 cm^{-1} that indicates the presence of the isothiocyanate group, together with the presence of the C=N stretching band at 1663 cm^{-1}. The addition of N-(2-aminoethyl) maleimide salt provoked the decrease of the isothiocyanate

band, and subsequently to the addition of the base DIPEA, the FTIR spectrum showed the complete disappearing of this band. The three FTIR spectra are shown in Figure 24.

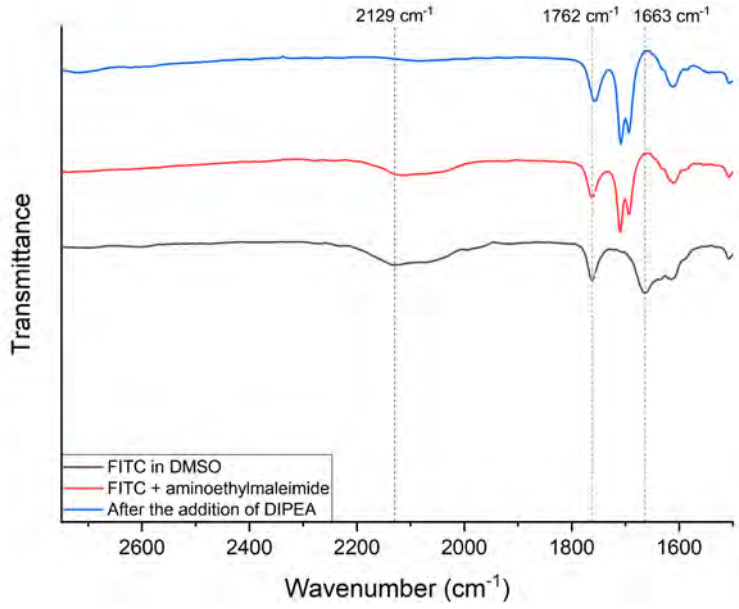

Figure 24. *Selected region of the FTIR spectra of FITC, mixture 1:1 of FITC and N-(2-aminoethyl) maleimide CF_3COOH salt, and the same mixture additioned with 0.9 equiv of DIPEA.*

The NMR spectroscopy was employed to assure that the disappearance of the bands associated to isothiocyanate was not due to a mere hydrolysis of this functional group. The ^1H spectrum, reported in Figure 25, confirmed the formation of the thiourea by the detection of the two NH signals at 8.12 and 9.98 ppm as well as by the shift of the CH_2(2') signal from 2.99 ppm to 3.75 ppm. All the proton signals were attributed through 2D homonuclear ^1H-COSY and ^1H-NOESY (not showed), as well as heteronuclear ^1H-^{13}C HSQC and ^1H-^{13}C HMBC experiments. From the point of view of ^{13}C, the heteronuclear experiments enable to recognize the thiourea quaternary carbon at 181.2 ppm through the development of a long range correlation with the CH_2(2') signal.

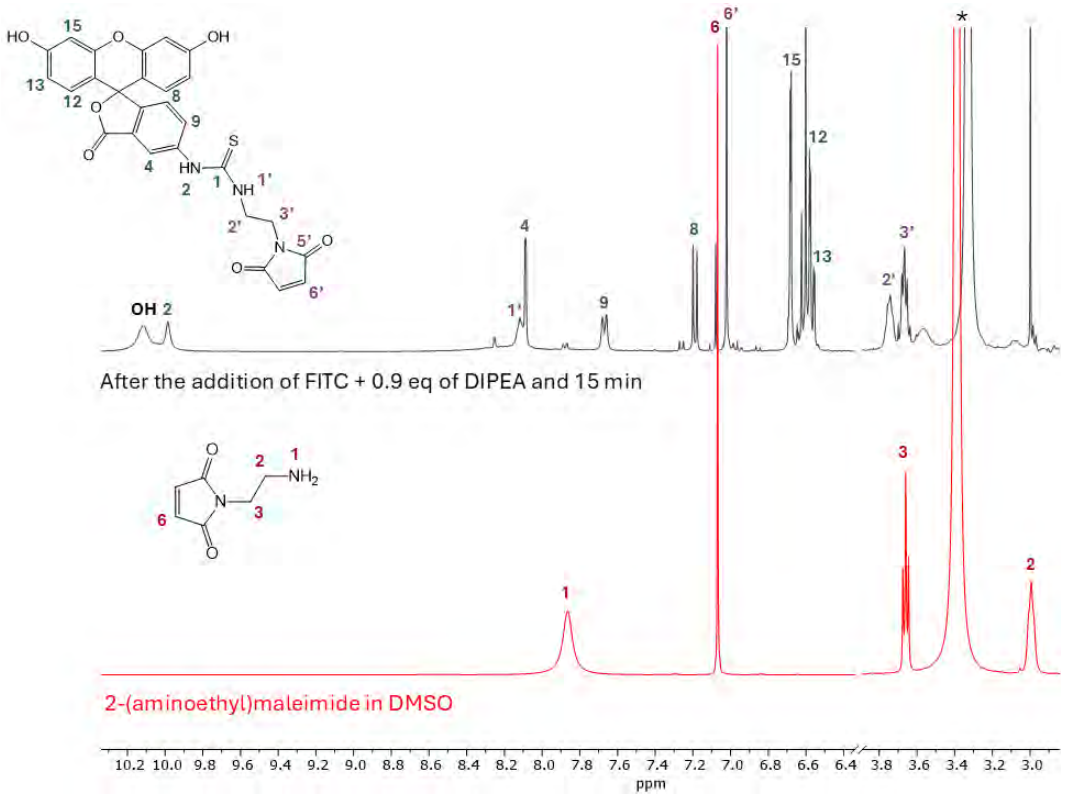

Figure 25. *^{1}H NMR spectra (9.4T, 300 K, DMSO/DMSO-d_6) of N-(2-aminoethyl) maleimide CF_3COOH salt (red trace) and its mixture 1:1 with FITC in the presence of 0.9 equiv of DIPEA (black trace). * marks the H_2O signal.*

This last reaction will be attempted using the fluorescein-maleimide adduct (**3b**). Notably, since we did not manage to isolate the S-S bis-biguanide, we attempted this last reaction on the crude product **1**. Thus, it is difficult to estimate the correct ratio between the two reagents and evaluate the feasibility of this reaction.

Conclusions

Metformin is a vastly used commercial drug for Type II diabetes treatment, whose action is mainly based on (but not limited to) the suppression of hepatic glucose production and on the improvement of insulin sensitivity and glucose uptake by skeletal muscles and adipose tissues. Beyond diabetes, metformin has been associated with a wide range of health benefits, such as weight loss, anti-aging, obesity, liver, renal and cardiovascular diseases treatment, as well as cancer prevention and treatment. Regarding its antitumoral action, in recent studies[7,8,40] a lower incurrence of various kinds of tumor has been reported in diabetic patients treated with this drug, suggesting a correlation between the use of metformin and an inhibition of the growth and proliferation of cancer cells. The exact mechanisms in which metformin exerts its antitumoral action remains uncertain, although various hypotheses have been formulated. It is stated, however, that the molecule is involved in the regulation of energetic metabolism of the cells.

Considering this background, this work aimed the preparation of a luminescent molecule bearing a terminal biguanide moiety to mimic metformin and obtain an insight on the antitumoral action of this drug, by studying the interaction of our biguanide with tumoral cells using techniques such as confocal microscopy. Being still an ongoing project, until now we focused on developing an efficient synthetic strategy to prepare such molecule. More in detail, the first step involved the synthesis of the biguanide group by reacting cystamine dihydrochloride with two equivalents of 1-cyanoguanidine to form a symmetric bis-biguanide bearing a disulfide bond to be reduced, giving two equivalents of a biguanide exposing a terminal thiol, then exploited for its linkage to a luminescent molecule. We attempted the reaction by refluxing various solvents (H_2O, methanol and butanol) and employing various amounts of HCl to catalyze the reaction, since both temperature and pH play a role in activating the nitrile group of cyanoguanidine. On the other hand, as protonated amines do not undergo the reaction due to the loss of their nucleophilic character, choosing the right amount of HCl to activate the cyanoguanidine without protecting the diamine plays a key role for the outcome of the reaction. The desired product, S-S bis-biguanide, was obtained carrying out the reaction in n-butanol and employing just the 2 equivalents of HCl provided by the cystamine dihydrochloride. However, the reactivity of primary amines at high temperature is high and not limited to C≡N, thus a byproduct was possibly obtained through a side reaction between the bisamine and the guanidine of cyanoguanidine and the subsequent reaction between the free nitrile group with partially reacted cystamine, obtaining a byproduct supposedly similar to the S-S bis-biguanide, but containing a symmetric biguanide in the middle of the molecule and two disulfide bonds.

The S-S bond of the product and of the byproduct was then selectively reduced employing an excess of $NaBH_4$, leaving the biguanide group as it is. The final part of the synthetic pathway involved the reaction between the thiol of biguanide-SH and the maleimide moiety of an adduct formed with a luminescent molecule and a maleimide. This adduct was formed by reacting fluorescein isothiocyanate with a N-(2-aminoetil) maleimide, exploiting the reactivity of the terminal amine group of the latter toward the thiocyanate group, forming a thiourea. The last reaction of the synthetic pathway was not carried out for time issues and will be attempted when the S-S bis-biguanide will be successfully isolated from the product mixture.

We also investigated a strategy to isolate the S-S bis-biguanide from the crude product of the first synthetic step. The separation of these molecules was not trivial, as they expose similar groups with similar polarity and characteristics. The washes with methanol suggested by the literature failed in isolating the desired product, but we managed to separate the product from part of the byproducts through a precipitation from H_2O/acetone. This partially purified mixture was then analyzed with UPLC-MS to determine the best eluting mixture and a peak that seemed to contain the symmetric byproduct

rather than the S-S bis-biguanide was isolated by HPLC equipped with a semi-preparative column. Further investigation on the isolation of the S-S bis-biguanide is still needed as well as testing different synthetic strategies as the one proposed above, to isolate a large amount of S-S bis-biguanide to carry out a deeper study on the last reaction of the synthetic pathway, with the final aim of preparing a luminescent biguanide pure enough to be employed for the biological investigation.

Experimental

Materials and instruments

Ultrapure water (Milli-Q, Millipore, resistivity = 18 MΩcm^{-2}) was used for the preparation of the aqueous solutions. Commercial reagents were used without further purification. N-(2-aminoethyl) maleimide was prepared by our research group as described in our previous work.[36] NMR experiments were acquired on a Bruker DRX400 spectrometer equipped with a Bruker 5 mm BBI Z-gradient probe head with a maximum gradient strength of 53.5 G/cm (π/2 pulse: ^{1}H 8.5 μs, ^{13}C 13 μs, ^{15}N 28 μs) operating at 400.13 MHz for ^{1} H, 100.62 MHz for ^{13}C NMR and 40.55 MHz for ^{15}N NMR. FTIR spectra were acquired on a PerkinElmer Frontier instrument equipped with an ATR accessory with a diamond/ZnSe crystal. The separation of the S-S bis-biguanide by UPLC-MS was performed on a 1260 Infinity II Prime LC UPLC coupled to a 6230 LC/TOF time-of-flight (TOF) mass spectrometer by Agilent technologies (Santa Clara, CA, USA) equipped with an ESI ion source, while by UPLC-MS on a Waters ACQUITY UPLC (Ultra-high Performance Liquid Chromatography) system (Waters corp., United States) equipped with a quaternary solvent manager system and a UV–Vis photo diode array (PDA). In both cases the separation was carried out on an ACQUITY UPLC® BEH C18 column (100 mm × 2.1 mm i.d.; 1.7 μm particle size). The biguanide separation with RP-HPLC was performed on an Agilent 1200 Series system with a semi-preparative column Luna C18 (250 x 10 mm, 5 mm) at a flow rate of 2 mL/min. Solvent A (0.1% TFA in CH_3CN) and solvent B (0.1% in water) were employed in the following gradient: 98% A at 0 min, 30% A at 25 min. The method was used with a UV detector at 220 and 260 nm.

Attempt to synthesize S-S bis-biguanide (1) in H_2O

The first attempt in the preparation of S-S bis-biguanide was carried out in H_2O employing 7 eq of HCl to catalyze the reaction. Cystamine hydrochloride (300.5 mg, 1.33 mmol) and 1-cyanoguanidine (246.8 mg, 2.94 mmol, 2.2 eq) were suspended in 2.45 mL of milliQ H_2O and 0.555 μL of HCl 37% were added to reach a total of 7 eq under N_2 atmosphere. During the heating process, the suspension completely solubilized, obtaining at first a yellowish solution that turned completely clear after some minutes. The mixture was refluxed overnight at 100 °C under inert N_2 atmosphere. It was then cooled down to RT and 862 μL (7 eq) of NaOH 32% were added, the water evaporated and the yellowish oil washed once with ethyl acetate and a second time with acetonitrile to separate it from NaCl. The NMR experiments carried out on the product suggested the unsuccess in preparing the desired product.

Attempt to synthesize S-S bis-biguanide (1) in MeOH

The second attempt in the preparation of S-S bis-biguanide was carried out in MeOH employing 4 eq of HCl. Cystamine hydrochloride (337.9 mg, 1.5 mmol) and 1-cyanoguanidine (226.9 mg, 2.7 mmol, 1.8

eq) were suspended in 1.5 mL of MeOH under N_2 protection and refluxed to 70 °C. After 1.5 h of heating 250 µL of HCl 37% were added to facilitate the dissolution of the reagents. After 29 h of heating the reaction was cooled to RT and left stirring under N_2 atmosphere overnight. 2-butanol was then added (5 mL) to the reaction mixture and the precipitated solid filtered. From the NMR experiments on the product it is unclear but unlikely whether the desired product was obtained.

Synthesis of S-S bis-biguanide (1) in *n*-butanol

The S-S bis-biguanide was successfully prepared using *n*-butanol as solvent without the addition of HCl except the 2 eq from cystamine hydrochloride. This time the glassware was left at 120 °C in the oven overnight before the synthesis.

Cystamine hydrochloride (452.0 mg, 2.01 mmol) and 1-cyanoguanidine (336.0 mg, 3.99 mmol, 2 eq) were suspended in 3 mL of *n*-butanol under N_2 protection and refluxed at 130 °C overnight. After 3 h of heating a yellow sticky solid was suspended in the clear solution, besides whom all the reagents were completely solubilized. At the end of the reaction the solid was filtered and dissolved with MeOH. The NMR spectra suggested the formation of the product in a mixture with a byproduct whose structure was tentatively determined. ^{1}H NMR of S-S bis-biguanide (9.4 T, 300 K, MeOD) δ 3.58 ppm (2H, m, CH(6,11)), 2.95 ppm (2H, m, CH(7,12)). ^{13}C NMR of S-S bis-biguanide (9.4 T, 300 K, MeOD) δ 160.6 ppm (C=NH(2,15)), 159.0 ppm (C=NH(4,13)), 39.9 ppm (CH_2(7,10)), 36.4 ppm (CH_2(6,11)).

A second attempt to synthesize S-S bis-biguanide in *n*-butanol was carried out increasing the amount of HCl to 4 eq. The reaction was carried out as described above, but adding 330 µL of HCl 37% and heating for 24 h. The NMR spectra suggested the formation of the product in a mixture with other byproducts that were not further investigated.

Reduction of S-S bis-biguanide to biguanide-SH (2)

The first attempt in the reduction of the disulfide bond was carried out using dithiothreitol (DTT) as reductant. A stock of the crude product containing S-S bis-biguanide was prepared by dissolving 6.5 mg in 5 mL of D_2O and one of DTT 10 mM was prepared dissolving in the same volume of H_2O 7.5 mg of molecule. In an NMR tube, 75 µL of DTT 10 mM were added to 75 µL of the stock solution containing the biguanide mixture under N_2 inert atmosphere and 450 µL of D_2O were added to reach a total volume of 600 µL. The mixture was heated to 50 °C for 30 min. The NMR spectra recorded to monitor the reaction suggest a partial reduction of the disulfide bond.

A second attempt was carried out as described above, but adding 7 µL of HCl 37% after the 30 min of heating to tentatively stop the reaction. The ^{1}H NMR spectra suggested again the re-oxidation of the product.

The successful reduction of the disulfide bond was achieved employing an excess of $NaBH_4$. In an NMR tube under N_2 inert atmosphere, to 35 mg of the crude product dissolved in D_2O, 4.3 mg of $NaBH_4$ powder were added, followed by the formation of bubbles. After 1 h of stirring at RT, first additional 3.3 mg and another excess after 1 additional hour were added, leaving the mixture under stirring at RT for 3 days. The NMR experiments carried out at the end of the reaction confirmed the successful reduction of the disulfide bond without reducing the biguanide moiety. ^{1}H NMR of S-S bis-biguanide (9.4 T, 300 K, D_2O) δ 3.18 ppm (2H, t, CH(6,11), J= 6.9 Hz), 2.56 ppm (2H, t, CH(7,12), J= 7.1 Hz). ^{13}C NMR of S-S bis-biguanide

(9.4 T, 300 K, MeOD) δ 160.7 ppm (C=NH(2,15)), 158.9 ppm (C=NH(4,13)), 46.0 ppm (CH_2(6,11)), 23.6 ppm (CH_2(7,10)).

Preparation of the rhodamine-maleimide adduct (3a)

The reaction between N-(2-aminoethyl) maleimide and rhodamine isothiocyanate was carried out following a procedure previously used by our research group.[36] Before starting the reaction, N_2/vacuum cycles were carried out to remove the residual moisture from the NMR tube. In anhydrous MeOD 1.7 mg of N-(2-aminoethyl) maleimide ($6.68 \cdot 10^{-3}$ mmol) and 3.2 mg of rhodamine isothiocyanate ($5.96 \cdot 10^{-3}$ mmol, 0.89 eq) and the mixture basified with 850 µL of Et_3N. The mixture was left reacting for 28 h at RT in the dark and under N_2 atmosphere.

Preparation of the fluorescein-maleimide adduct (3b)

A sample of FITC (12.7 mg, 0.0326 mmol) was dissolved in 4 mL of anhydrous DMSO in a Schlenk tube under nitrogen atmosphere. Then, 8.3 mg of N-(2-aminoethyl) maleimide CF_3COOH salt (0.0326 mmol) were added. Subsequently, to deprotonate the N-(2-aminoethyl) maleimide salt (**2**), 0.9 equivalents of DIPEA (5.0 µL) were added, and an immediate colour change was observed, passing from yellow to orange. The occurring of the reaction of the isothiocyanate group with the amine of compound **2** with the formation of compound **3b** was followed by both FTIR and ^{1}H NMR spectroscopy.
^{1}H NMR (9.4 T, 300 K, DMSO-d_6) δ 3.66 (CH_2(3'), m), 3.75 (CH_2(2'), br m), 6.59 (CH(13), dd, ^{3}J=8.47 Hz, ^{4}J=2.24 Hz)), 6.60 (CH(12), d, ^{3}J=8.47 Hz)), 6.69 (CH(15), d, ^{4}J=2.24 Hz)), 7.01 (CH(6'), s), 7.19 (CH(8), d, ^{3}J=8.52 Hz)), 7.68 (CH(9), br dd, ^{3}J=8.52 Hz, ^{4}J=1.75 Hz)), 8.11 (CH(4), d, ^{4}J=1.75 Hz)), 8.12 (NH(1') br t), 9.98 (NH(2), br s), 10.1 (OH, br s). ^{13}C NMR (9.4 T, 300 K, DMSO-d_6) δ 37.1 (CH_2(3')), 42.5 (CH_2(2')), 113.1 (CH(13)), 129.5 (CH(12)), 102.7 (CH(15)), 135.1 (CH(6')), 124.5 (CH(8)), 130.6 (CH(9)), 117.7 (CH(4)), 171.8 (C=O (5')), 181.2 (S=C(1)), 147.9 (C_q(3)), 169.1 (C_q(5)), 83.1 (C_q(10)), 110.2 (C_q(11)), 159.9 (C_q(14)), 152.3 (C_q(16))

References

(1) Foretz, M.; Guigas, B.; Bertrand, L.; Pollak, M.; Viollet, B. Metformin: From Mechanisms of Action to Therapies. *Cell Metabolism*. Cell Press December 2, 2014, pp 953–966. https://doi.org/10.1016/j.cmet.2014.09.018.

(2) Bailey, C. J. Metformin: Historical Overview. *Diabetologia* **2017**, *60* (9), 1566–1576. https://doi.org/10.1007/s00125-017-4318-z.

(3) Wu, H.; Esteve, E.; Tremaroli, V.; Khan, M. T.; Caesar, R.; Mannerås-Holm, L.; Ståhlman, M.; Olsson, L. M.; Serino, M.; Planas-Fèlix, M.; Xifra, G.; Mercader, J. M.; Torrents, D.; Burcelin, R.; Ricart, W.; Perkins, R.; Fernàndez-Real, J. M.; Bäckhed, F. Metformin Alters the Gut Microbiome of Individuals with Treatment-Naive Type 2 Diabetes, Contributing to the Therapeutic Effects of the Drug. *Nat. Med.* **2017**, *23* (7), 850–858. https://doi.org/10.1038/nm.4345.

(4) Rena, G.; Hardie, D. G.; Pearson, E. R. The Mechanisms of Action of Metformin. *Diabetologia* **2017**, *60* (9), 1577–1585. https://doi.org/10.1007/s00125-017-4342-z.

(5) Lv, Z.; Guo, Y. Metformin and Its Benefits for Various Diseases. *Frontiers in Endocrinology*. Frontiers Media S.A. April 16, 2020. https://doi.org/10.3389/fendo.2020.00191.

(6) Caturano, A.; Nilo, D.; Nilo, R.; Sircana, M. C.; Erul, E.; Zielińska, K.; Russo, V.; Santonastaso, E.; Sasso, F. C. Old Drug, New Science: Metformin and the Future of Pharmaceutics. *Pharmaceutics* **2026**, *18* (1), 77. https://doi.org/10.3390/pharmaceutics18010077.

(7) DeCensi, A.; Puntoni, M.; Goodwin, P.; Cazzaniga, M.; Gennari, A.; Bonanni, B.; Gandini, S. Metformin and Cancer Risk in Diabetic Patients: A Systematic Review and Meta-Analysis. *Cancer Prevention Research* **2010**, *3* (11), 1451–1461. https://doi.org/10.1158/1940-6207.CAPR-10-0157.

(8) Heckman-Stoddard, B. M.; DeCensi, A.; Sahasrabuddhe, V. V.; Ford, L. G. Repurposing Metformin for the Prevention of Cancer and Cancer Recurrence. *Diabetologia* **2017**, *60* (9), 1639–1647. https://doi.org/10.1007/s00125-017-4372-6.

(9) Brown, J. R.; Chan, D. K.; Shank, J. J.; Griffith, K. A.; Fan, H.; Szulawski, R.; Yang, K.; Reynolds, R. K.; Johnston, C.; McLean, K.; Uppal, S.; Liu, J. R.; Cabrera, L.; Taylor, S. E.; Orr, B. C.; Modugno, F.; Mehta, P.; Bregenzer, M.; Mehta, G.; Shen, H.; Coffman, L.; Buckanovich, R. J. Phase II Clinical Trial of Metformin as a Cancer Stem Cell-Targeting Agent in Ovarian Cancer. *JCI Insight* **2020**. https://doi.org/10.1172/jci.insight.133247.

(10) Rothermundt, C.; Hayoz, S.; Templeton, A. J.; Winterhalder, R.; Strebel, R. T.; Bärtschi, D.; Pollak, M.; Lui, L.; Endt, K.; Schiess, R.; Rüschoff, J. H.; Cathomas, R.; Gillessen, S. Metformin in Chemotherapy-Naive Castration-Resistant Prostate Cancer: A Multicenter Phase 2 Trial (SAKK 08/09). *Eur. Urol.* **2014**, *66* (3), 468–474. https://doi.org/10.1016/j.eururo.2013.12.057.

(11) Podhorecka, M.; Ibanez, B.; Dmoszyńska, A. Metformin – Its Potential Anti-Cancer and Anti-Aging Effects. *Postepy Hig. Med. Dosw.* **2017**, *71* (1), 0–0. https://doi.org/10.5604/01.3001.0010.3801.

(12) Hua, Y.; Zheng, Y.; Yao, Y.; Jia, R.; Ge, S.; Zhuang, A. Metformin and Cancer Hallmarks: Shedding New Lights on Therapeutic Repurposing. *J. Transl. Med.* **2023**, *21* (1). https://doi.org/10.1186/s12967-023-04263-8.

(13) Grytsai, O.; Ronco, C.; Benhida, R. Synthetic Accesses to Biguanide Compounds. *Beilstein Journal of Organic Chemistry* **2021**, *17*, 1001–1040. https://doi.org/10.3762/bjoc.17.82.

(14) Guo, L.-P.; Du, X.-D.; Lei, J.-H. Kinetics and Mechanism of the Additive Reaction of Aniline with Dicyandiamide. *Kinetics and Catalysis* **2009**, *50* (3), 359–366. https://doi.org/10.1134/S0023158409030045.

(15) Fortun, S.; Schmitzer, A. R. The Chemistry of Biguanides: From Synthetic Routes to Applications in Organic Chemistry. *Can. J. Chem.* **2020**, *98* (6), 251–260. https://doi.org/10.1139/cjc-2019-0371.

(16) Suyama, T.; Soga, T.; Miyauchi, K. A Method for the Preparation of Substituted Biguanides. *NIPPON KAGAKU KAISHI* **1989**, No. 5, 884–887. https://doi.org/10.1246/nikkashi.1989.884.

(17) Obianom, O. N.; Coutinho, A. L.; Yang, W.; Yang, H.; Xue, F.; Shu, Y. Incorporation of a Biguanide Scaffold Enhances Drug Uptake by Organic Cation Transporters 1 and 2. *Mol. Pharm.* **2017**, *14* (8), 2726–2739. https://doi.org/10.1021/acs.molpharmaceut.7b00285.

(18) Chen, H.; Dao, P.; Laporte, A.; Garbay, C. High Yielding Microwave-Assisted Synthesis of 2-(Arylmethyl)Amino-4-Arylamino-6-Alkyl-1,3,5-Triazines. *Tetrahedron Lett.* **2010**, *51* (24), 3174–3176. https://doi.org/10.1016/j.tetlet.2010.04.042.

(19) Mayer, S.; Daigle, D. M.; Brown, E. D.; Khatri, J.; Organ, M. G. An Expedient and Facile One-Step Synthesis of a Biguanide Library by Microwave Irradiation Coupled with Simple Product Filtration. Inhibitors of Dihydrofolate Reductase. **2004**. https://doi.org/10.1021/cc049953.

(20) Singh, S.; Wanjari, P. J.; Bhatia, S.; Sonwane, V. C.; Chakraborti, A. K.; Bharatam, P. V. Design, Synthesis, Biological Evaluation and Toxicity Studies of N,N-Disubstituted Biguanides as Quorum Sensing Inhibitors. *Medicinal Chemistry Research* **2015**, *24* (5), 1974–1987. https://doi.org/10.1007/s00044-014-1255-y.

(21) Bardovskyi, R.; Fabre, M.; Ronco, C.; Benhida, R. Mild Biamidine-Transfer Conditions for the Synthesis of Aliphatic Biguanides. *SynOpen* **2021**, *5* (4), 314–320. https://doi.org/10.1055/a-1681-4544.

(22) Martin, G. J. .; Martin, M. L. .; Gouesnard, J. Paul. *^{15}N-NMR Spectroscopy*; Springer-Verlag, 1981.

(23) Prati, F.; De Simone, A.; Armirotti, A.; Summa, M.; Pizzirani, D.; Scarpelli, R.; Bertozzi, S. M.; Perez, D. I.; Andrisano, V.; Perez-Castillo, A.; Monti, B.; Massenzio, F.; Polito, L.; Racchi, M.; Sabatino, P.; Bottegoni, G.; Martinez, A.; Cavalli, A.; Bolognesi, M. L. 3,4-Dihydro-1,3,5-Triazin-2(1H)-Ones as the First Dual BACE-1/GSK-3β Fragment Hits against Alzheimer's Disease. *ACS Chem. Neurosci.* **2015**, *6* (10), 1665–1682. https://doi.org/10.1021/acschemneuro.5b00121.

(24) Gräber, M.; Hell, M.; Gröst, C.; Friberg, A.; Sperl, B.; Sattler, M.; Berg, T. Oral Disinfectants Inhibit Protein-Protein Interactions Mediated by the Anti-Apoptotic Protein Bcl-XL and Induce Apoptosis in Human Oral Tumor Cells. *Angewandte Chemie - International Edition* **2013**, *52* (16), 4487–4491. https://doi.org/10.1002/anie.201208889.

(25) Fu, J.; Liu, S.; Hu, M.; Liao, X.; Wang, X.; Xu, Z.; Li, Q.; Quan, J. Biguanide MC001, a Dual Inhibitor of OXPHOS and Glycolysis, Shows Enhanced Antitumor Activity Without Increasing Lactate Production. *ChemMedChem* **2022**, *17* (6). https://doi.org/10.1002/cmdc.202100674.

(26) Silverstein, R. M.; Webster, F. X.; Kiemle David J. *Spectrometric Identification of Organic Compounds*, Seventh Edition.; Wiley, 2005.

(27) Sørensen, L. K. Determination of Metformin and Other Biguanides in Forensic Whole Blood Samples by Hydrophilic Interaction Liquid Chromatography–Electrospray Tandem Mass Spectrometry. *Biomedical Chromatography* **2012**, *26* (1), 1–5. https://doi.org/10.1002/bmc.1615.

(28) Lewis, I. R.; Edwards, H. *Handbook of Raman Spectroscopy*; CRC Press, 2001. https://doi.org/10.1201/9781420029253.

(29) *Oral Antidiabetics*; Kuhlmann, J., Puls, W., Eds.; Handbook of Experimental Pharmacology; Springer Berlin Heidelberg: Berlin, Heidelberg, 1996; Vol. 119. https://doi.org/10.1007/978-3-662-09127-2.

(30) Butler, J.; Spielberg, S. P.; Schulman, J. D. Reduction of Disulfide-Containing Amines, Amino Acids, and Small Peptides. *Anal. Biochem.* **1976**, *75* (2), 674–675. https://doi.org/10.1016/0003-2697(76)90129-9.

(31) Crawhall, J. C.; Segal, S. The Intracellular Ratio of Cysteine and Cystine in Various Tissues. *Biochemical Journal* **1967**, *105* (2), 891–896. https://doi.org/10.1042/bj1050891.

(32) Jocelyn, P. C. Chemical Reduction of Disulfides. In *Biochern. Biophys. Res. Commun*; 1987; Vol. 3, pp 246–256. https://doi.org/10.1016/0076-6879(87)43048-6.

(33) Clement, B.; Girreser, U. Characterization of Biguanides By15N NMR Spectroscopy. *Magnetic Resonance in Chemistry* **1999**, *37* (9), 662–666. https://doi.org/10.1002/(SICI)1097-458X(199909)37:9<662::AID-MRC518>3.0.CO;2-D.

(34) Renault, K.; Fredy, J. W.; Renard, P. Y.; Sabot, C. Covalent Modification of Biomolecules through Maleimide-Based Labeling Strategies. *Bioconjug. Chem.* **2018**, *29* (8), 2497–2513. https://doi.org/10.1021/acs.bioconjchem.8b00252.

(35) Potter, M. N.; Green, J. R.; Mutus, B. Fluorescein Isothiocyanate, a Platform for the Selective and Sensitive Detection of S-Nitrosothiols and Hydrogen Sulfide. *Talanta* **2022**, *237*, 122981. https://doi.org/10.1016/j.talanta.2021.122981.

(36) Galli, M.; Guerrini, A.; Cauteruccio, S.; Thakare, P.; Dova, D.; Orsini, F.; Arosio, P.; Carrara, C.; Sangregorio, C.; Lascialfari, A.; Maggioni, D.; Licandro, E. Superparamagnetic Iron Oxide Nanoparticles Functionalized by Peptide Nucleic Acids. *RSC Adv.* **2017**, *7* (25), 15500–15512. https://doi.org/10.1039/C7RA00519A.

(37) Pittelkow, M.; Lewinsky, R.; Christensen, J. B. Mono Carbamate Protection of Aliphatic Diamines Using Alkyl Phenyl Carbonates. In *Organic Syntheses*; Wiley, 2007; pp 209–214. https://doi.org/10.1002/0471264229.os084.21.

(38) Richter, M.; Chakrabarti, A.; Ruttekolk, I. R.; Wiesner, B.; Beyermann, M.; Brock, R.; Rademann, J. Multivalent Design of Apoptosis-Inducing Bid-BH3 Peptide–Oligosaccharides Boosts the Intracellular

Activity at Identical Overall Peptide Concentrations. *Chemistry – A European Journal* **2012**, *18* (52), 16708–16715. https://doi.org/10.1002/chem.201202276.

(39) Hermanson, G. T. The Reactions of Bioconjugation. In *Bioconjugate Techniques*; Elsevier, 2013; pp 229–258. https://doi.org/10.1016/b978-0-12-382239-0.00003-0.

(40) Stevens, R. J.; Ali, R.; Bankhead, C. R.; Bethel, M. A.; Cairns, B. J.; Camisasca, R. P.; Crowe, F. L.; Farmer, A. J.; Harrison, S.; Hirst, J. A.; Home, P.; Kahn, S. E.; McLellan, J. H.; Perera, R.; Plüddemann, A.; Ramachandran, A.; Roberts, N. W.; Rose, P. W.; Schweizer, A.; Viberti, G.; Holman, R. R. Cancer Outcomes and All-Cause Mortality in Adults Allocated to Metformin: Systematic Review and Collaborative Meta-Analysis of Randomised Clinical Trials. *Diabetologia* **2012**, *55* (10), 2593–2603. https://doi.org/10.1007/s00125-012-2653-7.

Acknowledgements

I'd like to express my great gratitude to my supervisor, Prof. Daniela Maggioni, for giving me the opportunity to undertake this PhD and the projects involved in it, for all the things she taught me, the great patience and availability and the good relationship we developed during these three years. Thank you also to Prof. Monica Panigati and Prof. Lucia Carlucci, for their important presence in the corridor and to Pasquale and Luca for all the NMR spectra recorded with the maximum priority.

Thank you also to Delia, who was my colleague in the first half of my PhD and fundamental for my initial survivance. Thanks to Veronica, who unfortunately worked with me only for the last two months, with whom I shared multiple debatable movies and conversations in the empty corridor.

A huge thank you also to all my Bachelor's and Master's students and all the people who were part of the laboratory for a while: Marianna, Mauro, Giulia, Sara, Natalie, and Giordano. Special thanks to Mauro, with whom I worked for a long time, sharing a beautiful collaboration, and to Ludovica and Daniela, whom I met in the lab and then developed a great friendship that I hope will last our entire lives. Thank you also to all the people who have taken part in the Maggiucci and Tendescion Ailand groups during the years and to the birrificio group for being my weekly Friday fixture for two years.

I'd also like to thank all the people that I met in Groningen who helped me feel at home. To Prof. Anna Salvati, for being a great teacher in a field that I knew so little about and for always making sure I was doing good and I was settling in. Thank you for giving me the opportunity to work in her laboratory with a fantastic group in a city I'll cherish forever. Thank you to all the Nano & Drug Targeting group for their warm welcome and for all their help. Special thanks to my office colleagues: Adam, Xinyu and Mia.

Thank you also to all my friends: both those I met in Groningen - Paolo, Sara, Mariangela and Lorenza - and those in Milan - Digio, Davide, Chiara, Marco, Benna, Martina and Mary.

Lastly, I'd like to thank my parents and my sister Francesca for their unconditional love and for encouraging me in everything I do.

Annex A: Abbreviations

Abbreviation	Definition
ACN	Acetonitrile
APTES	3-aminopropylethoxysilane
ATR-FTIR	Attenuated Total Reflectance - Fourier Transform Infrared
AuNP	Gold spherical nanoparticles
C	Thermal capacity
C_s	Specific heat capacity
cMEM	MEM + 10% FBS
DIPEA	N-ethyldiisopropylamine
DLS	Dynamic Light Scattering
DMF	Dimethylformamide
DMSO	Dimethylsulfoxide
DPBS	Dubecco's Phosphate Buffer Solution
DRS	Diffuse Reflectance Spectroscopy
DTG	Derivative Thermogravimetry
DTT	Dithiothreitol
EPR	Enhanced Permeability Retention
FBS	Fetal Bovine Serum
FITC	Fluorescein Isothiocyanate
FTIR	Fourier Transform Infrared
f-GNS	Surfactant-free gold nanostars
GNS	Gold nanostars
GNS@TX-100	GNS stabilized by the Triton X-100 surfactant
HATU	O-(7-aza-1H-benzotriazole-1-yl)-N,N,N,N-tetramethyluronium hexafluorophosphate
HPLC	High Performance Liquid Chromatography
HNT	Halloysite Nanotubes
HNT ALD	HNT purchased from Sigma-Aldrich
HNT USA	Non-commercial HNT extracted from Silver City, Utah, USA
HNT AUS	Non-commericial HNT extracted from Camel Lake, Australia
ICP	Inductively Coupled Plasma
ICP-MS	Inductively Coupled Plasma Mass Spectrometry
ICP-OES	Inductively Coupled Plasma Optical Emission Spectrometry
ISC	Intersystem Crossing
LC(CT)	Ligand Centered (Charge Transfer)
LSPR	Localized Surface Plasmon Resonance
MADLS	Multi-angle Dynamic Light Scattering
MB	Methylene blue

MEM	Minimum Essential Medium
MEF	Metal Enhanced Fluorescence
MEP	Metal Enhanced Phosphorescence
ME^1O_2	Metal Enhanced Single Oxygen Generation
MLCT	Metal-to-Ligand Charge Transfer
MS-ESI	Electrospray Ionization Mass Spectrometry
MTT	3-(4,5-dimethylthiazol-2-yl)-2,5-diphenyltetrazolium bromide
MTX	Mitoxantrone
MW	Microwaves
NIR	Near Infrared
NP	Nanoparticle
PAA	Polyamidoamine
PDA	Photodiode Array
PDT	Photodynamic Therapy
PL	Photoluminescence
PLQY	Photoluminescence Quantum Yield
PNA	Peptide Nucleic Acid
PS	Photosensitizer
PTT	Photothermal Therapy
PVP	Poly (vinylpyrrolidone)
RC	Regenerated Cellulose
RITC	Rhodamine Isothiocyanate
ROS	Reactive Oxygen Species
SERS	Surface Enhanced Raman Spectroscopy
UPLC	Ultra Performance Liquid Chromatography
TDP	Tetradecylphosphonic Acid
TEA	Triethylamine
TGA	Thermogravimetric Analyses
THF	Tetrahydrofuran
TLC	Thin Layer Chromatography
TPE	Two-photon excitation
TX-100	Triton X-100

Annex B: Publications and Communications

Pubblications

- Hady Hamza, Veronica Schifano, Giorgia Colciago, Marco Aldo Ortenzi, Anna Maria Ferretti, Gabriele Di Carlo, Maria Vittoria Dozzi, Riccardo Vago, Francesca Tessore, Daniela Maggioni. Halloysite nanotubes as a vector for hydrophobic perfluorinated porphyrin-based photosensitizers for singlet oxygen generation. Nanoscale, 2025, 17, 18935-18947

- Rosa Maria Dell'Acqua, Veronica Schifano, Maria Vittoria Dozzi, Laura D'Alfonso, Monica Panigati, Paola Rusmini, Margerita Piccolella, Angelo Poletti, Silvia Cauteruccio, Daniela Maggioni. Luminescent Iridium-Peptide Nucleic Acid Bioconjugate as Photosensitizer for Singlet Oxygen Production toward a Potential Dual Therapeutic Agent. Inorganic Chemistry, 2025, 64, 6898-6911

- Veronica Schifano, Elisabetta Ranucci, Anna Salvati, Daniela Maggioni. Decoration of Gold Nanostars with a Polyamidoamine-Ru(II) Complex to Increase $^1O_2$ Generation Efficiency in Photodynamic Therapy (*draft in preparation*)

Communications

- "An Ir(III)-Peptide Nucleic Acid (PNA) conjugate as a Singlet Oxygen Photosensitizer for Photodynamic Therapy'', XIV International School of Organometallic Chemistry (ISOC 2023), Camerino, 7-11 September 2023 *(poster and oral communication)*

- "Preparation and characterization of a PNA-Ir(III) conjugate for 1O2 production in PDT'', 17th European Biological Inorganic Chemistry Conference (EuroBIC-17), Munster, 25-29 August 2024 *(poster)*

- "An Ir-PNA Bioconjugate for 1O2 Production In PDT: Toward a Potential Dual Therapeutic Agent", 50th Congress of the Divisione di Chimica Inorganica of Società Chimica Italiana (INORG25), Naples, 9-12 September 2025 *(oral communication)*

- "Decoration of Gold Nanostars with a Polyamidoamine-Ru(II) Complex to Increase 1O2 Generation Efficiency in Photodynamic Therapy", 17th International Conference on Nanomaterials – Reasearch & Application (NANOCON2025), Brno, 15-17 October 2025 *(poster)*

Schools and conferences attended

- XIV International School of Organometallic Chemistry (ISOC 2023), Camerino, 7-11 September 2023
- 17th European Biological Inorganic Chemistry Conference (EuroBIC-17), Munster, 25-29 August 2024
- 50th Congress of the Divisione di Chimica Inorganica of Società Chimica Italiana (INORG25), Naples, 9-12 September 2025
- 17th International Conference on Nanomaterials – Research & Application (NANOCON2025), Brno, 15-17 October 2025